ORNL/TM-10469

ornl

OAK RIDGE
NATIONAL
LABORATORY

MARTIN MARIETTA

Ceramic Technology for Advanced Heat Engines Project Semiannual Progress Report for October 1986 Through March 1987

Prepared for
U.S. Department of Energy
Assistant Secretary for Conservation and Renewable Energy
Office of Transportation Systems
Advanced Materials Development Program

OPERATED BY
MARTIN MARIETTA ENERGY SYSTEMS, INC.
FOR THE UNITED STATES
DEPARTMENT OF ENERGY

Printed in the United States of America. Available from
National Technical Information Service
U.S. Department of Commerce
5285 Port Royal Road, Springfield, Virginia 22161
NTIS price codes—Printed Copy: A09 Microfiche A01

ORNL/TM-10469

METALS AND CERAMICS DIVISION

CERAMIC TECHNOLOGY FOR ADVANCED HEAT ENGINES PROJECT
SEMIANNUAL PROGRESS REPORT FOR
OCTOBER 1986 THROUGH MARCH 1987

D. R. Johnson
Project Manager

Date Published: August 1987

NOTICE: This document contains information of a preliminary nature. It is subject to revision or correction and therefore does not represent a final report.

Prepared for
U.S. Department of Energy
Assistant Secretary for Conservation and Renewable Energy
Office of Transportation Systems
Advanced Materials Development Program

Prepared by the
OAK RIDGE NATIONAL LABORATORY
Oak Ridge, Tennessee 37831
operated by
MARTIN MARIETTA ENERGY SYSTEMS, INC.
for the
U.S. DEPARTMENT OF ENERGY
under Contract DE-AC05-84OR21400

REPORTS PREVIOUSLY ISSUED

ORNL/TM-9325	Period March 1983-September 1983
ORNL/TM-9466	Period October 1983-March 1984
ORNL/TM-9497	Period April 1984-September 1984
ORNL/TM-9673	Period October 1984-March 1985
ORNL/TM-9947	Period April 1985-September 1985
ORNL/TM-10079	Period October 1985-March 1986
ORNL/TM-10308	Period April 1986-September 1986

CONTENTS

CERAMIC TECHNOLOGY FOR ADVANCED HEAT ENGINES PROJECT SEMIANNUAL PROGRESS REPORT FOR OCTOBER 1986 THROUGH MARCH 1987

SUMMARY

The Ceramic Technology For Advanced Heat Engines Project was developed by the Department of Energy's Office of Transportation Systems (OTS) in Conservation and Renewable Energy. This project, part of the OTS's Advanced Materials Development Program, was developed to meet the ceramic technology requirements of the OTS's automotive technology programs.

Significant accomplishments in fabricating ceramic components for the Department of Energy (DOE), National Aeronautics and Space Administration (NASA), and Department of Defense (DOD) advanced heat engine programs have provided evidence that the operation of ceramic parts in high-temperature engine environments is feasible. However, these programs have also demonstrated that additional research is needed in materials and processing development, design methodology, and data base and life prediction before industry will have a sufficient technology base from which to produce reliable cost-effective ceramic engine components commercially.

An assessment of needs was completed, and a five-year project plan was developed with extensive input from private industry. The objective of the project is to develop the industrial technology base required for reliable ceramics for application in advanced automotive heat engines. The project approach includes determining the mechanisms controlling reliability, improving processes for fabricating existing ceramics, developing new materials with increased reliability, and testing these materials in simulated engine environments to confirm reliability. Although this is a generic materials project, the focus is on structural ceramics for advanced gas turbine and diesel engines, ceramic bearings and attachments, and ceramic coatings for thermal barrier and wear applications in these engines. This advanced materials technology is being developed in parallel and close coordination with the ongoing DOE and industry proof-of-concept engine development programs. To facilitate the rapid transfer of this technology to U.S. industry, the major portion of the work is being done in the ceramic industry, with technological support from government laboratories, other industrial laboratories, and universities.

This project is managed by ORNL for the Office of Transportation Systems, Heat Engine Propulsion Division, and is closely coordinated with complementary ceramics tasks funded by other DOE offices, NASA, DOD, and industry. A joint DOE and NASA technical plan has been established, with DOE focus on automotive applications and NASA focus on aerospace applications. A common work breakdown structure (WBS) was developed to facilitate coordination. The work described in this report is organized according to the following WBS project elements:

0.0 Management and Coordination

1.0 Materials and Processing

  1.1 Monolithics
  1.2 Ceramic Composites
  1.3 Thermal and Wear Coatings
  1.4 Joining

2.0 Materials Design Methodology

  2.1 Modeling
  2.2 Contact Interfaces
  2.3 New Concepts

3.0 Data Base and Life Prediction

  3.1 Structural Qualification
  3.2 Time-Dependent Behavior
  3.3 Environmental Effects
  3.4 Fracture Mechanics
  3.5 NDE Development

4.0 Technology Transfer

This report includes contributions from all currently active project participants. The contributions are arranged according to the work breakdown structure outline.

0.0 PROJECT MANAGEMENT AND COORDINATION

D. R. Johnson
Oak Ridge National Laboratory

This task includes the technical management of the project in accordance with the project plans and management plan approved by the Department of Energy (DOE) Oak Ridge Operations Office (ORO) and the Office of Transportation Systems. This task includes preparation of annual field task proposals, initiation and management of subcontracts and interagency agreements, and management of ORNL technical tasks. Monthly management reports and bimonthly reports are provided to DOE; highlights and semiannual technical reports are provided to DOE and program participants. In addition, the program is coordinated with interfacing programs sponsored by other DOE offices and federal agencies, including the National Aeronautics and Space Administration (NASA) and the Department of Defense (DOD). This coordination is accomplished by participation in bimonthly DOE and NASA joint management meetings, annual interagency heat engine ceramics coordination meetings, DOE contractor coordination meetings, and DOE Energy Materials Coordinating Committee (EMaCC) meetings, as well as special coordination meetings.

1.0 MATERIALS AND PROCESSING

INTRODUCTION

This portion of the project is identified as project element 1.0 within the work breakdown structure (WBS). It contains four subelements: (1) Monolithics, (2) Ceramic Composites, (3) Thermal and Wear Coatings, and (4) Joining. Ceramic research conducted within the Monolithics subelement currently includes work activities on green state ceramic fabrication, characterization, and densification and on structural, mechanical, and physical properties of these ceramics. Research conducted within the Ceramic Composites subelement currently includes silicon carbide and oxide-based composites, which, in addition to the work activities cited for Monolithics, include fiber synthesis and characterization. Research conducted in the Thermal and Wear Coatings subelement is currently limited to oxide-base coatings and involves coating synthesis, characterization, and determination of the mechanical and physical properties of the coatings. Research conducted in the Joining subelement currently includes studies of processes to produce strong stable joints between zirconia ceramics and iron-base alloys.

A major objective of the research in the Materials and Processing project element is to systematically advance the understanding of the relationships between ceramic raw materials such as powders and reactant gases, the processing variables involved in producing the ceramic materials, and the resultant microstructures and physical and mechanical properties of the ceramic materials. Success in meeting this objective will provide U.S. companies with new or improved ways for producing economical highly reliable ceramic components for advanced heat engines.

1.1 MONOLITHICS

1.1.1 Silicon Carbide

Sythesis of High-Purity Sinterable Silicon Carbide Powders

H. A. Lawler and B. L. Mehosky [Standard Oil Engineered Materials Company (Carborundum)]

Objective/Scope

The objective of this program is to develop a volume scaleable process to produce high purity, high surface area sinterable silicon carbide powder.

The program is organized in two phases. Phase I, completed in July, 1986, included the following elements.

- Verify the technical feasibility of the gas phase synthesis route.
- Identify the best silicon feedstock on the basis of performance and cost.
- Optimize the production process at the bench scale.
- Fully characterize the powders produced and compare with commercially available alternatives.
- Develop a theoretical model to assist in understanding the synthesis process, optimization of operating conditions and scale-up.

Phase II, authorized in August, 1987, will scale the process to five to ten times the bench scale quantities in order to perform confirmatory experiments, produce process flowsheets and to perform economic analysis.

Technical Highlights

Background - The Gas Phase Route

Given the objective to produce a submicron silicon carbide powder of high purity and with more controllable prcperties than could be produced via the Acheson process, Standard Oil-Carborundum evaluated three candidate process routes:

1) Sol-Gel
2) Polymer Pyrolysis
3) Gas Phase Reaction

A gas phase route utilizing plasma heating was chosen as having the most proven technology, the highest product yield and good scaleability potential.

Further, Carborundum had previously sponsored proprietary research in gas phase synthesis and had demonstrated the feasibility of the approach.

Results of Phase I Activities

Phase I was concluded successfully with proof of sinterability and a small sample was submitted to Oak Ridge for their analysis. Specifics regarding the conduct of the Phase I workscope follow.

Design, Construct and Test Laboratory Scale Equipment

The Standard Oil Research and Development Laboratory in Warrensville, Ohio was chosen as the site of the laboratory scale gas phase synthesis system due to the ready availability of applicable engineering and technical resources. The design phase involved a complete review of the preliminary conceptual design and specifying appropriate subsystems in order to evaluate and control critical process parameters. A schematic of the conceptual design is shown in Figure 1.

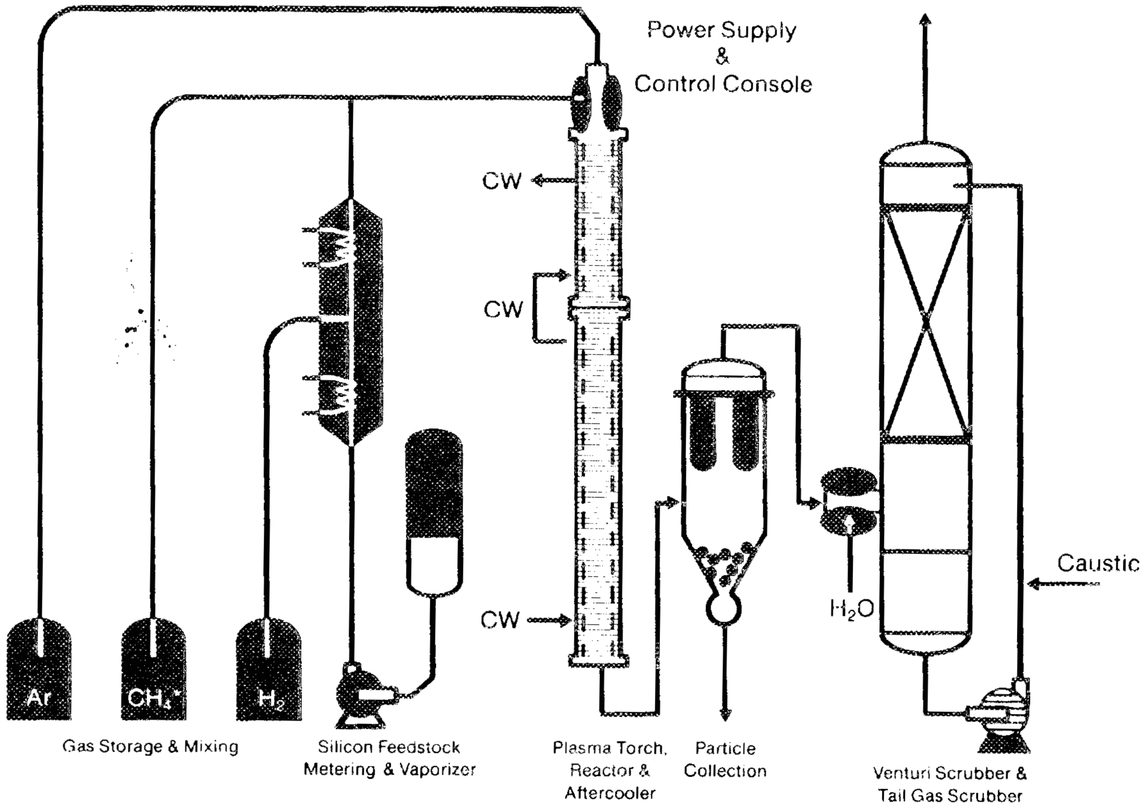

*Optional depending
on Silicon Feedstock

Figure 1. Conceptual Design and Simplified Process Flow Chart

Screening Experiments

After the plasma system was completed and debugged, a series of twenty-three experiments were run to evaluate the three candidate feedstocks (silicon tetrachloride, dimethyl dichlorosilane, and methyl trichlorosilane). When required, methane was used as a carbon source.

Temperature, carbon/silicon ratio, and reactant concentration were selected as variables for the screening experiments.

Though some plugging of the system due to the growth of a stalactite from the torch anode occurred, run times of about an hour were achieved with consistent results.

Based on analytical results (focussing on percent SiC, percent free carbon and percent free silicon (methyl trichlorosilane was selected as the preferred feedstock.

To assure that the powder produced was sinterable, a run under the best known conditions was conducted and a test of sinterability was made. Densities of sintered specimens of 89% and 92% of theoretical density were achieved.

Extended Parametric Studies

In order to further evaluate the process parameters of the chosen feedstock, fifteen further experiments were run in order to identify the best conditions for scaling up the process. In addition, one run with the addition of a boron dopant was made.

Theoretical Model

Concurrent with the above tasks, a subcontract was let with International Plasma Engineering, Inc. (Professor Boulous, et al). A theoretical model was developed to describe the flow and temperature field in the reactor, calculate the thermodynamic equilibrium for the H_2-Ar-CH_4-$SiCl_4$ system and study the chemical kinetics of possible homogenous reactions occurring in the plasma process. A literature review of nucleation and growth in an aerosol system was also conducted.

Results and Conclusions

A small sample of powder and a sintered specimen were submitted to the ORNL technical monitor as proof of sinterability. Powder chemistry and powder size characteristics are shown in Table 1 and are compared to other SiC powders. For this particular sample, 86% of theoretical density was achieved.

TABLE 1
SUMMARY OF THE CHARACTERISTICS OF THE POWDER PRODUCED UNDER THIS SUBCONTRACT COMPARED TO THE BASELINE POWDERS

	Phase I Gas Phase	Starck B-10	Starck A-10	Standard Oil
Chemistry (wt. %)				
Total Carbon	29.55	30.49	30.30	29.95
Free Carbon	0.35	1.83	1.54	0.36
Free Silicon	0.09	0.40	0.29	0.09
Oxygen	0.58	0.90	0.76	0.27
Iron	< 0.01	0.04	0.03	< 0.01
Silicon Carbide[1]	97.33	95.50	96.60	98.80
Physical Properties				
Major Phase	Beta	Beta	Alpha	Alpha
Median Particle Size (μm)	0.75	1.0	1.4	1.2
Surface Area (m^2/g)	10.0	15.3	14.3	9.4
Sinterability[2]				
Green Density (g/cm^3)	1.89	2.01	2.09	1.67
Fired Density (g/cm^3)	2.76	3.03	3.09	3.20

[1] Obtained from Carbon Balance
[2] With Typical Sintering Aids

Although sintering of this powder has not been optimized, the powder compares favorably to other commercially available powders such as the Starck A10 and B10 and is close to Standard Oil's α powders in terms of purity. Median particle size is smaller than any of the other comparable powders, but not so fine as to prevent adequate compaction. Principle impurities are copper (pick-up from the reactor) and chlorine (from the offgassing of HCI). Both of these can be easiliy removed but will also be reduced or eliminated with further development during Phase II.

Phase II Activities

Workplan

A breakdown of major tasks and milestones is shown in Figure 2.

ORNL granted a no-cost extension of Phase II thru December 31, 1987.

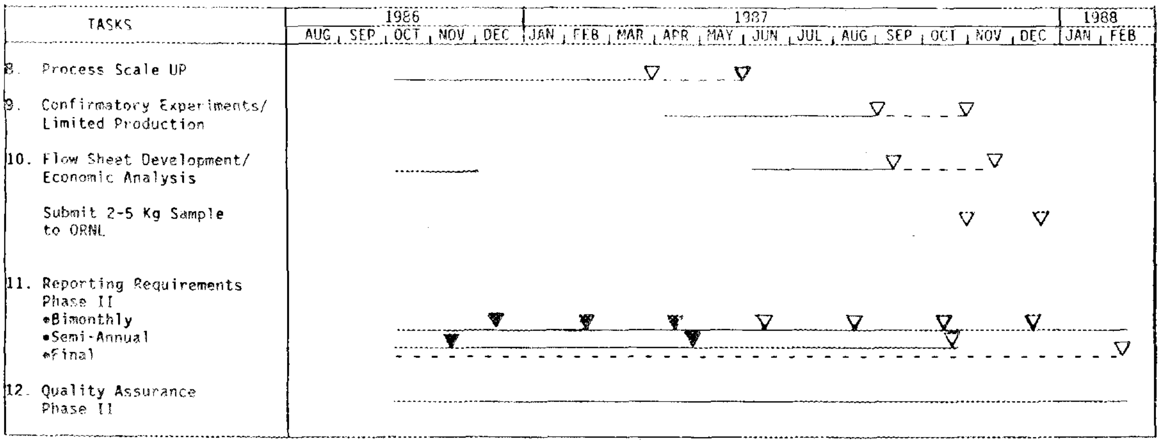

Figure 2 Milestone Chart

Task 8. Process Scale-up

Specification and purchase of all major components for the Phase II reactor system have been completed. The power supply has been tested at the vendor's shop and is in transit to Warrensville Laboratory. Final machining of the torch is underway, as is the fabrication of the high-frequency starting unit. The reactor has been completely fabricated, and the initial welding of the tail gas scrubber is in progress. Structural steel to support the larger pieces of equipment have been specified and ordered. The support racks for instrumentation mounting have been partially fabricated, and will be finished after the structural steel is completely in place.

The only significant item not on hand is the particulate collection unit. The unit is a stainless steel baghouse which must be custom fabricated. Shipment is scheduled for May 22, 1987. Initial commissioning activities will proceed without the unit, which will be installed as soon as it arrives.

Task 9. Confirmatory Experiments and Limited Production

The activities of Task 9, Confirmatory Experiments and Limited Production, will commence upon the completion of Task 8, Process Scale-Up.

Task 10. Flowsheet Development and Economic Analysis

The activities of Task 10, Flowsheet Development and Economic Analysis, are not scheduled until Task 9, Confirmatory Experiments and Limited Production, is well underway. However, Process Flow drawings (PFDs), detailed Piping and Instrumentation drawings (P&IDs) and piping specification drawings exist for the bench and pilot scale facilities. An effort is currently underway to transfer these drawings to a computer-aided drawings (CAD) system. The process flowsheets could then be easily edited and revised as warranted by later investigations. No rigorous detailed economic analysis has been performed to date on a commercial sized facility.

Status of Milestones

Phase I Activities

Task 1.	Design, Construct and Test Laboratory Scale Equipment	- Completed
Task 2.	Develop Theoretical Model	- Completed
Task 3.	Baseline Characterizations and Analytical Model Development	- Completed
Task 4.	Screening Experiments	- Completed
	.. Selection of Feedstock	- Completed
Task 5.	Extended Parametric Studies	- Completed
	.. Delivery of Sample to ORNL	- Completed
Task 6.	Reporting Requirements	- Ongoing

Phase II Activities

Task 7.	Quality Assurance	- Ongoing
Task 8.	Process Scale-Up	- Ongoing
Task 9.	Confirmatory Experiments and Limited Production	- Pending
Task 10.	Flowsheet Development and Economic Analysis	- Pending

Publications

None during the reporting period.

1.1.2 Silicon Nitride

Sintering of Silicon Nitride

G. E. Gazza (Army Materials Technology Laboratory)

Objective/Scope

The program is concentrating on sintering compositions in the Si_3N_4- Y_2O_3-SiO_2 system using a two-step sintering method where the N_2 gas pressure is raised to 7-8 MPa during the second step of the process. During the sintering, dissociation reactions are suppressed by the use of high N_2 pressure and cover powder of suitable composition over the specimens. Variables in the program include the sintering process parameters, source of starting powders, milling media and time, and specimen composition. Resultant properties determined are room temperature modulus of rupture, high temperature stress-rupture, oxidation resistance, and fracture toughness. Successful densification of selected compositions with suitable properties will lead to densification of injection molded or slip cast components for engine testing.

Technical Progress

Compositions of interest in this program lie generally in the Si_3N_4-$Y_2Si_2O_7$-Si_2N_2O triangle (subsequently refered to as triangle 1) and the Si_3N_4-$Y_2Si_2O_7$- $Y_5(SiO_4)_3N$ triangle (subsequently referred to as triangle 2). Total volume percent of Y_2O_3 and SiO_2 additives used in specimen compositions range from 8 to 14v/o and Y_2O_3/SiO_2 ratios range from 0.28 to 1.11. It has been previously shown in hot pressing and sintering studies that compositions located in triangle 1 possess excellent oxidation resistance and are not susceptible to thermal instability at intermediate temperatures, i.e., 700-1000C. However, little information is available on the creep resistance or static fatigue properties of these compositions which is of concern due to the high silica content in the composition and the potential for producing low viscosity or low melting phases. Processing problems can also be encountered working in this compositional range due to dissociation reactions involving Si_3N_4 and Si_{O2} producing SiO and N_2. The evolution of these gas species drives the composition toward the Y_2O_3-rich end of the phase diagram and may cross into a different phase field, particularly if weight losses are high during sintering. Compositional gradients (particularly with respect to oxygen) may occur in specimens causing different phases to develop near the specimen surface than in the interior. Therefore, control of such reactions is necessary for successful densification of silicon nitride where strict compositional and phase control are required. Although a broad range of compositions may be evaluated in the overall program, this report will focus on selected compositions located in Triangle 1 where the total volume percent of combined additive, i.e., Y_2O_3+SiO_2, for each composition varies from 8.5-10.5% and the Y_2O_3/SiO_2 ratio ranges from 0.42 to 0.50.

Experimental

Preparation of Starting Composition

In formulating the compositions to be studied and evaluated, the source of the starting powders and their characteristics are known to influence the process parameters required for sintering and the resultant microstructure and properties. Sources of silicon nitride powder being evaluated include Toyo-Soda TS-7 powder, UBE SN-E-10 powder, and KemaNord Siconide 1246 grade powder.

The powders are 90-95% alpha phase and contain 1.0-1.5% oxygen. The KemaNord contained less than 1200 ppm of Fe and Al while the Japanese powders contained less than 200 ppm of these impurities. The surface areas of all of the powders range from 10-14m^2/g. Both Japanese powders contain Cl with UBE reporting less than 100 ppm and Toyo-Soda 1000 ppm max. The various compositions selected for sintering were prepared by mixing one of the Si_3N_4 starting powders with Y_2O_3 and SiO_2 powders also including the amount of surface silica on the Si_3N_4 particles. The powders mixtures were milled in plastic jars or RBSN jars using either WC or Si_3N_4 milling balls and ethanol. Milling times were usually 12-24 hours using WC media in order to control WC pickup into the powder mixture. Milling in RBSN jars using Si_3N_4 balls ran 3-4 days. Powders milled in plastic jars were usually fired at 600C for 1-2 hours to eliminate the plastic and residual carbon. The powders were dried and sieved through a -325 mesh screen to remove agglomerates. The powder was uniaxially die pressed to a disc shape, then cold isostatically pressed at 150 MPa to increase the "green" density. Compositions focused upon in this report are:

Composition 40: 88.0m/oSi_3N_4-4.0m/oY_2Oa_3-8.0m/oSiO_2
Composition 37: 85.4m/oSi_3N_4-4.3m/oY_2Oa_3-10.3m/oSiO_2
Composition 39: 85.8m/oSi_3N_4-4.73m/oY_2Oa_3-9.47m/oSiO_2

Sintering

All sintering runs were made in a high temperature-high gas pressure furnace with graphite elements. Specimens were enclosed in a RBSN crucible with a loose fitting lid and embedded in a cover powder of appropriate composition to control specimen composition (weight changes) during sintering. A two-step sintering method was used where the gas pressure in the first step, 1.5-2.0 MPa, was held for 60 minutes, then raised in the second step to 7.0-8.0 MPa and held for 30 minutes. The sintering temperature used for the first step was 1950-1960C. For the second step (higher pressure), the temperature was raised to 1980C. After high temperature densification, some specimens were held at 1200C for 60-120 minutes to partially crystallize the specimen for XRD measurements to determine whether compositional control during sintering was sufficient to produce the desired phase development. Since the use of WC milling media (as well as Si_3N_4 media) is being studied for powder processing, the influence of milling media impurity pickup on sintering the compositions of interest was also examined. Using different starting powders, several batches of compositions 39 and 40 were prepared and milled with WC balls for different milling times to produce various amounts of WC impurity in the samples, as shown in Table 1. Milling times ranged from 7 to 24 hours. The KemaNord 1246 powder appeared to pickup the milling media impurity at a faster rate than the Toyo-Soda or UBE powders. This appears related to its lower surface area and broader particle size distribution. Sintering of the samples was accomplished at 1960C, 60 min., 2MPa, then 1980C, 30 min., 8MPa N_2 gas pressure. The samples for each different starting powder were sintered in separate runs but using the same sintering parameters. For the sintering parameters used, the best densities were obtained when a small amount of WC was present in the specimens. In order to determine whether both the W and C influenced densification, some powders were fired in air at 600-700C to oxidize the WC contained in the sample prior to sintering. Also, some WC powder was obtained, oxidized to WO_3, and then added to compositions, keeping the mol% of W in the sample the same as when WC was present.

A enhancement in specimen densification was observed for oxidized or unoxidized conditions. Since Mo appears to behave chemically similar to W, Mo_2C additions were made to various compositions and densification of specimens was also found to improve. Lowest effective amounts of WC producing full density specimens was 0.365-0.73m/o. Compositions (39, 37, & 40) only milled with Si_3N_4 bails and jars, and sintered at the time/temperature/pressure parameters cited above, densified to 95-98% of full density. Sintered discs 3.5-5.0 cm. diameter x 0.6-1.0 cm. thick are being machined into bars for mechanical property determination, oxidation studies, and microstructural examination.

Properties

Specimens are being machined from dense, sintered discs (Kem.1246 starting powder) for determination of room temperature modulus of rupture (RT MOR), fracture toughness, oxidation resistance, and stress-rupture properties. RT MOR tests were conducted using four point bending with specimens 1.5 mm thick x 2.0 mm wide x 30-40 mm long. MOR values are being determined for each basic composition, i.e., 40, 39, 37, where the compositions may also include different amounts of WC from milling. Data obtained thusfar show that the strength of composition 39 (containing 10.5v/o additive) is higher than composition 40 (containing 8.5v/o additive). Average strength for composition 40 is 545 MPa while that for composition 39 is 610 MPa. Other sintered bodies are currently being machined for further MOR measurements.

Oxidation resistance of compositions 40 and 39 were determined, in air, at temperatures of 1200C. After 120 hours, oxidation rate constant values for composition 39 where in the low 10^{-13} range while those for composition 40 were in the low 10^{-12} range. The appearance of the surface oxide on each composition also varied. On composition 39, the oxide was thin and coherent with the original maching marks still evident through the oxide film. On composition 40, the oxide appeared beaded with different wetting characteristics. A comparison of specimens is shown in Figure 1 (50x magnification under polarized light). The bands at the edges of each specimen are chamfers on the bars. A significant difference in chemistry between the bars, other than different $Y2O_3/SiO_2$ ratio, is that composition 40 contained approximately 2m/o WC while composition 39 contained only half that amount.

Specimens machined from discs of both compositions were tested in stress-rupture at temperatures of 900C and 1200C, in air, under a stress of 300 MPa. Specimens were tested as-sintered and oxidation in a furnace for 120 hours at 1200C. All bars tested at 900C survived 150 hours without failure. These bars will be tested at room temperature to determine residual strength. All composition 40 bars tested at 1200C failed in 30-300 seconds. The composition 39 bars generally survived all test conditions for 150 hours with the exception of a bar which failed in 19 hours due to a pre-existing flaw in the specimen.

Samples of the various sintered compositions (with and without various amounts of WC) are being prepared for microscopic examination by conventional metallography and SEM. Samples have also been submitted for analysis by wavelength dispersive spectroscopy.

XRD analysis on sintered and oxidized specimens shows the presence of beta phase Si_3N_4 and either gamma or beta $Y_2Si_2O_7$. Oxidation layers appear to be beta $Y_2Si_2O_7$ and cristobalite.

Status of Milestones

a) Scale up of compacts---------------compacts 1.5-2.0 in. diameter x 3/8 in. thick are being produced in order that specimens may be machined from them for property measurements. Properties being determined are RT modulus of rupture, fracture toughness, oxidation resistance, and stress-rupture at 900C and 1200C.

b) Specimens for microstructural analysis have been submitted for specimen processing by in-house service groups.

Presentations

"Sintering of Silicon Nitride", G. E. Gazza and D. N. Heichel, presented at proceedings of Contractors' Coordination Meeting, Dearborn, Michigan (Oct 26-30, 1986).

TABLE 1

Starting Powder	Comp. No.	% WC (m/o)	Sintered Density
Kem 1246	40	1.26	3.31
Kem 1246	40	0.10	3.02
Toyo-Soda	40	0.79	3.29
Toyo-Soda	40	0.47	3.28
Kem 1246	39	None	3.17
Kem 1246	37	None	3.23

Figure 1

Composition 39 (left) and composition 40 oxidized at 1200C for 120 hours (50 x under polarized left).

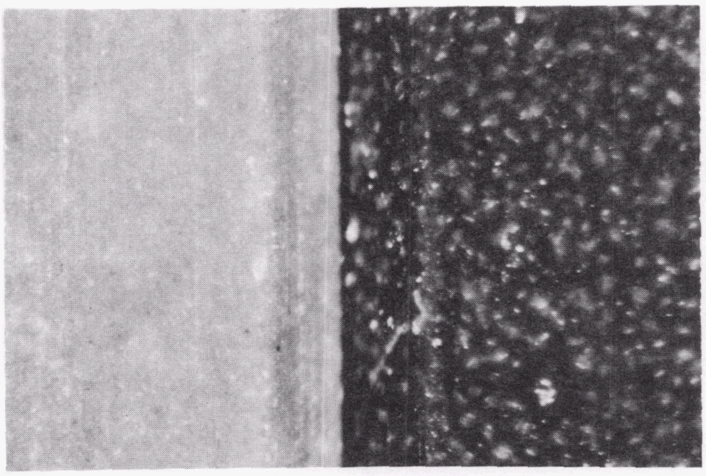

Synthesis of High Purity Sinterable Si_3N_4 Powders -- G. M. Crosbie (Research Staff, Ford Motor Company, Dearborn, Michigan)

Objective/scope

The goal of this task is to achieve major improvements in the quantitative understanding of how to produce sinterable Si_3N_4 powders having highly controlled particle size, shape, surface area, impurity content and phase content. Through the availability of improved powders, new ceramic materials are expected to be developed to provide reliable and cost-effective structural ceramics for application in advanced heat engines.

Of interest to the present powder needs is a silicon nitride powder of high cation and anion purity without carbon residue.

The process study is directed towards a modification of the low temperature reaction of $SiCl_4$ with liquid NH_3 which is characterized 1) by absence of organics (a source of carbon contamination), 2) by pressurization (for improved by-product extraction efficiency), and 3) by use of a non-reactive gas diluent for $SiCl_4$ (for reaction exotherm control).

Technical progress

Summary

A technical report was submitted describing the $SiCl_4$ vapor - liquid NH_3 powder synthesis process (to complete milestones for the original two-year contract). A draft of a design for a 100 kg/month Si_3N_4 pilot plant was reviewed with a chemical engineering consulting firm.

In the laboratory, improvements were achieved in yield, laboratory production rate, cation purity, and alpha/beta ratios over previous work.[1] Although variable from batch to batch, a yield of 83% has been achieved in one run. By directly adding liquid $SiCl_4$ to liquid NH_3, we are exceeding a 20 g Si_3N_4 per hour equivalent imide production rate in a 0.5 L reactor (and confirming the large exotherm). Cation purity is now at the target of <0.1% total cations, other than for an intended sintering aid of Al. An alpha/beta silicon nitride ratio of greater than 20 has been obtained with a 3 h decomposition at 1480°C. Oxygen contamination in the form of amorphous oxynitrides remains a problem.

Tests for effectiveness of rinsing out of by-product Cl by decantation were carried out in a series of six runs. Various minor modifications were made which apparently resulted in a reduction in oxygen contamination from 12.8 wt.% to 7.4 wt.%. An analytical method was developed (by K. R. Carduner) for quantitatively evaluating crystalline and amorphous contents of silicon nitride powders by ^{29}Si MAS-NMR. Sintering experiments (up to 1800°C at atmospheric pressure) of commercial powders have yielded ceramic densities of 3.2 g/cm^3 and a baseline time-temperature procedure for pressureless sintering.

Experimental observations and model calculations support a conclusion of vapor-liquid process scalability.

Yield

High percentage yields are a reflection of larger reacted quantities, improved effectiveness of rinsing out of Cl containing by-products, and minimization of solids accumulations in the reactor and transfer lines. In the case of the 83% yield, 76.6 g of $SiCl_4$ (21.2 g Si_3N_4 equivalent) were loaded and 17.5 g of hot-zone powder were recovered. The imide solids were separated from Cl in species dissolved in liquid NH_3 by decantation (no filtering). Most of the NH_4Cl was recovered from the wastage tank, as intended. (Chlorine residues carried with the intermediate product imide are known to form volatile imidochlorides which reduce hot zone yields to below 50%.)

Lower yield batches are explained by inlet or transfer tube clogging and ineffective rinsing. A 41.2% yield was obtained in another case where little or no NH_4Cl was found in the wastage vessel.

Cation Purity

Cation purity improvements have been brought into the target range of less than 0.1% total, except for Al. In a 1430°C decomposition batch, aluminum is analyzed at 2.03 wt.%. The aluminum content is from the decomposition vessel of Al_2O_3 and is considered a sintering aid. Other elements are reported below in contrast to those presented at the October 1986 ATD-CCM meeting:

	1986 ATD-CCM	(recent values)
Fe	0.16%	0.06%
Ca	0.06%	0.03%
Ti	0.03%	<0.005%
Total (listed)	0.25%	<0.095%
Al	0.6%	2.03%
Co		0.011%
Mo		0.0075%
Sn		0.0061%

These improvements are believed due to shorter times of contact of liquid NH_3 and $SiCl_4$ with pressure vessels and due to larger batch sizes.

Alpha Si_3N_4 Crystallization

In processes with a silicon diimide (silanediimide) intermediate, alpha silicon nitride crystallizes during the thermal decomposition of the intermediate. In this period, we have restored the practice of use of a low temperature hold (250 to 400°C) to allow residual NH_4Cl to sublime slowly. Also, with a thermocouple located in the center of the powder bed, we have observed a moderate exotherm (20 to 50°C center-to-muffle gradient at 1400°C center) for the onset of crystallization of the nominally 20 g batches, as expected.

In the powder synthesis project Task 2, titled "Characterization," there is stated a need "... to develop or demonstrate new and improved quantitative techniques ...." A technique has been developed by K. R. Carduner which can readily distinguish the individual concentrations of different amorphous and crystalline chemical species in silicon nitride powders.

Results are shown in the following table for two decomposition temperatures, each 3 hours, with slow approach to the hold temperature: Silicon Phase Analyses by MAS-NMR (courtesy of K. R. Carduner, Ford Research)

	Decomposition Temperature	
	1430°C	1480°C
Alpha/(Alpha + Beta) Ratio	1.0	0.955
Alpha/Amorphous Si_3N_4 Ratio	0.11	2.87
Alpha/Beta Si_3N_4 Ratio	>3	21.5
Percent Alpha Si_3N_4	6%	43%
Percent Beta Si_3N_4	N.D.	2%
Percent Amorphous Si_3N_4	53%	15%
Percent Amorphous Oxynitrides	41%	40%
Total	100%	100%

Such a low beta content is desired for mechanical properties of the sintered silicon nitride.

A manuscript describing the method has been submitted for publication (as listed in "Publications" section below). This work was carried out at Ford Research. The manuscript reflects that certain commercial Si_3N_4 powders which appear to be entirely crystalline by x-ray diffraction actually have 20 to 30% amorphous content as determined by magic angle spinning NMR (MAS-NMR).

Oxygen Contamination

Oxygen contamination remains a problem. Leco-type analyses of the above samples are 12.8% (1430°C) and 13.8% (1480°C).

In the past, we have lowered levels of oxygen by adding H_2 (from NH_3) to the carrier gas during decomposition. This reducing agent was not used in this period. This choice is the result of strategy to have the Si-N bonds formed at low temperature and to have the nitride formed by a single route. The choice should also increase the magnitude of a response when the responsible factor is changed.

Additonal steps have been taken to reduce oxygen contamination and some progress has been made. Modifications made included reduced count of fittings, replacement of possibly overworked compression fittings, and an O-ring design for the decomposition furnace seal. Components were helium leak tested before routine pressure testing. In a run made without breach of system integrity, Leco values of 7.1 and 7.8 wt.% oxygen were obtained. (The 7.4 wt.% value in the summary above is the average of these two.) These values are down from 12.8 wt.% of the Dec. 1986 - Jan. 1987 period and still represent tests done without the use of NH_3 in the decomposition carrier gas to provide reducing H_2. However, oxygen contamination is considered to remain a problem.

Chlorine extraction

In decantation to extract by-product chlorine, supernatant ammonia with dissolved $NH_4Cl \cdot 3NH_3$ is withdrawn to a wastage tank under the system pressure. Tests of effectiveness of rinsing by decantation were carried out in the format of a process capability test. We measured the mass of NH_4Cl recovered in the wastage tank (after depressurization and NH_3 evaporation) at the end of each of six runs. Except for minor modifications intended to reduce oxygen content, the runs were all scheduled to the same pattern. In particular, there were a fixed number of rinses (4) and a fixed time (5 min) for each extraction.

The resulting amounts of NH_4Cl recovered were variable with a bimodal distribution with modes about 4% and 38% of theoretical. (The theoretical value is taken to be all of the chlorine in the loaded $SiCl_4$. For four rinses at a decant ratio of 3 parts of 4, extracted chlorine would be $(1-(0.25)^4)$ or 99.6% of input Cl, assuming complete dissolution and the absence of adsorption.) In all but one case, the lower mode corresponds with abnormally low product recovery. These lower mode cases are assigned to be "exception cases" of inlet clogging with the liquid $SiCl_4$ - liquid NH_3 reaction being used to exclude any possible diluent gas oxygen.

The higher mode about 38% is believed to be more representative behavior. This departure from the equilibrium value suggests that the time for extraction is the limiting factor (for the present experimental conditions of 0^oC, 75 psig, and minimal agitation).

Sintering

We have carried out a partial factorial design of experiments to identify key time-temperature (t-T) factors in the pressureless sintering of commercially available silicon nitride powders with our equipment. Samples were prepared by dry-mixing with oxide aids, die-pressing and subsequent isostatic pressing. Under particular (t-T) conditions, we have obtained densities of 3.2 g/cm^3 (that is, 96-97% T.D.) with a combination of 10 wt.% Y_2O_3 and 2.25 wt.% Al_2O_3 sintering aids in less than or equal to 2 h at 1800^oC.

These ceramic densities are slightly higher than those of G. Woettig and G. Ziegler[2] for 1800^oC sintering of commercial diimide-precipitation powders processed by wet-milling. Thus, an experimental baseline (t-T) procedure for pressureless sintering of silicon nitride powders has been obtained.

Scalability

Experimental observations and model calculations support a conclusion of vapor-liquid process scalability. A summary of these points follows and is expanded in subsequent paragraphs: Heat and mass transfer mathematical models are discussed for two scale-up options that are appropriate to semi-continuous processes. Because of a nearly heat neutral reaction, heat transfer scale-up is not critical in either option. Mass transfer scale-up is via control of the gas-liquid interface area and contact time. Economic issues probably favor the "small reactor -- faster batch" option. Supporting the evaluation of scale-up potential are the operability as demonstrated in the laboratory and the closeness of correspondence of laboratory reaction conditions to those of a projected plant. A scale-up of greater than 100X from lab scale is judged to be a reasonable next step for a pilot plant.

The silicon tetrachloride vapor - liquid ammonia reaction is operated in a semi-continuous manner. $SiCl_4$ vapor flows nearly continuously until the batch is completed and the next volume of NH_3 is added. Two options (or design concepts) for scale-up (to obtain more product per unit of time relative to any given basis) of a semi-continuous process are: Option 1) larger reactor volume, proportionally higher gas flow rate, with the same batch time and Option 2) a reactor volume smaller than in the first option, a higher gas flow rate, and a shorter batch time. These two options are now examined qualitatively in terms of heat and mass transfer limitations and economics.

The heat transfer calculation is simplified for both of the two scale-up options, because we project a nearly heat neutral reaction zone. We have observed a small overall reaction endotherm at $0^{o}C$ with the laboratory apparatus. This observation is in support of a model calculation for a heat-neutral reaction zone near room temperature. Also, because we are on the endotherm side, the risk is minimized of a runaway or unstable reaction. A simple geometry vessel, without a heating or cooling jacket, can be considered for a commercial plant. The heat neutrality is important as the solids produced place additional constraints on the design if additional heat transfer surfaces were required.

One indicator of mass transfer scalability is that the reaction of $SiCl_4$ with NH_3 liquid is known to be fast. The gas-liquid reaction is likely to be absorption of $SiCl_4$ into the ammonia with an immediate reaction with NH_3. Since the kinetics of the chemical reaction are fast, the overall reaction rate is expected to be controlled by gas phase mass transfer. Using this as a design criterion for scale-up, we can address means to increase the area of gas-liquid contact and to increase the time of contact. Typically, these factors are improved by mechanical agitation, of which we have none in the laboratory apparatus. The contacting time can be related to bubble rise rate and the height of liquid in the reactor, for both Options 1 and 2. In particular, the necessary height for an overall reaction rate is less for greater interface area and absolute pressure. A wide range is available beyond that tested in the laboratory.

The economics of scale-up are considered in terms of raw materials, utilities, capital, and automation. The raw materials are available in large quantities at low cost. Since they are liquids, efficient means are available to purify them. Utility costs are primarily refrigeration for the condenser, since liquid nitrogen and ammonia are delivered under pressure. The materials of construction have not been exotic. The low temperature operation (near room temperature and below) that gives low chloride residue in the silicon nitride also leads to low Cl^- corrosion. The temperature of operation is not so low as to produce temperature gradient stresses that would become a limitation at larger scale. The semi-continuous operation is well-suited for automated operation with liquid-like flows. Automation is desirable because of increased personnel hazards with larger volumes of liquid ammonia and hydrogen evolved from the decomposition. The economics of scale-up probably favor Option 2, as a smaller tank has lower capital cost.

Laboratory testing has shown the operability of the novel imide route process under conditions similar to those projected for commercial plant operation. The reaction proceeds at 0^oC, in spite of an overall reaction endotherm. The product is primarily submicron, alpha-phase silicon nitride. Since the lab studies are run under pressure, the results are closer to projected plant practice than would be the case if studies were done under cryogenic conditions in glass apparatus. We have observed avoidance of inlet clogging, which has been a problem for direct reaction of $SiCl_4$ with liquid NH_3. Likewise, the transfer lines and reactor itself remain clear after batches are run. No foaming occurs as in some gas-liquid systems. Information on the characteristics of the imide intermediate has been obtained for design: purity, settling rate, and apparent slurry viscosity. Except for valves, the lab system has no moving parts for synthesis and transfer of the air-sensitive raw materials and intermediate products.

The correspondence of the lab work to the projected plant is close in several other ways. Since the intrinsic (T,P) conditions are above the normal boiling point of NH_3, the lab work reflects the greater solubility of the chloride by-product and presumably higher reaction rate to be found in practice under pressure. From early studies by chemists, much is known of the systems involved. From other imide-route nitrides on the market, the basic qualities of the powders are known which can result from those related imide routes to silicon nitride powders. In this work, a feasibility for adaptation to a uniquely low carbon powder is demonstrated.

Status of milestones

The milestones for scalability and preparation of a technical report were completed in this semiannual reporting period. A discussion of the scalability milestone accomplishment is given in the "Technical Progress" section above. The technical report describing the process for synthesis of silicon nitride powder was submitted March 18, 1987. Therefore, the final milestones for the original two-year program have been completed on time:

Demonstration of proof of scalability	November 1986
Complete draft technical report describing the process	March 1987

Publications

G. M. Crosbie, "Preparation of Silicon Nitride Powders," *Ceram. Eng. Sci. Proc.* 7(9-10) 1144-9 (1986).

G. M. Crosbie, "Si_3N_4 Powder Synthesis," presented at the 24th Automotive Technology Development Contractors' Coordination Meeting, Dearborn, Michigan, October 27-30, 1986. (Manuscript submitted for publication by the Society of Automotive Engineers, Warrendale, Pa.)

G. M. Crosbie, "Si_3N_4 Powder Synthesis," abstract accepted for presentation at Am. Ceramic Soc. Annual Meeting, Pittsburgh, Pa., April 26-30, 1987.

K. R. Carduner, R. O. Carter III, M. E. Milberg, and G. M. Crosbie, "Determination of Silicon Nitride Crystallinity and Silicon Phase Composition of Silicon Nitride Powder by ^{29}Si MASNMR," submitted for publication in *Analytical Chemistry*.

References

1. G. M. Crosbie, "Synthesis of High Purity Sinterable Si_3N_4 Powders," pp. 25-28 in *Ceramic Technology for Advanced Heat Engines Project Semiannual Progress Report for Period October 1985- March 1986*, ORNL/TM-10079, Oak Ridge National Laboratory, Oak Ridge, Tenn., August 1986.

2. G. Woettig and G. Ziegler, "Powder Characteristics and Sintering Behaviour of Si_3N_4 Powders," *Powder Metall. Intl.*, 18(1) 25-32 (1986).

1.2 CERAMIC COMPOSITES

1.2.2 Silicon Nitride Matrix

Transformation-Toughened Silicon Nitride

H. W. Carpenter (Rocketdyne Division, Rockwell International)

Objective/scope

The objective of this program is to develop high toughness, high strength refractory ceramic matrix composites that can be made at low cost and to near net shape for heat engine applications. The composite system selected for development is based on a silicon nitride matrix toughened by dispersions of ZrO_2, or HfO_2, or $(Hf, Zr)O_2$ modified with suitable additions of other refractory ceramics to control the physical behavior. The desired microstructure and optimum mechanical properties have been developed by expeditious laboratory methods including colloidal suspension, press forming, sintering, and hot pressing. Promising compositions and microstructures have been demonstrated and parameters are being optimized. Samples have also been fabricated by injection molding to demonstrate low-cost, high-volume production.

Technical progress

Si_3N_4 matrix plus ZrO_2 dispersoids modified with four different alloying agents have been studied. The four dispersoids are ZrO_2 alloyed with either (1) Y_2O_3, (2) CaO, (3) MgO, or (4) HfO_2 and TiO_2. Promising materials with potential structural applications have been developed from the first three compositions but the latter composition was not structurally stable. The effort is presently being concentrated on characterizing Si_3N_4 + ZrO_2 alloyed with either Y_2O_3 or CaO. Four-point MOR values to 1100 MPa and apparent toughness values to 13 MPa $m^{1/2}$ have been reported.

ZrO_2-Y_2O_3 Dispersions

Previously reported results on composites composed of Si_3N_4 plus 20 or 30 v/o ZrO_2 (stabilized with Y_2O_3) plus 4 w/o Al_2O_3 were highly encouraging. This composition readily sinters to a high density and exhibits 4-point MOR strengths to 1100 MPa. Work performed this period is summarized below.

Degradation at 700C and Transformation Toughening - Si_3N_4 and ZrO_2 react to form Zr-oxynitride, an undesirable compound because it depletes the ZrO_2 content without increasing toughness and it oxidizes at intermediate temperatures to monoclinic ZrO_2. The transformation to monoclinic ZrO_2 results in surface cracking. Lange (Ref. 1) has shown evidence that the formation of Zr-oxynitride can be prevented or retarded and that a transformable tetragonal ZrO_2 phase can be obtained by using ZrO_2 alloyed with Y_2O_3. It was shown earlier in this study that at least 8 w/o Y_2O_3 alloy content in the ZrO_2 was required to prevent the formation of Zr-oxynitride, and that transformable tetragonal was not present at that Y_2O_3 alloy content. Nevertheless, the material is still attractive from the stand point of high strength and low thermal conductivity.

Current results show that sintering temperature as well as Y_2O_3 alloy content of the ZrO_2 influence the intermediate temperature (500C to 1000C) oxidation problem. To date, all $Si_3N_4/ZrO_2(Y_2O_3)$ compositions sintered at 1750C (with one notable exception which is being investigated) exhibited oxidation degradation when aged in air at 700C, while all compositions sintered at 1800C did not exhibit oxidation degradation. Thus, a higher sintering temperature (1800C) eliminated the problem in the range of all ZrO_2-Y_2O_3 alloys (9 w/o to 13 w/o Y_2O_3) currently being evaluated. The implication to this is that it may still be possible to use a lower Y_2O_3 alloy content and, if less Y_2O_3 alloy can be used, it may still be possible to induce transformation toughening without the intermediate-temperature degradation. In order to explore this possibility, new compositions of Si_3N_4 plus 20 or 30 v/o or ZrO_2 alloyed with 8.0, 6.9, 4.5, 3.4, and 0.0 w/o Y_2O_3 are being prepared. The major differences in preparing these new samples is that a sintering temperature of 1800C or higher will be used, and that the 4 w/o Al_2O_3 addition used as a sintering aid will be replaced with 6 w/o Y_2O_3 + 2 w/o Al_2O_3 additions for compositions containing ZrO_2 powders with low Y_2O_3 alloy contents.

Transmission electron microscopy studies are in progress at the Rockwell Science Center to characterize these materials. Samples sintered at 1750C and aged at 700C (exhibiting zero strength) and samples of the same composition sintered at 1800C and aged at 700C (exhibiting increased strength) are being evaluated.

Strength Increase Due to Oxidation - An increase in strength after oxidizing in air at 700C has been observed in all samples sintered at 1800C. The data from samples composed of Si_3N_4 + 20 v/o and 30 v/o ZrO_2 (9 w/o Y_2O_3) + 4 w/o Al_2O_3 show this phenomena (Fig. 1). Strength increases rapidly to a maximum between 100h and 300h, and then gradually decreases. Maximum strength increase was 34% for the 20 v/o ZrO_2 composition and 26% for the 30 v/o ZrO_2 composition.

A white casing forms on these samples, presumably due to the oxidation of ZrO_{2-x} (grey) to ZrO_2 (white). The casing is about 0.25 mm thick after 500 hours at 700C and preliminary fracture analyses show that fracture originates at the white/grey interface. XRD analyses of the white and grey materials are the same.

Oxidation Kinetics - A series of samples were oxidized at temperatures from 700C to 1300C for selected times so that the thickness, weight gain, and the nature of the oxide layer can be characterized. These data and samples have not yet been evaluated.

High-Temperature Strength - The strengths to 1200C of four compositions containing 4 w/o Al_2O_3 as a sintering aid are shown in Fig. 2. The 3-point MOR of the materials containing 20 w/o ZrO_2 are slightly higher than those containing 30 v/o ZrO_2 and the strength of materials containing more Y_2O_3 alloy content in the ZrO_2 are slightly higher. However, the strength of the four compositions are relatively close together. Strength decreases with increasing temperature to approximately 700 MPa at 1000C and 500 MPa at 1200C. Four-point MOR has been shown to be about 18% lower at room temperature but it is about the same as the 3-point MOR at elevated temperatures. Although these strengths compare favorably with other Si_3N_4 materials reported in the literature, high-temperature strength can be increased appreciably by the use of other sintering aids and by heat treatment. Experience at Rocketdyne with our SN104 composition has shown that a mixture of Y_2O_3 + SiO_2 provides good sinterability plus high strength at elevated temperatures. In addition, this composition can be heat treated to exhibit even higher strength at elevated temperatures. With this in mind, a series of compositions containing Y_2O_3 + SiO_2 in place of Al_2O_3 were formulated in the Si_3N_4-Si_2N_2O-Y_2SiO_7 compatibility phase triangle. These formulations and the sintering results are presented in Table 1. Sintering parameters of 1860C, 2h were required to achieve near full densities. In fact, a higher sintering temperature may be required because the room-temperature strength of the composition Si_3N_4 + 30 v/o ZrO_2 (12 w/o Y_2O_3) + 8 w/o Y_2O_3 + 3.6 w/o SiO_2 was only 455 MPa, about half that when 4 w/o Al_2O_3 was used as the sintering aid. This has been the only composition in which strength has been measured so far. Although the room temperature strength is low, the strength at 1200C is slightly above that for the materials containing 4 w/o Al_2O_3 as the sinter aid (Fig. 2). MOR bars of the other compositions containing Y_2O_3 + SiO_2 as a sintering aid are available for testing.

Injection Molding - Strength data for injection molded bars of composition Si_3N_4 + 30 v/o ZrO_2 (9 w/o Y_2O_3) + 4 Al_2O_3 are given in Table 2. These MOR bars were tested in the as-fabricated condition unless noted, which means they had a skin of zirconium nitride and they were not perfectly straight or flat. They are typically 2.2 mm thick x 6.4 mm wide x 50 mm long. The 4-pt. MOR fixture (L_o = 30 mm, L_i = 10 mm) rotates on three of the four supports to accommodate imperfect bars. It has also been shown that the slab geometry of the bars produces MOR data that are about 20% lower than that produced on bars shaped like a beam. Nevertheless, the strength data for the injection molded bars are still only about half that of bars prepared by filter pressing. The low strength is due to the presence of large (.1 mm dia.) pores throughout the bars. Thirteen injection molded bars were isostatically pressed after binder removal in an effort to close the pores before sintering but the effort was not successful. The source of these pores will be determined so they can be eliminated. The strength increased when the tensile surface was ground even though the grinding exposed the large pores on the surface.

HfO_2 (Y_2O_3) Dispersoids - One of the approaches for increasing the service temperature of the materials in this program is to substitute HfO_2 for ZrO_2. This approach will be most beneficial in the Si_3N_4 + ZrO_2 (CaO) system, which is discussed in the next section of this report, where a tetragonal-to-monoclinic phase change occurs. However, the HfO_2(CaO) powders have not been received and a fully stabilized (10 m/o Y_2O_3) HfO_2 powder was on hand. A batch of 70 v/o Si_3N_4 + 30 v/o HfO_2 (Y_2O_3) + 4 w/o Al_2O_3 was prepared to determine whether any unexpected processing

problems or sintering reactions might occur. A slurry was prepared and 50-mm-dia. disc samples were formed by pressure filtration. Two samples were sintered at 1800C for 1h and the sintered discs were near full density (densities were 4.97 g/cc and 4.98 g/cc and porosities were .01% and .11%, respectfully). MOR bars are being diamond ground. XRD results showed only beta Si_3N_4 and fully stabilized HfO_2 peaks which were identical to the unmixed powders. These results are, therefore, encouraging.

ZrO_2-CaO Dispersions

Initial results of compositions Si_3N_4 + 10, 20, and 30 v/o ZrO_2 (5 w/o CaO) + 2 1/2 w/o MgO densified by hot pressing have also been highly encouraging. Strengths to 1100 MPa and apparent toughness values to 13.8 MPa $m^{1/2}$ have been obtained. These high strengths were obtained in spite of the fact that these materials exhibited agglomerated microporosity. During the last three reporting periods, samples were densified by sintering, rather than by hot pressing, and the microporosity content was even higher. Nevertheless flexural strength was still over 700 MPa. The ZrO_2 powder used to make these materials was not as pure nor as fine grained as desired.

Submicron, high purity ZrO_2 powders, containing 3.5, 6, and 10 w/o CaO were obtained after a long procurement time. Batches of 70 v/o Si_3N_4 + 30 v/o ZrO_2 (CaO) + 2 1/2 w/o MgO were colloidally prepared and filter-pressed discs were sintered at 1800C, 1860C, and 1900C for 1h. Results are presented in Table 3. A sintering temperature of 1860C was required to obtain a high density for the composition containing ZrO_2 (10 w/o CaO), a temperature of 1900C was required for the composition containing ZrO_2 (6 w/o CaO), while the composition containing ZrO_2 (3.5 w/o CaO) did not sinter to near theoretical density. Preliminary examination under the high-power optical microscope showed that these samples did not exhibit the agglomerated microporosity as did the samples made with the old ZrO_2 (5 w/o CaO) powder. A secondary phase that appeared as black inclusion was also observed. These black inclusions increased in size and in frequency with increasing CaO content. MOR bars are being prepared from the discs sintered at 1860C and 1900C.

Status of Milestones

All past milestones have been completed on time and progress toward the milestones for the next report period is on schedule.

Publications

None

References

1. F. F. Lange, L. K. L. Falk, and B. I. Davis, "Structural Ceramics Composites Based on Si_3N_4-ZrO_2(+Y_2O_3) Composites", unpublished, October 1985.

TABLE 1

Sintering Data For Compositions Of Si_3N_4 + 30 v/o ZrO_2 (12 w/o Y_2O_3) Containing Selected Y_2O_3 + SiO_2 Additions

Sinter Run	Identity	Sintering Temp./Time	Sintering Aid Additions		Sintered Density (g/cc)
			Y_2O_3(w/o)	(SiO_2(w/o)	
# 38	186-795-D3	1800C/1h	4.0	1.1	2.18
	180-795-D6		8.0	3.6	2.35
# 39	186-795-D1	1860C/2h	4.0	1.1	3.42
	180-795-D2		8.0	3.6	3.89
# 40	28-852-D4	1860C/2h	8.0	3.6	4.07
	28-852-D2		8.0	3.6	3.84
# 42	41-852-D2	1860C/1h	4.0	3.0	3.44
	28-852-D1		8.0	3.6	3.40
	38-852-D1		8.0	5.0	3.57
	40-852-D2		8.7	3.9	3.87
	37-852-D1		15.5	7.0	3.87
# 44	41-852-D1	1860/2h	4.0	3.0	3.78
	28-852-D2		8.0	3.6	4.12
	38-852-D2		8.0	5.0	3.82
	40-852-D1		8.7	3.9	3.96
	37-852-D3		15.5	7.0	3.93

TABLE 2

4-Pt MOR Data For Injection Molded Samples

Sinter Run	Procure	Surface Condition	Number Of Bars	Average Strength (MPa)	Standard Deviation (MPa)
S# 36	Standard	As Sintered	2	457	8
		Ground	8	595	96
S# 41	Standard	As Sintered	7	421	51
S# 45	Standard	As Sintered	4	356	51
	Note # 1	As Sintered	8	354	56
	Note # 1	Ground	5	538	41

Note # 1: Isostatically pressed after binder removal.

TABLE 3

Sintering Results For Si_3N_4 + 30 v/o* ZrO_2 (CaO) + 2 1/2 w/o MgO Composition

Sinter Run	Sintering Temperature C	CaO Alloy Content w/o	Wt. Loss %	Porosity %	Density (g/cm^3)
S# 46	1800	3.5	3.3	21	2.89
		6	2.5	14	3.29
		10	1.8	10	3.48
S# 48	1860	3.5	4.5	6.9	3.40
		6	1.2	0.2	3.66
		10	0.8	0.1	3.83
S# 49	1900	3.5	7.1	8.9	3.44
		6	1.3	0.2	3.80
		10	1.1	1.7	3.78

*The density of CaO stabilized ZrO_2 was not adjusted for the three different CaO contents for batch calculations. Therefore the volume percent may vary slightly.

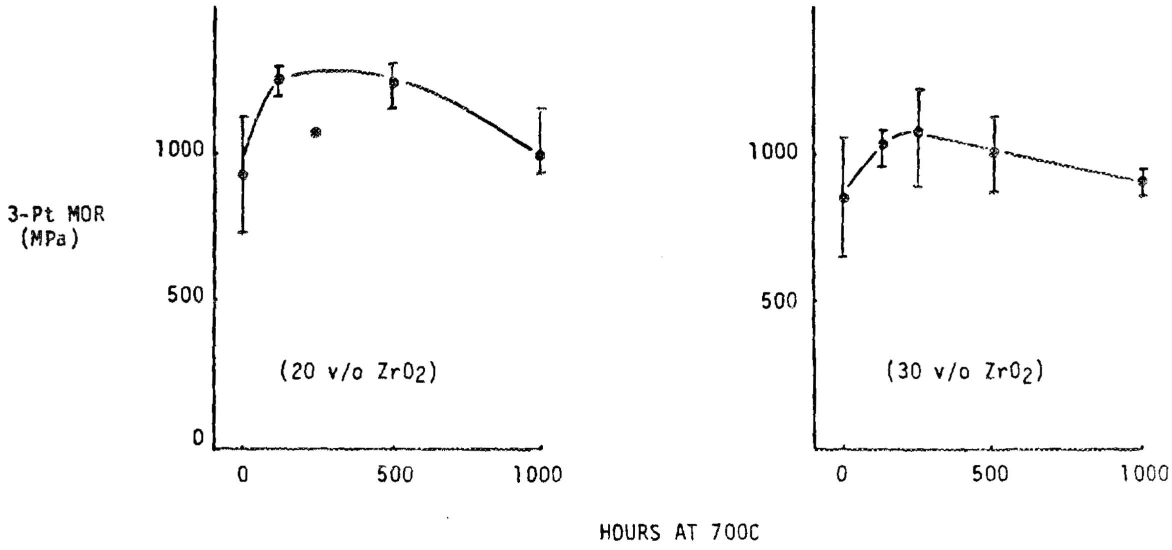

Figure 1 Room Tempeature Strength vs Aging Time at 700C in Air. Composition: $Si_3N_4 + ZrO_2$ (9 w/o Y_2O_3) + 4 w/o Al_2O_3

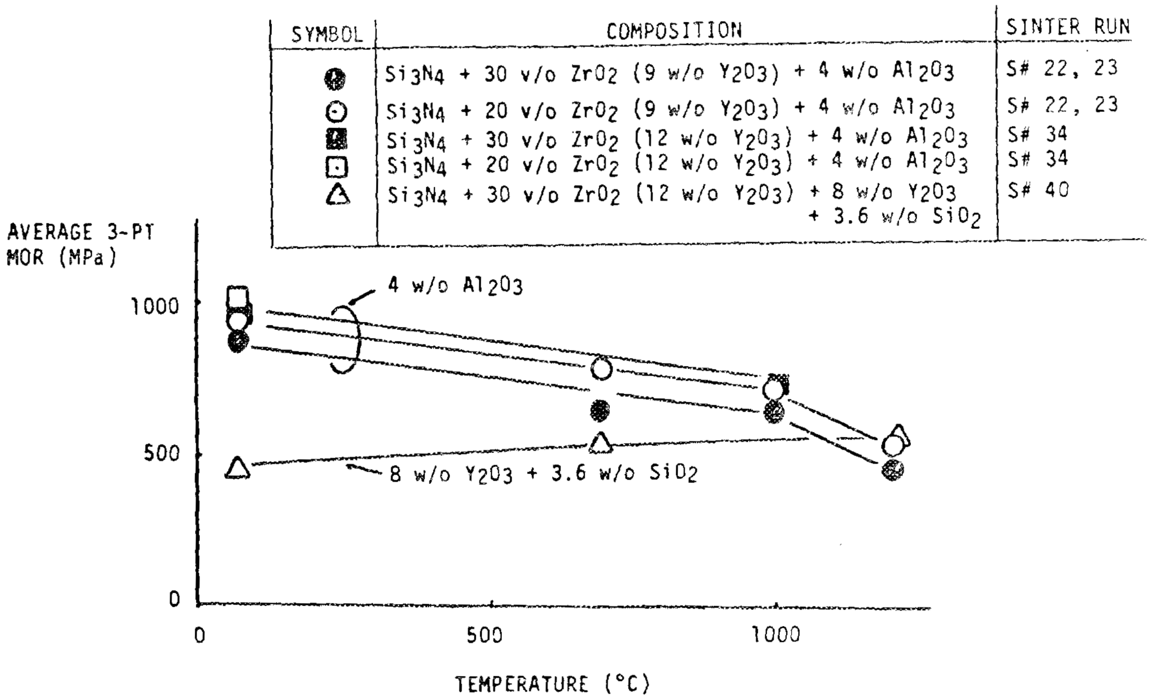

SYMBOL	COMPOSITION	SINTER RUN
●	Si_3N_4 + 30 v/o ZrO_2 (9 w/o Y_2O_3) + 4 w/o Al_2O_3	S# 22, 23
⊙	Si_3N_4 + 20 v/o ZrO_2 (9 w/o Y_2O_3) + 4 w/o Al_2O_3	S# 22, 23
■	Si_3N_4 + 30 v/o ZrO_2 (12 w/o Y_2O_3) + 4 w/o Al_2O_3	S# 34
⊡	Si_3N_4 + 20 v/o ZrO_2 (12 w/o Y_2O_3) + 4 w/o Al_2O_3	S# 34
△	Si_3N_4 + 30 v/o ZrO_2 (12 w/o Y_2O_3) + 8 w/o Y_2O_3 + 3.6 w/o SiO_2	S# 40

Figure 2 Flexural Strength vs Temperature for $Si_3N_4 + ZrO_2$ Mixtures With Al_2O_3 or ($Y_2O_3 + SiO_2$) as a Sintering Aid.

Silicon-Nitride-Metal Carbide Composites

S. T. Buljan (GTE Laboratories, Inc.)

Ceramic Matrix Composites - GTE Laboratories, Inc.

Objective/Scope

The objective of this program is to develop silicon nitride-based composites of improved toughness, utilizing SiC and TiC as particulate or whisker dispersoids, and to develop and demonstrate a process for near net shape part fabrication. Near net shape process development will explore forming by injection molding and consolidation by hot isostatic pressing or conventional sintering.

Technical Progress

Process Development

Powder Preparation

The system chosen for molding studies is AY6* + 30 volume percent SiC whiskers. Earlier research using hot pressed samples highlighted the critical importance of high whisker chemical purity and whisker size control if simultaneous strength and fracture toughness improvements are to be achieved. To date, only the Arco SiC whisker has met both size and purity requirements. Particularly critical to the outcome and the goal of obtaining high toughness, high strength composites is the step of powder preparation (Figure 1).

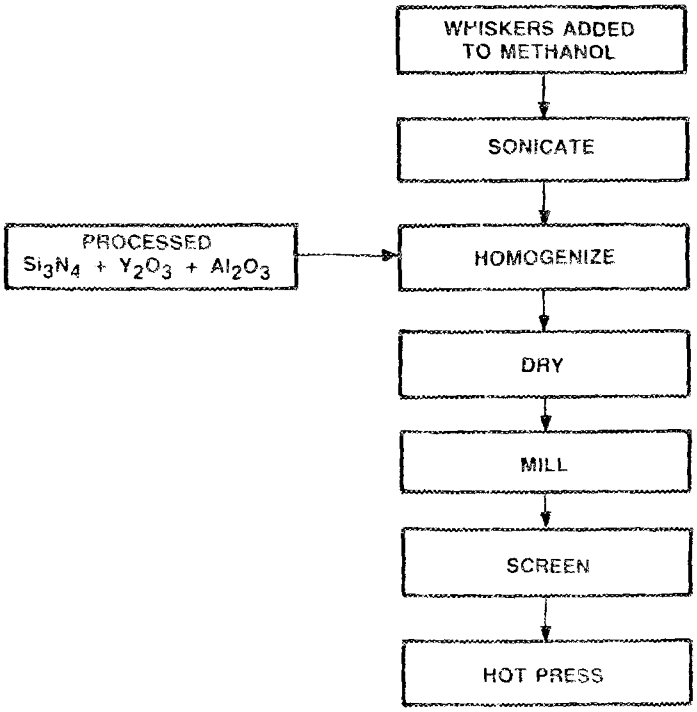

Figure 1: Flow Chart for Wet Processing of Si_3N_4-SiC Whisker Composites

---

*Si_3N_4 + 6 w/o Y_2O_3 + 1.5 w/o Al_2O_3

State-of-the-art processes for whisker fabrication are underdeveloped and yield materials with broad size distribution. As-received whiskers contain submicron particles and, more importantly, particles and hard whisker aggregates greater than 100 µm.

These aggregates and particulates, if processed into the composite, may act as fracture origin and reduce the composite strength. Particles of various sizes can be separated by sedimentation. A column was devised which allows removal of whisker/particle suspension at three different levels. For a given time of setting, the top portion of liquid contains the finest particles and floating debris, the bottom portion, the largest particles, which are to be removed, and the middle, a range of sizes between the two. It was not anticipated that clean separations of whisker lengths could be made using this technique. Whiskers were separated with a minimum of 98.8% of the material being recovered after separation. Table 1 shows the average length and relative amounts in each section (top, middle and bottom) for a typical separation, using a settling time which would allow particles with a 10 µm radius or larger to settle to the bottom of the column. Approximately 70% (middle section) of the starting material was deemed of appropriate quality for composite fabrication.

Table 1: Average Whisker Lengths and Relative Amounts Obtained from Different Column Levels

Material	**Average Whisker Length (µm) After Separation**			
	As-Received	**Top**	**Middle**	**Bottom**
Arco	17.5 ± 12.6	19.0 ± 8.7	17.5 ± 9.5	29.3 ± 14.5
	Relative Amounts of Whiskers (%) After Separation			
		Top	**Middle**	**Bottom**
Arco		29.7	68.3	1.9

Mechanical properties of composites containing 30 v/o of as-received or separated SiC whiskers are given in Table 2. As can be seen, the application of as-received whiskers results in a ≈20% reduced MOR, despite up to 40% increased fracture toughness over that of base AY6 material. Furthermore, a 40% reduction of MOR with respect to composites of equivalent fracture toughness containing separated whiskers is observed.

Table 2: Mechanical Properties of Si_3N_4-30 v/o SiC Whisker Composites Containing As-Received or Separated Whiskers

Whisker Source	K_{IC} (MPa•m$^{1/2}$)	MOR (MPa)	Calculated Flaw Size (μm)
As-Received	6.0 ± 0.1	597 ± 5	80
Separated	6.4 ± 0.5	975 ± 39	35
AY6 Monolith	4.7 ± 0.3	773 ± 67	30

Calculations indicate that the critical flaw size in a composite with as-received whiskers is of the order of 80 μm. Fractographic examinations of MOR bars broken at room temperature reveals a typical flaw size of 60 μm (Figure 2). Within the accuracy of assumptions included in calculations, these results are consistent with the premise that large particulates or whisker aggregates are the cause of reduced MOR. Examination of the separated fraction from the top of the column reveals the presence of large (> 100 μm) aggregates consisting of SiC whiskers and concentrated metallic impurities (Zn, Mn, Mg, K, Ca, P), probably remnants of the whisker precursor (Figure 3). The application of the above-described procedure prior to composite powder preparation results in a consistent attainment of design properties.

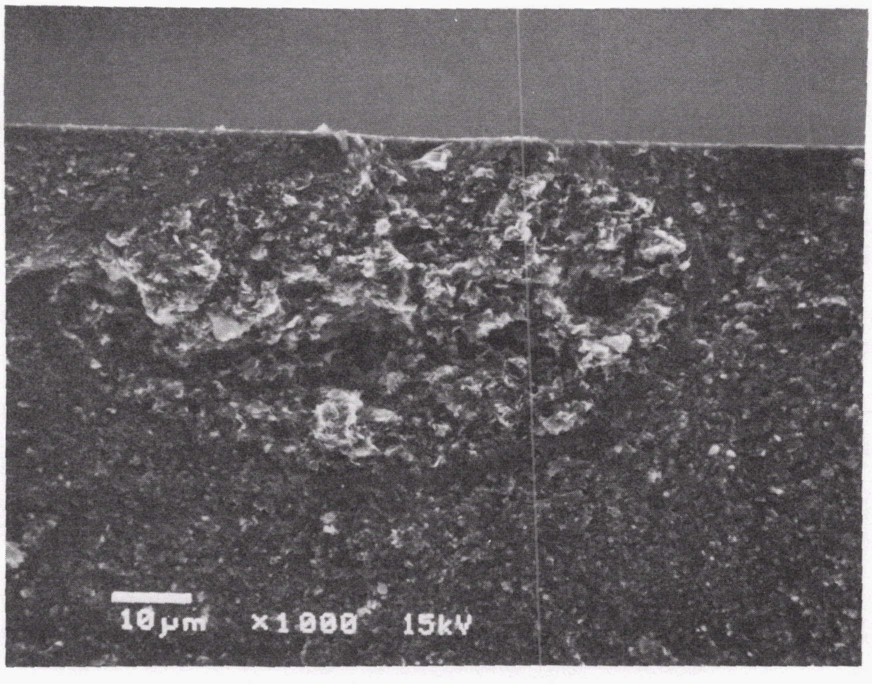

Figure 2: Fracture Origin of Si_3N_4 30 v/o SiC(w) Material Prepared with "As-Received" Whisker. MOR = 600 MPa; K_{IC} = 6.0 MPa·m$^{1/2}$.

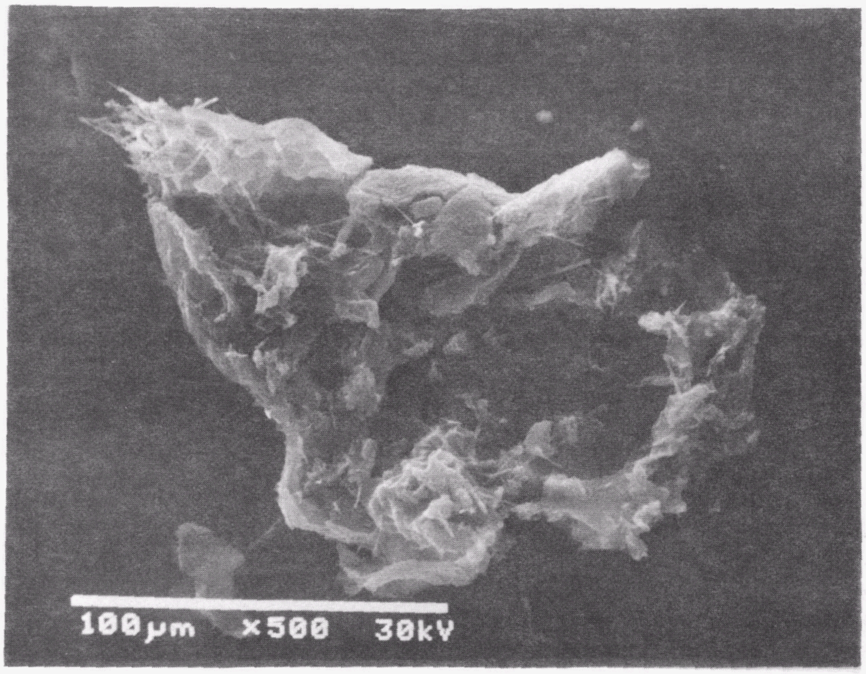

Figure 3: Particulate Material Contained in Arco SiC Whiskers

Injection Molding

The injection molding process for ceramic composites can be broken down into six major processing steps:

- **Mix Preparation** - The blending/milling of the desired composite composition which will give the desired properties in the final part.
- **Compounding** - Mixing the ceramic powder with an organic binder system such that the mixture behaves like a thermoplastic material.
- **Injection Molding** - Heating the mixture above its flow point and injecting it into a relatively cold metal die, where the mix solidifies.
- **Binder Removal** - Removal of the organic binder from the part, leaving behind a nondisrupted ceramic structure.
- **Densification** - Consolidation of the ceramic structure to a fully dense structure by sintering or hot isostatic pressing (HIP).
- **Non-Destructive Examination (NDE)** - Evaluation of part quality by means of visual, dimensional, and weight measurements as well as microfocus projection x-ray radiography.

Progress to date in applying injection molding technology to the fabrication of whisker-reinforced composites will be reviewed in terms of each major processing step.

Mix Preparation

Batches for injection molding have been prepared by two process routes, preblend and compound blend. In the preblend case, whiskers were added to AY6 prior to the compounding step. This approach is identical to the process used to produce feed powders for hot pressing. The alternate approach was to mix whiskers and AY6 in the compounder and use the high shear mixing action of the compounder to blend the two components. The latter approach was used for the bulk of the molding experiments.

Compounding

The compounding unit used is a Haake torque rheometer mixer. The unit measures the torque required to maintain a fixed mixing rpm as well as an integrated total torque for each batch. Information on "mixing viscosity" is thus gained as a function of shear rate, solids loading content, mixing procedure and mixing time.

Initial experiments using 30% Tateho SiC whiskers in AY6 were designed to identify the maximum solids loading level in the binder which would give a moldable mix. Mixes were compounded from 52 to 58 volume percent solids, finally setting on 53 v/o as the best compromise for the current binder and ceramic powder. Variations in powder particle size distribution and binder composition which can be used to further increase solids loading are currently being evaluated.

Both the preblend and the compounder blended powders showed comparable behavior. Initial torques were high as the powder was added to the binder in the mixing head. After all the powder was added the torque decreased toward a steady level.

A post-HIP examination of the microstructure of the two powder types indicated a presence of numerous aggregates (due to insufficient mixing) of AY6 in the compounder-blended composites. Increasing the compounding time from one to three hours was not sufficient to break down all of these aggregates. Therefore, the final molding experiments using the Arco whiskers will utilize preblended powders.

Injection Molding

The injection molding machine used in all molding experiments is a Ton Boy screw type injection molder with hydraulic clamping. It has a two-zone barrel heater and independent nozzle temperature control.

The die used for the majority of molding experiments was used previously in the DOE-sponsored CATE (Ceramic Applications in Turbine Engines) program. By altering the sprue position, the die can be configured to shoot either a single axial turbine blade, two test bars, or simultaneous filling of all three cavities. Figure 4 shows the fill pattern of the blade and one of the bar cavities. The gating is designed to minimize jetting and achieve smooth, uniform cavity filling.

Using this die, blades and bars have been molded at 53 v/o solids loading. The molding parameters have been defined in terms of desired barrel, nozzle, and mold temperatures as well as injection speed and pressure. It was also identified that minimizing mold release led to enhanced as-molded surface quality.

SEM photomicrographs of the injection-molded part indicate that good whisker aspect ratio is maintained through the molding process (Figure 5).

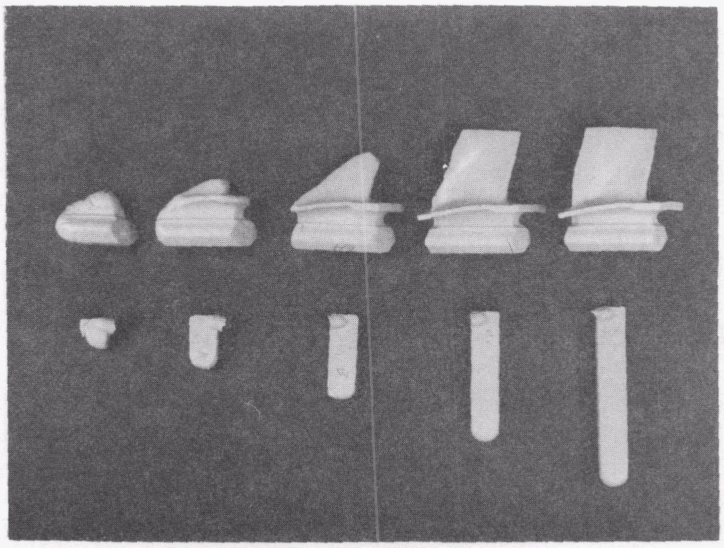

Figure 4: Series of Short Shots Showing Fill Pattern of Si_3N_4/Binder Mix in CATE Turbine Blade and Test Bar Die.

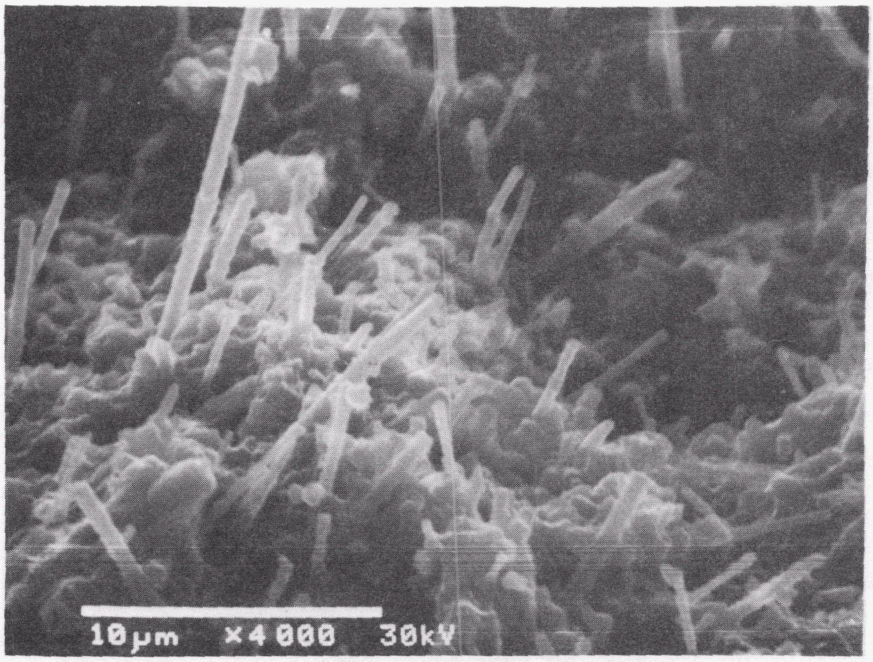

Figure 5: Fracture Surface of Injection-Molded Si_3N_4-30 v/o SiC (Whisker Composite Material

Microfocus x-ray examination of the as-molded bars containing Tateho whiskers indicated presence of high density (metallic) contaminants. Examination of the compounding and molding equipment showed no obvious source of galling and the source of the contaminants is still under examination.

Binder Removal

The molded parts, after numbering, were buried in a supporting Al_2O_3 setter sand. The burnout time/temperature profile used for composite binder removal is identical to that used for monolithic silicon nitride. The composite material exhibits a greater tolerance for rapid burnout cycles than monolithic materials.

Densification

All parts densified to date have used a single densification procedure. The parts are glass encapsulated using the licensed ASEA process and subjected to HIPing. Materials are densified to over 99% of theoretical density (TD = 3.236 gm/cc). After densification, the parts are a dull green in color. As in the case of hot pressed samples, fracture surfaces of the Tateho-containing composite showed negligible pullouts. Figure 6 shows a sequence of green, burned out and HIPed CATE blades made using AY6 + 30% Tateho SiC whiskers.

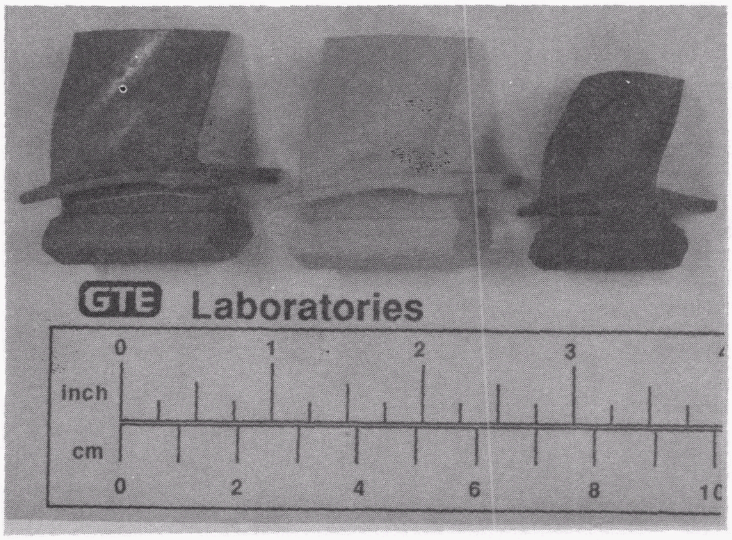

Figure 6: Injection-Molded CATE Blades Prepared from Si_3N_4 - 30 v/o SiC (Whisker) Composite in As-Molded, Dewaxed and Fired State

The main observation made from the densified samples was that a systematic and reproducible warpage occurred in the composite materials during densification. Test bars curved toward the injection molding gate during densification. The blades showed reproducible areas of distortion in the airfoil trailing edge, platform and dovetail. Efforts are now under way to isolate the cause of the distortion.

In summary, experiments to date have identified compounding, molding, binder removal and densification parameters capable of producing composites of 30% SiC whiskers in AY6. The primary outstanding issue is distortion during densification, which is being addressed.

The knowledge gained will be applied to injection molding demonstration of 30% Arco SiC whiskers in AY6.

Microstructure-Mechanical Properties

The extension of densification time from 90 to 400 minutes at the hot pressing temperature has been found to promote grain growth in monolithic AY6 and increase the material's fracture toughness and strength. Figure 7 compares the strength (4 point MOR) up to 1400 degrees C of two AY6 materials densified as described above to an AY6-30 v/o SiC whisker (Arco SC9) composite which required 400 minutes to densify. All three compositions had densities greater than 99% of theoretical. At 1000 degrees C, the AY6 material hot pressed for 400 minutes retains its higher strength compared to AY6 produced by standard process. Both monolithic ceramics exhibit lower values of strength compared to that reinforced with 30 v/o SiC whiskers. The data at higher temperatures (> 1200 degress C) show two monolithic materials to be essentially equivalent in strength. In this temperature regime, the softened intergranular glass phase controls the mechanical properties. Fractographic analysis has shown that at these higher temperatures subcritical crack growth related to intergranular glass phase viscosity occurs and results in strength degradation.

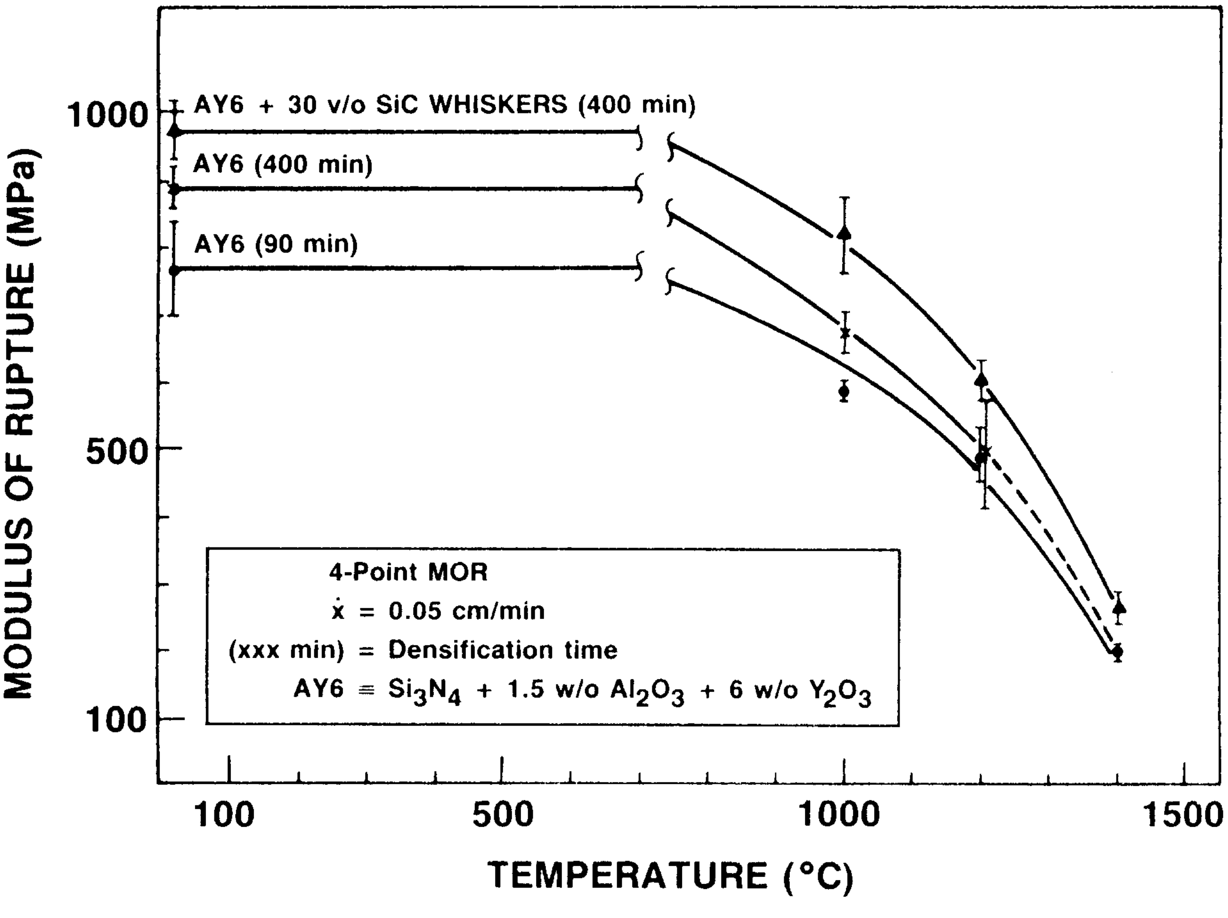

Figure 7: Modulus of Rupture of AY6-Si_3N_4 Ceramics and (a) AY6-30 v/o SiC whisker Composite up to 1400°C

As shown, the strength improvement by SiC whisker reinforcement is retained up to 1400 degress C under the fast fracture conditions imposed by this MOR test (crosshead rate = 0.05 cm/min). The increased strength at the higher temperatures appears to be related to an increased resistance to subcritical crack growth of the composite. Fractography of controlled flaw samples broken at 1200°C has shown an increase in crack depth of 82% and half crack length of 229% prior to fast fracture for the AY6 material hot pressed for 90 minutes. The respective increases for the AY6-30 v/o SiC whisker composite under the same conditions were 60% and 156%.

The results of creep studies conducted in collaboration with North Carolina State University have shown that, although the fast fracture strength is increased at 1200°C and above by whisker additions, under conditions of low strain rate, the steady state creep resistance of the monolith and composite are essentially the same at 1200°C, while the composite creeps faster at 1300 degrees C (Figure 8). This behavior has been atributed to an increased stability of the intergranular glass phase of the composite due to impurities contained in the Arco SC9 whiskers,[2] which reduces its tendency to crystallize. Under the conditions employed in this testing, a four hour anneal at the test temperature prior to test initiation, the monolithic AY6 was shown by TEM to contain a much larger percentage of devitrified glass phase compared to the composite. Hence, initially at 1250°C (1520°K) the composite exhibited a higher creep rate. However, eventually the creep curves of the two materials again became parallel. TEM analyses of tested specimens have indicated that the glass phase of the composite continues to devitrify during testing.

Mechanical property characterization of silicon nitride-based ceramics has also addressed the issue of potential rising R-curve behavior for composites containing SiC whiskers. MOR bars of monolithic AY6 and an AY6 + 30 v/o SiC whisker (Arco SC9) composite were indented with a single Vickers indentation. The indentation load was varied from 1 to 50 kg and the test bars annealed in argon at 1200°C for one hour to relieve the residual strain produced by the indentation process. The bars were broken in four point loading at a crosshead rate of 0.02 in./min. Fracture toughess was calculated from the strength of indented specimens and crack size data. Figure 9 is a plot of log MOR versus log indentation load. Both materials show linear decreases in log MOR as log load increases. Linear regression analysis of the data yields slopes of -0.3334 for AY6 and -0.3612 for the composite. Materials which exhibit a fracture toughness which is independent of crack extension have a slope of -1/3 for this type of plot. Fracture toughness of both materials is, within the limits of indentation cracks produced, independent of crack size.

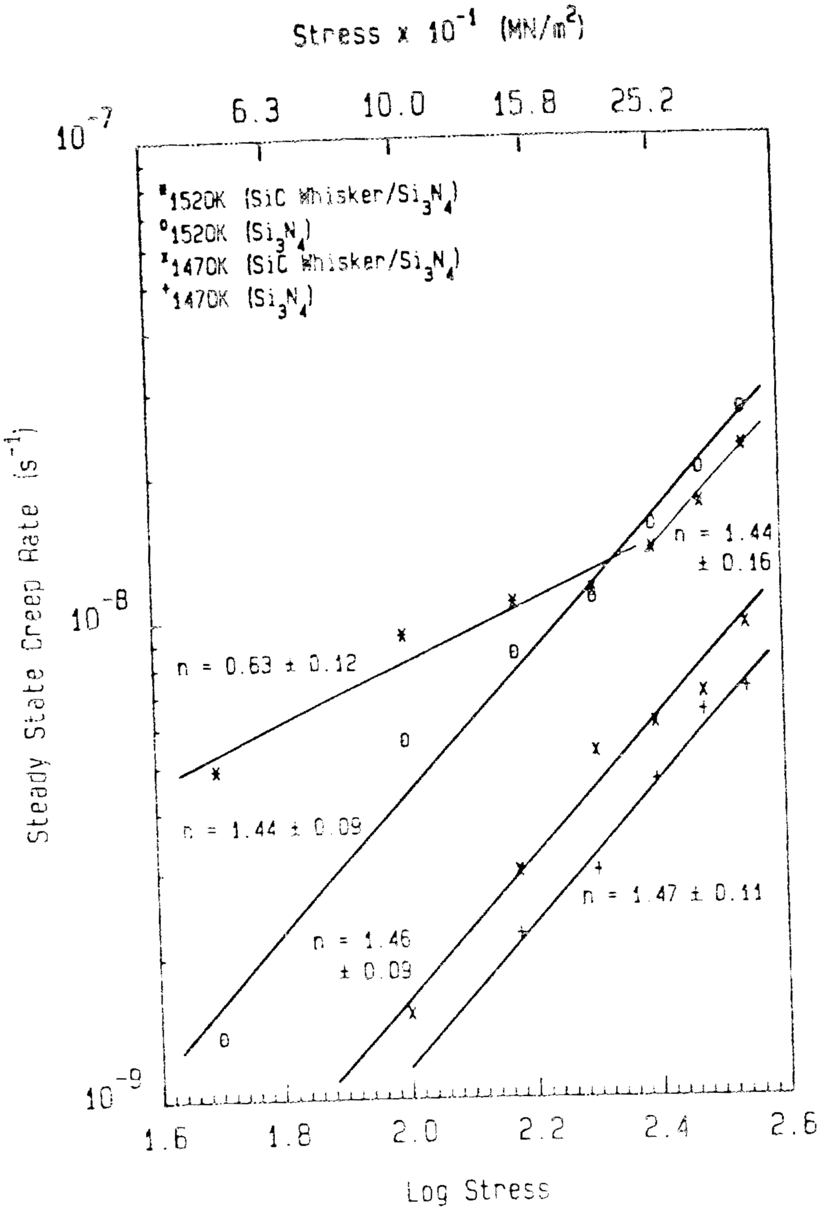

Figure 8: Steady State Creep Test of AY6 Si_3N_4 and an AY6-30 v/o SiC Whisker Composite (After R.D. Nixon, et al.)

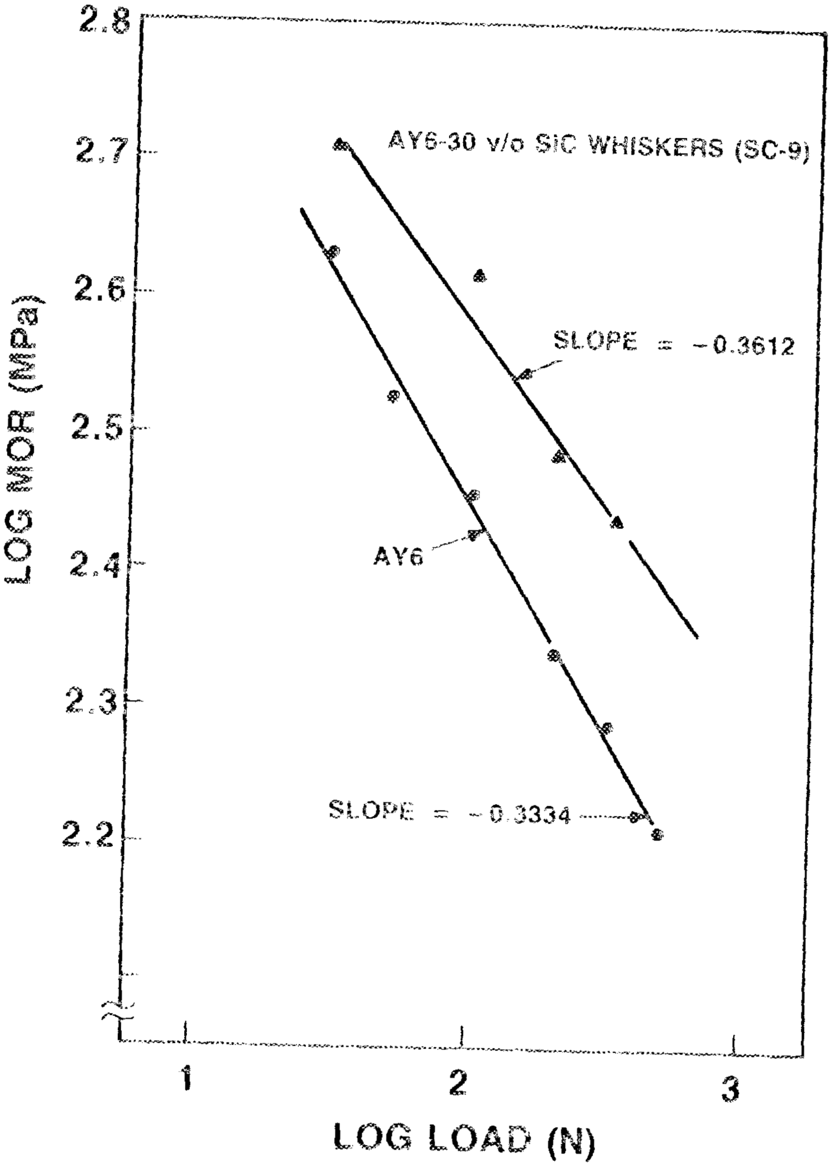

Figure 9: Measured Modulus of Rupture (MOR) of Si_3N_4 Monolith and 30 v/o SiC Whisker Composite Specimens with Vickers Indentations Produced at Various Loads.

Status of Milestones

Milestone 122304, Demonstration of Green CATE Turbine Blade, was completed by December 15, 1986. Overall execution of the program is on schedule.

Publications

S.T. Buljan, J.G. Baldoni, M.L. Huckabee, and G. Zilberstein presented "Dispersion-Toughened Si_3N_4" at the CCM, 11/30/86 (in print).

S.T. Buljan and G. Zilberstein presented "Microstructure Development in SiC Whisker-Reinforced Si_3N_4 Composites" at the MRS Meeting, Boston, MA, 12/3/86 (in print).

S.T. Buljan, J.G. Baldoni, and M.L. Huckabee, "Si_3N_4-SiC Composites," *Ceram. Bull.*, Vol. 66, No. 2, 1987.

References

1. R.D. Nixon, et al., "Deformation Behavior of SiC Whisker-Reinforced Si_3N_4," Mat. Res. Soc. Proceedings, *Advanced Structural Ceramics* (in print), presented at MRS Symposium, Boston, MA, 12/3/86.

SiC-Whisker-Toughened Silicon Nitride

M. Martin and H. Yeh (AiResearch Casting Company), and J. Schienle
(Garrett Turbine Engine Company)

Objective/scope

The objective of this twenty-four month program is to develop the technology base for fabricating a ceramic composites consisting of silicon carbide whiskers dispersed in a dense silicon nitride matrix. This is to be accomplished by using slip casting as the green shape forming method, and by using HIP'ping or sinter/HIP'ping as the densification method. An iterative experimental approach is used throughout the entire program.

The goal of the program is a two-fold increase in fracture toughness over the unreinforced silicon nitride matrix [92% GTE Sylvania (GTE) SN-502 Si_3N_4 + 6% Y_2O_3 + 2% Al_2O_3, designated as Code 2] without a degradation of other properties. AiResearch Casting Company (ACC) is responsible for developing the fabrication techniques and providing specimens to Garrett Turbine Engine Company (GTEC). GTEC is responsible for determining the physical and mechanical properties, including fracture toughness, and for evaluating the microstructure. Allied-Signal Engineered Materials Research Center (EMRC) provides analytical assistance.

Technical progress

Processing Activities

Si_3N_4/SiC Composites (Encapsulated HIP Studies)

Baseline silicon nitride and silicon nitride/silicon carbide whisker composite formulations (containing 10%, 20%, 30% and 40 weight % ARCO SC-9 silicon carbide whiskers) were prepared at ACC. A flow diagram for the whisker cleaning and composite slip making process is shown in Figure 1.

Powder preparation of the silicon nitride involved air classification to remove large (>40 micron) particles before milling and to maintain a narrow particle size distribution after ball milling. Cleaning of the silicon carbide whiskers was performed to remove contamination in the whiskers prior to incorporation with the milled silicon nitride matrix material. The incorporation of silicon carbide whiskers with the matrix powder was accomplished by liquid state blending/dispersion rather than milling, which was the method used previously. This is to avoid possible whisker damage and reduction in whisker aspect ratio.

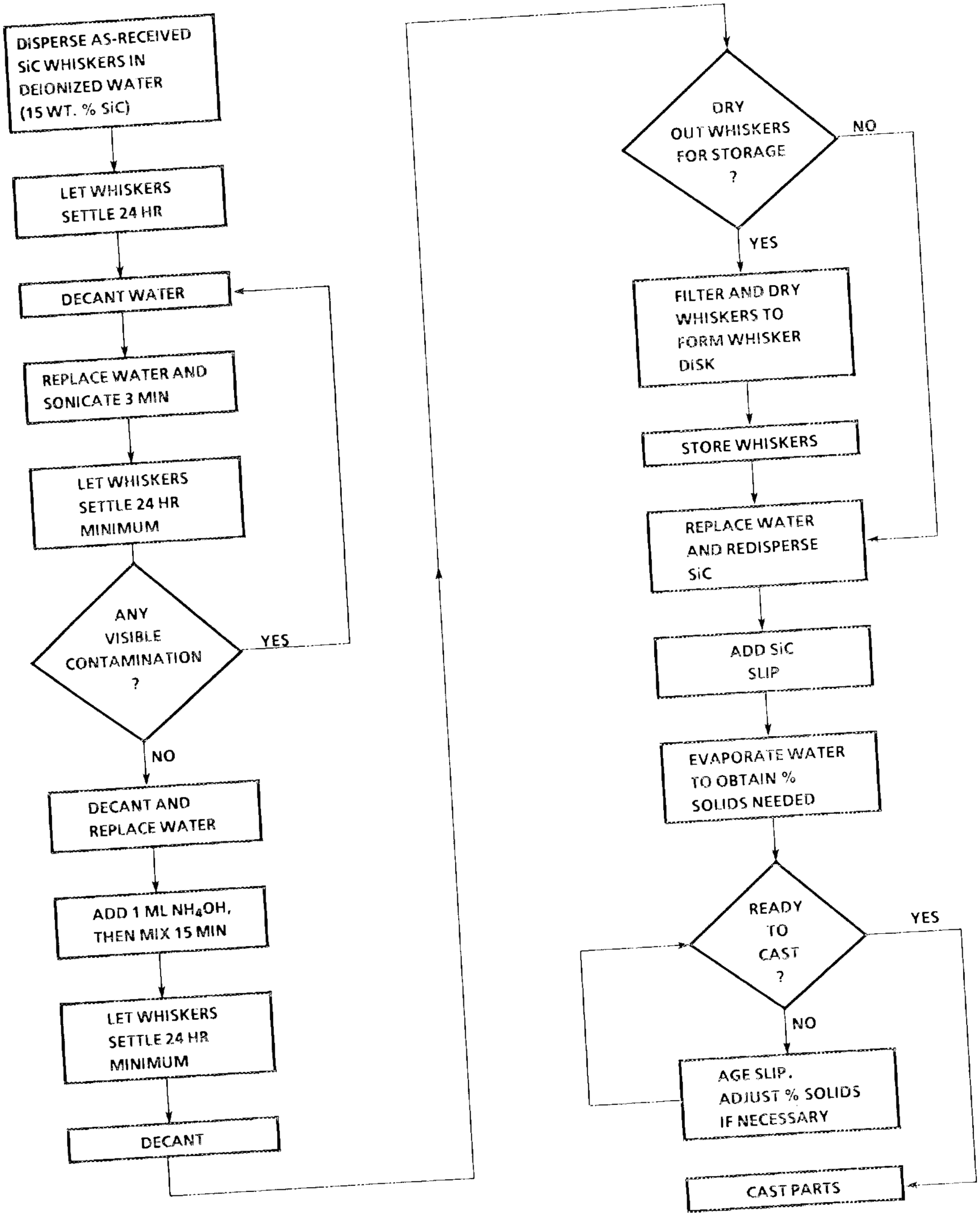

Figure 1. Flow Diagram for Whisker Cleaning and Composite Slip Making Process

Slip preparation involved mixing silicon nitride slip with a redispersed silicon carbide whisker slurry. The silicon nitride/silicon carbide slurries were placed on a hot plate and constantly stirred (using a Lightning mixer) to evaporate water and raise the solids content of the slip to 75% solids or to the highest possible % solids level while maintaining a stable slip rheology. (The baseline slip did not require evaporation.) Among the prepared slips, three slips (baseline, 10%, and 20%) had solids contents of 72 to 75 weight %. The 30% and 40% composite slips had lower solids content (approximately 60 weight %).

All formulations were slip cast into cylindrical billets 2½" in diameter and 3½" in length. The cylindrical specimens were dried at 120°F for two days and placed in a 400°C drying cycle for one day.

Sixteen composite billets (four each of 10, 20, 30, and 40 weight %) and four baseline billets were fabricated using the procedures described above. These twenty billets were fabricated in two batches. The first batch of billets was encapsulated in niobium for HIP'ping. A HIP run (1750°C in 28-ksi argon) containing four billets, one of each whisker loading, and one baseline billet was aborted due to an equipment problem. A subsequent HIP run containing the remaining four composite billets was aborted due to a niobium can leak, evidently caused by billet outgassing. The billets from both HIP runs were intact but further processing of these billets has been postponed.

The densification procedures for the second batch of billets was slightly modified. A 1000°C/2-hr presintering step in 10-psi argon was added to prevent outgassing during encapsulated HIP'ping. This step was added since TGA analysis of green composite after having been air-dried at 400°C indicated that vapor is released between 400°C and 700°C. Four of the billets, one of each whisker loading, were processed through presintering, encapsulating, and leak checking. These billets were subsequently HIP'ped at 1750°C in 28-ksi argon for 4 hr. Near-theoretical densities were achieved for all compositions (Table 1). Microstructural analysis (SEM and optical) was performed on small samples taken from outer portions of the densified billets. Figure 2 shows the optical micrographs of the polished sections of the composites containing the higher three SiC whisker loadings.

TABLE 1

HIP'ped DENSITIES OF Si_3N_4/SiC COMPOSITES

Whisker Loading, %	Density, gm/cc
10	3.23
20	3.23
30	3.23
40	3.20

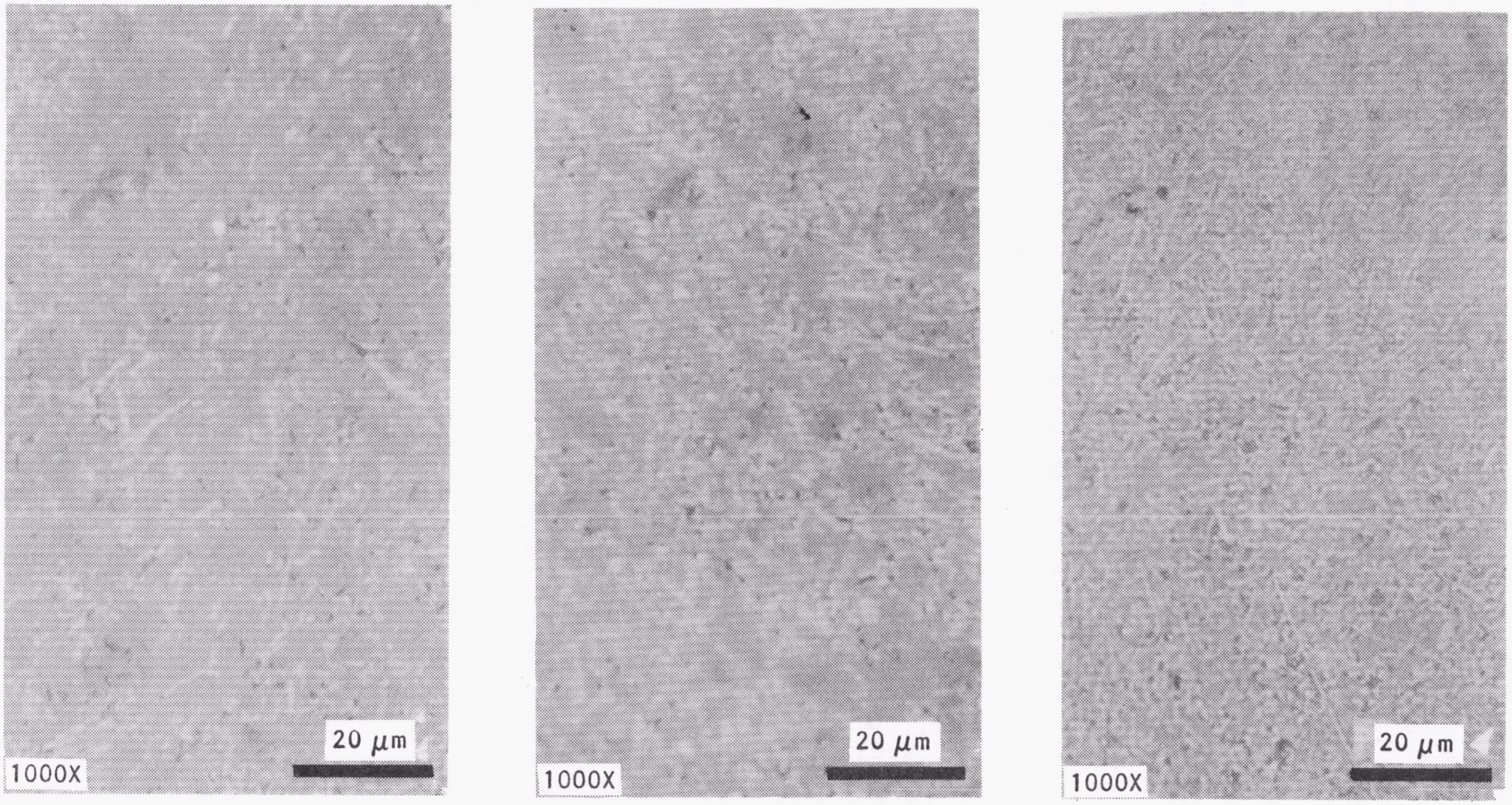

a. 20% SiC Whisker

b. 30% SiC Whisker

c. 40% SiC Whisker

Figure 2. Optical Micrographs of Composites HIP'ped at 1750°C and 28 ksi

The results indicated that all microstructures were good and contained uniformly-dispersed whiskers with high aspect ratio characteristics. Based on the microstructures, the 20, 30, and 40% SiC_w composites all have high potential for property improvement. Therefore, the optimum whisker loading will be selected based solely on mechanical property data which will be generated during the next reporting period. Additionally, all remaining composite billets (one each at 10, 20, 30, and 40% SiC_w loadings) will be processed through densification prior to selection of the optimum whisker loading.

Si_3N_4/SiC Composites (Unencapsulated Sinter-HIP Studies)

Several composite samples for sinter-HIP studies were co-processed at ACC with the billets fabricated for HIP'ping studies, as described in the previous section. Five sinter-HIP runs were experimented to densify unencapsulated Si_3N_4/SiC composites (10, 20, 30, and 40 weight % ARCO SC-9). The sinter-HIP parameters and results are summarized in Table 2.

TABLE 2

SUMMARY OF ACC SINTER-HIP RUNS FOR Si_3N_4/SiC COMPOSITES

Composition	Green Density, gm/cc	Sintered Density, gm/cc				
10 wt % SiC	2.02	2.12	2.31	--	--	2.30
20 wt % SiC	1.91	2.06	2.26	2.18	--	2.22
30 wt % SiC	1.42	1.52	1.64	1.51	1.83	1.78
40 wt % SiC	1.40	1.54	1.81	--	1.52	--
Sinter-HIP Parameters	Peak Temperature, °C	1750	1850	1800	1850	1900
	Atmosphere*	Nitrogen	Argon	Argon	Argon	Nitrogen
	Hold Time	4 hr	2 hr	3 hr	2 hr	20 min

*All runs were with 1500 psi pressure at peak temperature except the 1900°C run (200 psi).

For all runs, the composite sample did not exhibit any significant densification.

Additional sinter-HIP runs were performed at EMRC at 5000-psi pressure. The sinter-HIP parameters and results are shown in Table 3.

TABLE 3

SUMMARY OF EMRC SINTER-HIP RUNS FOR Si_3N_4/SiC COMPOSITES

Composition	Green Density, gm/cc	Sintered Density, gm/cc	
10 wt % SiC	2.02	2.17	2.26
20 wt % SiC	1.91	2.07	2.09
30 wt % SiC	1.42	1.41	1.44
40 wt % SiC	1.40	1.48	1.55
Sinter-HIP Parameters	Peak Temperature, °C	1800	1800
	Atmosphere*	Nitrogen	Argon
	Hold Time	4 hr	4 hr

*All runs were with 5000 psi.

These results were in agreement with the sinter-HIP results from 1500 psi-runs at ACC. No significant densification was observed.

Sintered Reaction Bonded Silicon Nitride (SRBSN) Composites

Compositions containing 0%, 10%, and 20% silicon carbide whiskers in the Al_2O_3 and Al_2O_3-free formulations were slip cast, dried, and nitrided. Additional composite samples previously made in the Al_2O_3 and Al_2O_3-free formulations, which contained 15% ARCO whiskers, were sinter-HIP'ped in both nitrogen and argon. The sinter-HIP parameters and results are summarized in Table 4. Only the baseline Code 7 material densified to near-theoretical density in both sinter-HIP runs. The Code 7 composite densified in argon but not in nitrogen. The Code 9 composite did not densify in argon or nitrogen. All specimens exhibited weight loss during sinter-HIP'ping (both runs). Microstructural analyses were conducted on specimens from the 1500-psi nitrogen sinter-HIP run. The results are noted in the COMPOSITE ANALYSIS section. All the results indicated that the Al_2O_3-free SRBSN composites cannot be fabricated into dense composites.

Composite Analysis

Microstructure of Si_3N_4 Matrix Composite HIP'ped at 1800°C

The microstructure of an ARCO SC-9 whisker-reinforced Code 2 Si_3N_4 matrix composite was characterized by scanning transmission electron microscopy (STEM) at the Allied Signal Engineered Materials Research Laboratory. This composite was fabricated and tested for strength and toughness during the previous semiannual reporting period. This composite was slip cast, presintered (1400°C in 10-psi nitrogen for 1 hr), encapsulated in niobium, then HIP'ped to full density (1800°C in 28-ksi nitrogen for 4 hr). A summary of the composite's properties is shown in Table 5.

TABLE 4

SUMMARY OF SINTER-HIP DATA FOR SRBSN COMPOSITES

Composition		Nitrided Density, gm/cc	Sinter-HIP'ped Density, (gm/cc)	
Matrix*	Reinforcement			
Code 7	---	2.69	--	3.26
Code 7	---	2.69	3.28	--
Code 7	---	2.69	--	3.25
Code 7	15 wt % ARCO	2.45	--	3.21
Code 7	15 wt % ARCO	2.45	--	3.21
Code 7	15 wt % ARCO	2.45	2.60	--
Code 7	15 wt % ARCO	2.45	2.56	--
Code 9	15 wt % ARCO	2.33	--	2.75
Code 9	15 wt % ARCO	2.33	2.29	--
Code 9	15 wt % ARCO	2.33	--	2.41
Code 9	15 wt % ARCO	2.33	2.33	--
Code 9	15 wt % ARCO	2.33	2.30	--
Sinter-HIP Parameters		Peak Temperature, °C	1800	1800
		Atmosphere	1500 psi Nitrogen	1500 psi Argon
		Hold Time	4 hr	2 hr

*Code 7 contains 6 wt % Y_2O_3 and 2 wt % Al_2O_3 sintering aids.
Code 9 contains 6 wt % Y_2O_3 sintering aid (no Al_2O_3).

TABLE 5

PROPERTIES OF 20 WEIGHT % SiC COMPOSITE HIP'ped AT 1800°C AND 28 KSI FOR 4 HR

Density, gm/cc	Strength*	Toughness,**
3.24	131 ksi (903 MPa)	6.45 ksi $\sqrt{in.}$ (7.10 MPa $\sqrt{in.}$)

*4 pt flexural, 1.5" outer span, 0.75" inner span, 1/8" x 1/4" cross section
**Chevron Notch bend test with 1/4" x 1/4" cross section

A general view of the composite microstructure is shown in Figure 3. The STEM results indicate that this composite has a fine-grained matrix. The average grain size is 0.57 microns. Most grains are equiaxed, but some are elongated. All grains were fully converted to the beta-phase. These results indicate that the composite's improved toughness (20% greater than 5.37 ksi $\sqrt{\text{in.}}$ for monolithic Code 2 Si_3N_4) is attributed to the SiC whisker reinforcement rather than to an acicular grained microstructure of the Si_3N_4 matrix. It is interesting to note that this material (20% SiC_w/80% Si_3N_4 matrix) exhibited a significant improvement over the monolithic in both strength and toughness, while other investigators observed a decrease in strength and only a slight improvement in toughness in a hot-pressed Si_3N_4 matrix composite containing the same amount of SiC whisker (20%).[1]

The results of the grain boundary and grain boundary pocket STEM analyses suggested that the secondary phases present after presintering reacted during HIP'ping to produce a homogeneous second phase. The grain boundary pockets are amorphous and have a composition of 13.7 ±2.4 at.% Al, 67.8 ±2.8 at.% Si, and 18.5 ±1.1 at.% Y (Figure 4). The composition of the grain boundaries was similar (14 at.% Al and 15 at.% Y) and seemed to be independent of whether a grain boundary separated two Si_3N_4 grains or a Si_3N_4 grain and a SiC whisker. However, the film separating SiC whiskers from Si_3N_4 grains was 5 to 10 nm in thickness, compared to 1 to 2 nm for grain boundaries between Si_3N_4 grains (Figure 5).

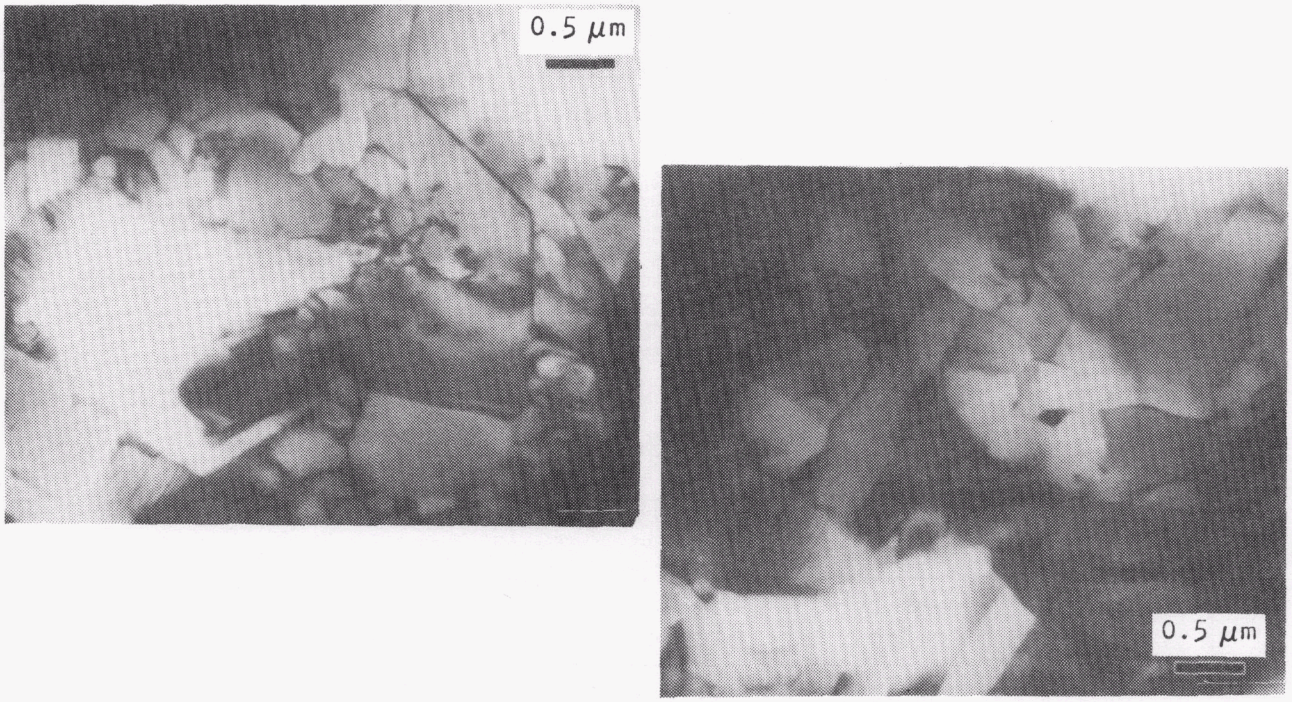

Figure 3. General View of 20% ARCO SC-9 Whisker-Reinforced Si_3N_4 Composite

---

[1] Buljan, S. T., Baldone, J. G., and Huckabee, M. L., "Si_3N_4-SiC Composites," Am. Ceram. Soc. Bull., 66 [2] 347-352 (1987).

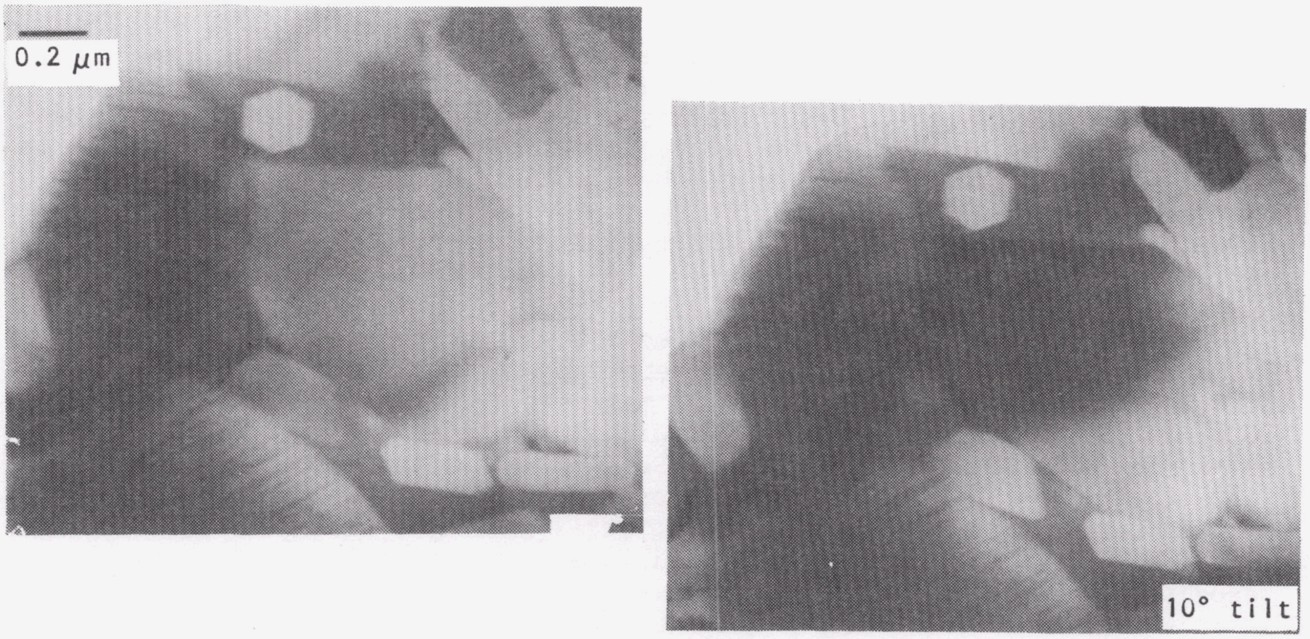

Figure 4. Non-Crystalline Grain Pockets as Demonstrated by Tilting the Sample for 20% ARCO SC-9 SiC Whisker-Reinforced Silicon Nitride

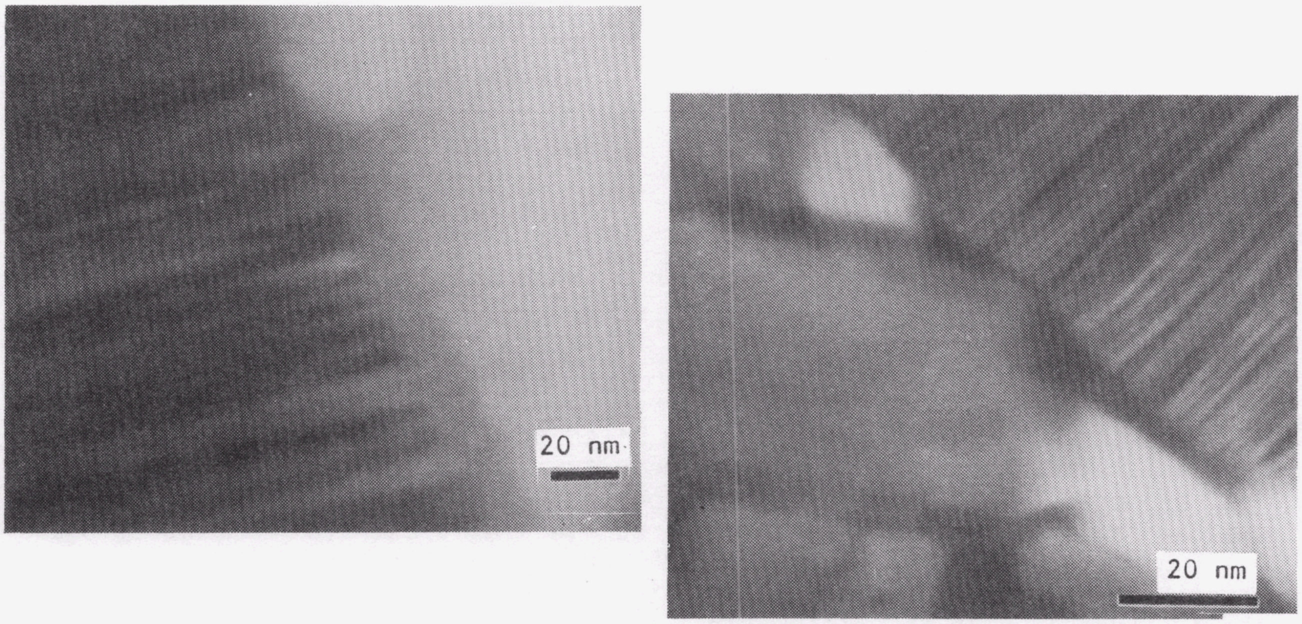

Figure 5. Grain Boundaries Between SiC Whiskers and Si_3N_4 Grains are 5 to 19 nm Thick Compared to 1 to 2 nm for Those Between Si_3N_4 Grains

The ARCO SC-9 whisker-toughened Si_3N_4 composite exhibited a slight degree of whisker degradation. Throughout the composite were micron-sized microcrystalline regions. In some of these regions very fine striated structures, which appear to be ARCO whiskers that have undergone a preliminary stage of degradation, are present. Based on this observation, the temperature for subsequent HIP runs for the program was reduced from 1800°C to 1750°C in order to reduce whisker degradation and to further improve the composite properties.

Strength, Toughness, and Microstructure of Si_3N_4 Matrix Composites HIP'ped at 1750°C

The strength and toughness of three SiC whisker-reinforced matrix composites fabricated during the previous reporting period were characterized at GTEC. All three composites had Code 2 matrices. One was reinforced with 20 wt.% ARCO SC-9; one was reinforced with 30 wt.% Tateho SCW #1; and one was reinforced with 20 wt.% Tateho SCW #1-S. All were slip cast, then presintered (1200°C in 10-psi nitrogen for 1 hr), encapsulated in niobium, then HIP'ped to full density (1750°C in 28-ksi nitrogen for 4 hr). The strength was measured using four-point bending with outer and inner spans of 1.5 in. and 0.75 in., respectively. The test bars were nominally 2 in. long and 0.250 by 0.125 in. in cross section. The fracture toughness was measured using Chevron Notched bend bars which were nominally 2 in. long and 0.250 by 0.250 in. in cross section. The results are shown in Table 6.

TABLE 6

PROPERTIES OF $SiC-Si_3N_4$ COMPOSITES* HIP'ped AT 1750°C

Material	Density, gm/cc	Strength, ksi (MPa)	Toughness, ksi $\sqrt{in.}$ (MPa $\sqrt{in.}$)
20% ARCO SC-9/Si_3N_4	3.23	69.8 (481)	5.45 (6.00)
30% Tateho SCW #1/Si_3N_4	3.23	51.4 (354)	4.34 (4.77)
20% Tateho SCW #1-S/Si_3N_4	3.23	54.6 (377)	4.15 (4.57)

*Containing metallic inclusions

All three composite materials exhibited poor strength and no improvement in fracture toughness. Fractography results indicated that the poor mechanical properties were attributed to large, dark inclusions. SEM micrographs of typical failure origins in the ARCO composite are illustrated in Figures 6 and 7. Figure 6 shows an origin in the ARCO composite which is high in iron, chrome, and nickel (possibly contamination from a stainless steel). Figure 7 shows an origin high in yttrium (from the Y_2O_3 sintering additive) which also has a small amount of iron present.

SEM analysis of the ARCO fracture surfaces suggested that the SiC whiskers were not severely degraded during HIP'ping (1750°C for 4 hr at 28 ksi). Figure 8 shows some SiC whiskers typical of those observed on the fracture surfaces.

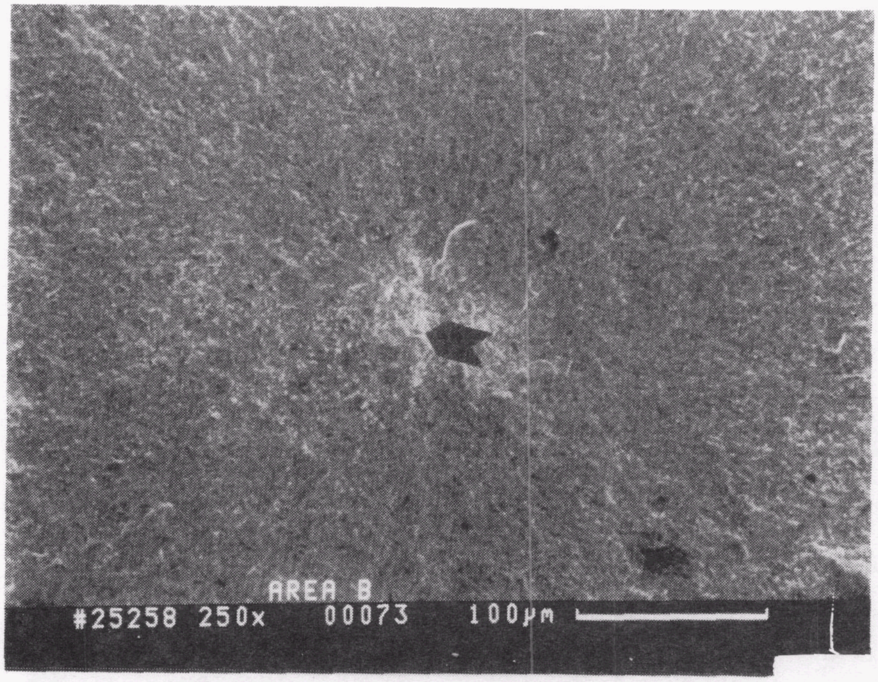

Figure 6. Failure Origins in the ARCO Whisker Composite Were Predominantly High in Iron, Chrome, and Nickel.

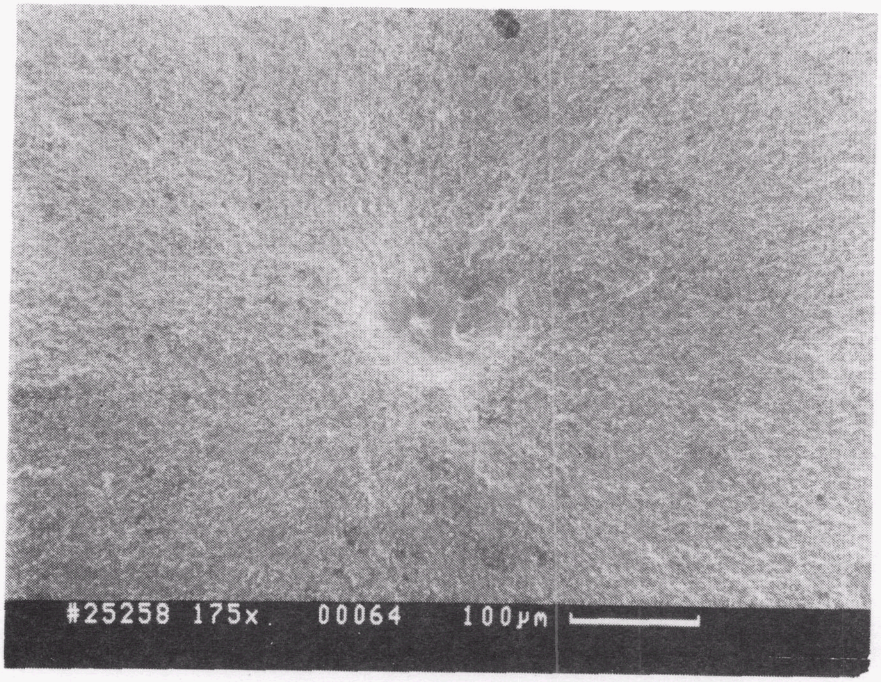

Figure 7. The ARCO Whiskers Composite Also Exhibited Some Failure Origins Which Were High in Yttria.

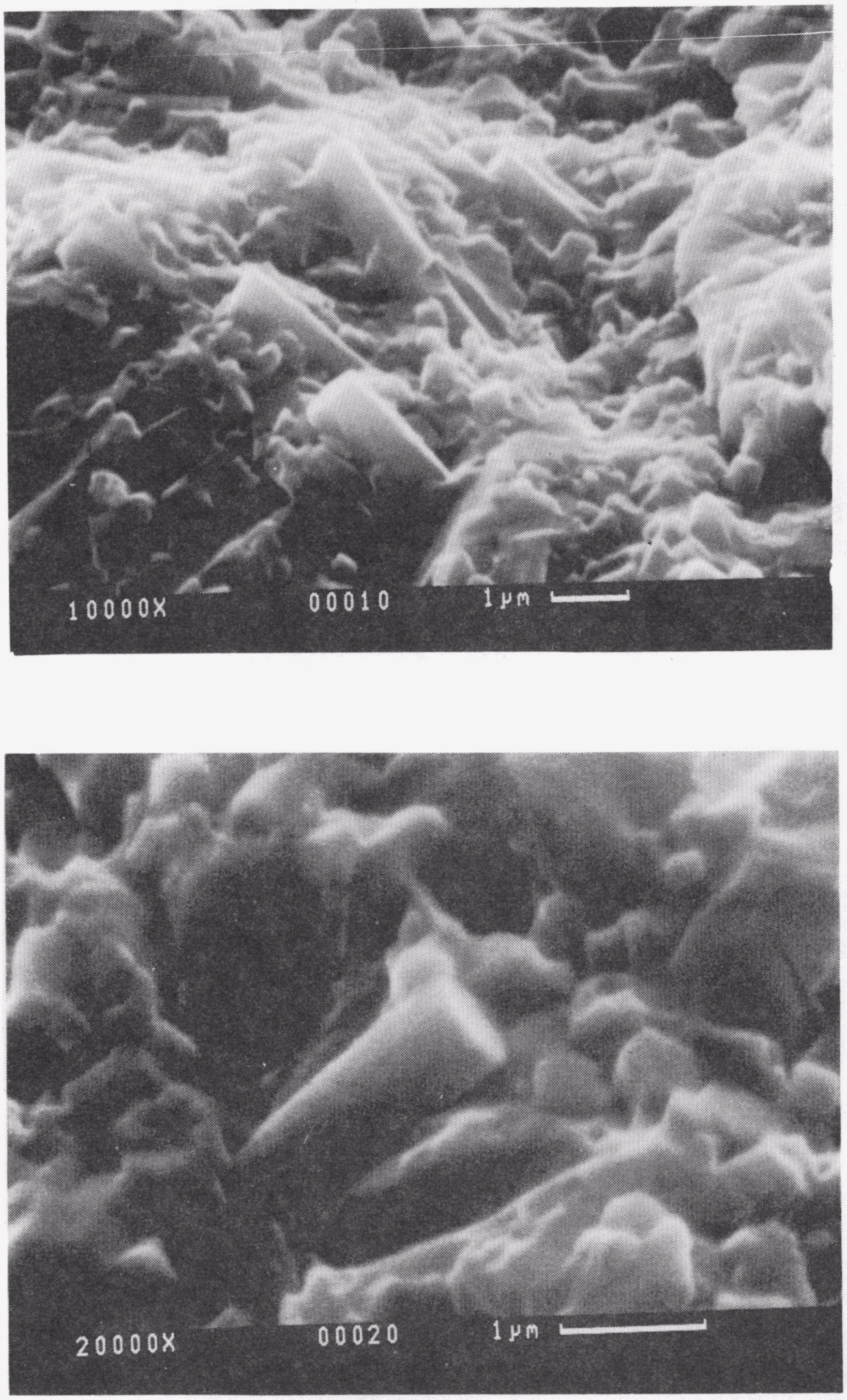

Figure 8. The ARCO Whiskers Observed on the Composites Fracture Surfaces

Metallography was performed on the ARCO whisker composite to determine the composite microstructure. The primary emphasis of this analysis was to identify the whisker distribution and orientation characteristics. Microstructures typical of the top, middle, and bottom of billets are shown in Figures 9, 10, and 11, respectively. The results suggest that the whiskers were relatively well dispersed, although there appears to be some degree of Si_3N_4 agglomeration. No whisker settling effects were observed (top, middle, and bottom of billet contain the same concentration of SiC whisker). The metallic inclusions, which were responsible for the poor mechanical properties discussed earlier, also appeared to be randomly dispersed. No preferred whisker orientation was observed in this composite.

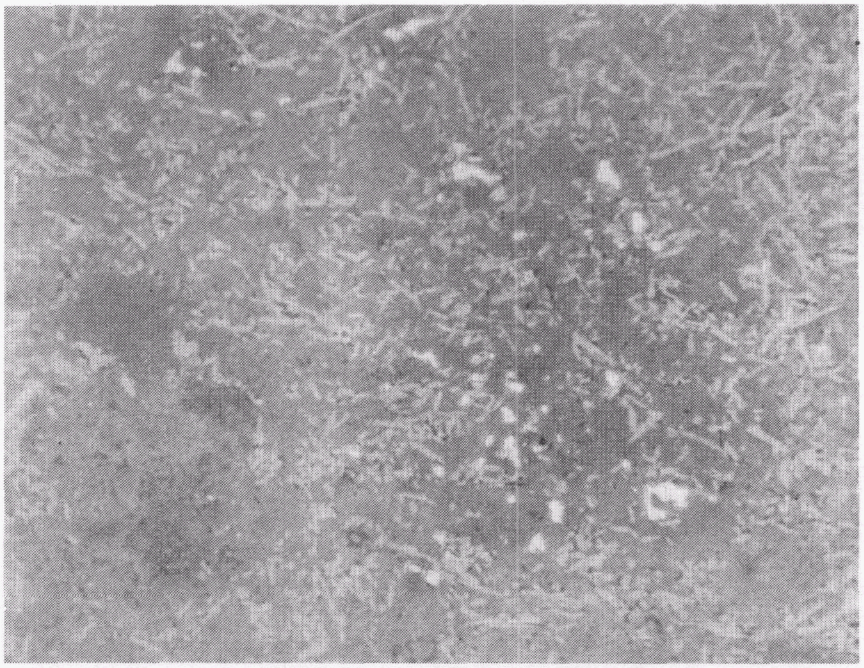

Figure 9. Micrograph from Top Section of Cylindrical Composite Billet

Sinter Reaction Bonded Si_3N_4 (SRBSN) Composites

The microstructures of Code 7 and Code 9 unencapsulated sintered-HIP'ped SRBSN composites were characterized. Emphasis was placed on determining the effect of sinter/HIP'ping (1750°C in 1500-psi nitrogen for 4 hr) on the SIC whiskers. These composites exhibited almost no densification during sinter/HIP'ping (Table 7) relative to co-processed monolithic Code 7, which reached near-theoretical density.

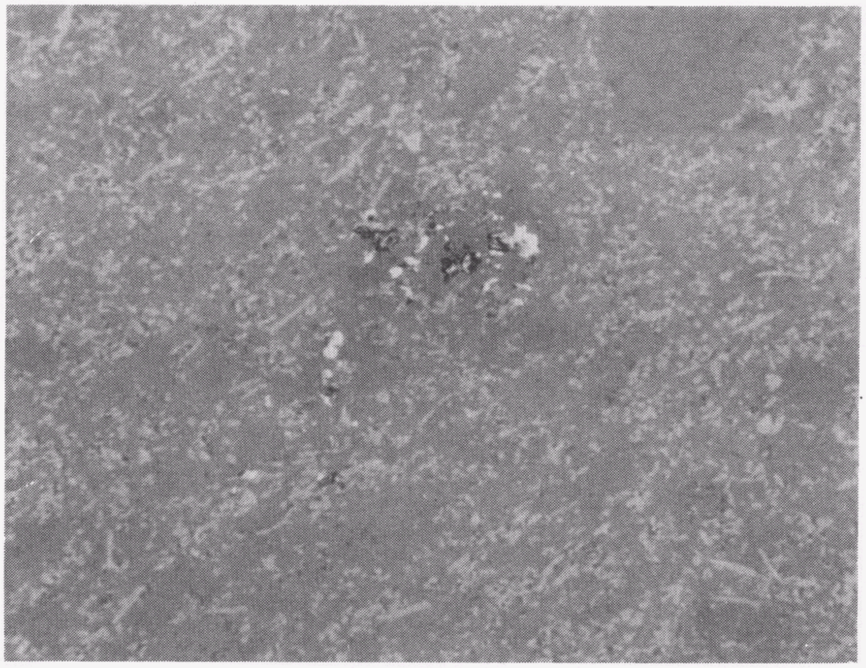

Figure 10. Micrograph from Middle Section of Cylindrical Composite Billet

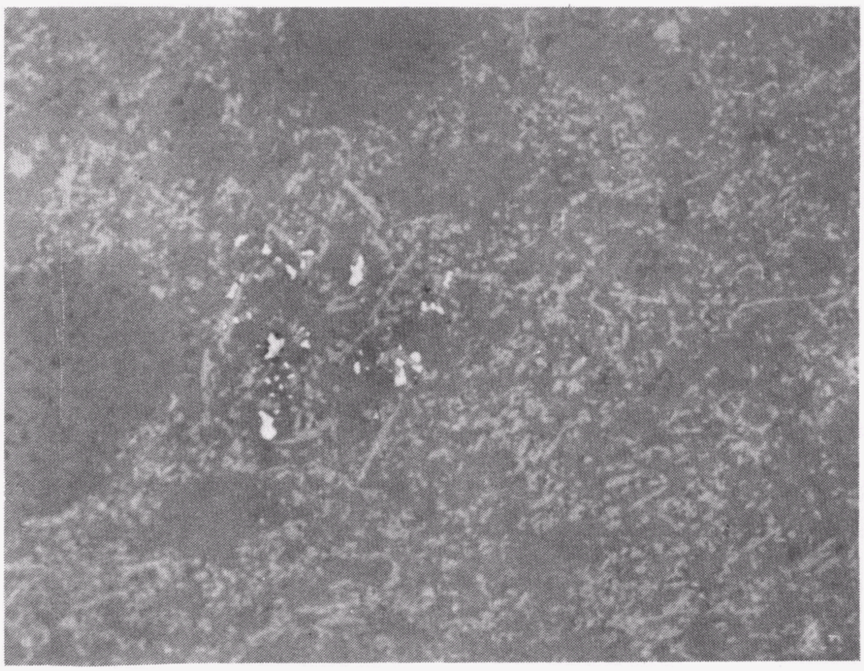

Figure 11. Macrograph from Bottom Section of Cylindrical Composite Billet

TABLE 7

SINTER/HIP RESULTS FOR SRBSN COMPOSITES

Matrix*	Reinforcement	Nitrided Density, gm/cc	HIP'ped Density, gm/cc	Percent Increase
Code 7	15% ARCO	2.54	2.67	5.1
Code 9	15% ARCO	2.30	2.20	-4.3

*Code 7 contains 6 wt % Y_2O_3 and 2 wt % Al_2O_3 sintering aids.
Code 9 contains 6 wt % Y_2O_3 sintering aid.

Preliminary SEM analysis of fracture surfaces provided no evidence of the presence of SiC whiskers in any of the composites. The results suggest the SiC whisker reacted during sinter/HIP'ping since the whiskers were present after nitridation (Figure 12). These composite specimens were analyzed further using metallography. The results, shown in Figures 13 and 14, agree with the preliminary SEM results. The microstructures are all porous Si_3N_4 bodies with no detectable whisker. The bright specks seen in all of the microstructures are most likely the iron catalyst for nitriding the silicon during the reaction bonding process. The Code 7 composites exhibited uniform microstructures while the Code 9 matrix composite had a mottled appearance.

X-ray diffraction (XRD) was performed on the SRBSN composites to determine whether a SiC phase was still present in the system. No evidence of SiC was observed. The major phase present was beta Si_3N_4 and the minor phase was $Y_2Si_3N_4O_3$ (yttrium silicon nitrate). Surprisingly, the peaks for this minor phase were quite strong and possibly suggested that 10 to 20 mole percent was present.

The conclusion based on these results is that the SiC whiskers in these SRBSN-based composites did react during the sinter/HIP process to form another phase, possibly beta Si_3N_4 and/or $Y_2Si_3N_4O_3$. In contrast, earlier Si_3N_4 powder-based composites, which were densified using encapsulated HIP'ping, still contained SiC whiskers. The differences in the whisker stability may be attributed to (a) protection of the whiskers by the encapsulant used for the Si_3N_4 powder-based composites, and/or (b) reaction induced by the presence of iron in the SRBSN-based composites (iron is used as a nitriding catalyst for reaction bonding). Efforts involving unencapsulated sinter/HIP'ping of Si_3N_4 powder-based composites, will provide additional information as to the cause of whisker degradation, since the nitriding catalyst (iron) will not be present.

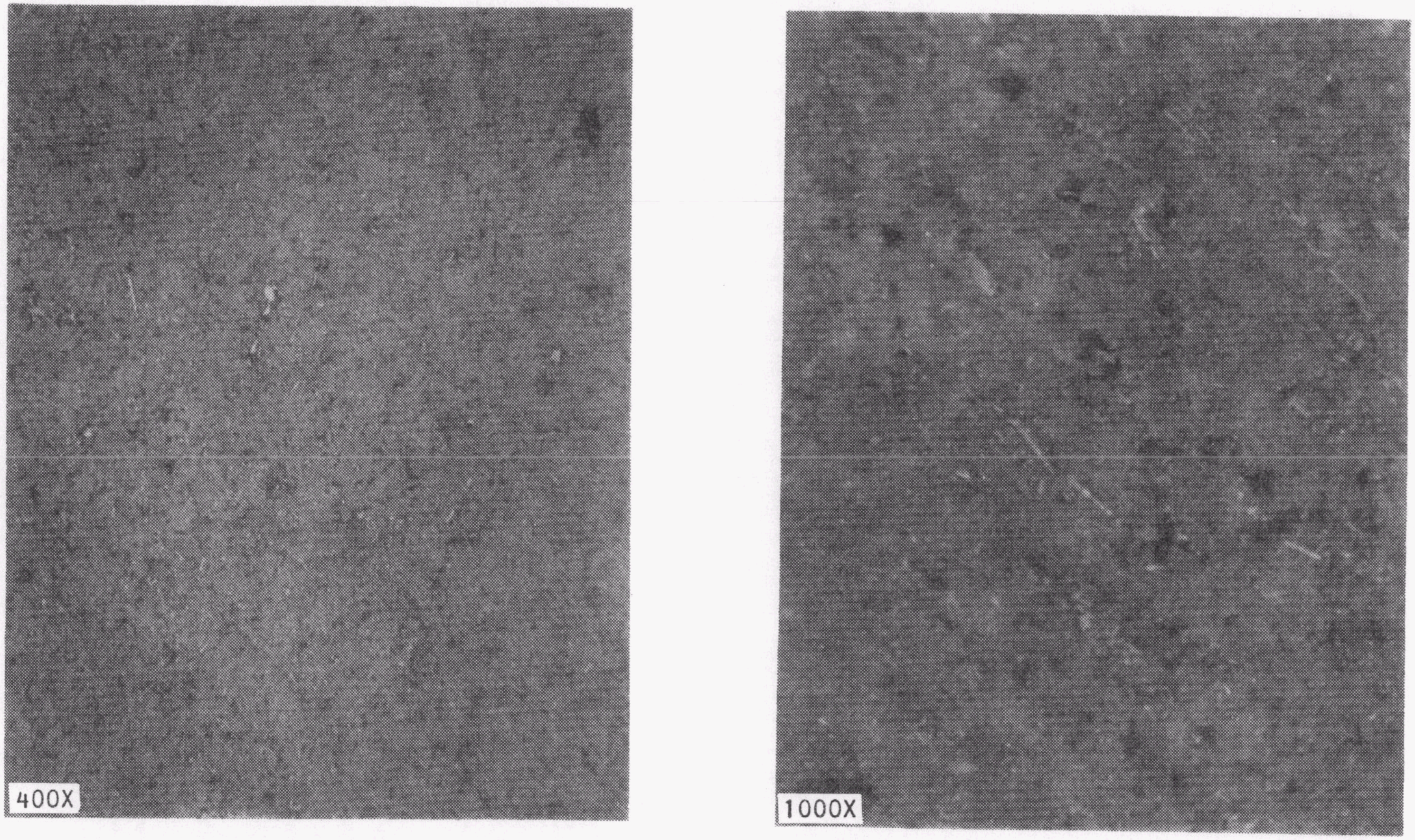

Figure 12. ARCO Whiskers Were Present in the Code 7 Matrix After Nitridation (Reaction Bonding).

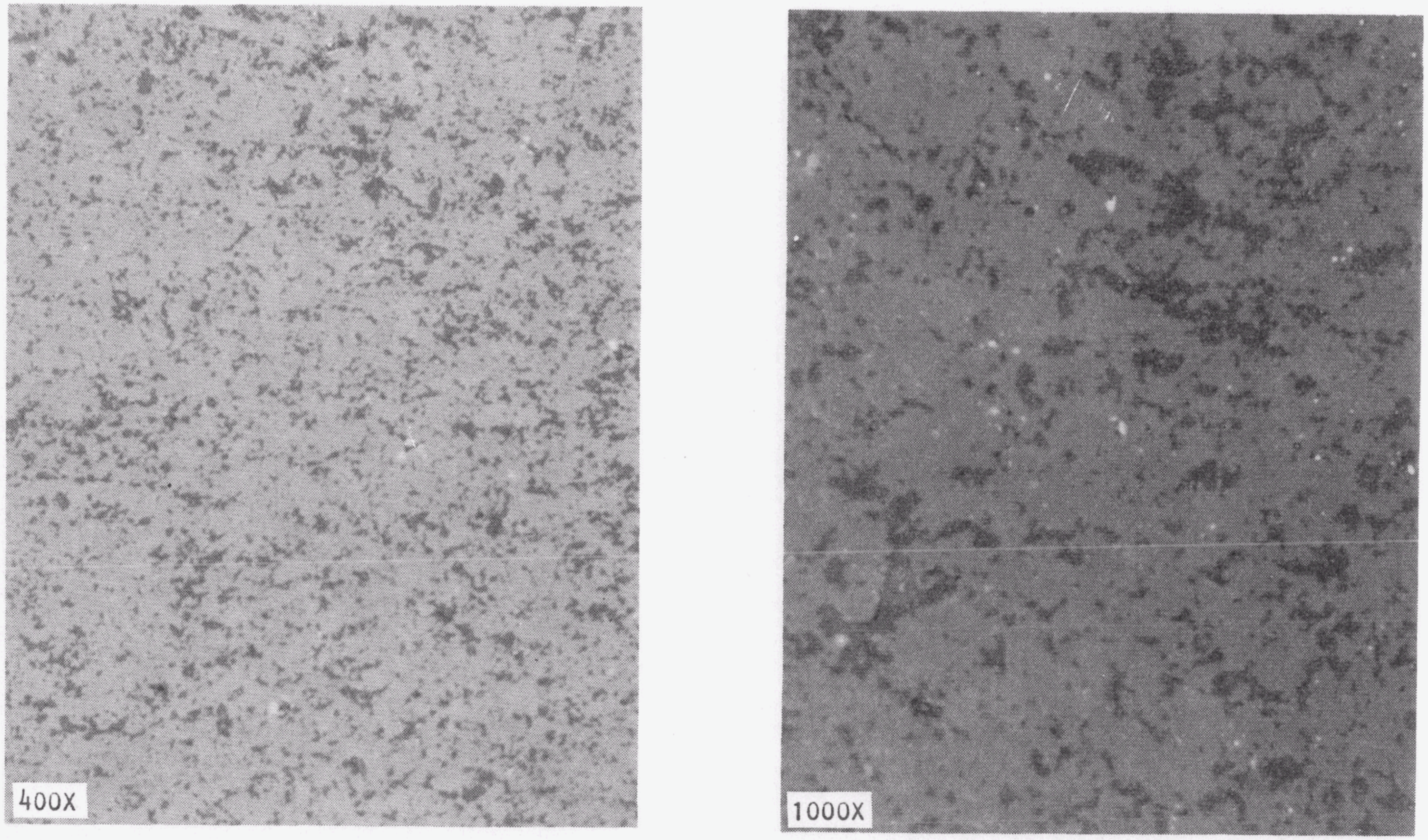

Figure 13. No SiC Whiskers Were Detected in the 15% ARCO - Code 7 Composite.

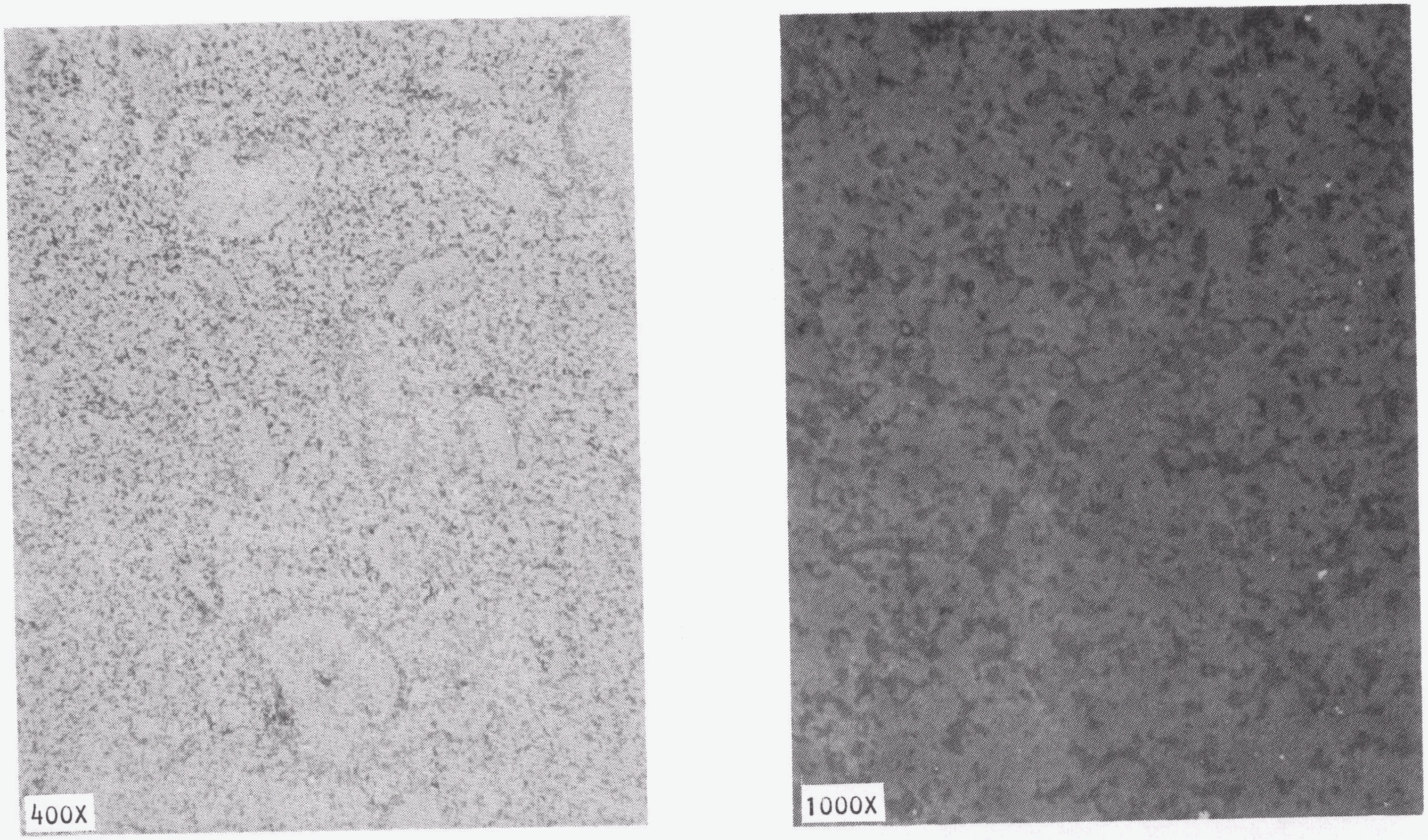

Figure 14. No SiC Whiskers Were Detected in the 15% ARCO - Code 9 Composite.

Whisker Analysis*

New batches of SiC whiskers (Tateho SCW #S-105, ARCO, Tokai Tokawhisker, and Versar VC1) were characterized by emission spectrography, LECO carbon analysis, X-ray photoelectron spectrography (XPS), and scanning transmission electron microscopy (STEM). In addition, analysis of Huber whiskers (two batches) was initiated.

Emission analysis results are shown in Table 8.

TABLE 8

EMISSION ANALYSIS OF SiC WHISKERS

Element	(Weight Percent)			
	Tateho	ARCO	Tokawhisker	Versar
Fe	0.053	0.014	0.024	0.047
Ni	0.007	<0.002	0.003	0.003
Ca	0.054	0.11	<0.04	0.13
Mg	0.005	0.017	<0.001	0.018
Mn	0.011	0.044	<0.001	0.020
Cr	<0.003	---	---	---
Cu	0.012	<0.001	<0.001	0.015
Ti	0.054	---	0.082	0.040
Na	<0.1	<0.1	<0.1	<0.1
Co	---	---	0.017	---
Al	0.098	0.066	0.002	0.070
Zr	---	---	---	0.011

--- indicates that the test yielded no trace. Tests were made for V, Sn, Zn, Pb, Mo, Sr, Ba, and B, but none of these was detected in any of the whiskers.

<X indicates trace amount below detection limit of X wt.%.

---

*Conducted at EMRC

The bulk chemistry of each of the new Tateho, ARCO, and Tokai whiskers is similar to the bulk chemistry of the earlier whiskers of the respective manufacturer. In each case, the impurity content is lower than the earlier version(s), particularly for the Tokai whiskers. One major drawback for the Tokamax whiskers was the very high bulk cobalt content which probably led to matrix degradation and explosive nitrogen release. The cobalt level has been drastically reduced in the new Tokawhiskers, although the appearance of cobalt species in the STEM analysis is still cause for some concern. The bulk impurity content of the Versar VC1 whiskers does not appear to be very different from those of the other whiskers.

The XPS surface chemistry analysis results are shown in Tables 9 through 12. Clearly, the surface chemistries of all the whiskers all appear to be converging toward a common point. This represents dramatic surface chemistry changes for both ARCO and Tokai. Since the old Tateho whiskers did not slip cast as well as the ARCO SC-9 whiskers, these changes may imply significant problems for slip-casting any of the new whiskers. Such difficulties would require a modification of the process or application of an appropriate coating. The new Tateho, ARCO, and Tokai whiskers all have low surface impurity content, reducing the chance of degradation during processing. Combining the results of the carbon analysis with those of the XPS analysis for the Versar whiskers, it appears likely that they contain a great deal of SiO_2. The Huber whiskers have significant amounts of surface impurities. In particular, the presence of Fe species is very disturbing. These impurities should be eliminated before the Huber whiskers are considered for use in the silicon nitride matrices.

TABLE 9

XPS SURFACE CHEMISTRY FOR TATEHO WHISKERS

Species	Atomic Percent (Binding Energy in eV)		
	SCW #1-S-105	SCW #1-S	SCW #1
C peak 1	34.4 (282.4)	28.9 (282.4)	28.1 (282.4)
peak 2	9.7 (283.7)	14.6 (284.1)	19.7 (284.2)
Si peak 1	33.6 (100.5)	29.0 (100.4)	27.3 (100.4)
peak 2	8.2 (101.7)	8.5 (101.8)	8.5 (101.6)
O peak 1	1.0 (529.3)	----	----
peak 2	13.1 (531.4)	17.4 (531.5)	15.0 (531.6)

TABLE 10

XPS SURFACE CHEMISTRY FOR ARCO WHISKERS

Species	Atomic Percent (Binding Energy in eV)	
	324-7	SC-9
C peak 1	34.4 (282.4)	16.8 (282.4)
peak 2	6.1 (284.0)	12.8 (283.9)
peak 3	2.7 (286.0)	
Si peak 1	35.2 (100.4)	19.3 (100.3)
peak 2	6.2 (101.9)	15.3 (102.2)
O peak 1	1.3 (529.9)	
peak 2	14.2 (531.8)	35.0 (531.6)

TABLE 11

XPS SURFACE CHEMISTRY FOR TOKAI WHISKERS

Species	Atomic Percent (Binding Energy in eV)	
	Tokawhisker	Tokamax
C peak 1	33.4 (282.4)	17.3 (282.4)
peak 2	12.3 (283.6)	12.9 (283.9)
Si peak 1	34.2 (100.4)	21.4 (100.5)
peak 2	8.1 (101.7)	14.7 (103.0)
O peak 1	12.1 (531.4)	33.7 (532.2)

TABLE 12

XPS SURFACE CHEMISTRY FOR VERSAR AND HUBER WHISKERS

Species	Atomic Percent (Binding Energy in eV)		
	Versar VC1	Huber Bag 1	Huber Bag 2
C peak 1	1.1 (282.4)	33.2 (282.4)	30.7 (282.4)
peak 2	3.9 (284.3)	14.2 (283.7)	12.1 (283.5)
peak 3	1.0 (286.2)		
Si peak 1	1.4 (100.8)	32.6 (100.4)	32.1 (100.4)
peak 2	29.8 (103.2)	7.1 (101.8)	7.3 (101.8)
O peak 1	62.8 (532.4)	0.6 (528.8)	1.8 (529.2)
peak 2		10.9 (531.1)	7.6 (530.8)
peak 3			4.0 (532.7)
peak 4			1.1 (534.7)
Cl peak			1.7 (268.5)
N peak 1		0.6 (397.0)	0.6 (396.9)
peak 2		0.5 (398.7)	0.5 (398.8)
Fe peak		0.4 (710.5)	0.7 (710.1)

The STEM morphology studies yielded mixed results. The ARCO whiskers (Figure 15) were more consistent and exhibited fewer morphological defects than all others, although these whiskers were slightly inferior to the SC-9 whiskers examined earlier primarily due to the presence of more debris. The morphology of the Versar VC1 (Figure 16) was quite good. Tateho (Figure 17) has improved their morphology significantly, although debris and hollow whiskers are still problems. The Tokai Tokawhiskers (Figure 18) exhibited the greatest morphological variations; the twisted morphology will probably cause problems during processing (e.g., clumping) and may lead to lower strengths. The Huber whiskers (Figure 19) appear to be significantly finer than the other whiskers examined. This can be expected to cause some problems during processing (i.e., difficulty in packing and/or whisker breakage), and it may also have an effect upon the mechanical properties.

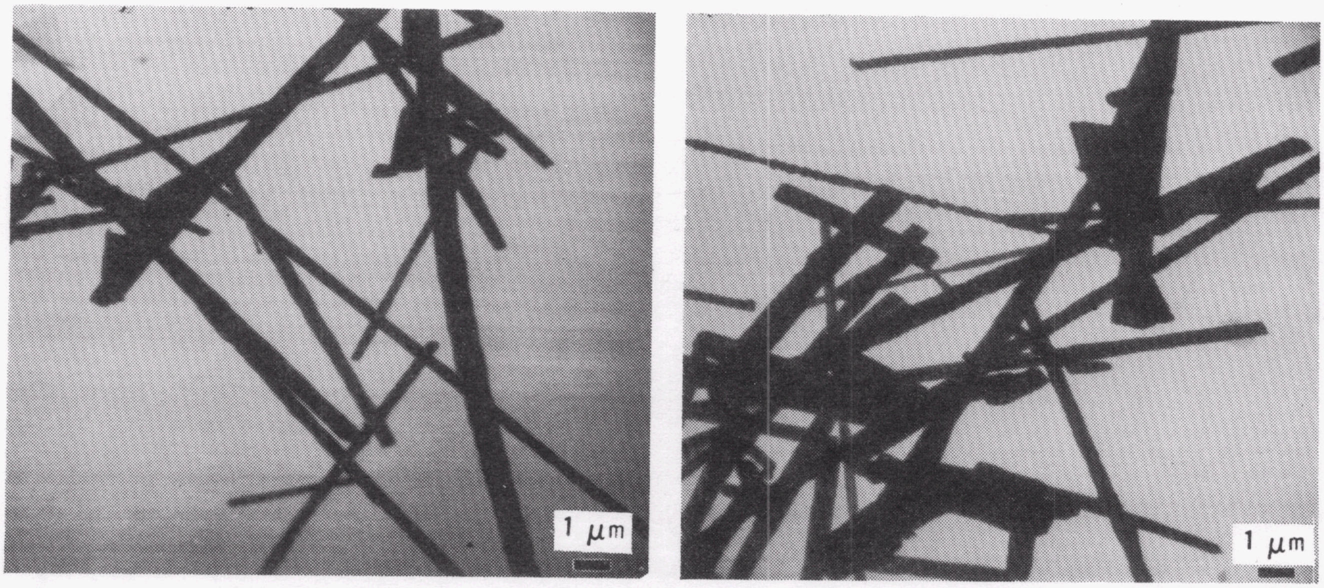

Figure 15. Variety of Morphologies for ARCO SiC Whiskers

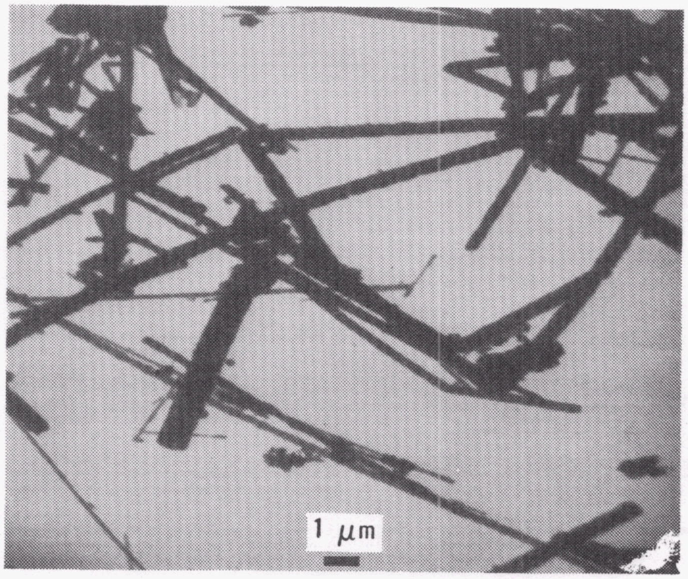

Figure 16. General Morphology of Versar VC1 SiC Whiskers

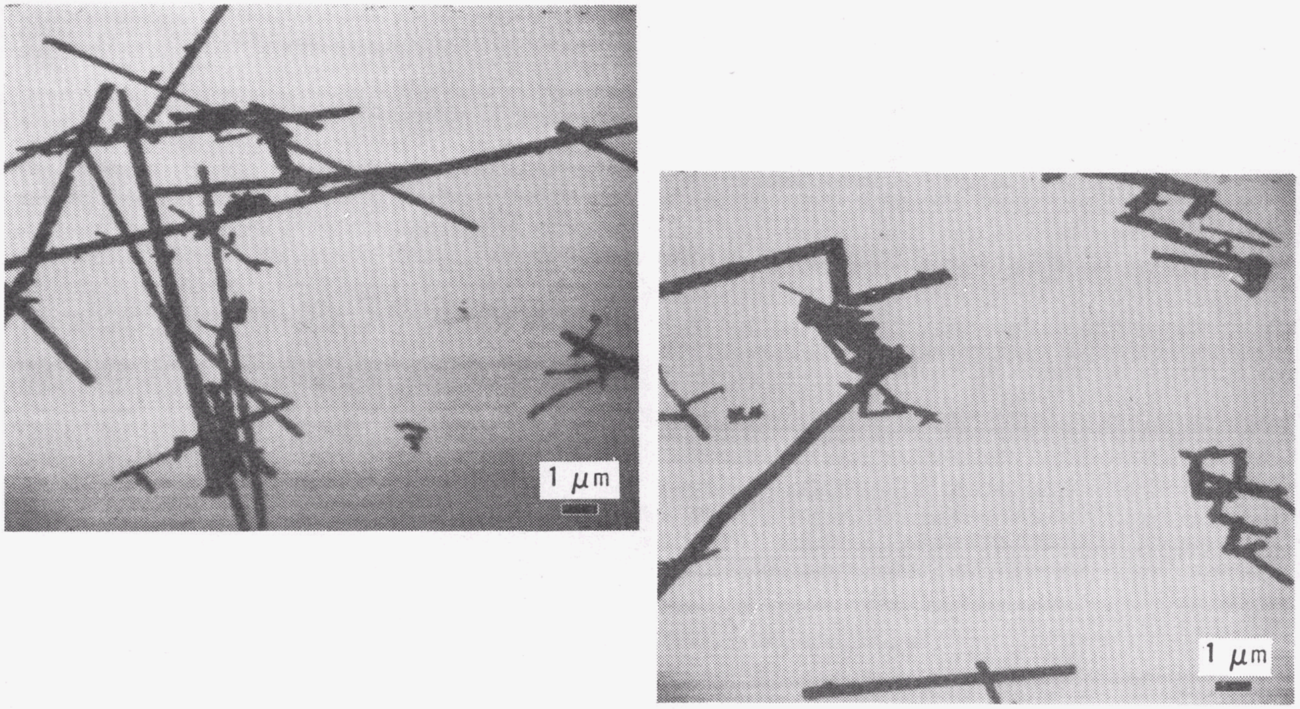

Figure 17. General Morphology of Tateho SCW #1-S, Lot T4-4 SiC Whiskers

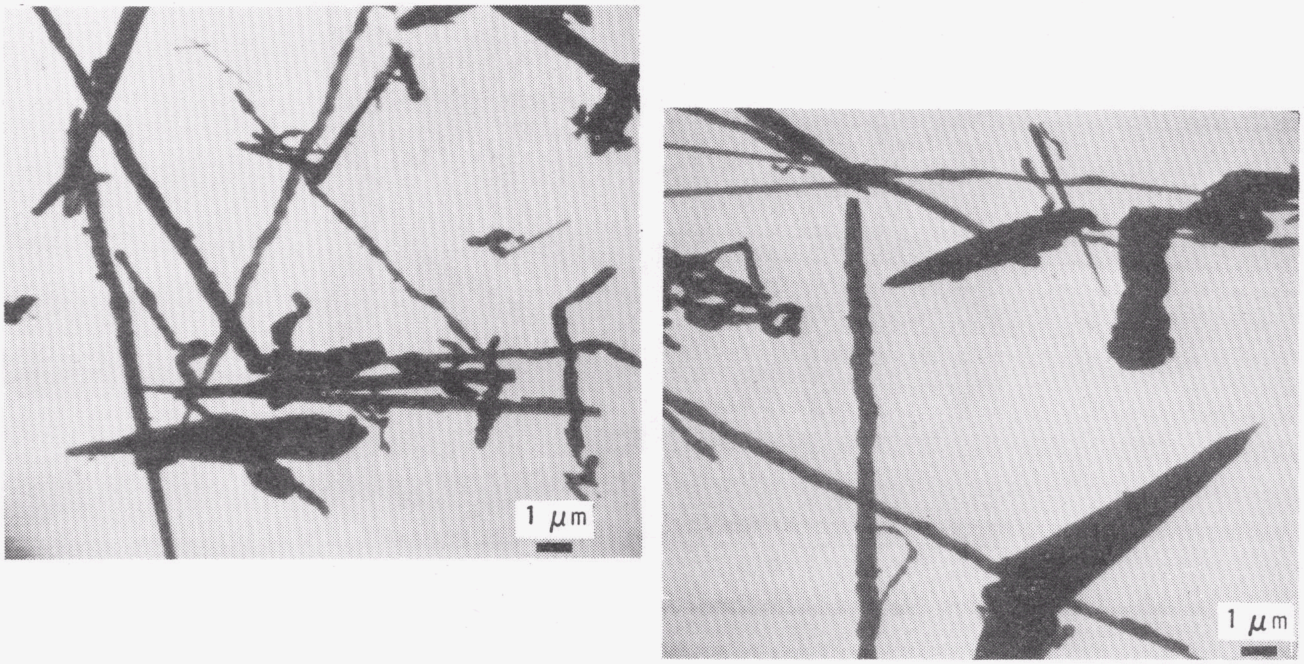

Figure 18. General Microstructure of Tokawhisker SiC Whiskers

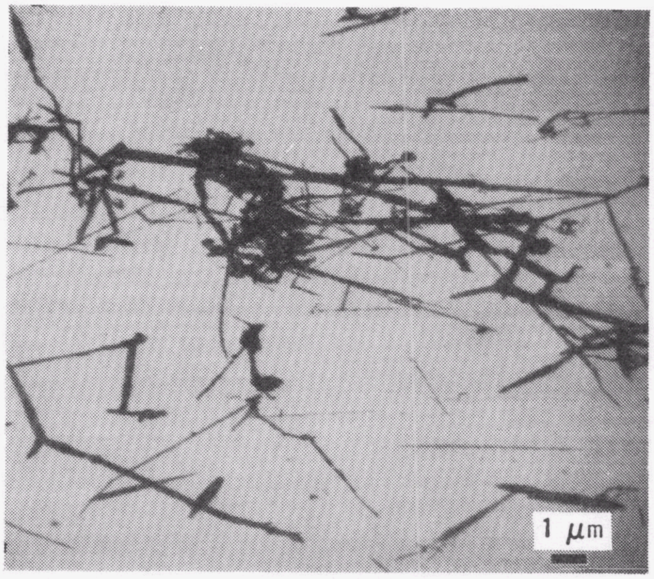

Figure 19. Fine Morphology of Huber SiC Whiskers

Status of Milestones

Milestones 3 and 4 were completed during this reporting period. Milestone 5 is 90% completed.

Development of Toughened Si_3N_4 Composites by Glass Encapsulated Hot Isostatic Pressure

Normand D. Corbin and Craig A. Willkens (Norton Company)

Objective/scope

This one-year effort is to develop fully dense Si_3N_4 matrix SiC whisker composites which show enhanced properties over monolithic Si_3N_4 materials. Composites will be prepared by an RBSN approach followed by high pressure HIPing. The emphasis of this study is on utilizing the ASEA HIP process which has the potential for producing near-net shaped complex geometries.

In addition, evaluations will be conducted to determine the role of whisker aspect ratio, coatings on whiskers, nitridation environments and HIP parameters on composite properties.

Technical progress

1.0 Evaluation Procedures

Microstructure evaluation - Powder and whisker morphology was observed using standard SEM techniques. Silicon powder size distributions were determined by a sedimentation technique. Surface areas were determined by a standard BET nitrogen adsorption method.

Composite samples were prepared for metallographic examination by polishing to a 1.0 micron diamond finish. Cross-sections and ground exterior surfaces were examined. These surfaces were used for microstructural evaluations and indentation fracture toughness measurements.

TEM specimens were prepared by slicing bulk samples with a low speed diamond saw to a thickness of ~0.5mm. The slices were ground to 125μm thickness using 20μm diamond disks. Three millimeter diameter disks were cut from the slices with an ultrasonic disk cutter. The specimens were then dimple ground with 3.0μm diamond paste to a thickness of ~1.5μm in the center of the specimen. The samples were ion milled with Argon gas at 6 kev and a 15° tilt. The samples were analyzed using a JEOL 200CX.

Composition Evaluations - Surface composition of powders and whiskers were evaluated using Scanning Auger Microanalysis (SAM) and Electron Spectroscopy for Chemical Analysis (ESCA or XPS). Analysis by SAM was conducted on whiskers to determine near surface composition as a function of depth to ~100-200Å. Samples were coated with a thin gold coating to alleviate sample charging. Depth profiles were determined using an argon ion gun with successive analysis taken after every 30 seconds of sputtering for up to 8.0 min. The gold, carbon, silicon, oxygen, nitrogen and boron concentrations were monitored as a function of sputtering time. The depth of penetration depends on the sputtering rate of the species analyzed. For pure carbon and Si_3N_4 the sputtering rates used are 20Å/min. and 50Å/min. respectively. The atomic concentrations were determined by normalizing peak heights with their respective sensitivity factors for a primary beam of 10 Kev. Beam diameter was approximately .3 micron.

Analysis by XPS was conducted to determine the binding energies of the surface constituents. In many instances these energies can be related to chemical species (ex. oxide, nitride, carbide) through the use of reference data. Semiquantitative chemical analysis of the surface (~20Å depth) was obtained by utilizing integrated peak heights and appropriate sensitivity factors for the elements under evaluation. For ESCA, analysis is taken from a relatively large area of the sample (~2mm x 2mm).

Bulk oxygen and nitrogen analyses were conducted using a combustion technique. Phase analysis was conducted by standard x-ray powder diffraction methods using Cu K_α radiation. Bulk chemical impurities were determined by semiquantitative emission spectroscopy.

Property Evaluations - Composite strengths were determined by 4-pt. flexural testing per the recommended U.S. Army Standard[1]. We use the 3mmx4mm specimen size with chamfered edges and a 320 grit surface finish. The high temperature fixtures have an upper span of 20mm and a lower of 40mm (room temp. spans are 19.1mm:38.1mm respectively). Samples are allowed to equilibrate 10 min. prior to testing at high temperature.

Two fracture toughness measurement techniques are being utilized. An indentation method[2] is used for qualitative K_{IC} determinations on small specimens. Five 10 kg Vickers indents are inserted with the resulting crack lengths measured at 400X. Hardness values taken from the 10 kg indent are used to calculate the respective K_{IC}. A controlled flaw method[3] is used for semiquantitative K_{IC} evaluations on larger quantities of materials. For this method we use flexural specimens and fixtures per the U.S. Army flexural test standard[1]. Vickers indentations between 10 and 40 kg are used for inserting the controlled flaw. Three specimens are evaluated and averaged for K_{IC}.

High temperature stress rupture is conducted in air with the same bend bar sizes and fixture spans as used for high temperature fast fracture. The testing conditions are similar to that described by Quinn.[4,5]

2.0 Reinforcements

Whisker Coatings - In order to understand the role of interfaces on composite toughness, a study is being conducted which utilizes CVD coated whiskers. To date, six different coatings have been attempted (Table 1). Four are multiple coatings designed to have a debonding/parting layer (BN or C) protected by an overcoating layer (SiC or Si_3N_4). A thick BN layer was attempted so that enough would remain after composite processing to significantly improve toughness. The thick SiC coating is an attempt to increase whisker diameter for our aspect ratio study. Photomicrographs of a dual-coated whisker is shown in Fig. 1. The coatings are on the order of 0.1μm thick. Auger results on the Si_3N_4/BN dual-coated whisker do not show the presence of a Si_3N_4 over-coating. Both boron and nitrogen are detected but the BN coating is not stoichiometric.

TABLE 1

COATED WHISKERS

PARTING LAYER	OVER COATING	WHISKERS* COATED	ANALYTICAL RESULTS
BN	SiC	1	~.1μm, SiC not detected, look like carbon
BN	Si_3N_4	1	~.1μm, Si_3N_4 not detected
C	SiC	1	~.1μm
C	Si_3N_4	1	~.1μm
--	SiC	T44	thin ~.1μm
BN	--	T44	thin ~.1μm

*Tateho SiC whiskers, 1=SCW#1 (rec. 12/85), T44=SCW#1-T44 (rec. 11/86)

In spite of the coating difficulties we decided to prepare composites using the dual-coated whiskers to determine how the coatings affect processing, in particular dispersion and densification. Evaluations on these first coatings will be used to guide future coating/interface studies. The K_{IC} of composites reinforced with coated whiskers were not different from uncoated whisker reinforced material (~3.0 MPa$\sqrt{m}$) (Table 2). It is anticipated that the coatings have deteriorated during composite processing. Earlier results at Norton Company have demonstrated that carbon interfacial layers can deteriorate during nitridation cycles[5]. An attempt to shorten the nitridation cycles to 8 hours was unsuccessful in fully converting the silicon matrix to silicon nitride, for all but the uncoated whisker composite.

Fig. 1 TATEHO Whiskers with SiC/BN Coating

TABLE 2

WHISKER COATING EFFECTS ON K_{IC}[1], HARDNESS[2], AND DENSITY

Whisker Coating[3]	Specimen Code	Silicon[5]	K_{IC} MPa$\sqrt{m}$	H GPa	Density g/cc
Unreinforced	(16#14)	NO	3.0±.1	13.9±1.5	3.10
Uncoated	(15#13)	NO	2.9±.1	17.0±.7	3.16
Si_3N_4 over BN[4]	(12#13)	NO	3.1±.1	13.2±1.1	3.04
Si_3N_4 over C	(14#13)	TR	2.9±.3	16.8±.7	3.09
SiC over C	(13#13)	-	-	-	2.74
SiC over C	(13W#13)	NO	2.6±.3	16.8±.5	3.15
SiC over BN	(58#20)	NO	3.9±.2	14.0±.1	3.19

1) K_{IC} by indentation at 10 kg, Anstis method.
2) Hardness at 10 kg with Vickers indent.
3) Coatings on Tateho SCW#1 whisker, rec. 12/85.
4) These were the coatings ordered, what was actually obtained is discussed in the text.
5) From optical microscopy NO = None Observed, TR = Trace Observed (<1%).
* 20 v/o whisker loading (except 13W#13 which had a lower %).
** 3μm jet milled silicon used except for 58#20.

Our future plans are to work closely with the coating vendor, to optimize coating composition and morphology for increasing the toughness of our materials. Further studies to minimize coating deterioration during processing will also be investigated.

Aspect Ratio - Thicker SiC whiskers, available from Huber and American Matrix have successfully been incorporated into dense Si_3N_4 matrices and are currently being evaluated. Fig. 2 compares the resulting microstructures.

Volume Fraction - Most of the studies to date were made using a constant whisker loading level of 20 v/o. Full densification was achieved for all systems studied. Samples have been made with 30 v/o whisker loading, and full densification was again achieved. Properties will be measured in the near future.

3.0 Green Body

Forming - A detailed evaluation of starting materials has been conducted with particular emphasis on the surface chemistry and surface charges of the starting components. Table 3 lists the basic analytical data on the whisker product primarily being utilized in our program. The bulk oxygen content of these whiskers is quite low and is primarily concentrated at the whisker surface (per ESCA). The discrepancy between the ESCA and Auger surface oxygen contents is unexplained. One possibility may be the desorption of adsorbed oxygen containing species during the Auger analysis as a result of electron beam heating. ESCA analysis uses x-ray excitation of the electrons which is less prone to cause sample heating. ESCA binding energy data for the carbon 1S peak and the silicon 2P peak shows the surface carbon is bonded to both silicon (SiC) and carbon (graphite?) while the silicon is primarily bonded to carbon (SiC) with very little bonded to oxygen (SiO_2). Noting the high concentration of oxygen detected on the surface (24 A/O), it appears much of the oxygen is bonded to other chemical species. An evaluation of the oxygen binding energy was not successful in determining other oxygen bonded species.

The Auger depth profile into a whisker surface is shown in Fig. 3. A carbon rich surface is apparent which is not fully removed until sputtered for 5 min. at which point stoichiometric SiC is obtained.

Surface Chemical Analysis by ESCA of the silicon powders used to date reveal that a significant amount of surface oxygen is associated with these materials (44-53 A/O). High resolution bonding energy scans show that Si-O bonding, typical of SiO_2, are present on all surfaces. The carbon content of the Kemanord powder is higher (~20 A/O vs. 8 A/O) than Elkem. The carbon (1S) peak shows carbon is primarily C-C or C-H bonded.

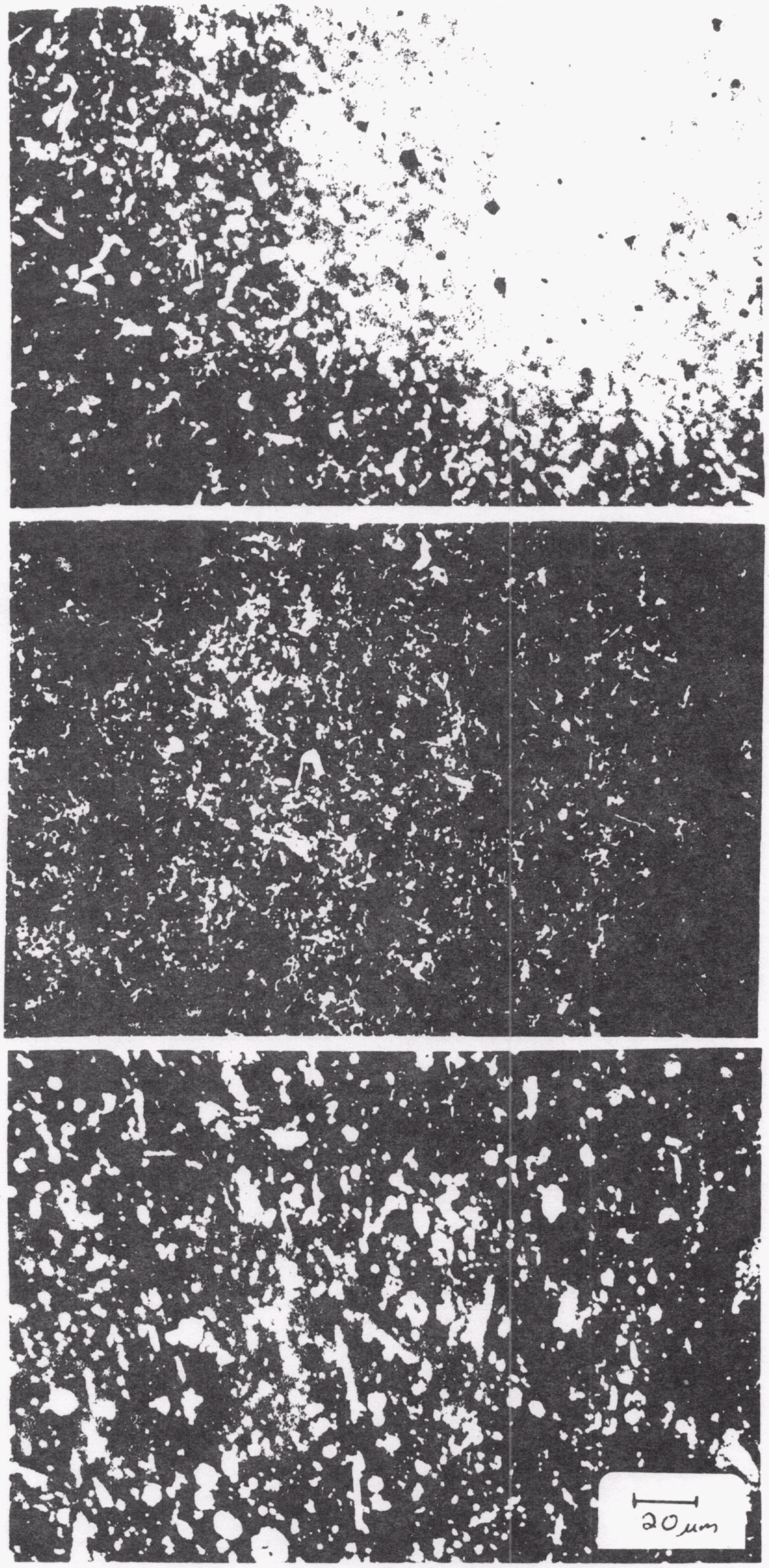

Polished Surfaces of Composites, 500X
TOP: 20 v/o Huber SiC/SRBSN (4% Y_2O_3)
MIDDLE: 20 v/o Tateho SiC/SRBSN (4% Y_2O_3)
BOTTOM: 20 v/o American Matrix/SRBSN (4% Y_2O_3)

FIGURE 2

TABLE 3

TATEHO WHISKER+ CHARACTERIZATION

BULK CHEMICAL ANALYSIS [a]	
Free Carbon	0.38%
Sulfur	27 PPM
Oxygen	0.4±.02%
Nitrogen	0.9 ±.02%

BULK CHEMICAL ANALYSIS[b] (%)	
AL	.132
ZR	.002
NA	.003
CA	.075
FE	.050
MG	.014
MN	.006
Ti	.004
Cr	.014
Cu	.003
Ni	.003
K	.009

Morphology (d, e)

Smooth Surfaces
~ 0.5μm thick whiskers
density = 2.95 g/cc

Phase Analysis[c]

Major β-SiC	(PDF #29-1129)
Minor α-SiC	(PDF #29-1130)

Surface Chemical Analysis

ESCA	Oxygen	24.0 atomic %
	Silicon	26.8 atomic %
	Carbon	49.1 atomic %

AUGER	Oxygen	7 atomic %
	Silicon	25 atomic %
	Carbon	68 atomic %

(+) SCW#1-S 105, T4-4 Type, Lot #S-178
(a) Leco Analysis
(b) Emission Spectroscopy
(c) X-ray diffraction
(d) SEM
(e) Helium pycnometer

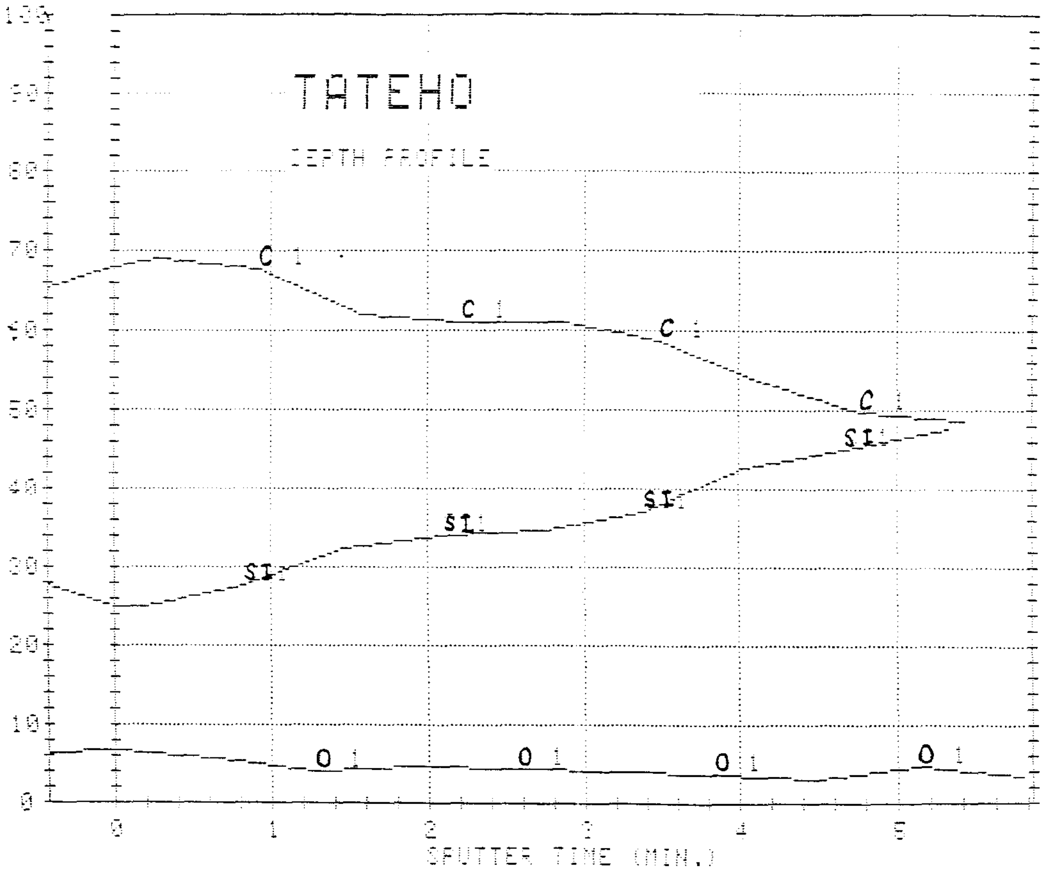

FIGURE 3 Auger Depth Profile Analysis of Tateho T44 Whiskers

Powder processing techniques were incorporated that allow for good microstructural uniformity and uniform whisker distribution (Fig. 2-middle). Tiles (3"x3"x3/8") are formed by wet bag, cold isostatic pressing.

Three silicon particle size distributions were evaluated (Table 4), processed by jet milling, wet milling and dry milling. The packing density of the unreinforced silicon followed expected trends, with the dry milled having the highest isopressed (45 ksi) green density due to a broader size distribution. The isopressed green density of the reinforced (20 v/o SiC-w as-received) silicon powder mixtures showed no variation in packing density. The whiskers control the packing density.

The wet milled silicon precursor results in the finest scale microstructure. The coarse jet milled silicon causes large (5-10μm) matrix regions to be present in the final product. These matrix rich regions are directly related to the coarsest fraction of the starting silicon powder.

TABLE 4

COMPOSITE GREEN BODY PROPERTIES BEFORE HIP

Sample Code	Silicon[1]	(g/cc) Silicon[2] Packing Density	(g/cc) Composite[5] Packing Density	(%) Silicon[3] Oxygen Content	(%) RBSN[6] Oxygen Content	(%) Composite[4] Alpha Si_3N_4 Content	(%) Free Silicon	Secondary Phases
(2030)	Jet milled d_{50}= 3μm	1.43	1.38	1.07	0.68	84	<0.1	Y_2O_3 Y_2SiO_5
(2029)	Wet milled d_{50}= 1.0μm	1.47	1.35	1.60	1.47	93	0.1	$Y_5(SiO_4)_3N$ Y_2O_3 (weak)
(2031)	Dry milled	1.51	1.33	-	1.00	72	0.1	Y_2O_3 $Y_5(SiO_4)_3N$ (weak)

[1] Kemanord Sicomill Grade IV Fe = 0.05%

[2] Silicon only, no sintering aid

[3] Leco combustion analysis

[4] Based only on composite matrix

[5] 20 v/o SiC-w/Si(6.3% Y_2O_3)

[6] RBSN having no sinter aid

Severe whisker damage occurred when isopressing whiskers and coarse (3µm) jet milled silicon above 30 ksi. The dry milled powder had less whisker damage. Apparently, the coarse particles acted as fulcrums during isopressing, causing the whiskers to undergo bending strain until they failed during high pressure CIP. The whisker damage which occurs during CIP is not readily apparent in the HIPed microstructure. This could either mean additional damage occurs during HIP which masks earlier damage or, more likely, damage is not apparent due to the random orientation of the whiskers in our composites.

Understanding the dispersion behavior of the whiskers in distilled water as a function of pH is useful for optimizing processing procedures and also gives an indication of whisker surface chemistry. The acoustophoretic mobility of two grades of Tateho whiskers was determined as a function of pH. Acoustophoretic mobility can be directly related to electrophoretic mobility. Empirically, Grade T44 was found to disperse better than a standard SCW#1 grade. The IEP (isoelectric point) was consistently lower in pH for T44 (Fig. 4). This was believed to be related to surface SiO_2. As mentioned earlier, ESCA data shows a lot of surface oxygen on this material but very little bonded as SiO_2. At low pH the surface charge (Fig. 4) was shown to be relatively high, in fact, higher than for the dispersed condition, but opposite in charge. The high surface charge present at low pH does not agree with the flocculated dispersion obtained empirically under these conditions.

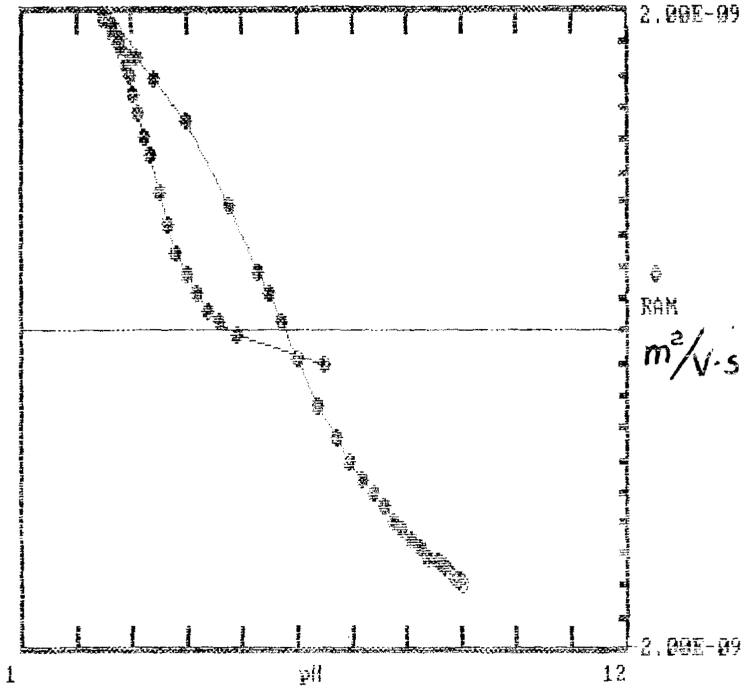

Figure 4 - Acoustophoretic Mobility of Tateho T44 SiC Whiskers, Acid-Base Titration

Shuhmann[7] has modeled nonhomogeneities on a surface and their discreteness of charge effects. A possible explanation for this case of SiC whiskers may be that discrete SiO_2 regions on the surface are acting as surface inhomogeneities. The average surface charge measured is determined by the predominant background surface (e.g. SiC). These SiO_2 sites at low pH having zero mobility/charge could flocculate the suspension and control dispersion/flocculation behavior. The influence of this effect on dispersion/flocculation would be enhanced by the large aspect ratio morphology of the whiskers.

Nitridation - Silicon carbide whiskers were heated alone in the nitridation cycles. The nitriding cycle appears to convert ~3-5% of the whiskers to alpha silicon nitride. An increase in nitrogen content of the whiskers is readily observed (0.9 to 3.1). Only a small reduction in oxygen content occurs (.4 to .3). Conversion of the original surface oxygen on the SiC whiskers to Si_3N_4 does not account for the total amount of Si_3N_4 observed. Therefore an additional reaction mechanism must also be occurring to account for the Si_3N_4 content. The majority of this conversion occurs within an 8-hour cycle with only a slight additional increase after the 36-hour cycle.

The RBSN monoliths and 20 v/o Tateho SiC-w/RBSN (4% Y_2O_3) composites were nitrided using a 36-hour cycle. Table 4 lists the resulting sample compositions. The alpha content for the matrix of these composites was highest for the wet milled silicon (93%). The residual silicon was very low in all cases ($\leq$0.1%). Secondary phases after nitriding included Y_2O_3, Y_2SiO_5 and $Y_5(SiO_4)_3N$ (apatite). The apatite phase formed primarily with the finer milled silicon.

After nitridation and HIPing different oxygen containing phases and bulk oxygen contents result when the different silicon powders are used. The finer silicon yields a higher oxygen content in the final product (1.8 vs. 3.6%). Control of the oxygen content and resulting phases will be vital to producing creep resistant materials.

Three nitridation processes were investigated; A (Standard 36-hr.), B (Special 36-hr.) and C (8-hr.). Controlled flaw K_{IC} data revealed that fracture toughness may be sensitive to the nitridation process, even though all samples are fully densified by HIP after the nitridation step. K_{IC} after HIP was shown to improve from 4.0 MPa $\sqrt{m}$ to 5.2 MPa $\sqrt{m}$ depending on the nitridation cycle for cycles B and A, respectively (Table 5). The fracture surfaces of these samples (Fig. 5) show dramatic differences. The higher K_{IC} sample

(Cycle A) possessed a significant amount of pullout and a generally rougher surface indicating a more torturous crack path. The lower K_{IC} sample (Cycle B) had a generally smoother looking surface, with no whisker pullout. Cycle B differed from Cycle A in that a higher nitriding reaction temperature was used, which resulted in a lower oxygen content and lower K_{IC}. An 8-hour Cycle (C) was evaluated for composites made with wet milled silicon. As compared to Cycle A, (Specimen #15) the shorter cycle resulted in a higher oxygen content and higher K_{IC} value (Table 5). It appears the nitridation cycle has a large effect on the properties of the fully densified (HIPed) composites. The following trend was observed: the "less severe" nitriding cycles (shorter time and/or lower reaction temperature) result in composites with higher K_{IC} and higher oxygen contents after the final HIP operation. In addition, the possibility of whisker damage during nitridation exists. We are planning to further study the effect of nitridation environments on composite properties.

TABLE 5

EFFECT OF NITRIDE CYCLE ON FINAL HIPed COMPOSITE/PROPERTIES

Sample(1) Code	Nitriding(5) Cycle	Silicon	Final[2] Oxygen Content	$\mathrm{MPa}^{.5}$ IFT(3) K_{IC}	$\mathrm{MPa}^{.5}$ CF(4) K_{IC}
2 #12	A	Wet milled Kemanord	3.6	4.2	5.2
3 #12	B	"	3.0	4.0	4.0
15	A	"	1.8	2.9	-
15X	C	"	2.6	3.3	-

1) 20 v/o Tateho/SRBSN (4% Y$%2O$%3)
2) Leco Combustion Analysis
3) IFT - Indentation Fracture Toughness
4) CF - Controlled Flaw Fracture Toughness
5) A - Standard 36-hour
B - Special 36-hour
C - 8 hour

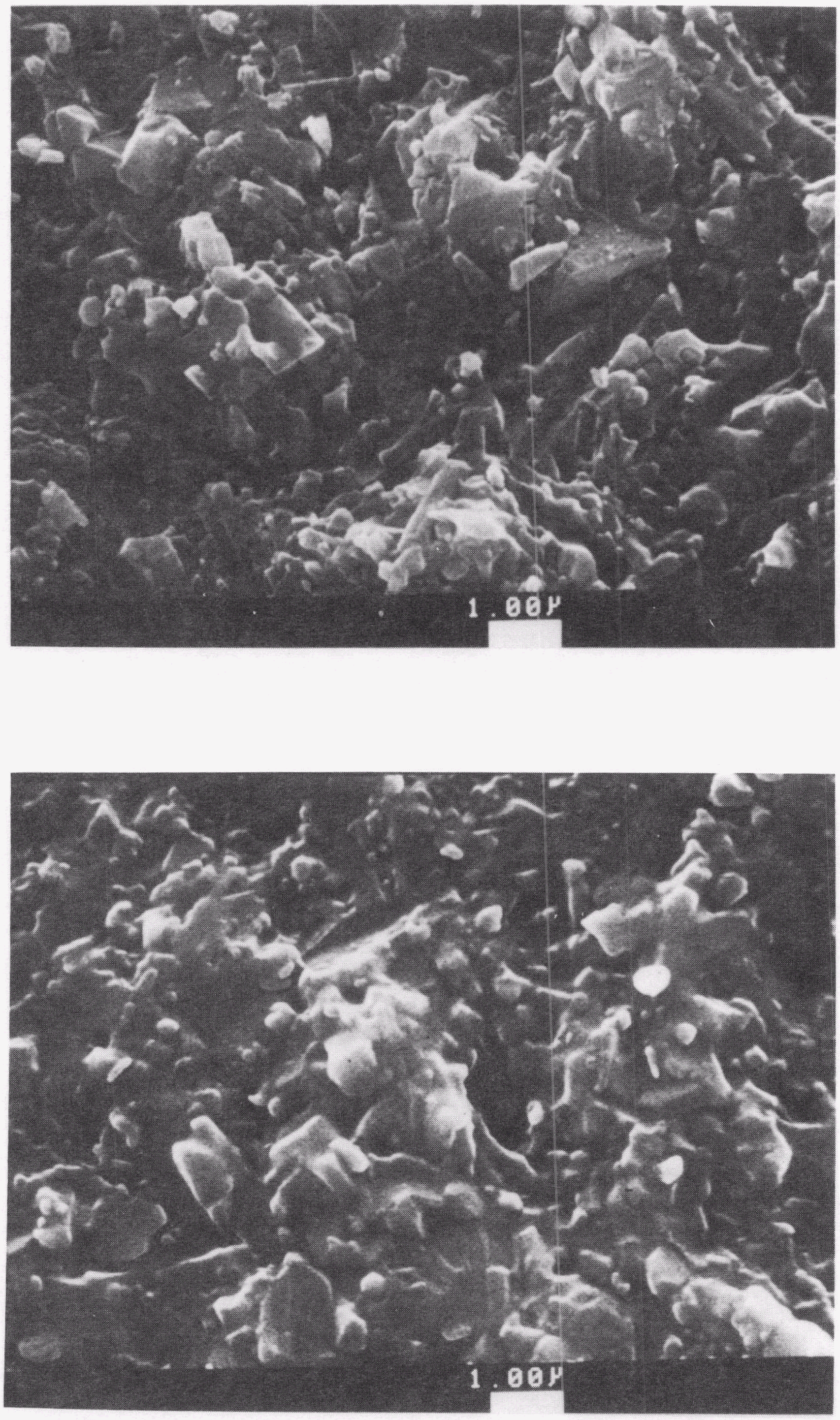

Fracture Surfaces of HIPed $Si_3N_4/SiC(w)$ Composites
with 4 w/o Y_2O_3 as Matrix Sintering Aid
TOP: $K_{IC} = 5.2$ MPa $\sqrt{m}$, High Oxygen, (2#12)
BOTTOM: $K_{IC} = 4.0$ MPa $\sqrt{m}$, Low Oxygen, (3#12)

FIGURE 5

4.0 Densification

HIP Parameters - A parametric study has been initiated to evaluate the effect of processing cycle on composite properties. Four cycles have been evaluated to date. In all cases full density has been obtained (3.21 to 3.25 g/cc). Table 6 compares the fracture toughnesses of these materials. The K_{IC} of composites prepared using wet milled Elkem silicon are sensitive to the HIP conditions used for processing. Best results are obtained using Cycle A. Composites prepared using the other silicon materials do not show a dependency of K_{IC} and HIP cycle. We are continuing to evaluate these materials to determine the role of interface composition and microstructure on K_{IC}.

Sintering Aids - Composite specimens are being prepared to evaluate the effects of sintering aids on properties, especially K_{IC}. The sintering aid systems to be evaluated are Y_2O_3-SiO_2-Al_2O_3 and MgO-SiO_2-Al_2O_3. Indentation fracture toughness data on a composites prepared with a 10% Y_2O_3 content in the matrix is 5.3 MPa$\sqrt{m}$ (Table 6). This is the highest value we have obtained by the indentation technique to date. Further evaluations are being conducted on this specimen to determine the mechanism for the toughness enhancement. Additional sintering aid studies are in process.

TABLE 6

FRACTURE TOUGHNESS[1] VS. HIP CONDITION AND MATRIX COMPOSITION

Sintering[3] Aid (w/o)	M or[4] C	Silicon Powder	Specimen Code	HIP Conditions[2] A	B	C	D
4% Y_2O_3	M	Wet milled Kemanord	(2187)	2.8±.1	2.7±.2	2.8±.4	2.8±.4
4% Y_2O_3	C	Jet milled Kemanord	(1N/2N)	3.7±.3	3.3±.1	3.7±.1	3.7±.1
4% Y_2O_3	C	Wet milled Elkem	(B1)	4.5±.2	-	3.5±.2	4.0±.2
10% Y_2O_3	C	Wet milled Elkem	(C4)	5.3±.3	4.0±.2	4.1±.2	4.9±.1
10% Y_2O_3	C	Dry milled Kemanord	(A2)	-	4.5±.1	-	4.4±.2

1) K_{IC} in MPa $\sqrt{m}$, indentation method per Antis, 10 kg indent.

2) A = 1790°C, 1 hr., 207 MPa.
B = 1790°C, 1 hr., 207 MPa with proprietary grain growth step.
C = 1790°C, 1 hr., 207 MPa with proprietary grain growth step.
D = 1790°C,.25 hr., 207 MPa.

3) Sintering aid content within matrix.

4) M = Monolith, C = Composite

* Composites with 20 v/o Tateho (grade #1S, 12/85) whisker loading.

5.0 Miscellaneous

TEM/STEM Studies - The microstructure of the Si_3N_4 matrix SiC whisker composite was analyzed using the TEM. The microstructure consisted of a Si_3N_4 matrix having a broad grain size distribution, crystalline and amorphous grain boundary phases, and SiC whiskers randomly oriented in the matrix. A brightfield electron micrograph of the microstructure of the Si_3N_4/SiC composite material is presented in Figure 6-top. The average grain size of the Si_3N_4 matrix was 0.40µm in diameter and 0.60µm in length. The grain size ranged from 0.10µm to larger than 1.0µm in diameter. The SiC whiskers were randomly oriented in the Si_3N_4 matrix and in some areas they were clustered together. The average whisker size was 0.4µm in diameter and 1.0µm in length.

The composite material contained three types of SiC whiskers: solid SiC whiskers, whiskers with two subzones, and, hollow whiskers. The solid SiC whiskers contain stacking faults and partial dislocations. The partial dislocations are shaped like a U or V and extend out from the core region. A transverse section of a solid SiC whisker is presented in Fig. 6-middle. The solid SiC whiskers have a small core region that contains small cavities. The second type of whisker is composed of two subzones, the SiC outer layer and an unknown inner layer that contains aluminum. A longitudinal section of a two zone whisker can also be seen in Fig. 6-middle. The sample also contained some hollow whiskers.

Selected area diffraction (SAD) was used to identify the whiskers. Two structures were identified β SiC and the 4H SiC polytype. Due to the random packing sequence, the whiskers are usually composed of a number of polytypes. The identity of the core phase in the two zone whiskers is still under investigation.

The whiskers appear well bonded to the matrix. Dark field microscopy was used to determine the nature of the intergranular phase. A continuous thin amorphous film is located in the grain boundaries. A whisker matrix interface is presented in Fig. 6-bottom. It is a very thin interface and no voids are present.

SAD was used to identify the crystalline intergranular phases, similar to the dark area adjacent to the whisker in Fig. 7-bottom. One intergranular phase was identified as $Y_5(SiO_4)_3N$, the apatite phase.

Areas of the future work are to; 1) Investigate whiskers more thoroughly, using microchemical analysis, 2) perform microchemical analysis on the intergranular phases in the composite samples, and 3) investigate other composite samples of interest.

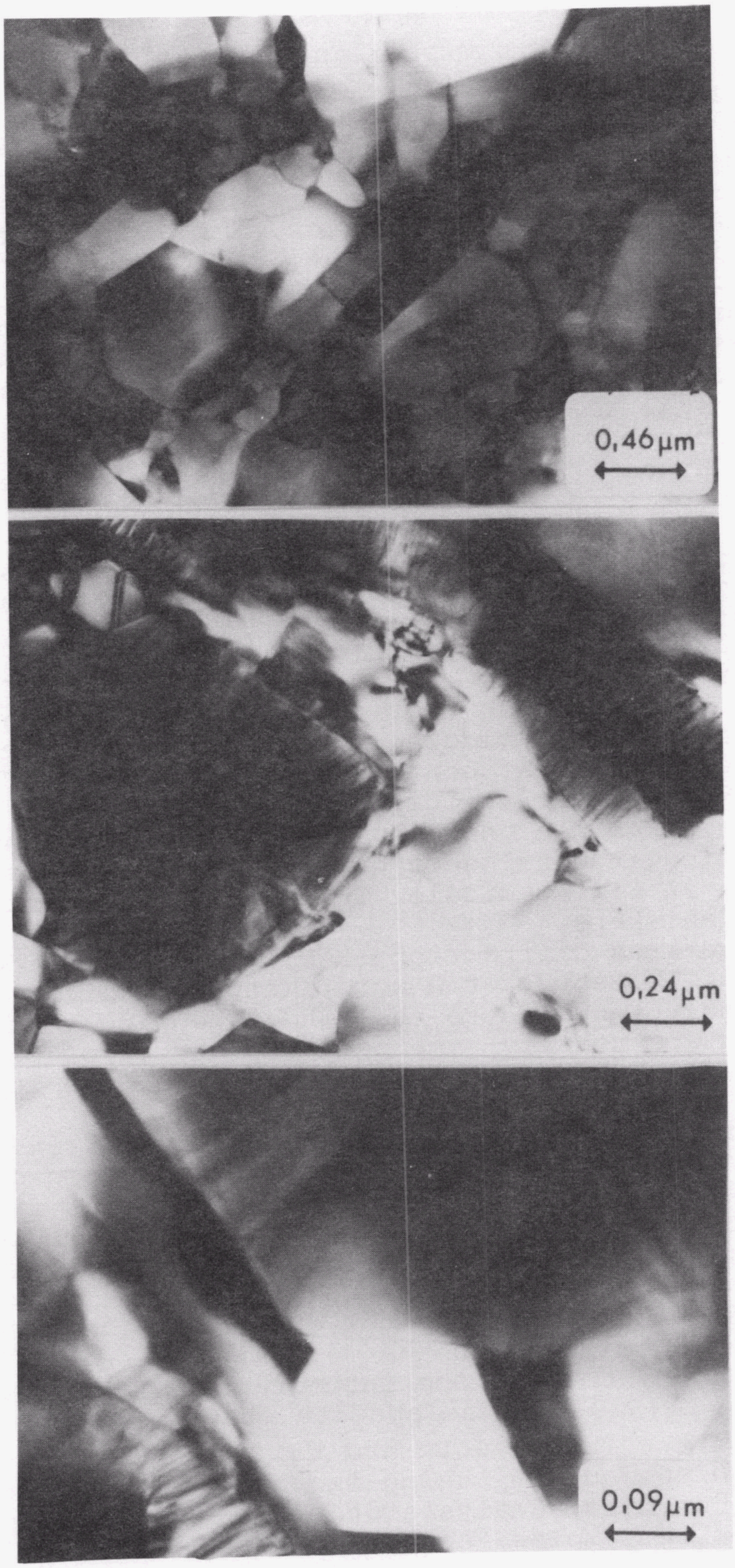

TEM Micrographs of Si_3N_4/SiC(w) Composites (Code 2N#10)
TOP: General Microstructure
MIDDLE: Two Whisker Types; Solid and Cored
BOTTOM: Whisker/Matrix Interface
FIGURE 6

Best To Date Specimens - Periodically a composite material will be fabricated by combining what we consider to be optimum processing conditions at that time. Enough material will be fabricated to allow for extensive evaluations. Of particular interest are; high temperature strength (1370°C), stress-rupture life, Weibull modulus and analysis by STEM. The first set of materials was prepared shortly after initiation of our program (October 1986). Table 7 lists data obtained on composite and monolith materials. The room temperature failure origins for the monolith were clusters of large residual pores associated with some large Si_3N_4 grains whereas all composite failure origins were large SiC particulates. No flaw origins could be identified when these materials were tested at high temperature. The high temperature failures could most likely result from a different mechanism. The fracture toughness of the composite was only slightly improved over the monolith. Initial stress-rupture data has also been listed. TEM evaluations on the composite material are discussed under a seprate section of this report. This initial data will be used as a baseline to monitor our material improvements.

Since initiating our program we have been able to make significant improvements in microstructural uniformity, toughness, and room temperature strength. The new set of composites under preparation for this evaluation include these improvements.

6.0 Summary

Of all the parameters evaluated to date, those which most effect fracture toughness appear to be composition related. Samples with higher oxygen content also have higher K_{IC}, (see Table 5). The nitridation conditions used also effect K_{IC}. The "less severe" the nitridation cycle (shorter time, lower temperature) the higher the K_{IC}. This is dramatically shown in Fig. 5 where the fracture surface of two materials prepared identically except for the nitridation cycle are compared.

Thus far, studies to vary the HIP processing cycle to change matrix microstructure have been unsuccessful in improving K_{IC} over recommended ASEA procedures. The incorporation of coated whiskers did not change fracture toughness but this is more likely a result of coating deterioration during processing than in effectiveness of the coating. We are working closely with the CVD vendor to make improvements.

TABLE 7

BEST-TO-DATE SPECIMENS, OCTOBER 1986

	Monolith	Composite
σRT[1]	532±58 MPa	583±72 MPa
σ1200°	610±24 MPa	508±19 MPa
σ1370°	505 MPa	425±6 MPa
K_{IC}[2] (RT)	4.5±.1 MPa$\sqrt{m}$	5.0±.1 MPa $\sqrt{m}$
K_{IC}[3] (RT)	3.5±.5 MPa$\sqrt{m}$	3.7±.3 MPa $\sqrt{m}$
STRESS RUPTURE		
- 1400°C/100 MPa	-	145 hours
- 1400°C/200 MPa	-	<.1 hr.
- 1300°C/200 MPa	-	170 hrs.
Total Oxygen w/o	2.1	1.8
Yttrium containing phases	δ-$Y_2Si_2O_7$ α-$Y_2Si_2O_7$	δ-$Y_2Si_2O_7$ $Y_5(SiO_4)_3$ N

1) Strength per MIL STD-1942 (MR)

2) Controlled flaw, 20 kg indent, Chantikul method

3) Indentation method, 10 kg indent, Anstis method

Specimen Codes: Monolith (1S, 3S), Composite (2N, 3N, 30I, IO)

Status of milestones

The first milestone has been completed. All others are on schedule.

1. Prepare and evaluate composites which utilize the first lot of CVD coated whiskers. Determine the effect of coatings on toughness - MAR 31, '87.
2. Determine HIP and nitridation processing parameters (time, temp., pressure) which reuslt in highest strength and K_{IC} for uncoated whisker reinforced Si_3N_4 - MAY 31, '87.
3. Prepare and evaluate composites which utilize whiskers of different aspect ratio, and composites which contain the 2nd lot of CVD whiskers. Determine optimum whisker l/d and coatings for improved toughness. Optimize SiC whisker distribution and green density. - SEP 31, '87.
4. Submit draft of final report to ORNL - NOV 31, '87.

Publications

None.

References

1. MIL-STD-1942 (MR), Flexural Strengths of High Performance Ceramics at Ambient Temperature, November 21, (1983).

2. Anstis, G.R., et al, "A Critical Evaluation of Indentation Techniques for Measuring Fracture Toughness: I, Direct Crack Measurements," J.Am.Ceram.Soc., 64 (9), 533-8 (1981).

3. Chantiful, P., et al, "A Critical Evaluation of Indentation Techniques for Measuring Fracture Toughness: II, Strength Method," J.Am.Ceram.Soc. 64(9), 539-43 (1981).

4. Quinn, G.D., "Guide to the Construction of a Simple 1500°C Test Furnace," U.S.Army Materials Technology Laboratory, AMMRC TR83-1, January 1983, NTIS ADA 125636.

5. Quinn, G.D., "Characterization of Turbine Ceramics after Long-Term Environment Exposure," U.S.Army Materials Technology Laboratory, AMMRC TR 80-15, April 1980, AD A117463.

6. Corbin, N.D., Rossetti, G. A., and Hartline, S.D., "Microstructure Property Relationships for SiC Filament - Reinforced RBSN," Cer.Eng.Sci.Proc., 7(7-8), 958-68 (1986).

7. Schuhmann, D. and D'Epenoux, B., "The Effect of Electrical Nonhomogeneities of Particles on Mean Surface Potential," J. Colloid and Interface Science, 116(1), 159-167(1987)

1.2.3 Oxide Matrix

Dispersion-Toughened Oxide Composites

T. N. Tiegs, L. A. Harris, and J. W. Geer (Oak Ridge National Laboratory)

Objective/scope

This work involves development and characterization of SiC-whisker-reinforced oxide composites for improved mechanical performance. To date, most of the work has dealt with alumina as the matrix because it was deemed a promising material for initial study. However, optimization of matrix materials is also being explored. The approach to fabrication is to first use hot pressing to identify compositions for toughening and then to explore pressureless sintering for fabrication to near net shape.

Technical progress

SiC Whiskers — The present understanding of toughening in whisker-reinforced ceramic composites indicates that crack-whisker interaction by crack bridging and deflection are the main mechanisms operating in high toughness materials. These mechanisms are dependent on the properties of the whisker-matrix interface, the size of the whiskers, and their inherent strength. To study the effects of these properties, whiskers from various sources were examined. Results of the fracture toughness of alumina–20 vol % SiC whisker composites are shown in Table 1. Considerable variation in the toughness values was observed from source to source and even from batch to batch from the same supplier.

Table 1. Fracture toughness of alumina–20 vol % SiC whisker composites influenced by SiC whisker source

Whisker source	Fracture toughness [K_{Ic} (MPa$\sqrt{m}$)]
Arco, Lot 1	8.3
Arco, Lot 2	7.4
Huber, Lot 1	3.6
Huber, Lot 2	5.6
American Matrix	5.4
Tateho, Lot 1	4.2
Tateho, Lot 2	3.9
Tokai Carbon	4.8
Versar	4.3
Los Alamos	9.1

Examination of fracture surfaces with a scanning electron microscope (SEM) showed considerable differences among composites with low and high fracture toughness (Fig. 1). In the high-toughness composites, the

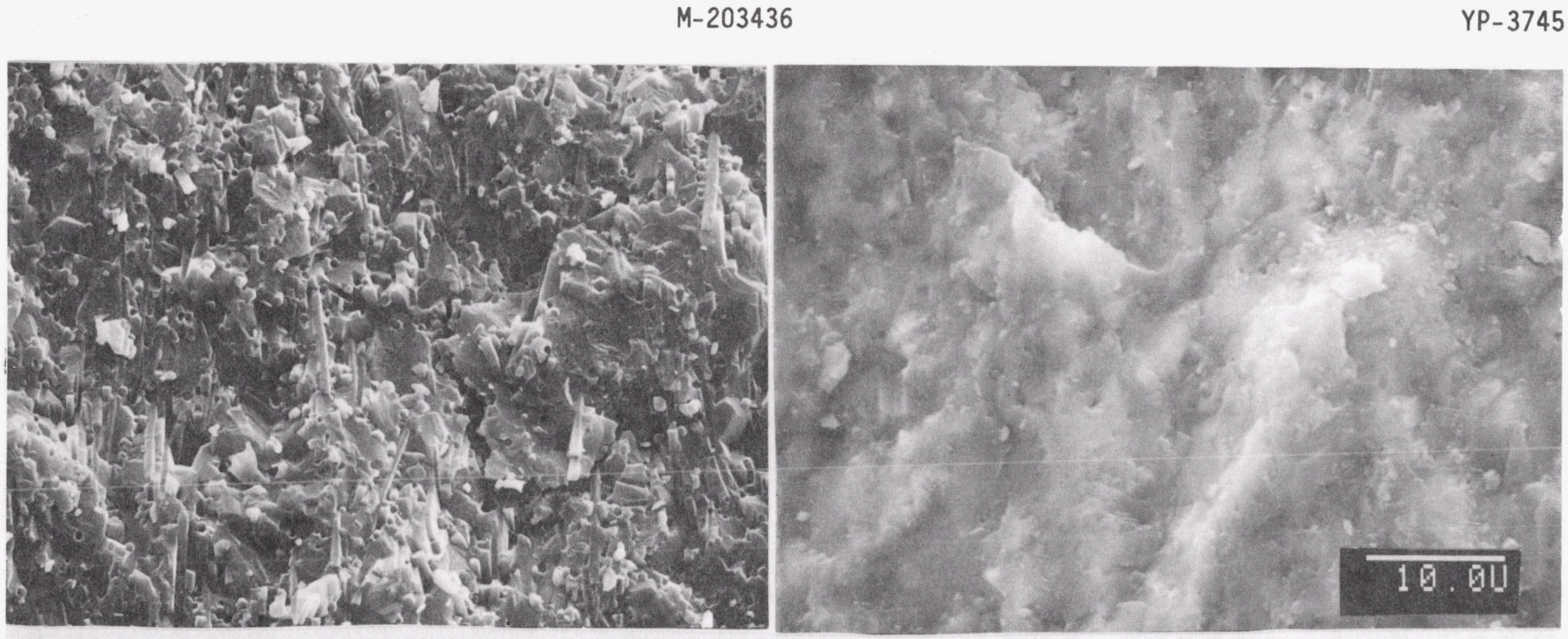

K1c=8.3 MPa m^0.5

K1c=3.9 MPa m^0.5

Fig. 1. SEM shows increased whisker-crack interaction in high-toughness composites.

surfaces are very rough and individual whiskers are readily observed. These are indicative of considerable crack-whisker interaction and of a relatively weak chemical bond at the whisker-matrix interface. On the other hand, the low toughness composites have relatively smooth fracture surfaces resembling transgranular fracture, which indicates that crack propagation is uninhibited by the whiskers in the low-toughness composites. The whisker-matrix bond is apparently too strong and, instead of the crack propagating along the interface, it propagates through the whisker.

Observations on alumina-SiC whisker composite materials with a transmission electron microscope revealed that the whisker-matrix interface is extremely thin (Fig. 2). To determine the effects of whisker surface chemistry on the interface, and consequently the fracture toughness, X-Ray photoelectron spectroscopy (XPS) of the whiskers was used. Generally, XPS showed that whiskers from composites with low fracture toughness were characterized by either high-surface oxygen or low-surface carbon. The whiskers from composites with high-fracture toughness were characterized by relatively low-surface oxygen and a suggestion of excess carbon on the surface.

The differences in the surface oxygen contents are illustrated in Fig. 3. The peak at ~100 eV binding energy is indicative of Si-C bonds, whereas the peak at ~103 eV is indicative of Si-O bonds. The high-surface oxygen, with indications of silica at the whisker surface, results in a strong bond at the interface and a composite with low toughness.

XPS results showing the differences in surface carbon between SiC whiskers is shown in Fig. 4. The low-energy peaks at 282 to 283 eV are attributable to SiC, whereas the peaks at 284 to 285 eV are indicative of surface carbon. The whiskers that went into the high-toughness composites had excess carbon on the surface, but the whiskers that went into the low-toughness composites had very little surface carbon.

Recent results have shown that the surfaces of SiC whiskers can be modified to decrease the surface oxygen and increase the surface carbon. Fracture toughness values for alumina-20 vol % SiC whisker composites with as-received and surface-modified whiskers are shown in Table 2. Although the initial toughness was low for the composites with surface-modified whiskers, an increase was apparent. The surface modifications are thought to lead to decreased bonding at the interface and result in greater crack-whisker interaction, as illustrated in Fig. 5.

In addition to surface modification and characterization, SiC whiskers from all available sources were examined by spark-source mass spectrometry to determine overall chemistry. Analytical chemistry results on the selected whiskers are given in Table 3.

Status of milestones

On schedule.

Publications

T. N. Tiegs and P. F. Becher, "Development of Alumina- and Mullite-SiC Whisker Composites: High-Temperature Properties," to be published in *Proceedings of Contractors' Coordination Meeting*, 1986.

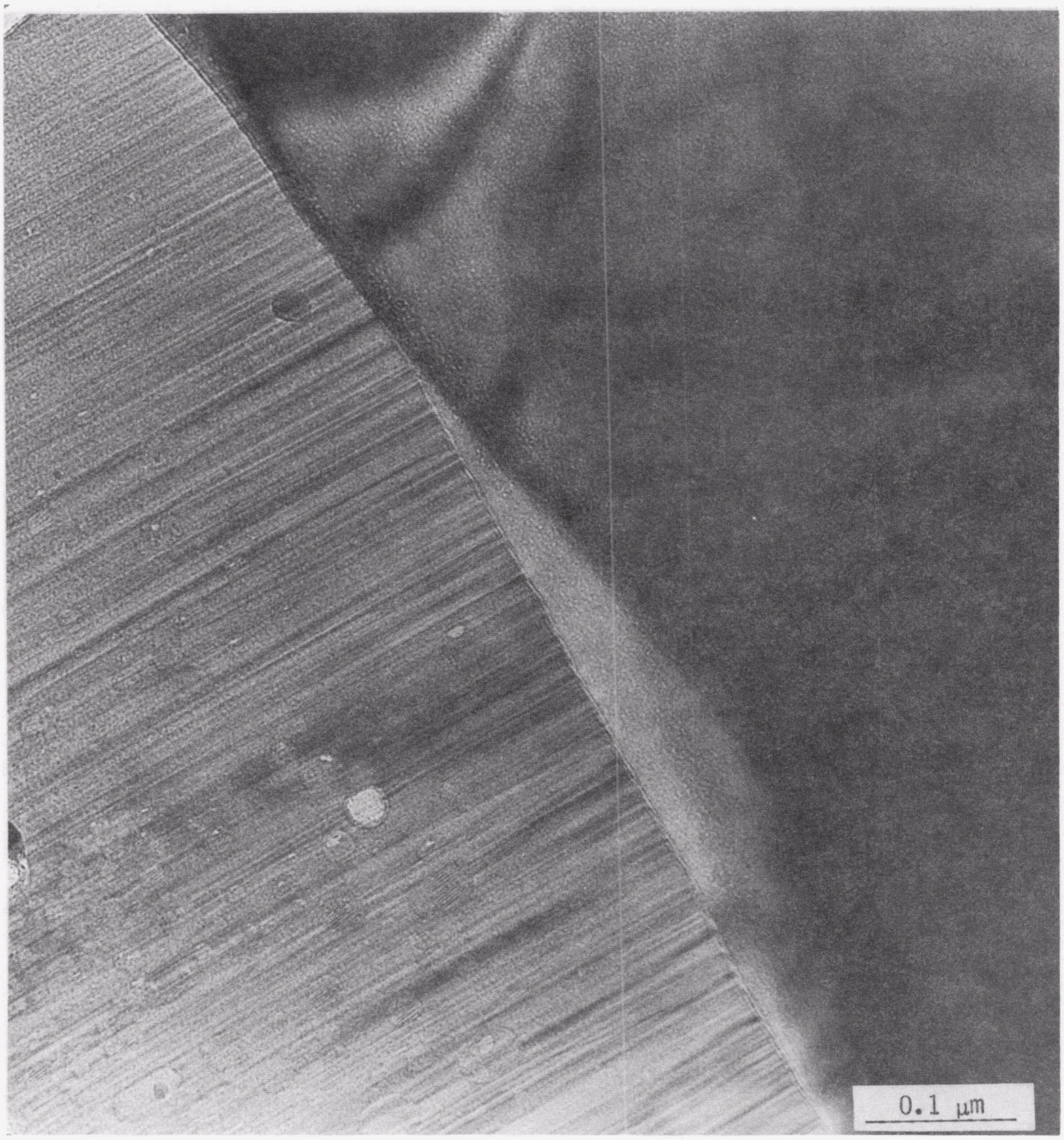

Fig. 2. TEM shows very thin interface between whiskers and alumina.

ORNL-DWG 86C-11173

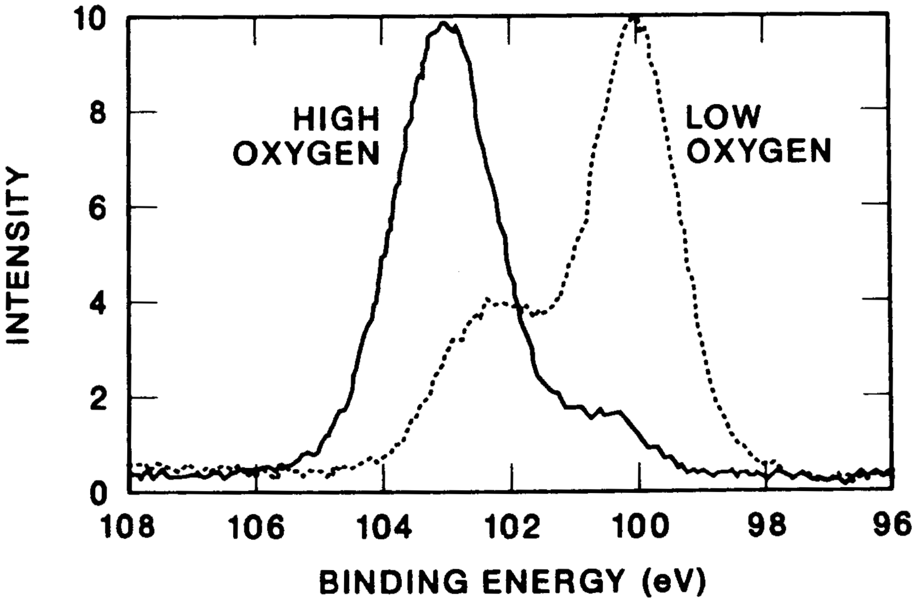

- BINDING ENERGY AT 100 eV → SiC
- BINDING ENERGY AT 103 eV → SiO_2
- SURFACE SiO_2 LAYER MAY RESULT IN STRONG BOND BETWEEN Al_2O_3 MATRIX AND WHISKER

Fig. 3. XPS of SiC whiskers reveals differences in surface chemistry.

ORNL-DWG 87-1930

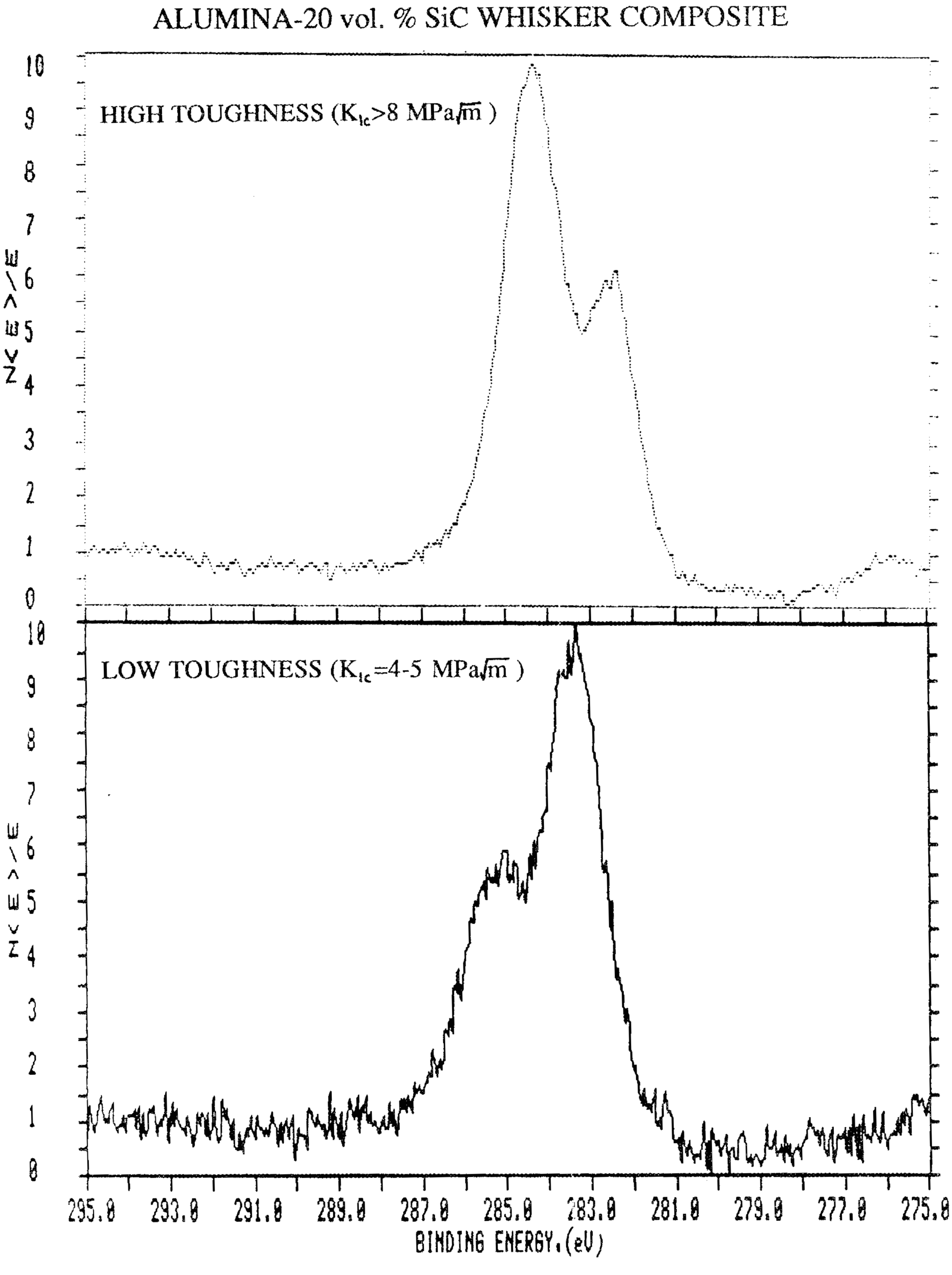

Fig. 4. XPS of whiskers used in high-toughness alumina matrix composites suggests excess carbon on surface.

M-23632

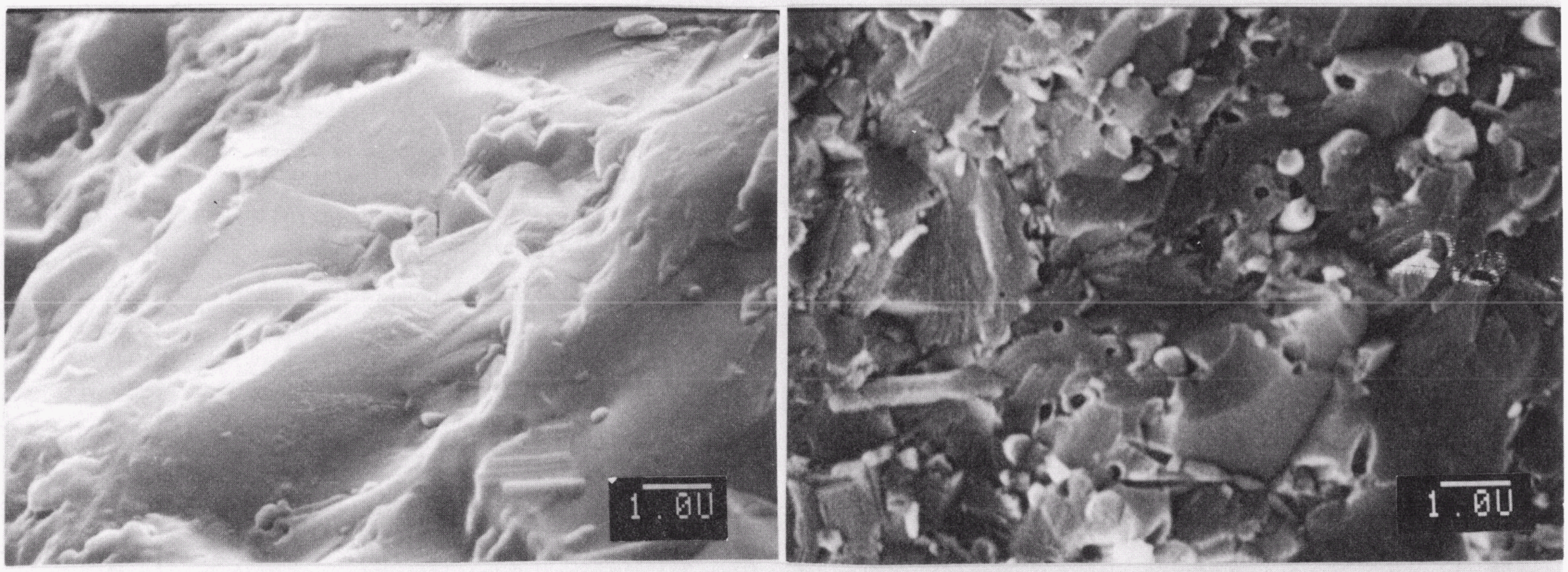

As Received

Surface Carbon Treated

K1c=3.9 MPa m^0.5

K1c=5.0 MPa m^0.5

Fig. 5. Surface-carbon treated whiskers show increased crack-whisker interaction and improved fracture toughness.

Table 2. Fracture toughness of alumina-20 vol % SiC whisker composites using as-received and surface-modified whiskers

Whiskers	Fracture toughness [K_{Ic} (MPa·$m^{1/2}$)]
As-received	3.9
Modification 1	4.5
Modification 2	5.0
Modification 3	5.4
Modification 4	6.0
Modification 5	4.3

Table 3. Chemical analysis of selected SiC whiskers (ppm)

	ARCO	Tateho	Huber	American Matrix	Versar Corp.	Tokai Carbon
O (wt %)	1.25	1.04	0.22	2.85	N.D.	N.D.
Al	120	500	30	200	30	10
B	<1	1	<1	≥1000	-	-
Ca	150	500	5	>1000	300	20
Co	<10	<10	<10	<10	<1	1000
Cr	15	50	20	200	30	50
Fe	60	300	300	200	50	50
K	10	25	<1	2	30	3
Mg	90	120	5	250	50	3
Mn	70	50	<1	5	50	5
Na	10	15	1	20	5	50
Ni	<10	<10	<10	200	10	10
Zr	<10	10	<10	60	10	3

ARCO Chemical Co., Greer, S.C.; Type SC-9.
Tateho Chemical Co., Japan; Type SCW-1S.
Huber Corp., Borger, TX; Type 7116.
American Matrix, Inc., Knoxville, TN; Experimental Lot.
Versar Corp., Springfield, VA; Type SCW-1.
Tokai Carbon Co., Japan; Type Tokamax.

Sol-Gel Oxide Powder

W. D. Bond, P. F. Becher, and T. N. Tiegs (Oak Ridge National Laboratory)

Objective/scope

Sol-gel processes can potentially synthesize materials that can be processed at modest temperatures; simultaneously, highly uniform composition is obtained in dense, fine-grain ceramics which incorporate dispersed second phases to increase fracture toughness. This research emphasizes the determination of the feasibility of sol-gel processes for (1) synthesizing powders of phase-stabilized zirconia and alumina and (2) synthesis of $Al_2O_3-SiO_2$ gels for conversion to mullite ($3Al_2O_3 \cdot 2SiO_2$) by reaction sintering. Sol-gel processes take advantage of the high degree of homogeneity that can be achieved by mixing on the colloidal scale and by the surface properties of the colloidal particles. The excellent bonding and sintering properties of colloids are a result of their very high specific surface energy.

Technical progress

Studies were continued on the preparation of colloidal zirconia, hafnia, and alumina by thermal hydrolysis reactions in an autoclave and the characterization of the product colloidal oxides. Work was also initiated on preparing $Al_2O_3-SiO_2$ gels for the synthesis of mullite ($3Al_2O_3 \cdot 2SiO_2$) ceramics.

Investigations of the morphology of colloidal oxides prepared by hydrothermal reaction are continuing. During this report period, work was focused on Al_2O_3 colloids. Oxide morphology is determined by transmission electron microscopy. In preparations of Al_2O_3 colloidal particles, we are investigating the effects of the type of precursor aluminum salt (nitrate or chloride), the salt concentration, and the hydrolysis temperature. In addition, we are investigating the effects of aging the colloids after hydrolysis of the salt is completed. At 0.02 $\underline{M}$ concentrations of the nitrate or chloride salt, complete conversion to large Al_2O_3 fibers (~1500 nm lengths) of the boehmite structure did not occur after a 60-h reaction time at 150°C. With the aluminum chloride precursor salt, modest amounts of spherical agglomerates (~200 nm diam) of tightly packed smaller fibers (50 nm length) were also formed. Smaller and irregular shaped agglomerates of the smaller fibrils were observed in product oxides from the nitrate salt precursor. At higher aluminum salt concentrations (0.3 to 0.5 $\underline{M}$), we observe only the large fibers of the boehmite structure in the hydrolysis products. The length and width of the fibers obtained are governed by both the reaction time and temperature. Our studies have shown that temperatures of at least 150°C are required to promote practical growth rates of the Al_2O_3 fibers. For example, at 125°C several days are required to grow fibers of ~30 nm length, whereas at 150°C the fibers grow to 500 nm in 4 to 6 h.

Gel particles of $Al_2O_3-SiO_2$ were prepared by chemical gelation of Al_2O_3-SiO_2 sols which were obtained by mixing Al_2O_3 sols and SiO_2 sols in ratios that are necessary for mullite synthesis. Silica sols are prepared by hydrolyzing tetraethyl orthosilicate in ammoniated ethanol solutions at pH values of ~12. Alumina sols were prepared by our previously reported method, which consists of the thermal hydrolysis of acid deficient aluminum nitrate in an autoclave at 175°C.

To date, our studies show that the colloidal oxides are less tightly agglomerated in powder particles when chemical gelation of Al_2O_3–SiO_2 occurs in water-ethanol solutions of ammonium hydroxide instead of in aqueous solution and then washed with dry ethanol. The dried gel particles (60°C) from alcohol processing were much softer and more easily crushed to fine powder than those processed in water. Similar benefits of alcohol processing for ZrO_2 powder preparation have been reviewed by Van de Graff and Burggraaf.[1] In our studies, we have observed that the tap densities of Al_2O_3–SiO_2 or ZrO_2 powders are reduced by about one-half when the oxide hydrogels are washed with dry ethanol prior to drying and calcination.

Status of milestones

Progress on Al_2O_3–SiO_2 gel powder synthesis variables (Milestone 12 33 04) is on schedule.

Publications

None.

References

1. M.A.C.G. Van de Graff and A. J. Burggraaf, "Wet Chemical Preparation of Zirconia Powders: Their Microstructure and Behavior," pp. 744-765 in Advances in Ceramics, Vol. 12, N. Claussen, M. Ruhle, and A. H. Heuer (eds.), American Ceramic Society, Inc., 1984.

Processing of Improved Transformation-Toughened Ceramics

J. B. Blum and G. A. Rossi (Norton Company), and C. E. Knapp
(Norton Research Corp., Canada)

Objective/scope

The objective of this program is the production of zirconia toughened ceramics (ZTC) which exhibit mechanical properties (strength and toughness) superior to those of the "state of the art" toughened ceramics, particularly at high temperature and after prolonged aging at high temperature. In addition, such ceramics should possess low thermal conductivity to minimize energy losses in heat engine applications.

The scope includes the powder synthesis and characterization, shape forming, pressureless sintering, characterization of the sintered ceramics, and reporting of results.

Our research will concentrate on three classes of zirconia toughened ceramics (ZTC), i.e. Mg-PSZ, (MgO-partially stabilized zirconia), Y-TZP (Y_2O_3-tetragonal zirconia polycrystals), and ZTA (zirconia toughened alumina). Most of the work will be done using rapidly solidified (R/S) powders, which offer several important advantages over the chemically derived (C/D) powders. However, the C/D powders or their mixtures will be used for testing new compositions, since melting/rapid solidification of small batches is expensive and impractical.

The ceramics should be made by pressureless sintering, but hot isostatic pressing will be used to evaluate the potential of each composition, before processing optimization is complete.

The goals of this program are minimum values of strength and toughness at RT and at 1000°C; in addition, the ceramics should meet the same requirements for RT strength and toughness after aging in air at 1000°C for 1000 hrs.

Technical Progress

During the last six months work has concentrated on the following areas:

1. Preparation of the ceramics using the R/S powders. At the end of 1986 it was decided to use the R/S powders for the rest of the contract period, since these powders have shown clear advantages over the C/D powders. However, it was also decided to use C/D powders or mixtures of them for the purpose of quickly evaluating new compositions, by using hot isostatic pressing after sintering to close the residual porosity.

2. Preparation of new compositions which possess the highest potential for meeting the program objectives, especially the minimum requirement for fracture toughness at 1000°C.

3. Identification of a reliable method for the measurement of fracture toughness at high temperature, after the disappointing results obtained with the MCF (multiple controlled flaw) method.

4. Improvement of our understanding of the properties of the 4 w/o Y_2O_3-TZP ceramics made with the R/S powder, in particular the relationship between microstructure, composition, and mechanical properties.

5. Reduction of the critical flaw size in the pressureless sintered ceramics, obtained by the elimination of hard agglomerates and foreign inclusions.

1. Mg-PSZ ceramics made with the R/S powder

It was previously reported that a unique microstructure was obtained in Mg-PSZ ceramics made with R/S powders, by sintering in the two phase (t + c) field at 1500°C and by aging at 1400°C. This microstructure contains two types of t-ZrO_2 particles, i.e. intragranular (the typical ellipsoids contained in the cubic grains) and intergranular. The intergranular t-ZrO_2 grains are typically about 3 um in size and their volume fraction, although it was not measured, appears to be consistent with the one predicted by the lever rule for the composition 3 w/o MgO-ZrO_2. These ceramics, therefore, are different from the NILCRA Mg-PSZ materials, which exhibit large (~60 um) cubic grains containing coherent t-ZrO_2 precipitates.

The presence of the 3 um intergranular t-ZrO_2 grains and the smaller size (5-10 um) of the cubic grains in our material could result in different mechanical properties, for example better wear resistance due to decreased grain pullout. However, the contribution to fracture toughness of the 3 um intergranular t-ZrO_2 grains is not known at present.

Attempts to produce uncracked pressureless sintered billets of these ceramics have not been successful. During the first experiments the billets fired in air showed a high percentage of m-ZrO_2 in the as-fired surface and it was concluded that cracking was the result of the stress induced by the t-m transformation, which, in turn, was believed caused by loss of MgO from the surface during firing. More recently, the green billets were fired buried in a bed of powder of the same composition and also in pure MgO powder. Although no m-ZrO_2 was detected by XRD on the as-fired surface, the fired billets were still cracked, but it seems that these cracks are process related, rather than induced by the t/m transformation. The reason is that a polished interior surface of the billets showed no m-ZrO_2 by XRD.

A sample was also analyzed by TEM, but the 3 um intergranular grains were found to be all m-ZrO_2. It appears that the t/m transformation occurred either during the sample preparation or under the electron beam.

Work will continue to try to make uncracked billets and to answer the question of the relative transformability of the intergranular vs. intragranular t-ZrO_2 particles, which affects the fracture toughness.

2. Y-TZP ceramics made with the R/S powders

2.1 Microstructural studies on the rapidly solidified crude and on the sintered ceramics

The R/S crude (4 w/o Y_2O_3) has shown the presence of the t'-ZrO_2 phase. This tetragonal phase has been reported in other materials rapidly cooled. It results from a displacive cubic to tetragonal phase transformation in Y_2O_3-ZrO_2.(1) Fig. 1 shows the twinned structure observed. The twinning is believed to result from mechanical deformation needed to accommodate strains arising from the phase transformation(1).

The sintered sample (4 w/o Y_2O_3) had equiaxed, predominately tetragonal grains (Fig. 2). No twinning was observed, but some grains did contain a dislocation substructure and had low angle boundaries, as seen in Fig. 3. The grains had rounded edges and a continuous glassy phase was observed at grain boundaries and three grain junctions. This microstructure is similar to those reported for other Y-TZP's(2).

2.2 Relationship between grain size and fracture toughness

A classified (particle size <1 um) 4.6 w/o Y_2O_3-ZrO_2 (R/S) powder was used to press discs, which were sintered at 1475°C to ~99% of TD. The discs were aged at 1500° and 1600°C for different times, cut, polished and thermally etched at 1400°C. The microstructure was obtained by SEM and K_{IC} with the microindentation method(3).

Table 1 shows that the fracture toughness increases with the average grain size, whereas the hardness is virtually unchanged.

Table 1

Relationship Between Aging Conditions, Grain Size, Hardness and K_{IC}

Aging T °C	Aging t (hrs.)	AGS (um)	K_{IC} MPa.m)	H_V (GPa)
1500	1	.56	7.6	15.2
1500	4	.66	8.3	15.0
1600	1	.75	8.0	15.1
1600	4	1.24	8.4	14.9
1600	6	1.60	9.0	15.0

Note: AGS = Average Grain Size, H_V = Vickers hardness

It is interesting to note that spontaneous cracking on cooling did not occur, an indication that the critical grain size for spontaneous transformation to m-ZrO_2 should be larger than 2 um. This conclusion is in agreement with Swain's results(4). He has aged samples of Toyo Soda TZ2Y (3.6 w/o Y_2O_3) and found that K_{IC} reaches a value of about 14 $MPa.m^{\frac{1}{2}}$ for a grain size of 1.9 um. No mention is made in his paper of spontaneous cracking on cooling. It is known(5) that the critical grain size for spontaneous transformation to m-ZrO_2 increases with the Y_2O_3 content and that, for the same grain size, a lower Y_2O_3 content gives a higher K_{IC}(6). Figures 4, 5, 6, 7 and 8 show the microstructures of the aged samples described in Table 1.

2.3 Low temperature dilatometry on Y-TZP samples

Five samples of different compositions and microstructures were sent to P. Becher of ORNL, who tested them in a low temperature dilatometer to try to detect the M_s and A_s temperatures. The samples are described in Table 2.

Fig. 9 shows the results obtained. The samples, 0.56 cm long, were cooled to -170°C at 10°C/min. Samples YZ110-C-S1475 and YZ110-MG-1500 seem to exhibit a small amount of t/m transformation, but no firm conclusion can be drawn from these data. These samples, according to P.Becher, behave similar to other fine grained Y-TZP ceramics containing 2-3 m/o Y_2O_3. In conclusion, it appears that these materials have an M_s temperature lower than -170°C. Since K_{IC} increases when M_s approaches the use temperature of the material(7), it should be possible to improve the toughness of the Y-TZP ceramics by careful manipulation of composition and microstructure, which both influence M_s.

2.4 Y-TZP ceramics made with R/S powder of higher purity

It was previously reported that high purity R/S powders contain less Ti, Si, Fe and Al than the regular R/S powders. Sintered and sintered/HIPed billets of the high purity material were made and tested for MOR at RT and at 1000°C. The results are shown in Table 3, where the MOR values for the low purity ceramic are also presented, for the sake of comparison.

Table 2

Sample Designation	d (Mg/m^3)	Designation
YZ110-MG-1500	6.02	4 w/o Y_2O_3-ZrO_2 made with rapidly solidified, mill grade powder, sintered at 1500°C
YZ110-C-S1475	6.03	4 w/o Y_2O_3-ZrO_2 made with rapidly solidified classified (<1 um) powder, sintered at 1475°C
YZ110-C-S/H	6.09	4 w/o Y_2O_3-ZrO_2 made with rapidly solidified, classified (<1 um) powder, sintered at 1475°C/HIPed at 1550°C
YZA-47-S1600	5.50	80 w/o (4 w/o Y_2O_3-ZrO_2) - 20 w/o Al_2O_3, made with rapidly solidified, mill grade powder, sintered at 1600°C
TZ2Y40A-SU-S1500	4.98	60 w/o (2 m/o Y_2O_3-ZrO_2) - 40 w/o Al_2O_3, Toyo Soda zirconia and Sumitomo alumina powders, mechanically mixed. Sintered at 1500°C.

Table 3

RT and 1000°C MOR (4 pt.) of low purity and high purity Y-TZP's (Sintered and Sintered/HIPed ceramics) (MPa)

Mat'.	Wt.% Y_2O_3	Avg. RT MOR	Max. RT MOR	Avg. 1000°C MOR	Max. 1000°C MOR
Low Purity Sintered	~4.5	970 (5)	1040	311*(3)	345*
High Purity Sintered	~4.5	875 (4)	930	440 (4)	460
Low Purity Sint./HIP	~4.5	1520 (6)	1680	539 (4)	565
High Purity Sint./HIP	~4.5	1475 (4)	1750	544 (4)	606

Note: Numbers in parenthesis are the bars broken. The numbers with the asterisk are obtained in 3 pt. bending. The typical chemical analysis of the low purity and high purity powders is as follows:

Low purity: Si = 0.05%; Ti = 0.15%; Al = 0.45%; Fe = 0.07%
High purity: Si = 0.03%; Ti = 0.04%; Al = 0.04%; Fe = 0.03%

It is not clear at present whether the higher strength values are due to the higher purity or also to other reasons (i.e. higher K_{IC}, fewer flaws).

3. Y-TZP ceramics containing Al_2O_3 as dispersed phase

3.1 Composition 80 w/o (4 w/o Y_2O_3-ZrO_2)-20 w/o Al_2O_3, R/S powders (Code name: YZA-47)

It was previously reported that the RT MOR (4 pt.) for this material was 1096 MPa and 425 MPa at 1000°C. More work has been done and billets were prepared by pressure casting to reduce the flaws, but cracking was frequently experienced. It now appears that the cracked billets were too low in yttria and underwent transformation from t-ZrO_2 to m-ZrO_2 on cooling. We were recently able to cast and sinter five good billets. The average MOR (4 pt.) was 976 MPa (18 bars), with a maximum of 1296 MPa. Fractography on ten of the samples has shown that, in most cases, large (20-50 um) voids were the strength limiting flaws, as seen in Fig. 10. We believe that these flaws resulted from organic inclusions which burned out during firing.

The strength values for this material are summarized in Table 4.

3.2 Composition 80 w/o (5.3 w/o Y_2O_3-ZrO_2)-20 w/o Al_2O_3, Toyo Soda C/D powder (Code name: Super Z)

Sintered and sintered/HIPed billets were made using the Super Z powder from Toyo Soda. The strength was measured at RT and at 1000°C. The values are reported in Table 4. The sintered ceramics exhibit very respectable strength, but after HIPing the gain is only marginal and the MOR value is much lower than those claimed by Toyo Soda in a recent US Patent (8). A reason could be the fact that the sintering and HIPing temperatures in this experiment were higher than those reported in the Toyo Soda patent.

3.3 Composition 80 w/o (3.6 w/o Y_2O_3-ZrO_2)-20 w/o Al_2O_3, made from commercial powders (Code name: TZ2Y/20A)

Toyo Soda TZ2Y (2 m/o Y_2O_3-ZrO_2) and Sumitomo AKP-30 alumina were ball milled in ethanol, after which the suspension was dried in a vacuum evaporator. The billets were sintered and also sintered/HIPed. The MOR values at RT and 1000°C are shown in Table 4 and are not as high as those of the Toyo Soda and our R/S ceramics. The probable reason seems to be the non uniformity of the microstructure, as seen in Fig. 11. Only traces of the m-ZrO_2 were found in the as-fired surface by XRD.

3.4 Composition 60 w/o (3.6 w/o Y_2O_3-ZrO_2)-40 w/o Al_2O_3 made from commercial powders (Code name: TZ2Y/40A)

The same powders used in experiment 3.3 were used and mixed according to the procedure described above. Sintered billets only have been made. The MOR values at RT and 1000°C are shown in Table 4. Also in this case the strength is fairly low. Less than 5% m-ZrO_2 was found on the as-fired surface by XRD. The microstructure is not very uniform and is shown in Fig. 12.

Table 4

MOR (4 pt.) at RT and 1000° for Sintered and Sintered/HIPed Y-TZP Ceramics Containing Alumina As Dispersed Phase (Values are in MPA)

Mat'l.	Avg. RT MOR	Max. RT MOR	Avg. 1000°C MOR	Max. 1000°C MOR
YZA-47 Sintered	976 (18)	1296	427 (8)	503
YZA-47 Sint./HIPed	1226 (4)	1598	510 (4)	517
SUPER Z Sintered	1171 (4)	1357	455 (4)	510
SUPER Z Sint./HIPed	1226 (3)	1440	593 (3)	675
TZ2Y/20A Sintered	710 (7)	841	282 (7)	324
TZ2Y/20A Sint./HIPed	1406 (7)	1571	482 (6)	710
TZ2Y/40A Sintered	661 (6)	703	282 (6)	303
TZ2Y/40A Sint./HIPed	N/A	N/A	N/A	N/A

Note: Numbers in parenthesis are the bars broken; N/A = not available.

4. Zirconia Toughened Alumina (ZTA) Ceramics

4.1 ZTA Ceramics made with the R/S powders

As previously mentioned, four batches of R/S powders with the compositions reported below have been made and pressureless sintered ceramics were obtained:

Mat'l. Code	Wt.% Al_2O_3	Wt.% ZrO_2	Wt.% Y_2O_3	Wt.% Y_2O_3 in Y/Z
AZY-55	78.6	21.4	0	0
AZY-57	76.5	23.2	0.33	1.4
AZY-56	76.4	23.0	0.60	2.6
AZY-54	76.1	22.9	1.02	4.4

Only material AZY-54 (with the highest w/o Y_2O_3) has given uncracked billets, whose RT MOR (3 pt.), measured on minibars (1x1x30 mm) was 1061 MPa.

Recently, green billets of the same materials have been HIPed at 1300°C and the following results were obtained for RT MOR (minibars) and for hardness:

Material Code	AVG MOR (3 pt.)	MAX. MOR (3 pt.	H_v (GPa)
AZY-55	Bars could not be made due to high % m-ZrO_2		
AZY-57	1013	1129	19
AZY-56	1040	1102	19
AZY-54	1233	1385	20

No K_{IC} values are available for these ceramics.

The reason for using hot isostatic pressing was to keep the grain size finer and retain a larger fraction of t-ZrO_2 after cooling to room temperature. This goal was achieved, as shown by the absence of cracking in all materials except AZY-55, which contains no Y_2O_3. The XRD patterns of the four ceramics HIPed at 1300°C (Fig. 13) show that the % m-ZrO_2 in the polished interior surface decreases with the increase in yttria content. Figs. 14 and 15 are SEM photomicrographs of the microstructures of materials AZY-57 and AZY-54, showing a fairly good distribution of the ZrO_2 grains in the Al_2O_3 matrix. However, a fraction of the zirconia appears trapped within the Al_2O_3 grains. The trapping is believed to occur when delta alumina, originally present in the powder, transforms to alpha alumina around 1200°C. Intragranular zirconia particles are not desirable for maximum toughness, since they are more resistant to transformation(9). More work will be done to control the delta -- alpha transformation and avoid the formation of intragranular ZrO_2 grains.

4.2 ZTA ceramics containing CeO_2

4.2.1 Composition 20 w/o (16 w/o CeO_2-ZrO_2)-80 w/o Al_2O_3

A powder of this composition was prepared by mixing in ethanol the Toyo Soda TZ12CE (12 m/o CeO_2-ZrO_2) and the Sumitomo AKP-30 alumina powders. The liquid was then evaporated with a rotary vacuum drier. Pressureless sintered billets, fired at 1500°C contained about 5% porosity and they were HIPed at 1550°C to virtually theoretical density (4.3 Mg/m^3). The microstructure, shown in Fig. 16, is not very uniform and grain pullout is evident after polishing. K_{IC} measured with the microindentation technique was about 6.5 $MPa.m^{\frac{1}{2}}$, but difficulties were encountered in measuring the crack length. The MOR (4 pt.) at RT and 1000°C are reported below:

RT AVG. MOR (MPa)	RT MAX MOR (MPa)	1000°C AVG. MOR (MPa)	1000°C MAX. MOR (MPa)
847 (4)	971	503 (4)	613

Note: Numbers in parenthesis are the bars broken.

Further attempts were made to produce a uniform aqueous suspension of the two powders, by using pH control and also by using steric stabilization (Darvan 821 A). These experiments failed to give a stable mixed suspension, due to the sedimentation of the TZ12CE powder.

4.2.2 Composition 22 w/o (16 w/o CeO_2-ZrO_2)-78 w/o Al_2O_3

A powder of this composition was prepared by adding colloidal sols of CeO_2 and ZrO_2 (supplied by NYACOL Corp.) to a suspension of AKP-30 alumina. The suspension was freeze-dried to avoid the formation of hard agglomerates and a small sample was pressed and sintered at 1600°C in a dilatometer. The fired density was about 99% of TD (TD = 4.33 Mg/m^3). The microstructure of this sample is shown in Fig. 17. It appears fairly uniform, but it shows grain pullouts as in the one discussed above. Unfortunately, large billets could not be made due to an accident which occurred in the cold isostatic pressing operation.

5. Aging at 1000°C/1000 hrs. of Y-TZP ceramics with and without Al_2O_3

Eight Y-TZP ceramics, with and without alumina, made with the rapidly solidified and chemically derived powders, sintered or sintered/HIPed, were aged for 1000 hrs. at 1000°C and slowly cooled in the furnace. Table 5 shows composition and firing conditions for these ceramics.

Table 5

Sample Code	Composition	Powder Used	Sint. T (°C)	HIP T (°C)
YZ-110-MG-S1500	4w/o Y2O3-ZrO2	R/S Low Purity	1500	--
YZ-46-MG-S1600	4.5w/o Y2O3-ZrO2	R/S High Purity	1600	--
YZA-47-S1500	3.2 w/o Y2O3 20 w/o Al2O3 76.8 w/o ZrO2	R/S High Purity	1600	--
TZ2Y-S1500	3.6w/o Y2O3-ZrO2	C/D (Toyo Soda)	1500	--
TZ2Y-S/H	3.6w/o Y2O3-ZrO2	C/D (Toyo Soda)	1500	1550
Z4Y20A-I-S/H	3.2 w/o Y2O3 20 w/o Al2O3 76.8 w/oZrO2	C/D (Method I)	1500	1550
SUPER Z-S1500	4.3 w/o Y2O3 20 w/o Al2O3 75.7 w/o ZrO2	C/D (Toyo Soda)	1500	--
TZ2Y/20A-S1500	2.9 w/o Y2O3 20 w/o Al2O3 77.1 w/o ZrO2	C/D (Toyo Soda + Sumitomo)	1500	--

The properties measured before and after the aging period are: %m-ZrO_2 by XRD, RT K_{IC} (microindentation) average RT MOR (4 pt.) and microstructure by SEM. Table 6 summarizes the results obtained.

Table 6

Properties of ceramics before and after aging at 1000°C/1000 hrs.

BEFORE AGING				AFTER AGING		
Material	%m-ZrO_2	MOR	K_{IC}	%m-ZrO_2	MOR	K_{IC}
YZ-110-MG-S1500	12	861(5)	9.2	82	cracked	5.0
YZ-46-MG-S1600	<5	875(5)	5.2	76	909(5)	13.3
YZA-47-S1500	<5	1096(2)	6.7	82	cracked	4.4
TZ2Y-S1500	<5	1233(6)	5.4	40	1213(5)	11.8
TZ2Y-S/H	<5	1371(8)	10.1	69	1240(5)	14.1
Z4Y20A-I-S/H	<5	1647(4)	4.8	7	1344(5)	4.4
SUPER Z-S1500	<3	1171(4)	3.9	0	1268(5)	4.0
TZ2Y/20A-S1500	<3	710(7)	4.4	3	854(5)	6.2

Note: MOR values are in MPa; K_{IC} values are in MPa·m ; numbers in parenthesis are # of MOR bars broken; MOR bar size is 3x3x30mm; K_{IC} was measured on the cross section of the billet; %m-ZrO_2 is from as-fired surface of billet.

From the data of Table 6, one can draw the following preliminary conclusions:

1) all materials containing 20 w/o Al_2O_3 showed no increase in % m-ZrO_2 and their strength was retained or improved, except for YZA-47-S1500.

2) the cracking of YZ-110-MG-S1500 and YZA-47-S1500 is not explainable at present and more studies are necessary.

3) the dramatic increase in %m-ZrO_2 on the billet surface is not accompanied by strength degradation in three of these ceramics.

4) there appear to be no correlation between change in toughness and change in strength.

5) the ceramics made with the C/D powders have shown better thermal stability.

The high %m-ZrO_2 in the Y-TZP samples after aging could be a surface effect. Polished cross sections were submitted for XRD to answer this question.

Figs. 18 through 25 show the microstructures of the eight ceramics <u>before</u> and <u>after</u> the aging treatment. In all cases no significant changes are visible. However, the grain size distribution curves, if available, could reveal an increase in the fraction of the coarse grains in the aged samples, which could explain the cracking of materials YZ-110-MG-S1500 and YZA-47-S1500. It must be remembered, however, that many factors may influence the tendency of the material to crack, viz, grain size distribution, yttria content, yttria distribution among individual grains, presence of yttria rich glassy phases which may have depleted yttria from the adjacent grains. Another reason for the cracking could be the t/m transformation induced by moisture in the critical temperature range of 200-300°C.

6. Powder processing/Shape forming methods

This part of the program has received much attention, but recently the main effort has focussed on producing R/S powders with the desired composition and free from foreign impurities, rather then characterizing the suspensions and optimizing their properties for the production of the best green parts by casting. HIPing was extensively used as a tool for a quick evaluation of new compositions, but the colloidal processing of the powders is still considered crucial for obtaining good and reproducible mechanical properties. We have now in house two "state of the art" instruments for the characterization of concentrated suspensions and we feel that they will provide invaluable information not available before.

7. Measurement of K_{IC} with the Double Torsion Method (DTM)

As mentioned previously, the MCF (multiple controlled flaw) method for the measurement of K_{IC} has proven unreliable at high temperature, since the cracks tend to heal and become invisible after the test.

Attempts were made to use the Indent Strength in Bending (ISB) method, but the "penny shaped" cracks on the fracture surface of the MOR bars were not clearly visible in most samples.

L.Chuck, our expert in mechanical properties of materials, previously at NBS, has suggested the use of the double torsion method (DTM) for K_{IC} measurement. Before the end of April we will have a high temperature fixture and the first measurements on the most promising materials will be done.

8. Alternate melting/rapid solidification technques

Norton Co. has recently acquired Plasma Materials, Inc. of Manchester, (N.H.). In this facility we have started producing rapidly solidified ceramic materials, but at present only very small quantities have been obtained, insufficient for making billets. The main problems encountered have been the collection of the R/S product and the control of the solidification rate. The first problem was solved, but the second one is still of major concern and now has first priority.

Status of Milestones

A new list of milestones for 1987 has been written, submitted to (and approved by) the ORNL contract manager. The list is shown below:

Milestone #	Description	Date
1	Identify M_s and A_s temperatures of Y-TZP ceramic using low temperature (Liquid N_2) dilatometry.	Mar. 31
2	Final evaluation of the Mg-PSZ ceramics made with the R/S powders.	Mar. 31
3	Develop ceramic fixture for measurement of hot fracture toughness with double torsion technique.	Apr. 30
4	Evaluate influence of microstructure of Y-TZP ceramics made with the R/S powders on MOR and K_{IC} at RT and HT.	Jun. 30
5	Evaluate MOR and K_{IC} at RT and HT for ZTA ceramics made with C/D and R/S powders, i.e. ZrO_2/Al_2O_3, Y-TZP/ Al_2O_3, Ce-TZP $(HfO_2)/Al_2O_3$.	Jul. 31
6	Select final composition and best processing method for final optimization.	Jul. 31
7	Optimize composition, processing, firing schedule to achieve program objectives.	Oct. 31
8	Measure thermal conductivity and thermal expansion coefficient of ceramic with optimized composition.	Oct. 31
9	Write final report to document results of the research contract.	Nov. 30

Milestone #1 has been met. Milestone #2 was not met due to the cracking problems previously mentioned and further work will be done. All other milestones are on schedule.

Publications

1. G. A. Rossi, C. E. Knapp, J. B. Blum and K. E. Manwiller: "Zirconia Toughened Ceramics For Heat Engine Applications". To be published in the Proceedings of the Twenty-Fourth Automotive Technology Development Contractors' Coordination Meeting, Dearborn, MI, 10/30/86.

References

1. A.H. Heuer, R. Chaim, V. Lanteri, "The Displacive Cubic → Tetragonal Transformation in ZrO_2 Alloys", Acta. Metall., 35, 661-666, (1987).

2. M. Ruhle, N. Claussen and A. H. Heuer, "Microstructural studies of Y_2O_3-Containing Tetragonal ZrO_2 Polycrystals (Y-TZP)", Science and Technology of Zirconia II, p. 352-370, Advances in Ceramics, Vol. 12, Pub. by the American Ceramic Society.

3. G. R. Anstis, P. Chantikul, B. R. Lawn and D. B. Marshall, "A Critical Evaluation of Indentation Techniques for Measuring Fracture Toughness: I, Direct Crack Measurements". J. Am. Ceram. Soc., 64, 9, 533-538, (1981).

4. M. V. Swain, "Grain Size Dependence of Toughness and Transformability of 2 mol% Y-TZP Ceramics", J. Mat. Sci. Lett., 5, 1159-1162, (1986).

5. F. F. Lange, "Transformation Toughening", J. Mat. Sci., 17, 240-246, (1982).

6. T. Masaki, "Mechanical Properties of Toughened ZrO_2-Y_2O_3 Ceramics", J. Am. Ceram. Soc., 69, 638-640, (1986).

7. P. F. Becher, "Toughening Behavior in Ceramics Associated with the Transformation of Tetragonal ZrO_2", Acta. Metall., Vol. 34, No. 10, pp. 1885-1891, (1986).

8. "High Strength Zirconia Type Sintered Body", U. S. Patent 4,587,225 (May 6, 1986).

9. B. W. Kibbel and A. H. Heuer, "Ripening of Inter- and Intragranular ZrO_2 Particles in ZrO_2-Toughened Al_2O_3", Science and Technology of Zirconia II, Advances in Ceramics, Vol. 12, p. 415-424, Pub. by the Am. Ceram. Soc. (1984).

13-1448

Fig. 1: Twinned tetragonal (t') microstructure of R/S raw material. The twins are believed to result from stress accommodation.

Fig. 2: Microstructure of sintered R/S material. Well defined, equiaxed grains about 1 um in diameter are evident.

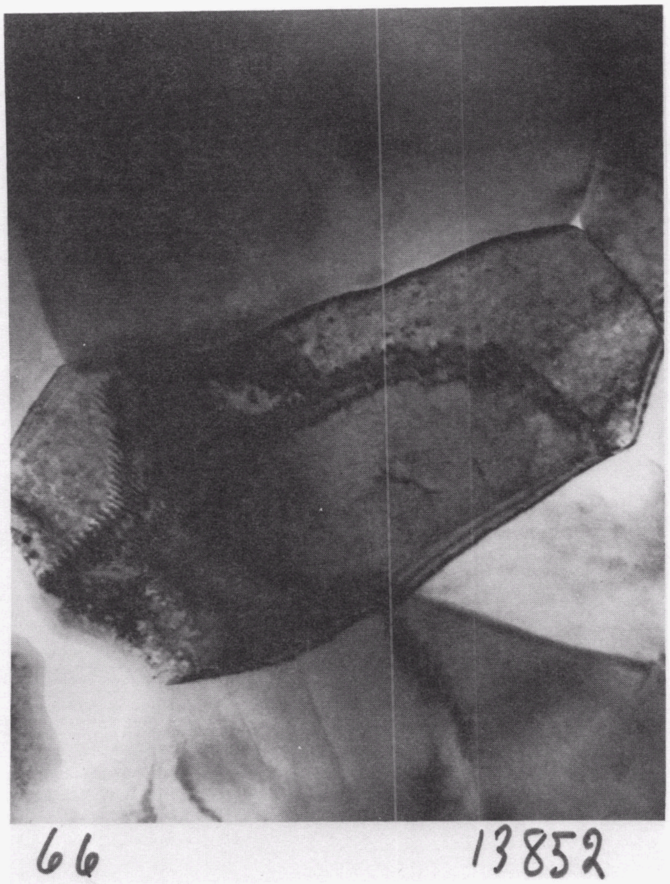

Fig. 3: Grain in sintered R/S material showing low angle boundary.

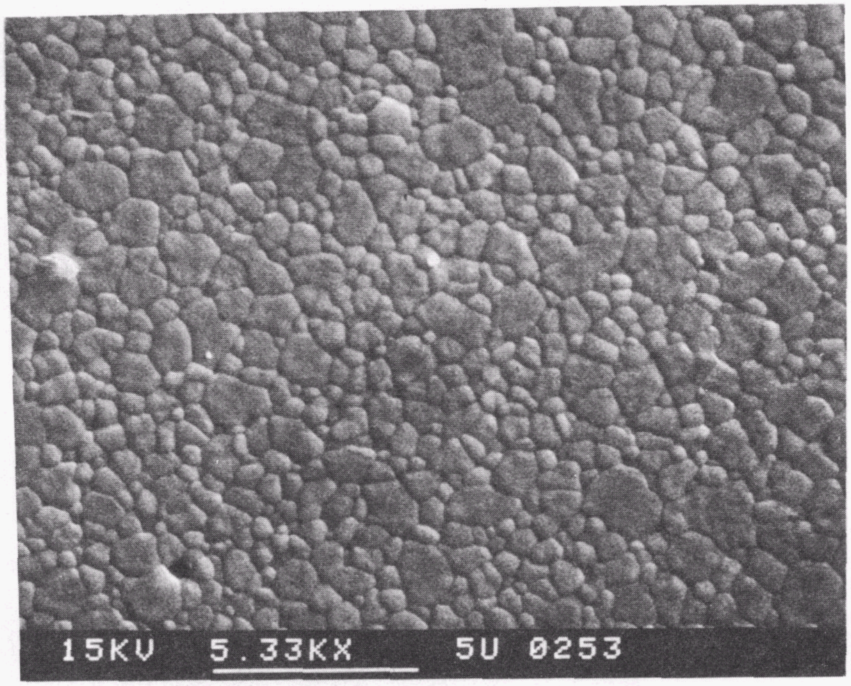

Fig. 4: Microstructure (SEM) of a 4.6 w/o Y_2O_3-ZrO_2 ceramic sintered at 1475^oC and aged at 1500^oC, 1 hr. Classified powder (particle size<1 um).

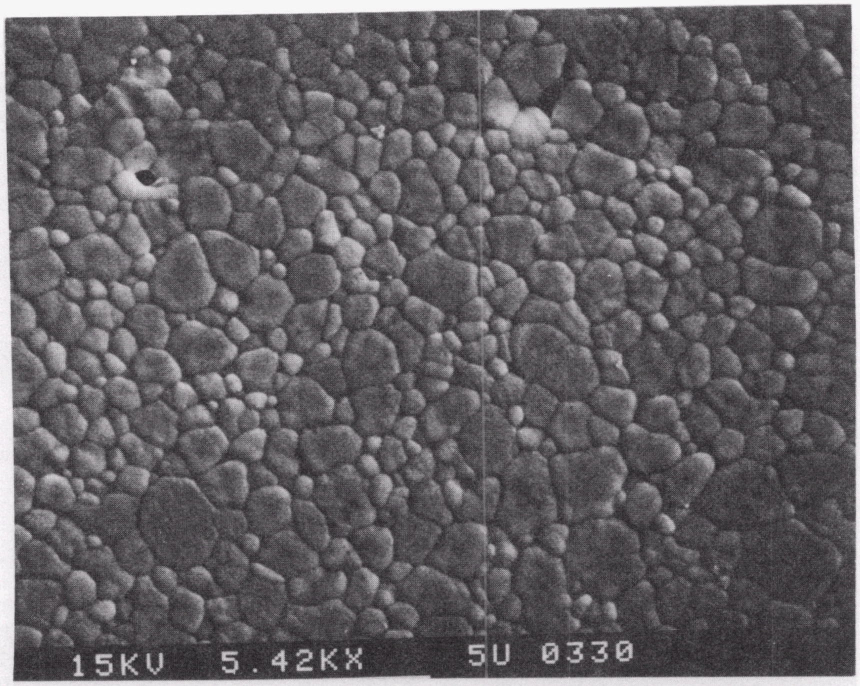

Fig. 5: Microstructure (SEM) of a 4.6 w/o Y_2O_3-ZrO_2. ceramic sintered at 1475°C and aged at 1500°C 4 hrs. Classified powder (particle size<1 um).

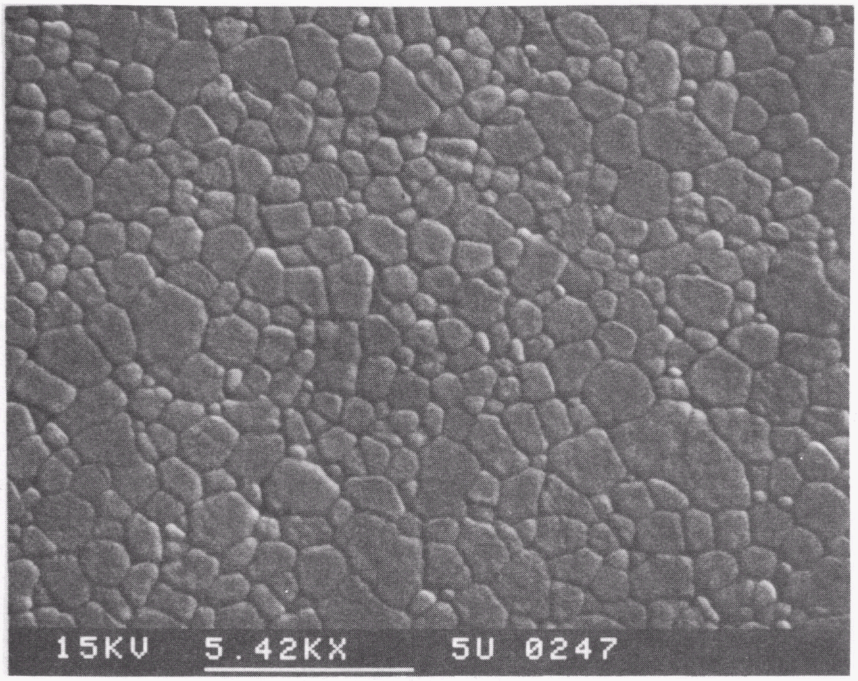

Fig. 6: Microstructure (SEM) of a 4.6 w/o Y_2O_3-ZrO_2 ceramic sintered at 1475°C and aged at 1600°C, 1 hr. Classified powder (particle size $<$ 1 um).

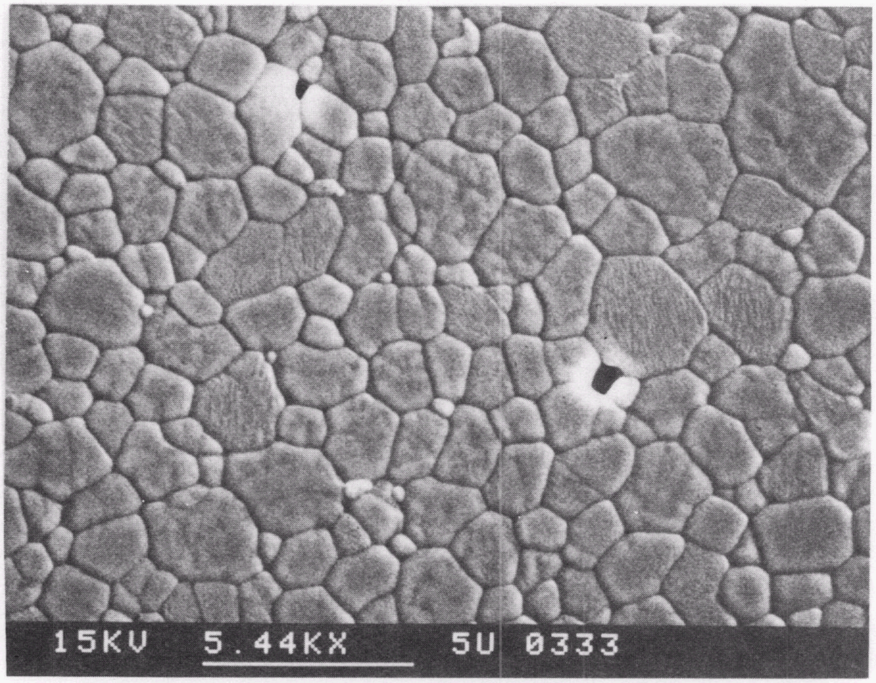

Fig. 7: Microstructure (SEM) of a 4.6 w/o Y_2O_3-ZrO_2 ceramic sintered at 1475°C and aged at 1600°C, 6 hrs. Classified powder (particle size< 1 um).

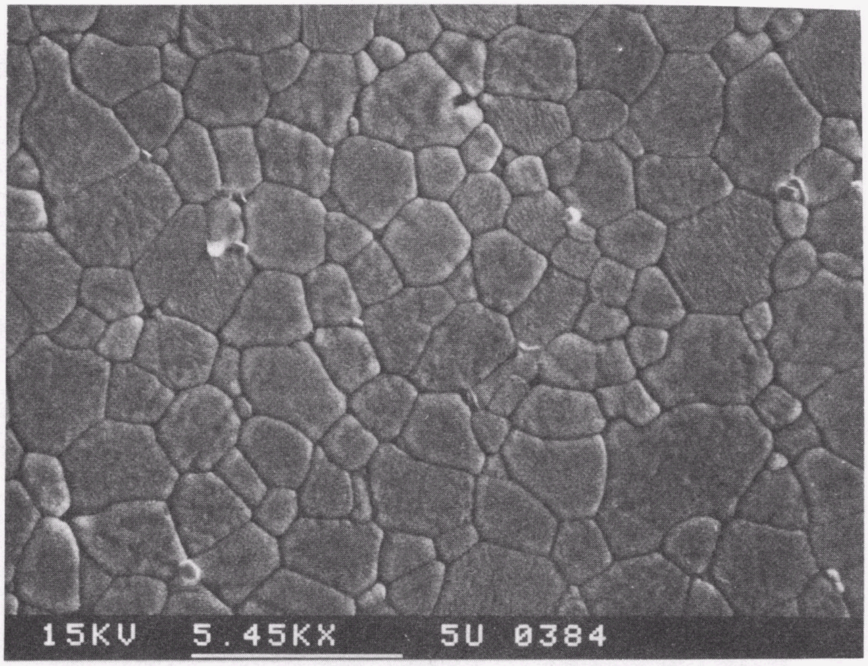

Fig. 8: Microstructure (SEM) of a 4.6 w/o Y_2O_3-ZrO_2 ceramic sintered at 1475°C and aged at 1600°C 6 hrs. Classified powder (particle size<1 um).

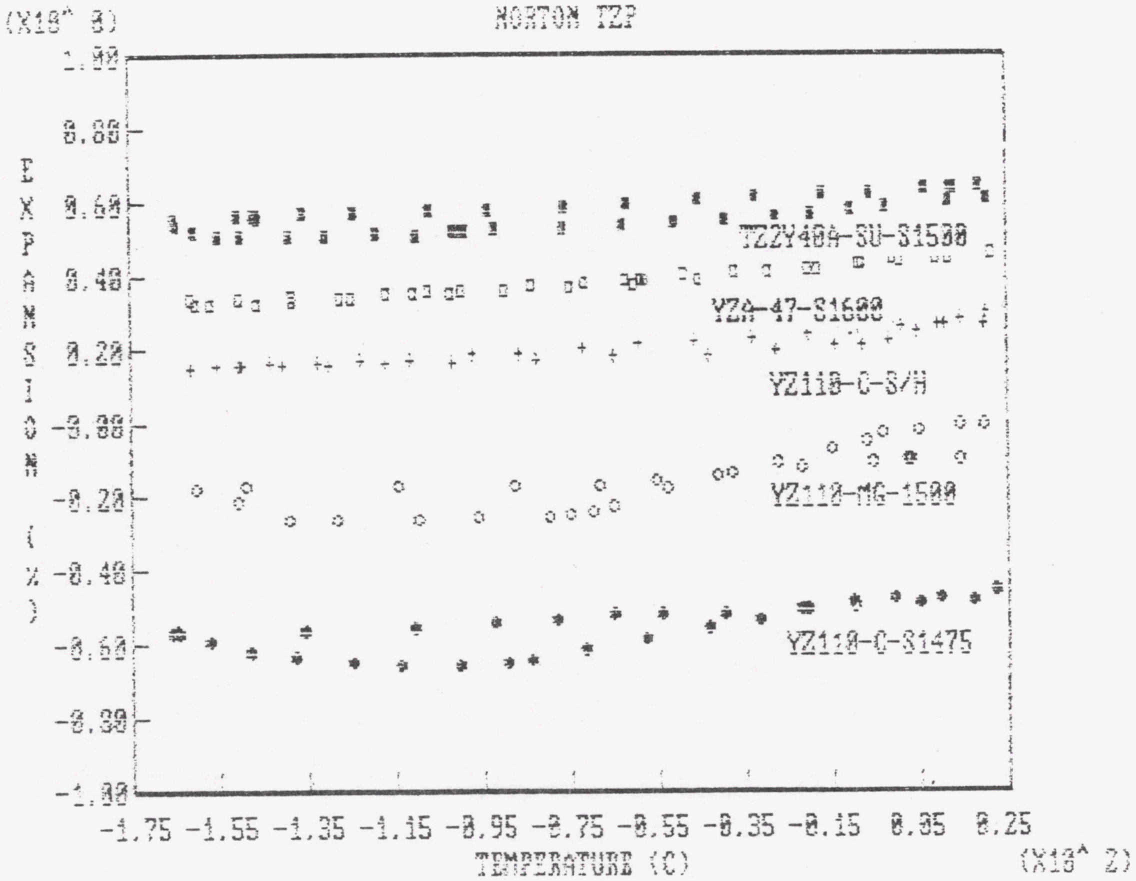

Fig. 9: Results of low temperature dilatometry experiment on five Y-TZP ceramics.

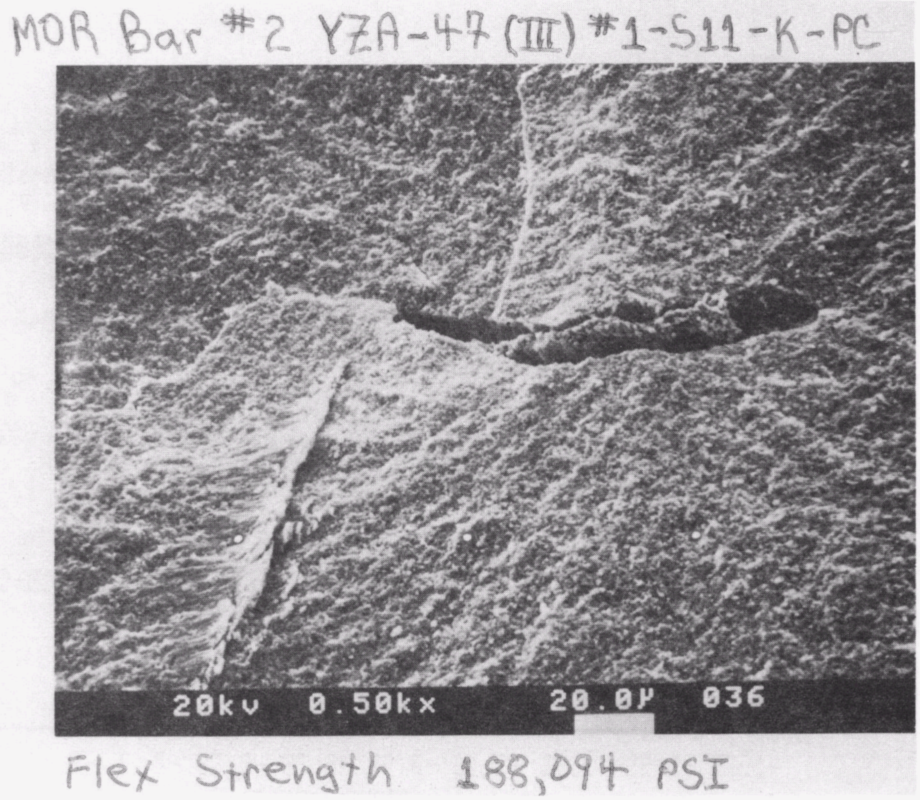

MOR Bar #2 YZA-47 (III) #1-S11-K-PC

Flex Strength 188,094 PSI

Fig. 10: Fractograph of sample of Z4Y20A (80% ZrO_2-4 wt.% Y_2O_3 + 20% Al_2O_3). The sample had a flexural strength of 1296 MPa. The critical flaw is the void located near the center of the picture.

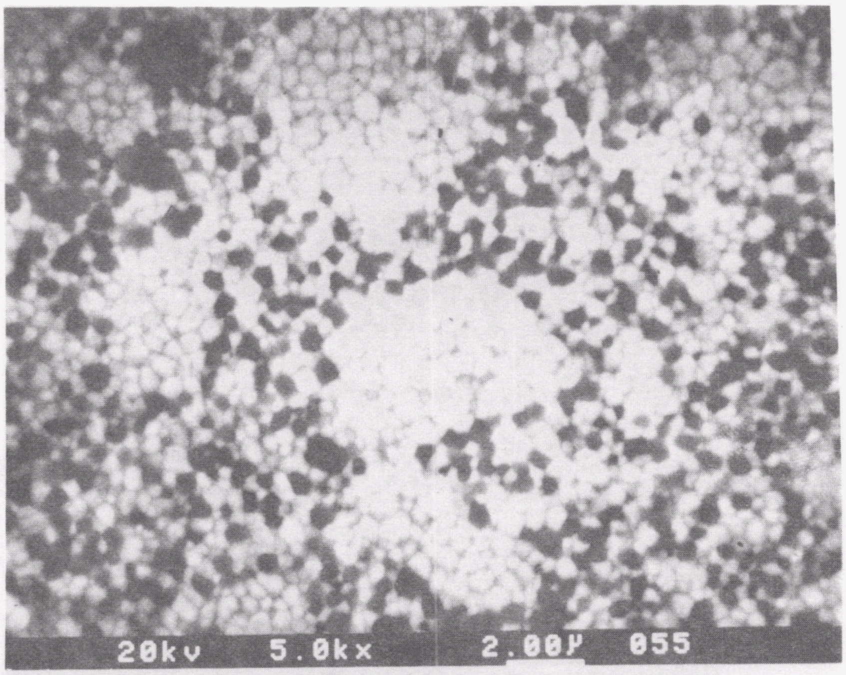

TZ2Y/20A-S1500

Fig. 11: Microstructure (SEM) of ceramic with composition 80 w/o (2 m/o Y_2O_3-ZrO_2)-20 w/o Al_2O_3, made by mixing commercial powders. Sintered at 1500°C.

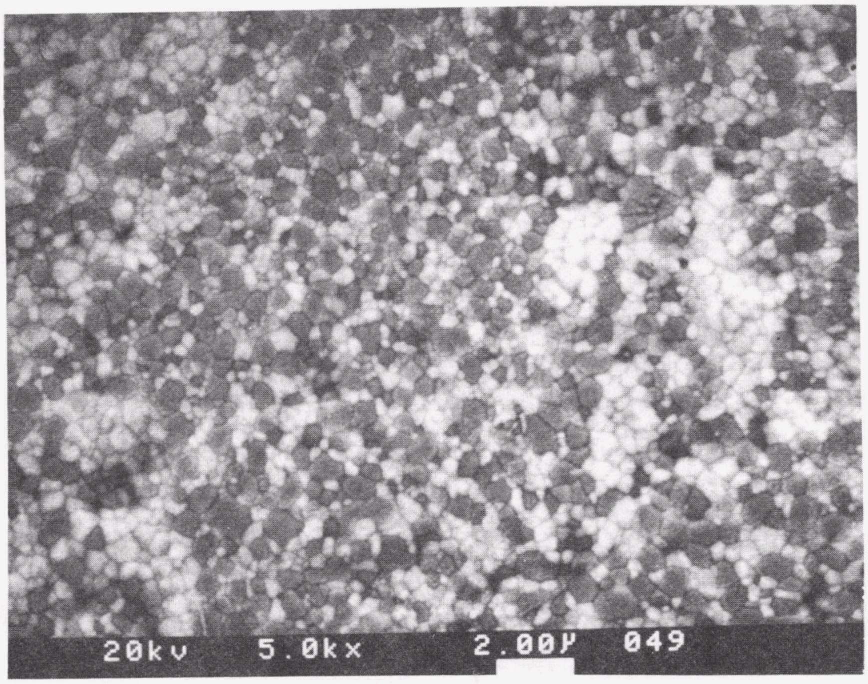

Fig. 12: Microstructure (SEM) of ceramic with composition 60 w/o (2 m/o Y_2O_3-ZrO_2)-40 w/o Al_2O_3, made by mixing commercial po9wders. Sintered at 1500°C.

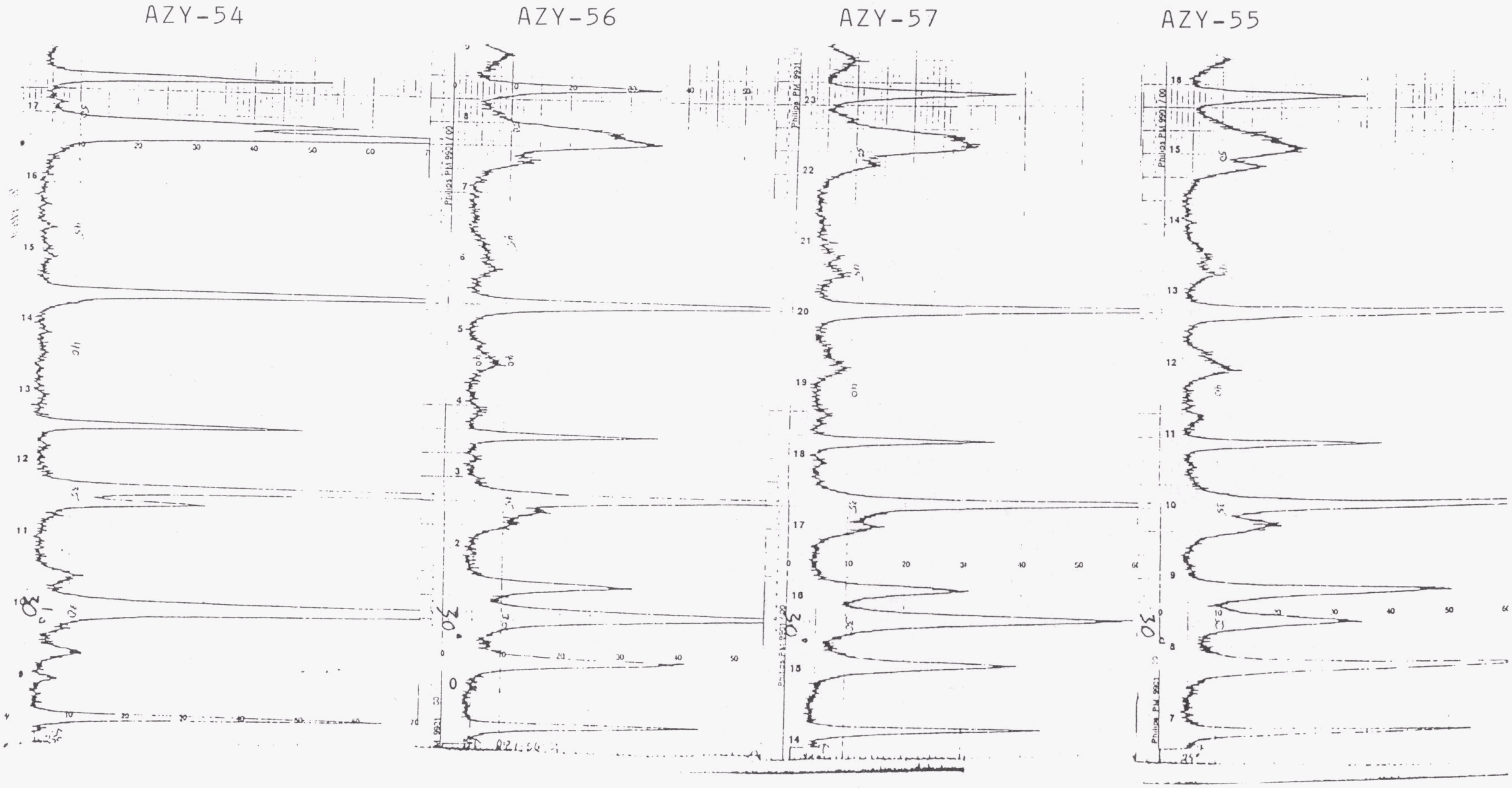

Fig. 13: XRD patterns of polished sections of ZTA ceramics made with the R/S powders, HIPed at 1300°C.

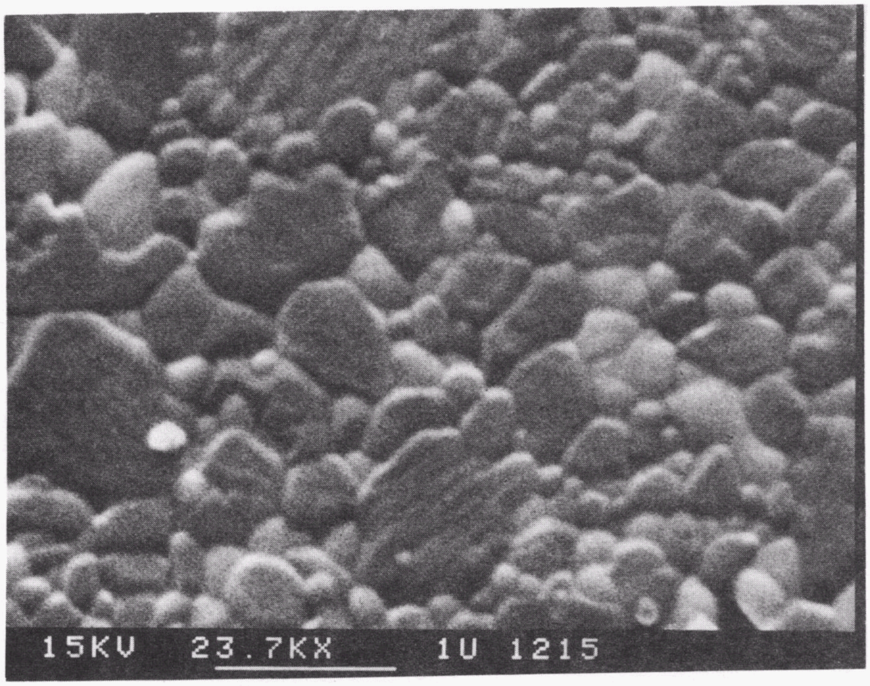

Fig. 14: Microstructure (SEM) of sample AZY-57, HIPed at 1300°C.

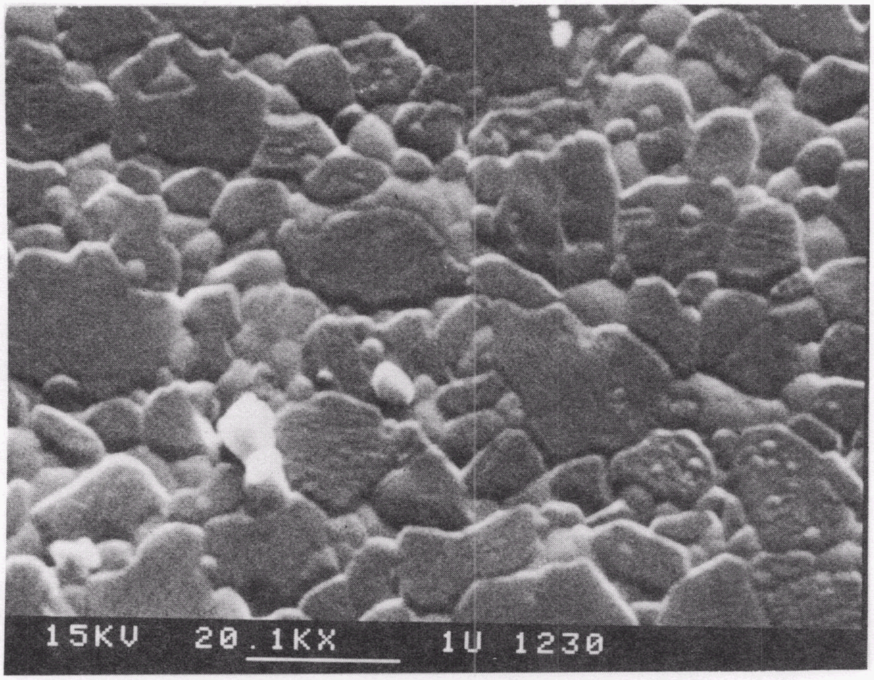

Fig. 15: Microstructure (SEM) of sample AZY-54, HIPed at 1300°C.

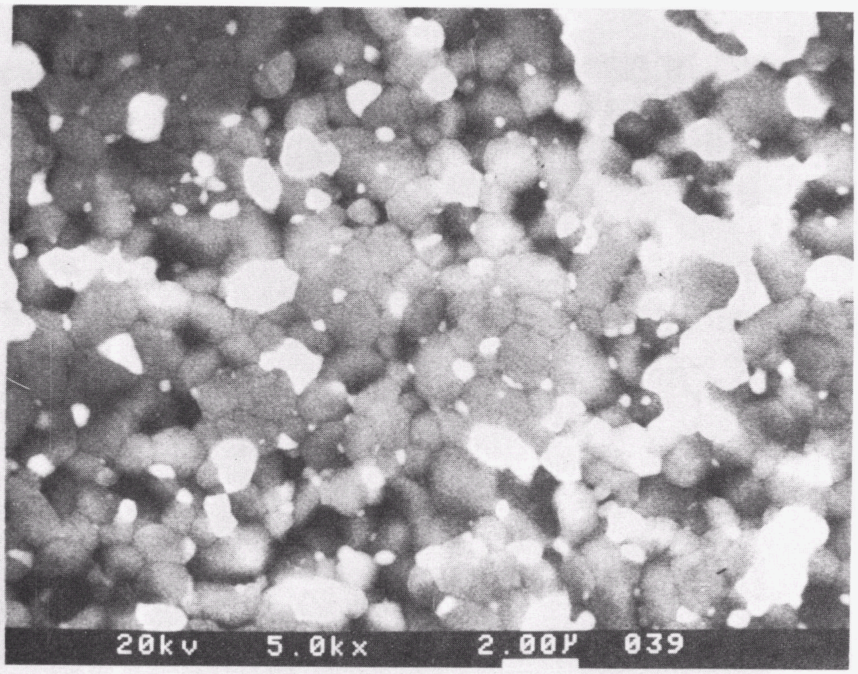

TZ12CE/80A-M/M-S/H

Fig. 16: Microstructure (SEM) of a ceramic with composition 20 w/o (12 m/o CeO_2-ZrO_2)-80 w/o Al_2O_3, made by mixing commercial powders. Sintered at 1500°C and HIPed at 1550°C.

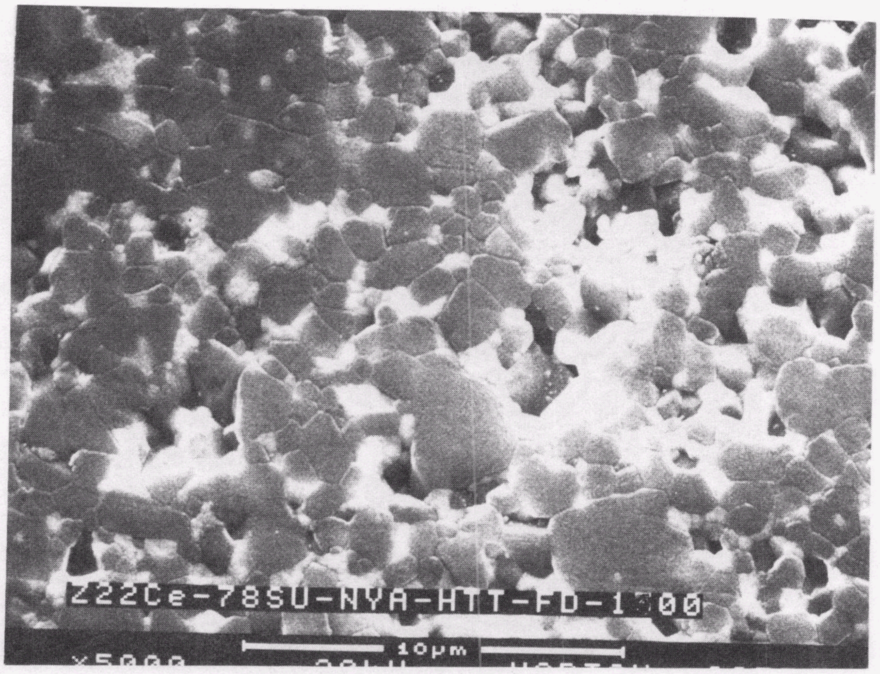

Fig. 17: Microstructure (SEM) of a ceramic with composition 22 w/o (12 m/o CeO_2-ZrO_2)-78 w/o Al_2O_3, made by colloidal method. Sintered at 1600 C.

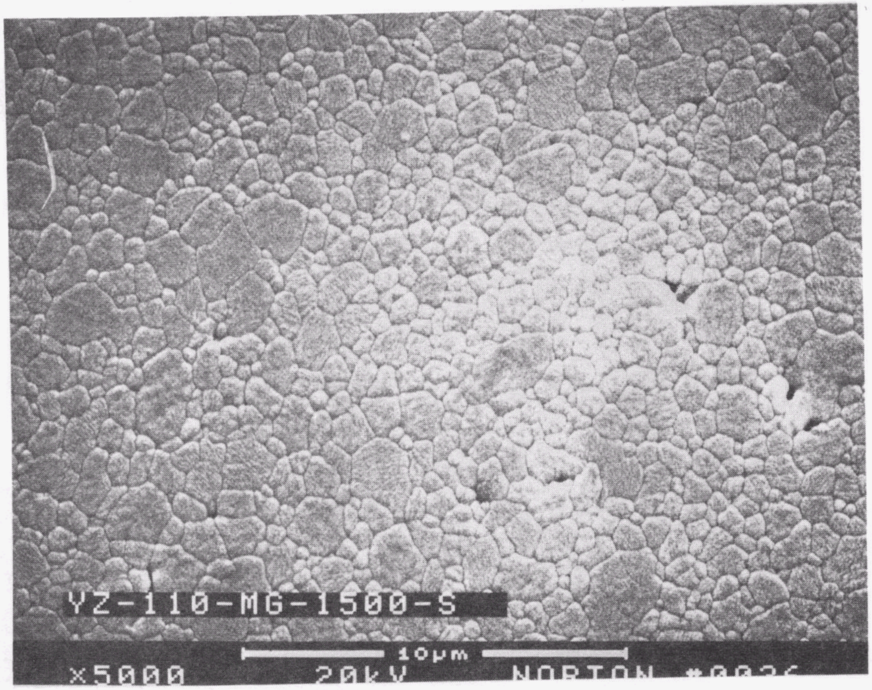

Fig. 18A: Microstructure (SEM) of sample YZ110-MG-S1500 (Table 5), before the aging period at 1000°C/ 1000 hrs.

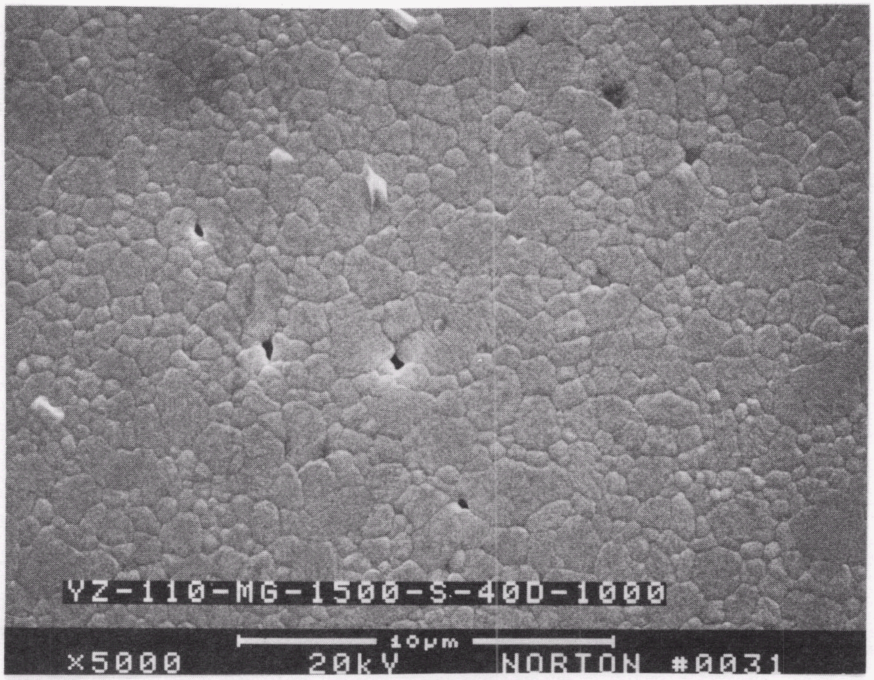

Fig. 18B: Microstructure (SEM) of sample YZ110-MG-S1500 (Table 5), after the aging period at 1000°C/ 1000 hrs.

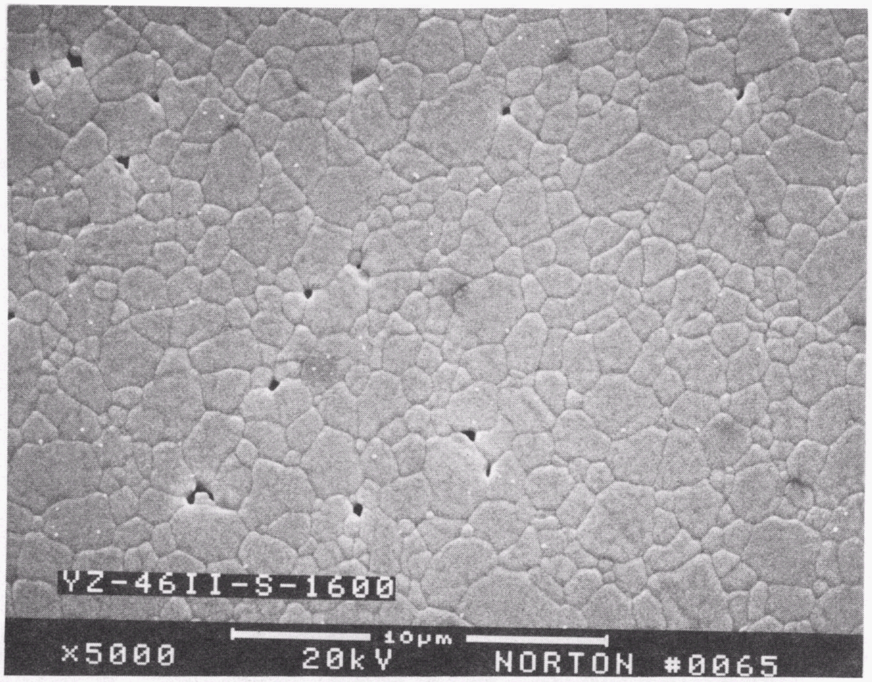

Fig. 19A: Microstructure (SEM) of sample YZ-46-MG-S1600 (Table 5), before the aging period at 1000°C/ 1000 hrs.

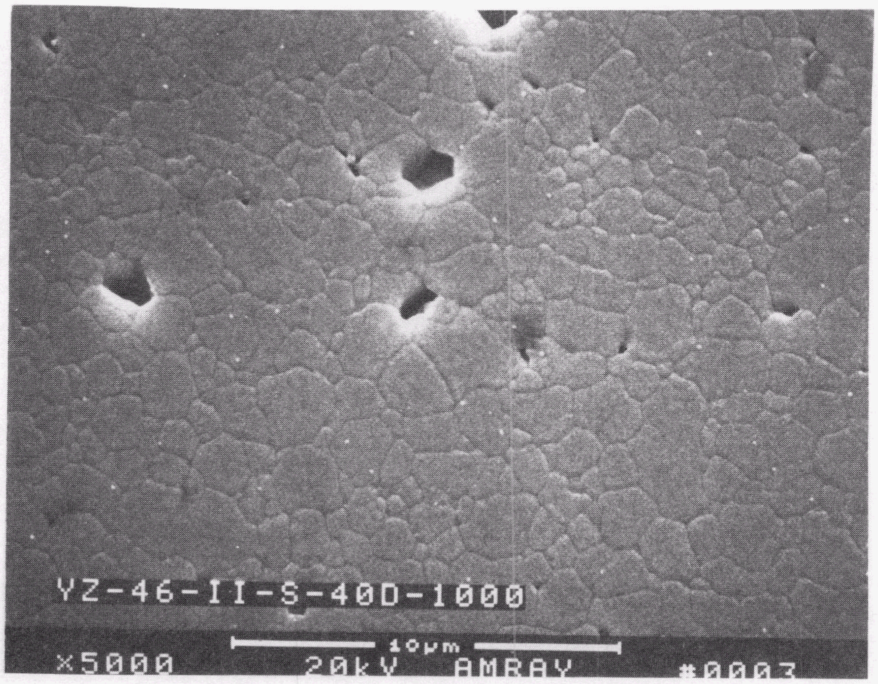

Fig. 19B: Microstructure (SEM) of sample YZ-46-MG-S1600 (Table 5), after the aging period of 1000°C/ 1000 hrs.

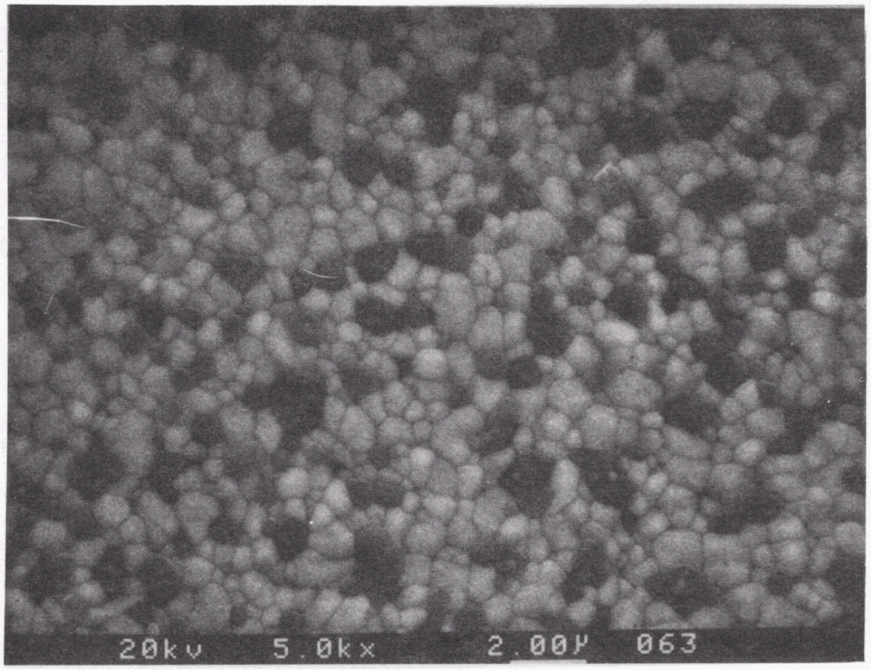

Fig. 20A: Microstructure (SEM) of sample YZA-47-S1500 (Table 5), before the aging period at 1000°C/ 1000 hrs.

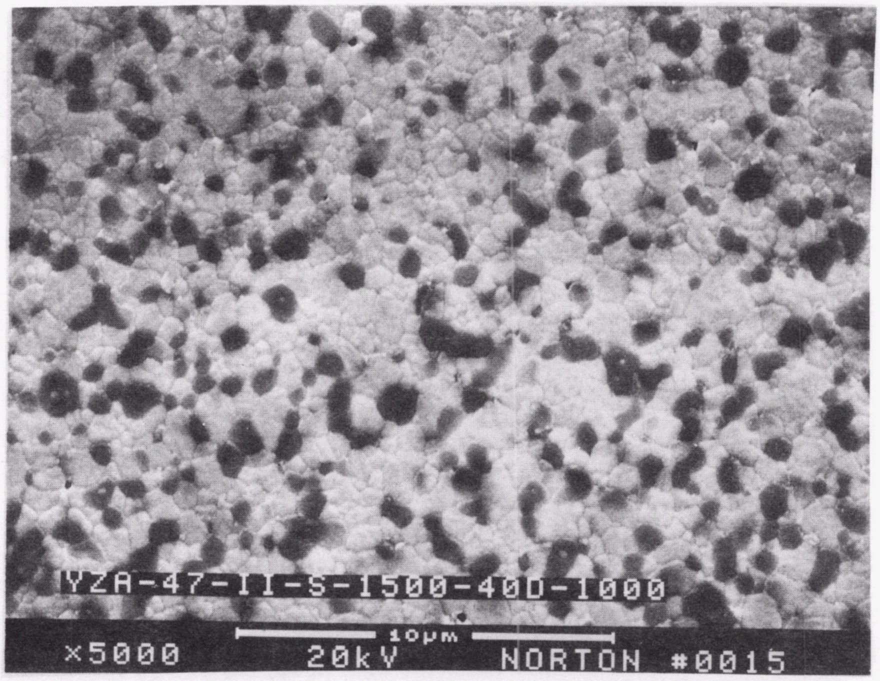

Fig. 20B: Microstructure (SEM) of sample YZA-47-S1500 (Table 5), after the aging period at 1000°C/ 1000 hrs.

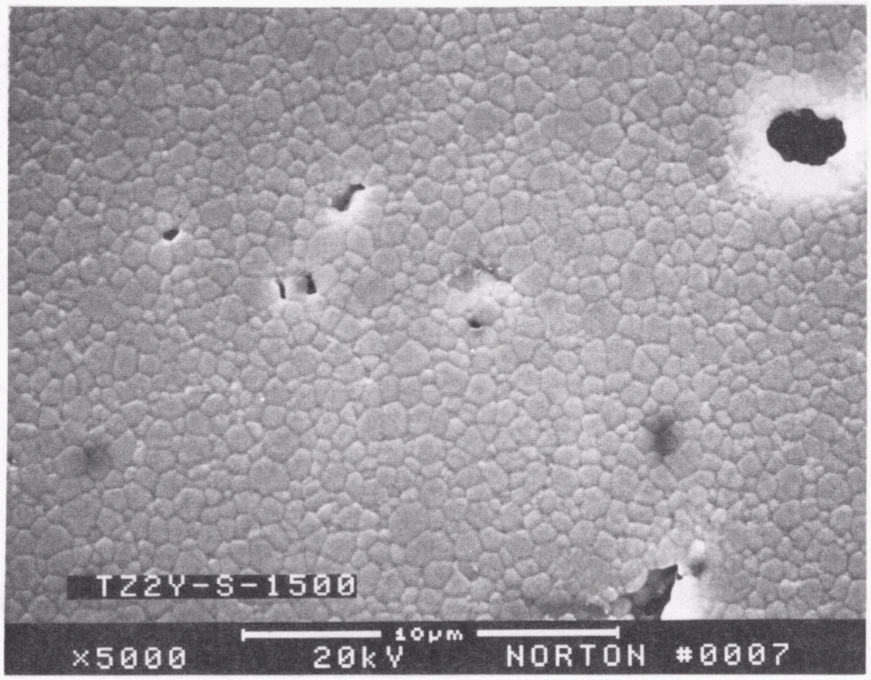

Fig. 21A: Microstructure of sample TZ2Y-S1500 (Table 5) before the aging period at 1000°C/1000 hrs.

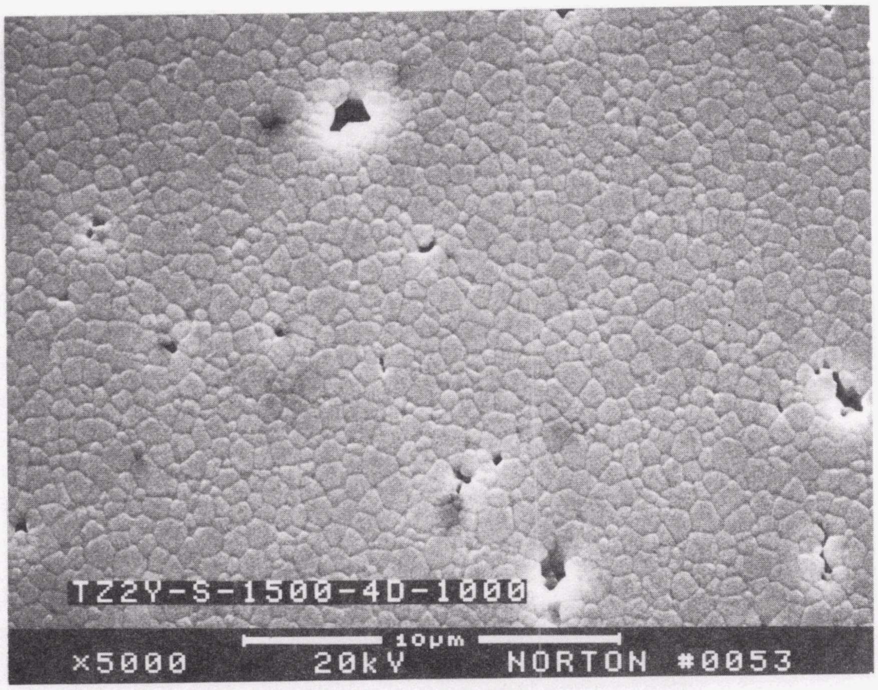

Fig. 21B: Microstructure of sample TZ2Y-S1500 (Table 5), after the aging period at 1000°C/1000 hrs.

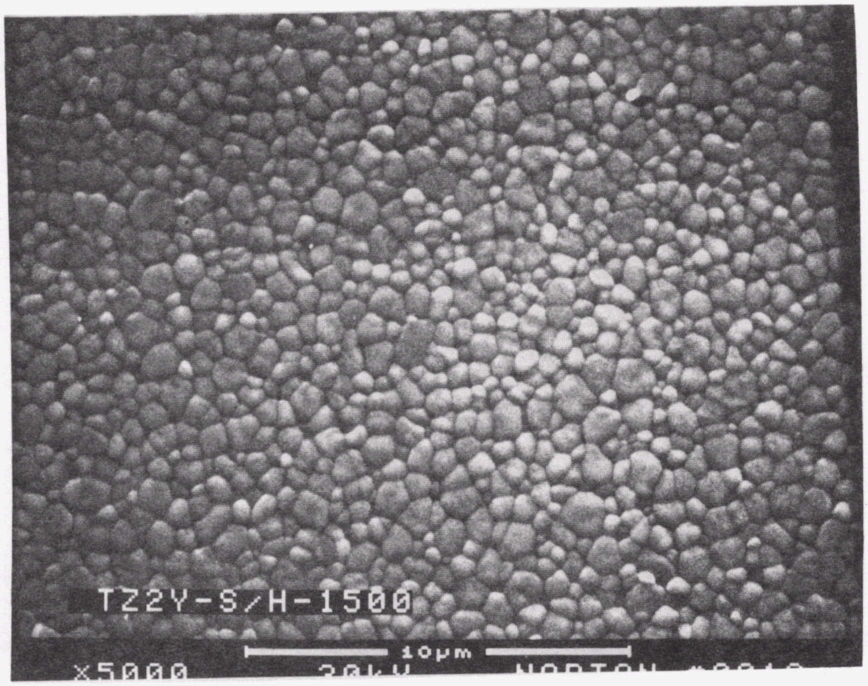

Fig. 22A: Microstructure (SEM) of sample TZ2Y-S/H (Table 5), before the aging period at 1000^{o}C/1000 hrs.

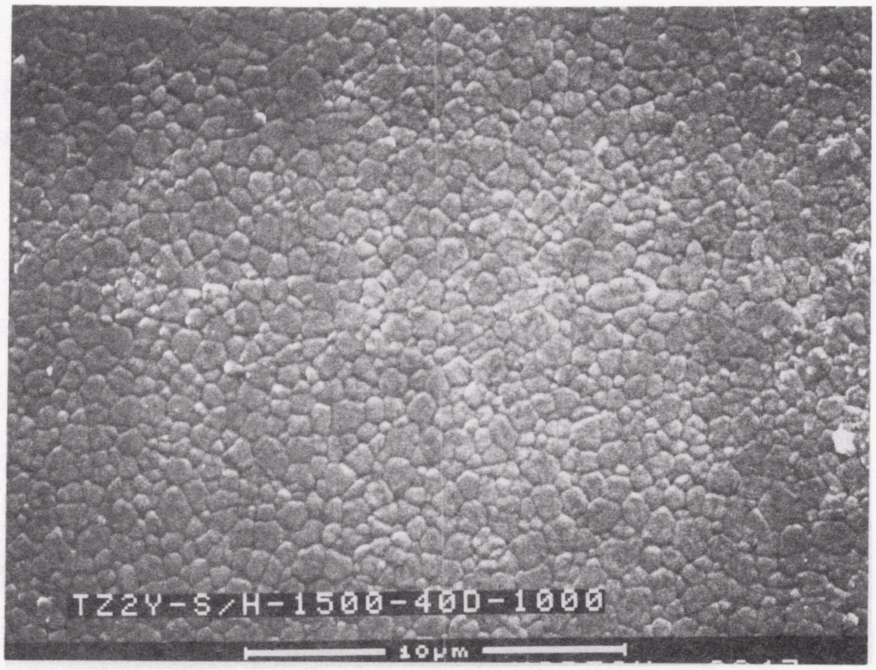

Fig. 22B: Microstructure (SEM) of sample TZ2Y-S/H (Table 5) after the aging period at 1000°C/1000 hrs.

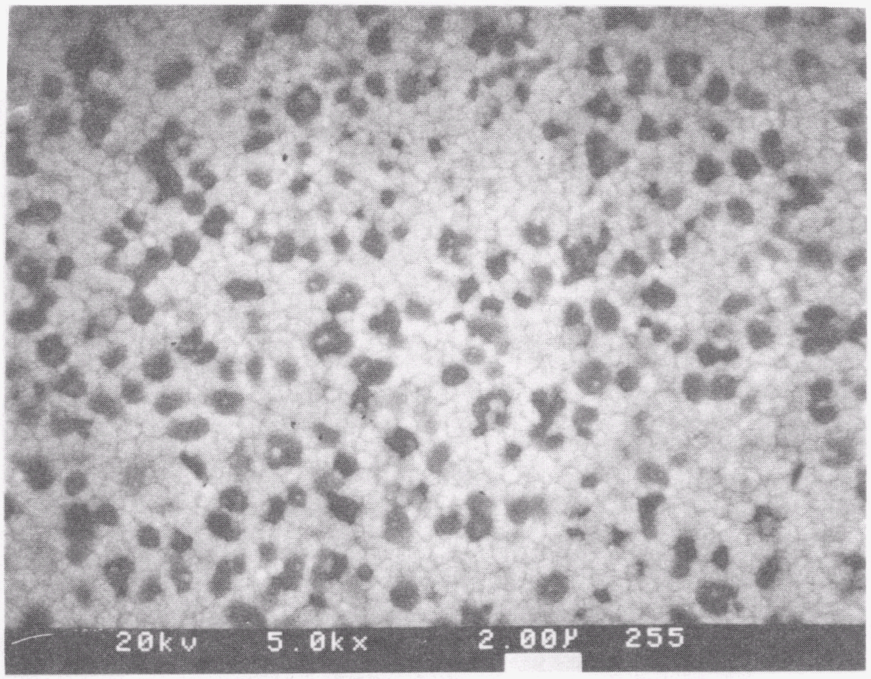

Fig. 23A: Microstructure (SEM) of sample Z4Y20A-I-S/H (Table 5), before the aging period at 1000°C/ 1000 hrs.

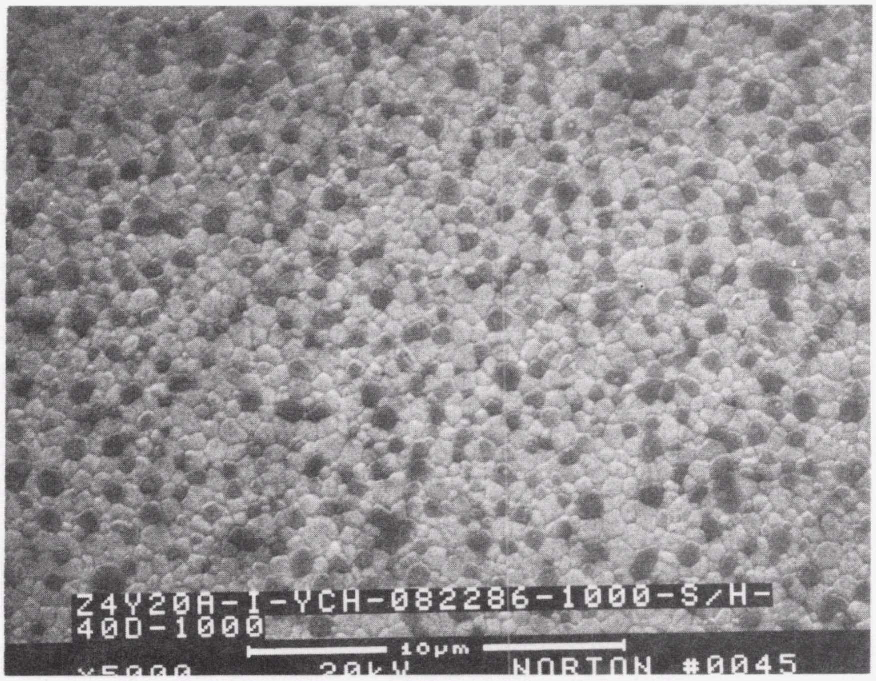

Fig. 23B: Microstructure (SEM) of sample Z4Y20A-I-S/H (Table 5), after the aging period at 1000°C/ 1000 hrs.

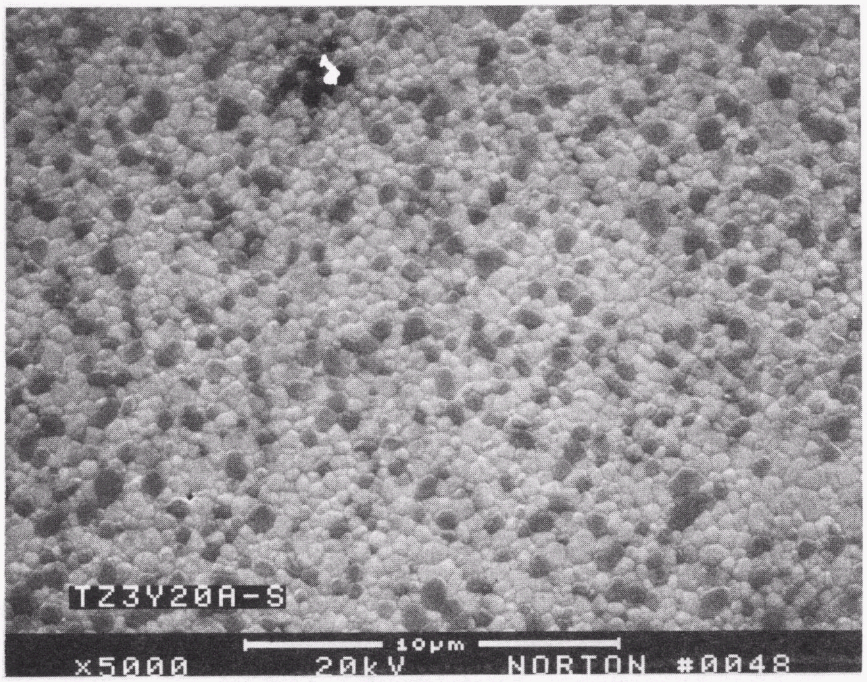

Fig. 24A: Microstructure (SEM) of sample Super Z-S1500 Table 5), before the aging period at 1000°C/ 1000 hrs.

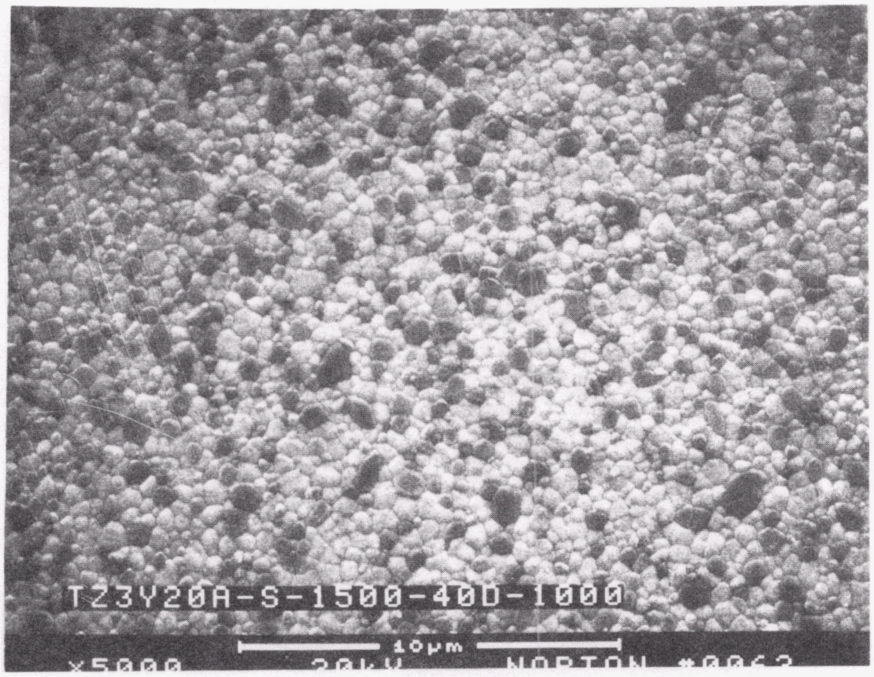

Fig. 24B: Microstructure (SEM) of sample Super Z-S1500 Table 5), after the aging period at 1000°C/ 1000 hrs.

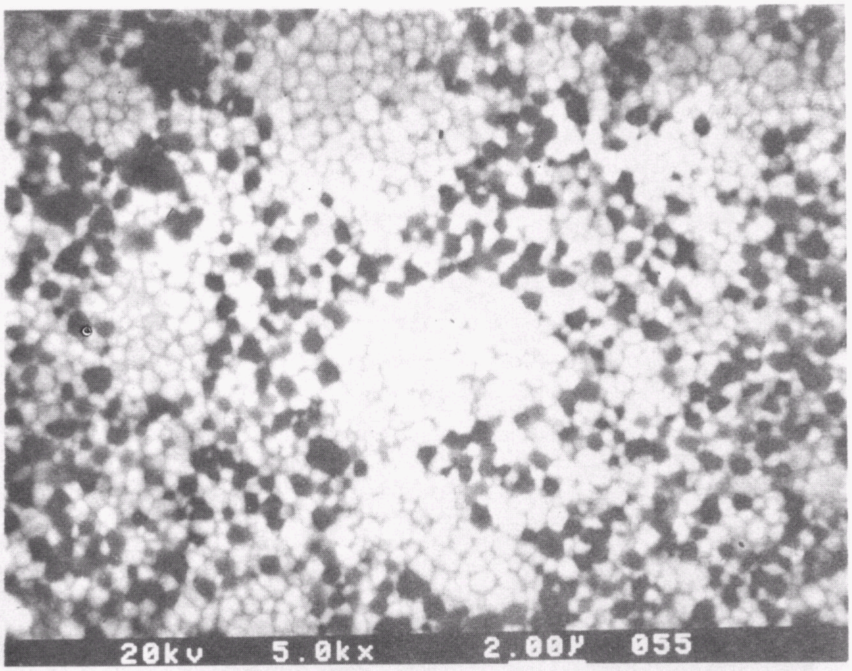

TZ2Y/20A-S1500

Fig. 25A: Microstructure (SEM) of sample TZ2Y/20A-S1500 (Table 5), before the aging period at 1000°C/ 1000 hrs.

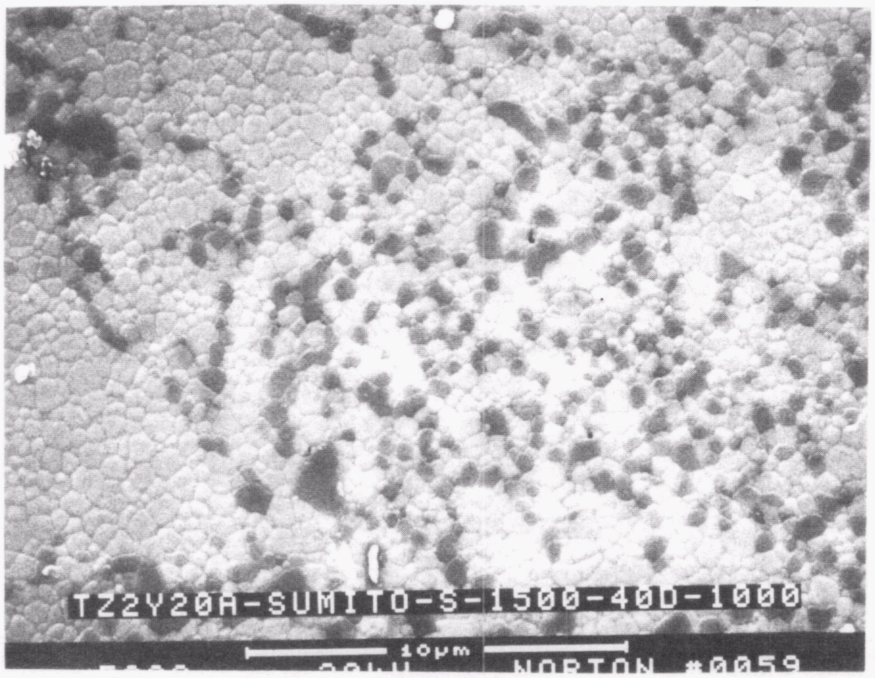

Fig. 25B: Microstructure (SEM) of sample TZ2Y/20A-S1500 (Table 5), after the aging period at 1000°C/1000 hrs.

Advanced Transformation-Toughened Oxides

J. Biel and T. Y. Tien (The University of Michigan)

Objective/scope

The goal of the current research is to improve the toughness and strength of the subject material. Previous results indicate toughness will be increased by increasing the v\o ZrO2 if the particle size is closely distributed around the critical size for transformation(1). When the ZrO2 particles grow too large during sintering spontaneous microcracking occurs which seriously degrades the mechanical properties. The problem of ZrO2 growth in this material becomes aggravated as its amount is increased due to particle agglomeration during forming and the particle growth mechanism of coalescence during sintering(2).

Strength will be improved by two mechanisms in this material. First by prevention of growth of large monoclinic zirconia particles which spontaneously microcrack. Second by elimination or minimization of processing defects and porosity in the pressureless sintered bodies.

All of these goals should be possible by improved processing of the material. Fine evenly sized starting powders are important and can be produced by co-precipitated methods. A key step during the forming process is the prevention of agglomeration by a dispersion agent. Of nearly equal importance is the development of powder consolidation methods which minimize pore size to allow quick sintering to near theoretical density without excessive grain or zirconia particle growth. The formation of dense evenly packed green bodies is possible using colloidal filtration methods(3,4,5).

Dispersion agents adsorb to particle surfaces from solution and create a repulsive force between particles. Dispersants are generally of three types, small charged molecules or ions which cause electrostatic repulsion between particles, adsorbed polymers which cause steric or entropic interference between particles and adsorbed polyelectrolytes which are charged polymers and have potential to cause both electrostatic and steric interference between particles.

A number of factors are important in determining the inter-particle repulsive forces caused by the adsorption of a dispersion agent. Among them are the amount and type of dispersion agent adsorbed as well as the suspension or liquid medium. Another factor which is little understood is the concentration of particles in suspension . This may become important during colloidal or pressure casting methods as the particle concentration becomes much higher than the particle concentration where most dispersant studies are performed.

Our current work has focused on these factors of agglomeration prevention by use of dispersion agents and on green body formation which takes advantage of the dispersed state. A brief summary of the experimental program is given next.

Technical progress

Experimental Methods:

Starting powders were produced by precipitation of salts from solution similar to methods already used(2). Al and Cr nitrate salts were dissolved in ethanol. Zr oxy-cl salt was dissolved in distilled water. All solutions were made to 1\2 M concentration and further diluted to 1\4 M before precipitation. The precipitation was done by dripping the mixed salt solution into a rapidly stirred bath of ethanol kept at a constant pH=8 by NH_4OH addition. The powders were given a quick calcination at 1300°c for 15 mins.. To break up agglomerates the powders were attrition milled for 1\2 hr..

Samples were formed by using a pressure casting method similar to slip casting. The slurries with a solids content of 10 v/o were suspended in distilled water and agglomeration was prevented by use of a polyelectrolyte. A polyacrylic acid was used and it was chosen based on the work done by R. Cannon on screening a large group of commercially available dispersion agents (6).

To optimize the use of the PAA a number of experiments were performed. Adsorption curves were measured using solution concentration measurements of polyelectrolyte before and after equilibration with a known amount of powder. The effect of adsorption amount on dispersion was determined by measuring the agglomerate size in suspension. Particle size distribution was determined using the change in light absorbance with sedimentation time. The zeta potential was measured to determine the level of electrostatic charge on the suspended particles and how that was affected by the polyelectrolyte adsorption. The effect of solution pH on the polyelectrolyte dispersion effects was also studied. The solution pH was adjusted by using HCL and NH4OH.

Green bodies were produced by pressure casting colloidal dispersions of the powders. A simple pressure filtration box was constructed using aluminum plate for the top and bottom and a section of rectangular aluminum tube for the body. An initial pressure of 15 psig was applied to the slurry with the pressure increased 5 psig every minute. Typically a 3-5 mm piece was cast in 15 mins. depending on the particle size and dispersion(4). Other pressure-time schedules for casting are being investigated. The pore size distribution in the green bodies as affected by the dispersion was measured using mercury porosimentry.

Pressureless sintering was done in a graphite furnace at low oxygen potential. Pressure cast samples were sintered at 1500°c for 1 hour to near theoretical density.

The fracture toughness measurements were made using the microindent crack length method(7). To calibrate the micro-indent method for this material a sample from the previous work(1) for which 4 pt. bend bar data was available was tested. The results of both methods to measure fracture toughness are in close agreement. Strength measurements were made using 2mm by 3mm cross section bars in four point bending.

Results and Discussion:

Co-precipitated powders were used to form green bodies using colloidal filtration methods followed by pressureless sintering. Initially a detailed study of the optimum colloidal dispersion was not made. Green bodies were produced with a density of 50-55% (measured from external dimensions). These sintered to near theoretical density at 1500°c in a graphite furnace.

Samples without HfO2 were produced with a tetragonal content of 80-90% after sintering for 1 hour. By aging these samples at 1500°c for six hours the tetragonal content could be lowered to around 50%. Samples with HfO2 were also sintered and had a lower tetragonal content depending on their HfO2 content. The room temperature fracture toughness of the samples are shown in fig.1.

The data indicates a significant improvement in toughness over previous samples(1,8) . Similar efforts at producing samples with 17.5-20v\o ZrO2 resulted in samples with a tetragonal content of 35-25% which is lower than the desired level. The particle size distribution will be growing away from the critical size for transformation and there is greater probability of spontaneous microcracking. To make further improvements efforts have been directed at better understanding of the polyelectrolyte-dispersion process. The level of polyelectrolyte adsorption, its effect on inter-particle repulsion in suspension and the resulting sintered microstructure are of primary interest.

The polyelectrolyte chosen for use is Darvan 821-A an ammoniated polyacrylic acid (PAA) which is anionic in nature. This choice was based on work conducted by R. Cannon(6). The adsorption curves for Al2O3:10 m/o Cr2O3 and ZrO2 (Zircar) are given in figs. 2,3 . The adsorption curves for the two materials shown are very similar. The saturation adsorption level increases with decreasing pH for both powders tested. This implies that the polyelectrolyte (PAA) molecules are more extended into solution at lower pH increasing the potential for steric repulsion and decreasing the electrostatic repulsion between particles. The opposite behavior should occur at higher pH. Polyelectrolytes may cause repulsion between particles using both electrostatic and steric factors and the relative importance of these mechanisms has not been firmly established(9,10,11).

To measure the adsorption effect on agglomeration in dilute suspensions particle size measurements were made. The results shown in Table 1 are the median values. The data shows the best dispersion and least agglomeration at the saturation level of adsorption. The effect of saturation adsorption at different pH levels on the measured particle-agglomerate size was also examined and found to make only a small difference for the powders tested. The results are also shown in Table 1 .

Zeta potentials were measured for 10-0-0 and 10-20-0 (material composition is expressed as m/o Cr2O3 - v/o ZrO2 - m/o HfO2) powders with and without polyelectrolyte adsorption.The data is given in Table 2. The zeta potential for the 10-0-0 and 10-20-0 (0v/o and 20v/o ZrO2 co-precipitated powders respectively) powders without polyelectrolyte are similar and are different from that of ZrO2. This indicates the ZrO2 must precipitate from solution first followed by the Al2O3:Cr2O3 which dominates the surface chemistry of the particle. This behavior has been observed in Al2O3/ZrO2 and ZrO2/SiO2 powders(12,13).

A relatively large amount of polyelectrolyte is adsorbed at low pH compared with higher pH levels. The zeta potential with polyelectrolyte at low pH is close to zero indicating little electrostatic repulsion between particles. At near neutral and high pH the zeta potential is higher with polyelectrolyte than without. The adsorbed polyelectrolyte is providing a higher level of electrostatic repulsion plus entropic repulsion to the particles(11). The measured zeta potential is highest at near neutral pH compared to that at high pH and may be due to a greater level of saturation adsorption at the neutral pH.

The adsorbed polyelectrolyte will keep the particles from agglomerating and when dried the dispersed powders are quite soft. To compare dry pressing and colloidal filtration methods a batch of 10-20-0 powder was attrition milled in distilled water and polyelectrolyte was added for full dispersion. Half of the slurry was used to make pressure casting while the other half was dried, sieved and isostatically pressed (25.5 ksi). Samples of each type were sintered together at 1500°c for the times shown in figs.4,5. The pressure cast samples sintered to a higher density than the dry pressed samples even though both types of samples had green densities of approximately 50%. The cause of this behavior is probably due to differences in pore size distribution(3). The results of mercury porosimetry tests on both types of samples is given in figs.6,7, and shows a smaller pore size distribution for the pressure cast sample.

A problem with making pressure castings has been that they curved towards the upper casting surface upon sintering. This may be due to a lower density in the upper layers caused by a change in conditions of particle deposition as the casting builds up and the rate slows down. The particle deposition rate slows down because the liquid is being forced through an ever thickening packed bed of particles. To maintain the same rate it is necessary to increase the driving force to compensate for the increased resistance to flow. This may be accomplished by linearly increasing the casting pressure with time. This practice has resulted in elimination of the curvature problem in the pressure castings produced on this project.

Pressure castings were made from fully suspended slurries at different pH levels to examine the pH variable on the pore size distribution. The pore size distributions were measured using mercury porosimetry and the results are shown in figs. 8-10 . The distribution of the acidic sample is significantly worse than samples with a higher pH. This result is somewhat surprising when the particle size measurements are considered but these measurements were made in dilute suspensions which may be significantly different from the concentrated conditions during pressure casting.

Based on these results near neutral pH slurry of 10-20-0 powder was pressure cast and sintered at 1500°c for 1 hour to near full density. The tetragonal content was measured as 60% using x-ray diffractometry methods. Bars were ground with a 2mm by 3mm crossection and tested in four point bending. The bars had a strength value of 904MPa which is significantly higher than the value of approximately 500 MPa reported by other investigators(1,8).

Acknowledgements:

The authors wish to thank Profs. S. Fogler and I-Wei Chen for helpful discussions. The financial support for this investigation was provided by the US Department of Energy, Division of Transportation Energy Conservation; Office of Vehicle and Engine Research and Development, Ceramics Technology for Advanced Heat Engines Programs; administered by the Army Materials Technology Laboratory.

References:

1) T.K. Brog, Transformation Toughening in the Alumina-Chromia/Zirconia-Hafnia System, Ph.D Thesis, University of Michigan, 1986.

2) A.K. Li, Sintering and Grain /Particle Growth of Composites in the System Alumina-Chromia/Zirconia-Hafnia, Ph.D. Thesis, University of Michigan.

3) J.W. Halloran, Role of Powder Agglomerates in Ceramic Processing, Forming of Ceramics, Advances in Ceramics v9.

4) I.A. Aksay, Microstructure Control Through Colloidal Consolidation, ibid..

5) I.A. Askay, F.F. Lange and B.I. Davis, Uniformity of Al2O3-ZrO2 Composites by Colloidal Filtration, J. Am. Cer. Soc.,66[6], c190-191, (1983).

6) K. Willinger and R. Cannon, Processing of Transformation Toughened Alumina, Center for Ceramic Research, Rutgers Univ..

7) A.G. Evans, E. Charles, Fracture Toughness Determinations by Indentations, J. Am. Cer. Soc., 59[7-8], (1976).

8) T.Y. Tien, T.K. Brog, A.K.Li, Toughened Ceramics in the System Al2O3:Cr2O3/ZrO2:HfO2, Int. J. High Technology Ceramics, 2, 207-219, (1986).

9) F.TH. Hesselink, Adsorption of Polyelectrolytes From Solution, from Adsorption From Solution, G.D. Parfitt ed. (1983).

10) O.A. Evers, et. al., Adsorption of Weak Polyelectrolytes From Aqueous Solution, J. Colloid Interface Sci., 111[2], 446-454, (1986).

11) Th.F. Tadros, Control of the Properties of Suspensions, Colloids and Surfaces, 18, 137-173, (1986).

12) M. Kagawa, et. al., Stability of Ultrafine Tetragonal ZrO2 Coprecipitated with Al2O3 by the Spray-ICP Technique, J. Am. Cer.Soc., 66(11), 751-54, (1983).

13) M. Kagawa, et. al., Surface Characterization of Ultrafine ZrO2-SiO2 Powders by Electrophoretic Mobility Measurements, ibid., 69(3), c50-c51, (1986).

Table 1, Ave. Particle Size as Affected by Polyelectrolyte-pH Conditions

material	pH	% of polyelectrolyte	ave. particle size microns
10-20-0	7.5	25	2.0
10-20-0	7.5	50	1.75
10-20-0	7.5	100	1.2
10-0-0	2.8	100	1.11
10-0-0	7.8	100	0.99
10-0-0	10	100	1.0
ZrO2	3	100	1.1
ZrO2	7.8	100	1.05
ZrO2	10	100	1.1

Table 2, Zeta Potential (mV)

material	pH	polyelectrolyte	zeta pot. (mV)
10-0-0	2.5	no	51
10-0-0	7	no	-36
10-0-0	10	no	-63
ZrO2	2.5	no	60
ZrO2	7	no	-41
ZrO2	10	no	-68
10-20-0	2.5	no	52
10-20-0	7	no	-33
10-20-0	10	no	-60
10-20-0	2.5	yes	10
10-20-0	7.8	yes	-74
10-20-0	10	yes	-70
10-0-0	2.5	yes	5
10-0-0	7.8	yes	-75
10-0-0	10	yes	-70

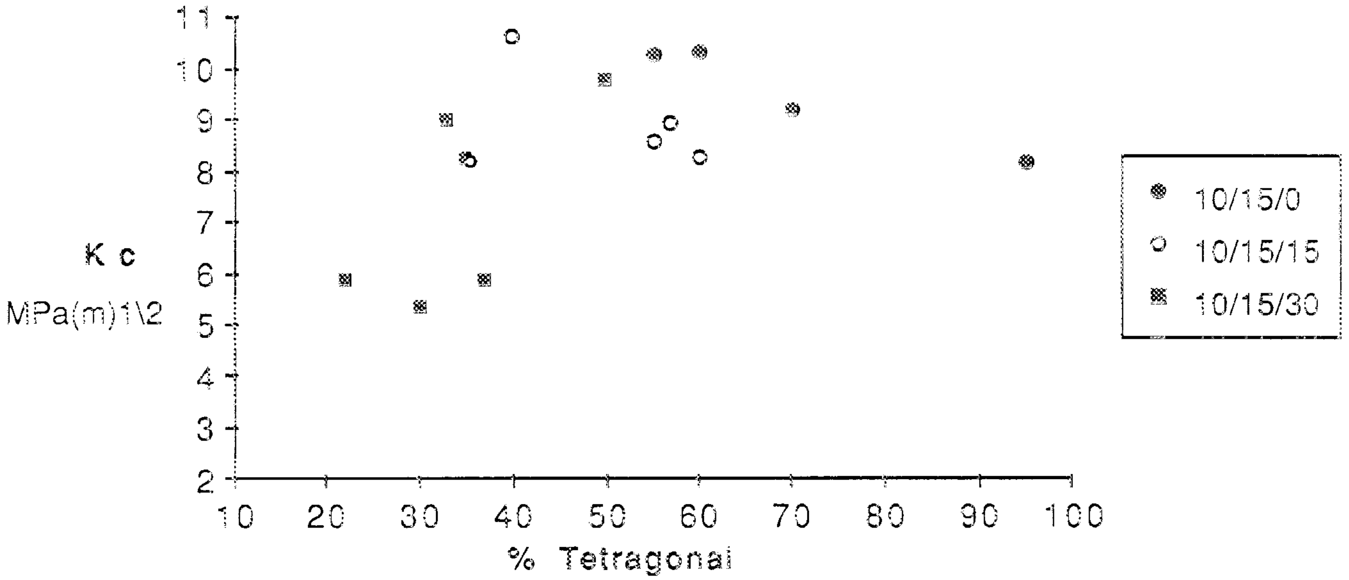

Fig.1, Toughness vs. %tetragonal for colloidal filtration samples.Composition is indicated in key as, m\oCr2O3/v\oZrO2/m\oHfO2.

Fig. 2, co-ppt Al2O3:Cr2O3 powder PAA adsorption showing stronger adsorption at lower pH.

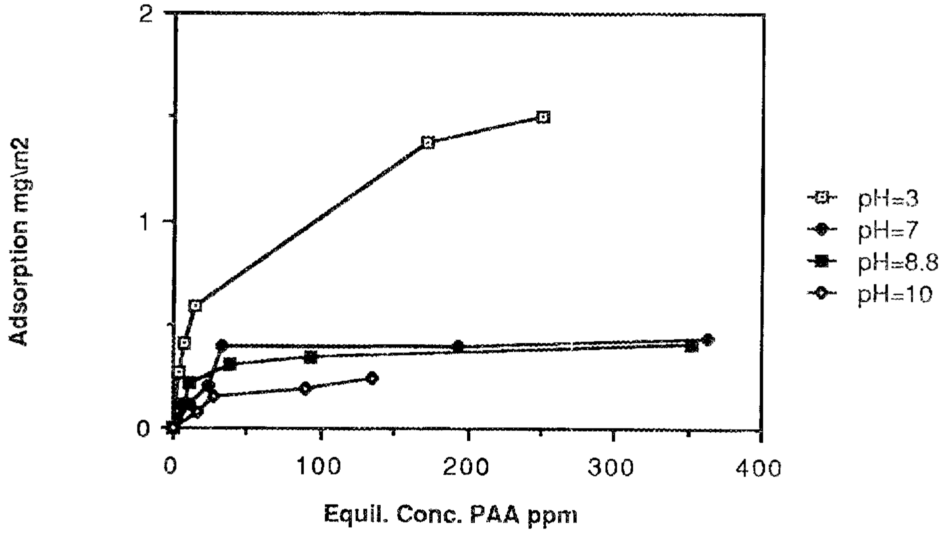

Fig.3, ZrO2 (Zircar) powder PAA adsorption showing high adsorption at pH=3 and low adsorption at pH=6.5,8.

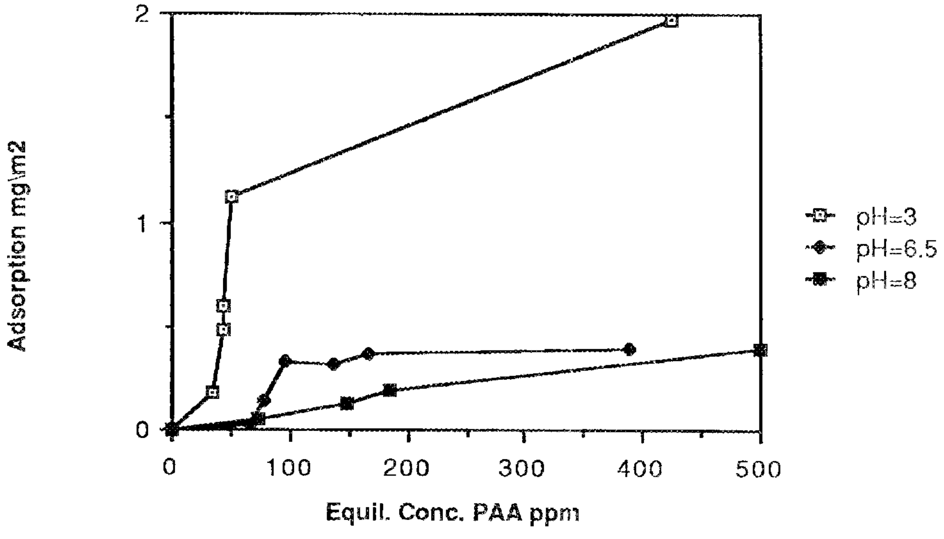

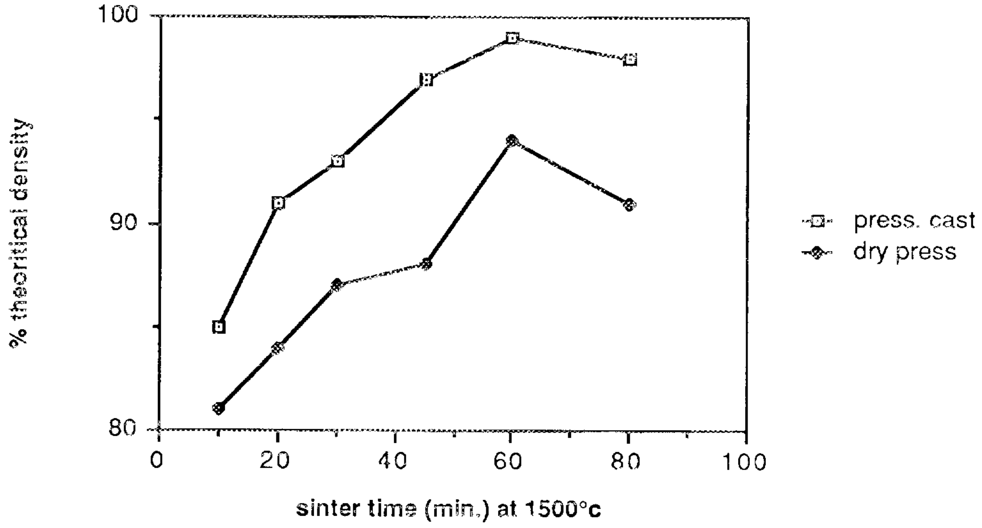

Fig.4, Density of p.c. vs d.p. samples

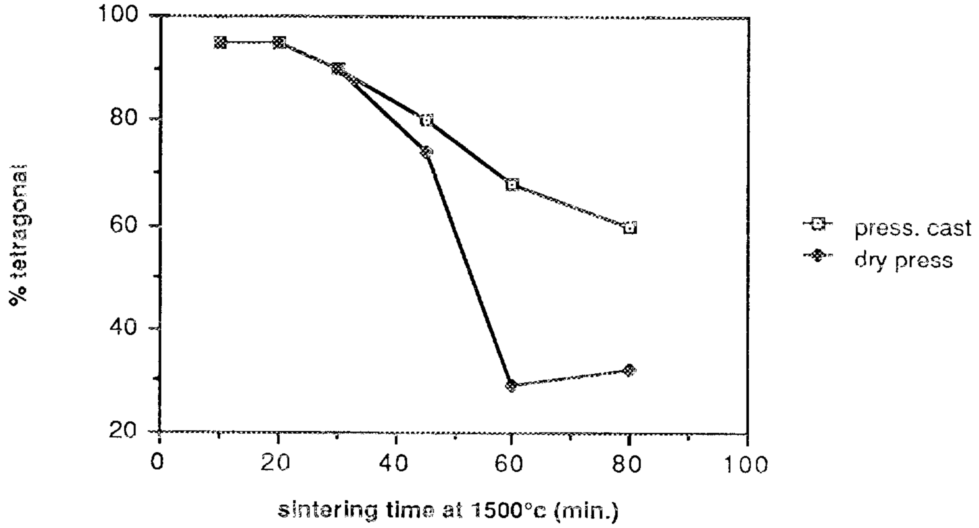

Fig.5, tetragonal content of p.c. vs d.p.

Fig. 6, Pore Size Distribution, Dry Press

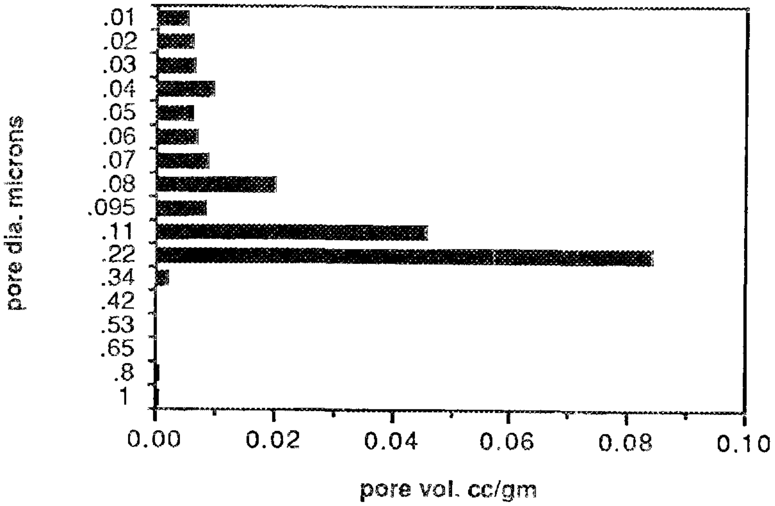

Fig. 7, Pore size Distribution, Press. Cast

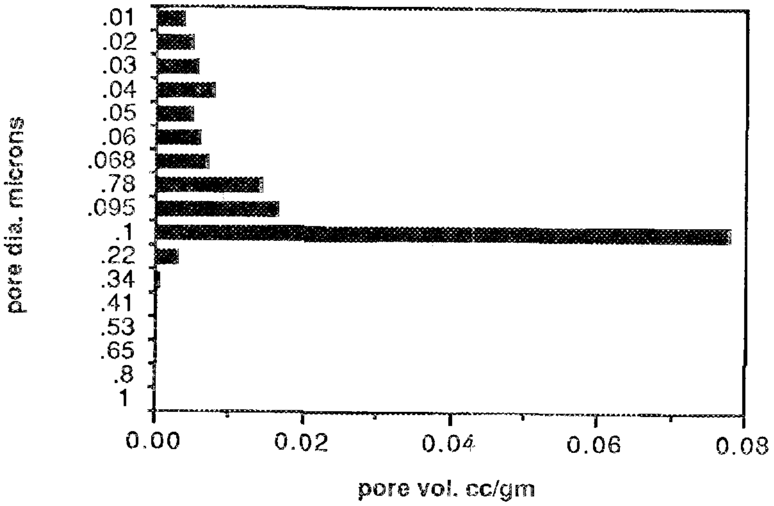

Fig. 8, Pore Size Distribution pH=3

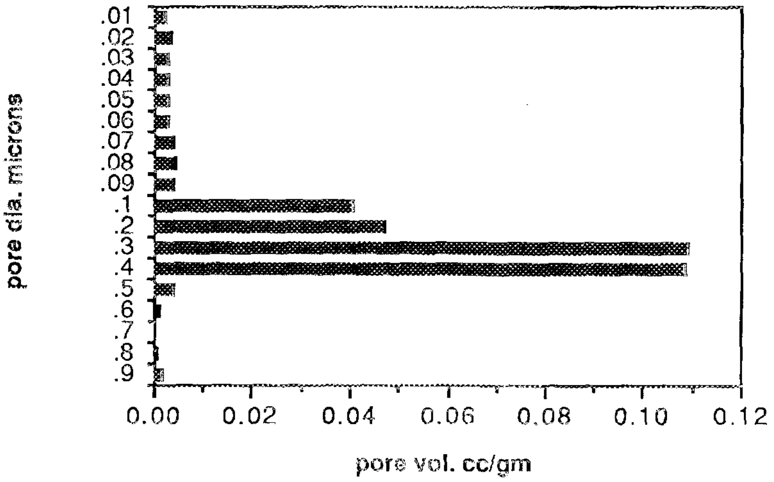

Fig. 9, Pore Size Distribution pH=7.8

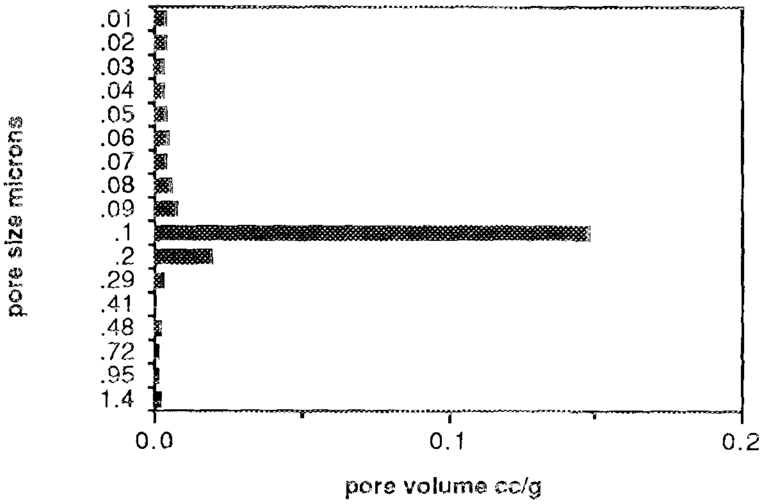

Fig. 10, Pore Size Distribution pH=10

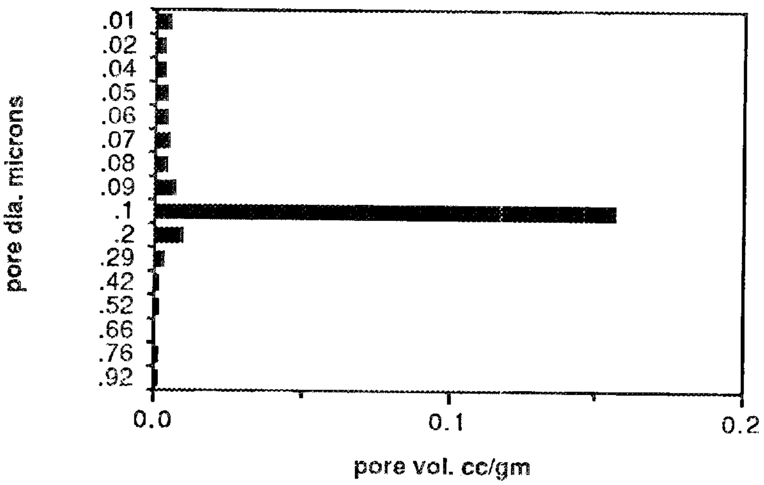

Processing and Characterization of Transformation-Toughened Ceramics With Strength Retention to Elevated Temperatures

R. A. Cutler, J. J. Hansen, D. W. Prouse (Ceramatec, Inc.) A. V. Virkar and D. K. Shetty (University of Utah).

Objective/Scope

Previous work[1] has shown that it is possible to increase the strength of Al_2O_3-ZrO_2 ceramics by incorporating transformation-induced residual stresses in sintered specimens consisting of three layers. The outer layers contained Al_2O_3 and unstabilized ZrO_2, while the central layer contained Al_2O_3 and partially stabilized ZrO_2. When cooled from the sintering temperature, some of the zirconia in the outer layers transformed to the monoclinic form while zirconia in the central layer was retained in the tetragonal polymorph. The transformation of zirconia in the outer layers led to the establishment of surface compressive stresses and balancing tensile stresses in the bulk. In theory, the residual stresses will not decrease with temperature until the monoclinic to tetragonal transformation temperature is reached since monoclinic and tetragonal ZrO_2 polymorphs have nearly the same coefficients of thermal expansion. The demonstration of the retention of residual stresses with temperature is a primary purpose of this project.

Previous work was accomplished using dry pressing techniques. The development of slip casting technology for layered composites will allow for better dispersion of zirconia in alumina and thereby facilitate higher volume monoclinic ZrO_2 in outer layers without strength degrading microcracking. A comparison between slip casting and dry pressing techniques will be made to identify higher strength materials for more detailed characterization during the second year of the project.

Technical Highlights

Characterization of Residual Stresses

Strength[2] and toughness measurements[3] on monolithic and three layer composites[1] have shown that substantial increases in mechanical properties occur due to the presence of residual stresses. A two parameter Weibull distribution was used previously to show that increasing strength and Weibull modulus are possible using three layer composites[4]. A three parameter Weibull expression,

$$F = 1 - \exp[-[(\sigma_f - \sigma_u)/\sigma_o]^m] \qquad (1)$$

where F is the fracture probability, σ_f is the fracture stress, σ_u is the "threshold stress" (i.e., the minimum stress for which fracture can occur), σ_o is a scale parameter and m is the Weibull modulus, was used to examine the change in σ_u as a function of compressive stresses (i.e., inner layer thickness, d_2, divided by total specimen thickness, d). The "threshold stress" was increased from zero in an iterative process to maximize the coefficient of determination (r^2). The threshold stress was taken as the stress at which r^2 was a maximum[5] (see Figure 1). Weibull plots (Figure 2) showed that the three parameter function gave a better fit of the data than the two parameter Weibull distribution. It is interesting to note that the threshold stress for the monolithic outer layer specimen was 370 MPa while that of the layered composite with d_1=375 micron was 660 MPa as shown in Figure 1. This tendency of increasing threshold stress with increasing compressive stress was not observed for the other three layer composites and larger sample populations are necessary before firm conclusions can be drawn. Increasing threshold stress is consistent with increasing strength due to the surface compressive stresses.

As further evidence of substantial residual stresses in layered composites made by the present technique, strain gauges were attached on fractured strength specimens and the opposite outer faces were successively removed by grinding as reported previously[1]. When the amount of material removed, δ, is small relative to the total thickness of the sample, the measured strain, $\varepsilon_M(\delta)$, can be used[1] to approximate $\Delta\varepsilon_o$ (the difference in length between the unconstrained inner and outer layers) by

$$\Delta\varepsilon_o \approx \varepsilon_M(\delta)d^2/\delta 3d_2 \qquad (2)$$

The slopes of the initial linear region of the data displayed in Figure 3 were used to calculate $\Delta\varepsilon_o$, as well as the residual compressive stresses. As expected, the monolithic outer and inner layer materials showed no change in strain upon grinding. The three layered bars for which strength was reported previously[2,4], however, showed increasing slopes with increasing residual stresses as shown in Figure 3. The average change in strain, $\Delta\varepsilon_o$ was calculated to be 1.49×10^{-3}, in excellent agreement with the values of 1.47×10^{-3} (calculated from XRD data[6]) and 1.39×10^{-3} (calculated from apparent toughness data[6]) reported previously. The residual stresses, calculated by substituting Equation (2) into

$$\sigma_c = -d_2E\Delta\varepsilon_o/d(1-\nu) \qquad (3)$$

where σ_c is the compressive stress, E is Young's modulus, and ν is Poisson's ratio were 526, 397, and 317 MPa for the 375, 750, and 1500 micron d_1 (outer layer thickness) specimens, respectively. These data are in good agreement with the change in strength reported previously[6].

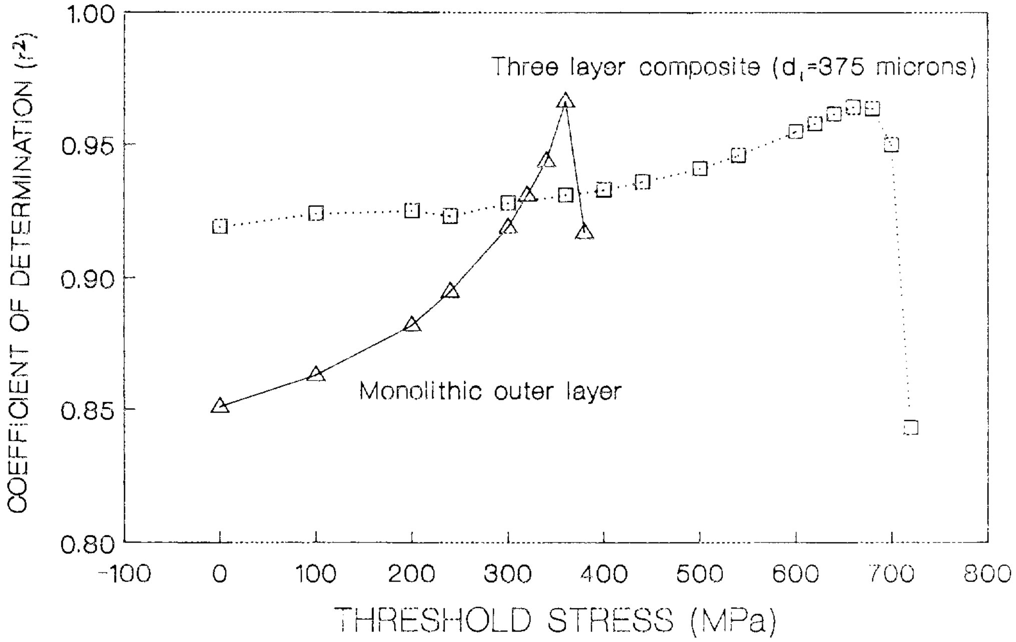

Figure 1. Change in coefficient of determination (r^2) as a function of threshold stress, σ_u.

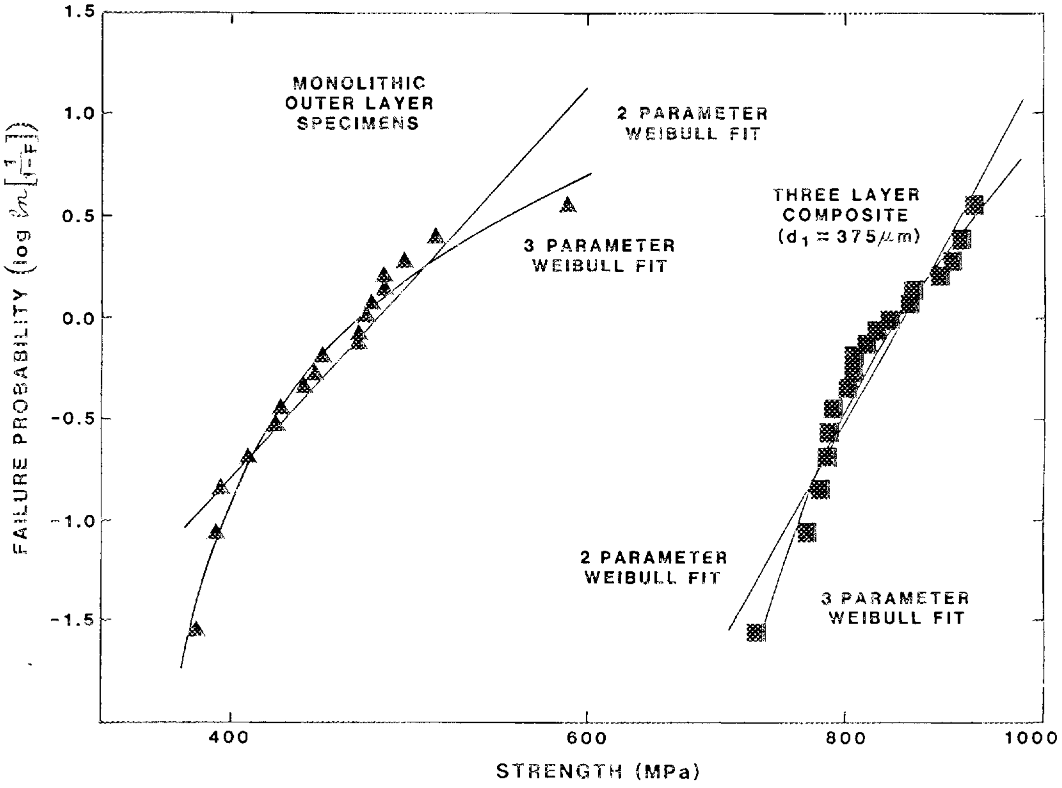

Figure 2. Comparison of two and three parameter Weibull distributions.

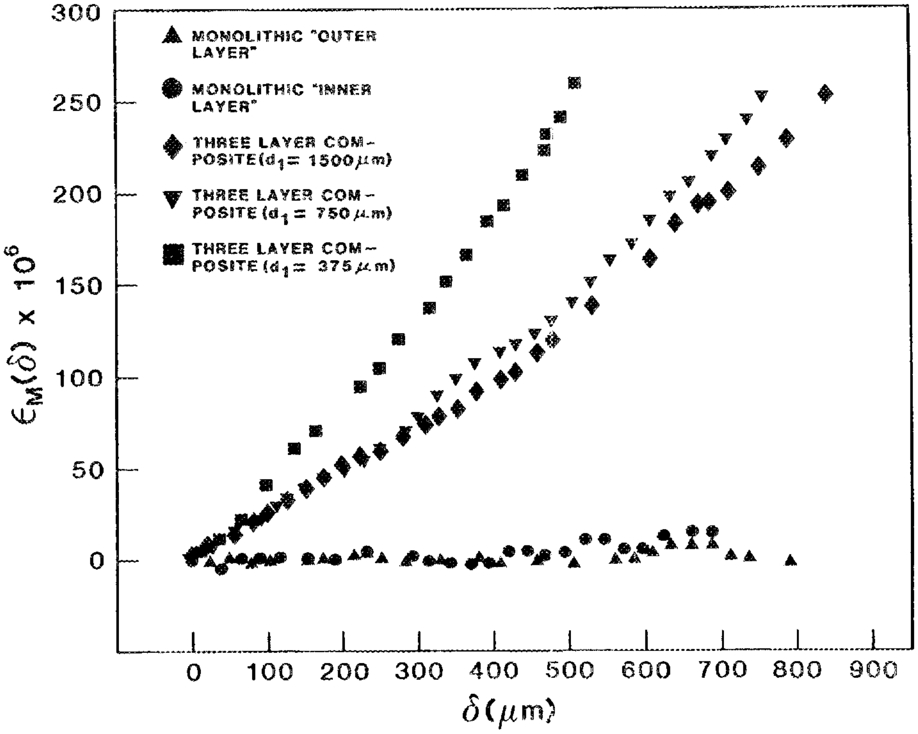

Figure 3. Strain determination in outer layers of Al_2O_3-15ZrO_2 bars as obtained using strain gage technique[1]. Note that monolithic specimens show no indication of residual stresses.

Slip and Tape Casting

Slip casting was investigated as a means of improving the uniformity of the outer layers of three layer composites and improving the density (minimizing the need for HIPping) of the composites. Three layer slip cast plates (100 mm x 100 mm x 6 mm) were made by pouring the outer layer slip into the mold first for a specified time, removing the remaining slip, and adding the inner layer slip into the mold until the cavity was fully cast. Monolithic inner and outer layer plates were also cast. The powders and processing used to make the Al_2O_3-15ZrO_2 composites were identical to that reported previously[1,4,6], except that the spray drying step was eliminated and slip casting was substituted for uniaxial and isostatic pressing. The fine powders (after air drying for 10 days) required heating rates of less than 0.3°C/hour to remove the water without producing cracks. Even with the slow heating rates, tensile cracks developed within the inner layer of three layer composites when the inner layer thickness exceeded 1/3 the total thickness. The tensile cracks were arrested in the outer layers, again evidence of the compressive stresses present in the outer layers of the composites. Further processing efforts will utilize nonaqueous slips to facilitate removal of the liquid after casting. The sintered plates were cut into bars for flexural tests.

The density of the monolithic inner material was 98.5 to 99.0% of theoretical after sintering as compared to 97.3 to 97.6% for the same composition made by spray drying and pressing. After HIPping there was no difference in density between slip cast and powder pressed bars for monolithic or three layer composites (see Table 1). Strength data (see Table 1) were obtained on monolithic composites and 2 three layer composites where the outer layer thickness was 1/10th the total thickness of the composite. The monolithic composites were about 100 MPa stronger when made by slip casting instead of spray drying, consistent with smaller critical flaw size. The limited data for three layer composites preclude firm conclusions. It is believed that the uniform outer layer thickness obtained by slip casting makes high strength bars, such as the 1.6 GPa three layer composite, possible. The strengths do show that slip casting has the potential to give substantially higher strengths in three layer composites than those obtained to date using pressing techniques.

Table 1
Slip Casting vs. Pressing of Al_2O_3-$15ZrO_2$ Composites

Description	Time[a] (min)	d_1[b] (μm)	Density(g/cc)		Strength[c] (MPa)	
			S.C.[d]	P.[e]	S.C.	P.
Outer[f]	90	6850	4.20[g]	4.21[g]	433±66(7)[g]	N.D.[h]
	90	6850	4.26[i]	4.27[i]	531±47(5)	451±48(18)
Inner[j]	90	6850	4.26[g]	4.14[g]	N.D.	N.D.
	90	6850	4.29[i]	4.30[i]	677±59(6)	545±50(18)
Three Layer Composite	1	700	4.26[g]	4.13[g]	N.D.	N.D.
	1	700	4.29[i]	4.30[i]	1604,920[k]	825±54(18)
	5	950	4.25[g]	N.D.	---[l]	N.D.
	10	1300	4.25[g]	4.14[g]	N.D.	N.D.
	10	1300	4.28[i]	4.29[i]	---[l]	696±88(20)
	20	1700	4.25[g]	4.16[g]	N.D.	N.D.
	20	1700	4.27[i]	4.29[i]	---[l]	N.D.
	40	2400	4.22[g]	4.16[g]	N.D.	N.D.
	40	2400	N.D.	4.28[i]	---[l]	570±62(10)

a. Slip casting time for outer layer (90 min. cast solid plate).
b. Outer layer thickness of slip cast plate (plate thickness was 6.8 mm).
c. Four point bend strength[4,6].
d. Slip cast.
e. Spray dried and pressed[4,6].
f. Monolithic outer layer specimens[1].
g. Sintered (1585 for 30 minutes in air).
h. Not determined.
i. Hot isostatically pressed (1525°C for 30 min., 200 MPa Ar).
j. Monolithic inner layer specimens[1].
k. Not determined due to cracking (cracks initiated in inner layer (tensile layer) or as a result of drying).

A strain gage was attached to a three layer Al_2O_3-$15ZrO_2$ slip cast specimen having a strength of 1.6 GPa (see Table 1) and the opposite side was ground in a similar manner to bars made with spray dried powder via powder pressing techniques[1]. The slip cast bar showed an inflection at the interface (see Figure 4) as predicted by Virkar[7]. The improved uniformity of the layers using slip casting is believed to be the reason why the inflection was observed using the slip cast bar and not with the specimens made by powder pressing. The residual strain using the initial slope of the data for the three layer slip cast bar in Figure 4 was calculated to be 1.2×10^{-3} and resulting compressive stress was 520 MPa.

Three layer bars having outer layers which where 1/12 the total thickness were made by tape casting and laminating 12 layers, each approximately 200 microns thick after sintering. The Al_2O_3-$15ZrO_2$ specimens had bend strengths of 592 MPa as compared to 840 MPa for the same composition made by uniaxially pressing spray dried powder. The strength of bars made via tape casting is quite good considering that mechanical mixing, not milling, was used to prepare the powders. Three layered composites made by tape casting showed no debonding between layers and excellent layer uniformity, as expected. Both tape and slip casting show much improved layer uniformity, as compared to bars prepared by powder pressing techniques.

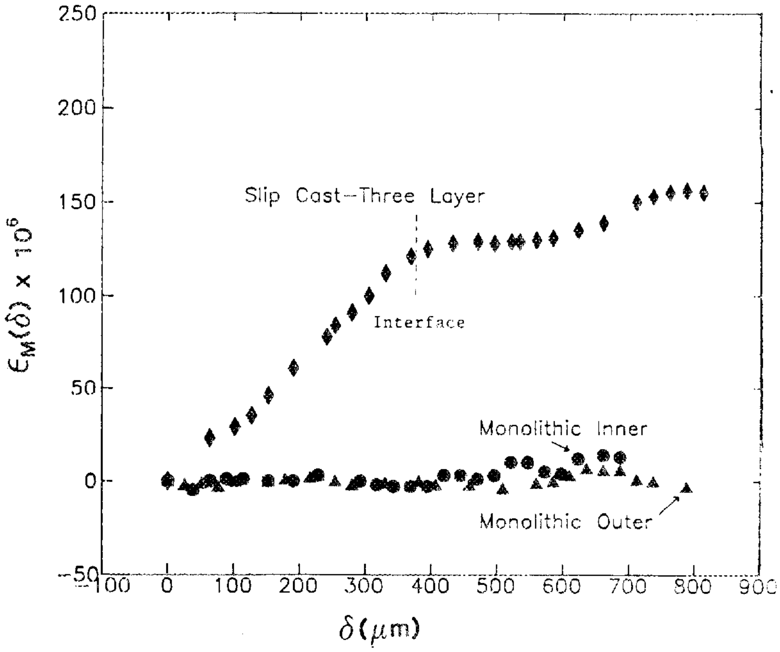

Figure 4. Strain determination in outer layer of three layer Al_2O_3-$15ZrO_2$ specimen made by slip casting in comparison to monolithic specimens showing no residual stresses. Note that the inflection in strain data coincides with the thickness of outer layer.

Toughness and Damage Resistance

Three layered Al_2O_3-15 vol. % ZrO_2 composites had bend strengths 375 MPa higher than the monolithic outer layer material at room temperature[2]. High temperature strength data, reported previously[2,4], showed retention of greater than 200 MPa at 750°C, with rapid loss of residual stresses above that temperature. Apparent toughness as a function of temperature (see Figure 5) was determined using the multiple indent technique[8] with monolithic "outer layer" and three layer (d_1=375 microns) composite bars. The three layer composites show more scatter than monolithic bars due to the variability (between bars) in the amount of outer layer removed while polishing one side of the bar, causing a change in residual stresses. It is believed that removal of a uniform amount of material from both outer layers would minimize this variability. The apparent toughness decreases with increasing temperature in a manner similar to strength data, as expected.

Indentation/strength measurements[9] were made on monolithic and three layer composites in the "as-sintered" condition by breaking the indented bars in four point bending. The strength of three layer composites where the crack size caused by indentation is contained well within the outer layer is given by

$$\sigma_f = \frac{2.02(K_{Ic})^{4/3}}{[(E/H)^{1/2}P]^{1/3}} + \sigma_c \qquad (4)$$

where K_{Ic} is fracture toughness, H is hardness and P is indentation load. Substituting Equation (3) into Equation (4) gives

$$\sigma_f = \sigma_f^o + d_2 E \Delta\varepsilon_o / d(1-\nu) \qquad (5)$$

where σ_f^o is the strength in the absence of compressive surface stresses as defined in Equation (4). A plot of fracture stress as a function of d_2/d, as seen in Figure 6, should yield a straight line with a slope related to $\Delta\varepsilon_o$ and an intercept of σ_f^o. Assuming a modulus of 365 GPa for E and taking ν as 0.25, a value of $\Delta\varepsilon_o$ of 1.20×10^{-3} was calculated from the slope of the plot in Figure 6. Assuming a hardness of 17 GPa, a value of K_{Ic} of 4.29 $MPa \cdot m^{1/2}$ was calculated from σ_f^o. Thus, indentation/strength measurements are another method for showing that residual stresses exist in three layer Al_2O_3-$15ZrO_2$ composites.

Indentation/strength measurements can also be used to assess the damage resistance of three layer composites as compared to monolithic ceramics. Accordingly, monolithic outer layer and three layer Al_2O_3-15 vol. % ZrO_2 bars (d_2/d=0.833) which were not ground after HIPping were indented with a 136° diamond pyramid indenter at loads of 50, 100, 150, 200, and 250 N before testing in four-point

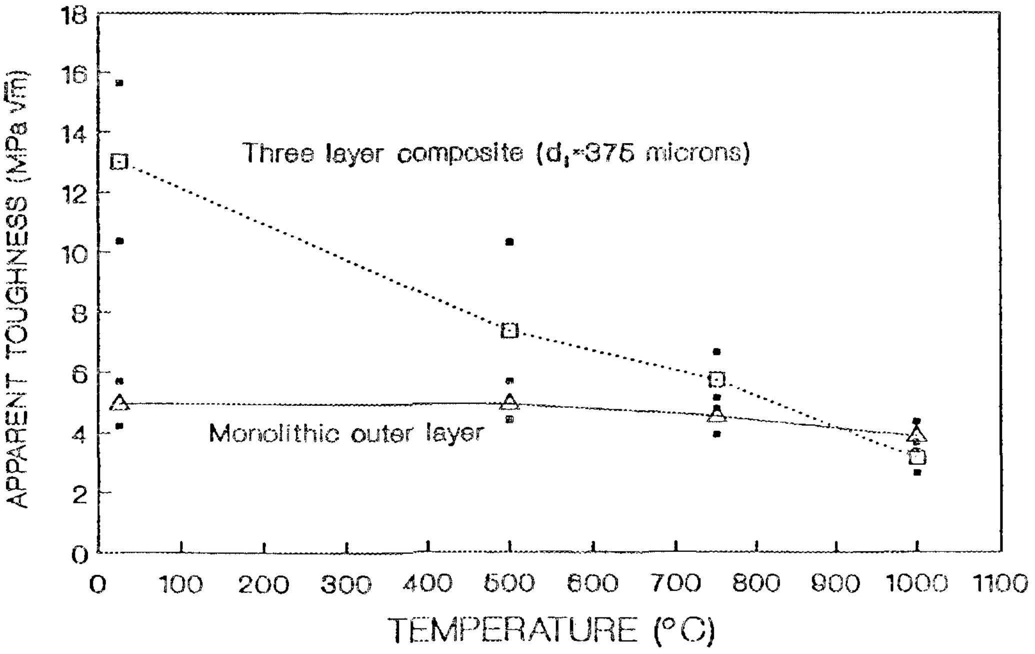

Figure 5. Apparent toughness of three layer Al_2O_3-15ZrO_2 specimens as a function of temperature.

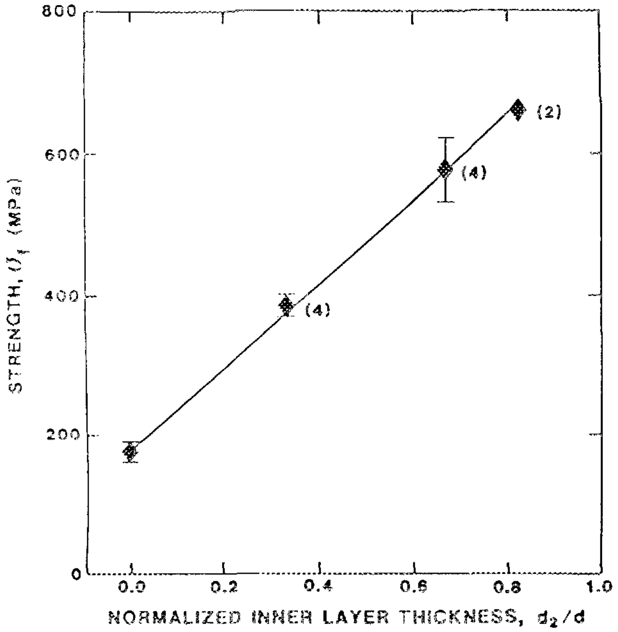

Figure 6. Strength of three layer Al_2O_3-15ZrO_2 specimens (indented at 100 N prior to strength testing) as a function of normalized inner layer thickness. A value of 4.29 MPa·$m^{1/2}$ for K_{Ic} was calculated from the intercept.

bending, in order to show the damage resistance of the three layer composites. Fractography confirmed that all the indented specimens failed from the indenter flaws. Table 2 shows strength data and calculated apparent toughness using the method of Chantikul et al.[9], along with apparent toughness measurements based on crack length measurements[10]. The residual compressive stress was calculated using Equation (5). A plot of σ_f versus $P^{-1/3}$ should yield a linear relationship where the intercept gives the residual stress and the slope can be used to determine K_{Ic}. Figure 7 shows such plots for the three layer composite specimens and the outer layer monolithic specimens. The significantly higher strengths of the three layer specimens relative to the monolithic specimens reflect their superior damage resistance due to the compressive residual stress. The three layer specimens showed an apparent insensitivity of strength to indentation load for loads greater than 50 N. It is not clear yet if this trend is real or it is due to the limited strength data obtained to date. Determination of crack size and shape, and further strength testing are underway.

Figure 7 shows linear regression fits (dotted lines) of both the three layer composite and the monolithic outer layer material with intercepts of 509 and 69 MPa, respectively. The fracture toughness values calculated from the slopes are 4.70 $MPa\cdot m^{1/2}$ for the three layer composite and 4.15 $MPa\cdot m^{1/2}$ for the monolithic outer layer specimens. If the data for the monolithic specimens are fitted with a straight line which is forced to go through zero and the same slope is used for the three layer composites (solid lines in Figure 7), the residual stress for the three layer composites is 472 MPa and the calculated toughness is 5.4 $MPa\cdot m^{1/2}$. The compressive surface stresses have therefore made the three layer composites more damage resistant by over 400 MPa.

In addition to the indentation/strength testing technique described above, an indentation technique that involves measurement of crack lengths[10] was also used to characterize the damage resistance of the three layer composites. The indentation/strength technique is preferred, however, because it does not involve measurement of crack lengths and no surface preparation is required prior to indentation. Apparent toughness, K_c^a, values given in Table 2 were determined using a crack measurement method proposed by Anstis, et al.[10] where

$$K_c^a = 0.016(E/H)^{1/2}P/c^{3/2} \tag{7}$$

where c is the crack length, and by the strength/indentation method proposed by Chantikul, et al.[9] where

$$K_c^a = 0.59(E/H)^{1/8}(\sigma_f P^{1/3})^{3/4} \tag{8}$$

Table 2
Indentation/Strength Data

Specimen Type	Indentation Load (N)	Strength (MPa)	Crack Length[a] (microns)	Apparent Toughness (MPa·m$^{1/2}$) K_c[a][4]	K_c[a][2]
Three Layer Composite[b]	0	840±79	---	---	---
	50	782±55	74	5.90±0.24	10.8±0.60
	100	698±62	97	7.54±0.30	11.5±0.73
	150	672±59	123	8.07±0.63	12.6±0.84
	200	667_50	145	8.40±0.44	13.5±0.76
	250	686±29	179	7.78±0.39	14.8±0.28
Monolithic Outer Layer[c]	0	445±79	---	---	---
	50	297±38	79	5.56±0.53	5.25±0.25
	100	235±21	138	4.88±0.90	5.20±0.35
	150	217±28	163	5.65±0.65	5.40±0.53
	200	184±14	211	5.08±0.16	5.13±0.29
	250	226±67	233	5.51±0.46	6.94±1.74

a. Crack length measured on polished specimens after indenting.
b. Al_2O_3-15ZrO_2 with outer layers 1/12 total thickness.
c. Monolithic outer layer specimens

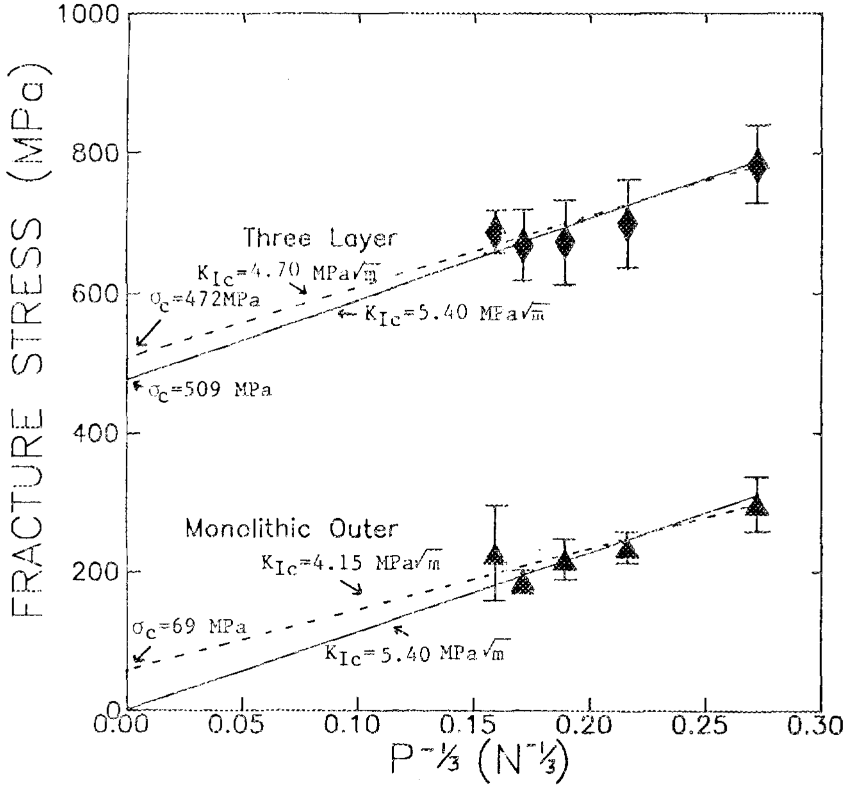

Figure 7. Strength as a function of cube root of inverse indentation load. Improved strength of three layer composites is evidence of damage resistance due to residual compressive surface stresses.

Fractured three layer and monolithic outer layer specimens were polished and indented at identical loads as the unground bars. The indents and resulting crack lengths were measured with values as shown in Table 2. As expected, the crack length increases with increasing load. No spalling or anomalous crack behavior was observed over the entire range of loads. The data in Table 2 show that determination of apparent toughness for specimens with residual stresses is sensitive to crack length. It is also interesting to note that the strength/indentation[9] and crack measurement[10] techniques for measuring fracture toughness give excellent agreement for monolithic specimens but apparent toughness values are much higher for the strength/indentation method. Previous work showed that apparent toughness values for three layer composites were similar when single indent[9] and multiple indent[8] techniques were compared. The present data show that apparent toughness is an ambiguous term to use when specimens have residual stresses. Strength measurements, as shown in Figures 6 and 7, should be used in preference to apparent toughness measurements in order to calculate K_{Ic}, the material property, for specimens with substantial residual stresses.

Optimization of ZrO_2 Size Distribution

Changing the ZrO_2 size distribution was investigated by using a zirconia powder (K906 from Teledyne Wah Chang) with a median particle size of 1.35 microns (all particles less than 3.7 microns, 90% less than 2.2 microns, and 90% greater than 0.65 microns). Specimens made with this 1.4 micron powder were compared with samples made with finer ZrO_2 powder (the outer layer zirconia powder used to obtain the data previously reported[8]). The finer ZrO_2 powder contained no particles greater than 1.8 microns and had an average particle size of 0.4 microns (90% less than 1.2 microns and 70% greater than 0.2 microns). Figure 8 shows the percent monoclinic ZrO_2 (data obtained by Dr. Rick Winterton (Dow Chemical Company) using elevated temperature x-ray diffraction) in the monolithic "outer layer" bars of 15 and 20 vol% 0.4 micron ZrO_2, as well as 15 vol. % 1.4 micron ZrO_2 as a function of temperature. The 1.4 micron ZrO_2 powder, although comparable in monoclinic content to the 0.4 micron ZrO_2 at temperatures up to 800°C, had twice as much monoclinic zirconia at 1000°C. While room temperature strengths of three layer composites of the two materials are comparable, it is predicted that improved retention in strength will occur by using the 1.4 micron zirconia which will not transform to the tetragonal phase until higher temperatures. An alternate method for increasing the ZrO_2 size is to increase the volume percent, allowing particle growth during sintering. The data for 20 vol. % ZrO_2, using the 0.4 micron ZrO_2, in Figure 8 indicates that smaller ZrO_2 particles

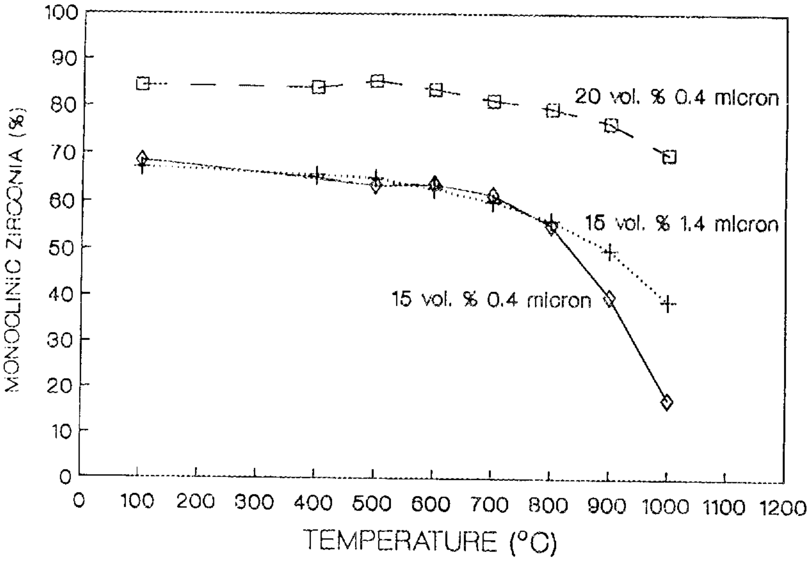

Figure 8. X-ray diffraction showing greater retention of monoclinic ZrO_2 by coarsening the ZrO_2 particle size.

coarsened during sintering leading to substantial improvement in the retention of the monoclinic polytype.

High temperature strength measurements were conducted to see if a correlation exists between XRD data (Figure 8) and strength measurements. The strength data for 20 vol. % ZrO_2 specimens are shown in Figure 9. The strengths fall off with increasing temperature, as for 15 vol. % specimens[2,4], but the three layer composites appear to be slightly stronger than monolithic specimens at 1000°C. Table 3 shows that a significant improvement in strength retention with increasing temperature was achieved by going to the higher volume loading of ZrO_2. It is believed that agglomeration of ZrO_2 and subsequent particle coarsening during sintering is the reason for the increased monoclinic content in the 20% ZrO_2 composition, as compared to the Al_2O_3-$15ZrO_2$ specimens. The lower strength of 20% ZrO_2 specimens could be due to microcracking, although limited scanning electron microscopy showed no evidence of microcracks. With improved dispersion techniques it should be possible to increase the strength of 20 vol. % ZrO_2 specimens.

HfO_2 and ZrO_2-50 mole % HfO_2 powders were supplied by Roger Peterson of Teledyne Wah Chang Albany. Al_2O_3-20 vol. % HfO_2 and Al_2O_3-20 vol. % (HfO_2-50 mol. % ZrO_2) powders were spray dried. These powders will be used

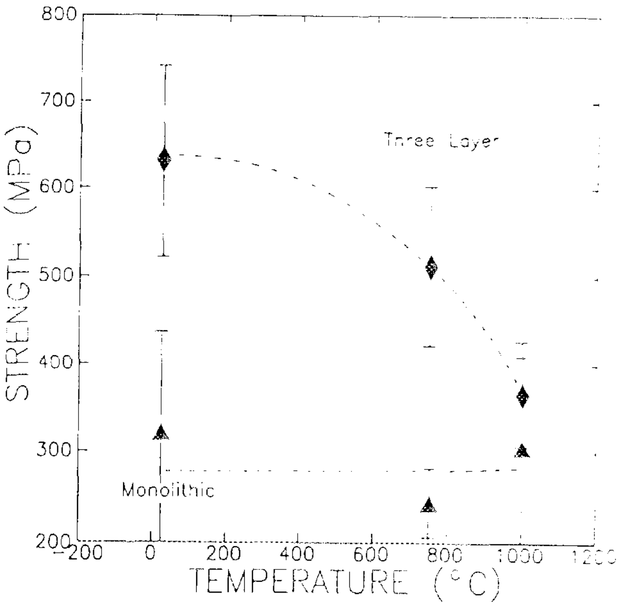

Figure 9. Strength of Al_2O_3-20 vol. % ZrO_2 specimens as a function of temperature.

as the outer layers of three layer composites in order to extend the temperature range over which compressive stresses are observed.

Status of Milestones

All milestones are on schedule.

Table 3
Strength Retention of Three Layer Al_2O_3-ZrO_2 Composites at Elevated Temperatures

Composition	Test Temperature (°C)	Strength (MPa)	Normalized Strength^{a}
Al_2O_3-15ZrO_2	25	825±54	1.00
	500	671±52	0.81
	750	573±98	0.70
	1000	304±104	0.39
Al_2O_3-20ZrO_2	25	632±110	1.00
	750	512±90	0.81
	1000	365±60	0.58

a. Strength divided by strength at 25°C.

Publications

A paper entitled "Transformation-Toughened Alumina with Improved Strength at Elevated Temperatures" was submitted to the Am. Ceram. Soc. for publication.

A paper entitled "Strength Improvement in Transformation Toughened Ceramics Using Compressive Residual Surface Stresses" (presented at the Fall MRS Meeting (Dec. 1-6, Boston, MA.) was submitted for publication.

References

1. A. V. Virkar, J. L. Huang, and R. A. Cutler, "Strengthening of Oxide Ceramics by Transformation Induced Stresses," 70[3] 164-170(1987).
2. R. A. Cutler, J. D. Bright, D. W. Prouse, A. V. Virkar and D. K. Shetty, "Processing and Characterization of Transformation Toughened Ceramics with Strength Retention to Elevated Temperatures," in Ceramic Technology for Advanced Heat Engines Project Bimonthly Technical Progress Report (ORNL/CF-86/259, June-July 1986), Oak Ridge National Laboratory, Oak Ridge, Tenn.
3. R. A. Cutler, J. J. Hansen, A. V. Virkar, and D. K. Shetty, "Processing and Characterization of Transformation Toughened Ceramics with Strength Retention to Elevated Temperatures," in Ceramic Technology for Advanced Heat Engines Project Bimonthly Technical Progress Report (Nov.-Dec. 1986), Oak Ridge National Laboratory, Oak Ridge, Tenn.
4. R. A. Cutler, J. D. Bright, A. V. Virkar and D. K. Shetty, "Transformation Toughened Alumina With Improved Strength At Elevated Temperatures," submitted to Am. Ceram. Soc. for publication.
5. D. K. Shetty, unpublished work.
6. R. A. Cutler, J. J. Hansen, A. V. Virkar, D. K. Shetty, and R. C. Winterton, "Strength Improvement in Transformation Toughened Ceramics Using Compressive Residual Surface Stresses," to appear in Proceedings of the 1986 Fall Materials Research Society Meeting.
7. A. V. Virkar, unpublished work.
8. R. F. Cook and B. R. Lawn, "A Modified Indentation Toughness Technique," J. Am. Ceram. Soc., 66, (11), C-200-C-201 (1983).
9. P. Chantikul, G. R. Anstis, B. R. Lawn and D. B. Marshall, "A Critical Evaluation of Indentation Techniques for Measuring Fracture Toughness: II, Strength Method," J. Am. Ceram. Soc., 64[9] 539-543 (1981).
10. G.R. Anstis, P. Chantikul, B.R. Lawn, and D.B. Marshall, "A Critical Evaluation of Indentation Techniques for Measuring Fracture Toughness: I, Direct Crack Measurements," J. Am. Ceram. Soc., 64[9] 533-38 (1981).

Injection Molded Composites

M. A. Janney (Oak Ridge National Laboratory)

Objective/scope

The goals of this activity are twofold: (1) to evaluate the ability of advanced ceramic-ceramic composites to be injection molded and processed using standard wax- and/or polymer-based binder systems; and (2) to develop advanced complex-shape-forming technologies that will eliminate some of the problems associated with wax- and polymer-based binder systems such as long binder removal times, cracking, and low green strength.

Technical progress

Rheology

In the last semiannual report, we presented work on the effects of whiskers on the rheology of alumina slurries in terms of the total solids loading and the whisker loading for Alcoa A16SG alumina and Tateho SCW-1S SiC whiskers. In this report, we describe the role of the source of the alumina (Sumitomo AKP50 and Reynolds RC-HP) on the rheology of the systems. The additives, mixing conditions, test conditions, etc. were the same as reported in the previous semiannual report.[1]

A summary of the flow curves for Sumitomo AKP50 alumina with Tateho SCW-1S whiskers at 40 vol % solids is shown in Fig. 1. For comparison, a similar plot for Alcoa A16SG is shown in Fig. 2. The general behavior of the Sumitomo slurries is similar to that of the Alcoa slurries except that the shear stresses are about an order of magnitude higher for the Sumitomo slurries. This increase in shear stress is not surprising considering that the Sumitomo powder has an average particle size of about 0.2 μm and the Alcoa power has an average particle size of about 0.7 μm. In particular, the Sumitomo slurries exhibit a reduction in viscosity when small amounts of whiskers (5 and 10%) are added, which is similar to the behavior of the Alcoa slurries. One small difference that was observed between the behavior of the Sumitomo and Alcoa slurries was that the Sumitomo slurries showed a reduction in viscosity at both 5 and 10% whiskers, as compared with the 100% alumina slurry, whereas the Alcoa slurries showed a reduction in viscosity only at 5% whiskers (Fig. 3). The reduction in viscosity of the particulate slurries on the addition of whiskers is probably a manifestation of improved particle packing with the whiskers filling voids between the alumina particles. We are working on the modelling of this phenomenon using some of the current theories of whisker and particle packing as the starting point for analysis.

Additional rheometry was performed on slurries made with Reynolds RC-HP powder at 55 vol % solids and 0 to 10% whiskers (Fig. 4). The flow curve for the base Reynolds alumina slurry was similar to that for Alcoa A16SG at 55 vol %, shown in Fig. 5, except that the shear stresses for the Reynolds slurry was somewhat lower than that for the Alcoa slurry, 140 vs 250 dyne/cm^2, respectively. On addition of the SiC whiskers, however, differences appeared. The Alcoa slurries showed a definite reduction in viscosity at 5% whiskers, similar to the behavior observed at 40 vol % solids for the Alcoa slurries. The Reynolds slurry did not exhibit any reduction in viscosity when whiskers were added. Further studies to determine the source of these differences are currently in progress.

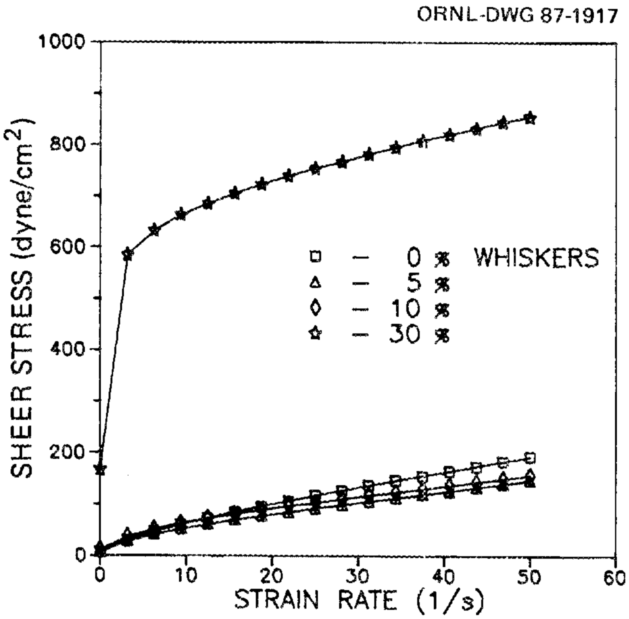

Fig. 1. Flow curves for 40 vol % solids slurries made with Sumitomo AKP50 alumina.

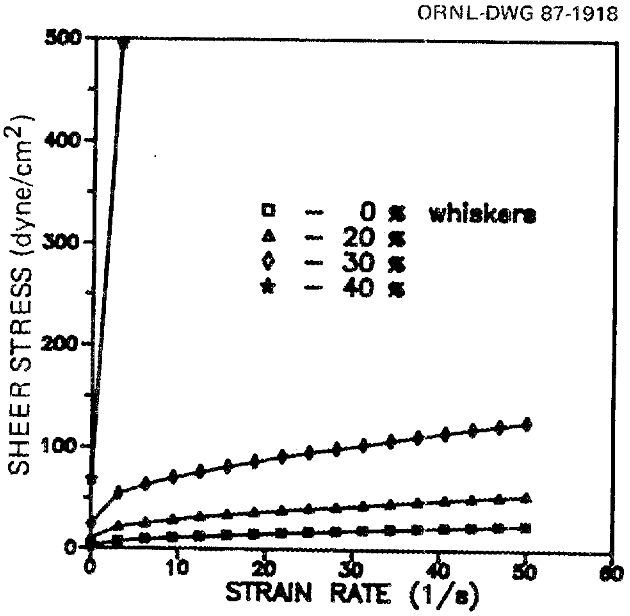

Fig. 2. Flow curves for 40 vol % solids slurries made with Alcoa A16SG alumina.

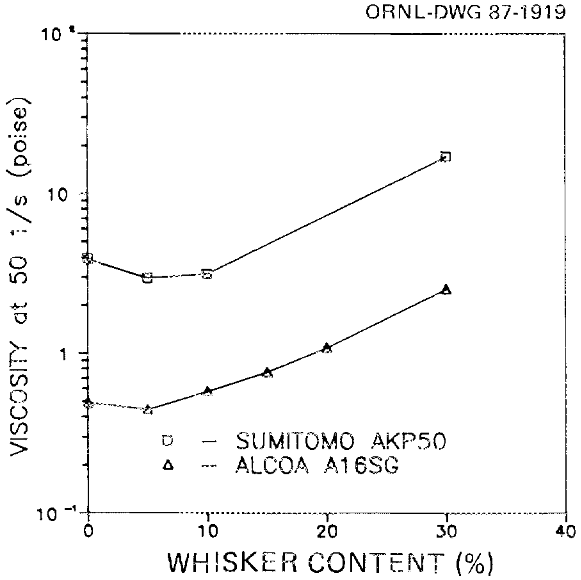

Fig. 3. The general behavior of Sumitomo AKP50 slurries was similar to that of Alcoa A16SG slurries.

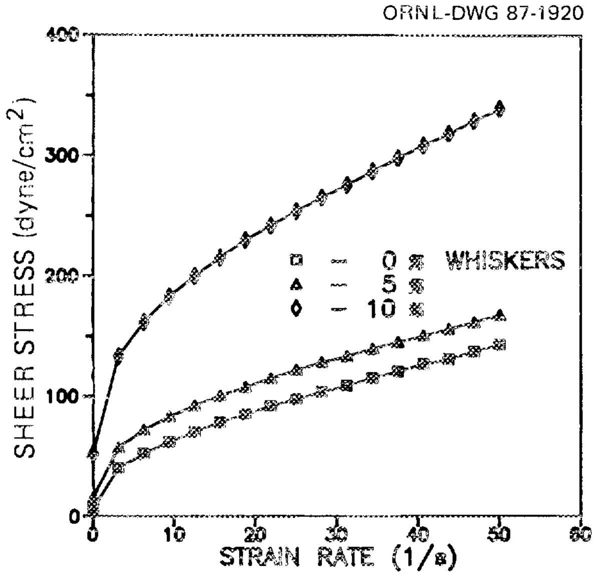

Fig. 4. Flow curves for 55 vol % solids slurries based on Reynolds RCHP alumina.

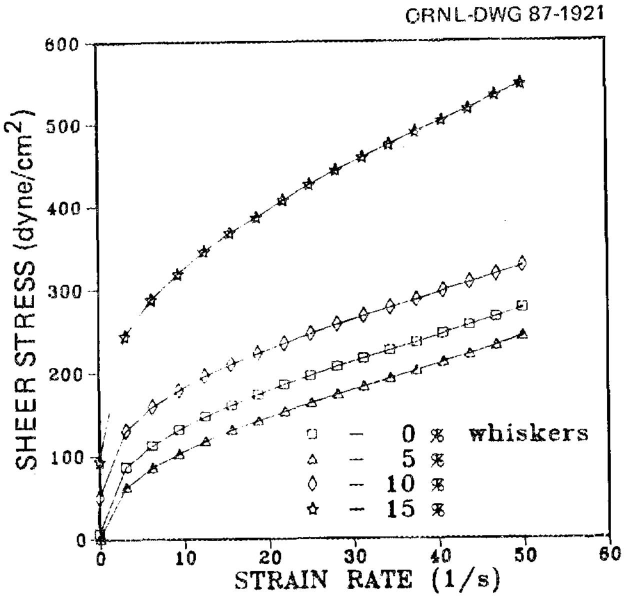

Fig. 5. Flow curves for 55 vol % solids slurries based on Alcoa A16SG alumina.

Status of milestone

A paper describing a new advanced forming technology has been submitted to the Ceramic Technology Program management, thus meeting one of the milestones (1.2.3.5.2) associated with this task. Submission to an open literature journal and general release of the document are awaiting patent clearance from the patent counsel at DOE-ORO.

Publications

None.

References

1. M. A. Janney, "Injection Molded Composites," in Ceramic Technology for Advanced Heat Engines Project Semiannual Progress Report for April Through September 1986, ORNL/TM-10308 (March 1987).

1.2.4 Silicate Matrix

Low Expansion Ceramics for Diesel Engine Applications

J. J. Brown, R. E. Swanson (VPI & SU), and F. A. Hummel (Consultant)

Objectives/scope

The major objective of this research is to investigate selected oxide systems for the development of a low expansion, high thermal shock resistant ceramic. Specifically, it is the goal of this study to develop an isotropic, ultra-low expansion ceramic which can be used above 1200°C and which is relatively inexpensive.

The need for stable, fabricable, low thermal expansion ceramics for use in advanced heat engines was first recognized in the Department of Energy Advanced Gas Turbine (AGT) technology programs. More recently, the need for ceramic materials having low thermal expansion for use in components of advanced low heat rejection diesel engines has also been recognized. Components for the AGT, including the regenerator and other parts in the hot flow path, operate under thermal cyclic or other conditions which require low thermal expansion in order for the components to have satisfactory life. Only two major ceramic systems--magnesia-alumina-silica and lithia-alumina-silica--have been evaluated extensively for use in fabricating these low expansion ceramic components. Compositions evaluated extensively in the magnesia-alumina-silica system are near the composition of the compound cordierite, whereas compositions evaluated in the lithia-alumina-silica system are near that of the compound spodumene. Advanced low heat rejection diesel engines also have demonstrated the need for low thermal expansion ceramics which have relatively high mechanical strength. Ceramic materials based upon either spodumene or cordierite have relatively low strength and high thermal expansion compared to fused silica, for example. It is of considerable importance to determine whether other ceramic systems exist in which the thermal expansion can be tailored so as to be very near zero over a relatively wide temperature range, extending to at least 1200°C.

The research program includes the following tasks: synthesis, property characterization, and fabrication of candidate low thermal expansion ceramics from four systems based upon aluminum phosphate, silica, mullite, and zircon. In the first two systems, the goal is to stabilize low thermal expansion, high temperature, high crystal symmetry phases via solid solution formation. In mullite, deviation from stoichiometry and solid solution formation is utilized to reduce the thermal expansion. In zircon, the crystal anisotropy and thermal expansion are reduced via solid solution formation. Based upon earlier data of the investigators, compositional ranges are evaluated by fabricating experimental specimens and determining phase content plus microstructure, thermal expansion, solidus temperature, and density. Those compositions which exhibit acceptable sintering, phase composition, and expansion characteristics are studied in more detail, including flexure strength, creep, thermal conductivity, and crystal structure. Finally, those ceramic compositions exhibiting the best combination of properties are evaluated as to their fabrication behavior in the form of specimens having masses up to about 0.5 kg.

Technical progress

Aluminum Phosphate

A. Background

An ultra-low coefficient of thermal expansion (CTE) corresponds to a ceramic material with high thermal shock resistance. Most of the analytical equations for thermal shock resistance are based on the following equation:

$$R = \frac{\sigma_f (1-\mu)}{E\alpha}$$

where σ_f is the stress required to fracture, μ is Poisson's ratio, E is the modulus of elasticity, and α is the linear expansion coefficient.[1] Since α is in the denominator, as its value approaches zero, the resistance to thermal shock will theoretically approach infinity. According to Hummel,[2] it has been shown experimentally that dense, low porosity materials with this ultra-low CTE do indeed have the best resistance to thermal shock.

The system $AlPO_4$-BPO_4-β-eucryptite ($Li_2O \cdot Al_2O_3 \cdot 2SiO_2$) has been targeted as a system that possibly contains the composition of an ultra-low expansion ceramic. In order to formulate different compounds with possible low expansion, a knowledge of the phase equilibrium and non-equilibrium relationships between the different components is necessary. Although a diagram with all three of these end members does not exist, a summary of work that has been done on various subsystems of this group follows.

$AlPO_4$ is a half-breed derivative of SiO_2. $AlPO_4$ has all the polymorphs of SiO_2 with similar structures and similar inversion temperatures. Crystal structures have been established for the α- and β-quartz and α- and β-cristobalite forms of $AlPO_4$. The α-quartz form of $AlPO_4$, called α-berlinite, has been assigned the space group $P3_121$ in the rhombohedral system with lattice parameters at 293K of a=4.937(2)Å and c=10.926(3)Å.[3] An earlier work lists room temperature parameters of a=4.9441Å and c=10.9392Å.[4] Recent work by Byrappa et al.[5] lists berlinite as being trigonal with a=4.942Å and c=10.97Å. They also describe the β-quartz form of $AlPO_4$, called β-berlinite, as being tetragonal with a=7.510Å and c=5.837Å. Ng and Calvo[6] further described the structure of β-berlinite as space group $P6_422$. They assign space group $P3_12$ to α-berlinite and describe it as having three formula units per unit cell, the same as quartz, but with the c-axis being doubled because of the double substitution of Al and P for Si.

Wright and Leadbetter have done much work on the α- and β-cristobalite forms of $AlPO_4$.[7–9] They describe the structure of α-cristobalite as being orthorhombic with four formula units per unit cell. This structure is pseudo-tetragonal and is almost identical to the analogous SiO_2 structure. The β-cristobalite form of $AlPO_4$ is also very similar to the analogous SiO_2 structure. Wright and Leadbetter described its structure using the space group $F\bar{4}3m$.[7] Allaf and Rouanet[10] list unit cell parameters for three different phases of

$AlPO_4$ as follows: α-cristobalite (orthorhombic), a=7.082Å, b=7.098Å, and c=6.993Å; β-cristobalite (cubic), a=7.08±0.01Å at 100°C-7.27±0.01Å at 1240°C; and tridymite (hexagonal), a=5.04Å and c=8.27Å. These values are in agreement with those reported by Wright and Leadbetter.[8]

Many researchers have worked on mechanisms and temperatures of the transformations in $AlPO_4$. Beck[11] in 1949 listed the following scheme:

$$\begin{array}{ccccccc} & 815\pm4^\circ C & & 1025\pm50^\circ C & & >1600^\circ C & \\ \text{Berlinite} & \leftrightarrow & \text{Tridymite } AlPO_4 & \leftrightarrow & \text{Cristobalite } AlPO_4 & \leftrightarrow & \text{Fused } AlPO_4 \end{array}$$

$$\begin{array}{llll} 586\pm2^\circ C & 93\pm3^\circ C & 130^\circ C\ (?) & 210\pm5^\circ C \\ \alpha \leftrightarrow \beta & \alpha \leftrightarrow \beta_1 & \longleftrightarrow \beta_2 & \alpha \leftrightarrow \beta \end{array}$$

He points out that all four phases can exist indefinitely at room temperature. According to Beck, berlinite will convert to tridymite and to cristobalite by way of tridymite. Amorphous $AlPO_4$ will convert to berlinite, tridymite, and cristobalite, again with tridymite being an intermediate stage in the conversion to cristobalite. Tridymite and cristobalite have reversible reactions: however, berlinite cannot be formed from either of these two, but from amorphous material. These reactions are all sluggish, but occur more quickly than the corresponding SiO_2 inversions. The $\alpha \rightleftarrows \beta$ transformations are all rapid, as with SiO_2. He finally states that the cristobalite form will rapidly convert to the tridymite form upon cooling to 815°C. However, with heating the reverse reaction proceeds slowly and only occurs above 1025°C. Hummel[12] expanded on this work by showing that the α to β cristobalite inversion was strongly dependent on thermal history.

Shafer and Roy[13] later showed that the quartz to tridymite inversion in $AlPO_4$ occurred at 705±7°C. Other sources confirm an α-toβ-quartz transition of 586°C.[6,14] Flaerke and Lachenmayr[15] found an α- toβ-tridymite inversion at 90°C and an α-to β-cristobalite inversion at 220°C for samples annealed at 1300°C for a prolonged time, which agree with inversion temperatures reported by Beck. Leadbetter and Wright[8] also found the α-to β-cristobalite inversion to be first order and in the vicinity of 200°C. Allaf and Rouanet[10] present a different view of the transformation scheme as shown in Figure 1.

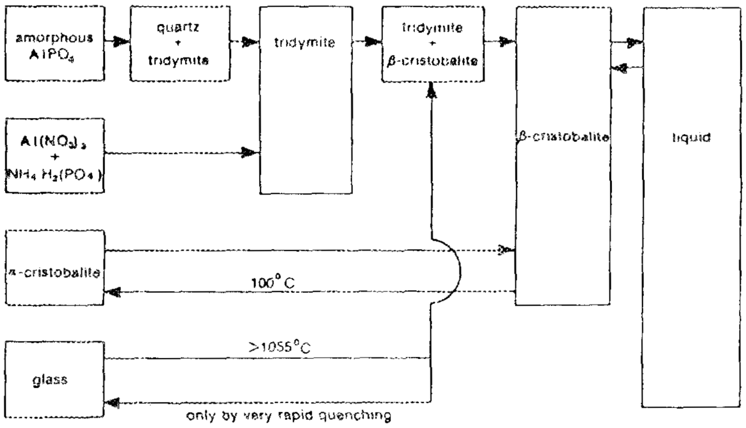

Figure 1. Diagram of $AlPO_4$'s Transformations.[10]

They state that the α-cristobalite to β-cristobalite inversion occurs at 100°C and that the two cristobalite polymorphs are the stable phases of $AlPO_4$ over the whole temperature range up to melting. The tridymite to cristobalite inversion is irreversible and tridymite is a metastable intermediate phase leading to the stable cristobalite phase when devitrification occurs. Devitrification will only occur above 1055°C.

$AlPO_4$ is known to decompose before melting; thus the exact melting point has not been determined. At 1600°C, a uniform weight loss of 0.2% per hour occurs.[16] This same reference estimates the melting point of $AlPO_4$ to be above 2000°C. Allaf and Rouanet[10] were able to melt and quench small samples of $AlPO_4$ by using a solar furnace and a splat cooling apparatus. They also observed the rapid decomposition of $AlPO_4$ as given by:

$$AlPO_4(s,l) \longrightarrow Al_2O_3(s,l) + P_2O_5(g)$$ [10]

The thermal expansion of $AlPO_4$ is similar to that of the analogous silica structures, as illustrated in Figures 2-4.

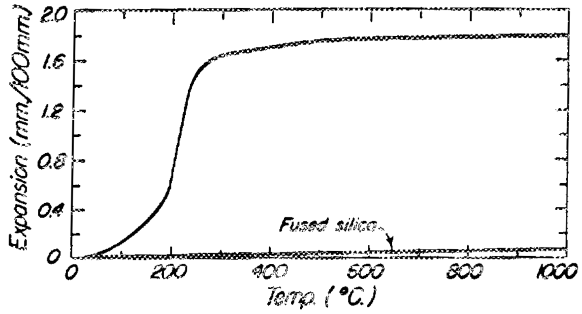

Figure 2. Thermal expansion of aluminum orthophosphate calcined at 1500°C for 1 h and refired for 2 h at 1500°C with 6% aluminum metaphosphate bond.[12]

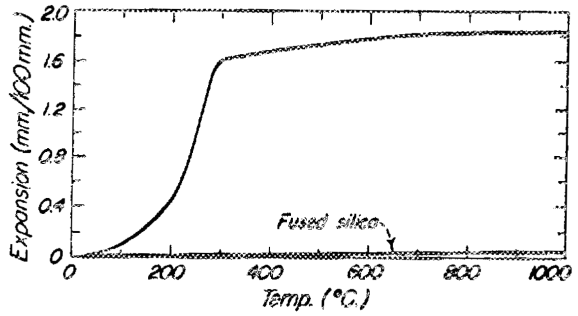

Figure 3. Thermal expansion of cristobalite prepared by calcination of Davison silica gel at 1500°C for 1 h and refired with 6% aluminum metaphosphate bond.[12]

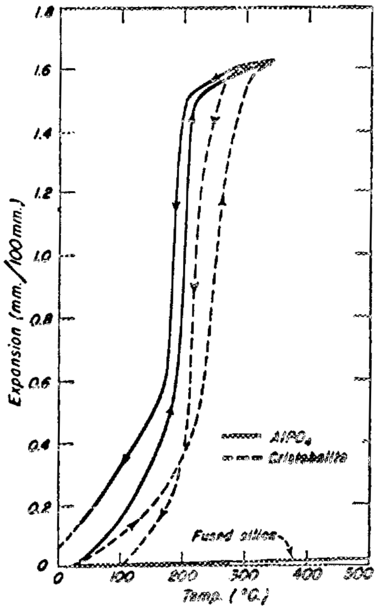

Figure 4. Thermal expansion of cristobalite and aluminum orthophosphate.[12]

BPO_4 is another compound which is a half-breed derivative of SiO_2. Polymorphs of BPO_4 exist which are analogous to those of SiO_2, but which have not been studied as extensively as those of SiO_2 and $AlPO_4$. The β-cristobalite structure of BPO_4 closely resembles that of $AlPO_4$.[7] BPO_4 will vaporize before melting, according to Hummel and Kupinski.[17] They claim that BPO_4 begins to vaporize around 1450°C and completely disappears within an hour at 1462°C. They detected no free P_2O_5, B_2O_3, or H_3BO_3 after partial vaporization of BPO_4, which led them to conclude that the compound does not decompose into its component oxides. Later work by Horn and Hummel[18] estimates the melting point of BPO_4 to be about 1300°C. This compound has yet to be successfully melted and quenched to a glass. The CTE for a bar of BPO_4 sintered at 1260°C for one hour is $\alpha = 90\text{x}10^{-7}/K$ in the temperature range 25 to 1000°C.[17]

β-eucryptite is a stuffed-derivative of SiO_2 with a high quartz-like structure. Half of the Si atoms are replaced by Al atoms and the charge balance is maintained by the addition of Li atoms. This gives a composition of $LiAlSiO_4$. Winkler[19] and Buerger[20] were among the first to study this material. Winkler described β-eucryptite as belonging to space group $C6_22$ with a $a=5.27\text{Å}$ and $c=11.25\text{Å}$. This corresponds to a doubling of the c-axis of the β-quartz structure. Buerger discovered that the a-axis of β-eucryptite was also doubled and assigned to β-eucryptite a monoclinic space group of the form PZ with $a=10.55\text{Å}$ and $c=11.22\text{Å}$. It is generally agreed that the Li atoms are 4-coordinated with O and are located in channels running parallel to the c-axis. Tscherry, Schulz, and Laves established the structure of β-eucryptite in a series of papers.[21-24] They state that at room temperature β-eucryptite has a structure similar to that of low quartz with an ordered arrangement of Li, Al, and Si atoms. It has a superstructure with space group $P6_422$ that shows a doubling of the high quartz-like a- and c-axes. The average structure is super-imposed on the superstructure and is described by space group $P6_222$. They list lattice constants of a=10.4818Å and c=11.1750Å for β-eucryptite which are comparable to those found by Buerger. Tscherry et al. describe a transformation from the low-temperature, ordered form of β-eucryptite to a high-temperature, disordered form which occurs at 400°C. They describe this as a first-order transition. Pillars and Peacor[25] did further work on β-eucryptite, and agreed with and expanded on the previously determined crystal structure. They disproved any first-order transition occurring at 400°C and showed the transition to be a combination of thermal vibrations and increasing disorder of Li atoms with increasing temperatures.

Eucryptite has two polymorphic forms: α-eucryptite (found in nature) and β-eucryptite (most often synthesized in the laboratory and described above). β-eucryptite and α-eucryptite undergo a reconstructive inversion. Roy et al. first reported the $\alpha \rightarrow \beta$ reaction to occur at 972 ± 10°C.[26] A later study by Isaacs and Roy[27] fixed the inversion temperature at 848 ± 5°C. Cooling from above to below this inversion temperature will result in a persistently metastable β-eucryptite phase.[28] Even prolonged heating at low temperatures will not result in the formation of α -eucryptite.

The crystal structure of α -eucryptite has been determined by Hesse.[29] The structure is trigonal with space group R$\bar{3}$ and with lattice parameters a=13.471Å and c=8.998Å and with eighteen formula units of $LiAlSiO_4$ per unit cell. The Al and Si atoms are disordered.

The melting behavior of β-eucryptite is described by Hatch.[30] He found that it melted incongruently around 1400°C.

CTE's for α-eucryptite have been measured as $110x10^{-7}$/K for the a-axis and $84.5x10^{-7}$/K for the c-axis.[31] β -eucryptite displays highly anisotropic behavior with expansion along the a-axis and contraction along the c-axis. The overall effect is a strong negative expansion. Three different groups of researchers have reported values of expansion coefficients for the a- and c-axes of β-eucryptite. These are given in Table 1.

Table 1. Expansion of the a and c parameters of β-eucryptite

along a-axis (K^{-1})	along c-axis (K^{-1})	Reference
$82.1x10^{-7}$	$-176x10^{-7}$	[32]
$81.1x10^{-7}$	$-169x10^{-7}$	[31]
$79x10^{-7}$	$-152x10^{-7}$	[33]

Different values have also been found for the expansion of sintered bars. Results of one experiment are illustrated in Figure 5.[34] In another experiment, Kondrat`ev found a value of $\alpha = -90x10^{-7}$/K between 20 and 850°C.[35] This value is more negative than that shown in Figure 5. Ikeda and Minagawa[36] discovered that these discrepancies are due to changes in sintering conditions, cooling conditions, and reheating conditions which affect thermal expansion properties.

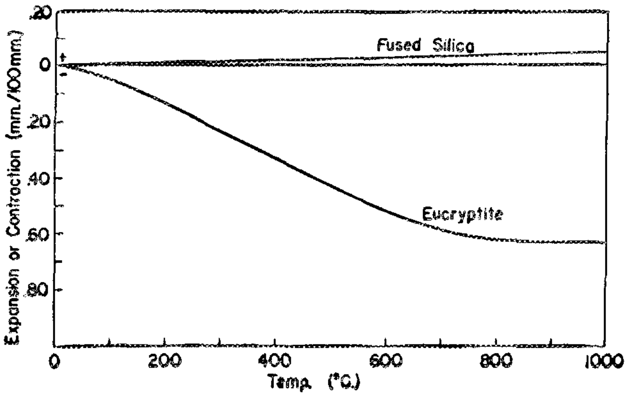

Figure 5. Thermal contraction of eucryptite as compared with expansion of fused silica.[34]

Work has been conducted with β-eucryptite to reduce the absolute value of the CTE. Increasing the solid solution SiO_2 content in β-eucryptite was successful in bringing the coefficient closer to zero.[37] However, substituting Ge^{4+} for Si^{4+} had no significant effect on the CTE.[31] Another study investigated the substitution of N^{3-} for O^{2-} in β-eucryptite. This substitution raised the overall expansion to a positive value, but reduced the expansion anisotropy.[38]

Work has been done on the binary diagrams $AlPO_4$-β-eucryptite and $AlPO_4$-BPO_4. A diagram for $AlPO_4$-β-eucryptite has not been completed; however, Perrotta[39] has a patent for a series of solid solutions extending from 5-65 mole % $AlPO_4$ with β-eucryptite. He reports that this range of compositions, when sintered into bars, has CTE from -70×10^{-7} to 11×10^{-7}/K at 1000°C. The solid solution forms when the compositions are heated for 16 hours at 1050°C or higher. Hummel and Langensiepen[40] have reported the formation of a solid solution between 50%$AlPO_4$/50% β-eucryptite (mol%) which has a thermal expansion as low as fused quartz.

Horn and Hummel[18] investigated the system $AlPO_4$-BPO_4. They maintain that in spite of a considerable difference in the ionic radii of B^{+3} and Al^{+3}, a complete series of solid solutions between BPO_4 and $AlPO_4$ exists above 1200°C. These solid solutions have the β-cristobalite structure and can be quenched metastably to room temperature. The stabilization is chemical rather than mechanical. Below 1200°C, long term heat treatments will cause exsolution and the appearance of $Al(PO_3)_3$ with compositions of 50% or greater $AlPO_4$ (mole percent). This study did not include work on the relationships between the quartz and tridymite phases of the two compounds. The exsolution and appearance of a three-phase region show that below 1200°C, the system is non-binary. Glasses could be formed between 10 and 70 mole percent $AlPO_4$. Electron microscope examination showed no phase separation in these glasses.[41] All of the above relationships were determined for compositions studied in a closed system, i.e. sealed platinum tubes. Work was also done using an open system to develop a tentative non-equilibrium diagram. The two $AlPO_4$-BPO_4 phase diagrams developed by Hummel and Horn are shown in Figures 6 and 7.[18]

Some discrepancies exist in the work by Horn and Hummel on $AlPO_4$-BPO_4. Both diagrams shown have been extrapolated from work done at temperatures well below the liquidus surface in most cases. The non-binary behavior of the system below 1200°C undermines the assertion of binary behavior above 1200°C.

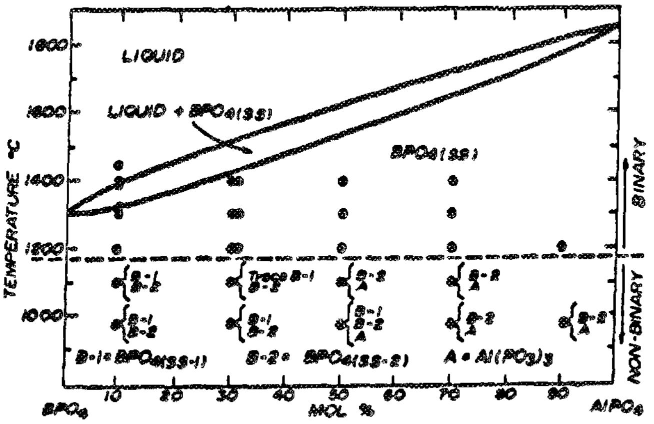

Figure 6. The binary system BPO_4-$AlPO_4$.[18]

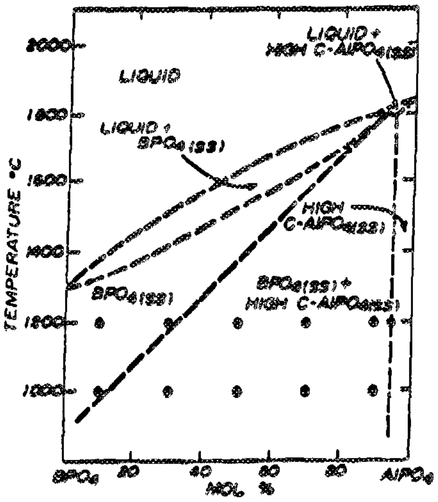

Figure 7. Tentative non-equilibrium diagram of the system BPO_4-$AlPO_4$.[18]

In a later work, Horn and Hummel[42] explain why the unexpected solid solution between $AlPO_4$ and BPO_4 should form. First they state that $AlPO_4$ is disordered cubic and isomorphous with BPO_4 when both are in their high cristobalite forms. They then state that solid solution is possible above 1200°C because at that temperature, both $AlPO_4$ and BPO_4 have ordered, tetragonal, high cristobalite forms. Generally the solid solution would not be expected because of the difference in atomic size and bonding characteristics of Al^{+3} and B^{+3} and because of the infrequency that the substitution is found in nature.

The appearance of $Al(PO_3)_3$ below 1200°C in the system $AlPO_4$-BPO_4 shows the system is non-binary. A better description of the system may be obtained by considering it to be a ternary system composed of Al_2O_3-B_2O_3-P_2O_5. Some work has been done on the bounding binary systems of this ternary system.

Kim and Hummel[43] have developed tentative phase relations for the system B_2O_3-Al_2O_3. They confirmed the existence of two binary compounds. The compound $2Al_2O_3 \cdot B_2O_3$ melts incongruently at 1030 ± 7°C to $9Al_2O_3 \cdot 2B_2O_3$ and liquid. The compound $9Al_2O_3 \cdot 2B_2O_3$ melts incongruently at 1440°C to Al_2O_3 and liquid. Although it is a naturally occurring compound, $Al_2O_3 \cdot B_2O_3$ could not be synthesized and was not observed.

The only well-documented compound occurring in the system $B_2O_3 \cdot P_2O_5$ is BPO_4. Most work on this sytem has been done at low temperatures with hydrated systems. A compound $B(PO_3)_3$ may be possible, but has yet to be verified.

Initial work on the system Al_2O_3-P_2O_5 has been done by Stone, Egan, and Lehr.[16] The tentative diagram determined by them is shown in Figure 8. The system seems to behave as a true binary system.

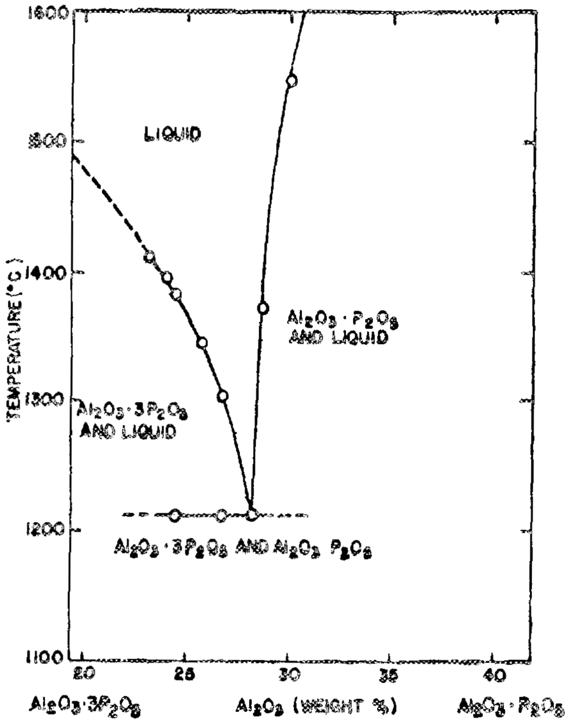

Figure 8. The binary system $Al_2O_3 \cdot 3P_2O_5$-$Al_2O_3 \cdot P_2O_5$.[16]

Three compounds have been identified in the Al_2O_3-P_2O_5 system. These are $Al_2O_3 \cdot 3P_2O_5$ ($Al(PO_3)_3$, $2Al_2O_3 \cdot 3P_2O_5$, and $Al_2O_3 \cdot P_2O_5$ ($AlPO_4$). Stone et al. found $2Al_2O_3 \cdot 3P_2O_5$ to have an upper temperature limit of stability in the range of 200 to 300°C. They expressed some doubt as to whether this was indeed a compound. It decomposes to $Al(PO_3)_3$ and $AlPO_4$. Pawlowski[44] also noted the existence of $2Al_2O_3 \cdot 3P_2O_5$, but stated that it decomposes to $AlPO_4$ with a loss of phosphorus. He listed the melting point of $Al(PO_3)_3$ as 1290°C whereas Stone et al. listed it as 1490±5°C from extrapolation. Tananaev et al.[45] list a compound $3Al_2O_3 \cdot P_2O_5$ that melts congruently at 2030°C and has two eutectics occurring at $27Al_2O_3 \cdot 13P_2O_5$ (1860°C) and at $173Al_2O_3 \cdot 27P_2O_5$ (1890°C).

Crystal structure analyses have been done for $Al(PO_3)_3$. Chistyakova et al. found a phase transition at 900 to $1000^\circ C$.[46] Pauling and Sherman[47] found the low temperature structure of $Al(PO_3)_3$ to be cubic with space group $T^6d\text{-}I\bar{4}3d$ and a=13.63Å. It has 16 formula units per unit cell. Van der Meer[48] describes the high temperature form of $Al(PO_3)_3$ as crystallizing with monoclinic space group Ic. The lattice parameters are given as a=10.423Å, b=18.687Å, and c=9.222Å and $\beta = 81.63^\circ$. There are 12 formula units per unit cell.

No diagrams have yet been found that describe a binary relationship between β-eucryptite and Al_2O_3, B_2O_3, or P_2O_5. No join seems to exist between Al_2O_3 and β-eucryptite in the ternary system $Li_2O\text{-}Al_2O_3\text{-}SiO_2$, which implies that these two compounds may not form a binary system.[49]

A good deal of work has been done on the ternary system $Al_2O_3\text{-}B_2O_3\text{-}P_2O_5$, but most of this work has dealt with establishing the extent of regions with glass-forming ability. Stanworth and Turner[50] were able to form some glass, but doubted that the extent of the region was large. Klein et al.[51] found two regions of glass-forming ability as well as a small range near B_2O_3, shown in Figure 9.

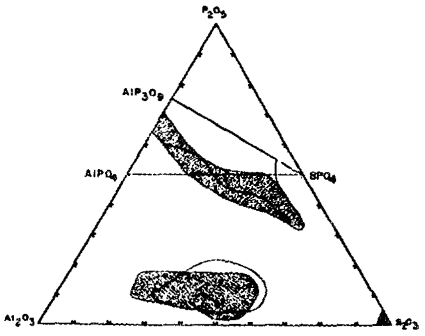

(Areas bounded by solid line are batch compositions; shaded areas are analyzed compositions.)

Figure 9. Regions of glass formation in the $Al_2O_3B_2O_3\text{-}P_2O_5$ system.[51]

They defined their glass-forming regions as being only those regions where a transparent glass formed. Thermal expansion coefficients for glasses in these regions varied between 30 and 65×10^{-7}/K. Some of the glasses, notably those high in B_2O_3, were phase separated. Hummel and Horn give a good summary of work done on the glass-forming regions of this system.[41] Their summary diagram is reproduced in Figure 10.

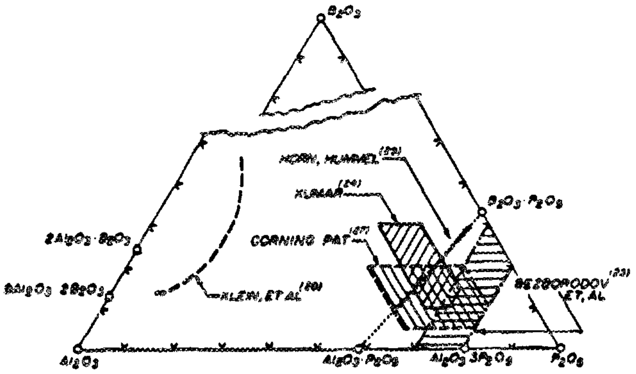

Figure 10. Fields of glass formation in the system B_2O_3-Al_2O_3-P_2O_5.[41]

Hummel and Horn also did work on the subsolidus compatibility relations in the system Al_2O_3-B_2O_3-P_2O_5.[41] Figure 11 shows the probable compatibility triangles they found. A join with complete solid solution exists above 1200°C between $AlPO_4$ and BPO_4. The join $9Al_2O_3 \cdot 2B_2O_3$-$AlPO_4$ exists above 1200°C and shows limited solid solution. The join $9Al_2O_3 \cdot 2B_2O_3$-BPO_4 also exists above 1200°C but has no solid solution. In contrast, the join $2Al_2O_3 \cdot B_2O_3$-BPO_4 exists only below 470°C. Work was not completed in the region bounded by BPO_4, $AlPO_4$, and P_2O_5 and containing $Al(PO_3)_3$.

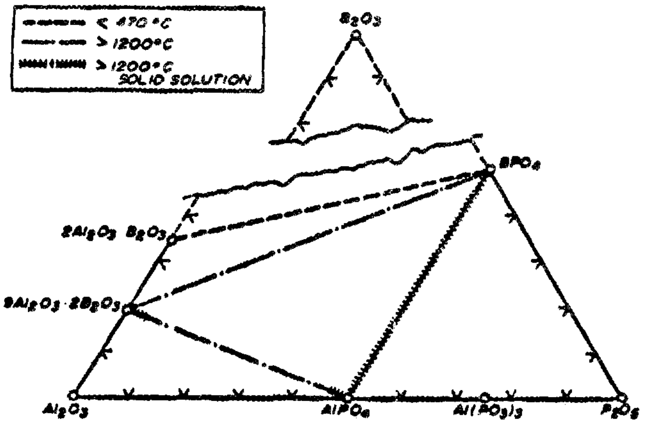

Figure 11. Probable compatibility triangles in the system B_2O_3-Al_2O_3-P_2O_5 below 470°C and above 1200°C.[41]

A summary of the information known on the system Al_2O_3-B_2O_3-P_2O_5-β-eucryptite is given by the proposed quaternary diagram illustrated in Figure 12.

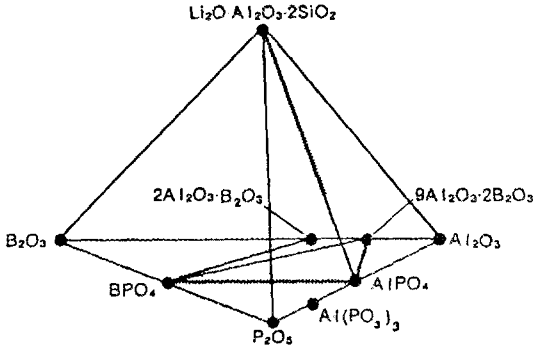

Figure 12. The extent of information on the quaternary system Al_2O_3-B_2O_3-P_2O_5-β-eucryptite.

The most satisfactory way of expressing the relationships between $AlPO_4$, BPO_4, and β-eucryptite seems to be a quaternary diagram composed of Al_2O_3-B_2O_3-P_2O_5- β-eucryptite. However, β-eucryptite decomposes at 1400°C. Below 1400°C, the assumption of a quaternary system may be valid, but if work is to be done above this temperature, the system may need to be expanded to a fifth-order system composed of

Al_2O_3-B_2O_3-P_2O_5-Li_2O-SiO_2.

B. Procedure

Processes have been developed for the consistent formation of $AlPO_4$, BPO_4, and β-eucryptite in the laboratory. The starting materials for the $AlPO_4$ are aluminum hydroxide, $Al(OH)_3 \cdot nH_2O$, and dibasic ammonium phosphate $(NH_4)_2HPO_4$, weighed to give a 1:1 Al_2O_3 to P_2O_5 ratio after accounting for weight loss. The starting materials for BPO_4 are boric acid, H_3BO_3, and dibasic ammonium phosphate, weighed to give a B_2O_3 to P_2O_5 ratio after weight loss. The starting materials for the β-eucryptite are lithium carbonate, Li_2CO_3; alumina, Al_2O_3; and silica gel, SiO_2, which are weighed to give a ratio of 1:1:2 $Li_2O/Al_2O_3/SiO_2$ after weight loss. In the case of the β-eucryptite, the raw materials were calcined at 200°C for 24 hours before weighing, and in the case of the $AlPO_4$, a weight factor for the $Al(OH)_3 \cdot nH_2O$ was determined.

The heat treatments and containers used for all samples are shown in Table 2. The raw materials for each batch are mixed under acetone using a mortar and pestle. The process is repeated between each firing.

After the final firing, samples are removed and reground dry with a mortar and pestle if they powder easily. Fused samples are reground under acetone or distilled water, then dried in a 200°C drying oven. The samples are analyzed by x-ray diffraction to determine whether the reaction is complete.

Samples have been prepared for differential thermal analysis

Table 2. Sample Compositions and Processing.

Sample	Compound	First Firing Temp/Time (°C/h)	Second Firing Temp/Time (°C/h)	Third Firing Temp/Time (°C/h)
KE-A1	$AlPO_4$	*1200/8	*1300/4	
KE-A2	$AlPO_4$	*1200/8	*1300/4	+1300/34.5
KE-A3	$AlPO_4$	*1200/8	*1300/4	
KE-A4	$AlPO_4$	*1200/8	*1300/4	
KE-A5	$AlPO_4$	*825/6	#1100/54	
KE-A6	$AlPO_4$	*825/6		
KE-B1	BPO_4	*800/5	*1150/7.5	
KE-B2	BPO_4	*800/5	*1150/7.5	
KE-B3	BPO_4	*825/6	#1100/54	
KE-B4	BPO_4	*825/6		
KE-A7	$AlPO_4$	+400/12	+1300/72	
KE-A7	$AlPO_4$	+400/12	#1300/72	
KE-A7	$AlPO_4$	*400/12	*1090/72	
KE-B5	BPO_4	+400/12	+1090/72	
KE-B5	BPO_4	+400/12	#1090/72	
KE-B5	BPO_4	*400/12	*1090/72	
KE-A8	$AlPO_4$	+400/18	+1080/70	
KE-A9	$AlPO_4$	+400/12.5	+1090/73	
KE-B6	BPO_4	*400/12.5	*1090/73	
KE-A10	$AlPO_4$	+400/17	+1080/72	
KE-B7	BPO_4	*400/17	*1080/72	
KE-E1	β-eucryptite	*120/24	+1300/48	+1300/36
KE-A11	$AlPO_4$	+400/12	+1080/80	
KE-B8	BPO_4	*400/12	*1080/80	
KE-E4A	β-eucryptite	~300/10.5	+800/20	+1300/49, +1300/24.5
KE-E4B	β-eucryptite	+800/67	+1300/50	+1300/27
KE-A12	$AlPO_4$	*400/9	+1085/72	
KE-B9	BPO_4	*400/9	*1085/72	
KE-E5	β-eucryptite	+800/12	+1300/48	+1300/38
KE-A13	$AlPO_4$	*400/12	*1100/72	
KE-A14	$AlPO_4$	*400/8	*1100/72	
KE-E6	β-eucryptite	*800/12	+1300/49	+1300/43
KE-A15	$AlPO_4$	*400/12	*1100/72	
KE-B10	BPO_4	*400/12	*1100/72	

---

*Alumina crucible.

+Pt crucible.

#Pt tube.

~Graphite crucible.

(DTA) and have been run. All samples are weighed on a mole percent basis then sealed in a platinum tube. Al_2O_3 is used as a reference and a heating rate of $5^{o}C/min$ is used. The compositions tested, heat treatment, source of powder, and results are given in Table 3. For compositions between 10-70% $AlPO_4$/90-30%BPO_4, the formation of a glassy phase is desired. X-ray diffraction patterns were run on a few of these samples to assure that a glassy phase had formed.

Some difficulties have been encountered in evaluating systems containing $AlPO_4$ and BPO_4. The volatility of B_2O_3 and P_2O_5 requires that compositions containing these compounds be sealed in platinum. The seals sometimes fail due to either the internal pressure from B_2O_3 or P_2O_5 or from the deleterious reaction of P_2O_5 with the platinum tube.[52]

A sample of $AlPO_4$ with a high impurity content of $Al(PO_3)_3$ was fired in an open alumina boat at 1300°C for six days to determine the stability of $Al(PO_3)_3$.

Bar samples were made to determine the CTE of different compositions. Bars were pressed in either 50-mm or 100-mm stainless steel dies using a methylcellulose-water solution as a binder. Bars were sintered on an alumina plate. Bar compositions and heat treatments are shown in Table 4. The mixed powders had no joint heat treatment prior to sintering. A fused silica dilatometer with a dial guage reading to 0.00254mm was used. Initial and final length measurements are made to the nearest 0.00254mm. Adding in a correction for the expansion of the fused silica push rod, the formula

Table 3. DTA Compositions, Heat Treatments, Powder Sources, and Results.

Composition mole%			Heat Treatment	Powder Sources	Maximum Temp. reached with DTA (°C)	Results
$AlPO_4$	BPO_4	β-eucryptite				
100	-	-	none	Aldrich*	1240	results not clear
90	10	-	A	Aldrich*	1220	212°C(endo),830°C,990°C,1180°C
70	30	-	B	Aldrich*	1220	212°C(endo),835°C,1020°C,1185°C
50	50	-	B	Aldrich*	1220	212°C(endo),828°C,975°C,1196°C
30	70	-	B	Aldrich*	1220	156°C(exo),not clear
10	90	-	B	Aldrich*	-	sample contained water from quenching
-	100	-	none	Aldrich	1220	results not clear
-	-	100	none	C	1140	846°C (both endo and exo characteristics)
33.3	33.3	33.3	none	C	1200	209°C(endo);1071°C,1149°C(change in slope)
50	-	50	none	C	1140	209°C(endo);862°C,906°C(change in slope),1114°C(exo)
70	-	30	none	C	1170	210°C(endo);661°C,848°C(change in slope), 1030°C(exo),1161°C(exo)
70	10	20	none	C	1200	206°C(endo);862°C,1166°C(change in slope)

A = prefired at 1300°C for 48 hrs. then furnace cooled.

B = heated to 1650°C (as determined by optical pyrometer) for 4 hrs. then water quenched.

* = Aldrich Chemical Company - $AlPO_4$ powder is amorphous, BPO_4 is crystalline.

C = laboratory synthesized - see Table 2

Table 4. Bar Sample Compositions, Heat Treatments, and Results.

Bar	Composition mole%			Thermal expansion (K^{-1})	Bar length (inch)	Permanent length change (inch)	Sintering temp./time °C/hr.	Notes
	$AlPO_4$	BPO_4	β-eucryptite					
KE- 1	100	-	-	178.5×10^{-7}	3.980	+0.015	1550/13	
KE- 2	-	100	-	74.9×10^{-7}	3.892	+0.003	1180/16.5	
KE- 3	50	-	50	-	-	-	1300/18	melted
KE- 5	70	-	30	-	-	-	1300/18	melted
KE- 6	33.3	33.3	33.3	-	-	-	1180/16.5	melted
KE- 7	-	-	100	-111×10^{-7}	2.296	+0.004	1300/18	
KE- 8	50	-	50	-25.7×10^{-7}	2.034	+0.001	1100/45	
KE- 9	70	-	30	-10.6×10^{-7}	1.948	-0.001	1100/45	
KE-10	33.3	33.3	33.3	-	-	-	1100/45	melted

used to calculate the thermal expansion is:

$$\alpha = \frac{\Delta L}{L_0 \Delta T} + 5 \times 10^{-7} (K^{-1})$$

Initial work on the ternary diagram Al_2O_3-B_2O_3-P_2O_5 used the same raw materials as used for $AlPO_4$ and BPO_4. Firings followed the same schedule as used for the first firings of these materials.

C. Results and Discussion

Pure $AlPO_4$ and BPO_4 were not formed using the heat treatments listed for compositions KE-A1 through KE-A6 and KE-B1 through KE-B4 listed in Table 2. Varying amounts of constituent oxides were identified using x-ray diffraction. The successful heat treatments for both $AlPO_4$ and BPO_4 were identical. For the initial firing, samples were held at 125, 155, 175, 300, and 400°C with the temperature being raised at approximately two-hour intervals. This treatment allowed for slow reactions around critical temperatures for the raw materials and prevented the violent expulsion of gases that could cause loss of sample. Holding the samples at 400°C allowed the reactions to initiate below the melting point of B_2O_3 and well below the range of any appreciable volatization of P_2O_5. Subsequent firing at 1080 to 1100°C allowed for completion of the reactions yet minimized volatization of B_2O_3 and P_2O_5. This heat treatment consistently gives $AlPO_4$ and BPO_4, as confirmed by x-ray diffraction.

β-eucryptite formed best when fired at 800°C, instead of 120°C, before firing at 1300°C. Better initiation of the reaction occurred and the final product was easier to grind. This treatment, shown for samples KE-E4 through KE-E6 in Table 2, gave a material which contains small amounts of impurities.

DTA results are shown in Table 3. The most striking result is that all samples having greater than 33.3% by mole $AlPO_4$ show an endothermic peak in the vicinity of 210°C. These peaks correspond to the $\alpha-\beta$ cristobalite inversion in $AlPO_4$. These results also support the concept of higher processing temperature resulting in a higher temperature inversion. All of the samples treated at 1650°C have inversions at 212°C while the samples synthesized at 1100°C in the laboratory have inversions from 206 to 210°C.

The presence of the peaks at 212°C and other temperatures in the DTA results for the binary $AlPO_4/BPO_4$ compounds may indicate complete solid solution did not form. However, the materials that formed have similar characteristics, as shown by similar temperature peaks.

Glass was difficult to form with the binary $AlPO_4/BPO_4$ compositions, even using the 1650°C heat treatments. At 1650°C, BPO_4 is completely volatized, while $AlPO_4$ remains as a solid. The reaction time may have been inadequate to allow reaction between these two phases.

Problems were encountered when heating platinum sample tubes to 1650°C followed by quenching. A number of tubes developed quench cracks. This allowed water to enter the sample. The walls of the tubes were likely embrittled by the attack of P_2O_5 on the platinum or the vapor pressure of the P_2O_5 and B_2O_3.

Ternary compositions and samples containing $AlPO_4$ and β-eucryptite were evaluated by DTA to predict the temperature at which melting begins. No conclusive temperature could be determined, but a range was established. Generally, samples containing small amounts of BPO_4 could be fired at 1100°C or lower, and samples containing mostly $AlPO_4$ could be fired at or slightly above 1100°C.

Bar sample compositions are listed in Table 4 along with their heat treatments and thermal expansion results. The coefficient listed is the straight line result between room temperature and 925°C. Expansion over the whole range is shown in Figure 13. The best result is for bar KE-9, which had an initial composition of 70% $AlPO_4$/30% β-eucryptite. This bar exhibited negative expansion. Bar KE-8, which had an initial composition of 50%$AlPO_4$/50% β-eucryptite, similarly had a low negative expansion.

X-ray diffraction analysis of these two samples following thermal expansion measurement showed that both had non-equilibrium compositions. Both contained mixtures of $AlPO_4$ and β-eucryptite solid solutions as well as some Al_2O_3 and $Al(PO_3)_3$. From Figure 12, this mixture of phases is metastable. The presence of Al_2O_3 in both samples indicates the volatization of P_2O_5, producing a final ratio depleted in $AlPO_4$. The thermal expansion results corroborate this change of composition. KE-9 has a slightly less negative expansion than Hummel and Langensiepen show for a bar containing 20%$AlPO_4$/80% β-eucryptite. KE-8 likewise has an expansion similar to Hummel and Langensiepen's 10%$AlPO_4$/90% β-eucryptite. While the composition may not have shifted this far, a loss of $AlPO_4$ did occur.

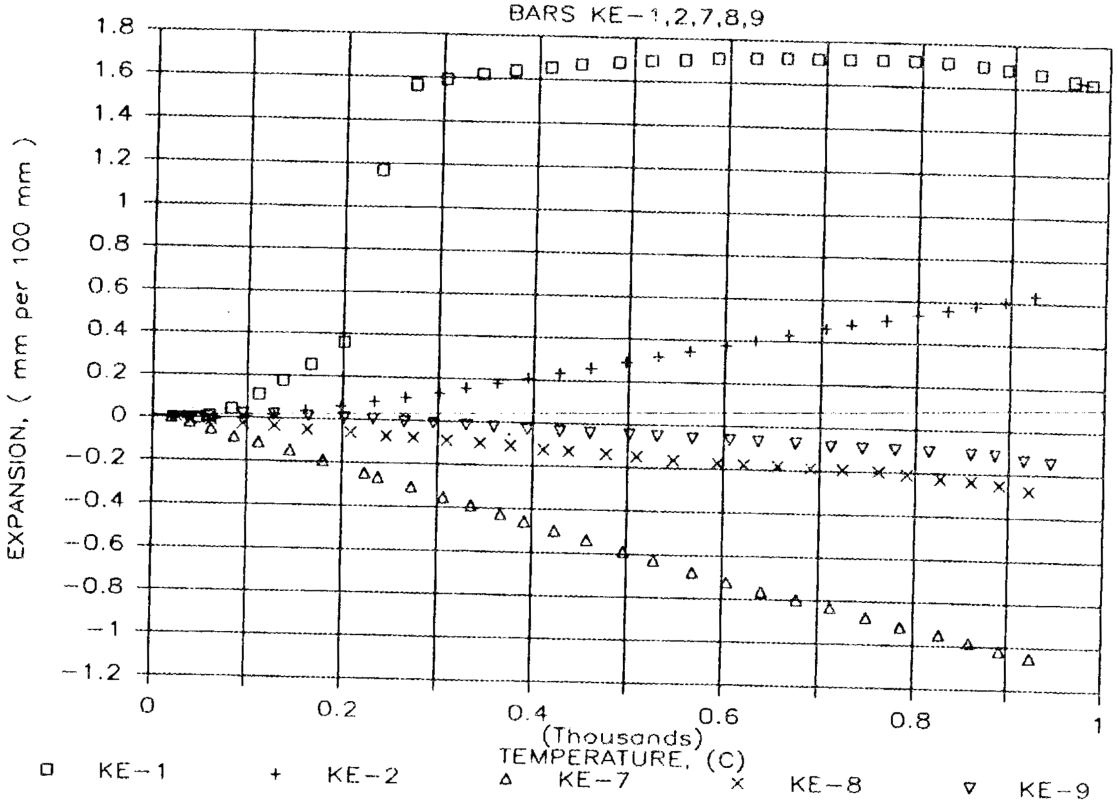

Figure 13. Thermal Expansion of $AlPO_4$-BPO_4-β-Eucryptite Samples

Four bars melted at temperatures lower than expected. These include: KE-3, KE-5, KE-6, and KE-10. Considering the melting points of the three materials--$T_m > 1800^{\circ}C$ for $AlPO_4$, $T_d = 1400^{\circ}C$ for β-eucryptite, and T_m=1300°C for BPO_4--the temperatures used would not be expected to cause melting. The compounds may flux each other or form low melting eutectics or peritectics. Ternary bars KE-6 and KE-10 contained some crystalline $AlPO_4$ and very small amounts of crystalline BPO_4 and β-eucryptite, the balance being a glass phase. Bars KE-3 and KE-5 softened and slumped more than melted according to x-ray diffraction results. Small amounts of glass were detected. Both contained a phase that probably was a solid solution of β-eucryptite and $AlPO_4$ or Al_2O_3. Bar KE-5 also contained $AlPO_4$. Some P_2O_5 may have either volatized from these bars or else come out of solution and melted to promote slumping.

Non-equilibrium compositions in bars and melting or slumping of bars at temperatures lower than expected indicate the need for a series of phase diagrams. DTA does not seem to be sufficient to establish processing times and temperatures needed to achieve equilibrium without slumping. Phase diagrams will show what to expect at equilibrium and point out regions of solid solution, which is desirable for this project.

D. Recommendations:

Exploratory work was begun on the ternary system Al_2O_3-B_2O_3-P_2O_5. Concentration was on the high P_2O_5 corner especially near $Al(PO_3)_3$.

When compositions in this region are fired to 300°C, they form a viscous gel when first removed from the furnace. This gel fuses to an extrememly hard mass upon cooling. This mass cannot be ground. This problem needs to be overcome before work can continue on this region of the diagram.

Compositions of $AlPO_4$ and β-eucryptite show promising results. Effort should concentrate on finding a high $AlPO_4$ solid solution. The effect of BPO_4 on this solid solution and its expansion should be examined. Phase diagrams of the quarternary system Al_2O_3-B_2O_3-P_2O_5-β-eucryptite will help determine which regions are most feasible for future work.

Silica

A. Background

The thermal expansion behavior of framework silicates and silica creates some interesting problems, since for essentially covalently bonded solids, their thermal expansion can be expected to be rather low due to the rigidity of the structural units, tetrahedra. This structure does not, however, lead to low thermal expansion. In the three-dimensional framework structure, all the tetrahedra are joined together through the bridging oxygen atoms. Although the tetrahedron itself is strongly bonded, the framework is not. The forces that hold the orientation of the tetrahedra through the bridging atoms are relatively weak. Therefore, it is the rotation or tilting of the tetrahedra that causes the structure to expand. The change of bond length with temperature is much smaller. Nonetheless, for structures such as simple cubic, the changes of bond length will be dominant rather than tilting bond angles. For example, good correlations have been found between thermal expansion α and Pauling valence (ionic charge divided by coordination number) for simple cubic structures such as alkali halides and fluorite, i.e. $\alpha = P^2$.[53] This simple relation can also be applied to complex structures such as spinel and olivine where octahedra share edges to form a three-dimensional framework structure. Since in this case the octahedra are unable to tilt freely, thermal expansion will be governed by changes in shape and size of individual tetrahedra, i.e. changes in bond length. This is also true for Si_3N_4 where the three-dimensional framework structure was formed by SiN_4 tetrahedra. The nitrogen atoms are in three-fold coordination with silicon atoms, forming a more rigid structure. Rotation along the nitrogen atom will be more difficult due to the three-fold coordination. As a result, the thermal expansion of Si_3N_4 is due mainly to anharmonic stretching vibrations between bonded atoms.[54]

In general, the thermal expansion of structures with a framework of linked polyhedra can be divided into two parts: (1) changes in size and shape of the polyhedra, and (2) rotating or tilting of bond angles of the polyhedra. Of the two, the effect of changes in bond angles (tilting) is usually much larger. For example, the study of alkali niobates (NbO_6-octahedra framework structure) showed that the average thermal expansion is $16x10^{-6}C^{-1}$ in $NaNbO_3$ where tilt can occur, and $4x10^{-6}C^{-1}$ in $KNbO_3$ where it cannot.[55] For tetrahedra framework structures, expansion due to the non-tilting effect can be much smaller because of stronger bonds (shorter bond length).

Change of bond angle often culminates in a phase transition, as was found for most alkali aluminum silicates and all silica. According to Taylor,[56-58] the thermal expansion of framework structures can be characterized by three stages, starting from a partially-collapsed state to a fully-expanded state. The first stage takes place from room temperature to the transition temperature. The transition is displacive, such as for the high-low transition in leucite, quartz, tridymite, and cristobalite. Expansion corresponding to this stage is the largest and the bond angles Si-O-Si or (Si,Al)-O-(Si,Al) show the greatest increase. The second stage starts at the transition temperature and ends at a temperature where the bond angles cease to change, i.e. the structure has reached the fully-expanded state at the end of this stage. In this stage, even though the high temperature form has been reached, the structure still shows a moderate expansion. During the final stage the structure shows zero expansion, and sometimes even contracts at the high temperature end. The near zero expansion is a result of negligible changes of bond length, while the contraction is probably due to an increase in the anisotropic thermal vibration of oxygen atoms, resulting in an apparent shortening of the Si-O bonds.[58,59]

Data from the structural analyses of cristobalite proved to support the aforementioned thermal expansion behavior.[60-62] The change from the partially-collapsed to fully-expanded state was brought about by rotation about the $\bar{4}$ axis. Although the rotation angle was not explicitly shown from the data, its influence on the Si-O-Si angle is apparent. The Si-O-Si angle of low cristobalite quoted by Smith and Fable[60] showed a large increase from 144.67° at -263°C to 148.45° at 200°C. Above the high-low inversion temperature of cristobalite, the Si-O-Si angle still showed a slight increase from 147.70° at 221°C to 148.9° at 310°C according to Peacor's single crystal studies,[61] or 146.7° at 300°C to 148.4°C at 500°C, based on Wright and Leadbetter's refinement.[62] Beyond 500°C, the Si-O-Si angle was changed only slightly. Although the angles measured by different investigators are not identical, the trend remains.

Therefore, to develop an ultra-low thermal expansion material using cristobalite, two problems need to be addressed. One is the large expansion associated with the high-low transition, and the other is the moderate expansion after the phase transition (the second stage). The former is in general much greater than the latter. The main goal is, therefore, to suppress the polymorphic inversion of cristobalite by stabilizing its high temperature phase. The high-low inversion involves changes of bond angles from a partially-collapsed state to a nearly fully-expanded state upon heating, or the reverse upon cooling. Therefore, in stabilizing high cristobalite, the structure has to be kept open and free from rotation as temperature changes. There are two ways that this can possibly be achieved. One is to substitute highly charged cations, such as phosphorous and tungsten, for silicon so as to increase the repulsive forces between cations, keeping the structure from collapsing. The other way is to fit large ions into the large holes, W sites, of the structure. The open high cristobalite structure contains two interstitial sites. One has 12-coordination (W sites) and the other has 6-coordination (S sites). The equivalent radius of the W sites, calculated by Takahashi, et al.[63] and extrapolated by Taylor and Henderson,[57] was given by 1.56Å and 1.59Å, respectively. It is because of the large holes that large ions are required to keep the structure open. This can be shown from the leucite group of compounds, leucite, Rb-leucite, and Cs-leucite (or pollucite). These are all isostructural with cristobalite, but only Cs-leucite showed a cubic structure without inversion. The other two inverted to the low temperature form upon cooling. The size effect of ions in maintaining an open structure is obvious.

It is also known that high cristobalite can be retained at room temperature by high dose neutron bombardment,[64] and by mechanical constraint. However, when the energy or the constraint is released, inversion occurs.

The current work in stabilizing high cristobalite is based on the concept of retaining an open structure. The high-low inversion of cristobalite was studied by reacting SiO_2 with TiO_2, $AlPO_4$, BPO_4, $CsLiWO_4$, and $CsLiMoO_4$. These compounds were chosen based on the consideration of crystal chemistry. With the exception of TiO_2, the compounds are isostructural with silica. An ultra-low expansion glass (lower than fused silica) can be prepared from the SiO_2-TiO_2 system.[65]

B. Experimental Procedure

The raw materials used in making compounds and preparing compositions are: $Al(OH)_3 \cdot nH_2O$, $(NH_4)_2HPO_4$, H_3BO_3, Cs_2CO_3, Li_2CO_3, MoO_3, WO_3, TiO_2, and silicic acid.

$AlPO_4$ and BPO_4 were prepared by mixing $Al(OH)_3 \cdot nH_2O$ or H_3BO_3 with $(NH_4)_2HPO_4$, and firing in platinum crucibles at 1200°C for 72 hours and 1050°C for 40 hours, respectively.

$CsLiWO_4$ and $CsLiMoO_4$ were prepared by mixing Cs_2CO_3, Li_2CO_3, and either WO_3 or MoO_3 according to the 1:1:2 molar ratio. The mixtures were fired in platinum crucibles at 900°C for 3 hours.

TiO_2 and the compounds described above were mixed with silicic acid according to the compositions shown in Table 5. All samples were ground in acetone for one hour. Compositions for TS-39 to TS-44 were formulated by mol% and then converted to wt%.

Table 5. Compositions Studied (wt%)

Sample No.	SiO_2	TiO_2	$AlPO_4$	BPO_4	$CsLiWO_4$	$CsLiMoO_4$
TS-15	97	3	—	—	—	—
TS-16	92	8	—	—	—	—
TS-17	90.5	9.5	—	—	—	—
TS-18	89.5	10.5	—	—	—	—
TS-19	87	13	—	—	—	—
TS-20	82	18	—	—	—	—
TS-21	78	22	—	—	—	—
TS-22	99	—	1	—	—	—
TS-23	98	—	2	—	—	—
TS-24	97	—	3	—	—	—
TS-25	96	—	4	—	—	—
TS-26	95	—	5	—	—	—
TS-27	93	—	7	—	—	—
TS-28	90	—	10	—	—	—
TS-29	85	—	15	—	—	—
TS-30	95	—	—	5	—	—
TS-31	92	—	—	8	—	—
TS-32	88	—	—	12	—	—
TS-33	95	—	—	—	5	—
TS-34	90	—	—	—	10	—
TS-35	80	—	—	—	20	—
TS-36	95	—	—	—	—	5
TS-37	90	—	—	—	—	10
TS-38	80	—	—	—	—	20
TS-39	83.18	3.69	13.13	—	—	—
TS-40	84.27	6.23	9.5	—	—	—
TS-41	85.39	8.83	5.78	—	—	—
TS-42	83.14	4.3	10.93	1.63	—	—
TS-43	84.21	5.6	8.55	1.64	—	—
TS-44	84.76	6.89	6.69	1.66	—	—

After calcining, samples were either made into bars (1x1x10 cm) or sealed in platinum (tubes or crucibles) and then heat-treated as listed in Table 6. Samples were furnace-cooled and temperatures dropped below 1000°C in less than 15 minutes for samples fired above 1000°C.

Table 6. Heat Treatment

Sample No.	Form	Calcing Temp/Time (°C/h)	Final Firing Temp/Time (°C/h)
TS-15 TS-21	Powder	--------	1630/40 in Pt crucible
TS-22 TS-29	Bar	1000/2	1500/24
TS-30 TS-32	Powder	800/2	1000/72 in Pt tube
TS-33 TS-38	Powder	--------	1000/72 in Pt crucible
TS-39 TS-41	Powder	1000/2	1500/72 in Pt tube
TS-42 TS-44	Powder	800/2	1000/72 in Pt tubes

Phase identification was performed using XRD and polarized microscopy. The high-low inversion temperatures were measured by thermal expansion curves, DTA, or DSC. Temperatures were calibrated by the melting temperature of indium and tin metals.

C. Results and Discussion

All inversion temperatures are compared to that of pure cristobalite, which inverts at 252°C after firing at 1500°C for 24 hours.

(1) SiO_2-TiO_2 System

Published information covering the phase relations in the SiO_2-TiO_2 system presents varying experimental observations.[66-68]

Uncertainties in this system are the solubility limits at both ends of the phase diagram and the eutectic composition. However, only the high silica portion of the system is of concern in our study.

Phase analyses of compositions TS-15 through TS-21 are listed in Table 7. The eutectic composition is at about 10% TiO_2, and the solubility of TiO_2 in SiO_2 appears to be less than 5%. Our previous results (shown in Table 8) indicate that the inversion temperature does not change at TiO_2 contents higher than 5%. The inversion temperature of cristobalite can be lowered by approximately 60°C where TiO_2 is introduced, possibly due to the large size of titanium ions.

Table 7. Phase Analyses of SiO_2-TiO_2 Mixtures at 1630°C

Sample No.	Composition (wt%)		Phase Present
	SiO_2	TiO_2	
TS-15	97	3	α-cristobalite(ss) + glass
TS-16	92	8	α-cristobalite(ss) + glass
TS-17	90.5	9.5	glass
TS-18	89.5	10.5	glass
TS-19	87	13	TiO_2(ss) + glass
TS-20	82	18	TiO_2(ss) + glass
TS-21	78	22	TiO_2(ss) + glass

Table 8. Inversion Temperatures of Cristobalite

Sample No.	Composition (wt%)		Inversion Temperature (°C)
	SiO_2	TiO_2	
TS-0	100		252
TS-1	95	5	191
TS-2	90	10	190
TS-3	85	15	190
TS-4	80	20	190

(2) SiO_2-$AlPO_4$ System

Phase analyses and the inversion temperature in the SiO_2-$AlPO_4$ system are shown in Table 9. A discontinued change in the inversion temperature was noted for the bar samples, which were finely divided. It was suspected that $AlPO_4$ was lost during firing. Therefore, compositions TS-26, TS-28, and TS-29 were prepared, and then sealed in platinum tubes following the same heat treatment as for the pressed bars (1500°C for 72 hr). Results from x-ray and DSC showed the presence of $AlPO_4$ in addition to low cristobalite (SiO_2) for TS-28 and TS-29, as shown in Table 10. The inversion temperature of cristobalite can be lowered by approximately 10°C when $AlPO_4$ dissolves in SiO_2.

Table 9. Phase Analyses and Inversion Temperatures for SiO_2-$AlPO_4$ Mixtures (Bar Samples)

Sample No.	Composition (wt%)		Phase Present	Inversion Temperature(°C)
	SiO_2	$AlPO_4$		
TS-22	99	1	α-cristobalite	255
TS-23	98	2	α-cristobalite	253
TS-24	97	3	α-cristobalite	252
TS-25	96	4	α-cristobalite	250
TS-26	95	5	α-cristobalite	253
TS-27	93	7	α-cristobalite	251
TS-28	90	10	α-cristobalite(ss)	235
TS-29	85	15	α-cristobalite(ss)	237

Table 10. Phase Analyses and Inversion Temperatures for SiO_2-$AlPO_4$ Mixtures (sealed in Pt tubes)

Sample No.	Composition (wt%)		Phase Present	Inversion Temperature(°C)	
	SiO_2	$AlPO_4$		SiO_2	$AlPO_4$
TS-26	95	5	α-cristobalite(ss)	237	----
TS-28	90	10	α-cristobalite(ss) + $AlPO_4$(ss)	236	217
TS-29	85	15	α-cristobalite(ss) + $AlPO_4$(ss)	236	214

(3) SiO_4-BPO_4 System

In this system the inverison temperature showed a continuous decrease with increasing BPO_4, as shown in Table 11. Since glass was formed, composition TS-32 does not represent the true solubility of BPO_4 in SiO_2. Therefore, more compositions or different heat treatment temperatures will be needed to test the solubility and inversion temperature.

Table 11. Phase Analyses and Inversion Temperatures for SiO_2-BPO_4 Mixtures

Sample No.	Composition(wt%)		Phase Present	Inversion Temperature(°C)
	SiO_2	BPO_4		
TS-30	95	5	α-cristobalite(ss)	215
TS-31	92	8	α-cristobalite(ss) + glass	189
TS-32	88	12	α-cristobalite(ss) + glass	184

(4) SiO_2-$CsLiWO_4$ and SiO_2-$CsLiMoO_4$ System

$CsLiWO_4$ and $CsLiMoO_4$ are isotructural with high (β) cristobalite, and do not show polymorphic inversions. However, since they are known as mineralizers, tridymite was formed for some compositions as shown in Table 12. Inversion temperature was not measured for tridymite.

Table 12. Phase Analyses and Inversion Temperatures for SiO_2-$CsLiWO_4$ and SiO_2-$CsLiMoO_4$ Mixtures

Sample No.	Composition(wt%)			Phase Present	Inversion Temp (^oC)
	SiO_2	$CsLiWO_4$	$CsLiMoO_4$		
TS-33	95	5	—	α-cristobalite + S_1-tridymite(tr) + glass	255
TS-34	90	10	—	S_1-tridymite + glass	
TS-35	80	20	—	S_1-tridymite + glass	
TS-36	95	—	5	α-cristobalite(ss) glass	247
TS-37	90	—	10	α-cristobalite(ss) +	250
TS-38	80	—	20	S_1-tridymite + glass	

(5) SiO_2-TiO_2-$AlPO_4$ System

In this system, the inversion temperatures of both cristobalite (SiO_2) and $AlPO_4$ do not seem to change for TS-39 and TS-40, as shown in Table 13. However, an anomaly appeared in TS-41. If the solubility limit was reached for both $AlPO_4$ and SiO_2, as shown from the relatively unchanged inversion temperatures for TS-39 and TS-40, the drastic change of inversion temperature for TS-41 is difficult to explain. More experiments on this system will be conducted.

Table 13. Phase Analyses and Inversion Temperatures for SiO_2-TiO_2-$AlPO_4$ Mixtures

Sample No.	Composition(wt%)			Phase Present	Inversion Temp (°C)	
	SiO_2	TiO_2	$AlPO_4$		SiO_2	$AlPO_4$
TS-39	83.18	3.69	13.13	α-cristobalite(ss) + $AlPO_4$(ss) + glass	194	135
TS-40	84.27	6.23	9.5	α-cristobalite(ss) + $AlPO_4$(ss) + TiO_2 + glass	195	131
TS-41	85.39	8.83	5.78	α-cristobalite(ss) + $AlPO_4$(ss) + TiO_2 + glass	118	88

(6) SiO_2-TiO_2-$AlPO_4$-BPO_4 System

In this system, the only crystalline phases present are TiO_2 and α-cristobalite. Therefore, only the inversion temperature of cristobalite is listed in Table 14. Since the inversion temperatures showed a continuous decrease, heat treatments at lower temperatures are necessary.

Table 14. Phase Analyses and Inversion Temperatures for SiO_2-TiO_2-$AlPO_4$-BPO_4 Mixtures

Sample No.	Composition(wt%)				Phase Present	Inversion Temp(°C)
	SiO_2	TiO_2	$AlPO_4$	BPO_4		
TS-42	84.13	4.3	10.93	1.63	α-cristobalite(ss) + glass	196
TS-43	84.21	5.6	8.55	1.64	α-cristobalite(ss) + TiO_2 + glass	180
TS-44	84.76	6.89	6.69	1.66	α-cristobalite(ss) + TiO_2 + glass	150

The high-low inversion of cristobalite is a complex phenomenon which reamins unclear. However, it is known that its inversion depends on two factors: impurity content (solute atoms) and forming temperature. Since the bond lengths (Si-O, O-O) do not show an appreciable change, it is believed that the inversion is related to the changes of bond angles with temperature. Either impurity atoms or heat treatment temperatures will play an important role in the behaviors of the bond angles, and thus the inversion temperature.

It can be concluded from the above results that each compound may have distinct effects on the inversion temperature. When more than one compound reacted with SiO_2, the effects do not appear to be additive. Instead, the effects are more likely to be synergistic, depending on complex crystal chemistry. Key factors in the stabilization of high cristobalite include the means and extent of substitution of silicon atoms end the mechanism by which large atoms can fill the large holes in the framework structures without forming a new phase.

Mullite

A. Background

Mullite is a potential candidate for regenerator disks of turbine engines and has high mechanical strength, high chemical stability, and moderate thermal shock resistance. Because the CTE, α ,is a major variable in thermal shock resistance, the goal of this study is the development of very low expansion mullite to improve its thermal shock resistance.

Although some low expansion ceramic families have been reported such as cordierite, silica glass, lithium aluminosilicates, and semi-refractory phosphates, etc., few studies have been conducted to lower the thermal expansion of mullite. Fenstermacher[69] reported (3:2) mullite to have slightly lower thermal expansion than (2:1) mullite; Lepold[70] developed low expansion mullite bodies, but notably they all contained substantial amounts of silica glass phase; Kim[71] confirmed that the solid solution of all compositions lying on or near the join $9Al_2O_3 \cdot 2B_2O_3$-$3Al_2O_3 \cdot 2SiO_2$ had linear CTE of approximately $41x10^{-7}/^{o}C$.

The present study focusses on the development of substitutional solid solutions of mullite by solid-state reaction. Previous work done on either oxide systems has shown that extended solid solution tends to lower thermal expansion. In addition, solid solution non-cubic oxides tend to reduce thermal expansion anisotropy which is significant since internal microcracking from an expansion anisotropy can lower its strength, and a more isotropic single phase gives lower localized stresses between grains in polycrystalline bodies.

Mullite has a solid solution range with average structure $Al_2^{VI}(Al_{2+2x}^{IV}Si_{2-2x}^{IV})O_{10-x}$,[72] where IV and VI represent the coordination number of the polyhedra and x is the number of oxygen atoms missing per unit cell ($0.2 < x < 0.6$). Mullite is now generally considered as a defect structure based on the sillimanite (Al_2SiO_5) polymorph.[72] The compositional variation of x is achieved by substitution of Si^{4+} ions by Al^{3+} ions in the tetrahedral chains of alternating Al and Si sequence. $2Al^{3+} + \square = 2Si^{4+} + O^{2-}$ is the charge-balancing substitution. A random distribution of Al^{3+} and Si^{4+} in the tetrahedra chain is generally observed.[73] However, mullite develops the incommensurate ordered structure (super structure) which gives a remarkable range of compositions, reflecting the flexibility of incommensurate ordering resulting from the variation in stoichiometry by changing the repeat distance of the ordering periodicity.

In the above structural and chemical expression of mullite(ss): $Al_2^{VI}(Al_{2+2x}^{IV}Si_{2-2x}^{IV})O_{10-x}(0.2 < x < 0.6)$, note that at $x = 0.2$ and $x = 0.6$, free silica and corundum, respectively, are usually found in the synthesized mullite bodies. So, in this study, a more restricted stoichiometric range was used: $0.25 \leq x \leq 0.4$. Compositions $x = 0.25$ and $x = 0.4$ correspond respectively to (3:2) and (2:1) mullite(ss).

The connection of octahedral and tetrahedral units gives relatively wide channels running parallel to the c-axis.[74] This configuration is suitable for the incorporation of ionic substitution. Before the substitutional cations were chosen, several crystal-chemical factors were taken into consideration:

(1) Ionic size: Empirically, ions of two elements can readily substitute for each other only if their ionic radii differ by less than 15%. If the radii of two ions differ by 15 to 30%, only limited substitution can occur.

(2) Temperature-dependent solubility: Higher temperatures

increase the amount of thermal disorder, and in turn, the space requirements of the structure become less rigorous. Mullite grown at a high temperature may display extensive ionic substitution that would be possible at a lower temperature.

(3) Electrical neutrality of the structure.

Additional factors which were considered in the selection of the compounds containing desired substitutional cations included a crystal structure similar to that of mullite and a high melting point.

Overall, the selection of substitutional cations must include consideration of increasing bond strength between cations and their surrounding anions in the structure of mullite. A cation-oxygen bond with low coordination should expand less than the same bond in a high coordination site because the total electrostatic energy associated with a particular cation is distributed among fewer bonds when coordination is low. The Pauling electrostatic bond strength is given as:

$$\text{bond strength} = \frac{Z}{CN}$$

where Z is the cation charge and CN refers to the cation coordination number. It is reasonable to expect that the structure with strong bonds expands less than that with weak bonds. Therefore, it is reasonable to expect that the expansion of a tetrahedral site is less than that of an octahedral site in mullite. This can also be described by Pauling's third rule which states that edge-sharing of two polyhedra decreases the stability of ionic structures. The edge-sharing of the [AlO_6] chain along c-axis in mullite obviously is less stable than the [SiO_4] and [AlO_4] of corner-sharing. Further, the corner-sharing tetrahedra correspond to the framework structure which is more open and would readily allow the [SiO_4] and [AlO_4] to tilt in order to minimize the free energy increase caused by increasing temperature.

It is almost impossible to find such a compound satisfying all above considerations. Three compounds chosen were titanium oxide, aluminum orthophosphate, and boron orthophosphate.

(1) TiO_2

The high temperature polymorph of TiO_2 is rutile, having a melting point of 1840±10°C. Ti^{4+} has sixfold coordination in edge-shared octahedra. Two edges of every octahedron are shared. $R_{Ti^{4+}} = 0.64$ Å.

(2) $AlPO_4$

This compound is a structural derivative of silica with Al^{3+} and P^{5+} ions in the tetrahedral-sites in the framework structure. It melts at about 1850°C, but a significant decomposition begins at around 1600°C.

$R_{Al^{3+}} = 0.57$ Å and $R_{P^{5+}} = 0.35$ Å.

(3) BPO_4

BPO_4 is also a structural derivative of silica with B^{3+} and P^{5+} ions in the tetrahedral sites in the framework structure. Its melting point is about 1300°C, and it also decomposes before melting at around 1100°C. $R_{B^{3+}} = 0.20$ Å.

According to Horn and Hummel,[75] $AlPO_4$ and BPO_4 form a continuous solid solution above 1200°C. One difference between $AlPO_4$ and BPO_4 is that $AlPO_4$ has a phase transformations comparable to that of silica, whereas BPO_4 has no such conversion.

B. Experimental Procedure

The synthesis of various mullite solid solutions was carried out mainly by solid-state reactions. Starting materials were reagent-grade silica (SiO_2), alumina (Al_2O_3), titanium oxide (TiO_2), silicic acid (SiO_2 nH_2O), aluminum hydroxide ($Al(OH)_3 \cdot nH_2O$), dibasic ammonium phosphate ($(NH_4)_2HPO_4$), boric acid (H_3BO_3), and magnesia (MgO). The weight factors of $SiO_2 \cdot nH_2O$ and $Al(OH)_3 \cdot nH_2O$ were carefully determined. The samples were weighed in the desired composition ratio of these raw materials, mixed and homogenized in acetone by hard mixing, air dried, and finally placed in a drying oven (100 to 200°C) overnight to remove volatiles.

$AlPO_4$ and BPO_4 were synthesized by sintering powder mixtures of $(NH_4)_2HPO_4$ with $Al(OH)_3 \cdot nH_2O$ and H_3BO_3, respectively, in desired stoichoimetric ratios. Both compositions were fired in covered alumina crucibles at 160°C for 2 hours, 400°C for 14 hours, and 1080° for 72 hours.

X-ray diffraction (XRD) phase identification was made on the sintered material using CuK_α radiation. The diffraction patterns were measured in a 2θ range of 15° to 72° with a scanning rate of 1° 2θ/min.

According to XRD analysis, the above heat treatment produced $AlPO_4$ with a minor amount of $Al(PO_3)_3$ (aluminum metaphosphate <5 wt%), and a rather pure BPO_4 phase. The powders of $AlPO_4$ and BPO_4 were used in forming the mullite solid solution. The decomposition rate of $AlPO_4$ was determined to be 2 wt% per hour at 1600°C. This was done in a platinum crucible fired in air.

For the system Al_2O_3-SiO_2-TiO_2(-MgO), the sample numbers, compositions, processing heat treatments, CTE, and the phase(s) present are shown in Table 15.

For the system Al_2O_3-SiO_2-BPO_4-$AlPO_4$, the sample numbers, compositions, sintering time, CTE, and the phases present are shown in Table 16.

In order to determine the bulk linear expansion of mullite-based bodies, bar specimens (100 by 10 by 10 mm) were pressed in a steel mold at 69 MPa. After the bar specimens were sintered, their linear expansions were measured by means of a fused-silica dilatometer. The rate of heating was controlled manually at 100°C per 15 minutes. Thermal expansion test results are presented in Figures 14 through 17.

The unit cell parameters of mullite(ss) from samples J-009 through J-012 were determined by the multiple regression method. The reflection planes used are (110), (120), (210), (001), (220), (111), (130), (401), (141), (230), (320), (041), (331), and (002). The results could only be compared relative to each other since the 2θ (theta) instrumental error was corrected, but the internal standard was not used. Table 18 gives the cell parameters and cell volumes of

Table 15. TiO_2 in Mullite-Based Compositions.

Sample No.	Composition (wt%)			Mullite Al_2O_3/SiO_2 molar ratio	Processing Heat Treatments		Thermal expansion coefficient (x 10^6/°C)	Phase(s) Present
	Mullite	TiO_2	MgO		Formation Temp/Time (°C/h)	Sintering Temp/Time (°C/h)		
J-006	89.75	10.25		3/1.76	1600/6+1200/8	1600/8+1200/11	5.2	*M + $^{+}$A
J-007	87.33	12.67		3/2	1600/6+1200/8	1600/8+1200/11	3.5	M + A
J-008	83.70	16.30		3/1.76	1600/6+1200/8	1600/8+1200/11	2.9	M + A
J-009	99.00	1.00		3/2	1600/8	1600/6+1200/8	4.8	M
J-010	98.00	2.00		3/2	1600/8	1600/6+1200/8	4.9	M
J-011	97.00	3.00		3/2	1600/8	1600/12+1200/19	4.5	M
J-012	96.00	4.00		3/2	1600/8	1600/12+1200/19	5.0	M
J-013	95.00	5.00		3/2	1600/12+1200/19	1600/6+1400/38	5.4	M + $^{\#}$R
J-014	94.00	6.00		3/2	1600/12+1200/19	1600/6+1400/38	5.6	M + R
J-015	94.50	5.00	0.50	3/2	1600/12+1200/19	1600/6+1400/38	5.3	M + R
J-016	92.99	6.00	1.01	3/2	1600/12+1200/19	1600/6+1400/38	5.6	M + R
J-017	83.70	16.30		3/2	1600/20	1600/12+1400/38	3.2	M + A
J-018	83.70	16.30		3/1.5	1600/20	1600/12+1400/38	3.9	M + A
J-019	81.00	19.00		3/1.76	1600/20	1600/12+1400/38	2.5	M + A
J-020	78.00	22.00		3/1.76	1600/20	1600/12+1400/38	2.3	M + A
J-021	83.70	16.30		3/1.76	1600/20	1600/12+1400/38	3.0	M + A
J-035	70.00	30.00		2/1		1100/4+1500/56	2.0	M + A
J-036	60.00	40.00		2.2/1		1100/4+1500/56	-	A + M + R

---

[*] M = Mullite Solid solution

[+] A = Aluminum titanate solid solution

[#] R = Rutile

Table 16. $AlPO_4$ and BPO_4 Additives in Mullite-Based Compositions.

Sample No.	Composition (wt%)			Mullite Al_2O_3/SiO_2 Molar Ratio	Sintering (°C/h)	CTE (x10^6/°C)	Phase(s) Present
	Mullite	$AlPO_4$	BPO_4				
J-022	93.00	7.00		3/2	(1600/5+1400/48)+(1500/72)	5.3	M^{*} + AP^{+} + C^{++}
J-023	88.00	12.00		3/2	(1600/5+1400/48)+(1500/72)	5.4	M + AP + C
J-024	83.00	17.00		3/2	(1600/5+1400/48)+(1500/72)	-	M + AP + C
J-025	78.00	22.00		3/2	(1600/5+1400/48)+(1500/72)	-	M + AP + C
J-026	88.00	12.00		2.76/2	(1600/5+1400/48)+(1500/72)	5.4	M + AP + C
J-027[a]	93.00		7.00	3/2	(1100/18+1250/28+1400/4+1550/18)	5.0	M + $AB^{\#}$ + C
J-028[a]	88.0		12.00	3/2	(1100/18+1250/28+1400/4+1550/18)	5.5	M + AB + C
J-029[a]	90.00	2.78	7.22	3/2	(1100/18+1250/28+1400/4+1550/18)	-	M + AB + C
J-030[a]	9.00	5.36	4.64	3/2	(1100/18+1250/28+1400/4+1550/18)	-	M + AB + C
J-031[a]	9.00	7.76	2.24	3/2	(1100/18+1250/28+1400/4+1550/18)	-	M + AB + C
J-032[b]	95.00	5.00		3/2	(1500/12+1600/8)	-	M + AP + C
J-033[b]	95.00		5.00	3/2	(1500/12+1600/8)	-	M + AB + C
J-034[b]	90.00	5.00	5.00	3/2	(1500/12+1600/18)	-	M + AB + C

---

[a] Samples sintered with synthesized mullite (3:2).

[b] Samples sintered with pure silica and alumina powders in sealed pt-tube, then quenched in water at room temperature.

[*] M = Mullite solid solution

[+] AP = $AlPO_4$

[#] AB = $(Al,B)PO_4$

[++] C = Corundum

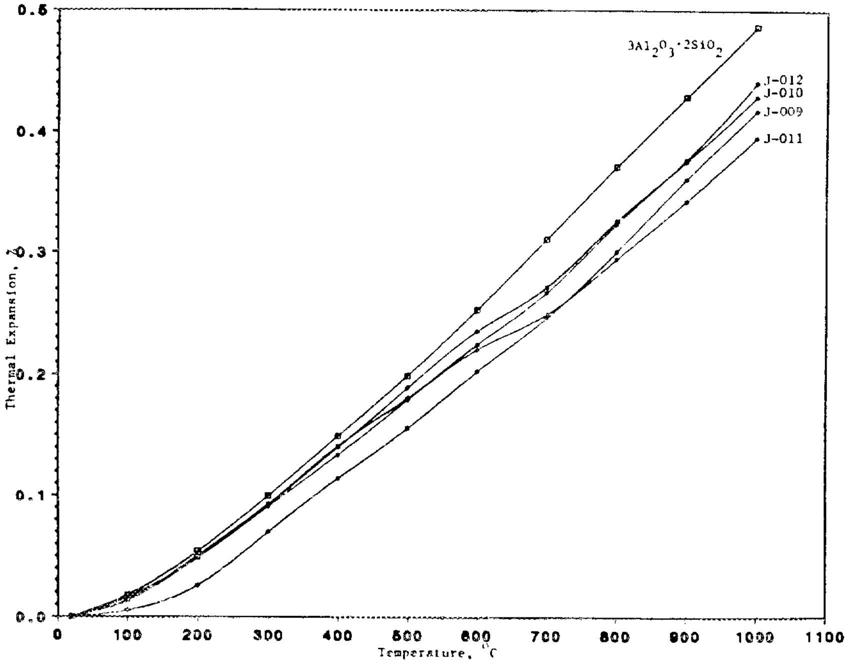

Figure 14. Thermal expansion of mullite solid solution containing Ti^{4+}.

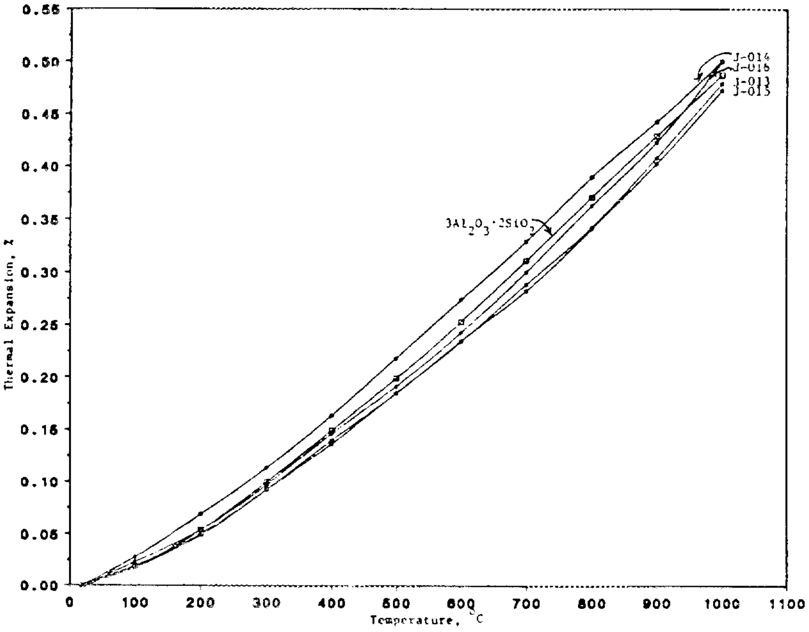

Figure 15. Thermal expansion of selected mullite-based ceramic compositions.

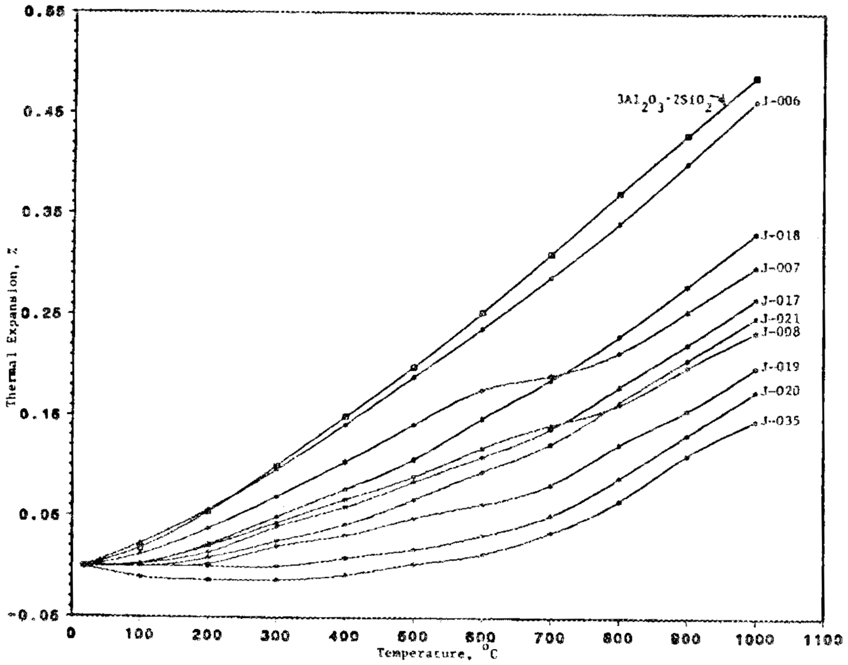

Figure 16. Thermal expansion of mullite (ss)-based bodies containing Al_2TiO_5 (ss).

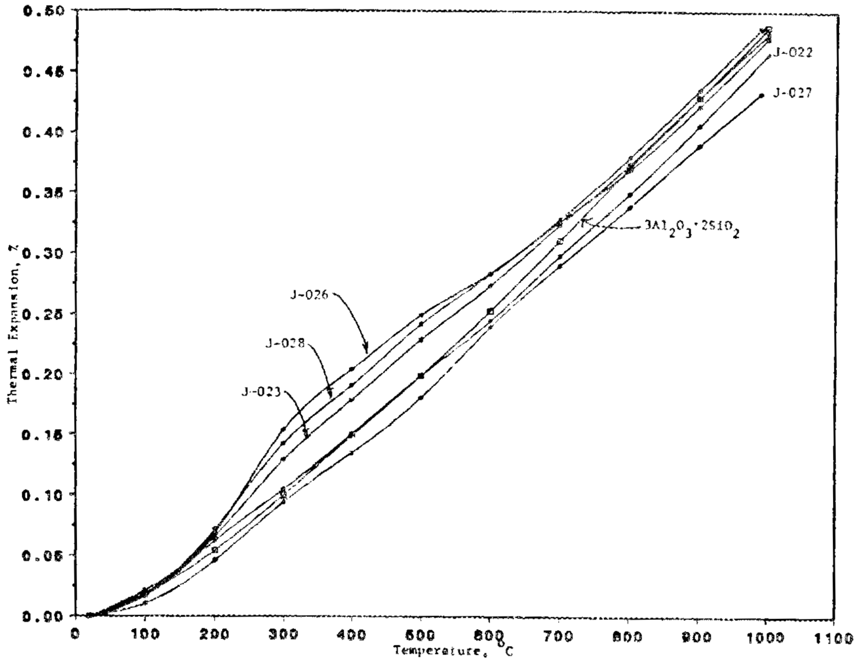

Figure 17. Thermal expansion of mullite-based ceramics with $AlPO_4$ and BPO_4.

these four samples.

Table 17. Cell Dimensions of Mullite at Room Temperature

Sample	a_o(Å)	b_o(Å)	c_o(Å)	V(Å^3)
J-009	7.539	7.684	2.883	167.01
J-010	7.551	7.690	2.893	167.99
J-011	7.549	7.692	2.888	167.70
J-012	7.555	7.699	2.890	168.10
3.2 mullite*	7.548	7.691	2.886	167.54

* Referenced from Ribbe[74]

C. Results and Discussion

1. Mullite system with TiO_2 additive

The solid solubility limit of TiO_2 in mullite is about 3 - 4% at 1600°C.[8] Samples J-009 through J-012 were synthesized to determine the effect of increased TiO_2 solubility on the CTE of mullite ($5.3x10^{-6}/^oC$ for 3:2 mullite). Overall, the results showed a slight decrease in CTE of mullite with the formation of a solid solution containing Ti^{+4}, as seen in Fig. 14. This is attributed to two mechanisms. First, the difference in radii between Ti^{4+} and Al^{3+} is only 12.3%; however, the difference between Ti^{4+} and Si^{4+} is 64.1%, making it unlikely for Ti^{4+} ions to substitute for Si^{4+} in the strongly bonded $[SiO_4]$ site. In turn, Ti^{4+} would readily substitute for Al^{3+} in the relatively weakly bonded $[AlO_6]$ site. As seen in Table 17, cell dimensions changed upon substitution. As cell edges a and c vary nonlinearly (might be seen as a slight increase), cell edge b increases. This gives an overall slight increase in cell volume compared to the cell volume in stoichiometric mullite. This may be caused by distortion of the $[AlO_6]$ chain by forming a $[TiO_6]$ site. The distorted $[AlO_6]$ sites tend to reduce the distortion upon heating and thus equalize bond lengths, leading to lower thermal expansion. Secondly, the Ti–O bond in TiO_6 is stronger than the Al–O in AlO_6, by Pauling's bond strength equation $(S_{Ti-O} = 4/6 > S_{Al-O} = 3/6)$. The stronger bond obviously results in a more rigid polyhedra. The octahedral edge-shared chain containing $[TiO_6]$ will be more stable and stronger. This will also contribute to a lower CTE.

The low solubility limit of TiO_2 in mullite is probably due to the difficulty in balancing the electrical neutrality required for such a substitution: $2Ti^{4+} + O^{2-} \leftrightarrows 2Al^{3+} + \square$. This requires the introduction of oxygen ions into the structure. The only site available for the O^{2-} ion is the oxygen vacancy site between two unit cells, and the number of vacancies is very limited.

Samples J-013 through J-016 were made to examine whether solubility of TiO_2 in mullite could be extended by adding MgO. The ionic radius of Mg^{2+} is 0.74Å, which is larger than $R_{Ti^{4+}}$. It was expected that this would compensate for a difference in charge when the substitution of Ti^{4+} for Al^{3+} in an octahedral site occurs. However, the results shown in Table 15 and Figure 15 indicate that such an exchange of cations does not extend the solubility limit of TiO_2 in mullite significantly even though x-ray analysis showed that addition of MgO reduced the rutile (110) peak intensity. Because of the presence of minor amounts of high expansion second phase rutile, the CTE could not be lowered.

Because the excess TiO_2 during sintering process formed aluminum titanate, an orthorhombic compound having high anisotropic axial CTE and very low bulk CTE, the bulk CTE was significantly lowered. But it is known that Al_2TiO_5 microcracks due to its high anisotropic axial expansion. Microcracking in the polycrystalline body very often gives anomalously low CTE. For this reason, the thermal expansion of bar specimens from two different batches with identical composition but different heat treatments was measured, as in Samples J-008 and J-021. CTE values were compared and showed remarkable agreement.

The effect of molar ratio of Al_2O_3/SiO_2 on the bulk CTE was also studied. Samples J-008, J-017, and J-018 were compared to show that Al_2O_3 to SiO_2 ratios of 3/1.76 result in lower CTE values than ratios of 3/2 and 3/1.5. This may be attributed to the consumption of Al_2O_3 when forming Al_2TiO_5. Based on simple calculations of change in composition during the reaction, a small amount of free SiO_2 (α-cristobalite) was expected. However, free SiO_2 was not detected by XRD analysis. Attention then was paid to the possibility of forming a solid solution of Al_2TiO_5 containing Si^{4+}. According to Ishitsuka,[77] the limited solid solution of Al_2TiO_5 can be formed when Si^{4+} substitutes for Al^{3+} in the structure. The substitution is effective in reducing the thermal decomposition rate of Al_2TiO_5. Furthermore, high thermal-expansion anisotropy of $Al_2(Ti,Si)O_5$ solid solution would possibly be reduced, and also explain the reproducible bulk CTE results. The exception should be mentioned on sample J-006 which gives an unusually high CTE. A general change in CTE upon the variation of compositions is shown in Table 15 and Figure 16.

2. Mullite System with $AlPO_4$ and BPO_4

The principal motivation of using $AlPO_4$ to form solid solutions of mullite was (1) the high melting point of $AlPO_4$; (2) the structural similarity between $AlPO_4$ and SiO_2; (3) the close ionic radii between P^{5+} and Si^{4+} ions; (4) the highly charged P cation which would form a stronger bond with O^{2-} in the tetrahedra site and (5), a naturally compensated charge neutrality in the substitutional reaction:
$Al^{3+} + P^{5+} \leftrightarrows 2Si^{4+}$.

Although the solid solubility limit of $AlPO_4$ in mullite was not known, a limited solid solution was expected. Samples J-022 through J-026 were synthesized with the desired composition range shown in Table 16. Samples were fired twice with phase identification by XRD analysis following each firing. The slightly changed d-spacing of mullite(ss) suggests a 1 to 2 wt% solubility limit. Pure $AlPO_4$ decomposes to Al_2O_3 and P_2O_5 at temperatures of 1400 to 1600°C (2 wt% per hour at 1600°C). Since nearly 90 vol% is mullite phase, even a low solubility of P^{5+} might affect the thermal expansion of the bulk samples. The CTE results shown in Figure 17 and Table 16 suggest no variation. On the other hand, sample J-032 which was synthesized in a sealed Pt tube (to prevent the loss of P_2O_5) and quenched from 1600°C to room temperature showed CTE results similar to those for samples synthesized in air, suggesting that the solubility limit of $AlPO_4$ in mullite is negligible.

A very low solubility limit may be explained as follows: (1) It is very difficult for both Al^{3+} and P^{5+} to substitute for Si^{4+} in tetrahedra sites because of the stability of the $[PO_4]$ unit. Bonding energy of the P-O bond is more negative than that of the Si-O bond according to O'Keefe,[78] making the individual P-O bonds very difficult to separate. (2) It is less difficult to form free Al_2O_3 at 1600°C than to form Al-rich mullite(ss).

Similar to $AlPO_4$, BPO_4 was also expected to form a limited solid solution of mullite. The differences between BPO_4 and $AlPO_4$ are: (1) the melting temperature of BPO_4 is lower than the temperature needed to form mullite, therefore mullite (3:2) was synthesized first then used to react with BPO_4. (2) $r(B^{3+})$ is small and tends to enter small coordination sites to form units such as $[BO_4]$, but at high temperatures, $[BO_4]$ is less stable than $[SiO_4]$. Samples J-027 and J-028 were prepared as shown in Table 16. The step-sintering schedule was used to give the slow heating rate, and the longer period of time at lower temperature to allow complete reaction. Also, similar to J-032, samples J-033 and J-034 were sealed in Pt tubes and quenched. These samples were examined by XRD and results are given in Table 16. The phase $(Al,B)PO_4$ was assumed because of the large d-spacing change compared with that of pure $AlPO_4$ and BPO_4 phases. All phases present are the same as mullite with $AlPO_4$.

A more significant change in d-spacing of mullite(ss) in samples J-033 and J-034 may suggest an extended solubility of BPO_4 and $(Al,B)PO_4$ in mullite upon quenching. The smallest amount of corundum was found in J-034. To evaluate this result, thermal expansion of samples J-027 and J-028 was measured as seen in Fig. 17. J-027 with 7 wt% BPO_4 was found to have a lower CTE than J-022. The estimated solubility limit for BPO_4 in mullite is thus about 3 to 5wt%.

D. Conclusions

(1) Within the solubility of TiO_2 in mullite, the CTE of mullite(ss) is lowered with increasing TiO_2 content.

(2) With the formation of a minor phase of $Al_2(Ti,Si)O_5$(ss) in a mullite matrix, the bulk expansion of mullite-based ceramic is lowered significantly.

(3) MgO additive will neither increase the solubility of TiO_2 in mullite, nor will it lower the CTE of mullite.

(4) $AlPO_4$ is ineffective in lowering the CTE of mullite due to the low solid solubility.

(5) BPO_4 is ineffective in lowering the CTE of mullite, although a 3 to 5wt% solid solubility may exist.

(6) The relative amounts of the phases present after sintering the mixtures of $AlPO_4$ and BPO_4 in the mullite composition appear to be similar to those when only $AlPO_4$ was fired in the mullite composition. However, when quenched, the relative amounts of phases present are close to those when only BPO_4 was fired in the mullite composition.

Zircon

A. Background

Zirconia exhibits three crystalline forms between room temperature and its melting temperature. It has monoclinic structure up to 1170°C, where it transforms to tetragonal system, followed by a final transformation to the cubic system at 237°C.[79]

By addition of a stabilizer such as CaO,[80-82] MgO,[83] Y_2O_3,[84-87] or many other rare earth oxides,[88-90] the structure is stabilized to the cubic form. A disadvantage of this fully stabilized zirconia, however, is its high CTE of $100 \times 10^{-7} K^{-1}$.[91] The high CTE's of these cubic-stabilized structures can be explained by applying the empirical equation by Hazen et al.[92]

Much effort to stabilize the tetragonal phase in zirconia has been based on the crystallite size and pressure effect.[93-96] Another method to stabilize the tetragonal phase included the addition of a previously known stabilizer (CaO, MgO, or Y_2O_3) plus ZnO. According to that study, at least 5% and up to 100% tetragonal structure can be obtained at room temperature.[97]

Although published information covers the presence of tetragonal phase in zirconia, the literature was found to contain very little data on the zirconia tetragonal solid solution. Therefore, two ZrO_2-TiO_2 and ZrO_2-CeO_2 binary systems and two ZrO_2-Y_2O_3-MgO and ZrO_2-CaO-MgO ternary systems were selected to investigate the effects of ZrO_2 tetragonal solid solution on CTE.

B. Experimental Procedures

Sample compositions used in these experiments are given in Table

18. The compositions of pure systems are shown in Table 19. Pure ZrO_2, TiO_2, and CeO_2 specimens were evaluated for reference purposes.

Table 18. Composition of Specimens

Specimens	Composition (mol%)	Specimens	Composition (mol%)
JK-001	pure ZrO_2	JK-011	$95ZrO_2$-$5CeO_2$
JK-002	$95ZrO_2$-$5TiO_2$	JK-012	$90ZrO_2$-$10CeO_2$
JK-003	$90ZrO_2$-$10TiO_2$	JK-013	$87.5ZrO_2$-$12.5CeO_2$
JK-004	$85ZrO_2$-$15TiO_2$	JK-014	$85ZrO_2$-$15CeO_2$
JK-005	$80ZrO_2$-$20TiO_2$	JK-015	$80ZrO_2$-$20CeO_2$
JK-006	$75ZrO_2$-$25TiO_2$	JK-016	pure CeO_2
JK-007	$70ZrO_2$-$30TiO_2$	JK-017	$90ZrO_2$-$5Y_2O_3$-5MgO
JK-008	$65ZrO_2$-$35TiO_2$	JK-018	$93ZrO_2$-$3.5Y_2O_3$-3.5MgO
JK-009	$60ZrO_2$-$40TiO_2$	JK-019	$90ZrO_2$-3CaO-7MgO
JK-010	pure TiO_2	JK-020	$90ZrO_2$-5CaO-5MgO
		JK-021	$90ZrO_2$-7CaO-3MgO

Table 19. Composition of Pure System

To give the reference, pure ZrO_2, TiO_2, and CeO_2 specimens were evaluated.

System	Purity
ZrO_2	99%
TiO_2	As: 0.0002%, Pb: 0.008%, Zn: 0.01%, Fe: 0.01% Water Soluble Salts: 0.15%
Y_2O_3	99.9%
CeO_2	99.9%
CaO	F:0.004%
MgO	Ba, Fe, Mn, K, Na, Sr, Pb, Ca, SO_4, Cl, NO_3, Ammonium Hydroxide: 0.0729%

Sample constituents were weighed to an accuracy of 0.001g, and magnetically stirred in acetone for 1 hr to ensure homogeneity. After drying, the powders were cold pressed into bar specimens using a small amount of binder. All bars were sintered at 1600°C for 12 hr, and allowed to furnace cool to room temperature.

XRD patterns were obtained to determine the phases present after sintering. A dilatometer was used to measure CTE at a heating rate of 5 or 10°C/min from room temperature to 1000°C. Thermal expansion values were corrected by adding the thermal expansion ($5.0 \times 10^{-7} K^{-1}$) of fused silica.

C. Results and Discussion

1. ZrO_2-TiO_2 System

Phase analysis results are shown in Table 20.

Table 20. Sintered Phases of ZrO_2-TiO_2 System

Specimens	Sintered phases
JK-001	Monoclinic ZrO_2
JK-002	Monoclinic ZrO_2(ss)
JK-003	Monoclinic ZrO_2(ss)
JK-004	Monoclinic ZrO_2(ss) + $ZrTIO_4$
JK-005	Monoclinic ZrO_2(ss) + $ZrTiO_4$
JK-006	Monoclinic ZrO_2(ss) + $ZrTiO_4$
JK-007	Monoclinic ZrO_2(ss) + $ZrTiO_4$
JK-008	Monoclinic ZrO_2(ss) + $ZrTiO_4$
JK-009	Monoclinic ZrO_2(ss) + $ZrTiO_4$
JK-010	Rutile

Specimens with up to 15 mol% TiO_2 did not show $ZrTiO_4$ peaks in their XRD pattern. Two different structures such as monoclinic ZrO_2 solid solution and $ZrTiO_4$ were detected in the samples of JK-005 through JK-009.

In Figures 18 through 21, thermal expansion data of JK-001 through JK-010 are shown. For pure ZrO_2 and TiO_2, the values of $76 \times 10^{-7} K^{-1}$ and $78 \times 10^{-7} K^{-1}$ were obtained, respectively. These values were found to be in good agreement with the data of other reported values.[98,99] In specimens of JK-002 and JK-003, the thermal expansion was slightly increased with increasing TiO_2. JK-004 through JK-009 samples showed phase transformation.

Table 21 shows the thermal expansion results before phase transformation and after phase transformation.

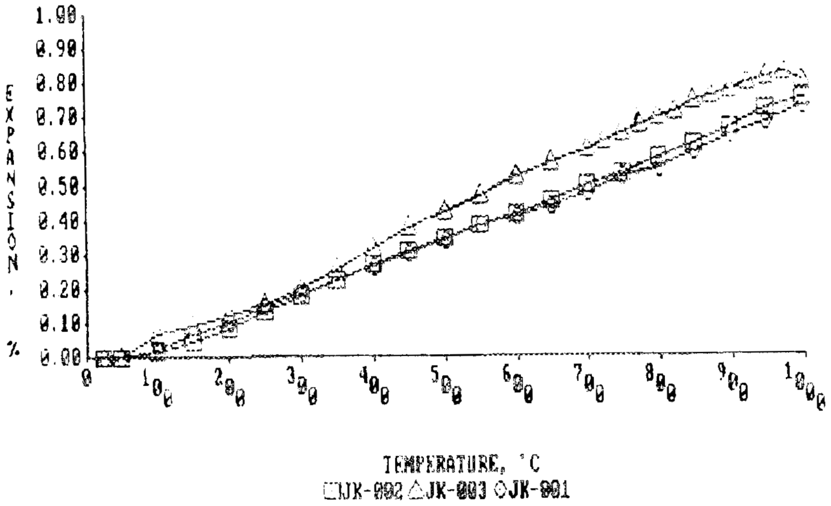

Figure 18. Thermal expansion of JK-001, JK-002, and JK-003.

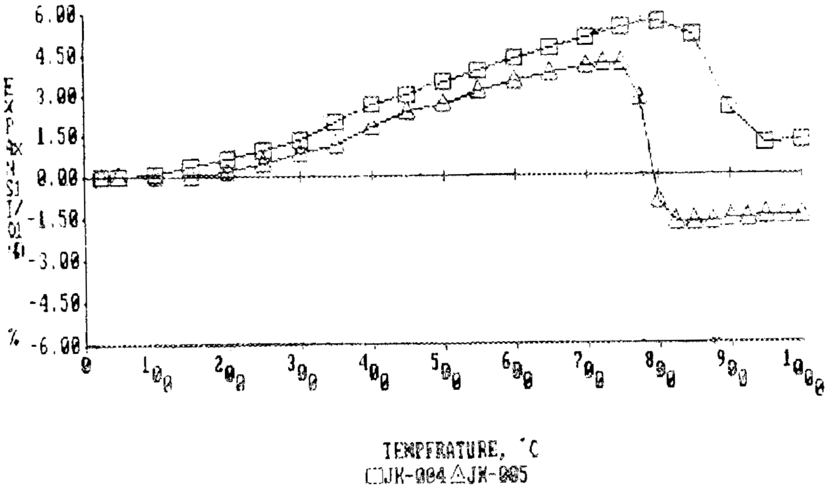

Figure 19. Thermal expansion of JK-004 and JK-005.

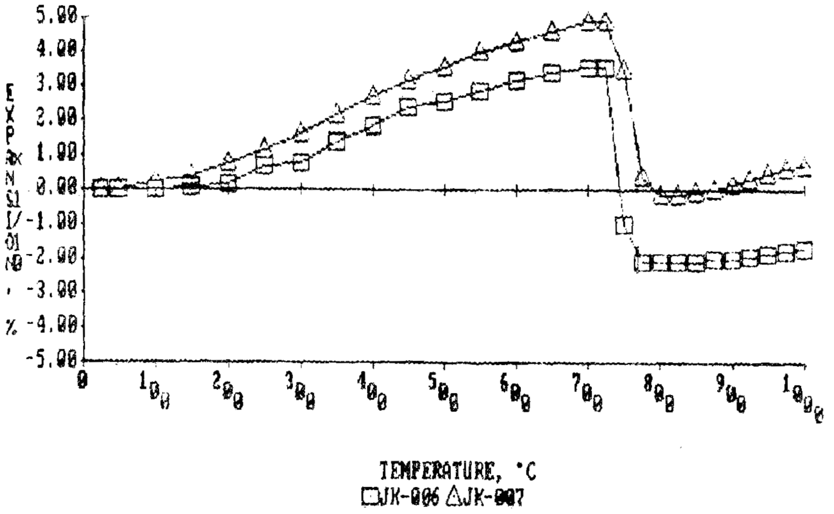

Figure 20. Thermal expansion of JK-006 and JK-007.

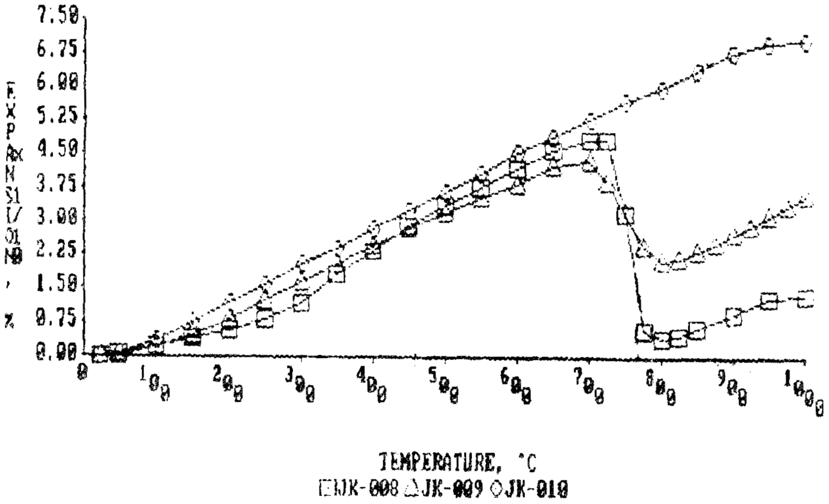

Figure 21. Thermal expansion of JK-008, JK-009, and JK-010.

Table 21. Effect of Phase Transformation on Expansion

Specimens	α Before phase transformation	α Following phase transformation
JK-004	58×10^{-7}	
JK-005	66×10^{-7}	17×10^{-7} (850°C -1000°C)
JK-006	63×10^{-7}	24×10^{-7} (825°C -1000°C)
JK-007	77×10^{-7}	53×10^{-7} (825°C -1000°C)
JK-008	74×10^{-7}	53×10^{-7} (800°C -1000°C)
JK-009	69×10^{-7}	80×10^{-7} (800°C -1000°C)

In JK-005 and JK-006, CTE's were lowered after phase transformation. From the phase diagram,[100] low CTE's are related to the ZrO_2 tetragonal solid solution. Microcracking due to phase transformation may explain the low CTE. However, in the samples JK-007 through JK-009, the values of thermal expansion are higher than those of JK-004 and JK-005. In compositions JK-007 through JK-009, phases after transformation might be considered as ZrO_2 tetragonal solid solution plus $ZrTiO_4$. In JK-003 through JK-009, thermal expansion was slightly increased in the temperature range from 300 to 400°C. This temperature range might be related to the transition into ZrO_2 tetragonal solid solution with ZrO_2 monoclinic solid solution from the already known phase information.[100]

Thermal expansion data of ZrO_2 tetragonal system were reported by Lang.[101] Axial thermal expansions of $123.4 \times 10^{-7} K^{-1}$ in the a-axis and $143.2 \times 10^{-7} K^{-1}$ in the c-axis were reported by using high temperature XRD. Even if the above results were based on out-of-date lattice parameters (a=3.639Å, c=5.275Å), which is different from recently reported lattice parameters (a=5.094Å, c=5.177Å),[102] thermal expansion results of the ZrO_2 tetragonal solid solution were remarkably reduced by the addition of TiO_2.

2. ZrO_2-CeO_2 System

Table 22 lists sintered phases of selected samples in the ZrO_2-CeO_2 system, and Fig. 22 through 24 show thermal expansion data.

Table 22. Sintered phases of ZrO_2-CeO_2 system

Specimens	Sintered phases
JK-011	ZrO_2 monoclinic(ss)
JK-012	ZrO_2 monoclinic(ss) + ZrO_2 tetragonal(ss)
JK-013	ZrO_2 monoclinic(ss) + ZrO_2 tetragonal(ss)
JK-014	ZrO_2 tetragonal(ss)
JK-015	ZrO_2 tetragonal(ss) $Ce_2Zr_3O_{10}$
JK-016	CeO_2 cubic

The 15 mol% CeO_2-ZrO_2 sample did not show expansion due to phase transformation of ZrO_2. On the other hand, specimens with up to 12.5 mol% CeO_2 showed expansion characteristic of a phase transformation. There are different reports about the composition at which phase transformation from monoclinic to tetragonal takes place.[103,104] From our results, a composition having more than 12.5 mol% CeO_2 is expected to have complete ZrO_2 tetragonal solid solubility at room temperature. In specimen JK-015, sintered phases were composed of ZrO_2 tetragonal solid solution with $Ce_2Zr_3O_{10}$.[105]

Before phase transformation with monoclinic ZrO_2 solid solution,

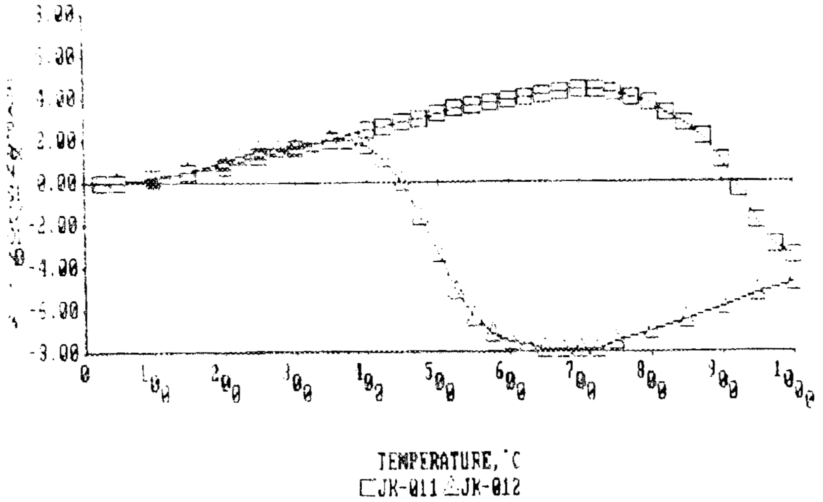

Fig. 22. Thermal expansion of JK-011 and JK-012.

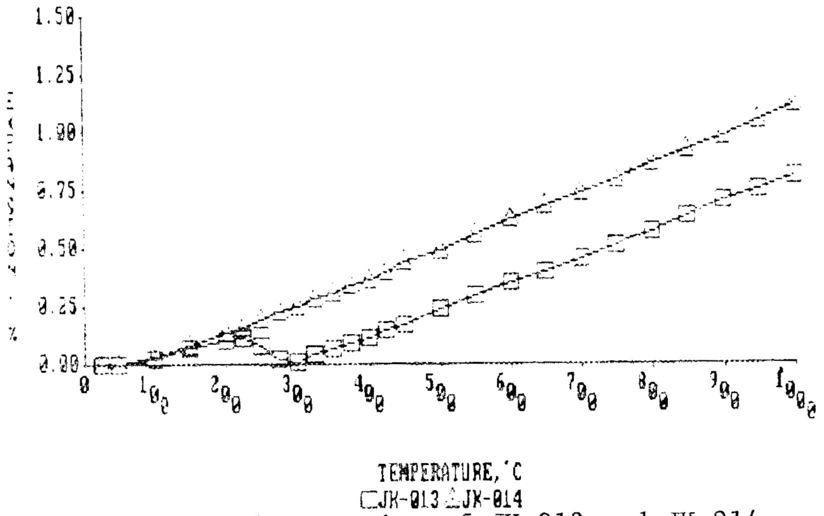

Fig. 23. Thermal expansion of JK-013 and JK-014.

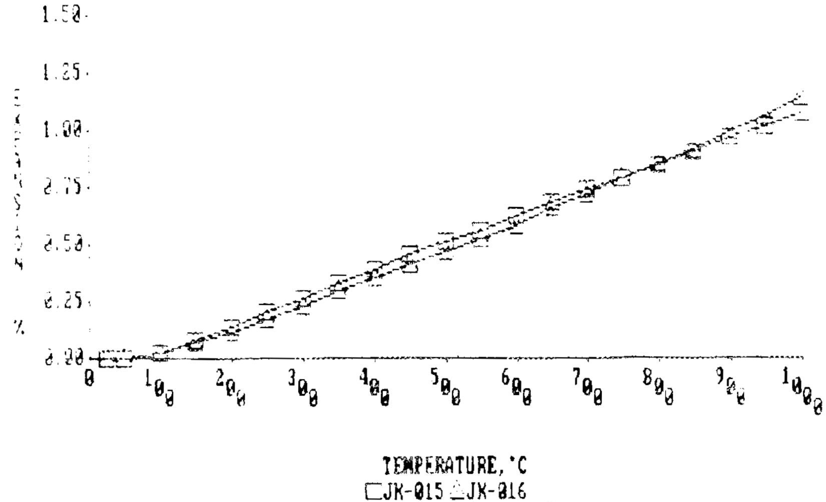

Fig. 24. Thermal expansion of JK-015 and JK-016.

CTE's were 66 to 76x10^{-7}K^{-1}. But after this transformation, in the region of tetragonal ZrO_2 solid solution, the CTE's were measured as 116 to 117x10^{-7}K^{-1}. For pure CeO_2, the value of 122x10^{-7}K^{-1} was obtained. A large difference in thermal expansion between ZrO_2-TiO_2 and ZrO_2-CeO_2 in spite of some metallic bonding characteristic might be explained as follows. Ti^{4+}(0.64Å) has a smaller ionic radius than Zr^{4+}(0.82Å), but Ce^{4+}(0.88Å) has larger ionic radius than that of Zr^{4+}(0.82Å), but Ce^{4+}(0.88Å) has larger ionic radius than that of Zr^{4+}.[106]

The substitution of a large ion, such as Ce^{4+}, into the ZrO_2 structure to form a solid solution results in a large strain. In the temperature range for the tetragonal solid solution (in the ZrO_2-TiO_2 and ZrO_2-CeO_2 systems), TiO_2 (alone) has tetragonal rutile structure, but CeO_2 (alone) has the cubic structure. The above mentioned characteristics of TiO_2 result in less strain-induced ZrO_2 tetragonal solid solution, and consequently low CTE. On the other hand, the addition of CeO_2 into ZrO_2 results in good mechanical strength due to large strain-induced solid solution transformation.

3. ZrO_2-Y_2O_3-MgO and ZrO_2-CaO-MgO Systems

Many binary systems based on ZrO_2 and doping additions of Y_2O_3, CaO, and MgO have been studied, and their CTE's are in the range of 60 to 100x10^{-7}K^{-1}.[80-87,102,107,108] However, the ZrO_2 ternary systems have not been extensively investigated. X-ray diffraction results for the selected systems are shown in Table 23. For specimens JK-017 and JK-021, the ZrO_2 monoclinic peaks were not detected. ZrO_2 tetragonal solid solution was stabilized in these two compositions at room temperature.

Table 23. Sintered Phases of JK-017-021

Specimens	Sintered Phases
JK-017	ZrO_2 tetragonal(ss)
JK-018	ZrO_2 tetragonal(ss) + ZrO_2 monoclinic(ss)
JK-019	ZrO_2 tetragonal(ss) + ZrO_2 monoclinic(ss)
JK-020	ZrO_2 tetragonal(ss) + ZrO_2 monoclinic(ss)
JK-021	ZrO_2 tetragonal(ss)

Thermal expansion data for JK-017 through JK-021 are plotted in Fig. 25 and 26.

All samples except JK-018 did not show thermal expansion behavior due to phase transformation. Thermal expansion results of JK-017 and JK-021 ($104\times10^{-7}K^{-1}$) which were composed of ZrO_2 tetragonal solid solutions were higher than those of of JK-018 through JK-020 (82 to $94\times10^{-7}K^{-1}$) made of ZrO_2 tetragonal and monoclinic solid solutions. With the exception of Mg, additive elements selected in these ternary systems have larger ionic radii than that of Zr^{4+}: $Ca^{2+}(1.04\mathring{A})$, $Y^{3+}(0.97\mathring{A})$, $Mg^{2+}(0.74\mathring{A})$.

After assembling all experimental results from JK-001 through 021, it may be concluded that the CTE of the ZrO_2 tetragonal solid solution can be expected to be lowered in the case of doping elements such as Ti^{4+} which have a smaller ionic radius than Zr^{4+}. This explanation can be extended to ZrO_2 binary systems which have CaO,

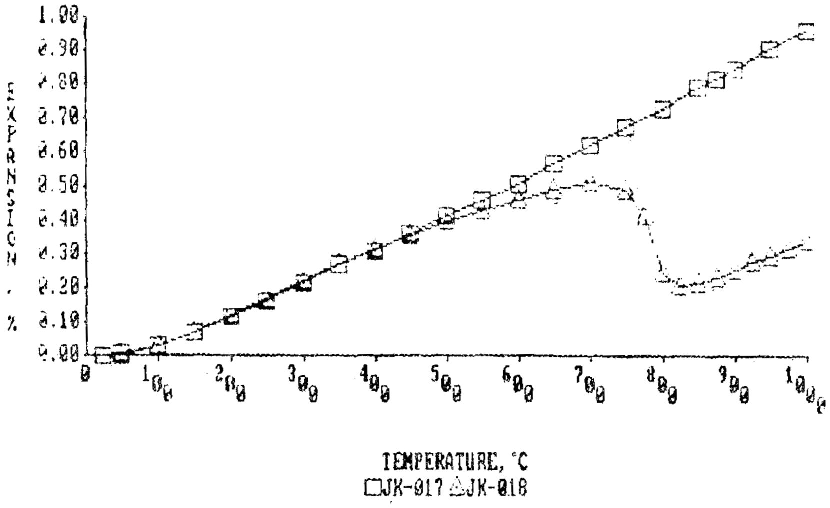

Figure 25. Thermal expansion of JK-017 and JK-018.

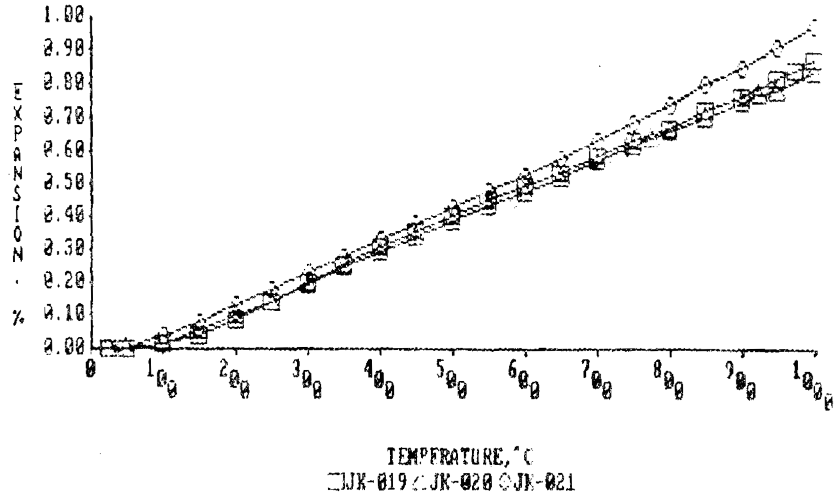

Figure 26. Thermal expansion of JK-019, JK-020, and JK-021.

MgO, Y_2O_3 as an alloy system. If we compare previously published results,[107-108] the thermal expansion of ZrO_2-MgO is the lowest among these three binary systems.

D. Summary

I. For the compositions of 20 and 25 mol% TiO_2 with ZrO_2, low CTE's (17×10^{-7}, $24 \times 10^{-7} K^{-1}$) were measured after phase transformation, which might include microcrack formation.

II. Specimens with up to 12.5 mol% CeO_2 in ZrO_2 system showed expansion characteristic of phase transformation.

III. ZrO_2 tetragonal solid solutions were obtained in ZrO_2-$5Y_2O_3$-5MgO and ZrO_2-7CaO-3MgO ternary systems at room temperature after sintering treatment.

IV. When making ZrO_2 tetragonal solid solution, ions smaller than Zr^{4+} might be more useful in achieving low thermal expansion.

Status of milestones

Status of milestones is presented in Table 24 and Figure 27. An automatic thermal expansion measurement system has been ordered. Task VPI 3.1 will be complete and on-schedule upon its installation and calibration, expected to occur by mid-June.

Publications

None this period.

Table 24. Key to major milestones

VPI 1.1	Process selection for phosphate- and silicate-based systems (Oct. 31, 1986)
VPI 1.2	Process selection for mullite- and zircon-based systems (Oct. 31, 1986)
VPI 2.1	Complete literature review (Oct. 31, 1986)
VPI 3.1	Complete upgrade of characterization facility (Dec. 31, 1986)
VPI 3.2	Complete upgrade of specimen fabrication, processing facilities (June 30, 1987)
VPI 4.1	Complete initial screening of phosphate-based systems (Dec. 31, 1987)
VPI 4.2	Complete initial screening of silicate-based systems (Dec. 31, 1987)
VPI 4.3	Complete initial screening of zircon-based systems (Dec. 31, 1987)
VPI 4.4	Complete initial screening of mullite-based systems (Dec. 31, 1987)
VPI 5.1	Complete second-stage property and characterization evaluation of phosphate-based systems (Sept. 30, 1988)
VPI 5.2	Complete second-stage property and characterization evaluation of silicate-based systems (Oct. 31, 1988)
VPI 5.3	Complete second-stage property and characterization evaluation of mullite-based systems (Nov. 30, 1988)
VPI 5.4	Complete second-stage property and characterization evaluation of zircon-based systems (Dec. 31, 1988)
VPI 6.0	Complete scale-up specimen fabrication of most promising low- expansion ceramics (Feb. 28, 1989)

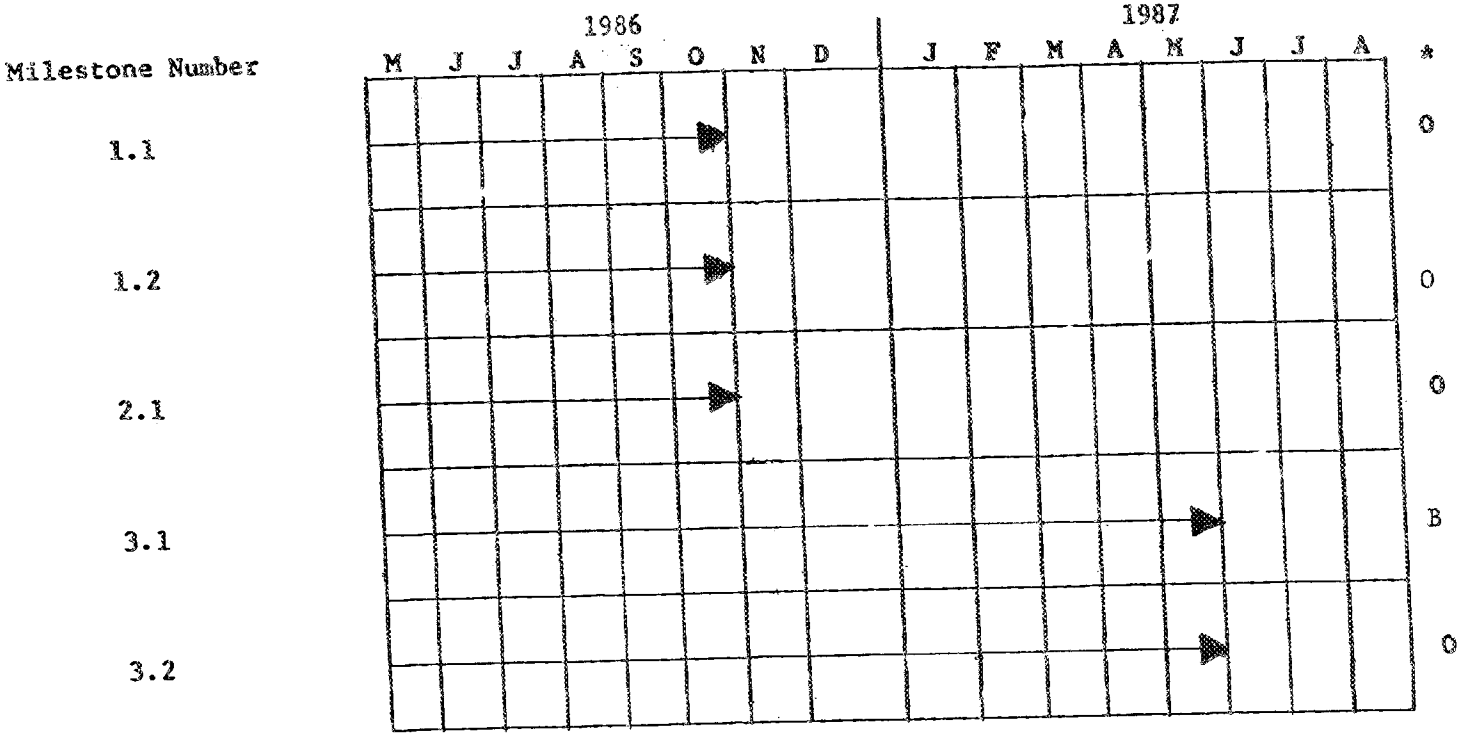

---

*On, ahead of, or behind schedule.

Figure 27. Milestone status.

References

1. W. D. Kingery, H. K. Bowen, D. R. Uhlmann, *Introduction to Ceramics*, 2nd Ed., John Wiley & Sons, New York, 1976.

2. F. A. Hummel, "A Review of Thermal Expansion Data of Ceramic Materials, Especially Ultra-Low Expansion Compositions," *Interceram*, 27-30 (Dec. 1984).

3. A. Goiffon, J. C. Jumas, M. Maurin, and E. Philippot, "Etude Comparee a diverses Temperatures (173, 293, et 373K) des Structures de Type Quartz des Phases $M^{III}X^{V}O_4$(M^{III}=Al,Ga et X^{V} = P,As)," *J. Solid State Chem.*, 61, 384-96 (1986).

4. M.Troccaz, C.Berger, M.Richard, and L. Eyraud, "$\alpha \rightleftarrows \beta$ Phase Transformations for the "Phospho-Quartz" Variety of Aluminum Orthophosphate," *Bull. Soc. Chim. Fr.*, 1967 (11), 4256-9.

5. K. Byrappa, J. Shashidhara Prasad, and S. Srikantaswamy, "High-Temperature X-ray Diffraction Studies of Berlinite Crystals," *J. Mater. Sci., Lett.*, 5(11), 1189-90 (1986).

6. H. N. Ng and C. Calvo, "X-ray Study of the Transformation of Berlinite ($AlPO_4$)." *Can. J. Phys.*, 54(6), 638-47 (1976).

7. A. F. Wright and A. J. Leadbetter, "The Structures of β-cristobalite Phases of SiO_2 and $AlPO_4$," *Phil. Mag.*, 31(6), 1391-1401 (1975).

8. A. J. Leadbetter and A. F. Wright, "The α-β Transition in the Cristobalite Phase of SiO_2 and $AlPO_4$: I. X-Ray Studies," *Phil. Mag.*, 33(1), 105-12 (1976).

9. A. J. Leadbetter and A. F. Wright, "The α-β Transition in the Cristobalite Phases of SiO_2 and $AlPO_4$: II. Calorimetric Studies," *Phil. Mag.*, 33(1), 113-19 (1976).

10. K. Allaf and A. Rouanet, "Relations entre les Phases de l'Orthophosphate d'Aluminium $AlPO_4$," *High Temp. - High Pressures*, 10(5), 591-7 (1978).

11. W. Beck, "Crystallographic Inversions of the Aluminum Orthophosphate Polymorphs and their Relation to those of SiO_2," *J. Am. Ceram. Soc.*, 32(4), 147-51 (1949).

12. F. A. Hummel, "Properties of some Substances Isostructural with Silica," *J. Am. Ceram. Soc.*, 32(10), 320-326 (1949).

13. E. C. Shafer and R. Roy, "Silica Structure Phases: III. New Data on the System $AlPO_4$," *Z. Physik. Chem.*, 11, 30-40 (1957).

14. K. Byrappa, S. Srikantaswamy, and G. S. Gopalakrisha, "Influence of Admixtures on the α-β Berlinite Transition," *J. Mater. Sci. Lett.*, 5(3), 347-8 (1986).

15. O. W. Flaerke and H. Lachenmayr, "Differential Thermal Analysis and X-ray Investigations on $AlPO_4$," *Ber. Deut. Keram. Ges.*, 39, 55-62 (1962).

16. P. E. Stone, E. P. Egan, Jr., and J. R. Lehr, "Phase Relationships in the System $CaO-Al_2O_3-P_2O_5$," *J. Am. Ceram. Soc.*, 39(3), 89-98 (1956).

17. F. A. Hummel and T. A. Kupinski, "Thermal Properties of the Compound BPO_4," *J. Am. Chem. Soc.*, 72(11), 5318-9 (1950).

18. W. F. Horn and F. A. Hummel, "The System BPO_4-AlPO_4," *Trans. J. Brit. Ceram. Soc.*, 77(5), 158-62 (1978).

19. H. G. F. Winkler, "Synthese and Kristallstruktur des Eukryptits, $LiAlSiO_4$," *Acta Cryst.*, 1, 27-34 (1948).

20. M. J. Buerger, "The Stuffed Derivatives of the Silica Structures," *Am. Mineral.*, 39(7-8), 600-14, (1954).

21. V. Tscherry, H. Schulz, and F. Laves, "Average and Super Structure of β-Eucryptite ($LiAlSiO_4$). Part I. Average Structure," *Z. Kristallogr.*, 135(3-4), 161-74 (1972).

22. V. Tscherry, H. Schulz, and F. Laves, "Average and Super Structure of β-Eucryptite ($LiAlSiO_4$). Part II Super Structure, *Z. Kristallogr.*, 135(3-4), 175-98 (1972).

23. H. Schulz and V. Tscherry, "Structural Relations Between the Low- and High-Temperature Forms of β-Eucryptite and Low Quartz," *Acta Cryst.*, 28, 2168-73 (1972).

24. H. Schulz and V. Tscherry, "Structural Relations Between the Low- and High-Temperature Forms of β-Eucryptite ($LiAlSiO_4$) and Low and High Quartz. II. High-Temperature Form of β-Eucryptite and High Quartz," *Acta Cryst.*, 28, 2174-2177 (1972).

25. W. W. Pillars and D. R. Peacor, "The Crystal Structure of Beta Eucryptite as a Function of Temperature," *Am. Mineral.*, 58, 681-90 (1973).

26. R. Roy, D. Roy, and E. F. Osborn, "Compositional and Stability Relationships Among the Lithium Aluminosilicates: Eucryptite, Spodumene, and Petalite," *J. Am. Ceram. Soc.*, 33(5), 152-9 (1950).

27. T. Isaacs and R. Roy, "The α-β Inversions in Eucryptite and Spodumene," *Geochim et Cosmochim. Acta.*, 15, 213-17 (1958).

28. J. H. Westbrook, "Temperature Dependence of Strength and Brittleness of Some Quartz Structures," *J. Am. Ceram. Soc.*, 41(11) 433-40 (1958).

29. K. F. Hesse, "Crystal Structures of Natural and Synthetic α-Eucryptite, LiAlSiO$_4$, *Z. Kristallogr.*, 172, 147-51 (1985).

30. R. A. Hatch, "Phase Equilibrium in the System Li$_2$O-Al$_2$O$_3$-SiO$_2$," *Am. Mineral*, 28, 471-96 (1943).

31. T. Y. Tien and F. A. Hummel, "Studies in Lithium Oxide Systems: XIII, Li$_2$O:Al$_2$O$_3$:32SiO$_2$-Li$_2$O: Al$_2$O$_3$:2GeO$_2$," *J. Am. Ceram. Soc.*, 47 (11) 582-584 (1964).

32. F. H. Gillery and E. A. Bush, "Thermal Contraction of β-Eucryptite (LiO·Al$_2$O$_3$·2SiO$_2$) by X-Ray and Dilatometer Methods," *J. Am. Ceram. Soc.*, 42 (4) 175-7 (1959).

33. V. Tscherry, H. Schulz, M. Czank, "Thermal Expansion of the Lattice Constants of β-Eucryptite Single Crystals," *Ber. Deut. Keram. Ges.*, 49 (5), 153-4 (1972).

34. F. A. Hummel, "Significant Aspects of Certain Ternary Compounds and Solid Solutions," *J. Am. Ceram. Soc.*, 35 (3) 64-66 (1952).

35. Yu. N. Kondrat'ev, "Order and Disorder in Lithium Aluminosilicates," *Izv. Akad. Nauk SSSR, Neorgan. Materialy*, 1 (5), 1395-8 (1965).

36. K. Ikeda and K. Minagawa, "Effect of Heat Treatment on Thermal Expansion Properties of Lithia Ceramics with β-Eucryptite Composition," *Yogyo Kyokai Shi*, 74(848), 109-13 (1966).

37. J. S. Moay, A. G. Verduch, and M. Hortal, "Thermal Expansion of Beta-Eucryptite Solid Solutions," Trans. *J. Brit. Ceram. Soc.*, 73 (6) 177-78 (1974).

38. G. R. Fischer, R. R. Wusirika, and J. E. Geiger, "The Crystal Lattice Thermal Expansion of an Oxynitride Glass-Ceramic Material of High-Quartz Structure," *J. Mat. Sci.*, 20, 4117-4122 (1985).

39. A. J. Perrotta, *Low Thermal Expansion Ceramic Material Comprising a Single Phase Solid Solution of Beta-Eucryptite and Aluminum Phosphate*, U. S. 3, 549, 394, 22 Dec. 1970, Appl. 18 Dec. 1967, p.1.

40. F. A. Hummel and J. B. Langensiepen, "Elimination of α⇄β Cristobalite Inversion of AlPO$_4$," *Korean Cer. Inds. Ass.*, 11(4), 4-5 (1986).

41. F. A. Hummel and W. F. Horn, "The Quaternary System B$_2$O$_3$-Al$_2$O$_3$-SiO$_2$-P$_2$O$_5$: I. Literature Review and Exploratory Data on the Ternary Subsystems," *J. Austral. Ceram. Soc.*, 17(1) 25-32 (1981).

42. W. F. Horn and F. A. Hummel, "The System BPO_4-$AlPO_4$-SiO_2 at 1200°C," *Trans. J. Brit. Ceram. Soc.,* 79, 109-11 (1980).

43. K. H. Kim and F. A. Hummel, "Studies in Lithium Oxide Systems: XII, Li_2O-B_2O_3-Al_2O_3m" *J. Am. Ceram. Soc.,* 45(10) 487-9 (1962).

44. S. Pawlowski, "Bond Properties of Aluminum Phosphates," *Epitoanyag,* 17 (9) 333-7 (1965).

45. I. Tananaev, V. Maksimchuk, Y. G. Bushuev, and S. A. Shestov, "Formation of Oxyphosphates in MPO_4-M_2O_3 Systems (M - Aluminum, Chromium, Yttrium)," *IZv. Akda. Navk SSSR, Neorg. Mater.* 14 (4) 719-22 (1978).

46. A. A. Chistyakova, V. A. Sivkina, V. I. Sadkov, A. P. Khashkovskaya, and L. G. Povycheva, "Aluminum Orthophosphates," *Izv. Akad. Navk SSSR, Neorg. Mater.,* 5 (3) 536-43 (1969).

47. L. Pauling and J. Sherman, "The Crystal Structure of Aluminum Metaphosphate," *Z. Krist.,* 96, 481-7 (1937).

48. H. Van der Meet, "The Crystal Structure of a Monoclinic Form of Aluminium Metaphosphate, $Al(PO_3)_3$," *Acta Cryst.,* B32, 2423-26 (1976).

49. R. Roy and E. F. Osborn, "The System Lithium Metasilicate-Spodumene-Silica," *J. Am. Chem. Soc.,* 71 (6) 2086-2095 (1949).

50. J. E. Stanworth and W. E. S. Turner, "Notes on the Possibility of Preparing Glasses Containing P_2O_5, Al_2O_3, B_2O_3 and SiO_2," *J. Soc. Glass Tech.,* 21, 368-82 (1937).

51. R. M. Klein, A. G. Kolbeck, and C. L. Quackenbush, "Glass Formation and Properties in the Aluminum Borophosphate System," *Bul. Am. Ceram. Soc.,* 57 (2) 199-216 (1978).

52. W. F. Horn and F. A. Hummel, "The Quaternary System B_2O_3-Al_2O_3-SiO_2-P_2O_5: II. Exploratory Data," *J. Austral. Ceram. Soc.,* 17 (2) 33-38 (1981).

53. H. D. Megaw, "Crystal Structures and Thermal Expansion," *Mat. Res. Bull.,*6, 1007-18 (1971).

54. C. M. B. Henderson and D. Taylor, "Thermal Expansion of the Nitrides and Oxynitride of Silicon in Relation to Their Structures," *Trans. Brit. Ceram. Soc.,* 75, 49-53 (1976).

55. H. D. Megaw, "The Thermal Expansion of Interatomic Bonds, Illustrated by Experimental Evidence from Certain Niobates," *Acta. Cryst.,* A24, 589-604 (1968).

56. E. Taylor, "The Thermal Expansion of the Sodalite Group of Minerals," *Miner. Mag.*, 36, 761-69 (1968).

57. D. Taylor and C. M. B. Henderson, "The Thermal Expansion of the Leucite Group of Minerals," *Amer. Miner.*, 53, 1476-89 (1968).

58. D. Taylor, "The Thermal Expansion Behavior of the Framework Silicates," *Miner. Mag.*, 38, 593-604 (1972).

59. D. W. J. Cruickshank, "Errors in Bond Lengths Due to Rotational Oscillations of Molecules," *Acta. Cryst.*, 9, 757-58 (1956).

60. J. J. Pluth, J. V. Smith, and J. Forber, Jr., "Crystal Structure of Low Cristobalite at 10, 293, and 473K: Variation of Framework Geometry with Temperature," *J. Appl. Phys.*, 57 (4) 1045-49 (1985).

61. D. R. Peacor, "High Temperature Single-Crystal Study of the Cristobalite Inversion," *Z. Krist.*, 38, 274-98 (1973).

62. A. F. Wright and A. J. Leadbetter, "The Structures of the β-Cristobalite Phases of SiO_2 and $AlPO_4$," *Philos. Mag.*, 31 (6) 1391-1401 (1975).

63. K. Takahashi, A. Osaka, and K. Ariyoshi, "Sizes of the Voids and of the Alkali Ions in a High-Cristobalite Type Network Structure," *J. Non-Cryst. Solid*, 69, 135-143 (1984).

64. M. Schenk, "Radiation-Induced Property Changes in Cristobalite (SiO_2), "*Phys. Stat. Sol.*, 36 K101 (1969).

65. M. E. Nordberg, *Glass Having an Expansion Lower than that of Silica,"* U. S. Pat. 2,26,059 (August 3, 1943).

66. N. E. Bunting, "Phase-Equilibria in the System TiO_2, TiO_2-SiO_2, TiO_2-Al_2O_3," *J. Research Nat. Bur. Standards*, 11 (5) 719-25 (1933).

67. A. R. Sheen and W. E. S. Turner, "Some Observations on the Influence of Titaniz on the Properties of Glass," *J. Soc. Glass Technol.*, 8 (31) 187 (1924).

68. R. W. Ricker and F. A. Hummel, "Reactions in the System TiO_2-SiO_2: Revision of the Phase Diagram," *J. Am. Ceram. Soc.*, 53 (7) 418-19 (1970).

69. J. E. Fenstermacher and F. A. Hummel, "High-Temperature Mechanical Properties of Ceramic Material: IV, Sintered Mullite Bodies," *J. Am. Ceram. Soc.*, 44 (5) 284-89 (1961).

70. M. H. Lepold and J. D. Sibold, "Development of Low-Thermal Expansion Mullite Bodies," *J. Am. Ceram. Soc.*, 65(9) C-147-C-149 (1982).

71. K. H. Kim, *Phase Equilibria in the System* Li_2O-B_2O_3-Al_2O_3-SiO_2 *and Some of Its Subsidiary Systems*, Ph.D. Thesis, The Pennsylvania State University (1961).

72. R. J. Angel and C. T. Prewitt, "Crystal Structure of Mullite: A Reexamination of the Average Structure," *Am. Mineral.*, 71, 1476-82 (1982).

73. H. Schneider, "Temperature-Dependent Iron Solubility in Mullite," *J. Am. Ceram. Soc.*, 70(3) C-43-C-45 (1987).

74. F. Liebau, E. P. Meagher, J. A. Speer, P. H. Ribbe, and G. E. Brown, *Orthosilicates, Reviews in Mineralogy*, Vol. 5, Second Ed., Mineralogical Society of America, Edited by P. H. Ribbe, Bookcrafters, Inc., Chelsea, Mich., 1982.

75. W. F. Horn and F. A. Hummel, "The System BPO_4 and $AlPO_4$," *Trans. J. Brit. Ceram. Soc.*, 77(5) 158-62 (1978).

76. C. Bandin, M. I. Osendi, and J. S. Moya, "Solid Solution of TiO_2 in Mullite," *J. Mater. Sci. Lett.*, 2(5) 185-87 (1983).

77. M. Ishitsuka, T. Sato, T. Endo, and M. Shimada, "Synthesis and Thermal Stability of Aluminum Titanate Solid Solution," *J. Am. Ceram. Soc.*, 70(2) 69-71 (1987).

78. M. O'Keeffe, B. Domenges, and G. V. Gibbs, "Ab Initio Molecular Orbital Calculations on Phosphates: Comparison with Wilicates," *J. Phys. Chem.*, 89, 2304 (1985).

79. F. A. Hummel, *Introduction to Phase Equilibria in Ceramic Systems*, Marcel Dekker, Inc., New York, 1984.

80. N. Stenton, M. R. Notis, and D. B. Williams, "Quantitative Electron Energy-Loss Measurements on the System ZrO_2-CaO," *J. Am. Ceram. Soc.*, 67(3) 227-32 (1984).

81. J. R. Hellman and V. S. Stubican, "Stable and Metastable Phase Relations in the System ZrO_2-CaO," *ibid.*, 66(4) 260-64 (1983).

82. V. S. Stubican and S. P. Ray, "Phase Equilibria and Ordering in the System ZrO_2-CaO," *ibid.*,60 (11-12) 534-37 (1977).

83. M. V. Swain, R. C. Garvie, and R. H. Hannink, "Influence of Thermal Decomposition on the Mechanical Properties of Magnesia-Stabilized Cubic Zirconia," *ibid.*, 66(5) 358-62 (1983).

84. C. Pascual and P. Duran, "Subsolidus Phase Equilibria and Ordering in the System ZrO_2-Y_2O_3," *ibid.*, 66(1) 23-27 (1983).

85. W. H. Rhodes, "Agglomerate and Particle Size Effects on Sintering Yttria-Stabilized Zirconia," *ibid.*, 64(1) 19-22 (1981).

86. R. Chaim, M. Ruhle, and A. H. Heuer, "Microstructural Evolution in a ZrO_2-12 wt% Y_2O_3 Ceramic," *ibid.*, 68 (8) 427-31 (1985).

87. V. S. Stubican, R. C. Hink, and S. P. Ray, "Phase Equilibria and Ordering in the System ZrO_2-Y_2O_3," *ibid*, 61(1-2) 17-21 (1978).

88. L. Tcheichvili, "The Stabilization of ZrO_2 with Rare-Earth Oxides with Atomic Numbers from 58 to 71," *Keramische Zeitschrift*, 30(3) 138-39 (1978).

89. R. Ruh, H. J. Garrett, R. F. Domagala, and V. A. Patel, "The System Zirconia-Scandia," *J. Am. Ceram. Soc.*, 60(9-10) 399-403 (1977).

90. R. K. Stewart and O. Hunter, Jr., "Stabilization of Zirconia by Erbia," *ibid.*, 53, 421-22 (1970).

91. W. D. Kingery, H. K. Bowen, and D. R. Uhlmann, *Introduction to Ceramics*, Second ed., John Wiley and Sons, New York, 1976.

92. R. M. Hazen and C. T. Prewitt, "Effects of Temperature and Pressure on Interatomic Distances in Oxygen-Based Minerals," *Am. Mineralogist*, 62, 309-15 (1977).

93. E. Tani, M. Yoshimuro, and S. Somiya, "Formation of Ultrafine Tetragonal ZrO_2 Powder Under Hydrothermal Conditions," *J. Am. Ceram. Soc.*, 66(1) 11-14 (1983).

94. T. K. Gupta, J. H. Bechtold, R. C. Kuznicki, L. H. Cadoff, and B. R. Rossing, "Stabilization of Tetragonal Phase in Polycrystalline Zirconia," *J. Mat. Sci.*, 12, 2421-26 (1977).

95. R. C. Garvie, "Stabilization of the Tetragonal Structure in Zirconia Microcyystals," *J. Phys. Chem.*, 82(2) 218-24 (1978).

96. E. D. Whitney, "Effect of Pressure on Monoclinic-Tetragonal Transition of Zirconia; Thermodynamics," *J. Am. Ceram. Soc.*, 45 (12) 612-13 (1962).

97. U. S. Patent No. 4,035,191.

98. R. Ruh, "Axial and Linear Thermal Expansion of ZrO_2 and HfO_2," *Bull. Am. Ceram. Soc.*, 60(4) 504-6 (1981).

99. K. V. Krishna Rao, "Thermal Expansion of Rutile and Anatase," *J. Am. Ceram. Soc.*, 53(3) 124-26 (1970).

100. F. H. Brown, Jr. and P. Duwez, "The Zirconia-Titania System," *J. Am. Ceram. Soc.*, 37(3) 129-32 (1954).

101. S. M. Lang, "Axial Thermal Expansion of Tetragonal ZrO_2 between 1150° and 1750°C, *ibid.*, 47(12) 641-44 (1964).

102. R. Stevens, *An Introduction to Zirconia*, Magnesium Elecktron Ltd., 1983.

103. P. Duwez and F. Odell, "Phase Relationships in the System Zirconia-Ceria," *J. Am. Ceram. Soc.*, 33(9) 274-283 (1950).

104. S. Somiya, S. Okikawa and S. Saito, "Thermal Expansion and Electrical Resistance of Sintered Bodies in the System ZrO_2-CeO_2," *J. Ceram. Assoc.*, Japan, 73(2) 25-29 (1965).

105. E. Tant, M. Yoshimura, and S. Somiya, "Revised Phase Diagram of the System ZrO_2-CeO_2 below 1400°C," *J. Am. Ceram. Soc.*, 66(7) 506-10 (1983).

106. F. D. Bloss, *Crystallography and Crystal Chemistry*, Holt, Reinhart and Winston, Inc., 1971.

107. D. C. Larson, J. W. Adams, L. R. Johnson, A. P. S. Teotia, and L. G. Hill, *Ceramic Materials for Advanced Heat Engines*, Noyes Pub., 1985.

108. D. L. Branson, "Thermal Expansion Coefficients of Zirconate Ceramics," *J. Am. Ceram. Soc.*, 48(8) 441 (1965).

1.4 JOINING

1.4.1 Ceramic-Metal Joints

Joining of Ceramics for Heat Engine Applications

M. L. Santella (Oak Ridge National Laboratory)

Objective/scope

The objective of this task is to develop strong, reliable joints containing ceramic components for applications in advanced heat engines. Currently, this work is focused on the joining of partially stabilized zirconia to nodular cast iron by brazing. Joints of this arrangement will be required for attaching monolithic pieces of partially stabilized zirconia to cast iron piston caps in order for the ceramic to provide the insulation necessary for use in low-heat-rejection diesel engines. A novel method for brazing zirconia to cast iron has already been established. The emphasis of this activity for FY 1987 will be investigating (1) the effect of thermal aging and testing temperature on the strength of joints between zirconia and cast iron, (2) the possibilities for using alternate ceramic and metallic materials in brazed components, and (3) residual stress patterns in ceramic-to-metal braze joints using indentation techniques.

Technical progress

There was significant activity in three technical areas during this reporting period:

(1) shear testing of braze joints between MS-ZrO_2 and nodular cast iron and MS-ZrO_2 and A286 steel;

(2) studying the effect of braze thermal cycles on the microstructure and hardness of grade 8003 nodular cast iron; and

(3) brazing silicon nitride.

Shear testing of MS-ZrO_2 Joints

The following zirconia-to-metal joints were shear tested at room temperature:

(1) active substrate braze joints between MS-ZrO_2 and nodular cast iron that were aged in air at 400°C for 100 h,

(2) active filler metal braze joints between MS-ZrO_2 and nodular cast iron that were aged in air at 400°C for 100 h,

(3) active substrate joints between MS-ZrO_2 and A286 steel that were brazed with LithoBT at 790°C, and

(4) active filler metal joints between MS-ZrO_2 and A286 steel that were brazed with Incusil-15 ABA.

The test results are given in Table 1. The data for the joints made to cast iron show considerable scatter for both brazing approaches but indicate that joints made by both processes may be stronger than the original data suggested. Additional testing of both types of joints is in progress so that some level of confidence in the data can be established.

The measured strengths of the active substrate joints between MS-ZrO_2 and A286 steel were low. Examination of the fracture surfaces

Table 1. Room-temperature shear strength of joints between zirconia and metal alloys

Specimen	Interface	Aging	Process/ filler metal	Shear strength (MPa)
MCB-72*	ZrO_2-Fe	400°C/100h	AS/604	114
MCB-178	ZrO_2-Fe	400°C/100h	AS/604	202
MCB-179	ZrO_2-Fe	400°C/100h	AS/604	43
MCB-95*	ZrO_2-Fe	400°C/100h	AF/Incusil	61
MCB-182	ZrO_2-Fe	400°C/100h	AF/Incusil	180
MCB-183	ZrO_2-Fe	400°C/100h	AF/Incusil	150
MCB-211	ZrO_2-A286	None	AS/LithoBT	67
MCB-212	ZrO_2-A286	None	AS/LithoBT	62
MCB-199	ZrO_2-A286	None	AF/Incusil	254
MCB-200	ZrO_2-A286	None	AF/Incusil	340

Notes:

1. All brazing was done in vacuum.
2. Brazing temperatures were: 604 to 735°C, LithoBT - 790°C, Incusil-15 ABA - 770°C.
3. Aging treatments were done in air.
4. All testing was done at room temperature.
5. Materials used were MS-ZrO_2, grade 8003 cast iron, A286 steel.
6. For the active substrate joints the ZrO_2 was vapor coated with 0.6 µm titanium.

*Data obtained in previous tests.

indicated that wetting and flow of the LithoBT filler metal on the titanium-coated zirconia was good but that bonding to the A286 was poor. Selection of a different filler metal alloy is indicated for this brazing approach. On the other hand, bonding of the Incusil-15 ABA filler metal to the MS-ZrO_2 and A286 steel was excellent as indicated by the high measured shear strengths of these joints. Testing and evaluation of these joints are continuing.

Thermal cycling of cast iron

The effect of braze thermal cycles on the microstructure and hardness of grade 8003 nodular cast iron was studied. Specimens of the as-recieved cast iron were heat treated with the thermal cycles used for making braze joints with braze alloy 604, which requires a peak temperature of 735°C, and Incusil-15 ABA, which requires a peak temperature of 775°C. The heating and cooling rates used for these specimens were relatively fast because the mass of the specimens was small. Also examined was a specimen of iron from the 112-mm-diam demonstration piece brazed with alloy 604 and a specimen heat treated to simulate the thermal cycle that would be used to braze a similarly sized piece with Incusil. In this case the heating and cooling rates were much lower than those used for the small specimen heat treatments.

Figure 1 compares the microstructures of the heat treated specimens with the microstructure of the as-received iron. Examination by optical metallography indicated that the initial microstructure of the iron was not significantly changed by any of the heat treatments except for the specimen subjected to the simulated demonstration piece braze cycle. In this case, the slow heating and cooling rate coupled with the 775°C peak temperature have changed the microstructure from one with a pearlitic matrix to one with a ferritic matrix in which only remnants of the original pearalite are retained. The Rockwell C hardness of each specimen was determined, and these results are given in Table 2. The only specimen to suffer a loss of hardness was the same one that underwent a significant change of microstructure, 87-0080, and the loss of hardness is consistent with the transformation from a pearlitic matrix to a ferritic matrix.

This experiment serves to reemphasize the need to maintain the lowest possible brazing temperature for the zirconia-to-cast iron joint if the overaging of the component materials is to be avoided and indicates that the active substrate process has a clear advantage in this regard.

Table 2. Rockwell C hardness of grade 8003 nodular cast iron specimens heat treated with brazing thermal cycles

86-1561	NA	32.4 ± 1.8	NA
86-1562	735	32.3 ± 0.3	7/10
86-1563	735	31.9 ± 0.8	95/40
86-1564	775	32.6 ± 1.8	70/40
87-0080	775	9.5 ± 0.9	11/13*

*Simulated demonstration braze thermal cycle.

Brazing silicon nitride

Specimens of Si_3N_4 (Kyocera SN-220) were brazed to three different alloys: (1) A286, a precipitation hardened, heat resistant steel; (2) ASTM B265 grade 1, commercially pure titanium; and (3) TZM, an alloy of Mo-0.5Ti0.09Zr-0.02C wt %. All of the Si_3N_4 surfaces used for brazing were vapor coated with a 1.0-µm-thick layer of titanium by vacuum

ORNL PHOTO 3761-87

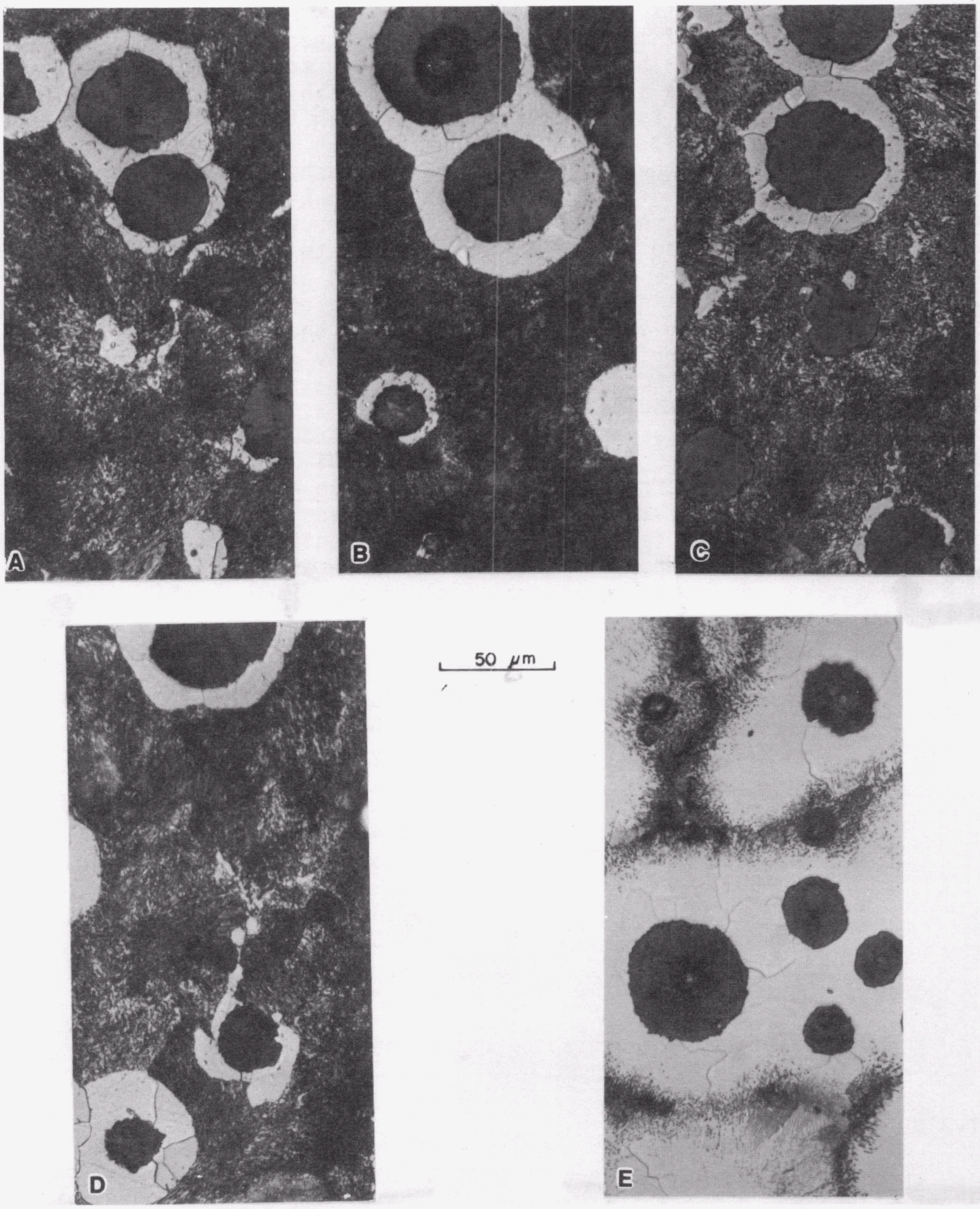

Fig. 1. Optical microstructure of grade 8003 cast iron after experiencing brazing thermal cycles: *(a)* as-received iron; braze 604 thermal cycle with fast *(b)*, and slow *(c)* heating and cooling rates; Incusil thermal cycle with fast *(d)*, and slow *(e)* heating and cooling rates.

evaporation. The braze alloy used was BAg-8a (Ag-28.0Cu-0.3Li wt %), and the brazing was done in vacuum at 790°C. The ductility of BAg-8a is very good.

Each of the three joints between Si_3N_4 and the metals cracked in the ceramic component upon cooling from the brazing temperature of 790°C. A photograph of the joints between Si_3N_4 and the titanium and the A286 steel, Fig. 2, shows the overall characteristics of the cracking. A short distance (0.5-1 mm) from the bond zone cracks formed and propagated through the Si_3N_4, leaving only a thin somewhat hemispherical fragment of the Si_3N_4 attached to the metal component of the joint. The joint between Si_3N_4 and titanium cracked similarly to the joint made with the A286. The joint between the Si_3N_4 and the TZM actually remained intact, even after sectioning for metallographic examination, but cracks of the same nature were evident in this specimen also.

An obvious explanation for the cracking is that it resulted from the strain that developed in the joined components because of the mismatch in thermal expansion coefficients between the metals and the Si_3N_4. The macroscopic mismatch strain, e_m, can be estimated using the expression

$$e_m = \Delta\alpha \; \Delta T,$$

where ΔT = 735°C for the BAg-8a braze alloy and $\Delta\alpha$ is the difference in linear thermal expansion coefficient for the materials used to form the joint. Using a value of 304 GPa for the Young's modulus for Si_3N_4, a stress due to the thermal expansion mismatch can also be calculated. Handbook values for the thermal expansion coefficients and the estimated strain and stress values are given in Table 3.

Table 3. Estimated mismatch strain and stress for joints between Si_3N_4 and metals

Material	α (µin./in./°C)	e_m	σ (MPa)
Si_3N_4	3.1		
TZM	5.6	0.0018	547
Ti	8.4	0.0039	1186
A286	16.5	0.0099	3010

The fracture strength of the Si_3N_4 was not determined experimentally but is reported to be 590 MPa in flexure. Comparison with the estimated mismatch stress values indicates that bonding Si_3N_4 to either the titanium or the A286 steel would undoubtedly generate stresses high enough to cause cracking in the ceramic, while the stress generated by bonding Si_3N_4 to the TZM would be on the order of the fracture strength of the ceramic.

ORNL PHOTO 1699-87

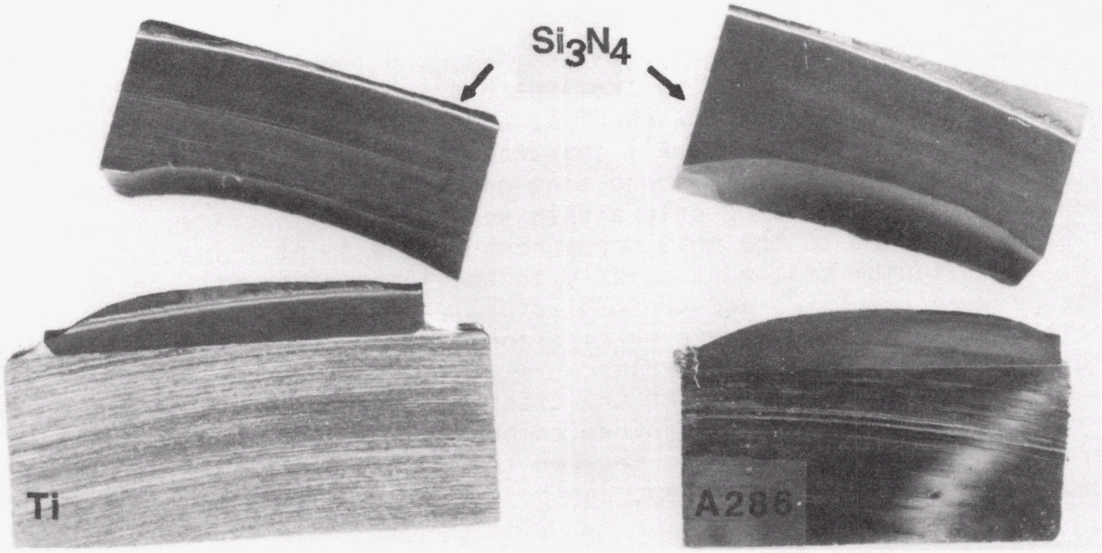

Fig. 2. Cross-sectioned braze joints of Si_3N_4–Ti (left) and Si_3N_4–A286 steel (right) that cracked spontaneously in the ceramic upon cooling from the brazing temperature of 790°C.

This experiment shows several important points: (1) the active substrate brazing approach can be used for brazing Si_3N_4 to metals; (2) having a ductile braze filler metal is not sufficient condition for preventing cracking of Si_3N_4 because of thermal expansion mismatch strains; (3) some means of accommodating or reducing the thermal expansion mismatch strains will probably be required for forming brazed butt joints of Si_3N_4 to metals.

Status of milestones

None

Publications

None

Presentations

1. "Characterization of Ceramic Braze Joints," by M. L. Santella and A. J. Moorhead was presented at the ASM Materials Week, Orlando, Florida, October 9, 1986.

2. "Characterization of Interfacial Reaction Products in Ceramic Braze Joints," by M. L. Santella and A. J. Moorhead was presented at the 18th International AWS Brazing Conference, Chicago, March 25, 1987.

2.0 MATERIALS DESIGN METHODOLOGY

INTRODUCTION

This portion of the project is identified as project element 2 within the work breakdown structure (WBS). It contains three subelements: (1) Three-Dimensional Modeling, (2) Contact Interfaces, and (3) New Concepts. The subelements include macromodeling and micromodeling of ceramic microstructures, properties of static and dynamic interfaces between ceramics and between ceramics and alloys, and advanced statistical and design approaches for describing mechanical behavior and for employing ceramics in structural design.

The major objectives of research in Materials Design Methodology elements include determining analytical techniques for predicting structural ceramic mechanical behavior from mechanical properties and microstructure, tribological behavior at high temperatures, and improved methods for describing the fracture statistics of structural ceramics. Success in meeting these objectives will provide U.S. companies with methods for optimizing mechanical properties through microstructural control, for predicting and controlling interfacial bonding and minimizing interfacial friction, and for developing a properly descriptive statistical data base for their structural ceramics.

2.2 CONTACT INTERFACES

2.2.2 Dynamic Interfaces

Studies of Dynamic Contact of Ceramics and Alloys for Advanced Heat Engines

K. F. Dufrane and W. A. Glaeser (Battelle Columbus Division)

Objective/scope

The objective of the study is to develop mathematical models of the friction and wear processes of ceramic interfaces based on experimental data. The supporting experiments are to be conducted at temperatures to 650 C under reciprocating sliding conditions reproducing the loads, speeds, and environment of the ring/cylinder interface of advanced engines. The test specimens are to be carefully characterized before and after testing to provide detailed input to the model. The results are intended to provide the basis for identifying solutions to the tribology problems limiting the development of these engines.

Technical progress

Apparatus

The apparatus developed for this program uses specimens of a simple flat-on-flat geometry, which facilitates specimen procurement, finishing, and testing. The apparatus reproduces the important operating conditions of the piston/ring interface of advanced engines. The specimen configuration and loading is shown in Figure 1. The contact surface of the ring specimen is 3.2 x 19 mm. A crown with a 32 mm radius is ground on the ring specimen to insure uniform contact. The ring specimen holders are pivoted at their centers to provide self-alignment. A chamber surrounding the specimens is used to control the atmosphere and contains heating elements to control the temperature. The exhaust from a 4500 watt diesel engine is heated to the specimen temperature and passed through the chamber to provide an atmosphere similar to that of actual diesel engine service. A summary of the testing conditions is presented in Table 1.

Materials

Monolithic alpha silicon carbide, silicon nitride, and three zirconia compounds were selected for the cylinder specimens. The compositions of the materials are presented in Table 2.

Plasma-sprayed coatings of chromium carbide and chromium oxide were applied on mild steel base metal for both ring and cylinder specimens. Chromium plated ring specimens and gray cast iron cylinder specimens were used for baseline data. Monolithic ring specimens were cut from the sides of the cylinder specimens.

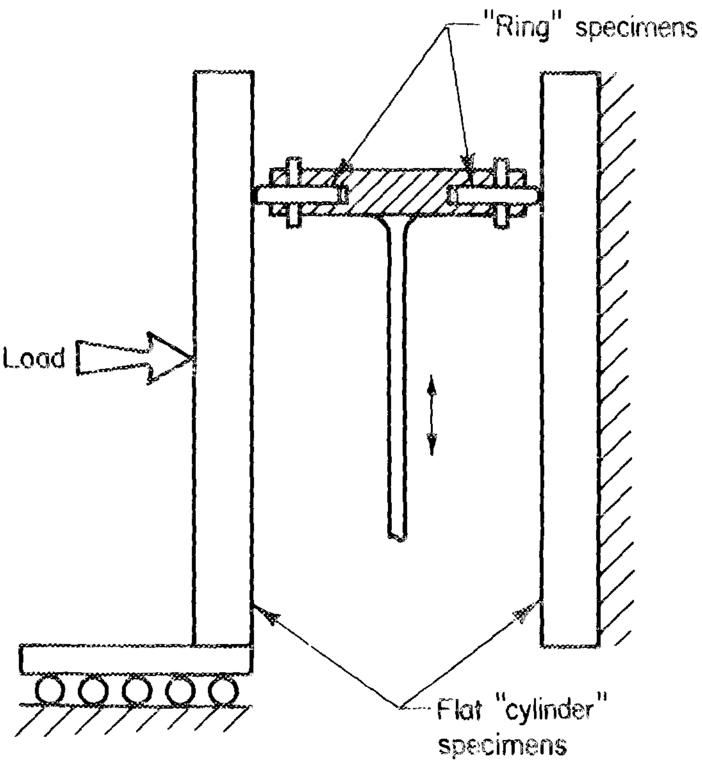

Figure 1. Test specimen configuration and loading

Wear rate studies

Earlier experiments in the program showed that ceramics in sliding contact will require lubrication for long-term sliding applications, such as the ring/cylinder interface of advanced engines. All attempts to run the five monolithic ceramics and several plasma-sprayed coatings of ceramics and metals resulted in high friction coefficients and high wear rates. Several of the material combinations responded well both to the liquid lubrication and to lubrication with powdered molybdenun disulfide. Since lubrication provided by self-lubricating processes typically have unacceptable wear rates and dry lubricants are extremely difficult to resupply reliably, liquid lubricants are of more interest for practical engines. However, the operating temperature with liquids is limited at least to some extent by the inherent thermal stability of the liquid itself. Earlier experiments established that 310 C was too high for SDL-1, a polyalphaolefin synthetic lubricant with relatively high temperature capabilities. Experiments at 260 C were more satisfactory. Therefore, a series of experiments was conducted with various material combinations at 260 C using the polyalphaolefin to measure the relative wear performance of various material combinations.

Table 1. Summary of testing conditions

Sliding Contact:	Dual flat-on-flat
"Cylinder" Specimens:	12.7 x 32 x 127 mm
"Ring" Specimens:	3.2 x 19 x 19 mm
"Ring" crown radius:	32 mm
Motion:	Reciprocating, 108 mm stroke
Speed:	500 to 1500 rpm
Load:	to 950 N
Ring Loading:	to 50 N/mm
Atmosphere:	Diesel exhaust or other gases
Measurements:	Friction and wear (after test)

Table 2. Current cylinder and ring specimens

Material	Abbreviation	Nominal Composition, Weight Percent
Magnesia Partially Stabilized Zirconia	MPSZ	3.3 % MgO 3 % HfO_2, bal ZrO_2
Yttria Partially Stabilized Zirconia (Z-191)	YPSZ	5.4 % Y_2O_3, bal ZrO_2
Alumina Transformation Toughened Zirconia	ATTZ	3.6 % Y_2O_3, 20 % Al_2O_3, bal ZrO_2
Sintered Alpha Silicon Carbide	SiC	SiC
Silicon Nitride	Si_3N_4	2 % W, 0.5 % Mg, 0.25 % Al, bal Si_3N_4
Chromium Carbide (plasma sprayed)	Cr_3C_2	20 % Cr_3C_2, 12 % Ni, 9 % W, bal Cr
Chromium Oxide (plasma sprayed)	Cr_2O_3	5 % Cr, bal Cr_2O_3
Chromium Plate	Cr	Cr
Gray Cast Iron	--	3.3 % C, 2.3 % Si, 0.7 % Mn, bal Fe

The friction and wear results of several experiments are presented in Table 3. The wear coefficients were calculated from the Archard wear equation:

$$k = \frac{3pV}{Lx},$$

where: k = wear coefficient (dimensionless),
p = hardness of wearing member,
V = wear volume,
L = applied load, and
x = sliding distance.

As a basis of comparison, the wear coefficient for an over-the-road diesel truck engine was calculated to be 5×10^{-9}, assuming an average loading of 17.5 N/mm (100 lbs/inch) and a radial chromium wear of 0.25 mm (0.01 inch) in 300,000 miles of operation. The wear coefficient of 8×10^{-8} for the chromium on cast iron in the test apparatus compares fairly well with that of actual service in that single order-of-magnitude variations in wear coefficients are not unusual. Further, the assumed average ring loading for the truck engine may be high and the higher operating speed of a truck engine would enhance the formation of hydrodynamic lubricant films. On this basis, the apparatus appears to be simulating the wear conditions of actual service in a satisfactory manner for a comparison basis.

The decrease in the lubricant capability at 260 C is reflected in the much higher wear coefficient of 1×10^{-5} measured with the chromium plated ring and a cast iron cylinder liner. The wear coefficient is clearly sensitive to the lubrication conditions for a given material combination. The best wear performance at 260 C has been obtained with self-mated Cr_2O_3 rings and Cr_2O_3 cylinder liners, which had wear coefficients of 1×10^{-6}. Similar ring wear performance was observed with both plasma sprayed and SCA-1000 drain cast Cr_2O_3 cylinder liner specimens. The performance of self-mated Si_3N_4 was somewhat higher at 3×10^{-6}. While clearly higher than the wear coefficient values measured at 100 C, wear coefficients of 10^{-6} are indicative of good sliding performance with the lubricant/materials systems. Wear coefficients of 10^{-5} and 10^{-4}, measured on the remaining examples in Table 3, are well beyond the acceptable range for practical piston ring applications.

These results are consistent with the reported low-heat-rejection engine results in that plasma-sprayed coatings of Cr_2O_3 have shown good performance at elevated operating temperatures relative to that of chromium plated rings or monolithic YPSZ rings. The results also indicate the need for lubricants with higher temperature capabilities to permit raising the operating temperature.

Inspection of Worn Ring Surfaces

The worn ring surfaces of Cr_2O_3 and Si_3N_4 were examined by scanning electron microscopy (SEM) to relate the wear process to the measured wear rates. As shown in Figure 2, the surfaces of the Cr_2O_3 ring specimens were quite rough on a microscale, even though they displayed the lowest wear coefficient of all the materials at 260 C. The surface features had a

Table 3. Comparison of Approximate Ring Wear Coefficients

Ring Material	Cylinder Material	Lubricant	Temperature, C	Ring Loading, N/mm	Friction Coefficient	Ring Wear Coefficient
Cr	Cast Iron	SAE 30	100	17.5	--	5×10^{-9}*
Cr	Cast Iron	SDL-1	100	12.3	0.03 - 0.04	8×10^{-8}
Cr_2O_3	Cr_2O_3	SDL-1	260	13.4	0.05 - 0.08	1×10^{-6}
Si_3N_4	Si_3N_4	SDL-1	260	12.3	0.05 - 0.06	3×10^{-6}
Cr	Cast Iron	SDL-1	260	15.7	0.07 - 0.1	1×10^{-5}
Cr_3C_2	Cr_2O_3	SDL-1	260	14.0	0.13	2×10^{-5}
Cr	Si_3N_4	SDL-1	260	12.3	0.14	1×10^{-4}
Cr	YPSZ	SDL-1	260	12.3	0.2 - 0.3	1×10^{-4}
YPSZ	YPSZ	SAE 10	20	12.3	0.13 - 0.16	2×10^{-4}
YPSZ	YPSZ	None	540	12.3	0.3 - 0.6	8×10^{-4}

* Typical actual diesel truck engine experience

general orientation in the direction of sliding and showed widespread evidence of local smearing, Figure 2a. At higher magnification, Figure 2b, the surface texture is suggestive of build-ups, possibly of wear debris and lubricant decomposition products. Local chemical attack may also be playing a role in forming the depressed areas. Fine abrasive scratches are visible locally, as would be expected. In view of the very low wear rates experienced by the Cr_2O_3, the surface texture would represent an equilibrium condition after high sliding distances. At the measured average wear rate, the sliding associated with four revolutions of the engine would be required to remove one atom layer from the surface. The surface texture observed was therefore the result of thousands of sliding cycles.

In contrast with the Cr_2O_3 surfaces, the Si_3N_4 ring surface consisted of bands of very smooth and roughened regions generally aligned with the sliding direction, Figure 3. At higher magnification, Figure 4a, the roughened bands consisted of widespread local fractures, which apparently released the near-surface material. Between the rough bands, the surface was highly polished, Figure 4b. Shallow abrasion scratches were present, as expected, but the general surface was indicative of a very mild polishing wear process.

The striking differences in surface texture between the Si_3N_4 and Cr_2O_3 ring surfaces suggest that the material chemistry may be playing an important role in the wear process. Both materials had relatively low wear rates, but different wear mechanisms were apparent. The highly polished areas on the Si_3N_4 are expected in low-wear-rate components. The roughened, microfractured areas are undesirable and a probable source of abrasive debris. The irregular surface on the Cr_2O_3 suggests that a smooth polished surface is not a requirement for low-wear-rate performance. Further examinations will be performed to provide more detailed information on the associated wear mechanisms.

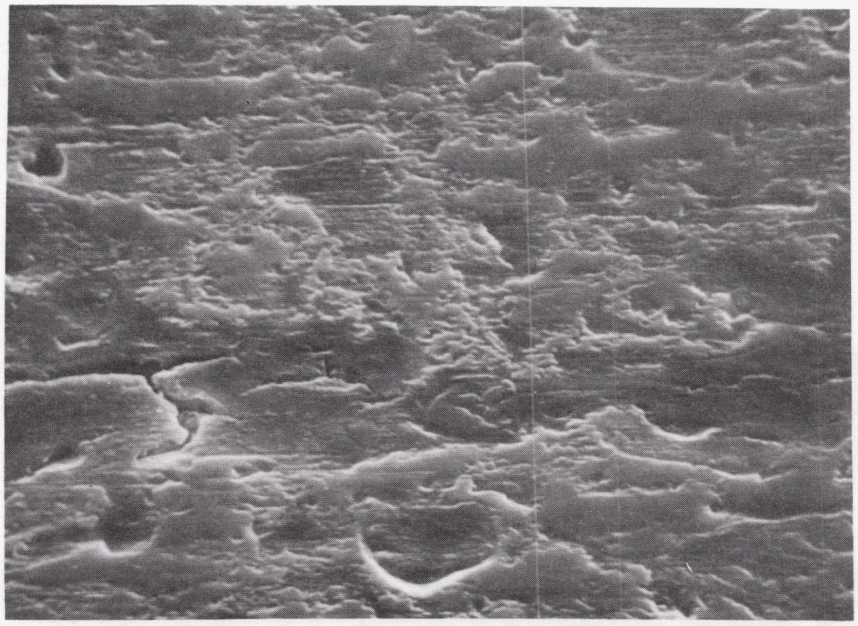

71327 2500X

a. Varying general roughness

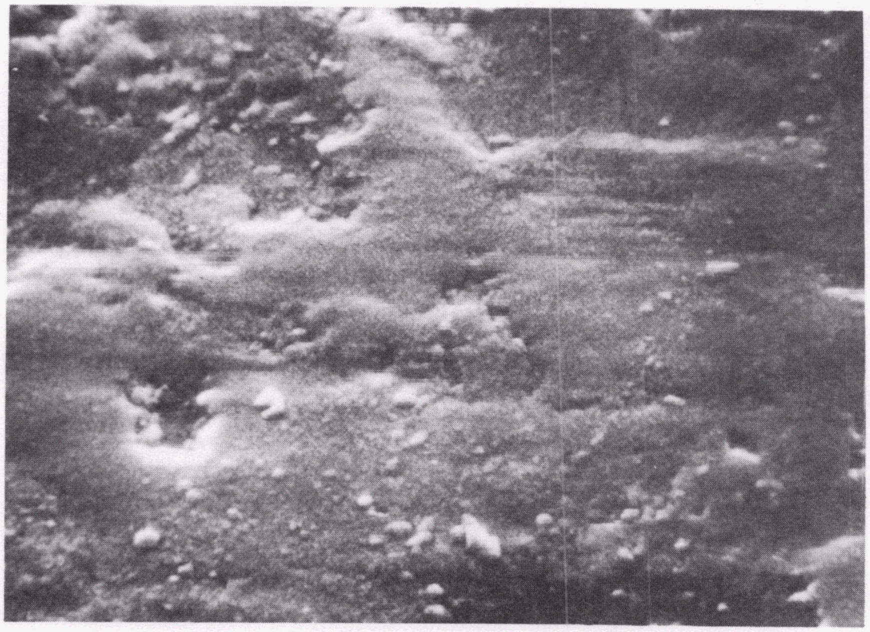

71348 20,000X

b. Details of relatively smooth area

Figure 2. Worn surface of Cr_2O_3 ring specimen after 12 hours of running

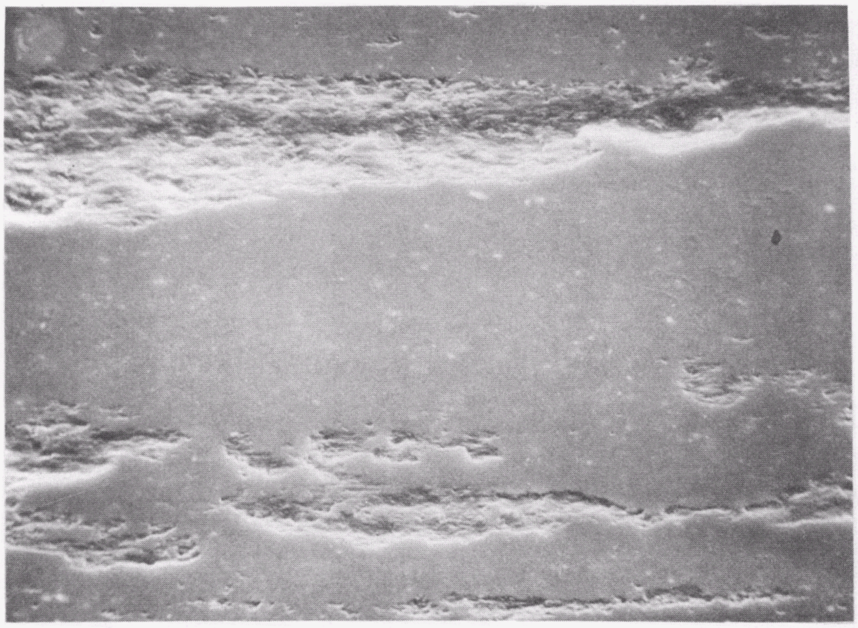

71318 1000X

Figure 3. Varying bands of smooth and roughened areas on worn Si_3N_4 ring surface

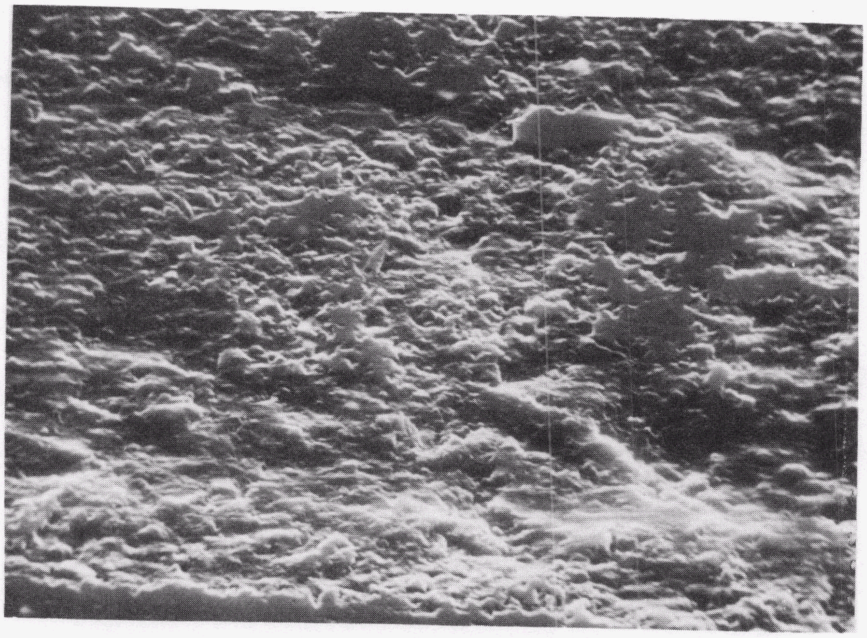

71320 2500X

a. Roughened area

71321 2500X

Smooth area

Figure 4. Detail of worn Si_3N_4 ring surface

Status of Milestones

The program is progressing in accordance with the milestone schedule.

Publications

K. F. Dufrane and W. A. Glaeser, "Dynamic Contact of Ceramics", presented at the *Contractor's Coordination Meeting in Dearborn, Michigan on October 30, 1986*. Submitted to SAE for publication.

K. F. Dufrane and W. A. Glaeser, "Performance of Ceramics in Ring/Cylinder Applications", *SAE paper 870416, 1987.*

2.3 NEW CONCEPTS

Advanced Statistics

W. P. Eatherly (Oak Ridge National Laboratory)

Objective/scope

The failure of brittle materials caused by flaw fields is generally treated quite satisfactorily by the use of Weibull statistics. The application of Weibull statistics is limited by lack of distributions for related functions such as tolerance limits and is generally restricted to low values of the Weibull exponent. The present effort under this program has been directed toward determining the higher moments of the Weibull distribution for any m-value and exploring these for goodness-of-fit tests.

Technical progress

Two reports are being prepared for publication. The first of these, the calculation of interpolation formulas for the Γ-function to ten significant figures, is relatively simple. The second represents the computation of the higher moments of the Weibull distribution in asymptotic form.

Extended table of the gamma function

The importance of the Γ-function to the statistics of brittle materials lies in the fact that, to the extent Weibull statistics apply, their characteristics are expressed as functions of the Γ-function. These functions depend on differences between Γ-functions that, at least for the moments of the distribution, rapidly approach zero. A ten-place table of Γ-functions appears to be sufficient to give good values of skewness up to a Weibull exponent value of $m \approx 50$, but it will give good values of kurtosis only up to $m \approx 20$.

The best table of Γ-functions I have found is in the National Bureau of Standards compilation. This ten-place table suffers, however, from too coarse a grid for the independent variable [i.e., an interval of 0.005 in x for $\Gamma(x)$]. The table may be tested for internal consistency by means of successive differences, and these become "rough" at the fourth difference. This roughness presumably arises from rounding the values of $\Gamma(x)$ back to ten places. If the interpolation of the table is performed directly from the tabulated values of $\Gamma(x)$, errors quickly move into the ninth place, and propagate into the third place when the fourth moment is calculated at $m = 20$. Thus, the accuracy of our earlier tables for the first four moments calculated directly from $\Gamma(x)$ has been overstated.

Interpolated values of $\Gamma(x)$ can be brought back to an accuracy of ±1 in the tenth place by smoothing the fourth difference. In practical terms, this simply means the interpolation formulas need not pass through the tabulated values but only pass in their neighborhood, that neighborhood being defined by the requirement that the tabulated value is rounded back to ten places.

The calculation of the interpolation formulas is essentially complete and will be issued soon as a document. Recalculation of the moments is trivial but has not yet been done.

Asymptotic equations for the higher moments of the Weibull distribution

As has been previously reported, equations for the moments of the Weibull distribution have been developed in asymptotic form to permit accurate calculation of the skewness and kurtosis for m values greater than 20. These equations take the form

$$\frac{\mu_n}{\theta^n} = \sum_{i=n}^{\infty} c_{ni}\, z^i \quad ,$$

where

$$z = \frac{1}{m}$$

and θ is the Weibull scale parameter. The coefficients c_{ni} are rather complicated finite series involving the Riemann zeta function and have been evaluated up to $i = 8$. A comparison of the numerical values from the asymptotic formulas and the direct calculation from the Γ-functions yielded a simple remainder formula:

$$\frac{\mu_n}{\theta^n} = \sum_{i=n}^{k} c_{ni}\, z^i + \frac{\hat{c}_{nk}\, z^{k+1}}{1 + 2\,z} \quad ,$$

where the remainder term is given by

$$\lim_{k\to\infty} \hat{c}_{nk} = n \quad .$$

With $k = 8$, the remainder term becomes negligible (less than one point in 10^6) at $m = 25$ for the second moment and at $m \approx 50$ for the third and fourth moments.

We have been totally frustrated in our attempts to derive the existence of this remainder formula. This is due to the complexity of the coefficients c_{ni} and the lack of ability to find any provably dominant terms within their finite series expressions. We have temporarily abandoned the attempt and will report the results of the calculations justifying the use of the remainder term on the basis of inspection only.

Status of milestones

The technical work for milestone 1.a (table of Γ-function) has been completed, and the table will be issued in July 1987.

Publications

None.

References

1. "Handbook of Mathematical Functions With Formulas, Graphics, and Mathematical Tables", Appl. Math. Ser. 55, Abramowitz and I. Stegun (eds.), p. 267, U.S. Department of Commerce, National Bureau of Standards, U.S. Government Printing Office, Washington, D.C. 20402.

Advanced Statistical Concepts of Fracture in Brittle Materials

C. A. Johnson and W. T. Tucker (General Electric Corporate Research and Development)

Objective/scope

The design and application of reliable load-bearing structural components from ceramics requires a detailed understanding of the statistical nature of fracture in brittle materials. The overall objective of this program is to advance the current understanding of fracture statistics, especially in the following three areas:

- Optimum testing plans and data analysis techniques.
- Consequences of time-dependent crack growth on the evolution of initial strength distributions.
- Confidence and tolerance bounds on predictions that use the Weibull distribution function.

The studies are being carried out largely by analytical and computer simulation techniques. Actual fracture data are then used as appropriate to confirm and demonstrate the resulting data analysis techniques.

Technical progress

During this reporting period, two milestones were completed and three others initiated. Results related to the completed milestones will be emphasized in this report. The first milestone (231303) studied the effects of sub-critical crack growth on the evolution of initial strength distributions, primarily using models such as power-law crack growth and Weibull strength distributions. The second milestone (231304) involved the derivation of confidence and tolerance bounds on predicted strengths using the Weibull distribution. The following two sections describe work related to these two milestones.

1. Evolution of Strength Distributions During Slow Crack Growth

The previous semi-annual report (1) summarized the effects of subcritical crack growth (SCG) on initial strength distributions during dynamic fatigue (constant-loading-rate) testing, using the crack growth relationship:

$$v = A K^{n} \tag{1}$$

and a Weibull distribution for the initial strength distribution. It was shown that progressively slower loading rates (longer times to failure) would not only result in lower failure strengths but would also result in less variability in strength (higher m value) than that of the initial (inert) distribution of strengths. At extremely slow loading rates the initially Weibull distribution of strengths was found to asymptotically return to a Weibull distribution, but with a higher m value of:

$$m_{slow} = m_{inert}\ (n+1)/(n-2) \qquad (2)$$

Since the previous semi-annual report, the study has been extended to include static fatigue (constant stress) testing and some preliminary consideration of exponential crack growth models.

Figure 1 was generated using power law crack growth according to Equation 1, and illustrates the relative behavior of static and dynamic fatigue on a material with an inert strength of approximately 650 MPa and a strength degradation exponent, n, of 5. The relationship describing time to failure in static fatigue as a function of applied stress can be derived by integrating Equation 1 in a similar manner to the integration of the dynamic fatigue loading schedule shown in earlier reports. The resulting time to failure in static fatigue is:

$$t_{static} = \left(\frac{2}{n-2}\right)\left(\frac{K_c^{\ 2}}{AY^2}\right)\left(\frac{\sigma_i^{\ n-2} - \sigma_f^{\ n-2}}{\sigma_f^{\ n}}\right) \qquad (3)$$

and can be related to the time to failure in dynamic fatigue by the following simple relationship:

$$t_{static} = t_{dynamic}/(n+1) \qquad (4)$$

The two curves on Figure 1 are therefore identical in shape and simply shifted in time by a factor of n+1. As in the case of dynamic fatigue, the static fatigue behavior asymptotically approaches a straight line relationship at low stresses and long times to failure, where the slope of the straight line is -1/n.

Figure 2 illustrates the effects of strength variability on static fatigue behavior by using a family of nine curves representing the 10, 20, through 90 percentile behaviors of a Weibull distribution (where the initial strengths have a Weibull modulus of 5). The lowest curve, for instance, represents the behavior of specimens with an initial strength equal to the 10 percentile behavior of the distribution (approximately 450 MPa for this choice of parameters). As for the case of dynamic fatigue, the family of curves on Figure 2 are identical in shape but displaced relative to each other. The displacement is not vertical but, rather, is along a line with a slope of -1/2.

In static fatigue testing, there is no variability in failure stress since the stress is held constant throughout each test and constant from specimen to specimen within a series of tests. Instead, the specimen to specimen strength variability is transformed into variability of the

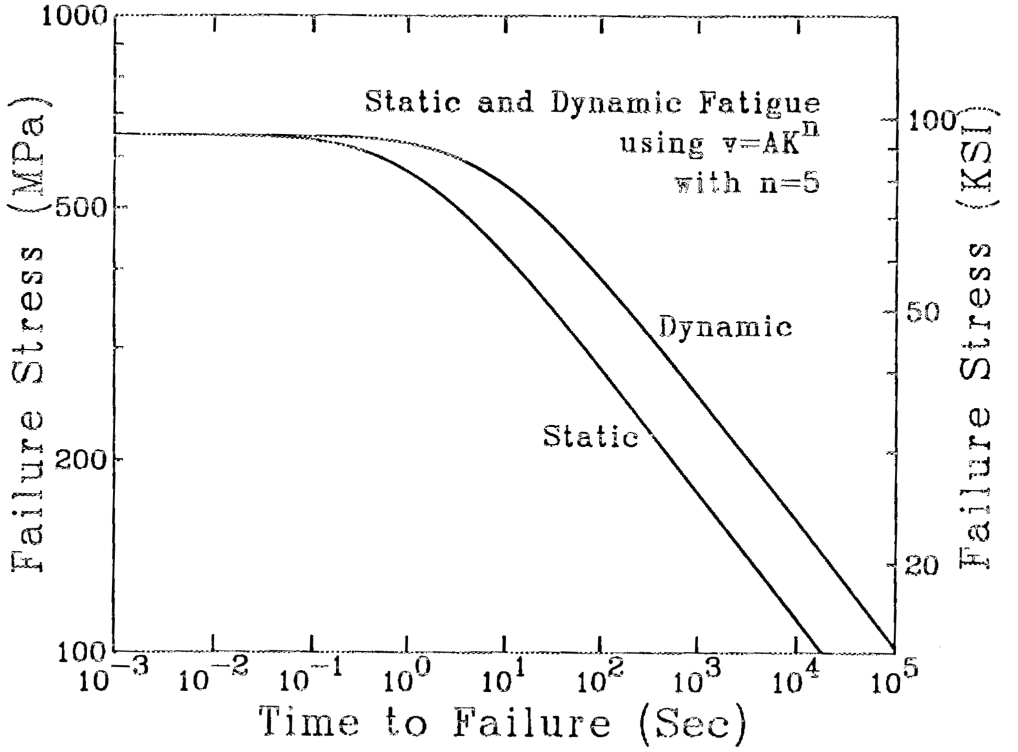

FIGURE 1: Comparison of static and dynamic fatigue behavior for power-law crack growth.

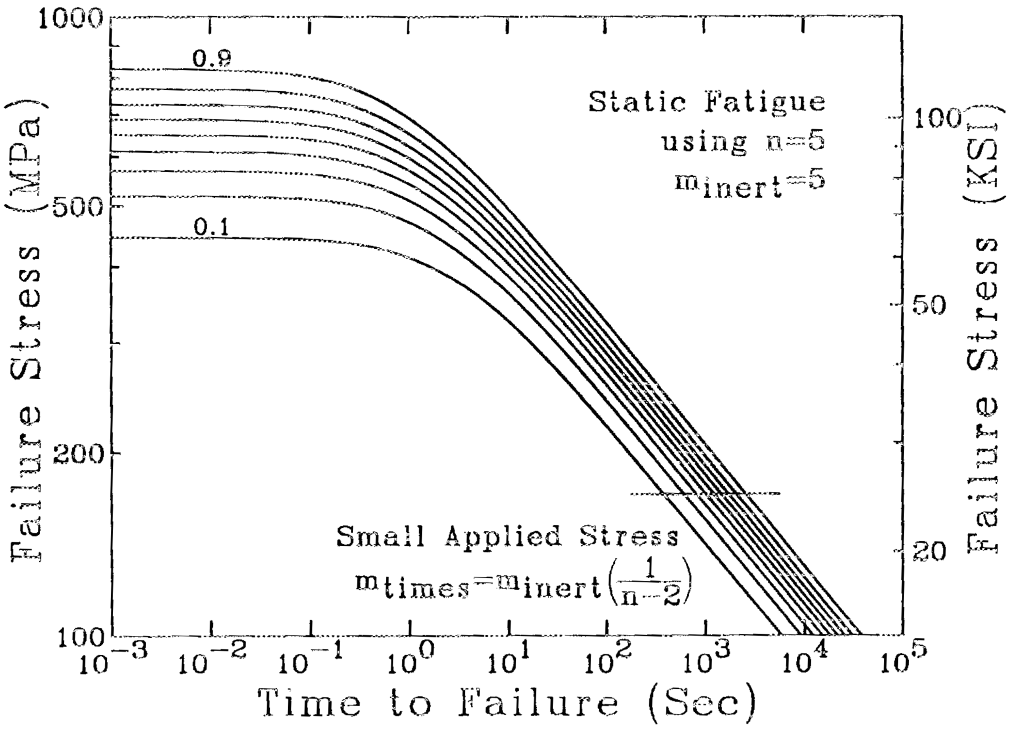

FIGURE 2: Static fatigue behavior for a family of inert strengths.

observed times to failure. The distribution of times to failure in static fatigue testing can be predicted on Figure 2 by the intersections of the family of static fatigue curves with a horizontal line at the applied stress. An example is included on Figure 2 at a stress of approximately 170 MPa.

For the case of crack growth according to Equation 1 with small applied stresses (such that failure occurs in the asymptotic region for each specimen) and with a distribution of inert strengths that is Weibull, it can be shown both graphically and by derivation that the distribution of times to failure in static fatigue is also Weibull in form. The Weibull modulus of times to failure at low stresses and long failure times is related to the Weibull modulus of the inert strengths as follows:

$$m_{\text{times}} = m_{\text{inert}}/(n-2) \qquad (5)$$

Therefore, the modulus of times to failure is generally much smaller than that for inert strengths. In fact, since typical strength degradation exponents are of the same order as typical Weibull moduli (5 to 30), the resulting Weibull modulus for times to failure in static fatigue should often be near unity.

A Weibull modulus of unity results in the exponential distribution which has the special feature that the time rate of failures is constant and independent of time. That is, if half the specimens fail in the first hour, then half the remaining specimens would be expected to fail in the next hour, and so forth. (This "half-life" description has obvious similarities to radioactive decay which is also described by the exponential distribution.)

The Weibull modulus of times to failure can be either greater or less than unity, but the rate of failure has different characteristics in the two regimes. When m of the failure times is greater than unity, the rate of failure is continuously increasing. That is, if half of the specimens failed in the first hour, then more than half of the remaining specimens should be expected to fail in the next hour. Conversely, when m is less than unity, the rate of failure is continuously decreasing such that in the above material, less than half of the remaining specimens should fail in the second hour.

In addition to power-law crack growth according to Equation 1, some preliminary consideration was given to the modification of initial strength distributions by exponential crack growth relationships of the following three forms:

$$v = A\ K/K_c \exp\ (nK/K_c) \qquad (6a)$$

$$v = A \exp\ (nK/K_c) \qquad (6b)$$

$$v = A\ K_c/K \exp\ (nK/K_c) \qquad (6c)$$

These three forms plus power-law crack growth were compared by Trantina in the analysis of high temperature static and dynamic fatigue of hot-pressed silicon nitride (2). In that study, Trantina found that the exponential forms were superior to power-law in fitting the observed behavior, and that the three exponential forms were virtually indistinguishable from each other within the range of observed times to failure.

Consideration of the exponential crack growth relationships of Equation 6 in the current study has revealed a disturbing characteristic common to all three. When plotted as Figure 2 for either dynamic or static fatigue, the exponential forms do not asymptotically approach a straight line but rather are always concave downward. When a family of curves representing a distribution of initial strengths are superimposed on one figure, the curves intersect at long times to failure. The net effect of the intersections is to invert the population of strengths. That is, the specimen with the highest inert strength will have the lowest strength at long times to failure, and vice versa. This inversion is permissible in a mathematical sense, but intuitively seems to violate some physical constraints. It is hoped that work can continue to further understand this characteristic of exponential crack growth relationships.

2. Confidence and Tolerance Bounds

Problems involving confidence and tolerance bounds on estimates of strengths can be categorized according to the type of loading and the presence or absence of size scaling. The following four cases will be considered:

- Uniform tensile stress and single specimen size
- Uniform tensile stress and multiple specimen sizes
- Common load factor (k) and multiple specimen sizes
- Differing load factors and multiple specimen sizes

In each of these cases it is assumed that the Weibull distribution with a size or volume term adequately describes the strength to failure:

$$P = 1 - e^{-\int(\sigma/\sigma_o)^m dV} \tag{7}$$

where P is the cumulative probability of failure, dV is the differential volume under a constant stress state, σ is the magnitude of that stress (at failure), m is the Weibull modulus, and σ_o is a normalizing parameter. Furthermore, it is assumed that the integral in Equation 7 can be evaluated to the form:

$$P = 1 - e^{-kV(\sigma_{max}/\sigma_o)^m} \tag{8}$$

where k is a dimensionless "load factor" describing the uniformity of the applied stress and σ_{max} is the maximum stress in the structure at the time of failure. For the case of uniform uniaxial tension (k=1), Equation 8 reduces to the form of the Weibull distribution commonly encountered in the statistical literature. Equation 8 is used in the following development of confidence and tolerance bounds.

The next four sub-sections discuss each of the four categories of confidence/tolerance problems listed above.

2.1 Uniform Tensile Stress and Single Specimen Size

This is the most straightforward of the four cases because there are no complications either from non-uniform stresses or from size scaling. Conversely, this is the least useful of the four because very few practical problems in design with brittle materials fit within the constraints of pure tension and no size scaling. However, these constraints reduce the problem to one that has been treated in the statistical literature for other problems that use the Weibull distribution. We refer to the books by Lawless (3), Mann, Schafer, and Singpurwalla (4), and Nelson (5), as well as the annotated bibliography of statistical confidence procedures for life data given in an earlier semiannual report (6).

2.2 Uniform Tensile Stress and Multiple Specimen Sizes

For this situation, the stress state is simple (k=1) but, at the very least, the test specimen and the component of interest differ in size. Suppose that the test specimens are denoted by unprimed quantities and the component structures are denoted by primed quantities. Let σ_p denote the quantile at p where $0 < p < 1$ and suppose we desire a confidence interval on $\sigma_{p'}$, with p′ a "usual" value of 0.01, 0.05, or 0.10. We now set σ_p equal to $\sigma_{p'}$, and employ Equation 8 in transforming the two quantiles at the two different volumes. This is done most simply by solving Equation 8 for $\ln(\sigma)$ and equating $\ln(\sigma_p)$ to $\ln(\sigma_{p'})$. After simple algebraic manipulation we obtain:

$$P = 1 - (1 - P')^{V/V'} \qquad (9)$$

In short we are finding a confidence interval on the quantile (actually a tolerance interval) at volume V that equals the desired quantile at volume V′. Thus, Equation 9 is useful in obtaining tolerance limits for component parts based on data taken on test specimens since the desired quantile at P′ for the component volume is equivalent, via Equation 9, to a quantile at the test conditions. Moreover, it is clear from inspection of Equation 9 that quantiles at more than two volumes can be transformed to a single volume so that more than one testing condition can be studied.

Furthermore, perusal of Equation 9 shows that the usual tabled values of P′, 0.01, 0.05, 0.10, are not adequate to obtain limits for any reasonable range of values of V and V′. Moreover, these tabled results are insufficient for test and design purposes. However, results of

Lawless (7) can be employed to overcome these difficulties. (We do not advocate use of the usual asymptotic normal theory methods since it is well known that these methods may require large sample sizes of the order of 100 or more.) The Lawless approach is a conditional one and requires integration of a conditional likelihood function in order to obtain the desired confidence limits. As a result of this, the Lawless method has not received wide usage. But, theoretical results on likelihood inference (see, for example, Hinkley (8)) show, at least for location-scale families, an exact relationship between the likelihood ratio method and the kernel of the likelihood function. Thus, the likelihood ratio method just gives a numerical approximation to the Lawless approach and it appears that the reluctance to employ the Lawless method is somewhat unfounded. Investigation of this methodology is still underway and specific conclusions and recommendations will be made concerning the use and properties of any proposed methodology developed.

2.3 Common Load Factor and Multiple Specimen Sizes

If the load factor, k, is the same for the test specimens and component structures then Equation 9 can still be employed to transform quantiles at operating conditions to those at test conditions. (The k's cancel out in the exponent in deriving Equation 9.) Thus any methodology developed for use with a uniform load and multiple sizes is also applicable with common load factors and multiple sizes.

2.4 Differing Load Factors and Multiple Sizes

This situation is the most difficult of the four to treat since the k's in the exponent of Equation 9 do not cancel out. If the Weibull integral can be evaluated and the implicit failure model that this integral implies is valid, then, in principle, likelihood inference methods can be applied. However, due to the possible complex way in which the k's may be functions of the Weibull modulus, convergence problems may exist. In any event, if one wants to estimate quantiles at component conditions the functional dependence of the k's on the unknown m must be known and a successful estimation scheme devised. Thus, failure models are important as well as the effects of multiaxial stress states in determining a complete estimation scheme.

Status of milestones

The three milestones due to be completed at the end of the third year of the program are on schedule.

Publications

C. A. Johnson and W. T. Tucker, "Modifications in Strength Distributions Due to Slow Crack Growth," in Proceedings of 24th Automotive Technology Development Contractors' Coordination Meeting, October 29 and 30, 1986, Dearborn, Michigan.

References

1. C. A. Johnson and W. T. Tucker, "Advanced Statistical Concepts of Fracture in Brittle Materials," in Ceramic Technology for Advanced Heat Engines Project, Semi-annual Progress Report for Period April-September 1986.

2. G. G. Trantina,"Strength and Life Prediction for Hot-Pressed Silicon Nitride," J. Am. Ceram. Soc., 62, 7-8, 1979.

3. J. F. Lawless, Statistical Models and Methods for Lifetime Data, John Wiley & Sons, New York, 1982.

4. N. R. Mann, R. E. Schafer, and N. D. Singpurwalla, Methods for Statistical Analysis of Reliability and Life Data, John Wiley & Sons, New York, 1974.

5. W. Nelson, Applied Life Data Analysis, John Wiley & Sons, New York, 1982.

6. C. A. Johnson and W. T. Tucker, "Advanced Statistical Concepts of Fracture in Brittle Materials," in Ceramic Technology for Advanced Heat Engines Project, Semi-annual Progress Report for Period October 1985-March 1986.

7. J. F. Lawless, "Construction of Tolerance Bounds for the Extreme-Value and Weibull Distributions," Technometrics, 17, 255-61, 1975.

8. D. V. Hinkley, "Likelihood Inference About Location and Scale Parameters," Biometrika, 65, 253-61, 1978.

3.0 DATA BASE AND LIFE PREDICTION

INTRODUCTION

This portion of the project is identified as project element 3 within the work breakdown structure (WBS). It contains five subelements, including (1) Structural Qualification, (2) Time-Dependent Behavior, (3) Environmental Effects, (4) Fracture Mechanics, and (5) Nondestructive Evaluation (NDE) Development. Research conducted during this period includes activities in subelements (1), (2), and (3). Work in the Structural Qualification subelement includes proof testing, correlations with NDE results and microstructure, and application to components. Work in the Time-Dependent Behavior subelement includes studies of fatigue and creep in structural ceramics at high temperatures. Research in the Environmental Effects subelement includes study of the long-term effects of oxidation, corrosion, and erosion on the mechanical properties and microstructures of structural ceramics.

The research content of the Data Base and Life Prediction project element includes (1) experimental life testing and microstructural analysis of Si_3N_4 and SiC ceramics, (2) time-temperature strength dependence of Si_3N_4 ceramics, and (3) static fatigue behavior of PSZ ceramics.

Major objectives of research in the Data Base and Life Prediction project element are understanding and application of predictive models for structural ceramic mechanical reliability, measurement techniques for long-term mechanical property behavior in structural ceramics, and physical understanding of time-dependent mechanical failure. Success in meeting these objectives will provide U.S. companies with the tools needed for accurately predicting the mechanical reliability of ceramic heat engine components, including the effects of applied stress, time, temperature, and atmosphere on the critical ceramic properties.

3.1 STRUCTURAL QUALIFICATION

Microstructural Analysis of Corrosive Reactions in Structural Ceramics

B. J. Hockey and S. M. Wiederhorn (National Bureau of Standards)

Objective/scope

The objective of this part of the program is to identify mechanisms of failure in structural ceramics subjected to mechanical loads in various environments. Of particular interest is the damage that accumulates in structural ceramics as a consequence of high temperature exposure to the environments and stresses normally present in heat engines.

Recent studies of high temperature failure of the non-oxide ceramics intended for use in heat engines indicate that for long term usage, damage accumulation will be the primary cause of specimen failure. Mechanical defects, even if present in these materials, are healed or removed by high temperature exposure so that the original defects have little influence on long term lifetime at elevated temperature. In this situation, lifetime can be determined by characterizing the nature of the damage and rate of damage accumulation in the material at elevated temperatures. In most structural ceramics of current interest, the fine grain size and chemical complexity of the microstructure precludes the use of routine characterization methods. Hence, there is a clear need for analytical transmission electron microscopy studies as an adjunct to the mechnical testing of these materials for high temperature applications.

In this project, the creep and creep-rupture behavior of several ceramic materials will be correlated with microstructural damage that occurs as a function of creep strain and rupture time. Materials to be studied include: sialons; hot-pressed silicon nitride; and sintered silicon carbide. This project will be coordinated with WBS 3.4.1.3, Tensile Creep Testing, with the ultimate goal of developing a test methodology for assuring the reliability of structural ceramics for high temperature applications.

In addition to the above, investigations of the microstructure of experimental batches of structural ceramics and composites will be conducted on a service basis for other projects included in the heat engine program. Characterization will be conducted by use of scanning and transmission microscopy to identify the phases present and the microstructural characteristics of these materials.

Technical progress

During the past six months the microstructure of as-received siliconized silicon carbide (SOHIO KX01) was compared with the microstructure of material that had been deformed at high temperatures in either flexure or tension. In flexural specimens, figure 1, the microstructure of the compressive side of the bend specimens was very similar to that of the as-received specimen. The material consisted of an interconnected network of silicon apparently wetting the surfaces of all grains of silicon carbide. This microstructure contrasts sharply with that from the tensile surface of the same specimens, figure 2, in which cavities have opened in the silicon phase of the composite material. Near the tensile surface, figure 2a, the cavities appear as small crack-like features within the narrowest of grain boundaries. As these grow, they arrest at the large pools of silicon that surround the carbide grains. Deeper within the material, figure 2b, the cavities are isolated, randomly distributed, and are much larger than those at the surface. This difference in the appearance of the cavities can be attributed in part to the triaxial nature of the stresses deeper within the flexure bar. Near the surface, plain stress conditions are primarily responsible for the growth of the cavities, whereas below the surface, where constraints on the flow are greater because of the absence of a free surface to relax stresses normal to the surface, plain stress conditions drive cavity growth. In the latter state of stress, cavities tend to open wider and to be more rounded in shape, as can be seen in figure 2b.

The origin of these cavities can be viewed in much greater detail by viewing the narrow interphases of silicon by transmission electron microscopy. Figure 3 shows a photomicrograph of a wide interphase boundary of silicon separating two grains of silicon carbide in material that has been deformed in tension to approximately 0.5 percent strain. Despite this strain, and despite the fact that deformation occurs only through the silicon phase, there is little evidence of dislocation generation within the silicon phase. This absence of significant dislocation densities is probably the result of recrystallization and migration of the dislocations responsible for deformation to the silicon/silicon carbide interface. A further observations is the cleanliness of the interface. In all our studies, there was little evidence of impurities or precipitates at these wide boundaries. Finally, the silicon phase formed relatively large single crystals that bonded the silicon carbide grains together. Aside from the twin boundary that is readily apparent in the silicon phase, the remainder of the intergranular silicon in figure 3 is a single crystal of silicon.

In contrast to the morphology just discussed for the wider silicon interphase boundaries, the narrower boundaries found between many of the silicon carbide grains (usually located in agglomerates Fig. 1) contain a wide variety of impurities and inclusions. In figure 4 for example, both iron-rich and calcium-rich inclusions are present in the silicon phase along this narrow grain boundary region. More generally, Ti-V-rich impurity inclusions are also found within grain boundaries of similar width. As these impurities both lower the melting point of the silicon and reduce the surface tension of the silicon/silicon carbide interface, they possibly provide a choice location within the solid for cavity nucleation. In addition, pre-existing cavities are often found near or within these narrow boundaries. As expected, examination of these boundaries show them to be sites for cavity nucleation and growth, figure 5. Apparently cavities generated within these boundaries are sufficiently narrow as to preclude their observation by optical microscopy. It is not until the cavity has spread apart as a consequence further deformation that they become visible optically. In the coming months, a model for the nucleation and growth of these cavities will be developed, to further explain the effect of these cavities on both the creep rate and the failure process.

Status of milestones

To date, all milestones have been met or are on target. We are in the process of analyzing the damage that accumulates in siliconized silicon carbide as a consequence of creep (Milestone 311101) and will be presenting a talk on the subject at the Annual Meeting of the American Ceramic Society on April 28.

Publications

None

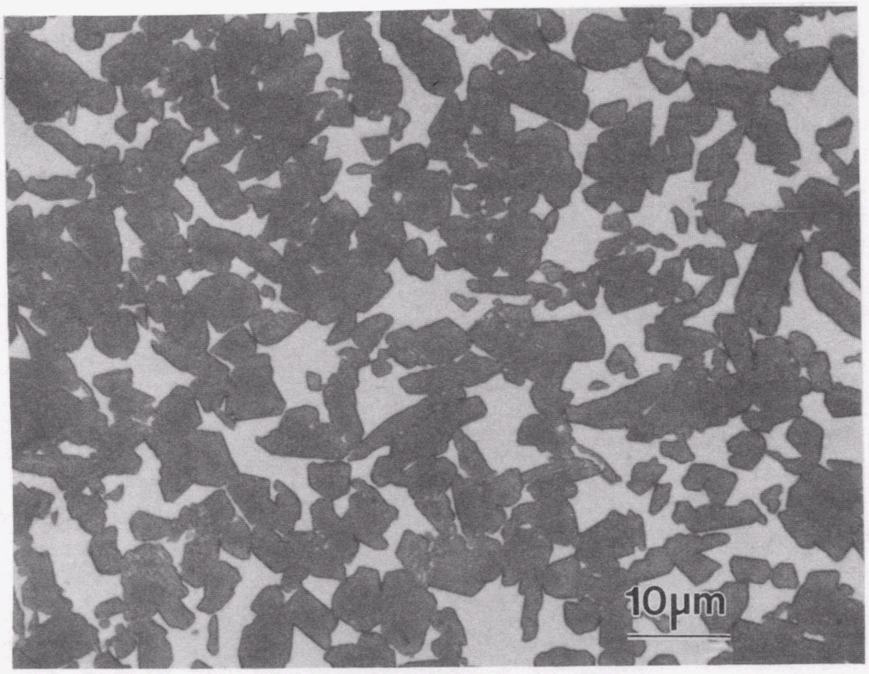

Fig. 1. Optical micrograph from compressive region of sample deformed in bending at 1300°C. Microstructure, consisting of SiC grains (dark areas) and intergranular silicon phase (lighter areas), is identical to that of as-received material.

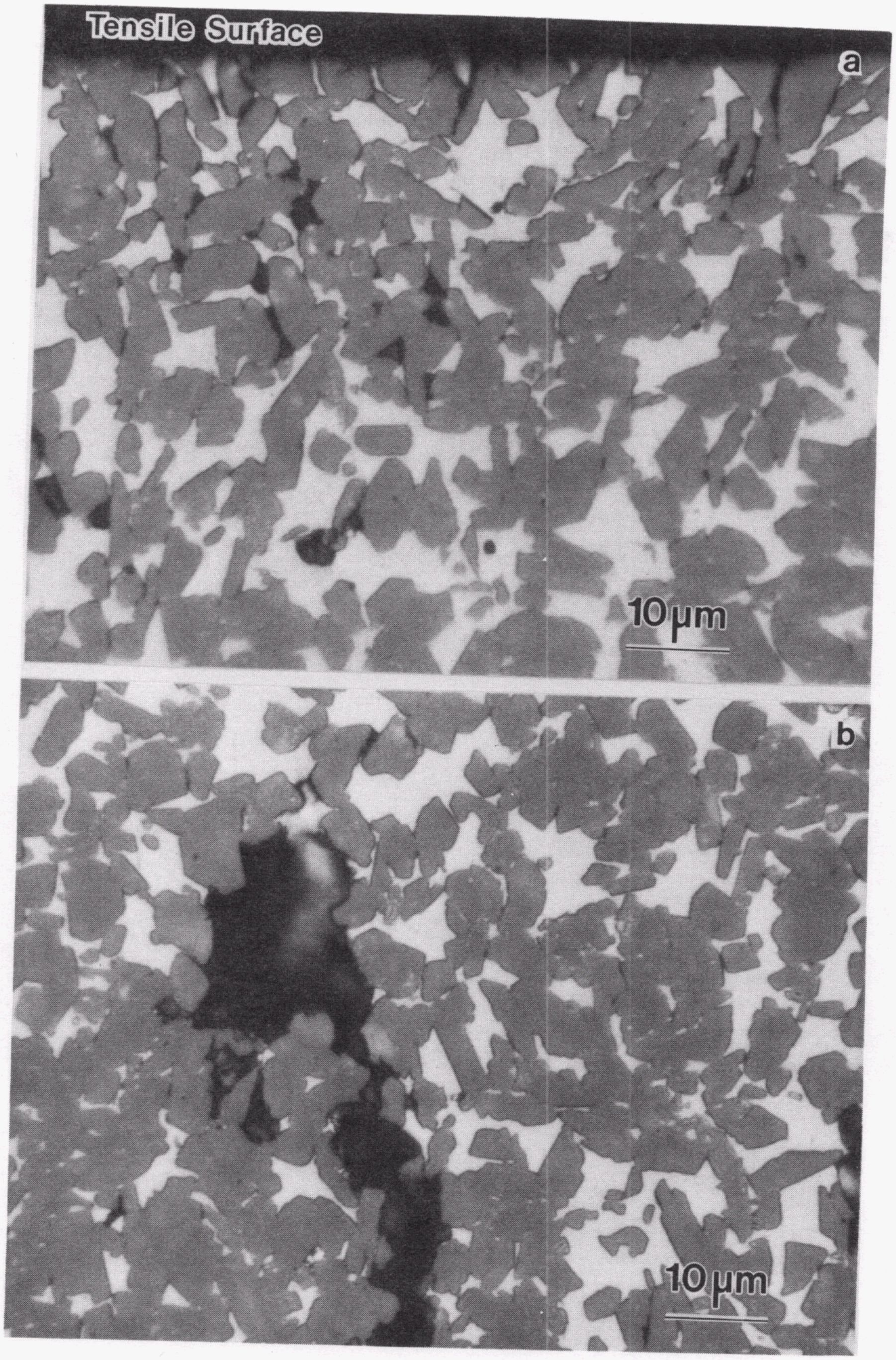

Fig. 2. a) Cross-sectional view from tensile region of bend sample after creep at 1300°C. Note cavities (black areas) formed within intergranular Si phase. Near tensile surface, cavities form predominantly at narrow grain boundaries.
b) Similar view from same creep sample but at greater depth (≈ 100-200 μm) below tensile surface. Note increased size of cavities.

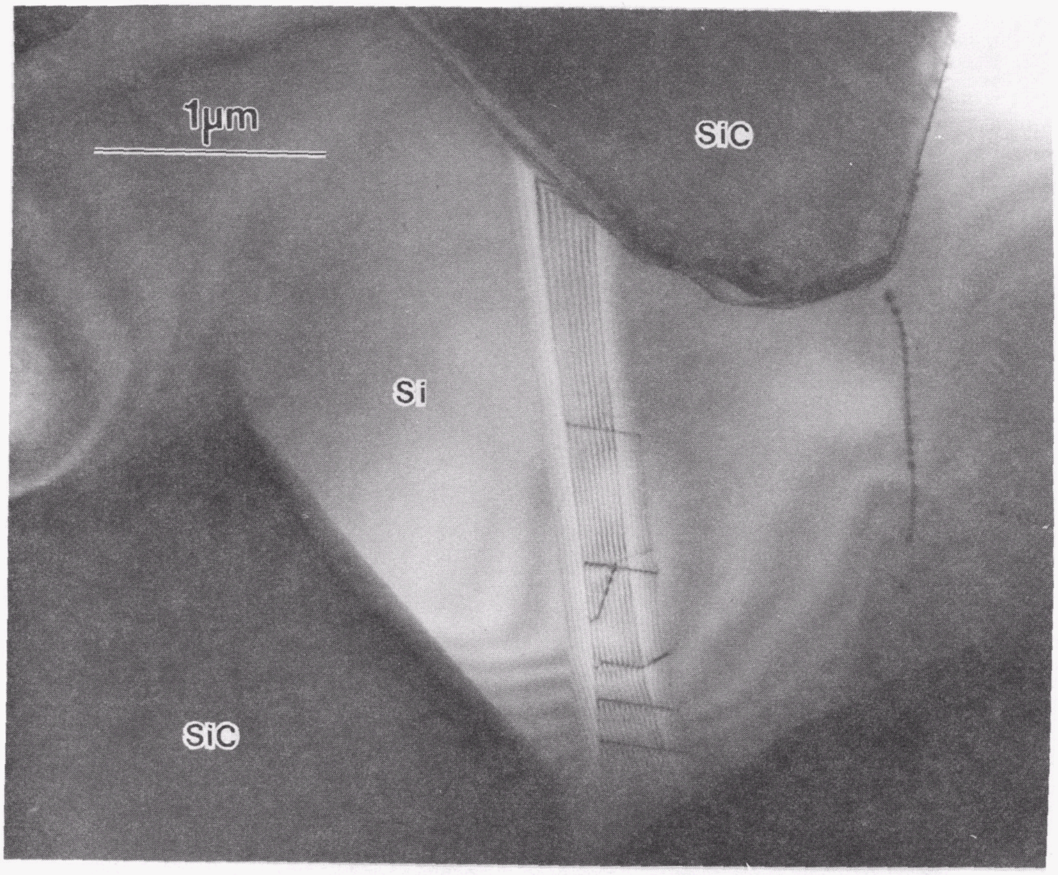

Fig. 3. Intergranular silicon phase located between widely separated SiC grains. Sample deformed in tension at 1300°C. With exception of twin and minor dislocation content, the silicon phase within such large regions is relatively unchanged after high temperature deformation.

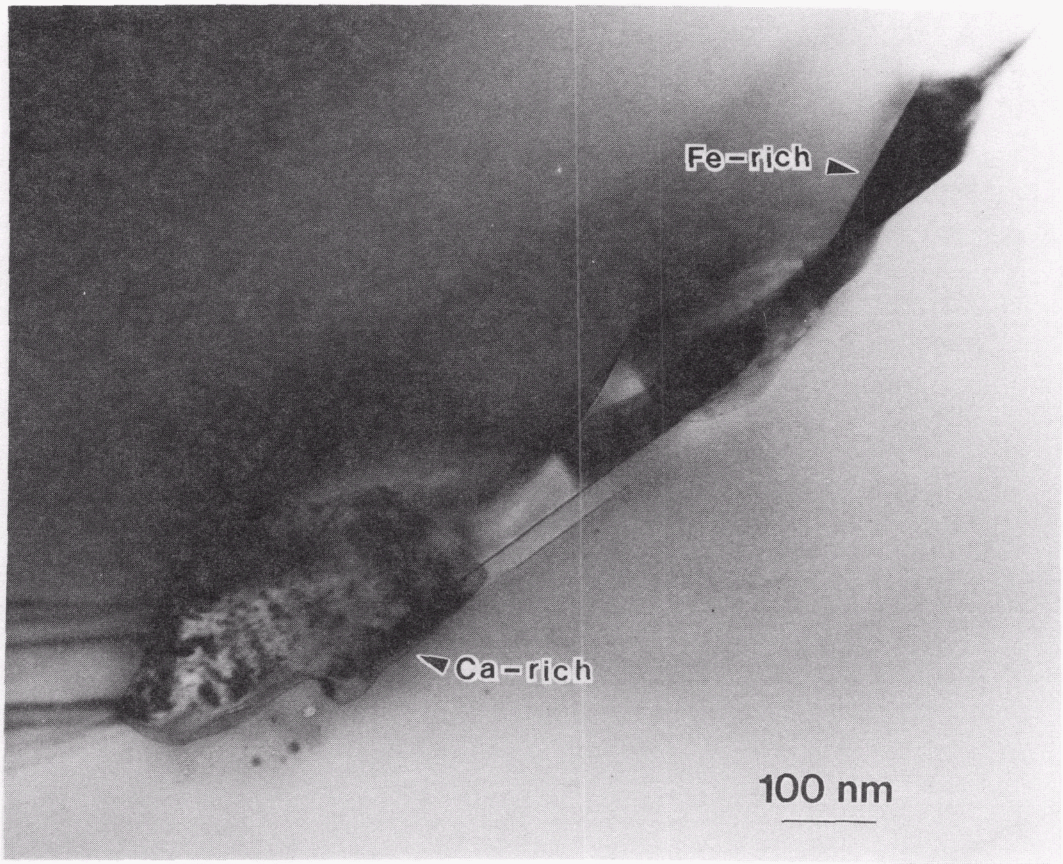

Fig. 4. Narrow interface region separating adjacent SiC grains. Impurities within intergranular Si phase are typically segregated to similar, narrow grain boundary regions. In this case, both Ca-rich and Fe-rich inclusions are present.

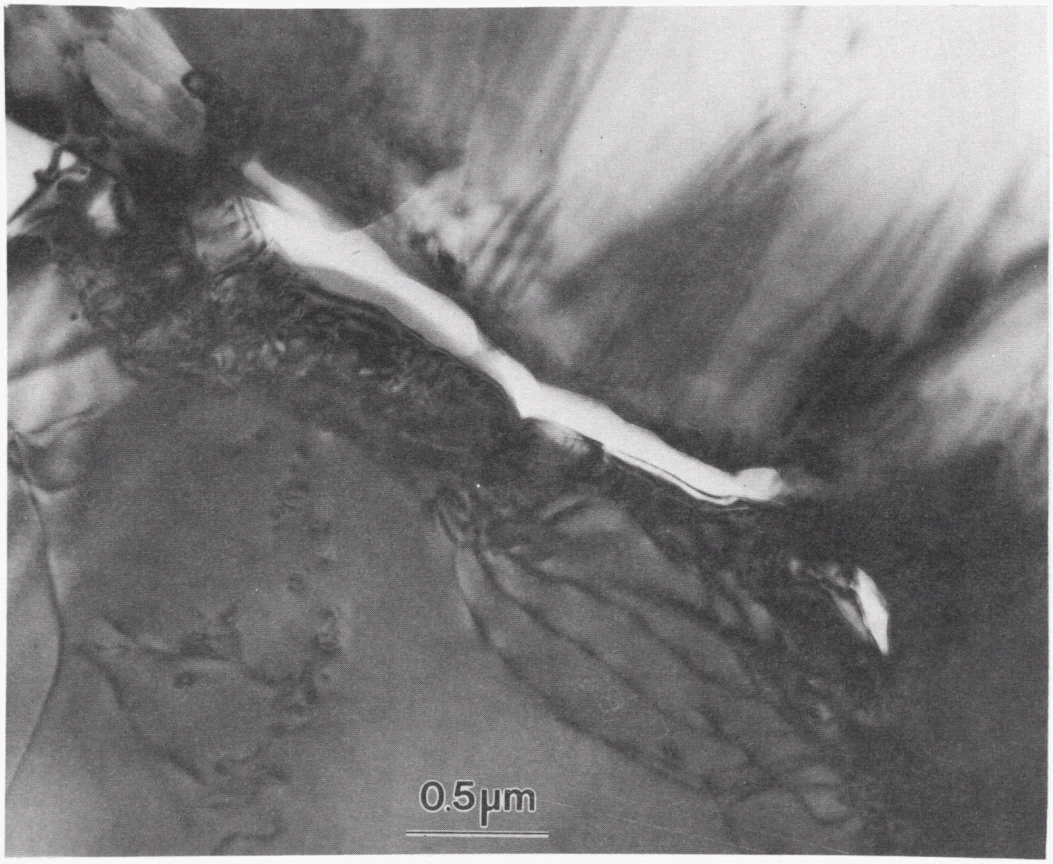

Fig. 5. Cavitated grain boundary region in sample deformed in tension at 1300°C. Depletion of Si phase from narrow grain boundary regions appears to represent initial stage in formation of creep cracks.

Physical Properties of Structural Ceramics

R. K. Williams and R. S. Graves (Oak Ridge National Laboratory)

Objective/scope

The structural ceramics presently considered for use in advanced heat engine applications usually contain more than one phase and several components. The thermal conductivities of these materials are low relative to metals, and this, along with thermal expansion plus fracture strength and toughness, is a prime factor in determining suitability of a given ceramic for a particular advanced engine component. The purpose of this research is to develop an improved understanding of the factors that determine the thermal conductivities of these complex structural materials at high temperatures.

Technical progress

The results of a study[1] of the effect of Cr_2O_3 content on the thermal conductivity of Al_2O_3 have been extrapolated to higher temperatures and compared with literature values. The Callaway equation

$$\lambda = \frac{k_B}{2\pi^2 v_s}\left(\frac{k_B T}{\frac{h}{2\pi}}\right)^3 \left\{ \int_0^{\theta_D/T} \frac{\tau_c\, x^4 e^x}{(e^x - 1)^2}\, dx + \frac{\left[\int_0^{\theta_D/T} \frac{\tau_c\, x^4 e^x}{\tau_N\, (e^x - 1)^2}\, dx\right]^2}{\int_0^{\theta_D/T} \frac{1}{\tau_N}\left(1 - \frac{\tau_c}{\tau_N}\right)\frac{x^4 e^x}{(e^x - 1)^2}\, dx} \right\} \tag{1}$$

was used to extrapolate the data to higher Cr_2O_3 contents and temperatures.[2] In this equation (1) k_B and h are Boltzmann's and Planck's constants, v_s is the velocity of sound, which can be calculated from the Debye temperature, θ_D, and τ_c is the combined relaxation time for the various scattering processes, τ_i:

$$T_c^{-1} = \sum_i \tau_i^{-1} \tag{2}$$

The parameter τ_N is the relaxation time for normal three phonon processes that do not directly generate thermal resistance but are included because they enhance the strength of phonon-point defect scattering, τ_p. The calculation assumes that the phonon-phonon scattering, τ_U, depends on composition and that grain boundary scattering anticipated for a grain size of 2 μm is present. Analysis of the lower-temperature data showed that the point defect scattering could be obtained from an equation based only on mass-difference, and that a heavy atom in a light matrix scatters less effectively than a light atom in a heavy matrix. In concentrated solutions, such as Al_2O_3-30 mol % Cr_2O_3, both effects must be included because both Al_2O_3 and Cr_2O_3 differ considerably from the average, virtual crystal masses.

The lower-temperature data and extrapolations were compared with the results of Tien et al.[3] These results, which were obtained by a comparative method, are for dense samples containing 15 vol % of a ZrO_2-based toughening phase. To obtain the thermal conductivity of the Al_2O_3 - Cr_2O_3 matrix phase, the data were adjusted via Maxwell's equation 4.

$$\lambda_c = \lambda \frac{\lambda_D + 2\lambda + 2V_D (\lambda_D - \lambda)}{\lambda_D + 2\lambda - V_D (\lambda_D - \lambda)} \quad (3)$$

In this equation, λ_c is the measured thermal conductivity of the composite, λ_D and V_D are the thermal conductivity and volume fraction of the dispersed phase, and the dispersed phase was assumed to have a thermal conductivity of 2.5 $W \cdot m^{-1} K^{-1}$. The results are shown in Fig. 1. At lower temperatures, the theory is in good agreement with the ORNL data and the Tien data[3] for the highest Cr_2O_3 content. At 400°C the theoretical extrapolation greatly exceeds the experimental values for low Cr_2O_3 contents; and the fact that the experimental value for pure Al_2O_3 is about a factor of 2 too low[5] suggests that the measurements may have been subject to some systematic experimental error.

In a later phase of this study, the role of photon energy transport is being investigated. The purpose of this study is to determine whether thermal diffusivity data adequately describe steady-state energy transport in partially transparent solids. Thermal diffusivity, specific heat, thermal conductivity, and optical property data will be compared to answer this question. Partially stabilized zirconia was chosen for this study because it is commercially available, has a low thermal conductivity, and is partially transparent. A stock of the material has been obtained and characterized and samples for a radial heat flow thermal conductivity experiment have been machined.

Status of milestones

311201 On schedule September 30, 1987

Publications

R. K. Williams, R. S. Graves, M. A. Janney, T. N. Tiegs, and D. W. Yarbrough, "The Effects of Cr_2O_3 and Fe_2O_3 Additions on the Thermal Conductivity of Al_2O_3," accepted for publication (May) in *J. Appl. Phys.*

References

1. R. K. Williams, R. S. Graves, M. A. Janney, T. N. Tiegs, and D. W. Yarbrough, "The Effects of Cr_2O_3 and Fe_2O_3 Additions on the Thermal Conductivity of Al_2O_3," accepted for publication (May) in *J. Appl. Phys.*
2. J. Callaway, *Phys. Rev.* **113**, 1046 (1959).
3. T. Y. Tien, T. K. Brog, and A. K. Li, p. 215 in *Proceedings of the 23rd Automotive Technology Development Contractors Coordination Meeting*, P-165, Soc. of Automotive Engineers, Inc., Warrendale, Pa., 1985.
4. J. M. Wimmer, H. C. Graham, and N. M. Tallan, p. 619 in *Electrical Conductivity in Ceramics and Glass, Part B*, ed. N. M. Tallan, Marcel Dekker, Inc., New York, 1974.
5. Y. S. Touloukian, R. W. Powell, C. Y. Ho, and P. G. Klemens, p. 93 in *Thermal Conductivity, Nonmetallic Solids*, IFI/Plenum, New York, 1970.

ORNL-DWG 87-1903

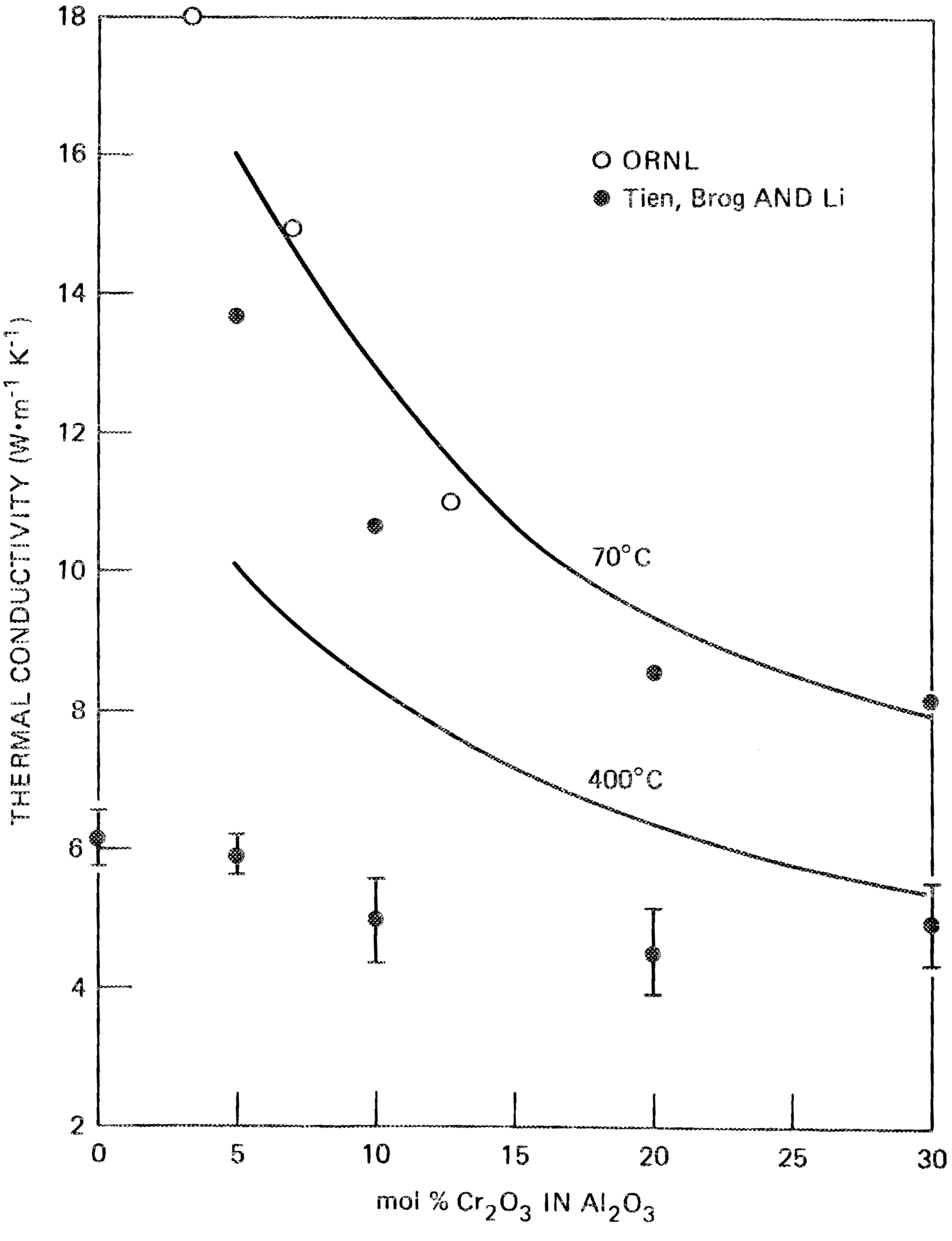

Fig. 1. Comparison of the effect of Cr_2O_3 additions on the thermal conductivity of AL_2O_3 as *(a)* obtained by extrapolating lower temperature data via Callaway's equation and *(b)* measured by Tien, Brog and Li.

Effect of Translucence of Engineering Ceramics on Heat Transfer in Diesel Engines- Syed Wahiduzzaman and Thomas Morel (Integral Technologies Incorporated)

Objective/scope

Ceramic materials are being used as thermal barrier materials, separating the engine metal substructure from the convective and radiative heat fluxes originating in the combustion gases. The heat transfer through the ceramic layer to the substructure will be increased by any translucense, which would allow a part of the radiation heat flux to pass through the barrier material. To quantify the effect of translucense of engineering ceramics on the heat transfer in diesel engines, Integral Technologies has conducted analytical studies using detailed computer codes which describe a realistic engine thermal environment including gas-to-wall heat fluxes, as well as the combined radiation/conduction heat transfer through a thermal barrier layer. A detailed parametric study was carried out in which the following parameters were varied, and their effect on heat barrier effectiveness was studied: 1) material absorption coefficient, 2) material conductivity, and 3) material thickness. An analysis of the results yielded bounds on critical properties, beyond which there is a reason for concern about this effect. Also, suggestions were made for methods to control any adverse effects.

Technical progress

The calculation of time-averaged heat fluxes and temperatures requires a time dependent heat transfer analysis of the heat transfer through the wall. Consequently, the present computational study was carried out using a one-dimensional coupled conduction-radiation heat transfer model which describes the time-dependent heat flux through a partially translucent ceramic layer backed by an opaque metallic layer.

To calculate the effects of translucence in a realistic manner, one has to represent all of the key physical processes involved. These include the transient heat conduction in the ceramic and in the substrate layer supporting it, and the heat radiation within the ceramic. The boundary conditions from the gas side describing the convection and radiation from the gases to the wall must come from a simulation of an engine operating under realistic conditions.

In the present work, the boundary conditions were supplied by the engine design analysis code IRIS, described by Morel et al.[1] This code simulates the operation of multi-cylinder engines, including the details of combustion and in-cylinder heat transfer. The convective heat transfer is calculated using a flow based model, which predicts the evolution of in-cylinder motions (swirl, squish, turbulence) as a function of crank angle in a spatially-resolved manner. The radiation heat transfer is calculated using a zonal radiation model employing a kinetics-based soot formation and burnup submodel. Both the convective and radiation heat transfer models have been validated by experiments (Morel et al,[2] Wahiduzzaman et al[3]).

properties of proposed ceramic materials should be among the properties that are measured and reported.

6. It is suggested that there may be a need to consider tailoring of ceramic properties to achieve opaqueness, as well as low conductivity and high temperature capability. Alternately, a layered approach may be considered where a three layer of opaque material is deposited on the surface to reduce the translucence of the ceramic layer.

7. The present results also provide guidance for the experimental portion of this work. They indicate the sensitivity of the heat flux to various radiative properties of the materials and thus suggest the degree of accuracy needed for their determination. The most sensitive are the absorption and scattering coefficients, while the back-scattering fraction and the refractive index are much less strong parameters in the range of values expected to cover the ceramics of interest. The reflectivity of the ceramic/substrate interface is important only if the optical thickness is very small and the ceramic is close to transparent. This knowledge is important in setting up the proposed experiments, and the data reduction scheme that will be used to deduce the radiative properties from the experiments.

Status of Milestones

All milestones have been completed.

Publications

No publications concerning this work were prepared during this period. A final report was submitted to ORNL on March 31, 1987.

References

1. T. Morel, R. Keribar, P. N. Blumberg and E. F. Fort (1986), "Examination of Key Issues in Low Heat Rejection Engines," SAE Paper 860316.

2. T. Morel, S. Wahiduzzaman, D. R. Tree and D. P. DeWitt (1987), "Effect of Speed, Load and Location on Heat Transfer in a Diesel Engine - Measurements and Predictions," SAE Paper 870154.

3. S. Wahiduzzaman, T. Morel, J. Timar and D. P. DeWitt (1987), "Experimental and Analytical Study of Heat Radiation in a Diesel Engine," SAE Paper 870571.

4. T. Morel, R. Keribar and P. N. Blumberg (1985), "Cyclical Thermal Phenomena in Engine Combustion Chamber Surfaces," SAE Paper 850360.

The transient heat conduction model used in this study is a modified version of a procedure described in Morel et al.[4] The model of heat radiation within translucent ceramic layers is based on a modified two-flux method, and is described in detail in the final report submitted recently to ORNL. For the purpose of the analysis, these models were coupled together and integrated in time in a simultaneous fashion.

Conclusions

1. A time-dependent coupled radiation/conduction model of a structural wall lined with a ceramic was developed, describing the radiation from gases penetrating into the structure, and acting there as distributed heat source. Then, a detailed parametric analysis was made in which the following parameters were varied:

    1) material radiative properties, i.e. absorption coefficient, scattering coefficient, refractive index, back scattering fraction and substrate reflectivity;
    2) material thickness; and
    3) material conductivity.

    The time dependent analysis was found to be important because of the need to represent the surface temperature swings, as well as to represent the correct phase relationships between the radiation heat flux penetrating into the ceramic and the conduction heat flux propagating at a much slower speed from the surface into the interior.

2. Translucence was found to have a significant detrimental effect on the heat barrier effectiveness under realistic diesel engine conditions. It allows the radiation heat flux to pass through the ceramic and be directly deposited on the substrate. This increases the convective heat transfer and thus the total heat flux, which can increase by 50 percent and more over the opaque case.

3. The effects of translucence depend strongly on the material absorption and scattering coefficients. Significant effects begin to be felt for absorption coefficients smaller than 10,000 m^{-1}, and scattering coefficients smaller than 20,000 m^{-1}. Above these values the ceramic is almost opaque from the point of view of the total heat flux. The above values are well within the range of expected properties of engineering ceramics.

4. An important quantity is also the barrier thermal effectiveness K/L. The lower its value, the larger the effects of translucence. It was determined, by a simplified analysis, that this dependence scales with a parameter defined as $K/L\ h_g$.

5. Significant translucence effects were found to occur within the range of radiative properties considered possible for engineering ceramics. This means that translucense is an effect that cannot be ignored in consideration of ceramic materials especially for ceramics that have very low conductivity. Thus, the radiative

3.2 TIME-DEPENDENT BEHAVIOR

Characterization of Transformation Toughened Ceramics

Jeffrey J. Swab (Army Materials Technology Laboratory)

Objective/scope

Because of their unusual combination of properties, transformation toughened zirconias (TTZ), specifically yttria tetragonal zirconia polycrystal (Y-TZP), are leading candidates for cylinder liners, piston caps, head plates, valve seats and other components for the adiabatic diesel engine. These materials are age-hardened ceramic alloy systems and as such, they are likely to be susceptible to overaging and loss of strength after long times at high temperatures (i.e., close to the age-hardening temperatures). Accordingly, a task was initiated to define the extent and magnitude of the overaging (if any) at engine operating temperatures (1000-1200°C) and the resulting impact on material performance.

It is also well known the Y-TZP's undergo a phenomenon at low temperatures (200-400°C) which leads to decreases in strength and fracture toughness and that this phenomenon is accelerated by the presence of water. As a result, a preliminary study to try and determine the effects of this phenomenon has been included in this task.

Technical progress

As indicated in previous reports the Hitachi (HIT) and Koransha "Hipped" (KH) have the best as-received room temperature strength and ability to retain that strength. As a result, additional heat treatments at 1100 and 1200°C for 500 hrs were done to determine if strength loss occurs at higher temperatures. Both materials showed no further strength loss after these treatments, Table 1.

Table 1
Strength Data for HIT and KH after Additional Heat Treatments

Material	HIT	KH
Condition		
As-Received MOR (MPa)	1169	1261
StD	265	140
500 hrs @ 1000 C MOR (MPa)	1062	1045
StD	215	89
500 hrs @ 1100 C MOR (MPa)*	1170	1135
StD	130	102
500 hrs @ 1200 C MOR (MPa)*	1098	1103
StD	74	116

* Lot Size = 15 bars

The results of the preliminary study of the effects of the low temperature treatments on these Y-TZP's indicates that this phenomenon is a problem in some but not all of the materials. The treatments at 200, 300 and 400°C w/~0.8 MPa water vapor pressure have been completed. Figure 1 shows the change in room temperature strength with treatment time. The Koransha "Sintered (KS) and NGK-Locke (NGK) showed no strength loss after these treatments and no decrease in density and MOE, Figures 2 & 3. This indicates that these companies have learned to overcome this low temperature problem. The Koransha "Hipped" (KH) showed slight degradation due to these conditions.

The Hitachi (HIT) which showed excellent strength retention after long time exposure at high temperatures (1000-1200°C) had a 68% strength loss after the treatment at 200°C. It also had strength losses after exposure to 300 and 400°C treatments. However, these losses were not a severe as the loss at 200°C. The density and MOE also showed corresponding changes in values with treatment temperature.

The Kyocera (KY) and Toshiba (TOSH) were included in these tests but none of the KY bend bars survived the 300 and 400°C treatments. None of the TOSH bend bars survived <u>any</u> of the treatments. These TZP's did not survive due to excessive macrocracking of the bend bar surface, Figure 4.

Due to a lack of material the AC Sparkplug (AC) TZP was not included in all the tests.

Status of milestones

The final draft of the in-house technical report, authored by Lise Schioler, on the work done for the first three years has been edited and corrections made. It is now in the Technical Reports section of MTL.

Room temperature flexural strength (MOR) on as-received and heat treated bend bars has been completed, but fracture toughness (Klc) will be delayed.

Publications

None.

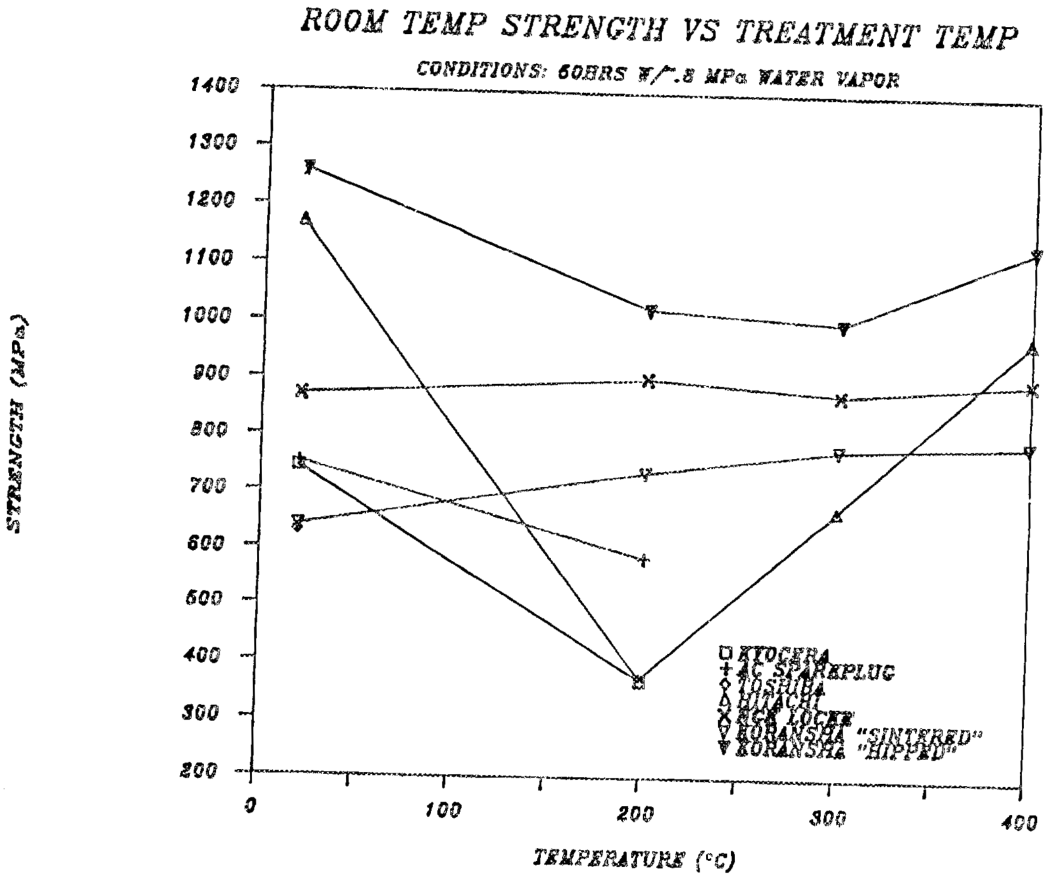
ROOM TEMP STRENGTH VS TREATMENT TEMP
CONDITIONS: 60HRS W/~.8 MPa WATER VAPOR
STRENGTH (MPa)
1400
1300
1200
1100
1000
900
800
700
600
500
400
300
200
0
100
200
300
400
TEMPERATURE (°C)
□ KYOCERA
+ AC SPARKPLUG
◇ TOSHIBA
△ HITACHI
X NGK LOCKE
▽ KORANSHA "SINTERED"
▼ KORANSHA "HIPPED"

Figure 1.

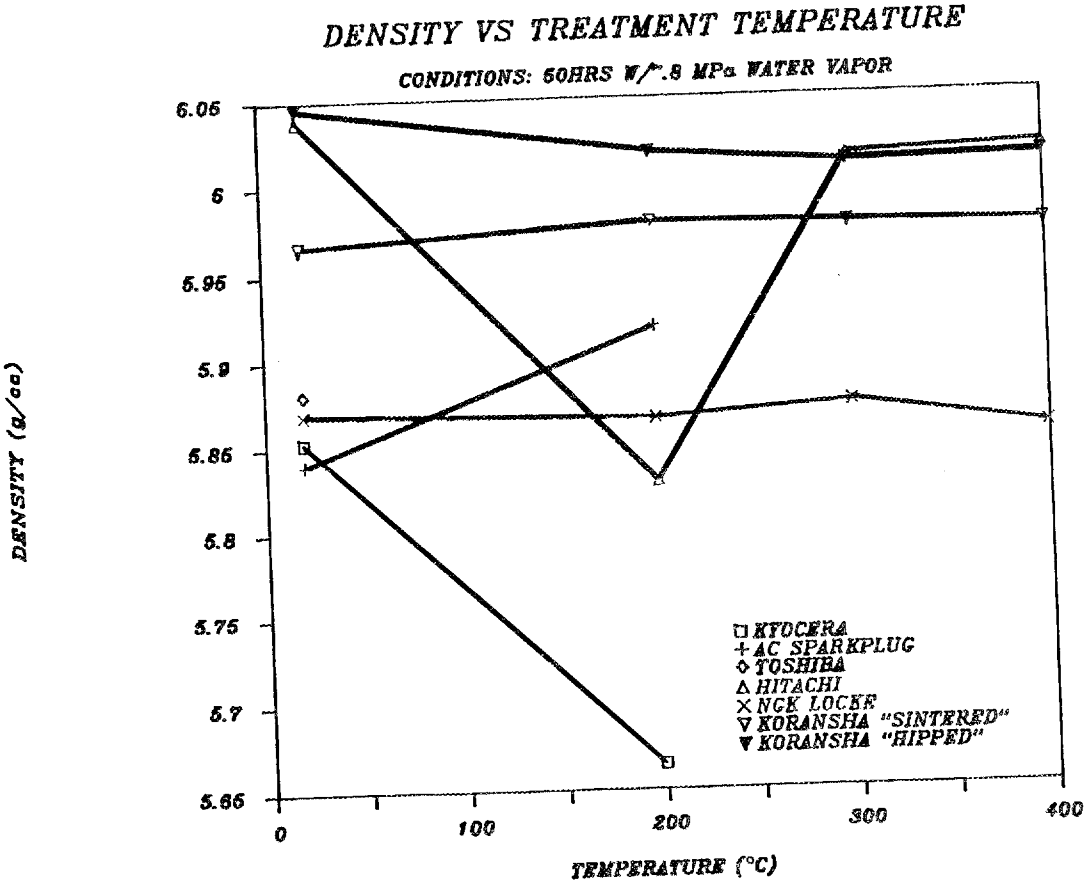
DENSITY VS TREATMENT TEMPERATURE
CONDITIONS: 50HRS W/.8 MPa WATER VAPOR
DENSITY (g/cc)
6.05
6
5.95
5.9
5.85
5.8
5.75
5.7
5.65
0
100
200
300
400
TEMPERATURE (°C)
□ KYOCERA
+ AC SPARKPLUG
◇ TOSHIBA
△ HITACHI
× NGK LOCKE
▽ KORANSHA "SINTERED"
▼ KORANSHA "HIPPED"

Figure 2.

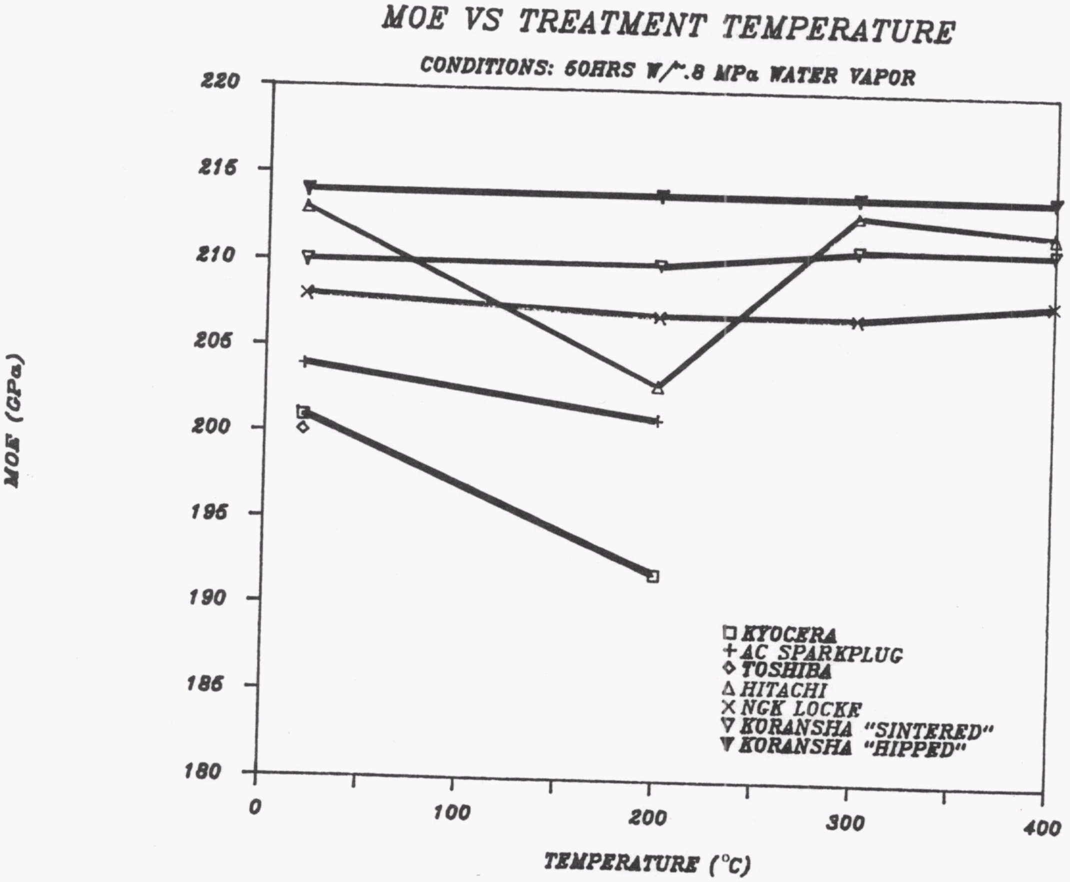

Figure 3.

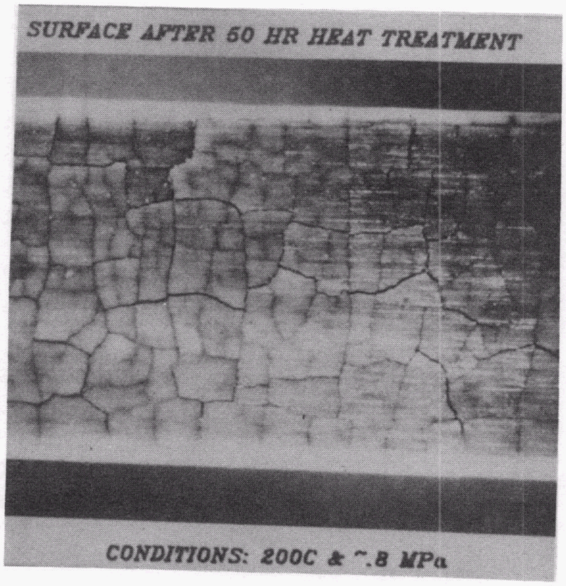

Figure 4.

Fracture Behavior of Toughened Ceramics

P. F. Becher and W. H. Warwick (Oak Ridge National Laboratory)

Objective/scope

Because of their excellent toughness, oxide ceramics such as partially stabilized zirconia (PSZ), dispersion-toughened alumina (DTA), and whisker-reinforced ceramics are prime candidates for many diesel engine components. The enhanced toughness of the PSZ and DTA materials is thought to be due to a stress-induced transformation (of the dispersed tetragonal ZrO_2 phase) that requires additional energy for catastrophic fracture to occur. However, these materials are still susceptible to slow crack growth and thus strength degradation. Also there is limited evidence that at temperatures above 700°C, time-dependent aging effects can reduce the concentration of the phase involved in the transformation process, leading to significant losses in toughness and strength. It is essential that mechanisms responsible for both the slow crack growth and aging behavior be well understood. Similarly the toughening behavior in whisker-reinforced ceramics and their high-temperature performance must be evaluated in order to develop materials for particular applications.

In response to these needs, studies have been initiated to examine toughening and fatigue properties of transformation-toughened and whisker-reinforced materials. Particular emphasis has been placed on understanding the effect of microstructure on processes responsible for time-dependent variations in toughness and high-temperature strength. In addition, fundamental insight into the slow crack growth behavior associated with these materials is being obtained.

Technical progress

The oxidation of SiC to SiO_2, the SiO_2-Al_2O_3 reaction couple can result in the formation of alumino-silicate glasses at ~1250°C and at sufficient time and temperature to the formation of mullites.[1,2] The formation of such glasses during the oxidation of SiC whisker-reinforced aluminas at elevated temperatures can be expected to influence the mechanical behavior of such composites. For example, Jakus et al.[3] have shown that alumina containing extensive (~8 vol %) glass phase exhibits creep-generated damage in the form of cracks at temperatures as low as 1000°C. On the other hand, recent studies indicate that the SiC whisker-reinforced alumina composites exhibit much lower creep rates at 1550°C in air than do comparable aluminas without the whiskers.[4] However, the presence of even localized impurities and glass phase can precipitate creep-induced damage in alumina and influence strengths at elevated temperatures.[5] As discussed by Wiederhorn, ceramics, especially SiC and Si_3N_4, can exhibit a range of response to high-temperature exposure in air under an applied stress.[6] In the early stages, strengthening may occur due to crack healing or blunting, while in the later stages, strength degradation via slow crack growth or creep damage generation can be observed.

Hot-pressed samples, 99+% of theoretical density, were machined to produce flexure bars. The flexure bars were prepared by surface grinding in a direction parallel to the length of the bars using a 180-220 grit diamond resinoid bonded wheel. The edges of all flexure bars were chamfered using a 6-micron polishing lap. The flexure bars (2.5 x 2.9 x >20 mm) were fractured using four-point loading with inner and outer span lengths of 6.35 and 19.05 mm at a stressing rate of 50 MPa/s. In these tests (the interrupted fatigue tests), flexure samples were heated to the desired temperature, a fixed stress applied (2/3 or 1/2 the fracture stress at the desired temperature) for a selected time period, and then the sample was fracture at that temperature.

The retained strengths increase with exposure for times up to 1000 h at temperatures of 800, 1000, and 1100°C (Fig. 1). At 1100°C, the retained strengths increase initially and then appear to remain more or less constant with increasing exposure time. However, at 1000 and 800°C, the retained strengths continuously increase with exposure time. These observations are consistent with strengthening by crack blunting.

At 1200°C, the composites exhibit considerable strength degradation with increasing exposure time whether subjected to an applied stress of 1/2 or 2/3 of the fracture strength at this temperature (Fig. 2). Optical microscopy analysis of the test samples reveals that crack nucleation and growth had occurred during the 1200°C testing within the maximum tensile stress region on the tensile surfaces. The extent of crack generation and growth increased with exposure time when the applied stress equaled 1/2 the fracture stress. Inspection of all the 1200°C test bars revealed that they had plastically deformed. A subsequent sample that was loaded to 1/2 the fracture stress for 192 h at 1200°C in air and then unloaded and cooled to 22°C exhibited a maximum permanent strain of 0.57%, based on its radius of curvature, and a creep strain rate of $\sim 8 \times 10^{-9}$ s^{-1}. As in the case of the fractured samples, the tensile surface of this sample contained numerous large cracks within the constant (maximum) tensile stress region. Similar crack generation was also observed in those samples subjected to an applied stress equal to 2/3 the fracture stress at 1200°C. These observations are comparable to the creep damage observed in alumina ceramics containing 8 vol % glass phase.[3] The composite thus exhibits strength degradation at 1200°C with and without an applied stress as a result of crack nucleation and growth induced by creep.

Studies of the rate of oxidation of the alumina-20 vol % SiC whisker-reinforced composites, as determined by weight change as a function of time, reveal a substantial increase in oxidation rates with increase in temperature. For example, for exposure times of under 100 hours, the oxidation rate at 1200°C is 10- to 15-fold greater than that at 1000°C, which is 2- to 4-fold greater than that at 800°C.[7] The substantial increase in oxidation rates (due to the SiC-oxygen reaction) at 1200°C coincides with the loss in fracture strength in the composites.

As seen by the lack of creep effects at 1100°C and below, one concludes that the viscosity of the glassy phase must be sufficiently decreased at 1200°C and above to allow the glassy phase to penetrate along the matrix grain boundaries and promote grain boundary creep, which leads then to crack generation. Observations of the fracture toughness samples tested at ≥1200°C support this conclusion. These studies revealed that transgranular fracture is the predominant fracture mode along the original indent crack in the composites tested at 1200°C.

ORNL-DWG 86-17106

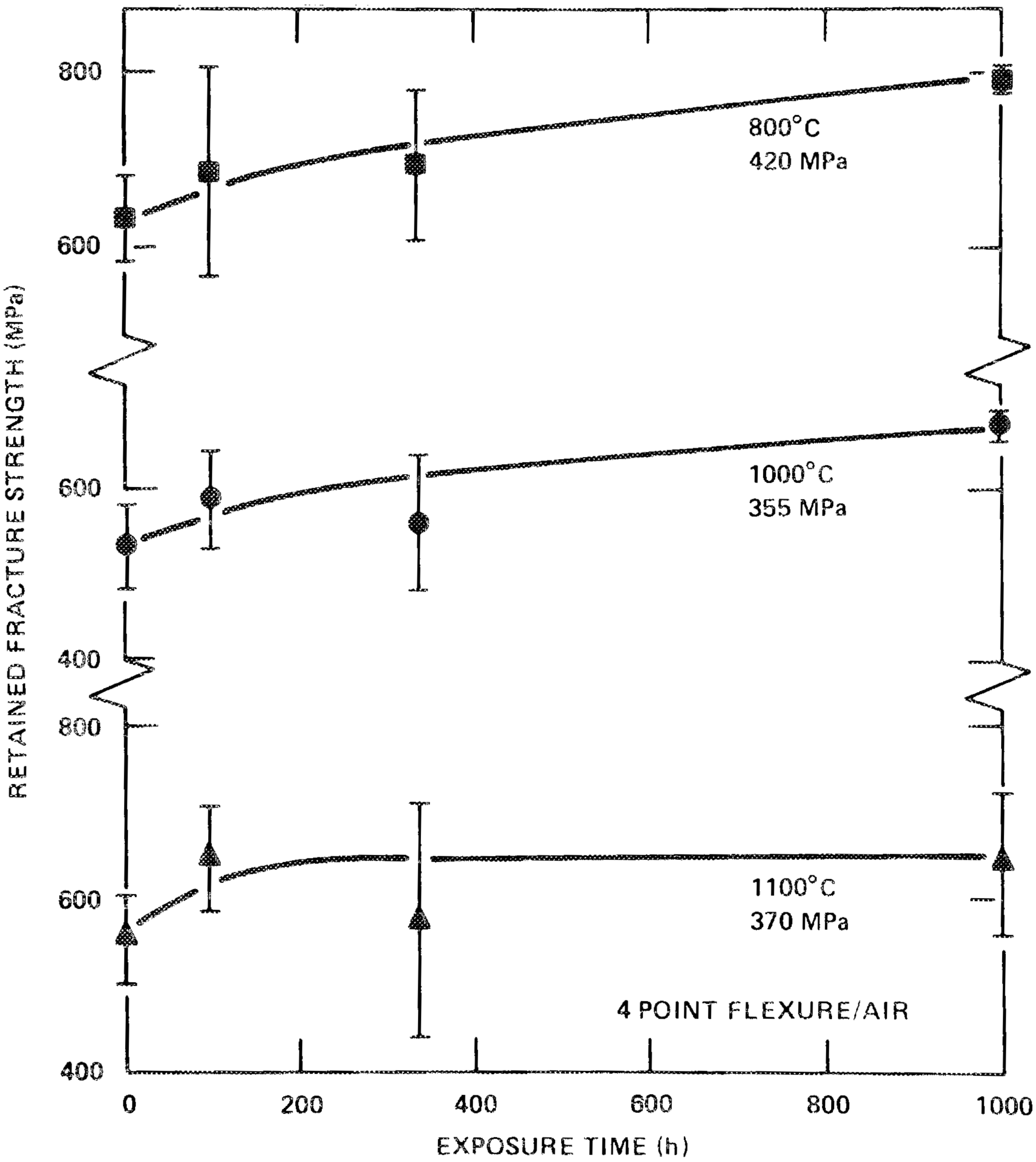

Fig. 1. The retained strength at temperature increases after exposure for various times for samples subjected to an applied stress at 800, 1000, and 1100°C. Note that at each test temperature the applied stress level is 2/3 of the fracture strength at that temperature.

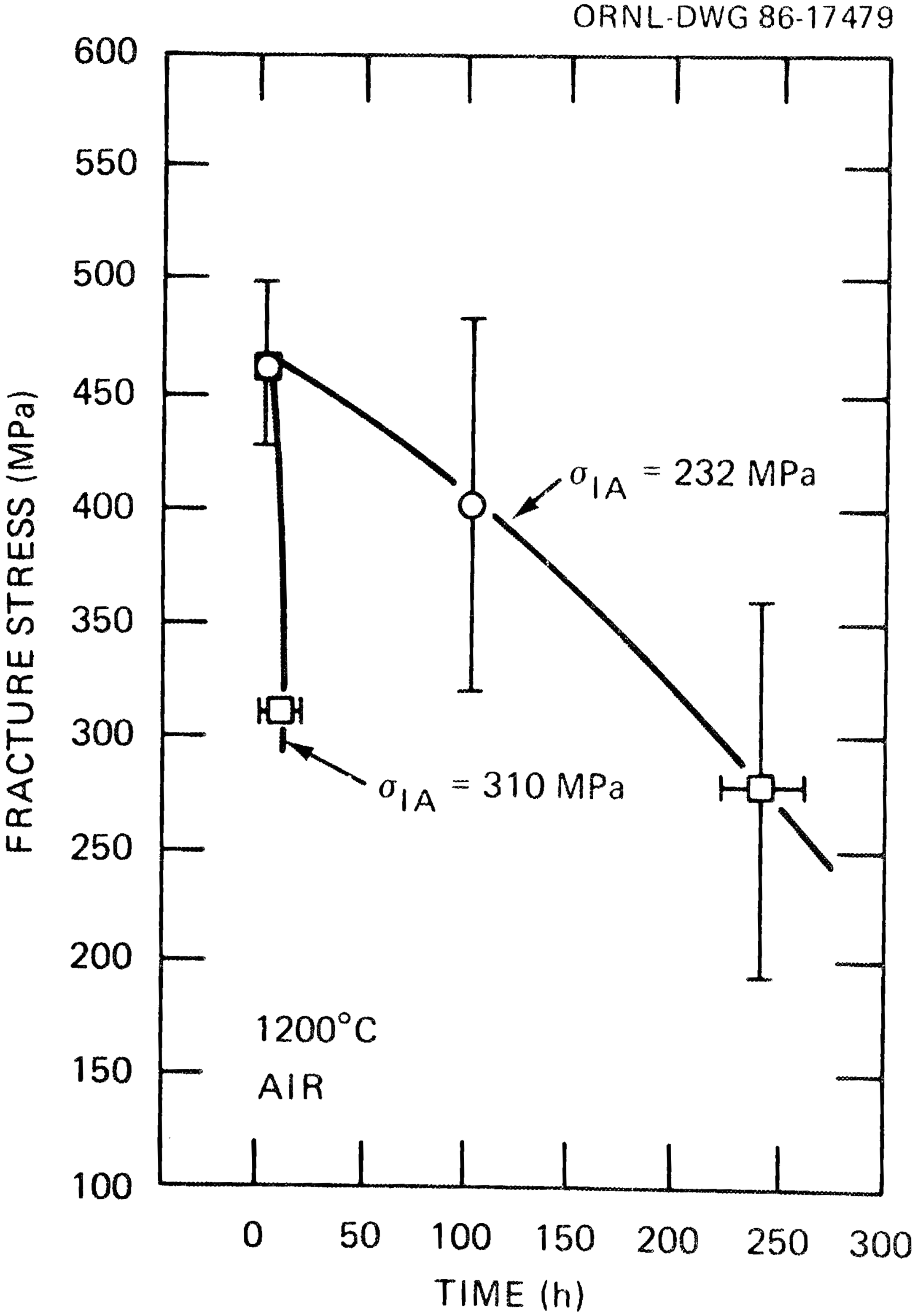

Fig. 2. At 1200°C, the retained strengths decrease with increase in exposure time and applied stress level.

However, within the crack tip region of the arrested indent cracks after fracture, one observes numerous intergranular separations consistent with grain boundary creep in the presence of a glassy phase.

The fracture toughness of the alumina–20 vol % SiC whisker composites in air remained constant (8.1–8.3 MPa $m^{1/2}$) at 22°C to at least 1000°C as determined by the multiple indent and fracture technique[8] (Fig. 3). These toughness values were obtained with long precracks and are in agreement with precracked, applied-moment, double-cantilever beam tests at room temperature. As a result of the introduction of long precracks, the toughness values are expected to be representative of the maximum toughness for materials that appear to exhibit R-curve behavior. This insensitivity of the fracture toughness to temperature is in contrast with the strong temperature dependence observed in transformation-toughened zirconia ceramics.[9]

At 1200 and 1400°C, there is a marked increase in the apparent toughness to values of 10 to 11 MPa $m^{1/2}$. However examination of the tensile surfaces of the samples tested at 1400°C reveals that the indent cracks exhibit significant crack opening displacements and that considerable additional crack formation has occurred. Although the indented samples were held at 1400°C for only 15–20 min, they were subjected to an applied stress of 160 MPa (or about half the stress required for fracture) during the entire heating (~60 min) and equilibration (15–20 min) cycle. This was done in an attempt to avoid crack blunting. The crack opening displacements and the numerous cracks observed here are similar to those features observed as a result of creep deformation in alumina ceramics.[5,6] As noted by Jankus et al, the growth of creep-damage cracks from an indent crack under stress is much more rapid than that associated with natural flaws,[3] which could explain the rather dramatic effects observed in the current short-term testing.

Although similar large opening displacements of the indent cracks and additional crack generation were not detected in the indented fracture samples tested at 1200°C, one does detect numerous grain boundary separations within the region of the final position of the crack tip after fracture. This and the fact that the apparent toughness values obtained are identical to that determined at 1400°C indicate that subsequent generated damage has occurred during toughness measurements of the composites at both 1200 and 1400°C in air.

Status of milestones

None.

Publications

None.

References

1. I. A. Aksay and J. A. Pask, *J. Am. Ceram. Soc.* 58(11-12), 507–12 (1975).
2. S. H. Risbud and J. A. Pask, *J. Mater. Sci.* **13**, 2449–54 (1978).

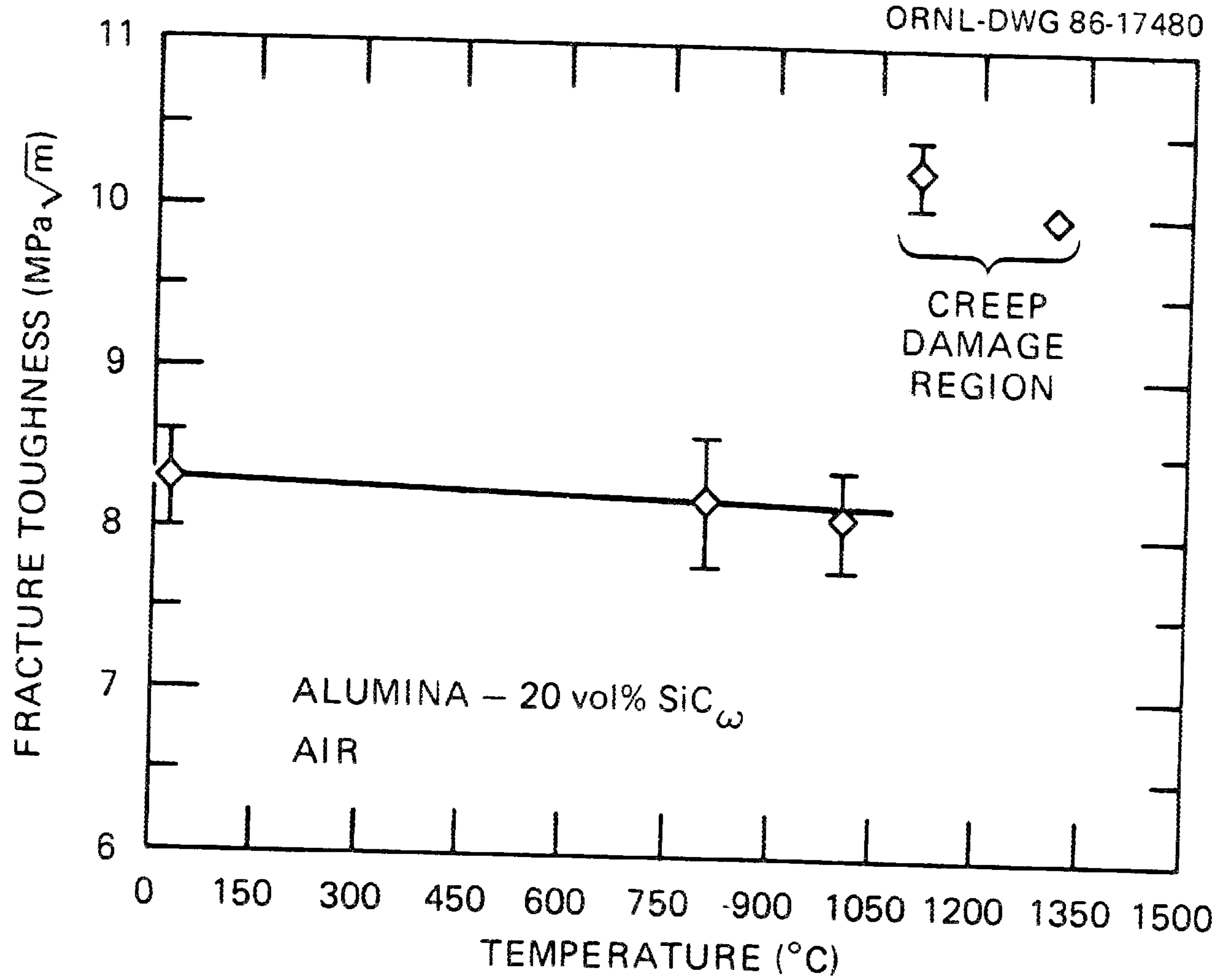

Fig. 3. Fracture toughness of alumina-20 vol % SiC whisker composite in air remains constant to at least 1000°C. Apparent toughness increases observed at 1200°C and above, but these are associated with creep crack nucleation and growth.

3. K. Jakus, S. M. Wiederhorn, and B. J. Hockey, *J. Am. Ceram. Soc.* **69**(10), 729–31 (1986).

4. A. H. Chokshi and J. R. Porter, *J. Am. Ceram. Soc.* **68**(6), C-144–C-145 (1985).

5. B. J. Dalgleish, S. M. Johnson, and A. G. Evans, *J. Am. Ceram. Soc.* **67**(11), 741–50 (1984).

6. S. M. Wiederhorn, pp. 197–226 in *Fracture Mechanics of Ceramics*, Vol. 5, R. C. Bradt, A. G. Evans, D. P. H. Hasselman, and F. F. Lange (editors), Plenum Press, New York (1983).

7. T. N. Tiegs and P. F. Becher, "Alumina-SiC Whisker Composites," *Proceedings of the 23rd Automotive Technology Development Contractors' Coordination Meeting*, Society of Automotive Engineers, Inc., Warrendale, PA, in press.

8. R. F. Cook and B. R. Lawn, *J. Am. Ceram. Soc.* **66**(11), C-200–C-201 (1983).

9. P. F. Becher, M. V. Swain, and M. K. Ferber, "Relation of Transformation Temperature to the Fracture Toughness of Transformation Toughened Ceramics," *J. Mater. Sci.* **22**(1), 76–84 (1987).

Cyclic Fatigue Of Toughened Ceramics

K. C. Liu and C. R. Brinkman (Oak Ridge National Laboratory)

Objective/scope

The objective of this task activity is to develop, design, fabricate, and demonstrate the capability to perform tension-tension dynamic fatigue testing on a uniaxially loaded ceramic specimen at elevated temperatures.

Three areas of research have been identified as the main thrust of this task: (1) design, fabrication, and demonstration of a load train column that truly aligns with the line of specimen loading; (2) development of a simple specimen grip that can effectively link the load train and test specimen without complicating the specimen geometry and, hence, minimize the cost of the test specimen; and (3) design and analysis of a specimen for tensile cyclic fatigue testing.

Technical progress

High-temperature testing of ceramic materials is being accomplished by two heating methods: inductance and resistance. The heating method by induction power was successfully demonstrated and discussed in the last report. Since then, a series of tensile tests were performed on commercial aluminum oxide at 1000°C. In some tests, strain was measured with a high-temperature extensometer capable of 10-microstrain (10^{-6}-in./in.) resolution. The specimens were loaded with a stress rate of 50 MPa/s (7.25 ksi/s).

Results of tensile tests and a preliminary fatigue test are summarized in Table 1. To facilitate comparison, Coors' test data are included in the same table. Two grades of aluminum oxide were tested — Coors' AD-94 with 94% Al_2O_3 and AD-998 with 99.8% Al_2O_3. Some specimens were tested at high temperature using nickel-base metal pullrods, and others using ceramic gripping fixtures (high-temperature pullrod assemblies) were similarly tested for exploratory purposes. The ceramic gripping fixtures are made from KYOCERA's high-performance silicon nitride SN-250, capable of high-temperature service to a maximum temperature of 1400°C. Details of the ceramic fixtures were illustrated and discussed previously in this series of progress reports.

The values of the elastic moduli shown in Table 1 were determined from the stress-strain curves plotted from the outputs of the load cell and the extensometer. The room temperature values are essentially the same for both ORNL and Coors. The average value of the three elastic moduli at 1000°C is 167 GPa (24.3×10^6 psi). No information is available from Coors for comparison.

Table 1 shows that all ORNL tensile data obtained for AD-94 at 1000°C have strength values above those of the Coors data. Specimen 33 clearly outperformed the others in this series. A comparison shows that the tensile strength of specimen 33 exceeds Coors' tensile and flexural strength by about 80 and 36%, respectively. Reasons for the higher strength are being investigated. Two possible reasons for these differences can be cited: (1) inconsistency in technique in using the monochromatic pyrometer for high-temperature specimen measurement, and (2) difference in soak time at high temperature before actual testing. First, it should be noted that high-temperature measurement by the monochromatic pyrometer is a subjective technique. Inevitably, some readout error may occur at the threshold temperature where a sharp drop-off in material properties may exist. As to the second possible cause, our investigation remains inconclusive at this time because of the limited test results. We anticipate that some of these possible problems will be minimized when a recently received two-color pyrometer is incorporated in follow-up testing.

Results of two tensile tests on Coors' AD-998 alumina at 1000°C are also included in Table 1. Both specimens were tested with the ceramic gripping fixtures and heated by an induction coil and susceptor. Both specimens show a tensile strength slightly higher than the flexural strength reported by Coors Company. No tensile data are available from Coors' literature for direct comparison.

Installation of the new resistance furnace and furnace bakeout have been completed. It contains six molybdenum disilicide heating elements capable of achieving temperature as high as 1650°C. Two exploratory tensile tests were performed for specimens 28 and 32 heated by the furnace. Results of the tests were somewhat disappointing because both specimens ruptured at the shank outside the reduced gage section. Examinations indicate that the fracture failure was initiated at the sharp point contact produced by the sharp edges on the tapered collars. The situation was subsequently corrected by removing the sharp edges on the tapered collars. Test results of the two specimens are included in Table 1. The tensile strength data are calculated based on the area of the reduced gage section.

Status of milestones

None due during this reporting period.

Publications

A paper entitled "Tensile Cyclic Fatigue of Alumina at Room and Elevated Temperatures," by K. C. Liu and C. R. Brinkman, was presented at the 24th Automotive Technology Development Contractors' Coordination Meeting held on October 27-30, 1986, at Dearborn, Michigan. The final manuscript has been submitted for publication in the conference proceedings.

Table 1. Results of tensile tests for Coors' aluminum oxide tested at 1000°C, including Coors' test data (Bulletin Nos. 205 and 953)

Data source	Specimen no.	Modulus of elasticity [GPa (10^6 psi)]		Tensile strength [MPa (ksi)]	Flexural strength [MPa (ksi)]	Heating method[a]	Pullrod assembly[b]
		25°C	1000°C	1000°C	1000°C		
				AD-94 Al_2O_3			
ORNL	29	-	166 (24.1)	115 (16.7)		I	M
	33	-	174 (25.3)	188 (27.2)		I	M
	28			131 (18.9)[c]		R	C
	32			124 (18.0)[c]		R	C
	31			108 (15.7)		I	C
	25[d]	284 (41.3)	162 (23.5)	-		I	M
Coors	Typical	283 (41)	-	103 (15)	138 (20)		
	Minimum	-	-	-	117 (17)		
				AD-998 Al_2O_3			
ORNL	37			205 (29.7)		I	C
	38			224 (32.5)		I	C
Coors	Typical	-	-	-	193 (28)		

[a] I = induction heating; R = resistance heating.

[b] M = metal pullrod; C = Ceramic gripping fixture.

[c] Fractured outside the reduced gage section.

[d] Tested in cyclic fatigue to 80 MPa (11.6 ksi) and failed at 400 cycles.

3.3 ENVIRONMENTAL EFFECTS

Static Fatigue Behavior of Toughened Ceramics

M. K. Ferber and T. Hine (University of Illinois)

Objective/scope

The objective of this program is to study the long-term mechanical stability of toughened ceramics for diesel engine applications. Materials under current investigation include (1) 2 varieties of an MgO partially stabilized zirconia (Mg-PSZ), (2) a yttria partially stabilized zirconia (Y-PSZ), and (3) a SiC whisker reinforced alumina. The work is divided into two tasks. The first involves the measurement of the time-dependent strength behavior of ceramic flexure-bar samples as a function of temperature and applied stress using the Interrupted Fatigue (I.F.) method. In the second task, the microstructures of selected I.F. specimens are characterized using SEM and TEM. In the case of the zirconia samples, x-ray diffraction and dilatometry studies are conducted to examine changes in their transformation behavior resulting from the high-temperature exposure.

Technical progress

(a) Interrupted Fatigue Testing

The fatigue behavior was determined using an interrupted fatigue (I.F.) technique in which the four-point bend strength S_f was measured as a function of time (t) temperature (T), and applied stress (σ_a). This method has several advantages over conventional static fatigue testing. First, since time is a controllable quantity, problems associated with an unpredictable fatigue life (as in the case of static fatigue) are avoided. In the present study, this feature allowed for periodic examination of test specimens so that changes in both the microstructure and phase assemblage could be ascertained. A second advantage is that processes responsible for both strength degradation and strength enhancement can be readily distinguished.[1]

All testing was conducted in a specially designed Flexure Test System (F.T.S.) capable of holding up to three bend samples. The general layout of the F.T.S. is shown in Fig. 1. The Test Frame contains the hardware for applying mechanical forces to each of three samples which are supported by Al_2O_3 four-point bend

SPECIALLY DESIGNED FLEXURE TEST SYSTEMS WERE ULTILIZED IN I.F. STUDY

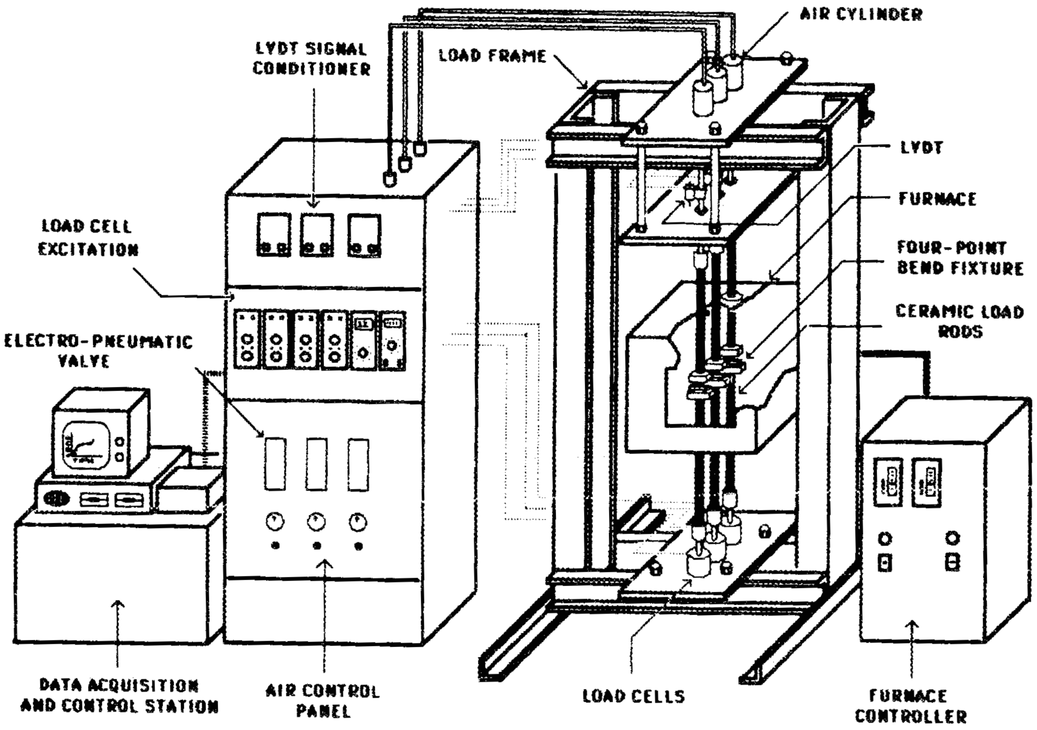

Figure 1. I.F. testing was conducted in specially designed Flexure Test System in which loads were applied pneumatically.

fixtures.[a] The loads are generated by pneumatically driven air cylinders located at the top of the support frame. These loads are transmitted into the hot zone of the furnace through aluminum oxide (Al_2O_3) rods . Each of the bottom three Al_2O_3 rods are also attached to a load cell which monitors the applied force as a function of time. Water-cooled adapters connect the aluminum oxide rams to both the load cells and the air cylinders. The computer monitors the load on each specimen and provides necessary adjustments in the air pressure (via the electro-pneumatic transducer) such that the desired stress level is maintained. Following the designated exposure time, the samples are fractured using a prescribed loading rate (345 KPa/s in the present study).

(b) MgO PSZ Ceramics

I.F. studies involving the MgO-PSZ materials were completed during this reporting period. Two commercial Mg-PSZ ceramics[b] designated TS-PSZ (thermal shock grade) and MS-PSZ (maximum strength grade/1983) were examined in this portion of the program. Both 1983 and 1984 vintages of the TS PSZ (designated TS(83) and TS(84)) were examined. Starting materials were obtained in the form of either circular discs 100 mm in diameter and 7.6 mm thick or rectangular plates (101.6 x 101.6 x 6.35 mm). Rectangular bend specimens (25.4 x 2.82 x 2.5 mm) were then machined from these shapes for subsequent mechanical property studies. The tensile surface of each sample was polished to a 0.25 µm finish and the edges beveled using a 6 µm diamond wheel.

As discussed previously,[2] the time-dependent strength behavior for the TS PSZ tested at 800 and 1000°C exhibited a strong dependence upon the applied stress. In particular, the application of stress promoted both strengthening and weakening processes depending upon time and temperature. The strengthening tendency was most prominent at 1000°C. X-ray data gave evidence that this effect was related to a preferential generation of the eutectoid decomposition phase along the tensile surface. In order to examine this possibility, additional x-ray analyses were used to measure the

---

[a] The F.T.S. design is based on a similar system originally developed by S. M. Wiederhorn and N. J. Tighe of the National Bureau of Standards.

[b] Manufactured by Nilcra Ceramics, USA Office, Glendale Heights, Illinois.

depth dependence of the volume fraction (V_f^m) of the monoclinic (m) phase generated in TS PSZ (84) samples exposed at 1000°C. In particular, V_f^m was determined as a function of distance from the tensile surface (y/H where H is the specimen thickness).

The resulting depth profiles are illustrated for the TS (84) PSZ exposed at 336 and 1008 h in Figs. 2(a) and (b), respectively. At both times, the (m) fraction decreased to a constant value within the bulk material. As indicated in Fig. 3, which provides a comparison of the average bulk V_f^m values with the corresponding surface quantities, this behavior was typical for the entire 24 to 1008 h exposure period. However, as shown in Fig. 2, the depth profiles at a given time were not significantly dependent upon the stress level. Therefore, the enhanced surface (m) formation was not sensitive to the applied stress. Finally, note that the high V_f^m values observed along the compressive surface (y/H=1) particularly for *t* =336 h were due to ground condition of that surface.

A major problem with the depth profile experiment was that material removal rates could not be precisely controlled. Consequently, V_f^m could not be accurately measured in the near surface regions. To overcome this limitation, additional Raman microprobe studies were conducted in which the ratio V_f^m/V_f^t was measured across the polished side of TS (84) specimens which had been exposed at 1000°C for 336 h. The results indicated that V_f^m/V_f^t was approximately constant to within 50 µm of the tension and compression surfaces. Therefore, the enhanced rate of (m) formation was limited to the near surface regions as indicated by the solid lines in Fig. 2.

The I.F. data for the TS PSZ tested at 800°C indicated that slow crack growth processes were activated at the higher applied stress levels. This subcritical crack growth is generally characterized by a velocity V which can be described by the expressions,

$$V = V_o \exp\ [-(q-bK_I)/RT]\Phi \qquad (1a)$$

where

$$\Phi = \{1-\exp[L(K_I-K_{th})/RT]\}. \qquad (1b)$$

In these equations, R is the gas constant, V_o is a pre-exponential constant, q is the stress free activation energy, b accounts for the K_I dependency (related to the activation volume), and L describes the threshold.[3,4] The crack growth parameters (V_o, q, b, L, and K_{th}) will be a function of material, temperature, and in some cases environment.

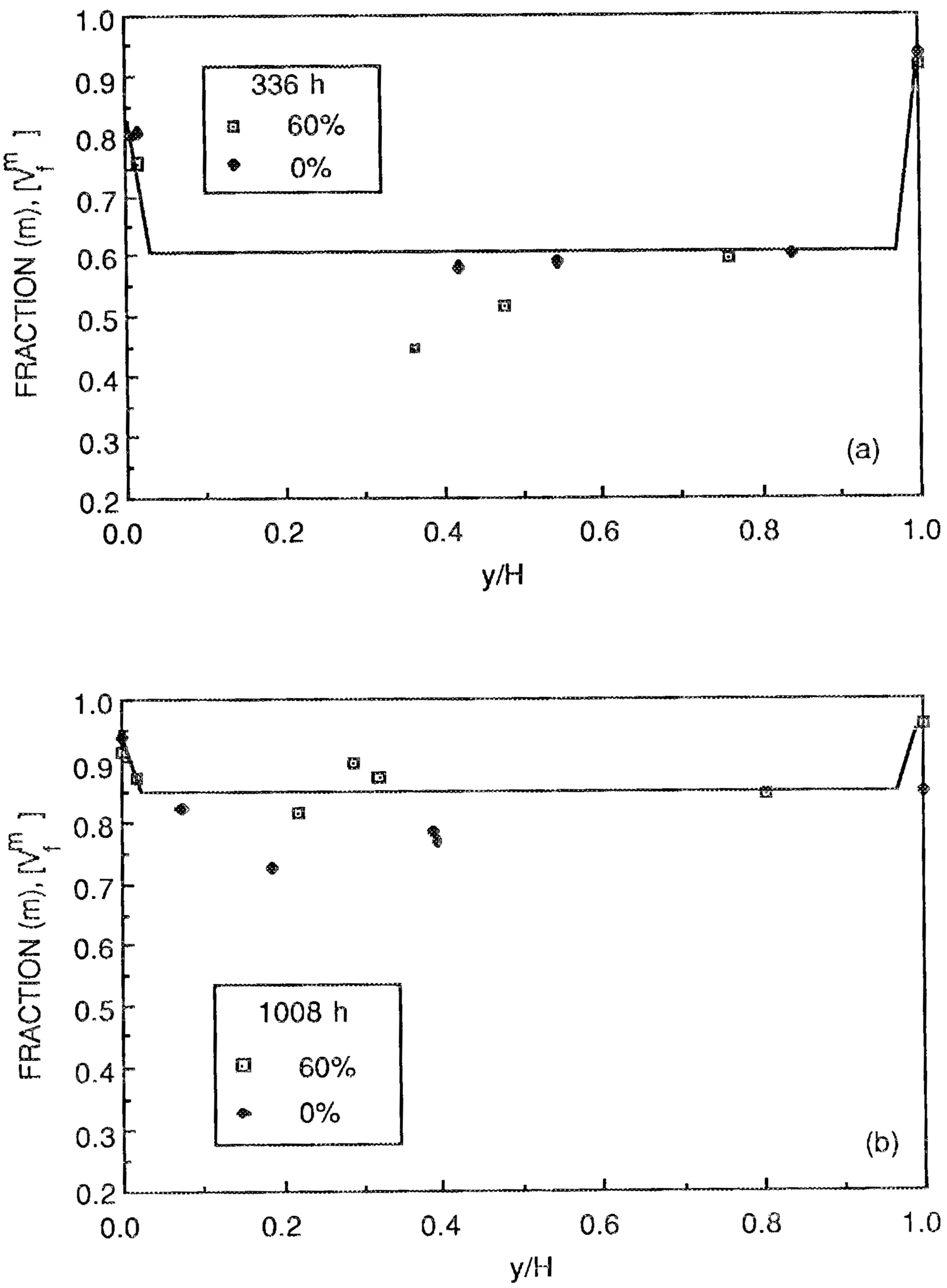

Figure 2. Volume fraction of the (m) phase in the bulk is consistently lower than that along the tensile surface for TS (84) samples exposed at 1000°C for (a) 336 h and (b) 1008 h.

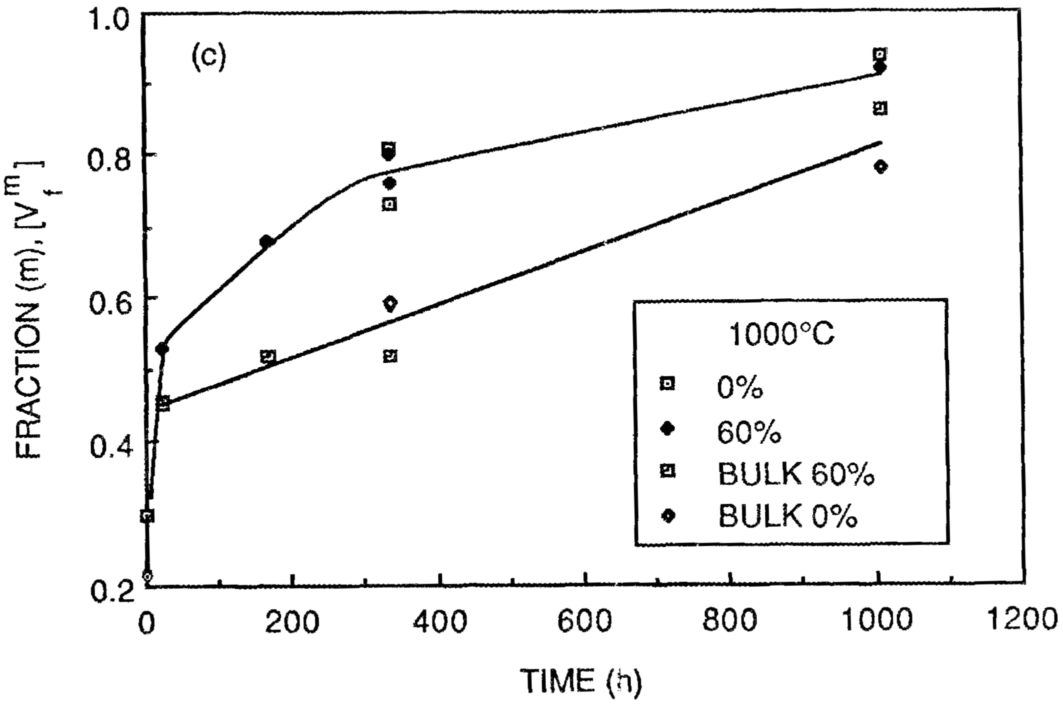

Figure 3. For a given exposure time, the fraction of (m) phase generated in the bulk is independent of stress level.

Subcritical crack extension can ultimately promote a time-dependent, loss in strength S_f. In particular, when a constant stress σ is applied to a test sample such that $K_I > K_{th}$ (the threshold for crack growth), then S_f will decrease with time in accordance with the relation,

$$t\,\sigma^{2} = C\int_{(\sigma/S_i)K_{IC}}^{(\sigma/S_f)K_{IC}} (K_I/V)\, dK_I \qquad (2)$$

where t is the exposure time, C is a constant, σ is the applied stress, S_i is the inert strength, and V is the subcritical crack velocity (given by Eq. 1). Fig. 4 illustrates the predicted I.F. behavior for some typical crack growth parameters. The actual calculations were made using a LOTUS 123 spreadsheet. The general trends in Fig. 4 are similar to those in the short-term I.F. data observed for the TS(84) PSZ samples tested at 800°C.[2] Such similarity suggests that slow crack growth processes were operative in this PSZ ceramic. Although the Fig. 4 curves indicate the possibility of time-dependent fracture (when $S_f = \sigma$), sample failure did not occur for the TS(84) material due to the long-term strengthening mechanism.

It is apparent that the major problem with the mathematical approach outlined above is that it does not account for potential strengthening mechanisms. For example if crack blunting occurs, then the equation for V must be modified accordingly.[5,6] In the present study, crack blunting effects were examined by assuming that an increase in the crack tip radius ρ resulted in a corresponding decrease in the effective stress intensity factor in accordance with

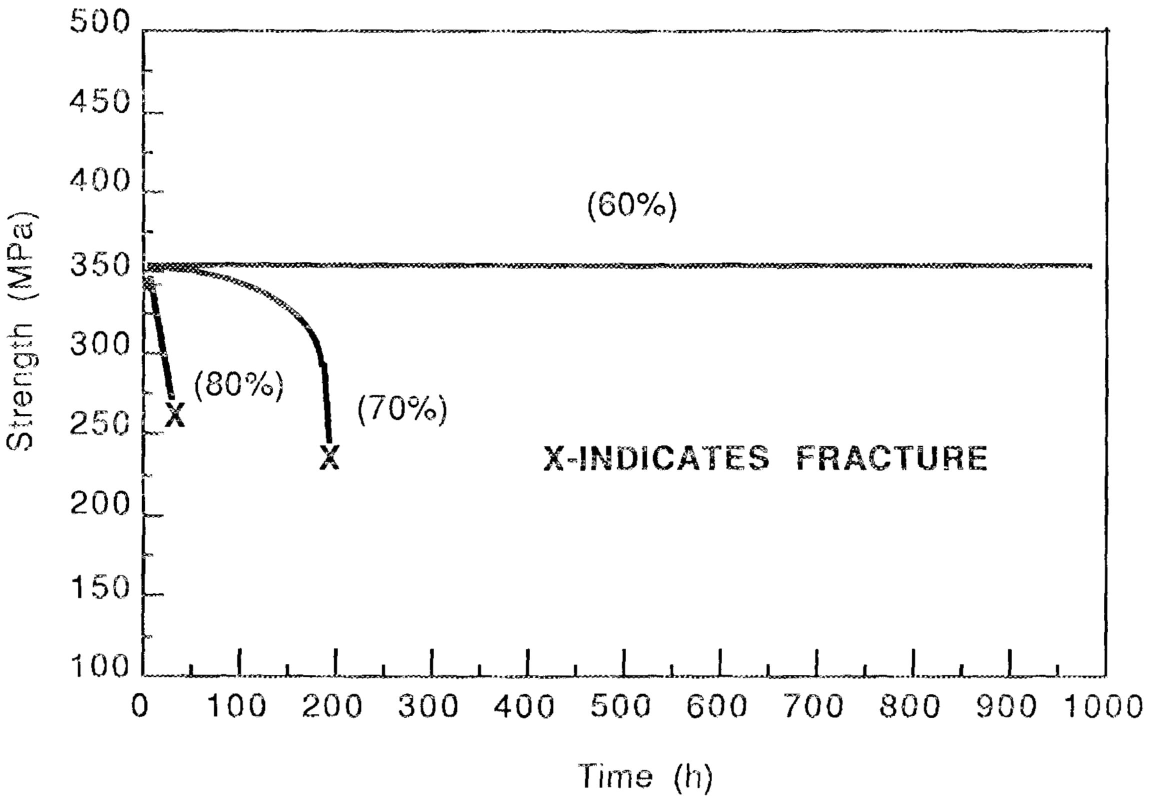

Figure 4. I.F. behavior predicted from V-K_I analysis reveals a rapid, short-term degradation in strength at the higher stress levels.

the expression,

$$K_I(\text{eff}) = K_I \; (\rho_0/\;\rho)^{1/2}, \qquad (3)$$

where ρ_0 is the crack tip radius at time=0. Several different kinetic laws describing the blunting process were incorporated into the computer spreadsheet. The resulting strength-time plots did not reflect the general trends observed experimentally for the TS(84) PSZ. Reasons for this discrepancy are currently under investigation.

I.F. testing of a SiC whisker reinforced alumina[c] was initiated this reporting period. Based upon input from the material supplier and contract monitor, a decision was made to focus the I.F. test matrix in the temperature range 1000 to 1100°C . The preliminary results for tests at 1000°C are shown in Fig. 5. The strength S_f of

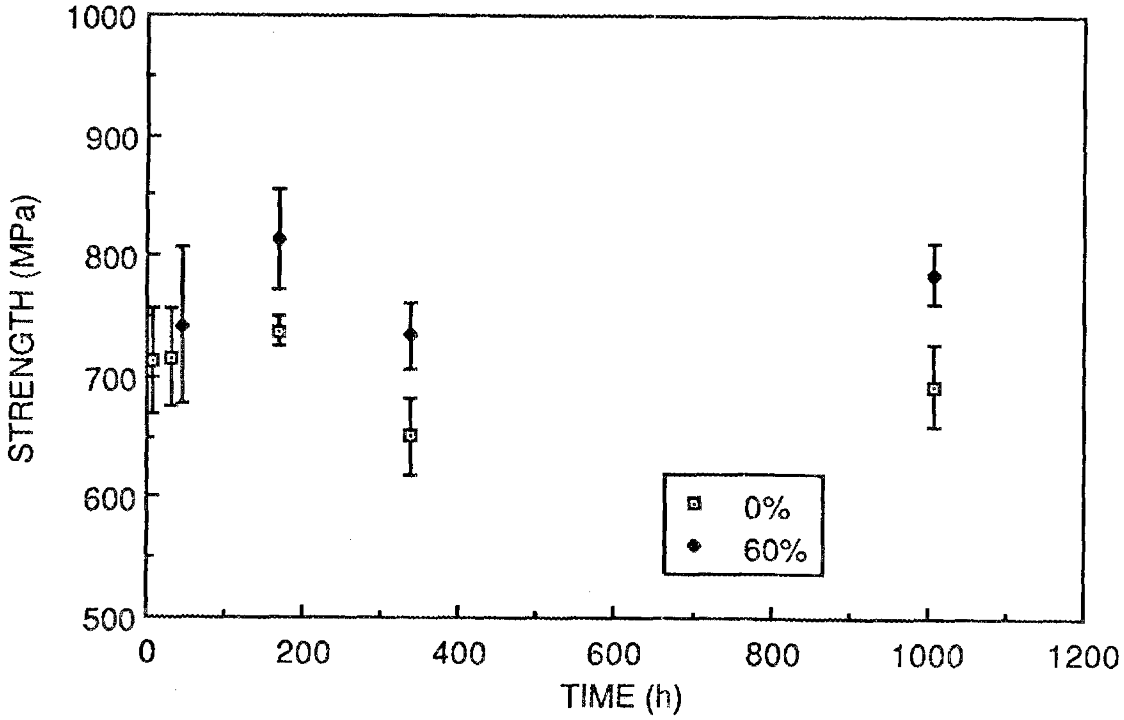

Figure 5. Strength for the SiC/alumina composite samples held under stress at 1000°C is higher than that for unstressed specimens.

---

[c] Supplied by Terry Tiegs, Oak Ridge National Laboratory, Oak Ridge, TN.

the stressed samples was significantly larger than that for the unstressed samples throughout the exposure duration t.. In addition, S_f for both stressed and unstressed conditions exhibited a short-term maximum for t =336 h and then increased again at t =1008 h. Preliminary SEM studies of fractured surfaces indicated that a whisker pullout mechanism was operative for all exposure times considered. Phase analysis studies are now underway.

Status of Milestones

A final report entitled, "Time-Dependent Behavior of MgO-PSZ Ceramics" was submitted to ORNL on March 27, 1987 in accordance with Milestone 331203. This report describes the the I.F. and microstructural results obtained for the TS and MS PSZ ceramics.

Publications

None.

References

1. S. M. Wiederhorn, "A Probabilistic Framework for Structural Ceramics "; pp. 197-226 in *Fracture Mechanics of Ceramics*, Vol 5., eds. R. C. Bradt, A. G. Evans, D. P. H. Hasselman, and F. F. Lange. Plenum, New York, 1983.

2. M. K. Ferber and T. Hine, "Fatigue Behavior of Partially Stabilized Zirconia Ceramics,to be published in Proceedings of the Twenty-Fourth Automotive Technology Development Contractors' Coordination Meeting, Society of Automotive Engineers, Warrendale, PA.

3. S. D. Brown, "Multibarrier Kinetics of Brittle Fracture: I. Stress Dependence of the Subcritical Crack Velocity, "*J. Am. Ceram. Soc.,* **62** [9-10] 515-24 (1979).

4. S. D. Brown, "A Multibarrier rate process Approach to Subcritical crack Growth, "pp. 597-621 in Fracture Mechanics of Ceramics, Vol. 4. Edited by R. C. Bradt, D. P. H. Hasselman, and F. F. Lange, Plenum, New York, 1978.

5. M. K. Ferber, "A Mathematical Description of Transient Crack Growth Behavior in Glass, "*J. Mater. Sci.,* **19** [8], 2570-5 (1984).

6. A. G. Evans and B. J. Dalgleish, "Some Aspects of the High Temperature Performance of Ceramics and Ceramic Composites," pp.1073-95 in *Ceramic Engineering and Science Proceedings* , American Ceramic Society, Sept.-Oct. 1986.

Environmental Effects in Toughened Ceramics

Norman L. Hecht (University of Dayton)

Objectives/scope

The University of Dayton Research Institute (UDRI) conducted and completed a study of "The Effect of Environment Upon the Mechanical Behavior of Structural Ceramics for Application in the DOE Ceramic Technology for Advanced Heat Engines Program." This effort was initiated in January 1985 through a subcontract with Martin Marietta Energy Systems Inc. The primary goal of this study was to determine the effect of environment upon toughening and strength in commercially available transformation toughened ceramics [partially stabilized ZrO_2 (PSZ) and dispersion toughened Al_2O_3 (DTA)]. Emphasis was placed on understanding the mechanism(s) responsible for environmentally induced strength degradation in the temperature range of 25°C to 1050°C. It was anticipated that the information and insights obtained from this program could be used to determine the long-term applicability of toughened ceramics for heavy duty diesel engine components.

Dynamic fatigue methods (4 point bend strength as a function of stressing rate) were used in a three-phase program to investigate strength and slow crack growth in environments containing controlled amounts of water vapor. Similar tests were also conducted in inert atmospheres (dry N_2) to distinguish intrinsic effects from environmentally induced conditions. In addition, the effects of aging (extended exposure at temperature and atmosphere) on the candidate materials at low temperatures (150°C-300°C) were studied. A description of the activities pursued and the results obtained are presented in this semiannual report.

In January 1987, the contract was extended for six months to investigate three additional materials (two Si_3N_4 and one SiC) according to an evaluation protocol developed in cooperation with the project monitor. Microstructure, chemistry, thermal expansion behavior, and mechanical properties at 25°C and 1500°C will be evaluated for the three materials suggested by the project monitor. Research results will be summarized in a final report submitted to ORNL.

Work plan

The work scope for this program initially consisted of three major tasks. An outline of these tasks is contained in Table 1. Eight commercial transformation toughened ceramics (Table 2) were identified for screening and initial evaluation. From the eight candidate materials screened, five were selected for further study in the second phase of the program.

The results of Task II were used for the selection of the two finalist materials to be evaluated more extensively in Task III.

Table 1. Work Scope.

TASK I	TASK II	TASK III
Evaluation of Potential Candidate Transformation Toughened Ceramics (TTC)	Investigation of five Selected Candidate Materials	Detailed Investigation of the Two Finalist TTC Materials
• Identification of TTC Suppliers • Screening Evaluation of Potential Candidate TTC Materials • Analysis of TTC Screening Data	• Finalize Candidate Selection for Matrix Testing Plan (four temperatures, two atmospheres, and two stressing rates) • Conduct Candidate Matrix Test Program • Conduct Aging Studies	• Selection of the Two Finalist Materials • Finalization of an Expanded Matrix Testing Plan • Implementation of MOR Testing Plan

Table 2. Transformation Toughened Ceramic Materials Identified for Evaluation.

Material Supplier	Material Designation	Material Description
Ceramatec Inc.	ZTA-XS121	ZrO_2 Dispersion Toughened Al_2O_3
Kyocera Int'l.	DTA-AZ301	Dispersion Toughened Al_2O_3 (19% ZrO_2)
Nilcra Ceramic (USA) Inc.	MS-PSZ	3 wt. % MgO Stabilized ZrO_2 (heat treated for high strength)
Nilcra Ceramic (USA) Inc.	TS-PSZ	3 wt. % MgO Stabilized ZrO_2 (heat treated for high thermal shock resistance)
Ceramatec Inc.	YTZP-XS241	~5 wt. % Y_2O_3 Stabilized ZrO_2 (with 10% Al_2O_3 addition)
NGK Locke Inc.	Z191	5 wt. % Y_2O_3 Stabilized ZrO_2
Kyocera Int'l.	PSZ-Z201	5.4 wt. % Y_2O_3 Stabilized ZrO_2
Ceramatec Inc.	CTZP	CeO_2 Stabilized ZrO_2 (with 10% Al_2O_3 addition)

The detailed matrix test plan used for evaluating the two finalist materials in Task III is presented in Table 3. The major objective of Task III was a more detailed investigation of slow crack growth for these materials. The MOR test results obtained in Task III were also statistically evaluated following the same format used in the analysis of the MOR data generated in Task II.

In compliance with our extended program, the three additional materials selected for evaluation (see Table 4) were ordered from the manufacturers. The protocol for evaluation is outlined in Table 5. In addition, a literature survey of SiC and Si_3N_4 has been initiated.

Table 3. Finalist MOR Matrix Test Plan.

Temperature	Environment*	MOR Crosshead Speed (cm/sec) 0.00004	0.0021	0.0064
25°C	Atm_1	x	x	x
	Atm_2	x	x	x
250°C	Atm_1	x	x	x
	Atm_2	x	x	x
500°C+	Atm_2	x	x	x
800°C	Atm_1	x	x	x
	Atm_2	x	x	x

*Environmental Conditions: Atm_1 - Dry N_2; Atm_2 - 90% N_2/10% H_2O.

+Only the MS-PSZ material was tested at 500°C

Table 4. Additional Structural Ceramics to be Evaluated.

Material	Manufacturer	Designation
Silicon Nitride	Norton Co.	XL144H Hipped and Sintered
Silicon Nitride	GTE Labs.	PY6, Injection Molded
Silicon Carbide	Sohio Eng. Matls.	Hexoloy Sintered Alpha

Table 5. Experimental Protocol.

Measurement	Technique/Conditions	Number of Specimens
Microstructure	SEM/Optical/TEM	3
Chemistry	XRD/EDAX	3
Density	Immersion at 25°C	5
Hardness	Microhardness at 25°C	5
Thermal Expansion[+]	Temp. Range 25-1500°C	5
Fracture Toughness[*]	Microindent and DCB at 25°C	10
Flexure Strength[x]	At 25 and 1500°C	10/10
Elastic Modulus	Sonic Velocity and Sonic Vibration Methods	3

[+] Thermal expansion will be measured on at least three of the specimens no less than two times from 25 to 1500°C in order to determine if expansion hysteresis effects are present.

[*] Fracture toughness will be measured by microindentation and double cantilever beam techniques and a comparison of the toughness values completed.

[x] Flexure strength will be measured in four-point flexure with an outer span of 1.50 in., an inner span of 0.75 in., and a specimen cross section of 0.125 x 0.250 in., with specimens loaded at a rate of 0.020 in. per minute.

Technical progress

Results obtained in Task III (The results obtained for Tasks I and II were presented in our last semiannual report - October 1986)

The Nilcra MS-PSZ and the Kyocera AZ301 materials were selected for more detailed investigation in Task III. The results of the MOR values obtained for the selected matrix test conditions are presented in Table 6. Included in Table 6 are the MOR values obtained for the MS-PSZ and AZ301 materials from Tasks I and II studies. The results of the statistical analysis of the data obtained is presented in Table 7. An evaluation of the dynamic fatigue analysis is presented in Table 8, and the computer generated graphs obtained from the data are presented in Figures 1 to 13.

Discussions of results

Analysis of Results from Task III

The AZ301 material was selected for further testing because it had flexure stengths significantly higher than any of the other candidate materials at all of the test temperatures and environments. The MS-PSZ material was selected because, of the materials tested, it was the most consistant and reproducible material and had moderate strength values at all of the test temperatures.

In general, the MOR and dynamic fatigue data (Tables 6 and 7) obtained in Task III for the AZ301 and MS-PSZ materials reinforced the results obtained and the basic trends observed in Task II. The MS material had an average flexure strength of 600 MPa at 25°C which dropped to ~240 MPa at both 800° and 1050°C. The AZ301 material had an average room temperature strength of 1000 MPa which dropped to about 600 MPa at 1050°C. For both the MS and AZ301 materials the highest average strengths were measured in the dry N_2 environment for most of the test conditions studied. Based on the research shown in Table 8, the loading rate was not a factor which effected the measured MOR values for the AZ301 material at any of the test temperatures or the MS material at 500°C and 800°C. The loading rate was a factor in the MS material at 25°C, 250°C, and 1050°C. For the MS material MOR values increased with increasing loading rates. The Task II MOR values were found to be slightly higher than the Task III MOR values for both the AZ301 and MS materials.

Table 6. Flexure Test Results for Task III.

Test Temperature (°C)	Test Atmosphere	Average MOR (MPa)		
		Crosshead Speed (cm/s)		
		0.00004 (CV)*	0.0021 (CV)*	0.0064 (CV)*
		Kyocera AZ301		
25	Dry N_2	1106 (11.5)	1212 (13.5)	1131 (17.9)
	10% H_2O	949 (21.6)	866 (22.7)	836 (23.2)
250	Dry N_2	--	--	997 (26.5)
	10% H_2O	808 (31.2)	967 (21.2)	938 (24.2)
800	Dry N_2	--	--	813 (24.0)
	10% H_2O	655 (32.2)	807 (11.6)	681 (28.5)
		Nilcra MS-PSZ		
25	Dry N_2	615 (6.0)	623 (10.6)	675 (5.7)
	10% H_2O	545 (5.1)	564 (4.6)	611 (6.5)
250	Dry N_2	--	--	531 (10.7)
	10% H_2O	461 (8.6)	491 (10.6)	523 (5.5)
500	10% H_2O	363 (7.0)	355 (9.0)	371 (8.0)
800	Dry N_2	--	--	250 (21.6)
	10% H_2O	249 (19.1)	214 (18.2)	238 (21.5)

*(CV) = Coefficient of Variance

(10 specimens were tested under each condition)

Table 7. Statistical Analysis of Flexure Test Results.

Test Conditions			MS-PSZ				AZ301			
Test Temp. (°C)	Test ATM	Crosshead Speed (m/s)	Mean (MPa)	Standard Deviation (MPa)	95% CL Range (MPa)	Relative Precision (%)	Mean (MPa)	Standard Deviation (MPa)	95% CL Range (MPa)	Relative Precision (%)
25	Dry N_2	.0004	615	37	53	4	1107	127	181	8
25	Dry N_2	.0021	622	66	95	7	1212	164	236	10
25	Dry N_2	.0064	675	39	55	4	1131	202	290	13
25	10% H_2O	.0004	546	28	40	3	949	205	293	15
25	10% H_2O	.0021	564	26	37	3	866	197	282	16
25	10% H_2O	.0064	611	40	57	5	836	194	277	17
250	Dry N_2	.0064	531	57	82	7	997	264	379	19
250	10% H_2O	.0004	460	40	57	6	808	252	361	22
250	10% H_2O	.0021	490	52	75	8	967	205	509	26
250	10% H_2O	.0064	523	29	41	4	938	227	325	17
500	10% H_2O	.0004	363	24	59	8	--	--	--	--
500	10% H_2O	.0021	356	33	83	12	--	--	--	--
500	10% H_2O	.0064	371	30	75	10	--	--	--	--
800	Dry N_2	.0064	251	54	77	15	813	195	279	17
800	10% H_2O	.0004	249	48	68	14	655	211	301	23
800	10% H_2O	.0021	214	39	55	13	807	93	232	14
800	10% H_2O	.0064	338	51	73	15	681	194	259	19
1050	Dry N_2	.0004	247	13	33	7	590	137	339	29
1050	Dry N_2	.0064	248	16	39	8	662	236	587	44
1050	10% H_2O	.0004	254	14	34	7	620	149	370	29
1050	10% H_2O	.0064	225	9	23	5	554	132	329	29

Table 8. Summary of Dynamic Fatigue Test Results for Task III.

Test Temp. °C	Conditions Atm.	AZ301 N	AZ301 A	MS N	MS A
25	Dry N_2	+124	1112	+68*	614
25	10% H_2O	-40	928	+52*	547
250	10% H_2O	+26	774	+43*	465
500	10% H_2O	--	--	+612	361
800	10% H_2O	+52	635	-57	238
1050	Dry N_2	+66	577	+1444	247
1050	10% H_2O	-47	600	-43*	248

$N = \frac{1}{\text{Slope}} - 1.$

A = Intercept.

* = Sufficient sample population to determine that the calculated slope value was statistically different from zero at the 95% confidence limit. Those values of n not starred are considered to not be statistically different from 0 (not subject to slow crack growth).

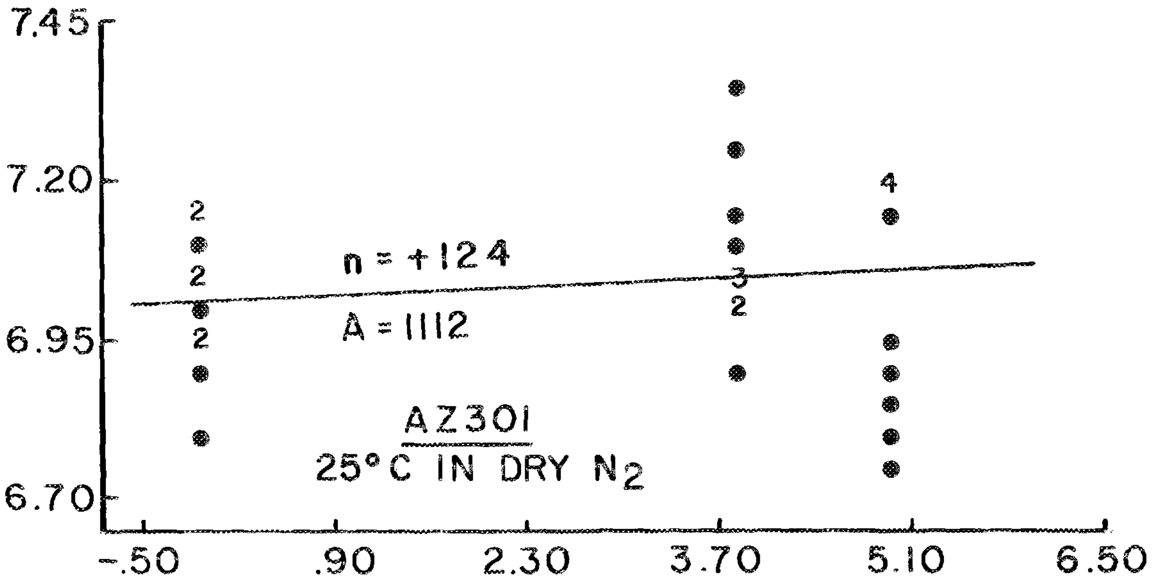

Figure 1. Dynamic Fatigue Results for AZ301 Material at 25°C in Dry N_2.

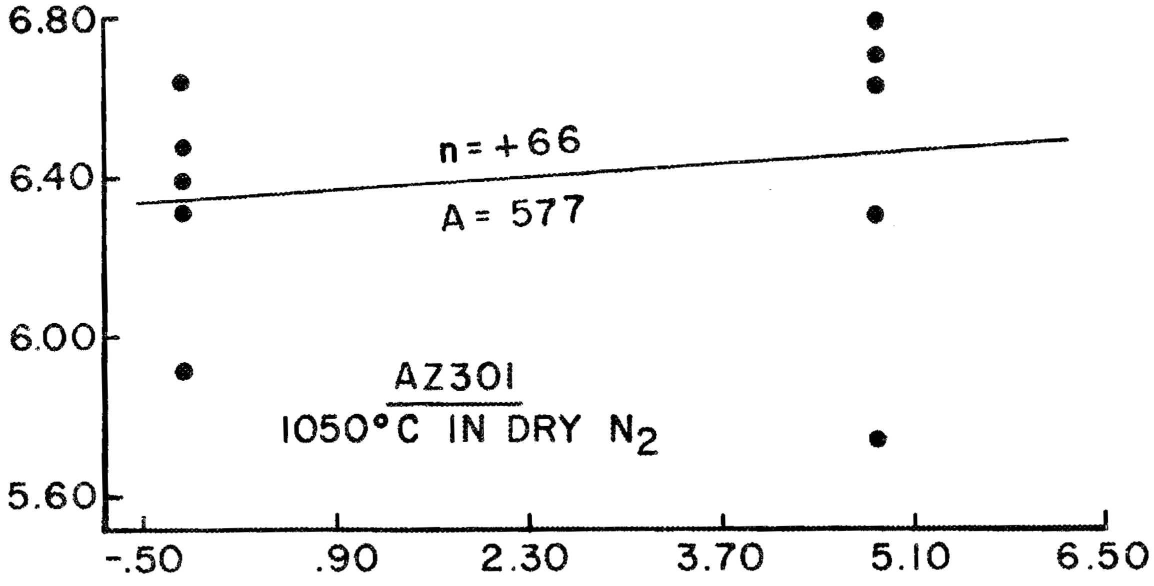

Figure 2. Dynamic Fatigue Results for AZ301 Material at 1050°C in Dry N_2.

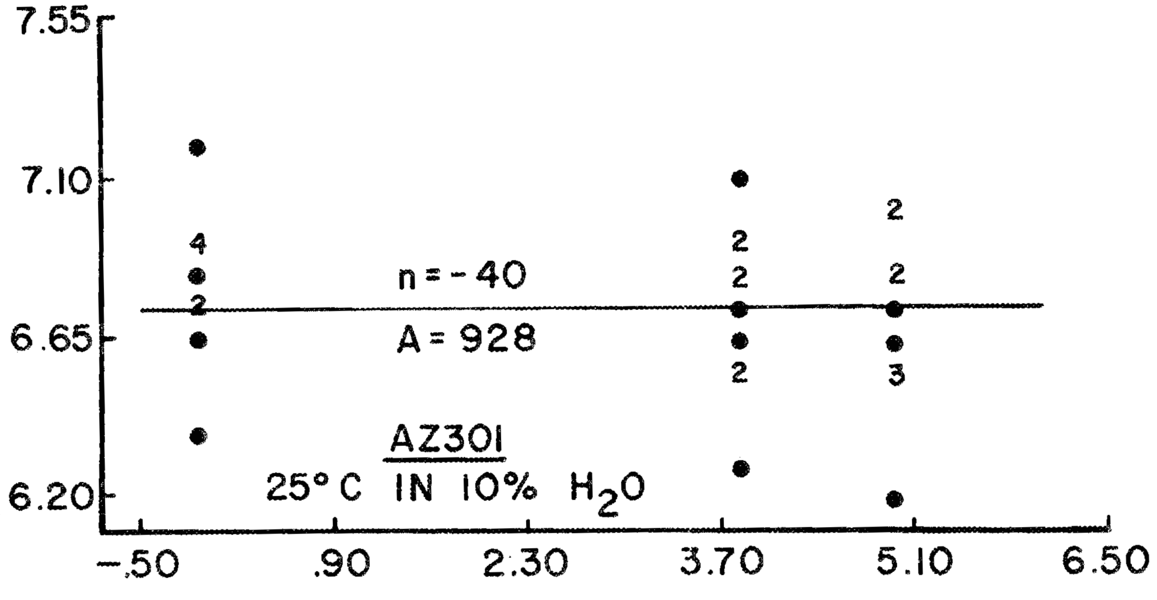

Figure 3. Dynamic Fatigue Results for AZ301 Material at 25°C in 10% H_2O.

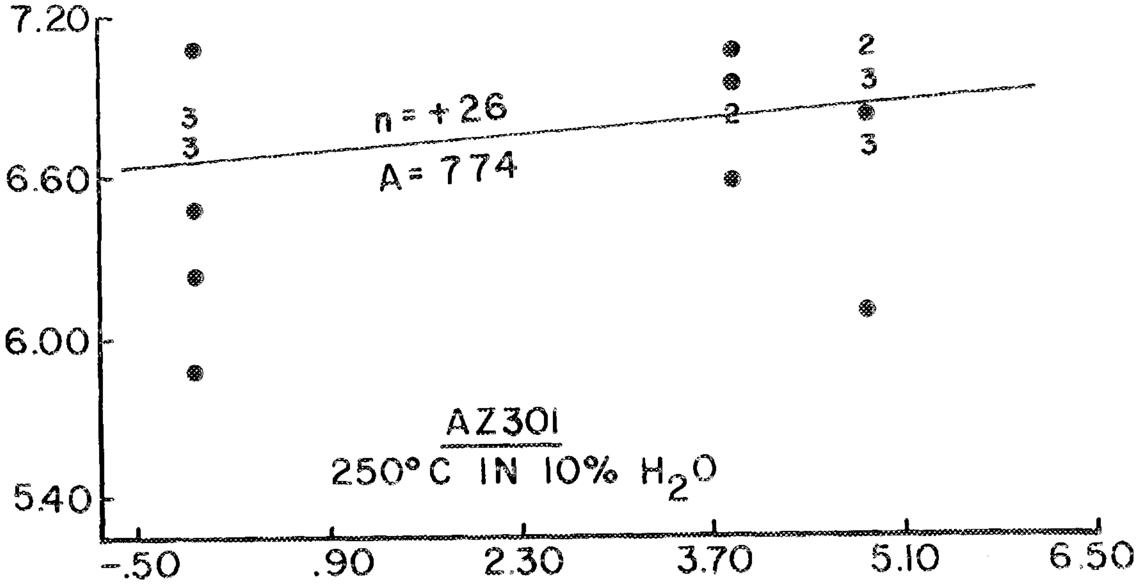

Figure 4. Dynamic Fatigue Results for AZ301 Material at 250°C in 10% H_2O.

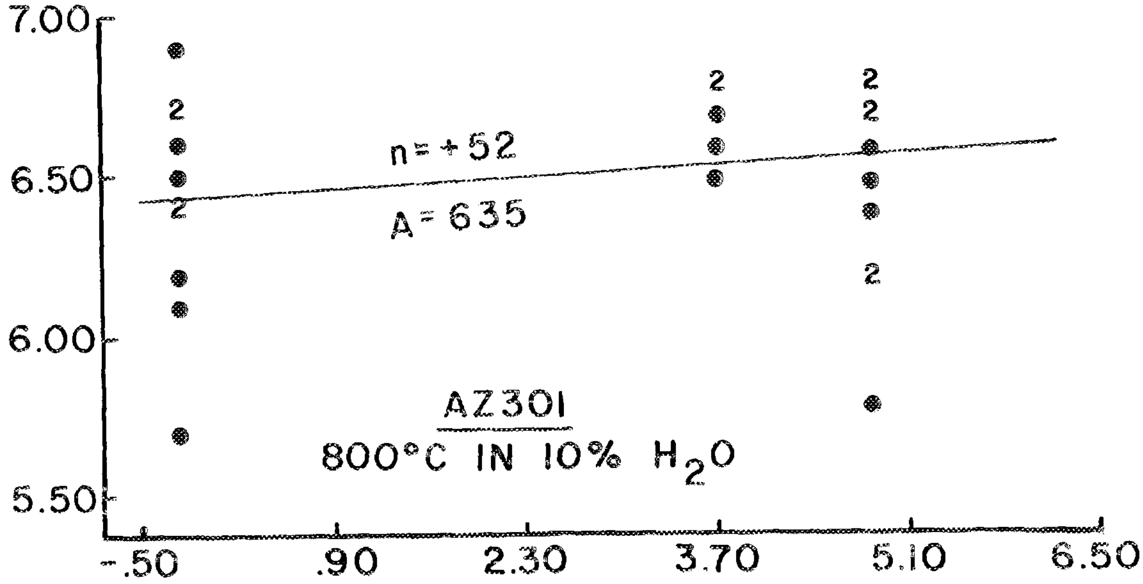

Figure 5. Dynamic Fatigue Results for AZ301 Material at 800°C in 10% H_2O.

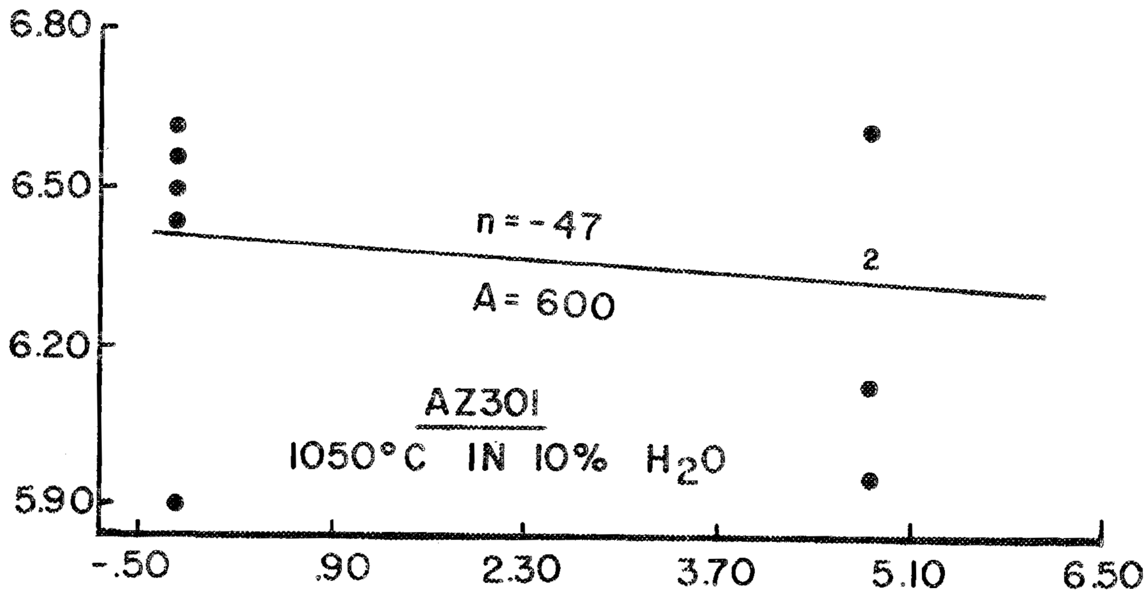

Figure 6. Dynamic Fatigue Results for AZ301 Material at 1050°C in 10% H_2O.

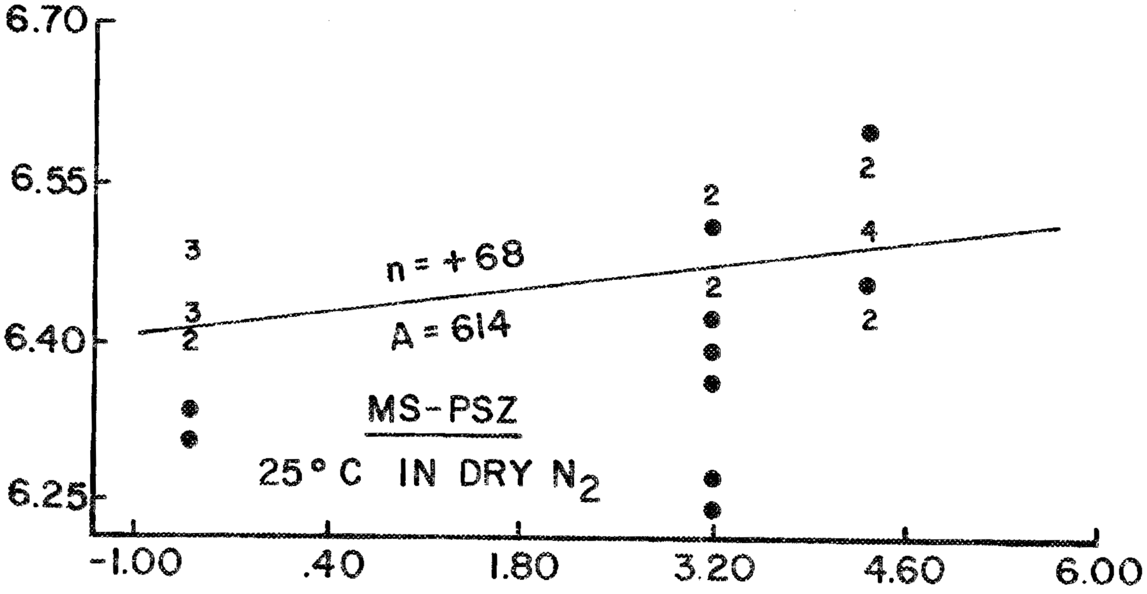

Figure 7. Dynamic Fatigue Results for MS-PSZ Material at 25°C in Dry N_2.

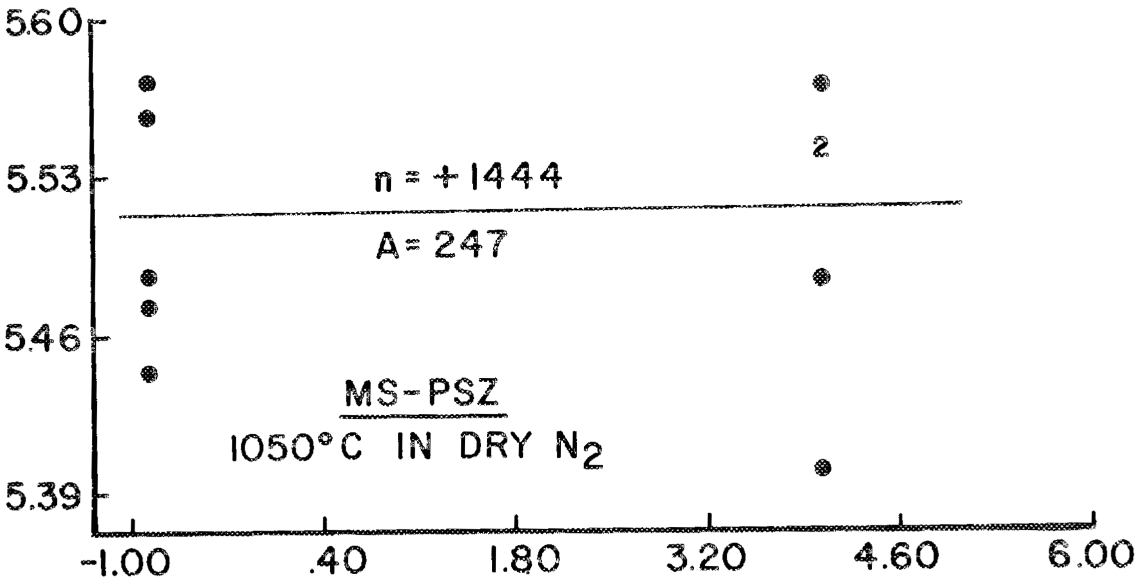

Figure 8. Dynamic Fatigue Results for MS-PSZ Material at 1050°C in Dry N_2.

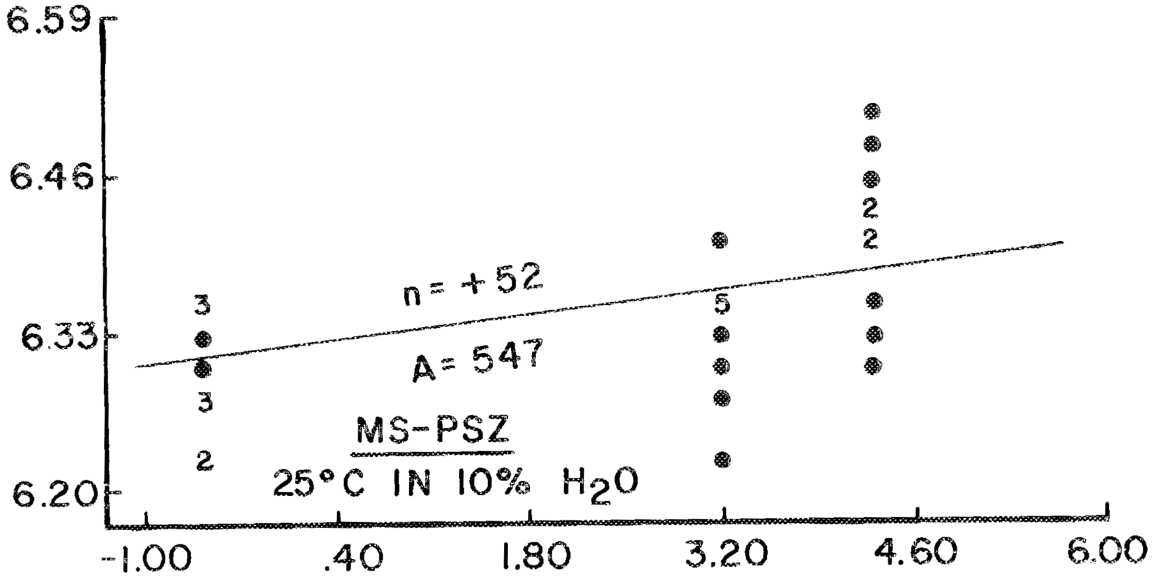

Figure 9. Dynamic Fatigue Results for MS-PSZ Material at 25°C in 10% H_2O.

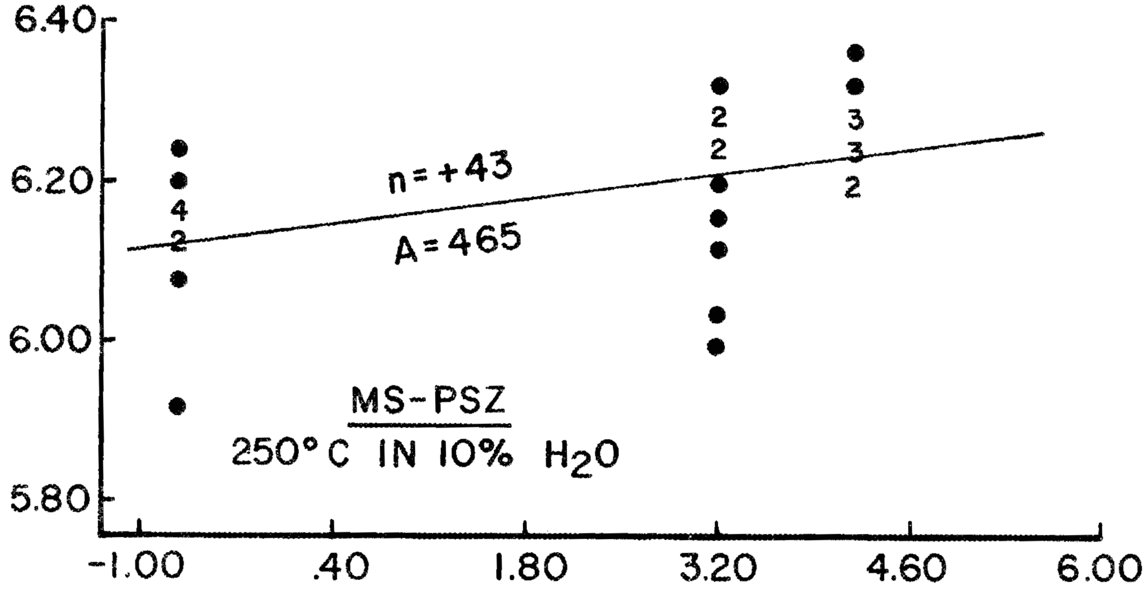

Figure 10. Dynamic Fatigue Results for MS-PSZ Material at 250°C in 10% H_2O.

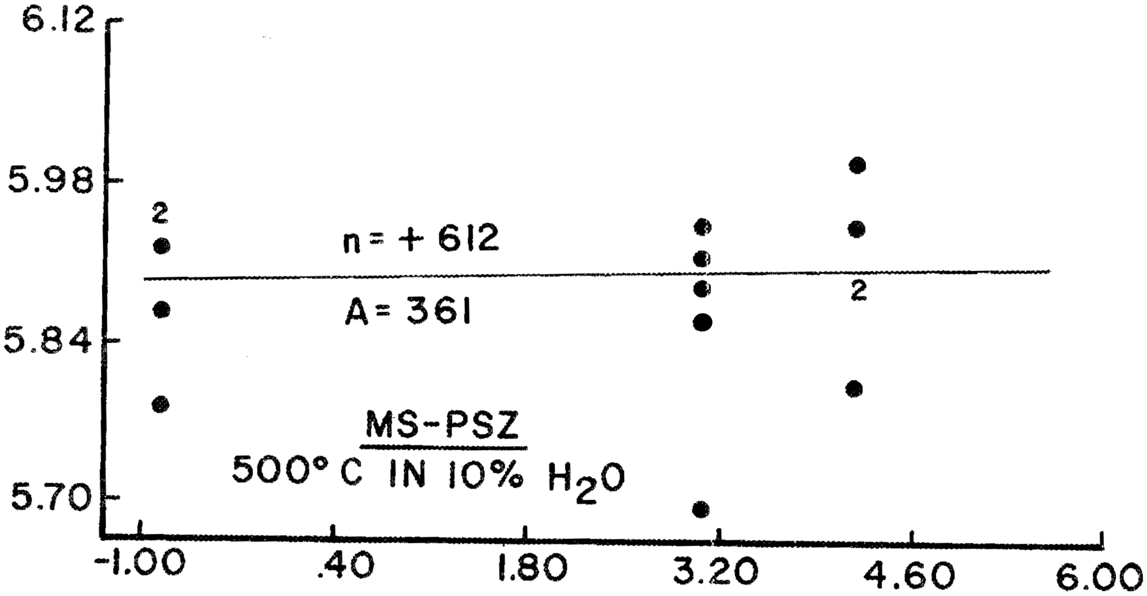

Figure 11. Dynamic Fatigue Results for MS-PSZ Material at 500°C in 10% H_2O.

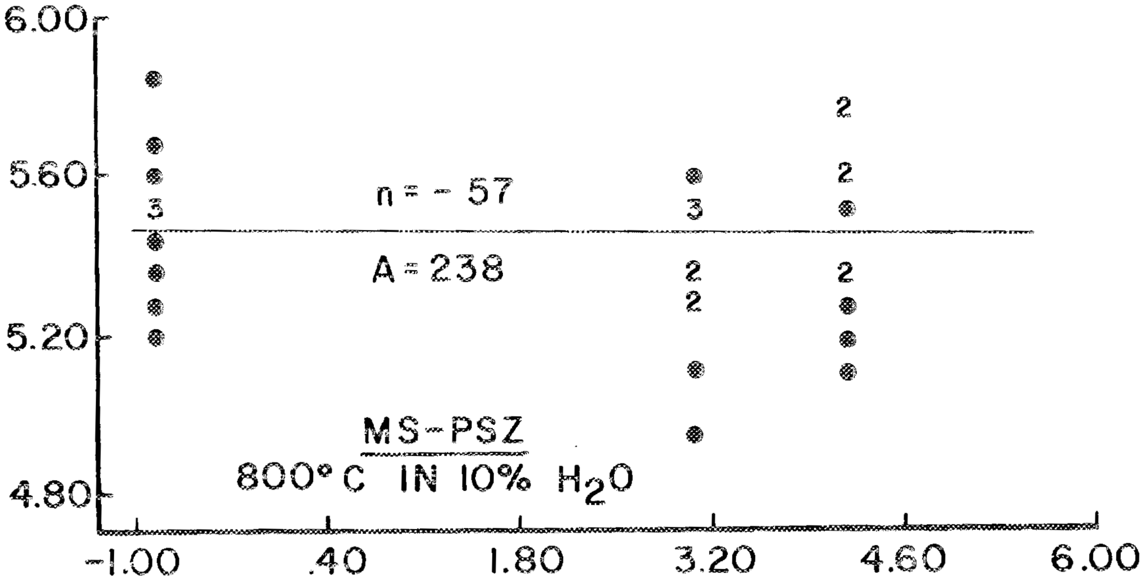

Figure 12. Dynamic Fatigue Results for MS-PSZ Material at 800°C in 10% H_2O.

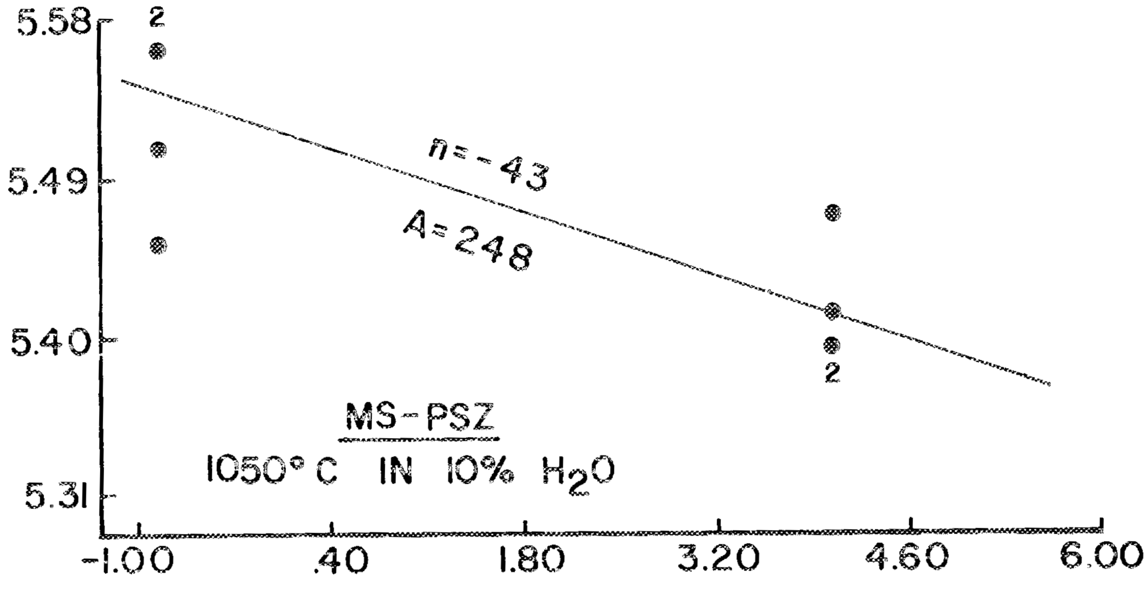

Figure 13. Dynamic Fatigue Results for MS-PSZ Material at 1050°C in 10% H_2O.

As shown in Table 8, the measured slopes and calculated n values for the AZ301 material are not significantly different from zero at any of the temperatures evaluated. It can be concluded from these results that the AZ301 material is not subject to slow crack growth. For the MS-PSZ material the dynamic fatigue analysis shows that the measured slopes and calculated n values at room temperature and 250°C were significantly different from zero indicating the occurrence of slow crack growth. At 500°C and 800°C the slope and n values are not significantly different from zero suggesting that slow crack growth does not occur at these temperatures for the MS material. At 1050°C the slope becomes negative and is significantly different from zero suggesting that a mechanism other than slow crack growth is operative. This effect may be due to the very large increase in monoclinic phase at this temperature.

It should also be noted that the use of the third loading rate added confidence to the results of the dynamic fatigue analysis. The data obtained confirmed that no slow crack growth occurred in the AZ301 material at any of the testing temperatures and that slow crack growth did not occur for the MS material at 500 and 800°C.

Conclusions

The flexure strength of the transformation toughened ceramics evaluated decreased linearly with increasing temperature. At 1050°C the transformation toughened zirconia ceramics evaluated showed a 60 to 80% decrease from room temperature flexure strengths. In addition, it was found that the fine grained TZP materials were subject to deformation, consistent with their reported creep behavior at 1000°C. It was also observed that the specimens tested in dry N_2 tended to have higher average MOR values than the MOR values for specimens tested in 10% H_2O at the same temperature. In addition it was noted that a majority of the specimens tested at fast loading rates had higher MOR values than those tested at slow loading rates. These results indicate the susceptibility of the commercial materials to environmental corrosion. The analysis of the dynamic fatigue calculations showed that the MS-PSZ and CTZP materials are definitely subject to slow crack growth at room temperature and 250°C.

Except for the CeO_2 stabilized ZrO_2, all of the evaluated transformation toughened ceramics exhibited some degree of sensitivity to low temperature (150-300°C) aging treatments in 10% H_2O. These aging treatments resulted in premature $t \rightarrow m$ transformation and changes in MOR values. It was also observed that several of the candidate materials are subject to premature transformation in aging treatments carried out in moisture free environments.

The current research program has served to facilitate the establishment of a data base for commercially available transformation toughened ceramics. Unfortunately, it is apparent that the commercially available transformation toughened ceramics studied do not have sufficiently high elevated temperature strength and resistance to environmental degradation required for high temperature structural applications in advanced heat engine systems. However, the compositions and processing procedures of these materials are being modified by the manufacturers, and it is anticipated that a number of new products will soon be available.

Future plans

A program to investigate microstructure chemistry, thermal expansion, and mechanical properties at 25°C and 1500°C for two Si_3N_4 materials and one SiC material that has been initiated will continue during the next reporting period.

Status of milestones

Milestone 331406 is in progress; all of the previous milestones have been completed.

3.4 FRACTURE MECHANICS

Improved Methods for Measuring the Fracture Resistance of Structural Ceramics

R. C. Bradt and A. S. Kobayashi (University of Washington)

Objective/scope

The long-term goals of this study are to develop and demonstrate a technique comprising a single measurement, or a technique comprising a set of correlative measurements for structural ceramics including monolithic and composite materials which will allow for the reliable and accurate determination of their resistance to fracture (crack propagation) over a broad temperature range from 20°C to 1400°C.

Technical progress

The laser interferometric strain gage (LISG) has been used successfully for fracture testing of all the materials studied in this program. Included are three monolithic ceramics: silicon carbide (Hexoloy SA), silicon nitride (GTE A2Y6) and a magnesium aluminate spinel (Coors hot pressed); and two composites: SiC whisker/alumina matrix (ARCO) Advanced Materials, HA9S) and SiC/SiC continuous fibre composite (Refractory Composites). Testing has been completed through 1400°C., using macroflawed, single-edge-notched, three-point bend bars.

Crack growth resistance curves (R-curves) were generated for all materials through 1400°C. Figure 1 shows an example of the trend of the K_R-curve behavior for the continuous fibre composite at various temperatures through 1400°C. Figure 2 is the relationship between K_{IC} and temperature using the chevron-notched specimens for all of the materials.

The continuous fiber SiC/SiC composite was used to represent the brief mechanistic study into the observed rising R-curve behavior, shown in Figure 3. Here, the test was interrupted at a predetermined crack length and removed from the machine for re-sawing of the wake area behind the crack tip. On continuation of the test, the fracture energy was observed to return to its original value found at the beginning of the test, for $a=a_0$. This indicates a significant contribution from the developing process zone wake to the noted rise in crack resistance as the crack extends.

Figures 4a and 4b illustrate the fracture toughness behavior of the SiC whisker/Al_2O_3 matrix composite and the Si_3N_4 monolithic, for both the chevron-notched and straight-notched bend bars. Note that for the composite, the chevron-notched specimen always shows a higher fracture toughness, whereas the reverse is true for the case of the Si_3N_4 monolithic material. It has been found that all of the materials in this study that exhibit R-curve behavior show a similar trend to the SiC whisker/Al_2O_3 matrix composite. This is consistent with the wake model in that the chevron notch allows for a significant amount of crack growth prior to calculation of K_{IC} at the maximum load, P_{max}, and the development of a wake zone behind the crack tip. If no wake develops, as in the case of materials, such as the Si_3N_4 which exhibit flat R-curves, the effect of the sharp crack at P_{max} in the chevron-notched specimen will represent a closer approximation of K_{IC} than the relative bluntness of the notch tip in the straight-notched specimen.

The results of the finite element analysis and a previously developed computer program were used to calculate the R-curves from the digitized load/CMOD data. A stable crack was grown into a transparent magnesium aluminate specimen to varify the crack length determined through the numerically evaluated compliance calibration curve.

Status of milestones

Although the present status is still lagging the projected milestones, elevated temperature fracture testing is now complete, and the micro-flaw and MOR tests have begun, and are expected to move rapidly with the well established test methods.

Publications

The following papers have been submitted for publication:

Fracture Toughness Testing of Ceramics Using a Laser Interferometric Strain Gage, (American Ceramic Society)

Crack Initiation and Arrest in a SiC Whisker/Al_2O_3 Ceramic-Ceramic Composite, (American Ceramic Society)

A 3-D Finite Element Analysis of a Chevron-Notched, Three-Point Bend Fracture Specimen, (International Journal of Fracture)

The following papers are being finalized for submission for publication:

1. Elevated Temperature Fracture Resistance of a Sic Whisker/Al_2O_3 Matrix Composite
2. Elevated Temperature Fracture Resistance of a Silicon Carbide
3. Elevated Temperature Fracture Resistance of a Silicon Nitride

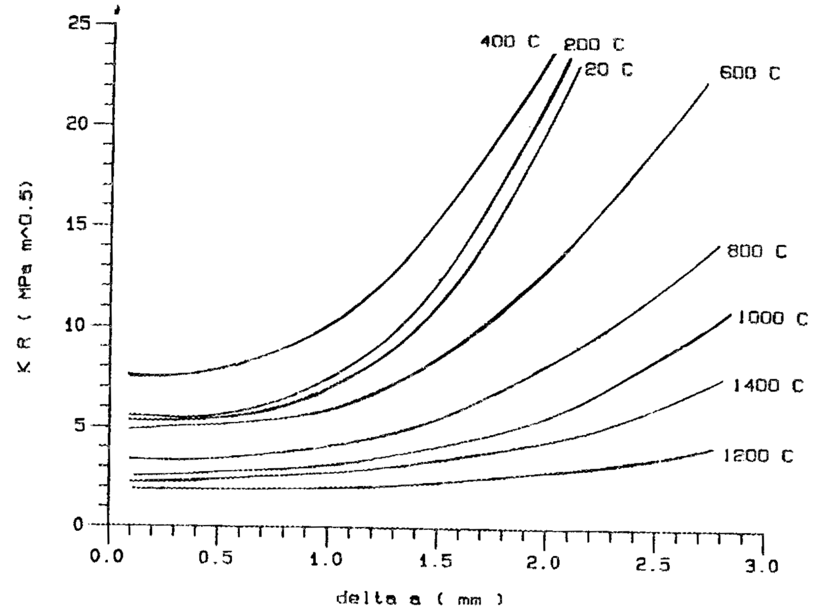

FIGURE 1
R-CURVES FOR AN SiC/SiC COMPOSITE FOR THE TEMPERATURE RANGE OF 20 C TO 1400 C.

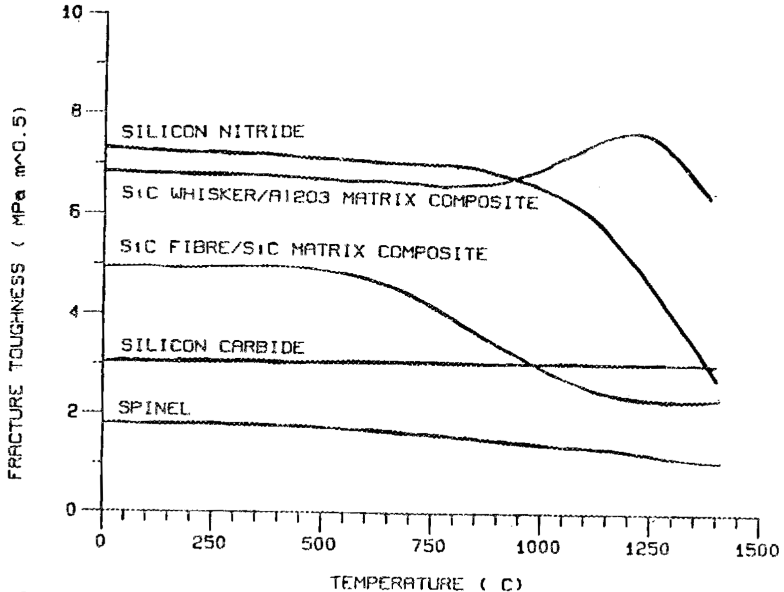

FIGURE 2
FRACTURE TOUGHNESS VERSUS TEMPERATURE FOR FIVE MATERIALS USING CHEVRON-NOTCHED, THREE-POINT BEND SPECIMENS.

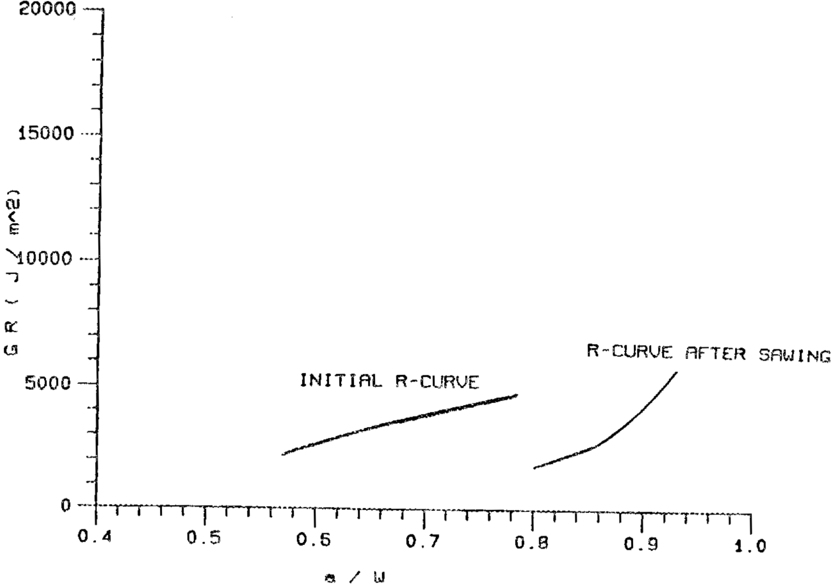

FIGURE 3
RESULTS OF THE EXPERIMENT ON THE WAKE MECHANISM.

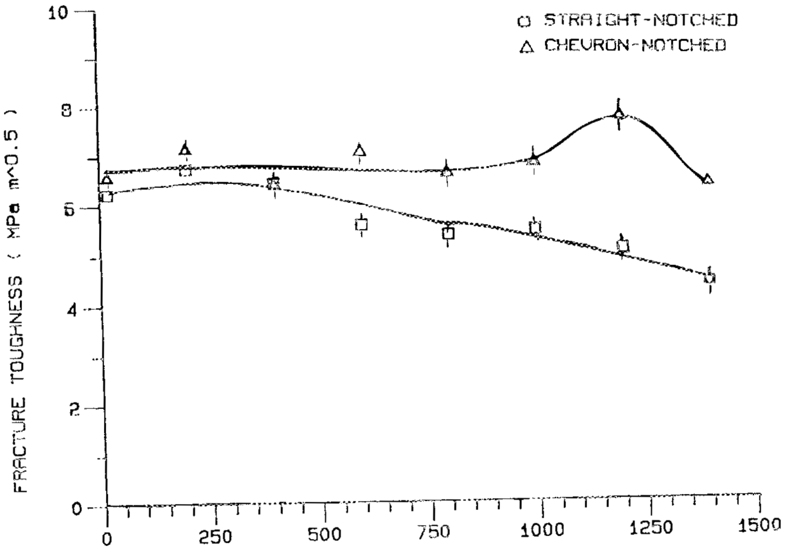

FIGURE 4a FRACTURE TOUGHNESS VERSUS TEMPERATURE FOR SiC WHISKER/Al2O3 MATRIX COMPOSITE, SINGLE-EDGE NOTCHED, THREE-POINT BEND SPECIMENS.

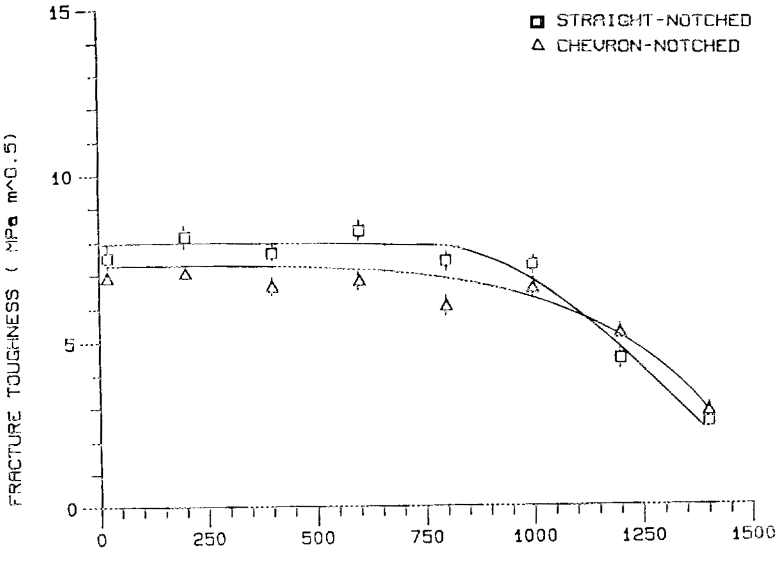

FIGURE 4b FRACTURE TOUGHNESS VERSUS TEMPERATURE FOR SILICON NITRIDE SINGLE-EDGE-NOTCHED, THREE-POINT BEND SPECIMENS.

Testing and Evaluation of Advanced Ceramics at High Temperature in Uniaxial Tension

J. Sankar, V. S. Avva, and R. Vaidyanathan (North Carolina A & T State University)

Objectives/scope

The purpose of this effort will be to test and evaluate advanced ceramic materials at temperatures up to 1500°C in uniaxial tension. Testing may include fast fracture strength, stepped static fatigue strength, and cyclic fatigue strength, along with analysis of fracture surfaces by scanning electron microscopy. This effort will comprise the following tasks:

Task 1. Specifications for Testing Machine and Controls + (Procurement)
Task 2. Identification of Test Material (s) + (Procurement of Specimens)
Task 3. Identification of Test Specimen Configuration
Task 4. Specifications for Testing Grips and Extensometer + (Procurement)
Task 5. Specifications for Testing Furnace and Controls + (Procurement)
Task 6. Development of Test Plan
Task 7. High Temperature Tensile Testing
Task 8. Reporting (Periodic)
Task 9. Final Report

It is anticipated that this two (2) year program will help in understanding the behavior of ceramic materials at very high temperatures in uniaxial tension.

Technical progress

During the reporting period, the evaluation of the alignment characteristics of the test equipment and the hydraulic self-aligning grip systems continued. As mentioned in the previous Semiannual progress report, the uniaxiality of the self aligning hydraulic grip mechanism was tested with the help of a special "Spider arm" load applicator instrumented with strain gages. The load applicator consists of a radial "Spider arm" with eight radial cantilever arms made of a high strength aluminium alloy, with indentations to seat the hydraulic pistons.

Strain gages were bonded on four cantilever arms which were 90 deg. apart. In each arm, a strain gage was mounted on top and bottom to monitor the distribution of the resulting tensile and compressive strains on the arms after application of the load. A quarter bridge circuit was used for the strain measurement. The strains were monitored continuously using a switching and balancing unit and a digital strain indicator, while a tensile load was being applied. A load range of 17.79

kN (4 Kips) was used and the strains were measured while the load was varied using the set point control, the maximum load being 14.23 kN (3.2 Kips). To counter the transverse sensitivity of the foil strain gages, the strains were measured both during the loading and unloading cycles. After completion of this test in position # 1, the load applicator (spider arm) was rotated by 45 deg. (position # 2) and the strains were again measured in each arm, under incremental loading conditions. Eight such tests were performed (position # 1 to # 8) thus completing the cycle. Tables 1 and 2 are typical data obtained for positions 1 and 2, 45 deg. apart from each other for grip # 1. Similar tests were conducted for grip # 2 also.

Fig. 1 shows the graphical plot of the results obtained for piston 1 in Table 1. Since the spider arm used for measuring the strain is aluminium, the results produced a slightly non-linear curve. In order to make comparisons easier, a least square fit of the data was plotted, assuming a straight line equation for these data points. From Fig. 1, it can be observed that both the non-linear curve and the least square fitted straight line almost overlapped each other, validating the assumption as a reasonable one. The obtained slopes ('m' values) of the least square straight lines on the compression side is always higher than that of the tension side. This is most likely due to membrane (stretching) effects, resulting in higher strain values in tension than in compression for a particular load. The difference between these two further increases as the load is increased. Further, it can be observed that there is a slight difference in the slopes between the loading and unloading leg of the tension or compression side. The viscous effect of the adhesive used in mounting the strain gages is thought to be the reason for this discrepancy.

Figures 2 through 8 show the load-strain least square fitted straight lines lines for the data obtained of pistons 3,5,7,2,4,6 and 8 respectively (Tables 1 and 2). All the slopes obtained in this way for all the pistons in the 8 tests conducted for the grip # 1 during the tensile loading and unloading are tabulated in Tables 3 and 4. It can be seen that the average slope for the individual pistons varies slightly from the grand average. Possible reasons for this deviation are:

1. Misalignment in the positions of strain gages.
2. Relative viscous deformation of the adhesive layers of the strain gages.
3. Possible difference in piston movements.
4. Possible difference between the actuator and load cell alignment.

Tables 5 and 6 represent the slopes of all the pistons in compression during loading and unloading.

The alignment between the actuator and load cell with the self aligning hydraulic mechanism installed was tested with the help of two dummy aluminium specimens (Figs. 9-10), which almost resembled the actual specimen configuration.

For a rough calibration check, the aluminium specimen in Fig. 9 was used. The specimen was bonded with 4 strain gages (CEA-06-250UW-350 type) 90 deg. apart along the circumference of the gage section to monitor the distribution of the resulting tensile strains along the circumference after application of the load. A load range of 44.48 kN

Table 1. Calibration results for Grip # 1, 0 deg. rotation from original position : Position # 1.

Load in kN			0.0	1.78	3.56	5.34	7.12	8.90	10.7	12.5	14.2
Load in Kips			0.0	0.4	0.8	1.2	1.6	2.0	2.4	2.8	3.2
			STRAIN IN MICROSTRAIN cm/cm (IN/IN)								
Piston # 1	Ten.	L	+ 0	+052	+099	+149	+200	+250	+297	+346	+398
		U	- 6	+054	+109	+161	+210	+259	+305	+353	+398
	Com.	L	- 0	-046	-091	-135	-179	-221	-264	-306	-350
		U	- 0	-055	-105	-150	-194	-234	-274	-313	-351
Piston # 3	Ten.	L	+ 0	+057	+106	+157	+208	+257	+309	+359	+410
		U	+ 0	+057	+111	+164	+215	+265	+314	+363	+410
	Com.	L	- 0	-049	-096	-142	-188	-234	-280	-326	-371
		U	- 0	-053	-104	-152	-199	-243	-287	-330	-372
Piston # 5	Ten.	L	+ 0	+067	+122	+172	+220	+266	+313	+360	+410
		U	+ 27	+091	+145	+197	+243	+287	+329	+372	+413
	Com.	L	- 0	-060	-114	-162	-206	-248	-290	-332	-375
		U	- 0	-063	-118	-170	-215	-258	-297	-338	-377
Piston # 7	Ten.	L	+ 0	+049	+097	+144	+193	+244	+293	+344	+394
		U	- 10	+049	+103	+158	+209	+259	+304	+351	+394
	Com.	L	- 0	-048	-092	-137	-182	-228	-272	-320	-365
		U	- 0	-053	-104	-155	-203	-248	-289	-329	-367

Note : Ten. denotes Strain gage measuring Tensile strains
Com. denotes Strain gage measuring Compressive strains
L : Readings in loading leg
U : Readings in unloading leg

Table 2. Calibration results for Grip # 1, 45 deg. rotation from original position : Position # 2.

Load in kN				0.0	1.78	3.56	5.34	7.12	8.90	10.7	12.5	14.2
Load in Kips				0.0	0.4	0.8	1.2	1.6	2.0	2.4	2.8	3.2
				STRAIN IN MICROSTRAIN cm/cm (IN/IN)								
Piston # 2	Ten.	L	+	0	+061	+111	+160	+209	+259	+308	+358	+408
		U	-	0	+065	+122	+175	+225	+270	+316	+363	+409
	Com.	L	-	0	-052	-096	-137	-181	-223	-266	-310	-353
		U	-	0	-055	-107	-155	-197	-238	-276	-316	-355
Piston # 4	Ten.	L	+	0	+061	+109	+157	+206	+255	+306	+356	+406
		U	+	0	+061	+117	+168	+217	+264	+312	+359	+407
	Com.	L	-	0	-053	-097	-141	-184	-229	-275	-320	-364
		U	-	0	-053	-104	-151	-196	-239	-282	-324	-366
Piston # 6	Ten.	L	+	0	+057	+106	+153	+200	+247	+294	+341	+389
		U	+	7	+064	+118	+165	+211	+256	+301	+345	+390
	Com.	L	-	0	-055	-102	-145	-189	-232	-276	-319	-363
		U	-	0	-056	-109	-153	-197	-240	-283	-323	-364
Piston # 8	Ten.	L	+	0	+061	+108	+152	+198	+246	+295	+343	+392
		U	+	0	+062	+117	+169	+217	+261	+308	+352	+393
	Com.	L	-	0	-054	-096	-137	-179	-222	-267	-310	-355
		U	-	0	-056	-108	-156	-200	-241	-282	-321	-357

Note : Ten. denotes Strain gage measuring Tensile strains
Com. denotes Strain gage measuring Compressive strains
L : Readings in loading leg
U : Readings in unloading leg

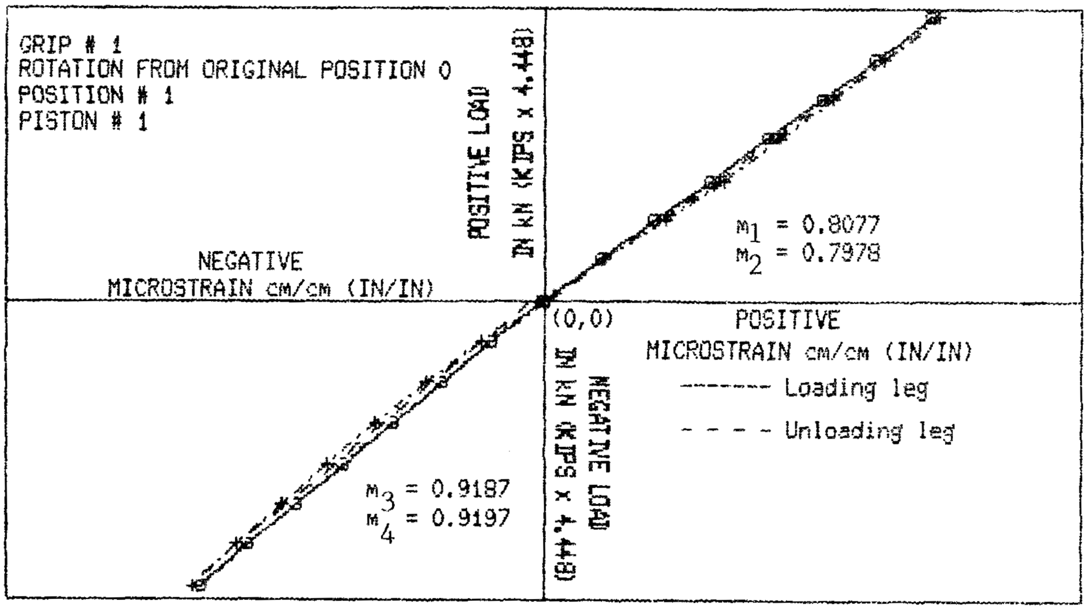

Fig. 1. Load-Strain response results of Piston 1 from Table 1. Observe the non-linear behavior of the curves and the least square linear fit of the data points.

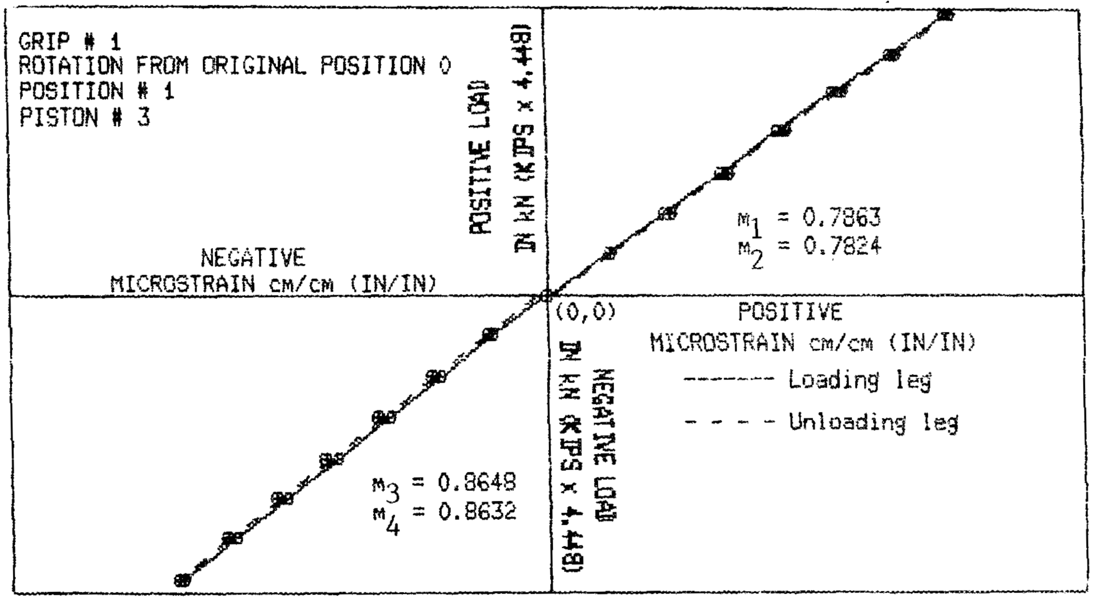

Fig. 2. Least square fitted straight line response of Load-Strain results of Piston # 3 (Table 1.).

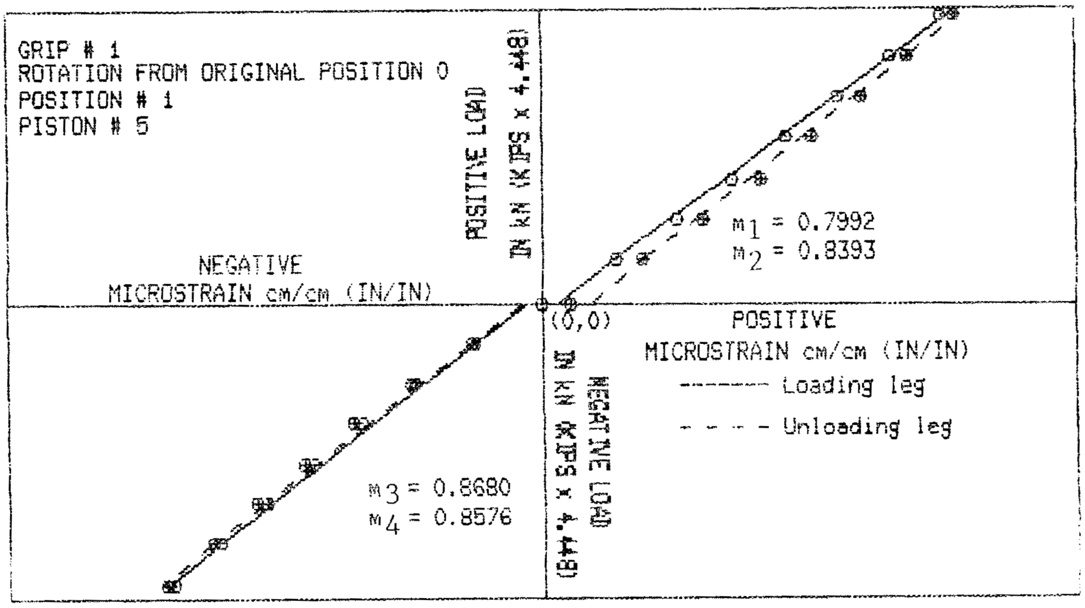

Fig. 3. Least square fitted straight line response of Load-Strain results of Piston # 5 (Table 1.).

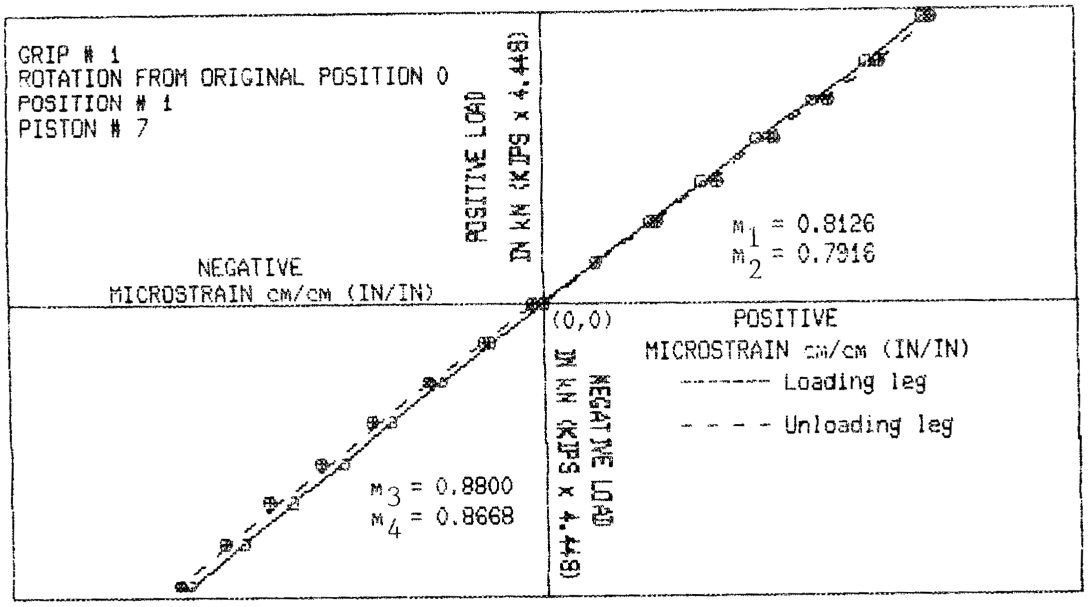

Fig. 4. Least square fitted straight line response of Load-Strain results of Piston # 7 (Table 1.).

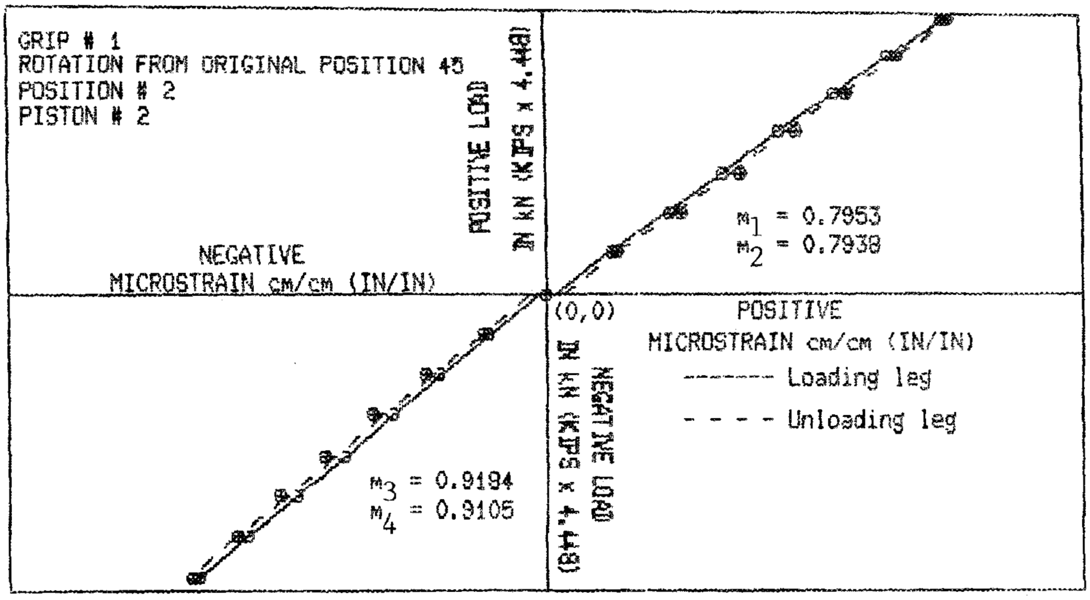

Fig. 5. Least square fitted straight line response of Load-Strain results of Piston # 2 (Table 2.).

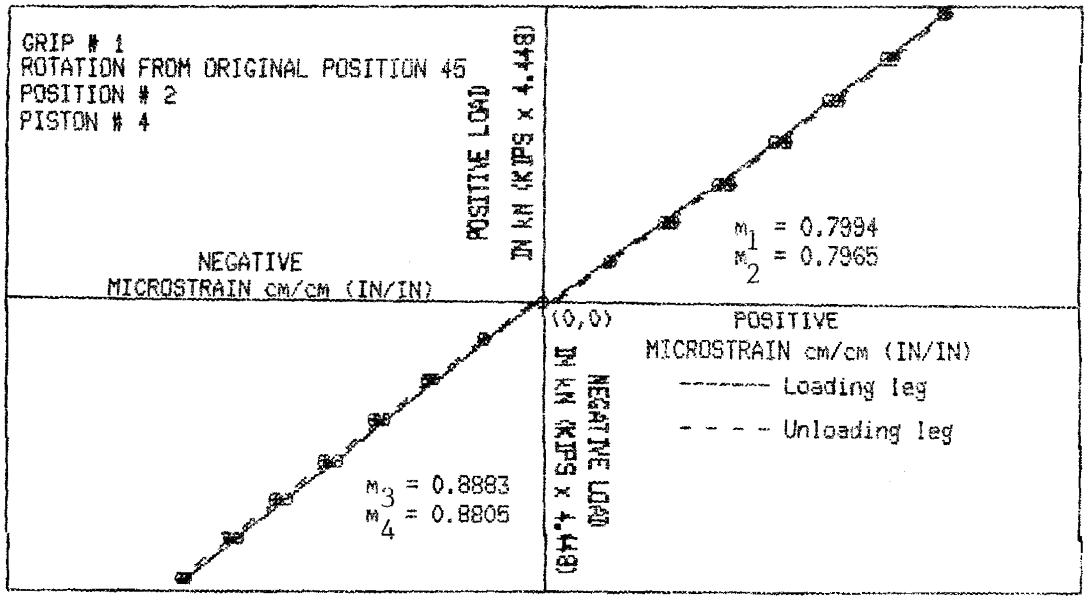

Fig. 6. Least square fitted straight line response of Load-Strain results of Piston # 4 (Table 2.).

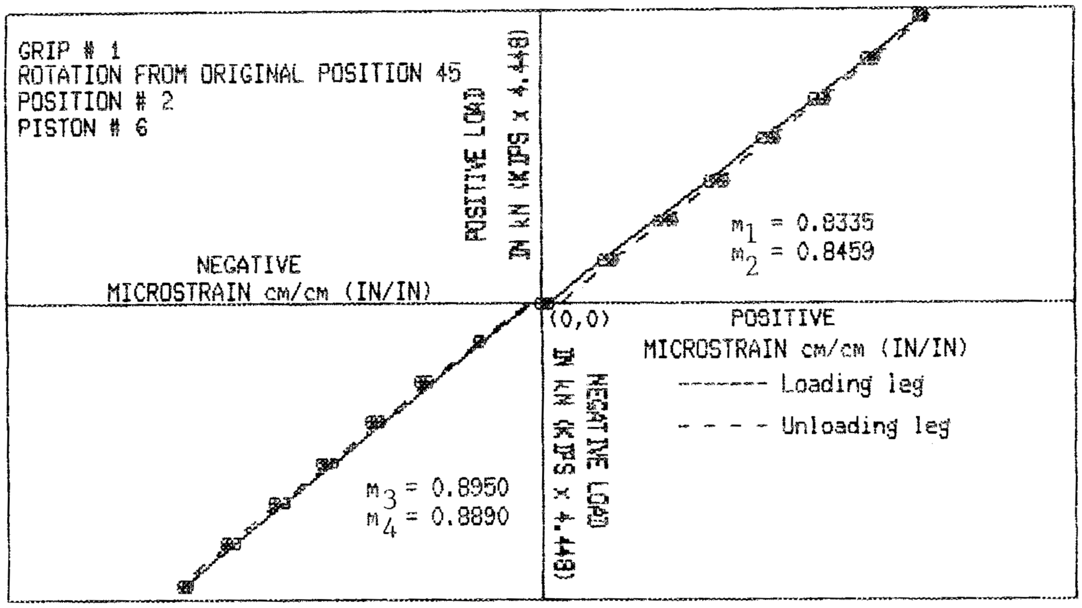

Fig. 7. Least square fitted straight line response of Load-Strain results of Piston # 6 (Table 2.).

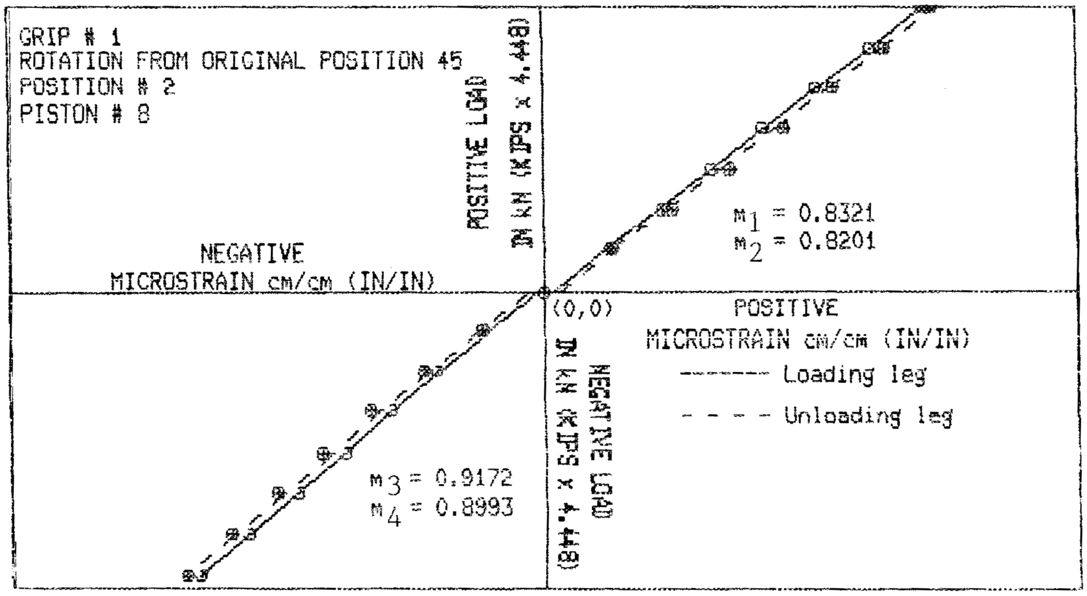

Fig. 8. Least square fitted straight line response of Load-Strain results of Piston # 8 (Table 2.).

Table 3. Slopes of the load-strain response curves for Grip # 1 for the loading leg on Tension side.

Test #	Piston #							
	1	2	3	4	5	6	7	8
1	0.8077		0.7863		0.7992		0.8126	
2		0.7953		0.7993		0.8335		0.8321
3	0.8281		0.7828		0.7933		0.8197	
4		0.8390		0.7732		0.7898		0.8259
5	0.8412		0.8187		0.7656		0.7971	
6		0.8528		0.8115		0.7903		0.8108
7	0.7542		0.8132		0.8115		0.7855	
8		0.8072		0.7892		0.7446		0.7973
Avg.	0.8078	0.8236	0.8003	0.7933	0.7924	0.7896	0.8037	0.8165
Grand Avg. :=		0.8034						

Table 4. Slopes of the load-strain response curves for Grip # 1 for the unloading leg on Tension side.

Test #	Piston #							
	1	2	3	4	5	6	7	8
1	0.7978		0.7824		0.8393		0.7916	
2		0.7938		0.7965		0.8459		0.8201
3	0.8258		0.7823		0.7831		0.8621	
4		0.8365		0.7987		0.7860		0.8372
5	0.8451		0.8148		0.7482		0.7950	
6		0.8474		0.8115		0.7834		0.7997
7	0.7525		0.8258		0.8056		0.7743	
8		0.7935		0.7734		0.7940		0.7737
Avg.	0.8053	0.8178	0.8013	0.7950	0.7941	0.8023	0.8058	0.8077
Grand Avg. :=		0.8037						

Table 5. Slopes of the load-strain response curves for Grip # 1 for the loading leg on compression side.

Test #	Piston #							
	1	2	3	4	5	6	7	8
1	0.9187		0.8648		0.8680		0.8800	
2		0.9184		0.8883		0.8950		0.9172
3	0.9174		0.9063		0.8723		0.8809	
4		0.9312		0.9024		0.8797		0.8986
5	0.9110		0.9107		0.8730		0.8934	
6		0.9132		0.8939		0.9137		0.9020
7	0.8364		0.8781		0.8997		0.9083	
8		0.8810		0.8376		0.9035		0.8928
Avg.	0.8959	0.9110	0.8890	0.8806	0.8675	0.8980	0.8907	0.9027

Grand Avg. := 0.8919

Table 6. Slopes of the load-strain response curves for Grip # 1for the unloading leg on compression side.

Test #	Piston #							
	1	2	3	4	5	6	7	8
1	0.9197		0.8632		0.8576		0.8668	
2		0.9105		0.8805		0.8890		0.8993
3	0.9104		0.9032		0.8587		0.8710	
4		0.9241		0.8941		0.8731		0.8786
5	0.8983		0.9044		0.8586		0.8871	
6		0.8995		0.8875		0.9042		0.8824
7	0.8305		0.8747		0.8898		0.8948	
8		0.8744		0.8182		0.8909		0.8875
Avg.	0.8897	0.9021	0.8864	0.8701	0.8662	0.8893	0.8799	0.8870

Grand Avg. := 0.8838

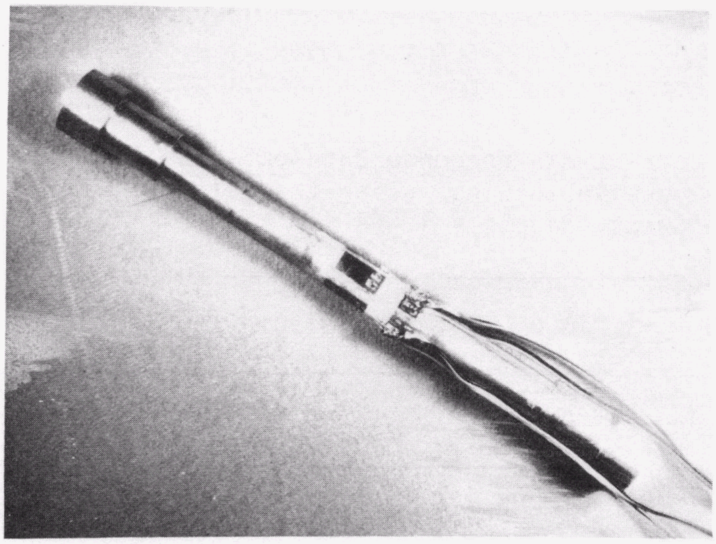

Fig. 9. Close up view of Aluminium Sample # 1 (A & T Sample)

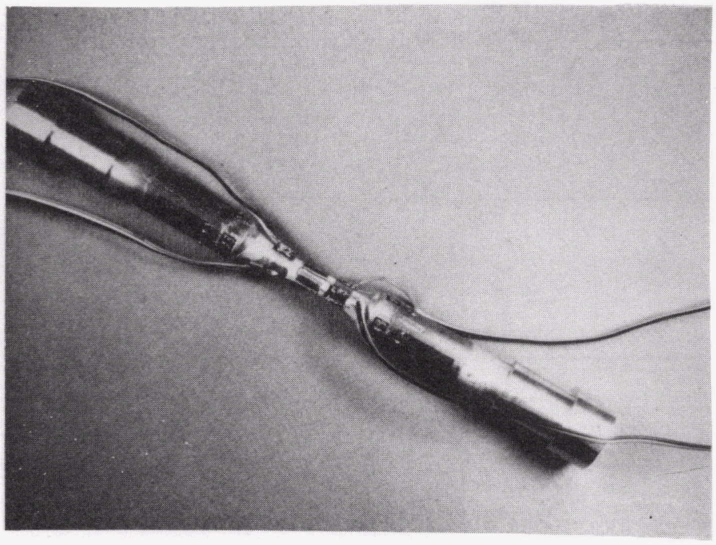

Fig. 10. Close up view of Aluminium Sample # 2 (ORNL Sample)

Table 7. Load-Strain response data obtained for Aluminium Sample on tensile loading. using the Self aligning Hydraulic Grips, Sample # 1. (A & T sample)

Load in kN		0.0	4.45	8.90	13.34	22.24	31.14
Load in Kips		0.0	1.0	2.0	3.0	5.0	7.0
		Strain in Micro Strain cm/cm (IN/IN)					
Gage # 1	L	+ 0	+ 511	+1007	+1515	+2559	+3619
	U	+ 0	+ 484	+ 998	+1518	+2551	+3625
Gage # 2	L	+ 0	+ 494	+1037	+1582	+2666	+3749
	U	+ 65	+ 513	+1068	+1612	+2673	+3752
Gage # 3	L	+ 0	+ 520	+1050	+1562	+2594	+3620
	U	+ 0	+ 534	+1046	+1562	+2594	+3622
Gage # 4	L	+ 0	+ 541	+1037	+1537	+2559	+3603
	U	- 52	+ 518	+1010	+1515	+2557	+3602

Note :
1. L denotes readings in Loading cycle.
2. U denotes readings in Unloading cycle.

Table 8. Load-Strain response data obtained for Aluminium Sample on tensile loading, using the Self aligning Hydraulic Grips, Sample # 2. (ORNL sample)

Load in kN		0.0	0.89	1.78	2.67	4.45	6.23
Load in Kips		0.0	0.2	0.4	0.6	1.0	1.4
		Strain in Micro Strain cm/cm (IN/IN)					
Gage # 1	L	+ 0	+ 429	+ 812	+1205	+2000	+2772
	U	- 134	+ 405	+ 772	+1149	+1945	+2756
Gage # 2	L	+ 0	+ 382	+ 788	+1200	+2004	+2816
	U	- 314	+ 428	+ 845	+1247	+2022	+2811
Gage # 3	L	+ 0	+ 352	+ 754	+1146	+1944	+2752
	U	+ 107	+ 309	+ 727	+1140	+1940	+2751
Gage # 4	L	+ 0	+ 400	+ 779	+1155	+1944	+2728
	U	+ 288	+ 336	+ 704	+1086	+1906	+2724

Note : 1. L denotes readings in Loading cycle.
2. U denotes readings in Unloading cycle.

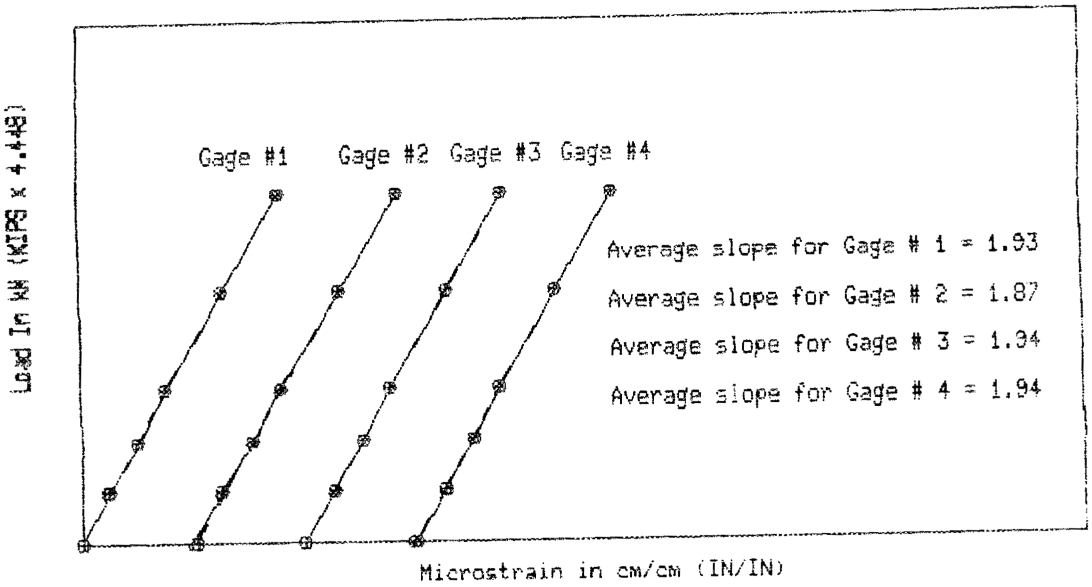

Fig. 11. Load-Strain response curves for Dummy Aluminium Sample, Sample # 1

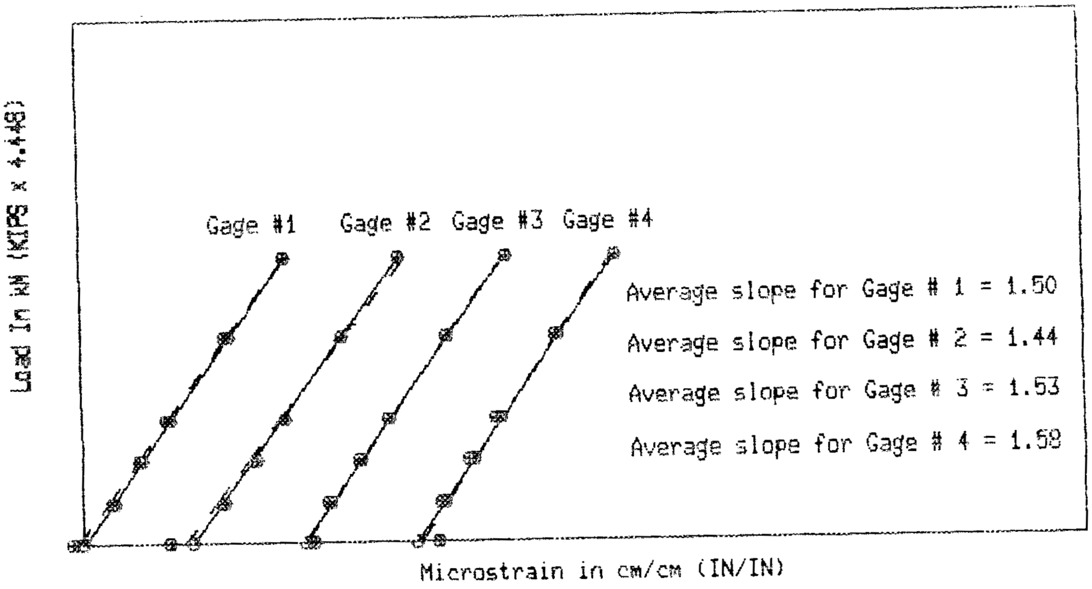

Fig. 12. Load-Strain response curves for Dummy Aluminium Sample, Sample # 2

(10 Kips) was used and the strains were measured while the load was varied using a set point control, the maximum load being 31.14 kN (7Kips). Table 7 shows the typical data obtained for this specimen. Fig. 11 shows the load strain least square fitted straight lines for the data obtained in Table 7. To check the calibration further, an aluminium sample (Fig. 10) with a gage section almost matching that of the actual ceramic test specimen configuration was used. The sample was supplied by Ken Liu of the ORNL.

The test was similar to the test for the specimen in Fig..9 except that the load range was 8.90 kN (2 Kips), the maximum load applied being 6.23 kN (1.4 Kips) and the strain gages used were EA-13-031DE-350 type. The typical data obtained for this specimen is given in Table 8. Fig. 12 shows the load strain least square fitted straight lines for the data obtained in Table 8. From Figs 11-12, it can be observed that the average slopes of the load strain response curves are almost identical, the possible deviations due to the misalignment in the positions of the strain gages. It must be said here that a great amount of care should be exercised while mounting the specimen in the grips. The strain measurement techniques used in the tests are extremely sensitive and even the slightest variation in the sample mounting technique can produce a big change in the strain values.

It is concluded from these results that the operation and the accuracy of this self-aligning hydraulic grip system used looks promising for conducting the uniaxial tension test of ceramics.

Status of Milestones

Tasks 1-4 are complete. High temperature grips have already arrived and furnace specifications and extensometry are being discussed with the furnace manufacturers. Test plan for the program (Task 6) is ready and the testing will start as soon as the samples arrive.

Publications

1. J. Sankar, R. Vaidyanathan, V. S. Avva, A. D. Kelkar and K. C. Liu, "A New approach for Testing Ceramics in Uniaxial Tension", paper submitted to "Test, Measurement and Inspection for Quality Control" conference, Detroit, Michigan, September 1987.

Standard Tensile Test Development

S. M. Wiederhorn, L. Chuck, T.-J. Chuang and D. E. Roberts
(National Bureau of Standards)

Objective/scope

This project is concerned with the development of test equipment and test procedures for measuring the tensile strength and creep resistance of ceramic materials at elevated temperatures. Inexpensive techniques of measuring the creep and strength of ceramics at elevated temperatures are being developed and will be used to characterize the mechanical behavior of structural ceramics. The test methods use self aligning fixtures, and simple grinding techniques for specimen preparation. Creep data obtained with tensile test techniques will be compared with data obtained using flexure and compressive creep techniques. The ultimate goal of the project is to assist in the development of a reliable data base that can be used for structural design of heat engines in vehicular applications.

Technical progress

Tensile Testing of Siliconized Silicon Carbide.

During the past 6 months, a pin and clevis fixture has been used to obtain creep data on siliconized silicon carbide. The test specimen configuration is indicated in figure 1. The specimen is held in the test apparatus by an α-SiC pin through each end of the specimen. As with specimens for the clothespin design, each specimen is made by simple grinding operations using a shaped grinding wheel. The cost of the specimen is approximately the same as that for the clothespin design fixture ~ $75. Creep is measured from the gauge section of the specimen using flags of the same design as that used earlier in this study. Creep data obtained at 75 MPa and 1300°C indicate a similar behavior to that already obtained in this study, a relatively short transient creep period followed by a lengthy steady state creep period, figure 2. The creep data obtained by the pin and clevis device is consistent with that obtained by the clothespin apparatus used earlier. As can be seen in figure 3, the creep data plot on a single curve; both sets of data suggest a change in creep mechanism for stresses exceeding ≈100 MPa. As discussed earlier, this change in mechanism can be attributed to cavitation within the gauge section at the higher stresses. This observation supports the data obtained by Carroll and Tressler on the same material at 1100°C. Since cavitation eventually results in component failure, more recent experiments on the project are being directed towards the collection of creep rupture data and the correlation of such data with the creep rate at elevated temperatures. Specifically, we are exploring the possibility that the failure mechanism of this material can be described by a Monkman-Grant type of plot. We expect to have relevant information to report on this subject by the next semi-annual report.

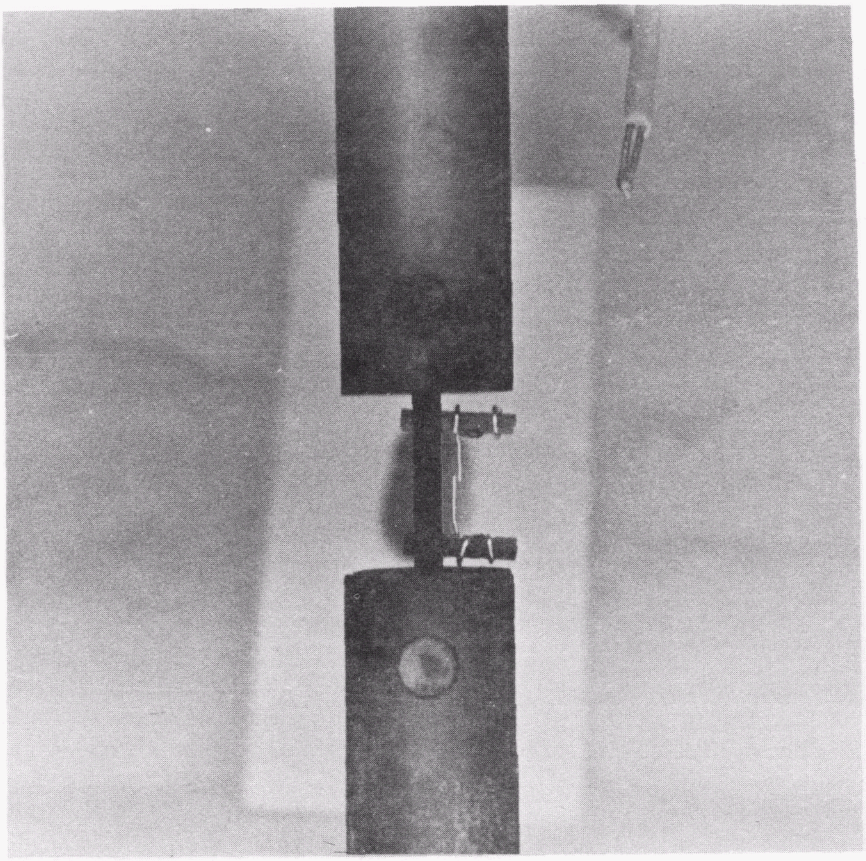

1. Test specimen configuration: the specimen is held to the test apparatus by an α-SiC pin through each end of the specimen; as with specimens for the clothespin design, each specimen is made by simple grinding operations using a shaped grinding wheel.

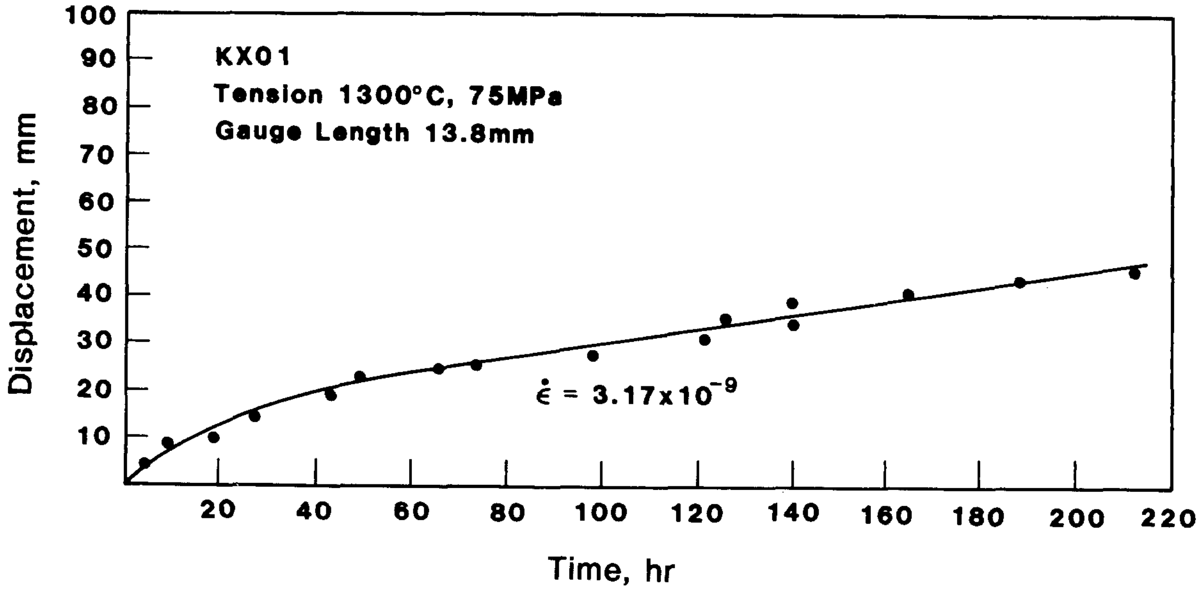

2. Creep data obtained at 75 MPa and 1300°C using the pin and clevis design. The creep behavior is similar to that already obtained in this study: a short transient creep period is followed by a lengthy steady state creep period.

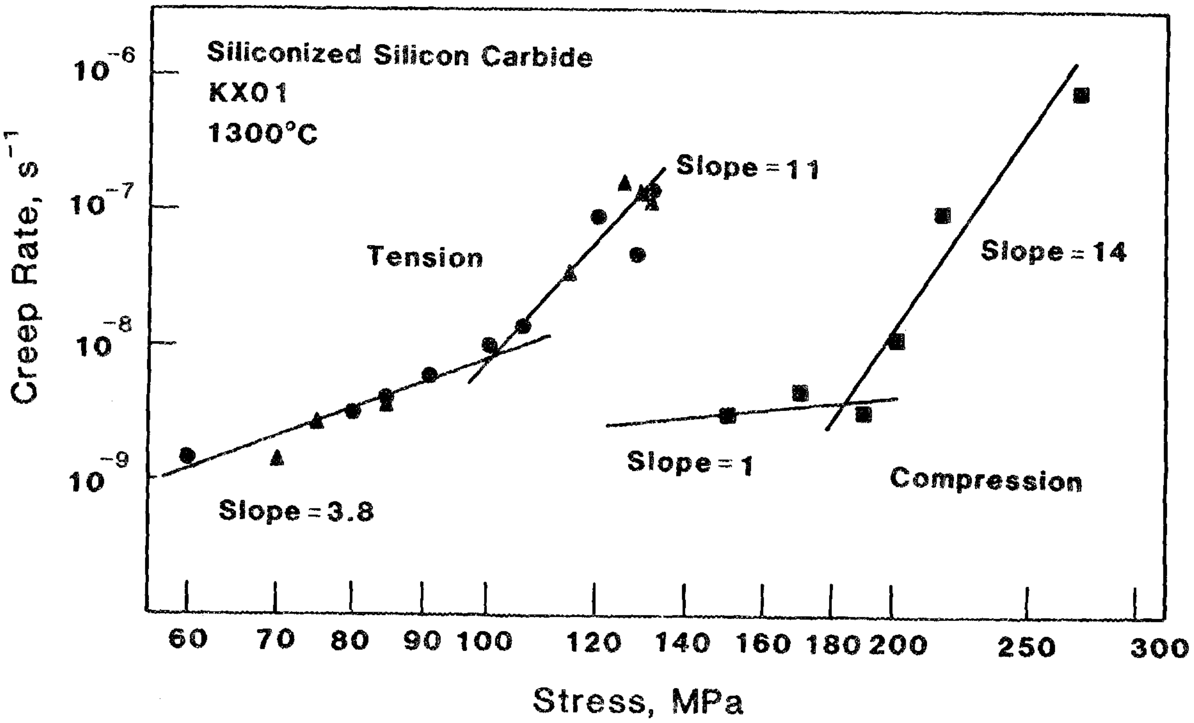

3. A comparison of creep data obtained by the pin and clevis device ● with similar data obtained using the clothespin design ▲ shows that the creep data plot on a single curve, both sets of data suggesting a change in creep mechanism at a stress exceeding ≈100 MPa. A comparison of compressive creep data obtained to date with the tensile creep data suggests that siliconized silicon carbide is far more resistant to creep in compression than it is in tension.

Compressive Testing of Siliconized Silicon Carbide

Although compressive testing has proven more difficult than first imagined, we have finally overcome these difficulties (specimen alignment and sticking of specimens) and now have a configuration that works. The test geometry adopted for the study is illustrated in figure 4. Specimens ≈8x3x3 mm were mounted between two pedestals made of the same grade of siliconized silicon carbide. Creep was measured from the edge of the pedestal using a traveling optical telescope. To view the pedestal, it was necessary to remove some of the insulation in the wall of the furnace lying just behind the specimen. This created a dark background so that the edge of the pedestal could be sharply imaged in the eyepiece of the microscope. The accuracy of gauge length measurement is estimated to be ±3 μm. To improve specimen alignment, the upper pedestal was rounded by gently hand polishing with diamond paste (15 μm) on a soft cloth lap. Hand holding the pedestal during polishing assured the center to be raised above the edges of the pedestal. To support the load, 2x2x1 cm blocks of creep resistant α-SiC were used on each end of the loading train. Finally, to prevent sticking of the α-SiC blocks to the silicon carbide push rods, thin discs of aluminum oxide (Vistal) were used as spacers. By following this procedure, creep measurements were easily obtained and sticking of the specimen to the load train was avoided.

Currently, compressive creep data are being collecting at 1300°C in the stress range 100 to 270 MPa. An example of compressive creep data on siliconized silicon carbide is shown in figure 5. Within the scatter of the data, we see evidence for a very short transient creep stage. As in the case of the tensile creep data, the transient stage is over relatively quickly for this material.

The creep data obtained to date is compared in figure 3 with the tensile creep data. As can be seen, siliconized silicon carbide is far more resistant to creep in compression than in tension. At 150 MPa for example, the creep rate in tension is approximately 400 times that obtained in tension. As a tentative explanation for the lower creep rate in compression, we suggest that creep in compression is due to contact between SiC grains, so that deformation of the SiC skeletal network controls the creep rate. Since silicon carbide is more difficult to deform than silicon, the creep rate at a given stress is expected to be much greater in tension than in compression. Additional creep studies and microstructural analyses of the deformed specimens will be needed to confirm this view. The type of behavior discussed above does, however, lead to stress redistributions and to the shifts in the neutral axes that have been reported earlier on this project.

Theoretical Analysis of Creep in Flexure

With the development of a method to obtain compressive creep data, it is now possible to predict creep behavior in flexure from more elementary creep data. In particular it is possible to show that anomalous behavior of creep bars in flexural loading is due to the differences in behavior in tension and compression.

Compressive Creep Test Configuration

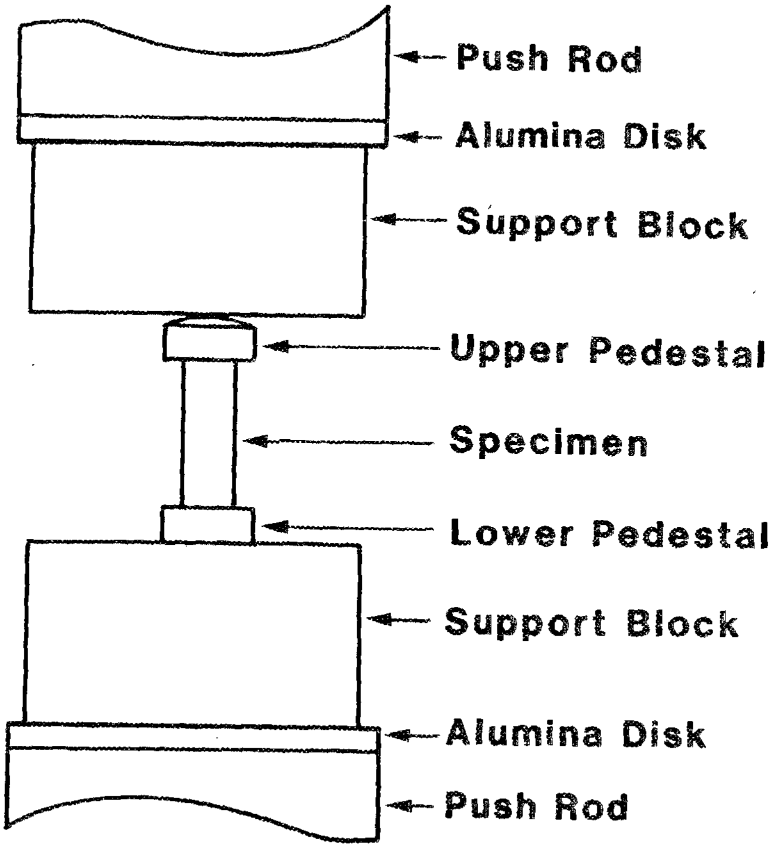

4. Test geometry adopted for the study of compressive creep in high temperature structural ceramics. Displacement measurements are made directly from each pedestal by direct observation with a travelling telescope.

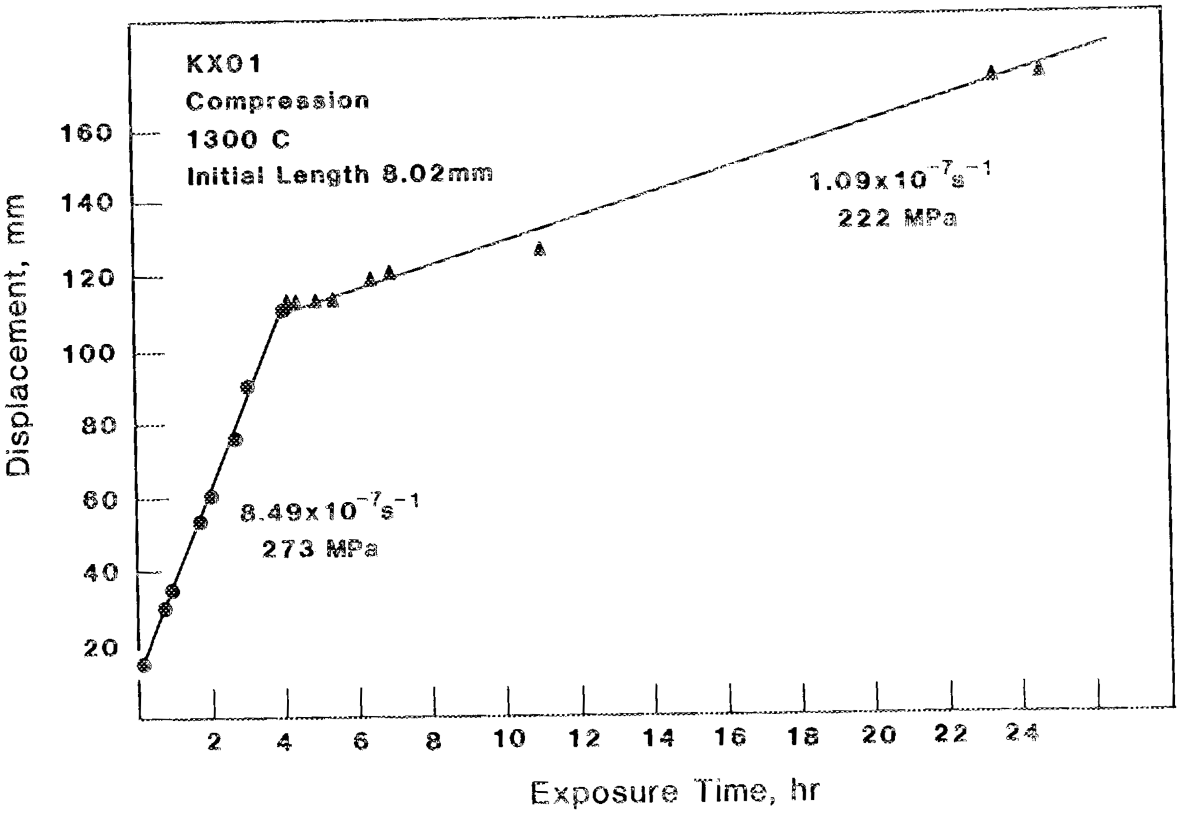

5. An example of compressive creep data obtained on siliconized silicon carbide. Within the scatter of the data, we see little evidence of a transient creep stage.

The transient creep of a ceramic bend bar under constant load was analyzed using a scheme developed earlier by Cohrt et al. The methodology assumes that the beam is formed by an infinite number of parallel fibers, each modelled as a Maxwell fluid consisting of an elastic spring and a dashpot connected in series. The numerical solution produces a time history of stress along the beam depth, ranging from a linear (elastic) distribution at initial loading to a nonlinear distribution at steady state. Also available from this numerical solution are the transient periods and the time-dependent migration of the neutral planes in stress and strain, the latter being measurable and thus experimentally verifiable. The theoretical analysis confirms experimental data in three ways: the analysis predicts long periods of transient behavior, even when the material itself is in steady state creep; the analysis correctly predicts the size of the cavitation zone in bend bars; and finally, the analysis qualitatively predicts the motion and final position of the plane of neutral strain. It is hoped that analyses of this type can be expanded and used to develop criteria for failure of components that are subjected to complex modes of loading.

Tensile and Compressive Testing of SIALON Type Materials

During the coming year studies will be started on commercial grades of sintered silicon nitride. The material to be investigated will be Kyocera silicon nitride, grade SN220M, obtained from a slip cast turbine rotor (courtesy of Dr. L.C. Lindgren, Allison Co.). These have been forwarded to the NBS Grinding Shop to be made into specimens. Tests will commence on these during the coming year. In addition to these commercial grades of silicon nitride, studies will be initiated on an experimental grade of β_{10}-7G SIALON, hot-pressed by Mr. Ching-Fong Chen a graduate student working for Prof. Tien at the Department of Materials Science and Engineering, The University of Michigan, Ann Arbor, MI. Mr. Chen has been doing all of the electron microscopy and mechanical testing for his thesis at the National Bureau of Standards, Ceramics Division, with nominal support of this project (mainly shop work). During the next six months he will be collecting compressive and tensile creep data on the SIALON material he is studying. Since the microstructure of the SIALON material is very similar to the Kyocera material that we will be studying, a comparison of the three types of creep data should be transferable to the present program. At present, compressive specimens are being tested and tensile specimens are being prepared at the NBS Grinding Shop. At the end of this report period, we expect to have data to report on the SIALON material.

Status of milestones

Test technique development: To date all milestones have been met or are on target. The clothespin design test fixture and the pin and clevis test fixture are both operational and are being characterized for degree of bending. If agreement is obtained between these two techniques and if the fixtures can be shown to apply a uniform stress in the gauge section, the construction of a third type of test fixture (powder grip design) will be canceled.

Comparison of creep data obtained in tensile testing with that obtained in compression and bending: This portion of the program is ahead of schedule. Creep data has already been obtained in tension and in bending; compressive creep equipment have been constructed, and data are being collected on both siliconized silicon carbide and SIALON. Data collection on this portion of the program is expected to be completed for the siliconized silicon carbide as of 7/87. Two lectures on this subject will be presented at the Annual Meeting of the American Ceramic Society in May. A paper on this subject has been written and will be submitted for publication by 8/87.

Inter-laboratory comparison of tensile test method: Although the milestones for this portion of the program lie in the future, a comparison is being made between our data and that collected at Pennsylvania State University on the same material. We view this comparison as a prelude to a inter-laboratory comparison on tensile test techniques for ceramic materials at elevated temperatures. In addition, the possibility of collaborative work with Mr. Leon Chuck of the Norton Co.

Publications

"High Temperature Mechanical Properties of SIALON Ceramic: Creep Characterization," C.F. Chen and T.-J. Chuang, Ceramic Engineering and Science Proceedings, in press.

"Transient Behavior of Structural Ceramics under Flexural Creep," T.-J. Chuang, S.M. Wiederhorn and C.F. Chen, Third International Conference on Creep and Fracture of Engineering Materials and Structures, Swansea, UK, April 5, 1987.

"Standard Tensile Test Development," S.M. Wiederhorn, Leon Chuck, T.-J. Chuang and Karl Jakus, 24th Automotive Technology Development Contractors' Coordination Meeting, October 29, 1986.

3.5 NONDESTRUCTIVE EVALUATION DEVELOPMENT

Nondestructive Characterization

R. W. McClung (Oak Ridge National Laboratory)

Objective/scope

The purpose of this program is to conduct nondestructive evaluation development directed at identifying approaches for quantitative determination of conditions (including both properties and flaws) in ceramics that affect the structural performance. Those materials that have been seriously considered for application in advanced heat engines are all brittle materials whose fracture is affected by structural features with dimensions on the order of the dimensions of their microstructures. This work seeks to characterize those features using high-frequency ultrasonics and radiography to detect, size, and locate critical flaws and to measure nondestructively the elastic properties of the host material.

Technical progress

Ultrasonics — W. A. Simpson, Jr., and K. V. Cook

Many of the variations in ceramic properties (e.g., density, elastic wave velocity, attenuation, etc.) that we routinely measure involve changes of <1 dB in the value of the ultrasonic quantity being measured. (This is generally not true for the detection of flaws, however, which often produce large changes in the ultrasonic amplitude.) To display these small variations, we previously developed a gray-scale presentation technique in which the value of a digitally acquired ultrasonic variable is represented by varying shades of gray on an electrostatic plotter/printer. We also wrote a routine which permits any range of the raw pixel values to be expanded to cover the full range of gray levels, thus enhancing the contrast between regions of similar pixel values on the sample. Although this package has been extremely useful in displaying subtle variations in ultrasonic properties, it suffers from two shortcomings. First, the contrast between adjacent gray levels is not readily discernible, because the eye is far more sensitive to color changes than to amplitude changes. Second, because the intensity of a single dot on the plotter/printer cannot be varied, it is necessary to average several adjacent pixels of the image to generate the gray-scale display. This averaging, which is similar to the use of a half-tone screen in printing, reduces the obtainable resolution.

To address the problems of gray-scale imaging, we have written a software package that permits the ultrasonic data to be displayed in color on an IBM PC-AT. Since the colors may be selected by the user, variations of as little as 0.03 dB may be depicted in easily discernible hues. In addition, since each pixel of the display is assigned a color, the full resolution of the original data is preserved. Using this new package, we have already located several areas on our zirconia modulus of rupture (MOR) standards where there is enhanced scattering from the microstructure that was not noticed in gray scale.

To illustrate the use of this package, Fig. 1 shows the variation in ultrasonic transmission for two polycrystalline silicon samples being

YP-3207

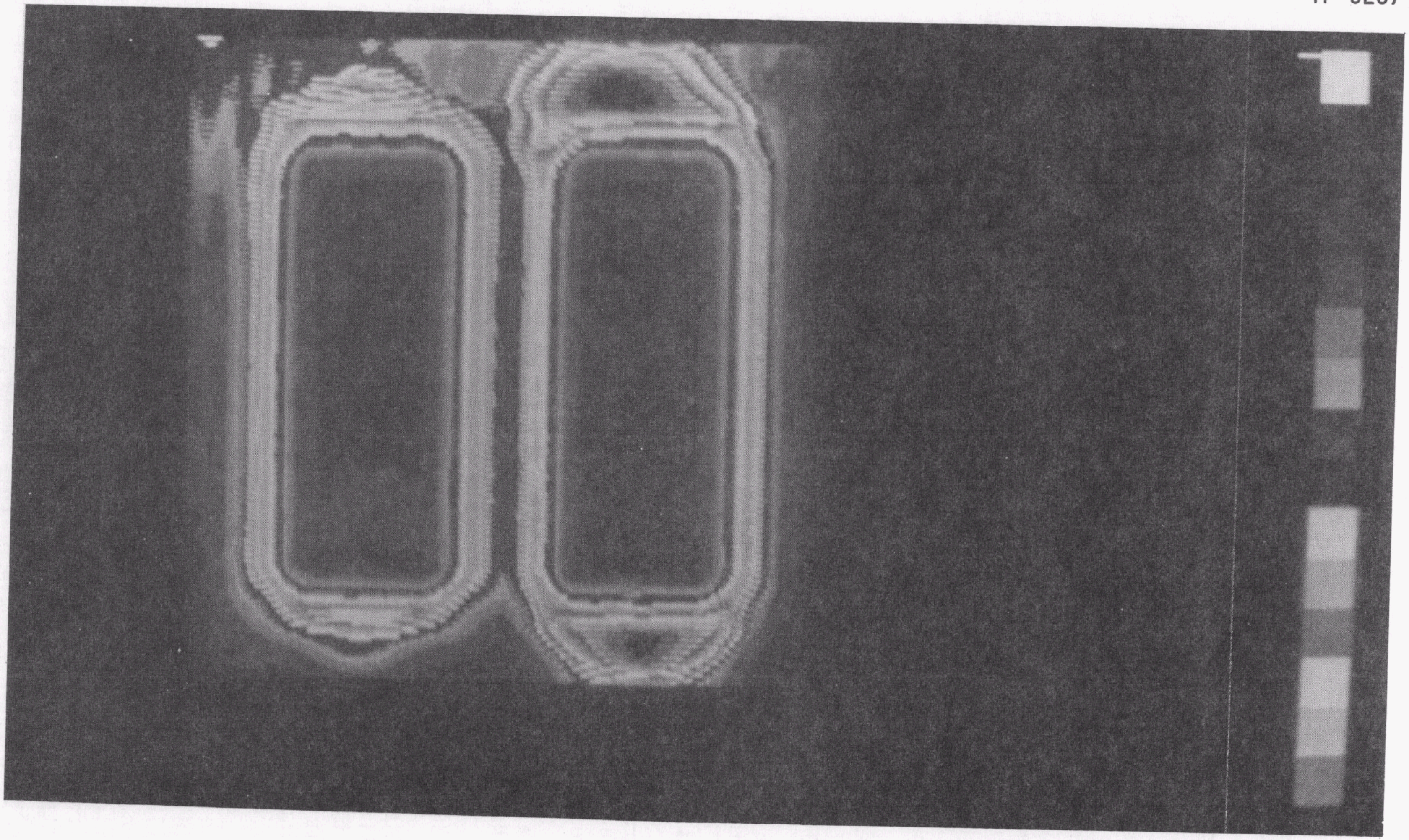

Fig. 1. Color representation of ultrasonic transmission through two silicon bars.

examined for small variations in attenuation. (Although the original figures are in color, the major salient features are discernable in this reproduction.) For both samples the transmission appears to be very uniform, varying by only a single color level in the sample on the left. The white fiducial marks to the left of the color bar delineate the digitizer range being displayed (0 to 254 in this case). Figure 2 shows the same data but with a narrow range of pixel values, again indicated by the fiducial marks, expanded to cover the full range of colors. Considerable variation in the transmission can now be seen, with adjacent color values representing variations of about 0.04 dB.

Figure 3 shows the transmission color results obtained on a silicon carbide whisker-reinforced alumina. Three distinct features of the sample structure can be discerned. First, there is a random global variation in the transmission caused most likely by changes in the elastic properties or the microstructure. Second, there are very localized high-amplitude variations in the transmission amplitude caused by scattering from the whisker clumps in the alumina matrix. Last, there are periodic striations in the results caused by forming or machining marks on the surfaces of the sample which were not seen in the gray-scale results. Expansion of the appropriate pixel range yielded an image of the whisker clumps identical to the gray-scale results, except that the relative amplitudes of scattering from the clumps could now be differentiated.

We have improved our system for inspection of International Energy Agency (IEA) silicon nitride MOR bars. A new transducer having a frequency/focal length combination better suited to the evaluation of these bars has been obtained. With this transducer, 125-μm flaw standards at 2-mm depth can be detected in the bar at full-scale digitizer amplitude and with a gain reserve of 30 dB. The system has also been reprogrammed for a fourfold increase in inspection speed with no loss in sensitivity. These changes indicate that a much faster test is now possible with significant increases in both sensitivity and detection depth.

We have now completed volumetric ultrasonic inspection of a number of the IEA silicon nitride MOR bars. Several indications whose amplitude equals or exceeds that from a 125-μm reference standard have been found. A few of these indications could be detected from either side of the bar, even though for at least one of these orientations the source could not be located near the focal plane of the transducer. In general the results are similar to those obtained earlier on sintered silicon nitride, although the current samples appear to be somewhat "quieter" ultrasonically than earlier specimens.

We continued work on surface wave inspection of ceramics. Machined standards have been fabricated with very small (125 μm) diamond-tipped drills and inspected using 50-MHz surface waves. Both notch and hole standards have been fabricated, and, as expected, all were easily detected. The notch standards were designed to simulate a crack, but the width of the notch (125 μm) makes this a rather poor simulation. Accordingly, we are preparing actual cracks in silicon nitride bars by Knoop indentation of the surface. Since the crack depth can be controlled by varying the load, this approach should provide near ideal standards.

The software is now in place to generate color maps of distribution of surface flaws in a ceramic sample as determined by surface wave inspection. In these maps, color corresponds to the amplitude of the surface wave scattered by a crack, which generally correlates with crack size. For surface-breaking cracks, the scattered signal often consists of

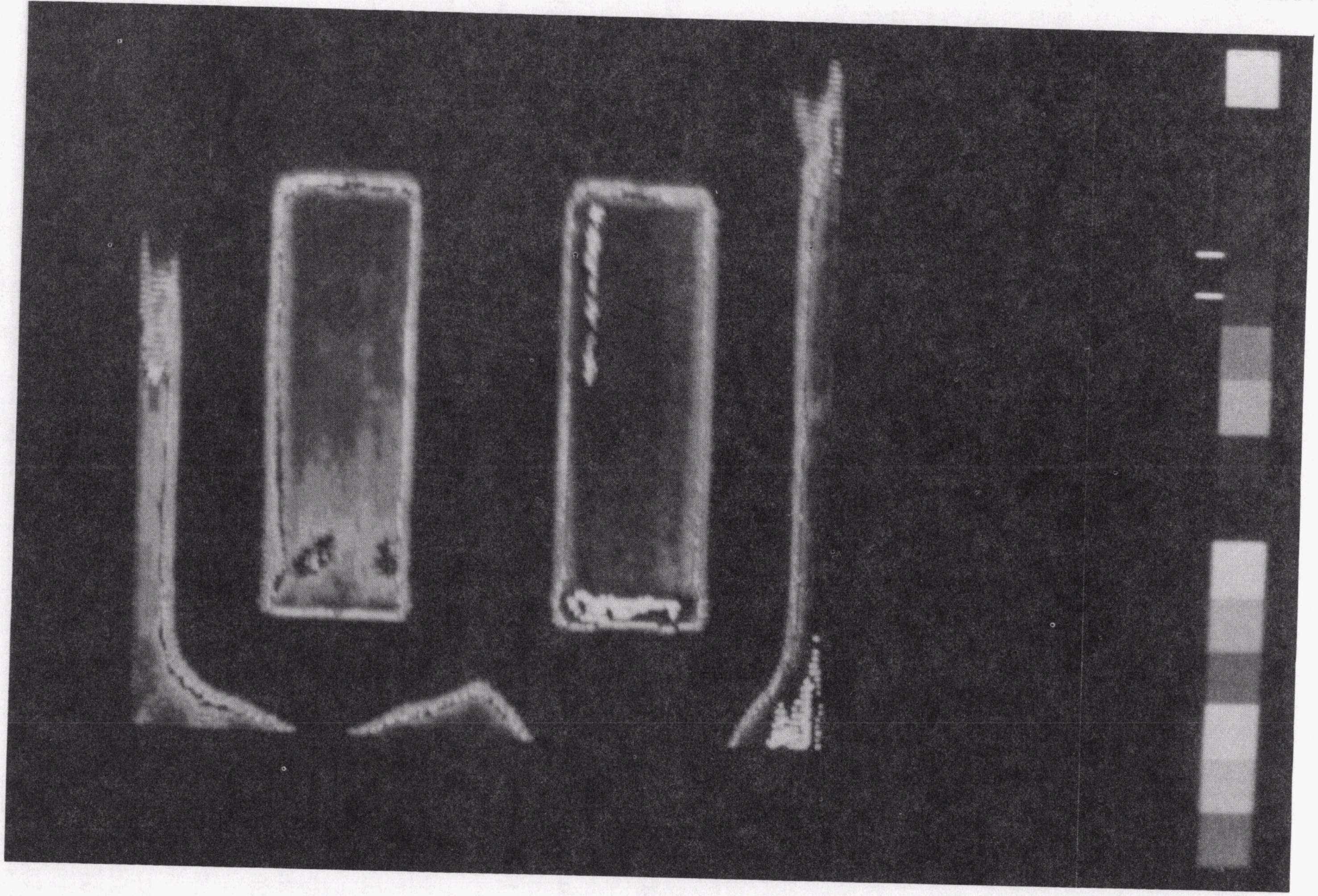

Fig. 2. Expanded pixel range of ultrasonic transmission through two silicon bars.

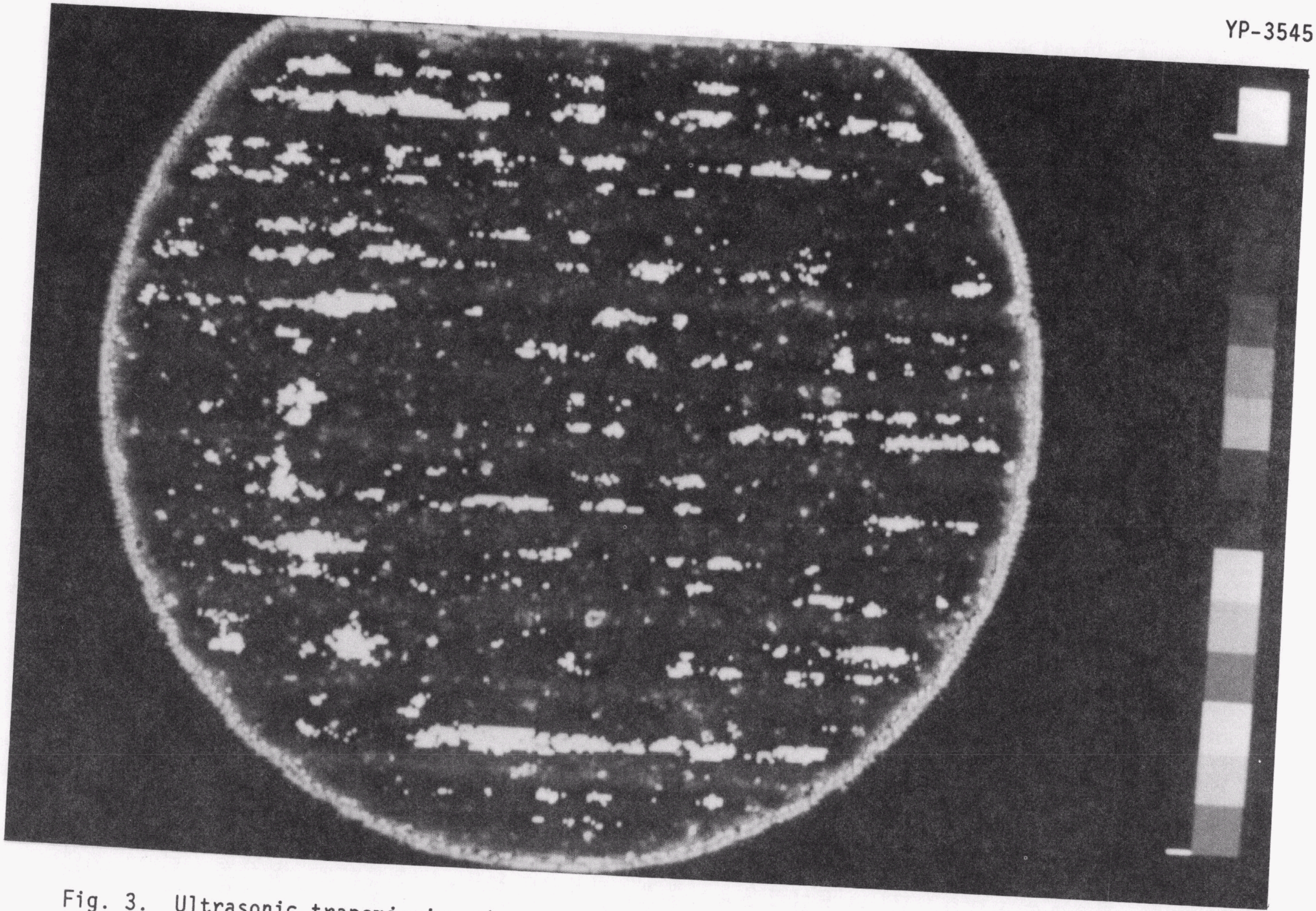

YP-3545

Fig. 3. Ultrasonic transmission through a composite ceramic sample.

two waves, one of which is reflected at the subsurface tip of the crack. When present, this condition provides an independent measure of the crack depth, since the temporal separation between these signals depends on the surface wave velocity and the crack depth. We have therefore provided the capability for displaying the frequency content of the scattered wave, from which the separation may be obtained easily.

Three ceramic billets have been obtained from Stephen Dahar at Dow Chemical Company. These billets consist of two silicon nitride samples, one a monolithic material and the other reinforced with silicon carbide whiskers, and an alumina sample containing silicon carbide whiskers. Each billet is about 76 × 76 × 9.5 mm (3 × 3 × 3/8 in.). We have agreed to characterize the billets (examination for flaws and determination of elastic properties and attenuation characteristics) ultrasonically. The samples will then be cut into MOR bars and tested destructively.

Radiography – B. E. Foster

Visits were made to five suppliers of real-time imaging and/or computed tomography equipment to determine the sensitivity that could be obtained with ceramic MOR bars. We used four MOR bars containing flat-bottom holes with diameters of 75, 100, 125, and 250 μm and depths from 10 to 70 μm representing equivalent penetrameter sensitivities of 1.0 to 3.4%.

Sensitivities obtained varied from 1.9 to over 3.4% (zero holes imaged) with the different equipment in both the real-time and CT mode of operation. A second visit was necessary to one of the suppliers because of equipment malfunction. A 10-cm cube of Plexiglas containing a flat-bottom hole with a diameter and depth of 375 μm (representing an equivalent penetrameter sensitivity of 0.26%) was also used on this second visit. The hole in the Plexiglas was imaged but none of the holes in the MOR bars were detected. Apparently spatial resolution was the limiting factor and it is thought that a smaller beam slice thickness of 0.25 mm (instead of the 1.0 mm used) would permit detection of most of the holes in the MOR bars. Additional contacts and visits are planned.

A radiographic technique using 50-kV X rays has been developed for evaluation of the IEA MOR bars. A penetrameter (image quality indicator) was fabricated for use on each radiograph. The penetrameter is a section of an MOR bar with two flat-bottom holes that are 0.25 mm (0.010 in.) in diameter by 0.025 mm (0.001 in.) deep and 0.13 mm (0.005 in.) in diameter by 0.05 mm (0.002 in.) deep. We require that both holes be visible on each radiograph, thus assuring a penetrameter sensitivity of at least 1.6%. A total of 817 MOR bars have been radiographed and measured dimensionally (width and height).

Status of milestones

No milestones were due in this period.

Publications

None.

Computed Tomography

W. A. Ellingson, M. W. Vannier, and H. C. Yeh (Argonne National Laboratory)

Objective/scope

The purpose of this program is to develop X-ray computed tomographic (CT) imaging for application to structural ceramic materials. This technique has the potential for mapping density distributions, detecting and sizing high- and low-density inclusions, and detecting cracks in green-state and densified ceramics. CT imaging is capable of interrogating the full volume of a component, and is non-contacting. It is also relatively insensitive to part shape and thus can be used to inspect components with complex shapes such as turbocharger rotors, rotor shrouds, and large turbine blades.

Technical progress

In our previous work on this project[1-4], we have discussed the advantages of X-ray computed tomography and pointed out some of the problems that need to be considered in applying CT scanners to ceramics. Of particular concern are the differences between isotope sources[5] and polychromatic sources[1] relative to beam-hardening corrections. We previously evaluated[2] linearization beam-hardening correction methods which, in theory, could be put into the CT scanner reconstruction algorithm as a polynomial or a look-up table. The problem with this correction is that it is time-consuming and relatively difficult to implement.

During this reporting period, we have explored a second software solution to the beam-hardening problem: a so-called dual-energy correction method.[6-7]

A basic assumption underlying dual-energy reconstruction is that over an X-ray energy range of interest, the explicitly energy-dependent mass attenuation coefficient (μ/ρ) (E) of all materials can be expressed with sufficient accuracy as a linear combination of the Compton and the photoelectric coefficients [8,9]. Thus, it can be shown that the mass attenuation coefficient of any material can be expressed as a linear combination of the coefficients of two so-called basis or calibration materials:[6]

$$\left(\frac{\mu}{\rho}\right)(E) = a_1 \cdot \left(\frac{\mu}{\rho}\right)_1 (E) + a_2 \cdot \left(\frac{\mu}{\rho}\right)_2 (E) \ , \qquad (1)$$

where subscripts 1 and 2 refer to reference materials 1 and 2, respectively. The two basis materials should be sufficiently different in their atomic number z, and thereby in their Compton and photoelectric attenuation characteristics, to give satisfactory results (this is determined empirically). In CT imaging, the line integral over the linear attenuation coefficient, $\int \mu(r,E)ds$, is determined for each focus position and detector element. This integral can be expressed as

$$\int \mu(r,E)ds = (\tfrac{\mu}{\rho})_1\ (E)\cdot\delta_1 + (\tfrac{\mu}{\rho})_2\ (E)\cdot\delta_2\ , \qquad (2)$$

where

$$\delta_i = \int \rho_i(r)ds \quad . \qquad (3)$$

The symbols δ_i and $\rho_i(r)$ represent the "area density" in g/cm^2 and the local mass density in g/cm^3, respectively, of basis material i. When materials other than the basis materials are present, the densities are referred to as equivalent basis material densities, a linear combination of which reflects the physical density of the attenuating material.

The equivalent "area densities" δ_1 and δ_2 of the two basis materials (Eq. 3) have to be determined for each ray path. By measuring the attenuation with two different spectra, we obtain two nonlinear equations for each ray path:

$$I_h = \int I_{oh}(E)\cdot\exp\left[-(\tfrac{\mu}{\rho})_1\ (E)\cdot\delta_1 - (\tfrac{\mu}{\rho})_2\ (E)\cdot\delta_2\right]dE\ , \qquad (4)$$

$$I_\ell = \int I_{o\ell}(E)\cdot\exp\left[-(\tfrac{\mu}{\rho})_1\ (E)\cdot\delta_1 - (\tfrac{\mu}{\rho})_2\ (E)\cdot\delta_2\right]dE\ , \qquad (5)$$

where I and I_o are the attenuated and primary intensities and the subscripts h and ℓ refer to the high- and low-kVp X-ray head voltages, respectively. Equations (4) and (5) can be solved for the equivalent "area densities" δ_1 and δ_2, which characterize the unknown material.

The basis material decomposition is thus accomplished by calculating the δ_1 and δ_2 values from the measured projection values. Materials with an atomic number Z different from those of the two basis materials will contribute to both δ_1 and δ_2 in a specific fashion.[9] The values δ_1 can be interpreted as components in a two-dimensional vector space with the basis materials defining the basis vectors.

The dual-energy correction is usually accomplished by use of table look-up procedures; the basic procedure is outlined in Fig. 1.

A dual-energy package was implemented on a medical CT imaging scanner during this reporting period. The package was evaluated on both liquid Freon TF and a green-state injection-molded Si_3N_4 turbocharger rotor (see Fig. 2). The particular turbocharger rotor selected for testing had at least one known defect, a circumferential crack, which is visible in Fig. 3.

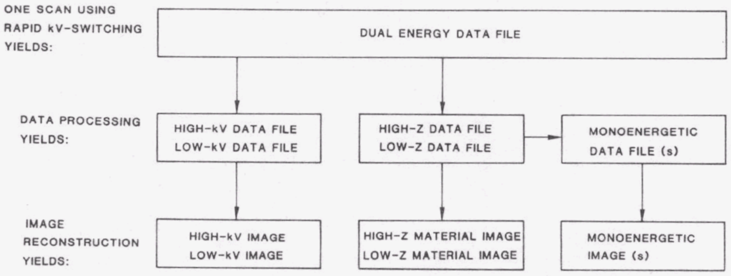

Fig. 1. Processing Scheme for Dual-Energy Data Evaluation. (From Ref. 6)

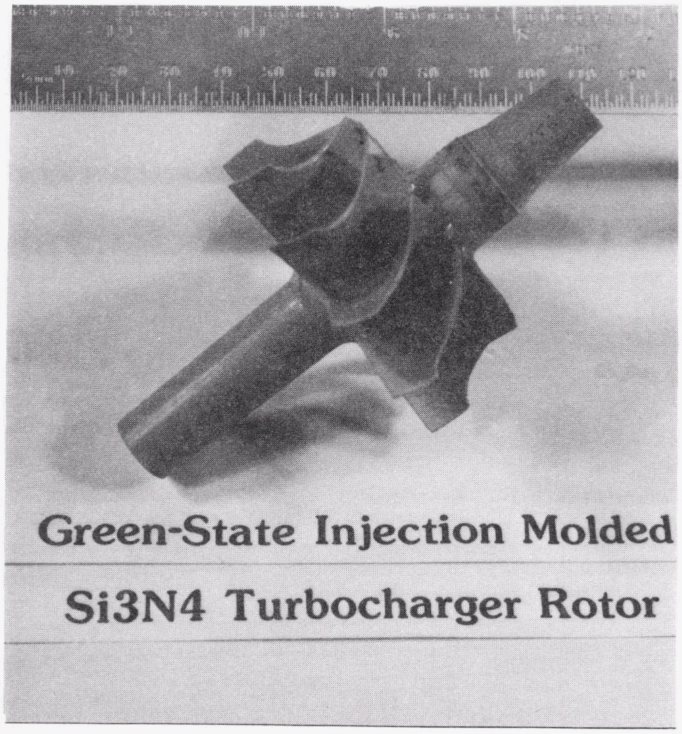

Fig. 2. Green-State Turbocharger Rotor Used in Experimental Dual-Energy CT Scan Tests.

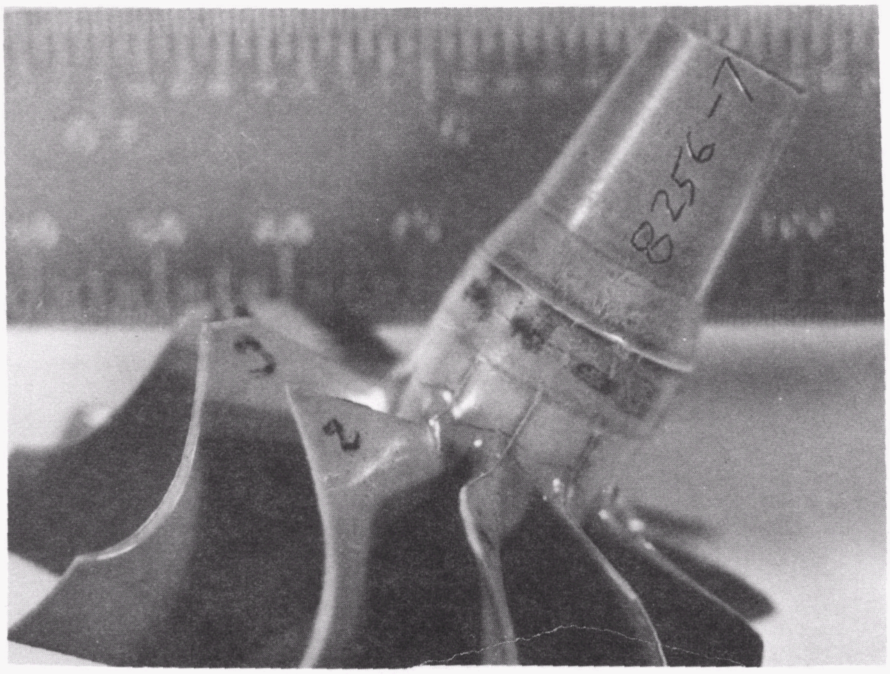

Fig. 3. Close-up Photograph of Turbocharger Rotor, Showing Circumferential Surface-breaking Crack.

An axial CT section of the entire rotor, with a slice thickness of 2 mm, was taken using the dual-energy beam-hardening correction. Figure 4 shows the image produced from the "Hi-kV" image reconstruction data file. The crack is detected at "A" in the figure. The streak labeled "B" in Fig. 4 may be a second crack, or an artifact in the image. We plan to cut the rotor open to establish the nature of this feature.

Transaxial CT sections were also obtained. Figure 5, a section through the vanes, shows edge artifacts (the star pattern in the hub) but also shows an apparent low-density region near the core of the shaft. In order to obtain better information on the shaft, we obtained transaxial sections just upstream of the vanes, as shown in Fig. 6. Again, the "Hi-kV" reconstruction data were used to reconstruct the image. Figure 6 clearly shows regions of high and low density. A densitometer trace through these regions (Fig. 7) reveals the wide variation in density across the two regions.

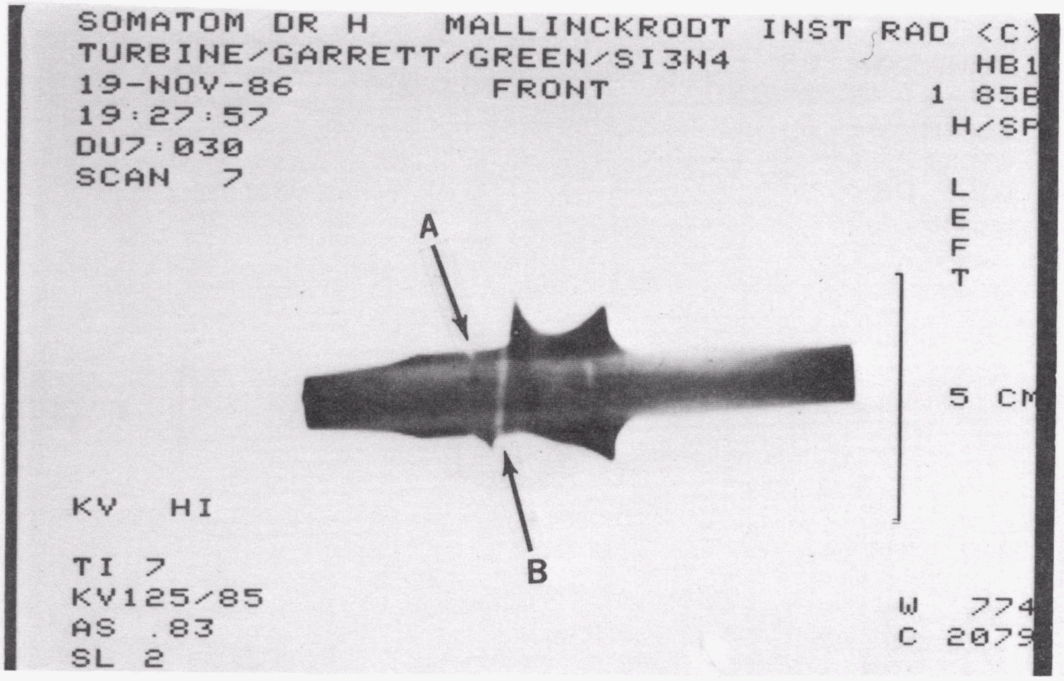

Fig. 4. Axial CT Image of Rotor Shown in Figs. 3 and 4, Obtained With the Dual-Energy Beam-hardening Correction.

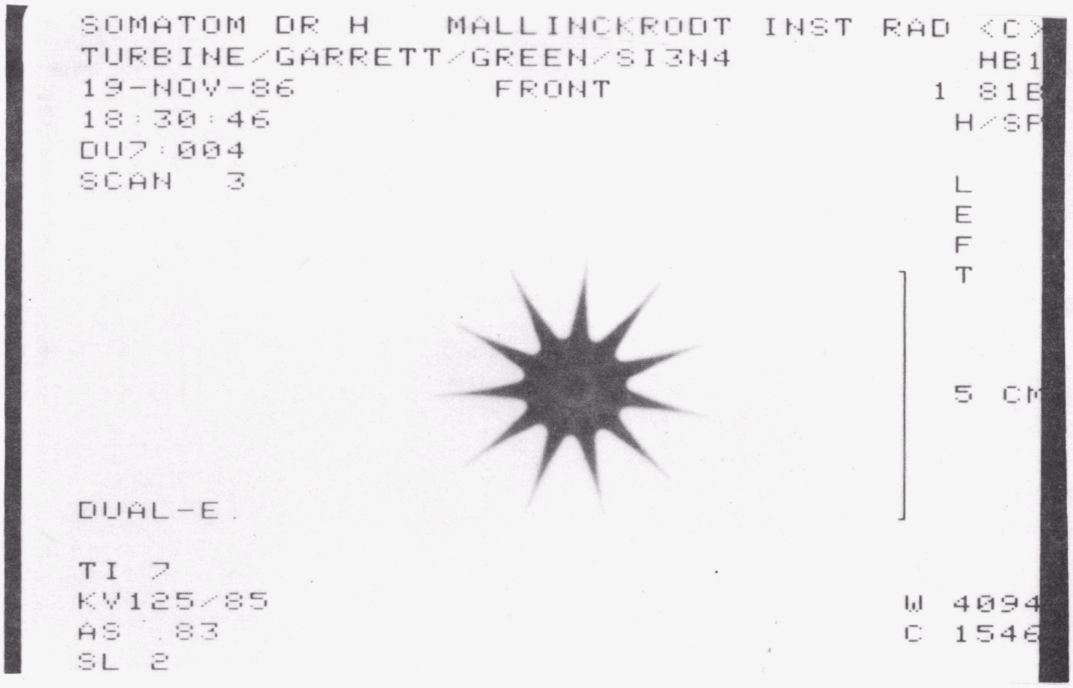

Fig. 5. Transaxial CT Image of Same Rotor, Taken through the Vanes.

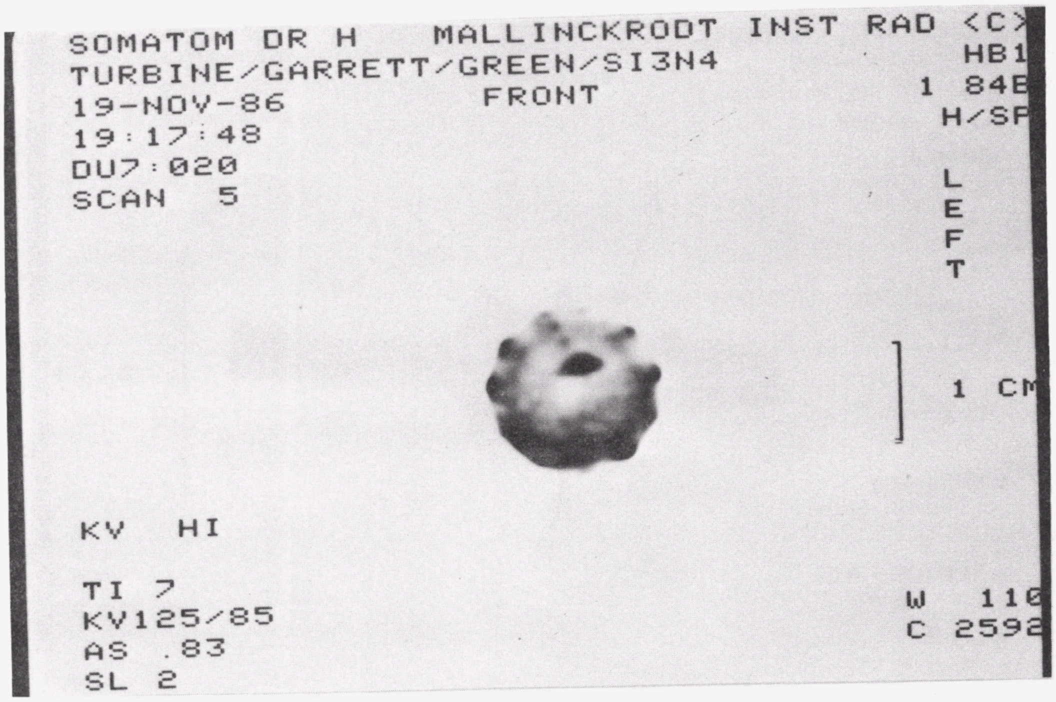

Fig. 6. Transaxial CT Image of Same Rotor, Taken Upstream of the Vanes.

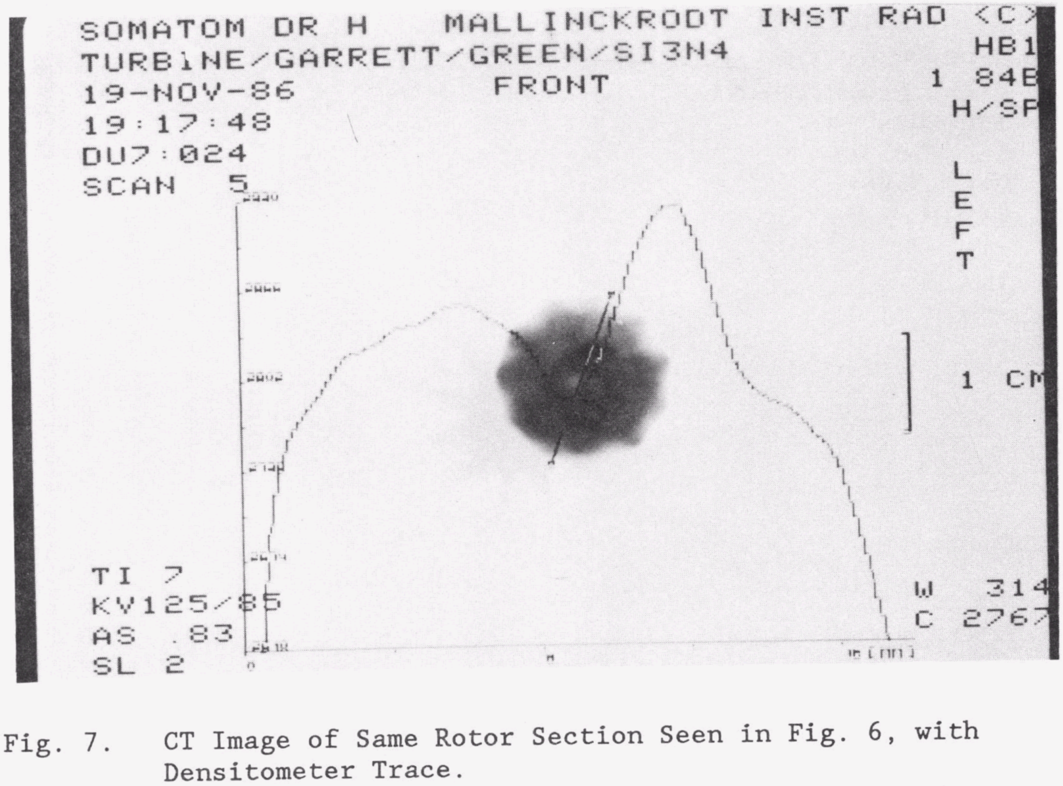

Fig. 7. CT Image of Same Rotor Section Seen in Fig. 6, with Densitometer Trace.

Status of milestones

All milestones are on schedule.

References

1. E. Segal and W. A. Ellingson, "Beam-Hardening Correction Methods for Polychromatic X-Ray CT Scanners Used to Characterize Structural Ceramics," to be published in the Proceedings of the 2nd Intl. Symposium on the Nondestructive Characterization of Materials, Montreal, Canada, July 21-23, 1986.

2. E. Segal, W. A. Ellingson, Y. Segal, and I. Zmora, "A Linearization Beam-Hardening Correction Method for X-Ray Computed Tomographic Imaging of Structural Ceramics," to be published in the Proceedings of the Review of Progress in Quantitative NDE, La Jolla, CA, August 3-8, 1986.

3. W. A. Ellingson and E. Segal, "Computed Tomography," pp. 326-339 in *Ceramic Technology for Advanced Heat Engines Project Semiannual Progress Report for Period October 1985-March 1986*, ORNL/TM-10079, Oak Ridge National Laboratory, Oak Ridge, Tenn., August 1986.

4. W. A. Ellingson, E. Segal, and M. W. Vannier, "Computed Tomography," in *Ceramic Technology for Advanced Heat Engines Project Semiannual Progress Report for Period April-September 1986*, ORNL/TM-10308, Oak Ridge National Laboratory, Oak Ridge, Tenn., in press.

5. B. D. Sawicka and W. A. Ellingson, "Photon CT Scanning of Advanced Ceramic Materials," Atomic Energy of Canada Limited, Chalk River Nuclear Laboratories, Ontario, Canada, Report AECL-9384 (February 1987).

6. W. A. Kalendar, W. H. Perlman, J. R. Vetter, and E. Klotz, "Evaluation of a Prototype Dual-Energy Computed Tomographic Apparatus: I. Phantom Studies," *Med. Phys.* 13(6), 334-339 (May-June 1986).

7. A. J. Coleman and M. Sinclair, "A Beam Hardening Correction Using Dual-Energy Computed Tomography," *Phys. Med. Biol.* 30(11), 1251-1256 (1985).

8. R. E. Alvarez and A. Macovski, "Energy-Selective Reconstruction X-Ray Computerized Tomography," in *Phys. Med. Biol.* 21, 733-744 (1976).

9. L. A. Lehmann, R. E. Alvarez, A. Macovski, and W. R. Brody, "Generalized Image Combinations in Dual kVp Digital Radiography," *Med. Phys.* 8, 659-667 (1981).

Methodology for Intelligent Processing of Reliable Engineering Ceramics

T. M. Resetar, G. E. Schaefer, J. W. McCauley (U.S. Army Materials Technology Laboratory)

Objective/scope

Any engineering system requires certain material properties for performance. In an ideal world, any extrinsic property of a material is a function of its intrinsic characteristics. Therefore, by identifying the unique characteristics of the material the properties are also defined in an unambiguous way. The converse is not true. Identification of a property does not uniquely define a material. This is the fundamental ambiguity of advanced materials. In the real world the unique characteristics of any material not only consists of chemistry and physical structure of its constitutive components, but also includes defects.

Materials characterization has been very succinctly defined by a National Academy of Sciences Materials Advisory Board report. "Characterization describes those features of the composition and structure (including defects) of a material that are significant for a particular preparation, study of properties, or use, and suffice for reproduction of the material." The unique signature of any material therefore is:

P = equals f(c,M,PD)
C = equals chemistry, phases
M = equals microstructure (physical structure)
PD = equals processing defects

Therefore, any property of a material can be unambiguously defined by its unique signature. Quantification of this unique signature for powder and final ceramic products is the overall goal of this project.

Technical progress

Our approach is to start with the unique signature concept and to evolve this into computer interrogatable data base framework for a selected variety of advanced ceramic materials - powders and final products. This is a particularly difficult aspect of the program and will require several iterations before a satisfactory data base is achieved.

The first attempt to define an acceptable basic set of powder characteristics appears on Table I. They were derived from the preliminary draft of a report (Ref. 2) authored by Resetar and McCauley on the powder characterization subtask of the IEA program. This chart was distributed to U.S. participants in the IEA ANNEX II and was accepted as the framework for a data base format. This data base will be used for recording, storing, analyzing, comparing and retrieving powder characterization information.

An important aspect of the data base is that certain characteristics may be determined by two or more completely different and independent measurement techniques. This is especially true for particle size distribution and certain chemistry requirements like oxygen content. The headings in Table I are broad enough to encompass a variety of classic powder characterization techniques to include various property information specific to each different material.

After undertaking the task of creating a usable, interrogatable data base framework for material characteristics, it was realized that many iterations would be necessary as our data base knowledge and expertise grew. Even though the format may change, the basic set of quantifiable powder characteristics would not. (Table I) Therefore, this basic set was and will be the keystone in development of the data bases.

With this in mind, the next task was to transcribe the preliminary powder characterization charts (Ref. 2) onto computer disks for use with the Rainbow personal computer (Digital, Inc.) and Symphony (version 1.01) software. These charts contain the recommended preliminary format for the data base and were amended, then approved at various IEA Annex II meetings.

Table II shows the particle size and distribution chart. This particular format includes the geometric median diameter (d_{50}) and the distribution (standard deviation) calculated from d_{84} and d_{16}. One concern on this particular chart is the number of modes within a powder sample and how to record multimodal powders. Other pertinent information (i.e., an increased number of data points, other statistical descriptors) may be added at a later date as the situation warrants.

Table III includes morphological descriptors such as surface area, permeametry number, aspect ratio and other calculable quantities. This chart can also be easily revised to include other parameters.

The next three tables (IV, V, VI and VII) will contain the chemical characteristics of the powders to be studied. Included is a summary chart (Table IV) which condenses the information presented on Tables V and VI. Table VII contains phase information. These chemical charts may have to be modified to fit specific materials, and also be able to contain similar information from independent sources (i.e. oxygen analysis by neutron activation and LECO method).

Prior to the arrival of the IEA Program powder, the complete unique signature characterization of Zr metal powder has been completed and includes complete independent oxygen analysis by the LECO method and neutron activation analysis. Particle size distribution has been measured by sedimentation, SEM image analysis, electrozone sensing, and turbidimetric techniques. This data is now being inserted into trial data bases which will be able to be used on an expert system since burn rate data (direct powder property) has been measured on all of the powders. The current collection of data for zirconium powder appears on Table VIII. This format closely follows the proposed framework for quantifiable powder characteristics.

The problem of multiple methods for determining particle size distribution is illustrated for Zr metal powder on Table IX. This illustrates the problem very nicely. All of the methods are perfectly acceptable, however, the physical model used in the technique for determining the particle size differs for all of these methods. If the various measurements are normalized to each other by using the Hatch-Choate equation one can see that the actual (true) differences are small. This problem must be resolved in the data base methodology.

Status of milestones

3.5.1.4 - Materials Characterization Methodology, MTL.

351401. - Quantifiable Characteristics May 31 1986.

351402. - Preliminary Data Base Format	September 30 1986.
351403. - Zr Metal Powder Characterization/Data Base	June 30 1987.
351404. - Zr Oz Powder/SiC Ceramic Characterization	October 31 1987.
351405. - Other IEA Powder and Ceramics	June 30 1988.
351406. - Total Data Base Incorporation/Analysis	January 31 1988.

Publications

None

References

1. J.W. McCauley, "The Role of Characterization in Emerging High Performance Ceramic Materials, "Am. Ceram. Soc. Bull., 63(2), 263-265 (1984).

2. "Summary Report for International Energy Agency (IEA) Annex II - Cooperative Program on Ceramics for Advanced Engines and Other Conservation Applications: Subtask 2: Powder Characterization Studies," J.W. McCauley and T.M. Resetar; January 1986 (revised April 1986) (16 pp.).

Table 1. Basic Set of Quantifiable Powder Characteristics

CHARACTERIZATION

A. PHYSICAL CHARACTERISTICS:

1) Particle Size (dg, dv)
2) Particle Size Distribution (σg)
3) Surface Area (Sw)
4) Permeametry # (Fisher Sub-Sieve Size)
5) Material Density (Pycnometer, etc.)
6) Aspect Ratio (Long/Short)

B. CHEMICAL CHARACTERISTICS:

1) Major Elements
2) Minor Elements
3) Trace Elements
4) Volatile Analysis
5) Weight Loss in Air to 110°C
6) Phase Analysis (X-ray Diffraction)

C. PHYSICAL DEFECTS:

1) Agglomeration: Percent/Size

D. OTHER CHARACTERISTICS:

Table II. Preliminary Data Base Format for Powder Size and Distribution

POWDER CHARACTERIZATION

PHYSICAL CHARACTERISTICS
TABLE 1-A: SIZE AND DISTRIBUTION

OPERATOR____
LABORATORY______________________________________
DATE____
POWDER____

	POWDER ID									
LAB CODE	IEA	LAB	MODES	d50(1)	Sigma* (1)	d50(n)	Sigma* (n)	METHOD	Normalization **	Standard

TMR
4/87

Sigma = 0.5(d_{84}/d_{16})

** Normalization: Value normalized to selected internal reference material

COMMENTS:

Table III. Preliminary Data Base Format for Powder Morphology

POWDER CHARACTERIZATION

PHYSICAL CHARACTERISTICS
TABLE I-B: MORPHOLOGY

OPERATOR ____________________
LABORATORY ____________________
DATE ____________________
POWDER ____________________

LAB CODE	POWDER ID		Surface Area		(TAP DENSITY)/ (X-RAY DENSITY)	PERMEAMETRY # (FSSS)		[S_w (meas.)]/ [S_w (calc.)]	ASPECT RATIO (Long/Short)	OTHER
	IEA	LAB	VALUE	STD. USED		VALUE	STD. USED			

TMR
4/87

Table IV. Preliminary Data Base Format for Summary of Chemical Characteristics of Powders

POWDER CHARACTERIZATION

CHEMICAL CHARACTERISTICS
TABLE 2-A: SUMMARY

OPERATOR ______________________
LABORATORY ______________________
DATE ______________________
POWDER ______________________

	POWDER	ID	Majors						Standards		
LAB CODE	IEA	LAB	A	B	C	Total Minors	Total Trace	Total Volatiles	1	2	3

TMR
4/87

Table V. Preliminary Data Base Format for Minor Elements of Powders

POWDER CHARACTERIZATION

CHEMICAL CHARACTERISTICS
TABLE 2-B: MINOR ELEMENTS

OPERATOR ______________________
LABORATORY ______________________
DATE ______________________
POWDER ______________________

	POWDER ID		% Minor Elements							
LAB CODE	IEA	LAB	A	B	C	D	E	F	ETC.	TOTAL

TMR
4/87

Table VI. Preliminary Data Base Format for Trace Elements of Powders

POWDER CHARACTERIZATION

CHEMICAL CHARACTERISTICS
TABLE 2-C: TRACE ELEMENTS

OPERATOR ______________________
LABORATORY ____________________
DATE __________________________
POWDER ________________________

			% Trace Elements										
	POWDER ID		Non-Volatiles						Volatiles				
LAB CODE	IEA	LAB	A	B	C	D	E	TOTAL	F	G	H	I	TOTAL

TMR
4/87

Table VII. Preliminary Data Base Format for Chemical Phases of Powders

POWDER CHARACTERIZATION

CHEMICAL CHARACTERISTICS
TABLE 2-D: PHASES

OPERATOR ________________________
LABORATORY ______________________
DATE ____________________________
POWDER __________________________

LAB CODE	POWDER ID		Non-crystalline %	Crystalline %			Foreign Matter *
	IEA	LAB		A	B	C	

TMR
4/87

---

* Loss on ignition to X °C

Table VIII. Preliminary Data Base Format for Zirconium Powder, Type I

ZIRCONIUM POWDER

Type I

	Sedigraph		*g(84)-	Sw (BET)	FSSS	Sw(BET)/	%	%	Oxygen Content (w %)		ten'/sec
Sample	dg(50%)(um)	*g(84,16)	*g(16)	(M2/g)	APS (um)	Sw(dg)	Free Zr	Mg	Leco	Neut.Act.	Burn Time
J5040A-1	4.8	1.93	-0.43	1.42	3.15	7.42	88.3	.7			3.5
J5040A-2	5.1	2.03	-0.53	2.16	3.1	11.99	87.1	1.2	5.53	4.148	3.3
J5040A-3	5.2	2.05	-0.45	1.67	3.00	9.45	87.4	1.2	5.83	4.21	3.9
J5040A-4	4.9	2.12	-0.7	2.41	2.90	12.85	86.3	1.2			4.3
J5052A-1	4.8	2.06	-0.25	1.88	3.32	9.82	86.5	.27	4.77	3.817	4.1
J5054A-3	5.52	2.01	-0.4	1.46	3.7*	8.77	88.6	.25	4.82	3.763	4.5
J5062A-1	5.20	2.10	-0.35	1.67	3.10	9.45	86.3	.25	6.15	3.154	3.4
J5064A-1	5.20	2.02	-0.47	1.53	3.10	8.66	85.4	.50	6.15	4.679	3.8
J5072A-1	5.10	1.91	-0.33	2.52	3.60	13.99	90.3	.75			5.5
J5072A-2	5.15	1.82	-0.19	2.64	3.45	14.80	90.3	.75			6.7
J5072A-3	5.25	1.85	-0.09	3.02	3.60	17.25	90.0	1.00			6.2
J5072A-4	5.50	1.79	-0.15	2.68	3.60	16.04	91.1	.75			5.9
J5075A-3	6.30	1.99	-0.39	1.25	3.55	8.57	91.4	.50	4.27	3.342	3.6
J5075A-4	5.50	2.16	-0.08	1.62	3.38	9.70	88.3	.25			2.7
J5079A-1	5.80	2.19	-0.01	1.52	3.25	9.59	87.7	.23	4.87	3.728	3.0
J5087A-1	5.30	1.75	0.23	1.17	3.65	6.75	91.4	.25	4.19	3.217	4.1
J5087A-2	6.10	1.79	-0.34	1.05	4.00	6.97	92.3	.25			5.7
J5088A-1	6.80	1.74	-0.3	0.98	3.7*	7.25	92.1	.30	3.89	3.064	5.8
J5092A-2	5.92	1.83	-0.21	1.34	3.6*	8.63	92.5	.50			4.3
J5092A-3	5.70	1.86	-0.42	0.97	4.10	6.02	93.1	.50	3.61	2.96	4.8
J5092A-4	5.20	1.99	-0.35	1.20	3.60	6.79	92.6	.50			3.7
J5092A-5	6.20	1.81	-0.51	1.02	4.20	6.88	92.6	.25	3.69	2.987	5.1
J5095A-1	6.30	1.91	-0.24	1.20	4.20	8.23	92.6	.30	4.12	3.265	3.7
J5095A-2	5.90	1.84	-0.28	1.01	4.18	6.37		1.3			5.0
J5095A-3	5.80	1.73	-0.37	1.17	3.2*	7.39	91.9	.25	3.64	3.244	4.2
J5095A-4	6.41	1.83	-0.3	1.13	3.61*	7.88		.50			4.4
J5098A-2	6.88	1.75	-0.38	1.14	3.3*	7.44	94.4	.30			3.6
J5098A-4	6.60	1.70	-0.43	0.97	3.6*	6.97	92.9	.30		3.144	4.7
J5102A-1	6.80	1.81	-0.31	1.13	3.83*	7.38	91.7	.70	4.14	3.225	4.1
J5106A-5	5.81	1.77	-0.4	1.19	3.6*	7.52	91.9	.40	4.02	2.821	4.9
J5113A-1	6.18	1.82	-0.28	0.99	4.4*	6.66	92.7	0.25	3.66	4.232	5.2

*Ventron Data

Table IX.

COMPARISON OF OBSERVED AND CALCULATED* Zr POWDER DIAMETER FROM VARIOUS TECHNIQUES.

Sample	Type	SEDIGRAPH		TURBIMETER		COULTER COUNTER		MICROSCOPY (SEM)	
VENTRON #		$d_g = d_{vs}$ μm	$\bar{\sigma}_g$	d_s(OBS) μm	d_s(CALC) μm	d_v(OBS) μm	d_v(CALC) μm	d_{gc}(OBS) μm	d_{gc}(CALC) μm
5079 A-1	I	5.80	2.19	3.00	2.31	3.30	3.14	1.03	1.25
5072 A-3	I	5.25	1.85	3.90	2.98	5.50	3.60		2.03
5092 A-3	I	5.70	1.86	2.90	3.20	3.90	3.87	1.45	2.17
5042 A-2	II	1.75	1.56	1.17	1.30	1.72	1.44	1.00	1.07
5043 A-3	II	1.80	1.54	1.30	1.36	1.75	1.49	1.15	1.13
5078 A-1	?	3.15	1.75	2.40	1.97	2.50	2.30	1.80	1.44
MEAN	I	5.66	1.90	3.10	3.05				
MEAN	II	1.84	1.64	1.30	1.27				

*Using Hatch-Choate Equations

4.0 TECHNOLOGY TRANSFER

4.1 TECHNOLOGY TRANSFER

4.1.1 Technology Transfer

Technology Transfer
D. R. Johnson (Oak Ridge National Laboratory)

Technology transfer in the Ceramic Technology Project is accomplished by a number of mechanisms including the following:

Trade shows. A portable display describing the program has been built and used at several trade shows and technical meetings, most recently at the Annual Meeting of the American Ceramic Society, April 26-30, 1987, in Cincinnati, Ohio.

Newsletter. A Ceramic Technology Newsletter is published regularly and sent to a large distribution.

Reports. Semiannual technical reports, which include contributions by all participants in the program, are published and sent to a large distribution. Informal bimonthly management and technical reports are distributed to the participants in the program. Open-literature reports are required of all research and development participants.

Direct Assistance. Direct assistance is provided to subcontractors in the program via access to unique characterization and testing facilities at the Oak Ridge National Laboratory.

Workshops. Topical workshops are held on subjects of vital concern to our community.

International Cooperation. Our program is actively involved in and supportive of the cooperative work being done by researchers in West Germany, Sweden, and the United States under an agreement with the International Energy Agency. That work, ultimately aimed at development of international standards, includes physical, morphological, and microstructural characterization of ceramic powders and dense ceramic bodies, and mechanical characterization of dense ceramics. Detailed planning and procurement of ceramic powders and flexural test bars have been accomplished. Exchange of preliminary data on ceramic and powder characterization results has been started by those laboratories participating.

IEA Annex II Management

V. J. Tennery (Oak Ridge National Laboratory)

Objective/scope

The IEA Annex II agreement between the United States, the Federal Republic of Germany, and Sweden on structural ceramics is directed toward cooperative research and development oriented to the identification and adoption of standardized methods for characterizing these materials. This agreement includes four subtasks: (1) information exchange, (2) ceramic powder characterization, (3) ceramic chemistry and structural characterization, and (4) ceramic mechanical property characterization. Each country is providing selected ceramic powders and sintered structural ceramics for use in the research work Subtasks 2, 3, and 4 in all three participating countries. Participating laboratories in these countries have agreed to share all resulting data with the purpose of using the knowledge gained from the work for developing standard measurement methods for characterizing ceramic powders and sintered structural ceramics.

The lack of such standard measurement methods has been an impediment to the evolution and development of structural ceramics, from the point of view of both the manufacturer and the user. This Annex II agreement was conceived to accelerate the development of standard methods for determining important properties of these evolving materials.

In the United States, many companies and their research staffs have agreed to contribute significant resources in performing the required measurements. For example, in Subtask 2, 12 laboratories are participating; in Subtask 3, 7 laboratories are participating; and in Subtask 4, 8 laboratories are participating.

The research in Subtask 2 includes five ceramic powders that are being studied in the initial phase of this subtask. For Subtasks 3 and 4, three sintered ceramics are being studied, one from each of the three countries. The ceramic from the United States is a silicon nitride, SNW-1000 from GTE-Wesgo; that from Germany is a hipped SiC from ESK Kempton; and that from Sweden is a silicon nitride from ASEA Cerama.

Technical progress

The major technical status changes since the last semiannual report is reviewed briefly as follows:

Subtask 2

Ceramic Powder Characterization

The U.S. National Bureau of Standards (NBS) is distributing all ceramic powders for Annex II; the first was a zirconia from Toyosoda in Japan, and specimens were distributed to all participating laboratories in all three countries in January. The second to be distributed is the "reference powder," which is the LC-10 silicon powder from H C. Stark in Germany. Final riffling has been completed, and nearly all of the 2400 vials required for this material have been prepared. Flame sealing is planned by the end of May. It is anticipated that this powder will be distributed by the NBS by the end of June. No results have been received from the participating U.S. laboratories performing work in this subtask.

Subtasks 3 and 4:

Ceramic Chemical, Structural, and Mechanical Characterization ESK Silicon Carbide from the Federal Republic of Germany

The SiC bars from Germany to be studied in the United States were received at ORNL in October 1986.

Subtask 3 Results

In support of the work in Subtask 3, sets of ten bars each were sent by ORNL to the ten participating laboratories in the United States involved in the chemical and structural characterization research in this subtask. In addition, LOTUS templates were prepared and distributed by ORNL for use by the participating laboratories in submitting and exchanging their results from this work. Preliminary results from these measurements are anticipated by the end of May.

Subtask 4 Results

In support of the work in Subtask 4, 400 flexure bars were distributed by ORNL in November to the five U.S. participating laboratories. An additional 200 bars, which are the international archive for this material, are being held at ORNL. The 400 flexure bars have been fractured by the participating laboratories to provide a total data set for 395 specimens (measurements on 5 specimens were invalidated because of test machine problems at the participating laboratories). These data have been returned to ORNL in the form of LOTUS 1-2-3 templates generated and furnished earlier by ORNL and the University of Illinois. Statistical analyses of these data sets have been completed, and a preliminary report has been written and distributed for comment. In addition, a final report, "Analysis of Flexural Strength Data for ESK Silicon Carbide Measured in the United States, IEA Annex II, Subtask 4," has been written and distributed to all Subtask 4 participants in the United States. The results of this work clearly show that measurement of the four-point flexure strength of a carefully prepared structural ceramic in a number of experienced laboratories results in a significant spred in the critical Weibull distribution parameter alpha (or m). The value of this parameter is particularly critical in predicting and determining the reliability of structural ceramic materials under mechanical stress. The "maximum likelihood analysis" technique has been demonstrated to be very superior in determining the Weibull modulus (alpha or m) compared with the least squares or linear regression technique often used in the United States.

Furthermore, the Kolmogorov-Smirnov goodness-of-fit test was demonstrated as being very useful in testing these flexural strength data sets for determining their "fit" with the Weibull distribution function. In summary, the results show that the flexure strength of the ESK silicon carbide evaluated in the United States clearly came from a Weibull distribution, with significance values for the goodness-of-fit tests generally being well above 0.99. Only one individual data set, that from Sohio Engineered Materials, had a significance leel below 0.99; it had a value of 0.415, which was still substantially higher than this statistic when the data set was tested against a Gaussian distribution. The results for the data sets from each of the five laboratories (approximately 80 specimens per set) and the analysis results obtained when data for all 395 specimens are combined, including the Kolmogorov-Smirnov statistics, ae given in Tables 1 and 2. In addition to the shape and scale parameters (alpha or m and beta) that best describe the Weibull distribution function for each of these six data sets, other important Weibull distribution properties including the mean, variance, and mode were calculated and are given in Table 3. In addition to these measurements, each participating laboratory is performing fractography analysis on selected specimens from the weakest, medium strength, and strongest specimens from that laboratory's 80-bar set. These results are expected to be sent to ORNL by the end of May. A complementary summary report on the fractography results will be written and distributed after all of the fractography results are received.

Subtasks 3 and 4

GTE Wesgo SNW-1000 Silicon Nitride from the United States

As of April 30, a total of 1122 machined bars of the German metric standard size of the SNW-1000 ceramic had been received by ORNL, and the remaining 318 are expected by the end of May. At that time, the required NDE measurements will be concluded, and it is anticipated that the distribution of these bars for Subtasks 3 and 4 will begin by the middle of July. Following completion of the 1440 German metric bars by GTE, the required 640 bars of the AGT size will be delivered to ORNL and subsequently distributed. Some additional bars will also be received by ORNL and held in an archive. The AGT size bars are expected to be ready for distribution to the three U.S. cooperating laboratories by the end of August.

Subtasks 3 and 4

ASEA Cerama Hipped Silicon Nitride from Sweden

The bars of silicon nitride from ASEA Cerama in Sweden are expected to be received at ORNL by the middle of May. Depending upon the amount of

Table 1.

Weibull parameters and goodness-of-fit statistics
for six flexure strength data sets
of ESK hipped silicon carbide

Participant	GTE Labs	Sohio	Allison	NASA Lewis	Garr. Turb.
Weibull distribution function parameters					
Weibull parameters					
Alpha (func.fit)	7.16	6.82	4.91	6.59	6.60
m by max. likelihood	7.16	6.82	4.91	6.59	6.60
Beta (func.fit) (MPa)	541.17	517.01	508.88	556.72	554.01
Kolmogorov-Smirnov goodness-of-fit statistics					
D+	0.048534	0.071237	0.079603	0.063649	0.080716
D-	0.053023	0.098843	0.068261	0.047503	0.065303
DN	0.053023	0.098843	0.079603	0.063649	0.080716
Sign.level	1.000000	0.415088	0.999792	0.999999	0.999760

Statistics for entire 395 specimens of silicon carbide

Weibull parameters

Alpha	6.09
Max. likelihood	6.0
Beta (MPa)	535.82

Kolmogorov-Smirnov Goodness-of-fit statistics

D+	0.030714
D-	0.021805
DN	0.030714
SIGN.LEVEL	0.999993

Table 2.

Gaussian distribution parameters and Weibull modulus
determined by two methods for ESK silicon carbide

(using Lotus template)

Participant	GTE Labs	SOHIO	Allison	NASA Lewis	Garr. Turb.
Avg. strength (MPa)	506.91	482.11	468.69	519.23	516.50
Std. deviation (MPa)	81.81	88.07	99.45	90.28	90.54
Weibull modulus					
Least squares	7.332	6.043	5.697	6.783	6.750
Max. likelihood	7.160	6.816	4.914	6.587	6.601
No. of specs.	75	80	80	80	80

Results for combined strength values from all five laboratories

Avg. strength (MPa)	498.02
Std. deviation (MPa)	92.43
Weibull modulus	
Least squares	6.410
Max. likelihood	6.095
Number of specs.	395

TABLE 3

Weibull parameters and distribution characteristics
for six flexure strength data sets
of ESK hipped silicon carbide

Participant	GTE Labs	Sohio	Allison	NASA Lewis	Garr. Turb.
Weibull parameters					
Alpha	7.16	6.82	4.91	6.59	6.60
Beta	541.17	517.01	508.88	556.72	554.01
Mean	506.82	483.06	466.75	519.12	516.64
Variance	6953	6912	11,820	8509	8404
Mode	529.92	505.13	485.82	542.99	540.39

Results for combined strength values from all five laboratories

Weibull Parameters	
Alpha	6.095
Beta	535.82
Mean	497.52
Variance	9029
Mode	520.30

repackaging, randomizing, etc. required for these bars before distribution, it is anticipated that these specimens will be distributed by about the middle of June.

Status of milestones

On schedule.

Publications

1. A summary report, "Analysis of Flexural Strength Data for ESK Silicon Carbide Measured in the United States, IEA ANNEX II, Subtask 4," by V. J. Tennery was written and distributed to all U.S. participants in Subtask 4 in the United States at the end of April. This report will be the primary basis for information exchange with Germany and Sweden concerning Subtask 4 research on the ESK SiC ceramic from Germany.

Standard Reference Materials

A. L. Dragoo, D. B. Minor, C. R. Robbins, J. F. Kelly, J. P. Cline
(National Bureau of Standards)

Objective/scope

Ceramics have been successfully employed in engines on a demonstration basis. The successful manufacture and use of ceramics in advanced engines depends on the development of reliable materials that will withstand high, rapidly varying thermal stress loads. Improvement in the characterization of ceramic starting powders is a critical factor in achieving reliable ceramic materials for engine applications. The production and utilization of such powders require characterization methods and property standards for quality assurance.

The objectives of the NBS program are (1) to assist with the division and distribution of five ceramic starting powders for an international round-robin on powder characterization; (2) to provide reliable data on physical (dimensional), chemical and phase characteristics of two silicon nitride powders: a reference and a test powder; and (3) to conduct statistical assessment and modeling of round-robin data. This program is directed toward a critical assessment of powder characterization methodology and toward establishment of a basis for the evaluation of fine powder precursors for ceramic processing. This work will examine and compare by a variety of statistical means the various measurement methodologies employed in the round-robin and the correlations among the various parameters and characteristics evaluated. The results of the round-robin are expected to provide the basis for identifying measurements for which Standard Reference Materials are needed and to provide property and statistical data which will serve the development of internationally accepted standards.

Technical progress

The technical progress covered in this report includes descriptions of work on the preparation of powder samples for the IEA/ANNEX II round-robin and of the development of a data template for electronic reporting of the round-robin data.

Division, Distribution and Certification of Ceramic Starting Powders. During the final riffling of the zirconia powder (Toyo Soda TSK-ZR-3Y[a],) which was described in the previous report, vials of powder were randomly selected for certification analyses. In addition,

---

[a] Certain commercial equipment, instruments, or materials are identified in this report in order to adequately specify the experimental procedure. Such identification does not imply recommendation or endorsement by the National Bureau of Standards, nor does it imply that the materials or equipment identified are necessarily the best available for the purpose.

samples; the usual conditions for rejection of a vial were partial spillage or fracture of a vial. Eight randomly selected vials, plus 1 or 2 preliminary vials were submitted for each certification analysis. The following characteristics and methods were used to establish the uniformity of the powder samples:

Bulk density - helium (He) pycnometry
Specific surface area - B.E.T.
Particle size - photon correlation spectroscopy (PCS)
(quasi-elastic light scattering)
Chemical composition:
  Zr, Y, Al - x-ray fluorescence (XRF)
  Total elemental - neutron activation analysis (NAA)
Phase composition - x-ray diffraction (XRD)

The procedures adopted for each analysis and results are described here for each of the methods listed above, with the exception NAA which will be described in the next report.

(a) Procedures

(1) Bulk Density. Bulk densities were determined with an automatic He pycnometer (Micromeritics 1320). The instrument was allowed to warm up for 3 to 4 hours to reach thermal equilibrium. It was nulled with cup and cover in place, and the calibration was verified against a standard steel ball of known volume.

The entire contents of a sample vial were transferred to the cup to maximize the amount of sample used for analysis. The cup was dried in a vacuum oven at 90-100 °C for 12 h. The oven then was backfilled with Ar, the sealable cover was placed on the cup, and the cup was placed in a desiccator and allowed to cool to room temperature. Once the sample was thermally equilibrated, it was weighed and transferred to the pycnometer.

Five determinations of density were made on each sample. Samples were evacuated for 3 minutes before commencing a determination. The mean of the 5 determinations was taken as the density of the sample.

It was found that exposure of a sample to room air for more than 5 minutes resulted in determinations which showed a successive decrease toward an asymptotic value. Reproducible values were obtained by maintaining samples under dry conditions.

(2) Specific Surface Area.

Surface area analyses were carried out on 8 samples. Each sample was outgassed in nitrogen at 250 °C for 2 h prior to analysis. The analysis was performed with helium as the carrier gas and nitrogen as the absorbate; the ultra pure gases blended and then dried by passage through a liquid nitrogen cold trap. Three point B.E.T. analysis was used.

(3) Particle Size. The mean particle size and spread of the size distribution were measured by photon correlation spectroscopy (PCS) using a Coulter N4 particle size analyzer. Particle size is determined from the diffusion coefficient associated with the Brownian motion of particles suspended in a liquid. The instrument measures the correlated flicker of laser light scattered by the moving particles. Only a few milligrams of sample are required for the measurement. The analytical range of the instrument is 3 to 3000 nm. The instrument used in our work uses a single reflectance direction - i.e., 90° to the incident beam, and appears to be subject to some measurement bias and variability when used for particle size measurements of particle size distribution with a significant breadth.

The following list gives sources of expected variability and procedures for determining their effects

1. Sample-to-sample variability. Analyze replicate samples.
2. Within sample variability. Since a small amount of powder is required for the analytical sample, the amount withdrawn from the larger sample may not be representative. Blend total sample before taken analytical sample. Analyze replicate aliquots of suspension and replicate suspensions.
3. Instrumental variability. Analyze monosize standards to verify performance. Use two standards which bracket the analytical range of interest.
4. Failure to attain thermal equilibrium in analyzed suspension. Ultrasonic dispersion of a powder results in some heating of the suspension. Heating of the suspension reduces the viscosity of the liquid and yields a larger particle diffusion coefficient, with the result that the observed size appears finer than the true value. A delay of 5 min. or longer may be required to allow liquid in cuvette to equilibrate with the spectrometer.
5. Settling of coarser particles from the suspension. This may be a problem if a long delay time is required to reach thermal equilibrium. Settling of coarser particles will shift the distribution to finer particles. Particles may be resuspended by agitating the suspension by withdrawing it into a pipette and expelling the liquid back into the cuvette. Repeat this operation several times. The shearing action of the liquid passing through the orifice of the pipette may also tend to break up any loosely bound agglomerates which may have reformed following ultrasonic agitation.
6. Agglomeration. If the suspension has not been ultrasonically agitated for sufficient time, or if agglomerates have reformed after agitation was stopped, the agglomerates will tend to skew the particle size distribution to the larger sizes. Varying amount of agglomerates will cause variation in the observed mean. This effect can be investigated by increasing the agitation time and by trying several different dispersants. Agglomeration is expected to be a problem in the measurement of the size of particles below 100 nm.
7. Operator effect. Have two or more operators conduct the measurement.

Based on the above considerations, the following procedures were developed for the analysis of the zirconia powder samples:

a. Pour sample onto a fresh weighing paper. With a small spatula blend the powder, then transfer about 3 mg of powder to a weighing paper. Verify that the mass of powder is in the range of 2-4 mg. Always use the full amount of powder on the tip of the spatula since tapping off a portion may introduce a bias in the size of the particles taken for analysis.

b. Add the 3 mg sample to 20 ml filtered, distilled water. Add dispersant (One drop of 10 percent Darvan C solution was used in this study. Solution was prepared by diluting Darvan C 1:10 with filtered, distilled water). Ultrasonicate the suspension for at least 15 minutes.

c. Verify instrument performance by measuring the particle size of 2 standards - e.g., aqueous suspensions of monosized latex spheres - with mean sizes that bracket size range to be analyzed.

d. Withdraw about 1.5 ml of the suspension with a disposable pipette, squeeze the fluid in and out of the pipette several times to obtain a good mix in the sample. Add the 1.5 ml aliquot to 1.5 ml water in a cuvette. Mix the 3 ml of liquid well using the pipette as before. Place the cuvette in the spectrometer.

e. Wait 5 min. for sample to equilibrate thermally and for convection currents to die out.

f. Operate the spectrometer in Manual Mode analysis; the default settings of the Automatic Mode may not yield optimized measurement of the autocorrelation function. Three runs of 300 s were used in the present work. Output was set for printout of tables and distributions plots for each run.

g. Mix the suspension in the cuvette by agitating with a pipette. Repeat the analysis without a delay time. The results of "f." and "g." should agree if settling or agglomeration have not occurred.

h. Re-ultrasonicate the remaining 20 ml suspension for 2-5 min, and repeat the analysis. Three replicate analyses are to be run.

i. Repeat measurement with a replicate sample.

Eight samples and 1 preliminary sample were analyzed. No significant difference was observed with respect to the preliminary sample.

(4) X-Ray Fluorescence (XRF). XRF was used to determine fluorescence intensities associated with Zr, Y and Al in 8 selected samples and 2 preliminary samples. Two 4 g samples were taken from each vial and pressed in spec caps in a hydraulic press at 16 tons pressure, using 1.5 g of lithium tetraborate powder as a backing to ensure complete filling of the caps. The samples were measured once in

a PW 1400 x-ray spectrometer using a Cr target x-ray tube operated at 40 kkV, 10 mA for zirconium and yttrium, and 60 kV, 50 mA for aluminum. The HOMTST computer program was used for testing of elemental inhomogeneity. This work was performed by the Center for Analytical Chemistry, National Bureau of Standards.

(5) X-Ray Diffraction (XRD). XRD was used to determine the phase composition of 8 selected samples and 2 preliminary samples. Diffraction patterns were measured on a Philips diffractometer equipped with a sample spinner and graphite diffracted beam monochromator. The diffractometer was mounted on an XRG 3100 generator which utilized a long fine-focus, Cu target x-ray tube. The generator was operated at 40 kV, 35 mA. Samples were run at a scan rate of 2 degrees per min, and output was recorded on an analog strip-chart recorder.

(b) Results

The results are summarized in Table 1 for the 5 methods described above. The results are presented in terms of the standard deviation, s, and the coefficient of variation,

$$v = s/X \quad , \qquad (1)$$

where X is the mean. The results for the coefficient of variation for the different methods may be compared with the coefficient of variation of the weights of the samples prior to the final riffling (Splitting Yield) as a measure of the relative bottle-to-bottle variation. Khan obtained a v of 0.00125 and an estimated relative sample error of

Table 1. Summary of Certification Tests

Characteristic	Unit	Method	No. of Samples	Std. Dev.	Coef. of Variation
Bulk Density	g/cm^3	He pyc.	9	0.02	0.003
S.S.A.	m^2/g	3 pt. BET	9	0.4	0.02
Particle Size	nm	PCS	9	10	0.05
Composition:					
[Y]/[Zr]	--	XRF	10	0.0006	0.002
[Al]/[Zr]	--	XRF	10	0.0003	0.06
[monocl]	%	XRD	10	0.4	0.05
Splitting Yield (Stage 3)			96		0.017

0.0042 for riffling of 60:40, coarse:fine, sand mixtures. Since the splitting process used here involved one manual splittings, two splittings with a spinning riffle, and transfers of powder from container to riffler and vice-versa, v = 0.017 is considered reasonable for the overall process. Taking relative maximum estimated error, e, as

$$e = 3v/\sqrt{n} \quad , \tag{2}$$

where n is the number of samples, $n \approx 9$, the estimated error is seen to be approximately equal to the coefficient of variation.

The estimated measurement errors listed in Table 2 are based on replicated measurements for a each of the samples. With the exception of the particle size measurements, the coefficients of variation are less than the estimated measurement errors which implies that no sample-to-sample variation can be inferred from the measurements. Only the bulk density measurements and the [Y]/[Zr] measurements had estimated errors of measurement which allow agreement to estimated error of 0.017 to be tested. Both of these measurements yielded values of v well below 0.017, in agreement with the expectation that these properties would be unaffected by variations in the splitting process.

The results for the measurement of the particle size distribution suggest that a small amount of sample-to-sample variation is present. A plot of the residues versus sample number is shown in Figure 1. Using the sample numbers showing the largest deviations from the norm, possible groups of samples have been flagged which may show significant deviations. However, due to the large measurement error which is present, this identification is tentative.

Table 2. Estimated Measurement Error

Characteristic	Coef. of Variation (Table 1.)	Estimated Measurement Error
Bulk Density	0.003	0.009
S.S.A.	0.02	0.05
Particle Size	0.05	0.03
Composition:		
[Y]/[Zr]	0.002	0.003
[Al]/[Zr]	0.06	0.1
[monocl]	0.05	0.1

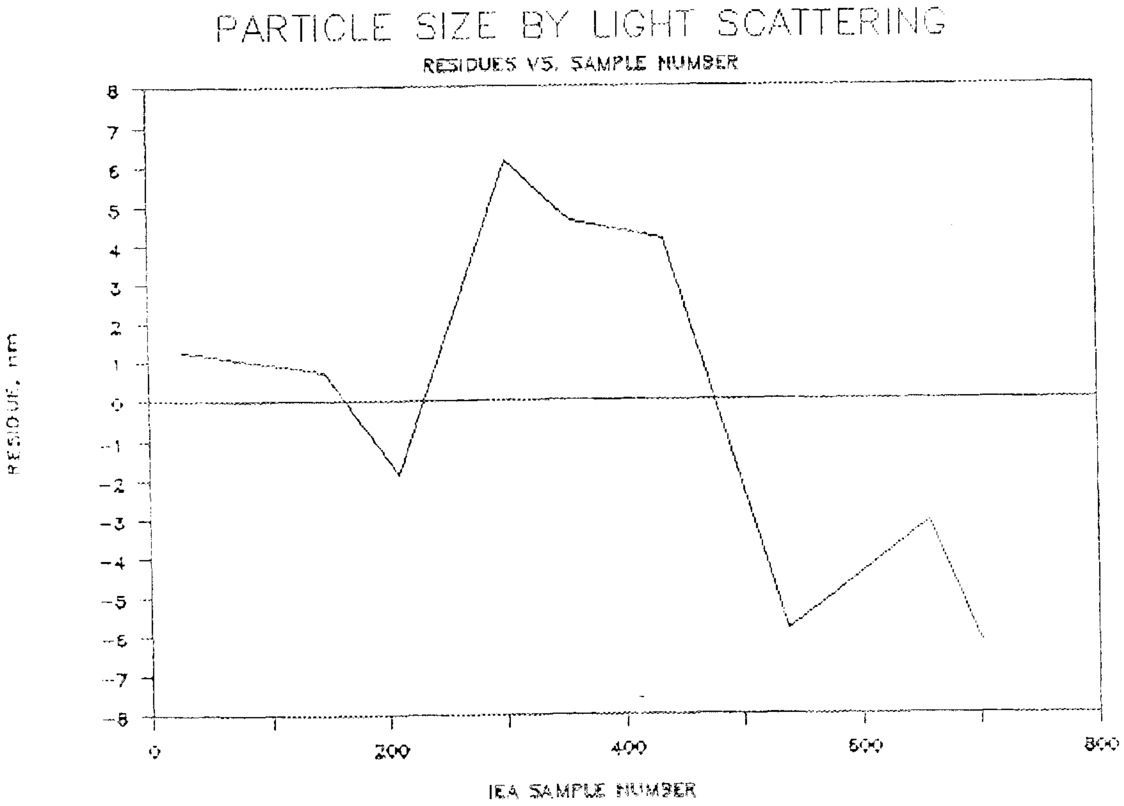

Figure 1. Residues of the averaged sample mean particle size with reference to the grand mean particle size vs. IEA Sample Number. Particle size was determined by photon correlation spectroscopy.

Two effects were noted which influenced the particle size measurement. First, coarse particles were apparently lost during the delay time used to establish thermal equilibrium. Samples which were analyzed with delay time and then remixed with pipette agitation and immediately reanalyzed yielded a small increase in mean particle size (2-5 nm) and larger spread of the particle size distribution. Allowing a cuvette to stand overnight between first and second analysis resulted in about -20 nm change and considerable narrowing of the particle size distribution. Further investigation of the particle size measurements with other dispersants will be carried out in attempt to improve the stability of the suspensions.

The second effect involved occasional thermal drifts of about 0.5 °C of the spectrometer. During a full operating day, the latex reference suspensions should be run at least twice, and more frequently if changes in the spectrometer thermal condition is indicated.

Although the results of the XRF characterization indicated statistically significant differences in absolute fluorescence intensities due to zirconium and yttrium, the rationalized intensities were within acceptable limits of variation. No significant differences for Al were found; however, the analytical sensitivity for Al was poor so that small differences (e.g., less than 1 percent) were not ascertained for this element. Al was the major impurity reported by the manufacturer of the powder and is the principal contaminate expected from the riffling process.

The XRD characterization indicated that the powders consisted of identical mixtures of two phases: cubic yttrium zirconium oxide (yttria-stabilized zirconia), PDF #30-1468[a]; and monoclinic zirconium oxide (baddeleyite, syn), PDF #36-420. Measurements of peak heights were used to calculate ratio I(baddeleyite)/I(cubic) for assessment of the relative amounts of the two phases. Variations in ratio from sample to sample were considered to be within experimental error.

(c) Division of Powders

At the present time 2000 vials of the silicon nitride reference powder have been prepared. The final stage riffling of this powder is being performed under dry Ar, as was the case with the zirconia powder. Riffling of this powder is expected to be completed during the week of April 20 to 24. The vials are scheduled to be flame-sealed at Construction Technology Laboratories, Inc., on May 11. Packaging and mailing of the flame-sealed vials is scheduled for May 20-22.

Blending and manual splitting of the three remaining powders is scheduled to be carried out the week of May 18. Riffling of the GTE-Ube Silicon Nitride powder is projected to begin June 1.

Data Template. A template for recording and performing first-stage processing of particle size distribution data is being prepared for Lotus 1-2-3 Version 2. An initial form of the template which was prepared in October 1986 is being extensively revised to provide menu-guided data entry, data analysis and data presentation. The template extends the number of data fields to provide for input of distribution data. A portion of the table of contents for the particle size distribution template is given in Figure 2.

Reference

1. Khan, A. A. M.Sc. Thesis, Bradford University; 1968.

---

[a] JCPDS-International Centre for Diffraction Data Powder Diffraction File (PDF). Numbers refer to data cards in the PDF.

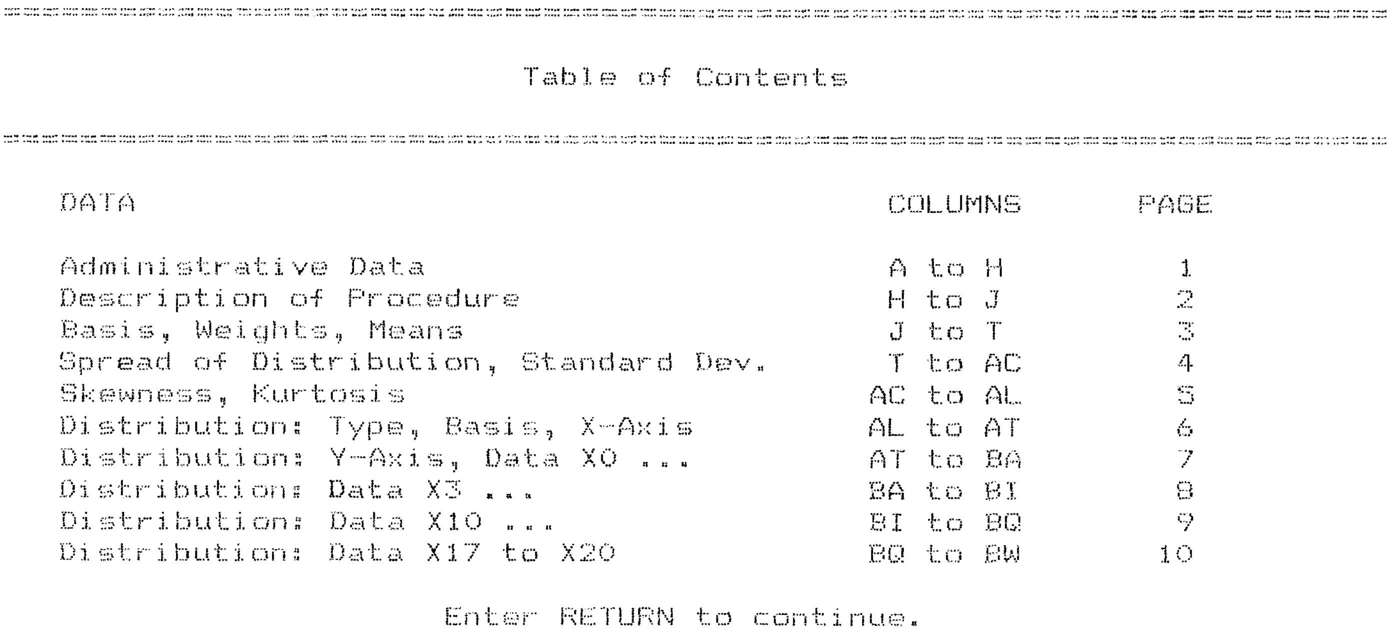

```
================================================================================

                            Table of Contents

================================================================================

   DATA                                              COLUMNS       PAGE

   Administrative Data                                A to H          1
   Description of Procedure                           H to J          2
   Basis, Weights, Means                              J to T          3
   Spread of Distribution, Standard Dev.              T to AC         4
   Skewness, Kurtosis                                AC to AL         5
   Distribution: Type, Basis, X-Axis                 AL to AT         6
   Distribution: Y-Axis, Data X0 ...                 AT to BA         7
   Distribution: Data X3 ...                         BA to BI         8
   Distribution: Data X10 ...                        BI to BQ         9
   Distribution: Data X17 to X20                     BQ to BW        10

                          Enter RETURN to continue.
```

Figure 2. Table of Contents for Lotus template for particle size distribution data.

ORNL/TM-10469

INTERNAL DISTRIBUTION

1-2. Central Research Library
3. Document Reference Section
4-5. Laboratory Records Department
6. Laboratory Records, ORNL RC
7. ORNL Patent Section
8. S. Baik
9. R. L. Beatty
10. P. F. Becher
11. J. Bentley
12. T. M. Besmann
13. A. Bleier
14. E. E. Bloom
15. K. W. Boling
16. W. D. Bond
17. R. A. Bradley
18. C. R. Brinkman
19. V. R. Bullington
20. A. J. Caputo
21. R. S. Carlsmith
22. P. T. Carlson
23. J. A. Carpenter, Jr.
24. J. V. Cathcart
25. R. H. Cooper
26. S. A. David
27. J. H. DeVan
28. W. P. Eatherly
29. J. I. Federer
30. W. Fulkerson
31. R. L. Graves
32. D. L. Greene
33. M. A. Janney
34-38. D. R. Johnson
39. R. R. Judkins
40. M. A. Karnitz
41. M. P. Kertesz
42. T. B. Lindemer
43. K. C. Liu
44. E. L. Long, Jr.
45. W. D. Manly
46. R. W. McClung
47. D. L. McElroy
48. A. J. Moorhead
49. J. L. Rich
50. C. R. Richmond
51. J M Robbins
52. M. W. Rosenthal
53. M. L. Santella
54-77. A. C. Schaffhauser
78. J. H. Schneibel
79. J. L. Scott
80. G. M. Slaughter
81. E. J. Soderstrom
82. D. P. Stinton
83. R. W. Swindeman
84. V. J. Tennery
85-87. P. T. Thornton
88. T. N. Tiegs
89. J. R. Weir, Jr.
90. F. W. Wiffen
91. R. K. Williams
92. C. S. Yust
93. A. Zucker

94. Donald F. Adams
University of Wyoming
Laramie, WY 82071

95. Jane W. Adams
Corning Glass Works
Corning, NY 14831

96. Donald J. Adrian
High Velocity Tool Corp.
2015 Indiana Street
Racine, WI 53405

97. Bruce J. Agle
Sundstrand Corporation
4400 Ruffin Road
Post Office Box 85757
San Diego, CA 92138-5757

98. Richard T. Alpaugh
U.S. Department of Energy
Forrestal Building CE-151
1000 Independence Avenue
Washington, DC 20585

99. H. Arbabi
Brunel University
Uxbridge Middlesex UB8 3PH
UNITED KINGDOM

100. James P. Arnold
U.S. Army Belvoir
R&D Center
ATTN: FTRBE-EMP
Fort Belvoir, VA 22060

101. V. S. Avva
North Carolina Agricultural and
Technical State University
Greensboro, NC 27411

102. John M. Bailey
Caterpillar Tractor Company
100 NE Adams
Peoria, IL 61629

103. Murray Bailey
NASA Lewis Research Center
21000 Brookpark Road, MS 77-6
Cleveland, OH 44135

104. R. R. Baker
Ceradyne Advanced Products, Inc.
3169 Red Hill Avenue
Costa Mesa, CA 92626

105. J. Gary Baldoni
GTE Laboratories, Inc.
40 Sylvan Road
Waltham, MA 02254

106. A. L. Bement, Jr.
TRW, Inc.
23555 Euclid Avenue
Cleveland, OH 44117

107. M. Bentele
Xamag, Inc.
259 Melville Avenue
Fairfield, CT 06430

108. Clifton G. Bergeron
University of Illinois
204 Ceramics Building
Urbana, IL 61801

109. William D. Bjorndahl
TRW, Inc.
One Space Park
Building 01, Room 2060
Redondo Beach, CA 90278

110. James A. Black
American Matrix, Inc.
118 Sherlake Drive
Knoxville, TN 37922

111. John Blum
Norton Company
High Performance Ceramics
Goddard Road
Northboro, MA 01532-1545

112. Paul N. Blumberg
Integral Technologies Inc.
415 E. Plaza Drive
Westmont, IL 60559

113. Wolfgang D. G. Boecker
Standard Oil Engineered
Materials Company
Post Office Box 832
Niagara Falls, NY 14302

114. Han Juergen Bossmeyer
BMW Technologies, Inc.
800 South Street
Waltham, MA 02154

115. Raymond J. Bratton
Westinghouse Electric
Corporation
1310 Beulah Road
Pittsburgh, PA 15235

116. Catherine E. Brown
E. I. DuPont de Nemours
& Company
Wilmington, DE 19898

117. J. J. Brown
Virginia Polytechnic Institute
and State University
Blacksburg, VA 24061

118. W. Bryzik
U.S. Army Tank Automotive
Command
Warren, MI 48090

119. S. T. Buljan
GTE Laboratories, Inc.
40 Sylvan Road
Waltham, MA 02254

120. John M. Byrne, Jr.
PPG Industries, Inc.
One PPG Place
Pittsburgh, PA 15272

121. Donald J. Campbell
Air Force Wright Aeronautical
Laboratory
AFWAL/POX
Wright-Patterson AFB, OH 45433

122. Harry W. Carpenter
Rockwell International
6633 Canoga Avenue
Canoga Park, CA 91304

123. David Carruthers
Garrett Turbine Engine Company
111 South 34 Street
Post Office Box 5217
Phoenix, AZ 85010

124. Jere G. Castor
Garrett Turbine Engine Co.
111 S. 34th Street
Post Office Box 5217
Phoenix, AZ 85010

125. Se-Tak Chang
Sundstrand Turbomach
4400 Ruffin Road
San Diego, CA 92138-5757

126. R. J. Charles
General Electric Company
Post Office Box 8
Schenectady, NY 12301

127. En-sheng Chen
B&C Engineering Research
13906 Dentwood Drive
Houston, TX 77014

128. Albert A. Chesnes
U.S. Department of Energy
Forrestal Building CE-151
1000 Independence Avenue
Washington, DC 20585

129. Frank Childs
EG&G, Inc.
Post Office Box 1625
Idaho Falls, ID 83415

130. Gilbert Y. Chin
Bell Telephone Laboratories
Murray Hill, NJ 07974

131. Melvin H. Chiogioji
U.S. Department of Energy
Forrestal Building CE-15
1000 Independence Avenue, SW
Washington, DC 20585

132. William J. Chmura
The Torrington Company
59 Field Street
Torrington, Connecticut 06790

133. Eugene V. Clark
Turbine Metal Technology, Inc.
7327 Elmo Street
Tujunga, CA 91042-2204

134. William L. Cleary
ORI, Inc.
1375 Piccard Drive
Rockville, MD 20850

135. Jack L. Clem
J. M. Huber Corporation
Post Office Box 2831
Borger, TX 79008-2831

136. Philip R. Compton
National Aeronautics and
Space Administration
Washington, DC 20546

137. Harry E. Cook
Chrysler Motors Corporation
1200 Chrysler Drive
Highland Park, MI 48288-1118

138. Stephen Copley
University of Southern
California
Los Angeles, CA 90089-0241

139. John A. Coppola
Standard Oil Engineered
Materials Company
Post Office Box 1054
Bldg. 91-2
Niagara Falls, NY 14302

140. Normand D. Corbin
Norton Company
High Performance Ceramics
Goddard Road
Northboro, MA 01532-01545

141. Charles H. Craig
Defense Technology Security
Administration
400 Army-Navy Drive, Suite 300
Arlington, VA 22202

142. William J. Croft
U.S. Army Materials Technology
Laboratory
Arsenal Street
Watertown, MA 02172

143. Gary M. Crosbie
Ford Motor Company
Post Office Box 2053
Room S-2079
Dearborn, MI 48121

144. Floyd W. Crouse, Jr.
U.S. Department of Energy
Post Office Box 880
Morgantown, WV 26505

145. Raymond Cutler
Ceramatec, Inc.
163 W. 1700 South
Salt Lake City, UT 84115

146. David A. Dalman
Dow Chemical Company
Midland, MI 48640

147. Stephen C. Danforth
Rutgers University
Post Office Box 909
Piscataway, NJ 08854

148. Stanley J. Dapkunas
National Bureau of Standards
Gaithersburg, MD 20899

149. Robert F. Davis
North Carolina State University
232 Riddick Laboratory
Box 7907
Raleigh, NC 27695

150. Evelyn M. DeLiso
Rutgers University
Post Office Box 909
Piscataway, NJ 08854

151. Alan L. Dragoo
National Bureau of Standards
Gaithersburg, MD 20899

152. Keith F. Dufrane
Battelle Columbus Laboratories
505 King Avenue
Columbus, OH 43201

153. Paul Dyer
Air Products and Chemicals, Inc.
Post Office Box 538
Allentown, PA 18105

154. Robert J. Eagan
Sandia National Laboratories
Albuquerque, NM 87185

155. Christopher A. Ebel
Norton Company
High Performance Ceramics
Goddard Road
Northboro, MA 01532-1545

156. J. J. Eberhardt
U.S. Department of Energy
Forrestal Building CE-12
1000 Independence Avenue, SW
Washington, DC 20585

157. E. E. Ecklund
U.S. Department of Energy
Forrestal Building CE-151
1000 Independence Avenue
Washington, DC 20585

158. William A. Ellingson
Argonne National Laboratory
9700 South Cass Avenue
Argonne, IL 60439

159. Graydon A. Elliott
U.S. Army Research and
Technology Laboratory (AVSCOM)
Fort Eustis, VA 23604

160. A. Erdely
26 Av. Gore des Eaux-Vives
1208 Geneva
SWITZERLAND

161. Charles D. Estes
U.S. Senate
Washington, DC 20510

162. Peggy Evanich
National Aeronautics and Space
Administration
Washington, DC 20546

163. Anthony G. Evans
University of California
Santa Barbara, CA 93106

164. Robert C. Evans
NASA Lewis Research Center
21000 Brookpark Road
Cleveland, OH 44135

165. Katherine T. Faber
Ohio State University
2041 College Road
Columbus, OH 43210

166. John W. Fairbanks
U.S. Department of Energy
Forrestal Building CE-151
1000 Independence Avenue
Washington, DC 20585

167. Larry Farrell
Babcock and Wilcox
Old Forrest Road
Lynchburg, VA 24505

168. H. W. Foglesong
Dow Corning Corporation
3901 S. Saginaw Road
Midland, MI 48640

169. Thomas F. Foltz
Avco
Two Industrial Avenue
Lowell, MA 01851

170. Robert G. Frank
General Electric Company
One Neumann Way, Mail Drop M-87
Post Office Box 156301
Cincinnati, OH 45215-6301

171. George E. Gazza
U.S. Army Materials Technology
Laboratory
Arsenal Street
Watertown, MA 02172

172. Charles M. Gilmore
The George Washington University
Washington, DC 20052

173. Paul Glance
Concept Analysis
950 Stephenson Highway
Troy, MI 48007-7013

174. Fred M. Glaser
U.S. Department of Energy
Washington, DC 20545

175. Joseph W. Glatz
Naval Air Propulsion Test Center
Box 7176, PE 34
Trenton, NJ 08628

176. Stephen T. Gonczy
Allied Signal Research Center
50 UOP Plaza
Des Plaines, IL 60016-6187

177. Robert J. Gottschall
U.S. Department of Energy
Washington, DC 20545

178. Kenneth Green
Coors Porcelain Company
17750 N. 32 Street
Golden, CO 80401

179. Lance E. Groseclose
General Motors Corporation
Post Office Box 420
Indianapolis, IN 46206-0420

180. T. D. Gulden
GA Technologies, Inc.
Post Office Box 81608
San Diego, CA 92138

181. M. D. Gurney
NIPER
Post Office Box 2128
Bartlesville, OK 74005

182. J. J. Habeeb
Esso Petroleum Canada
Post Office Box 3022
Sarina, Ontario
CANADA N7T 7MI

183. H. T. Hahn
Pennsylvania State University
227 Hammond Building
University Park, PA 16802

184. Nabil S. Hakim
General Motors Corporation
36880 Ecorse Road
Romulus, MI 48174

185. John W. Halloran
Ceramic Process Systems
840 Memorial Drive
Cambridge, MA 02139-3758

186. R. A. Harmon
25 Schalren Drive
Latham, NY 12110

187. Stephen D. Hartline
Norton Company
High Performance Ceramics
Goddard Road
Northboro, MA 01532-1545

188. Willard E. Hauth
Dow Corning Corporation
Midland, MI 48640

189. Kevin L. Haynes
McDonnell Douglas Astronautics
Company
Box 516 E456/HQ/3N/MS329
Saint Louis, Missouri 63166

190. Norman L. Hecht
University of Dayton Research
Institute
300 College Park
Dayton, OH 45469-0001

191. S. S. Hecker
Los Alamos National Laboratory
Post Office Box 1663
Los Alamos, NM 87545

192. Peter W. Heitman
General Motors Corporation
Post Office Box 420, W-5
Indianapolis, IN 46206-0420

193. Richard L. Helferich
The Duriron Company
Incorporated
Post Office Box 1145
Dayton, OH 45401

194. H. E. Helms
General Motors Corporation
Post Office Box 420
Indianapolis, IN 46206-0420

195. Thomas L. Henson
GTE Products Corporation
Hawes Street
Towanda, PA 18848-0504

196. Thomas P. Herbell
NASA Lewis Research Center
21000 Brookpark Road, MS 105-1
Cleveland, OH 44135

197. Hendrik Heystek
Bureau of Mines
Tuscaloosa Research Center
Post Office Box L
University, AL 35486

198. Robert V. Hillery
General Electric Company
Cincinnati, OH 45215

199. Jonathan W. Hinton
Standard Oil Engineered
Materials Company
Post Office Box 1054
Niagara Falls, NY 14302

200. Stephen M. Hsu
National Bureau of Standards
Gaithersburg, MD 20899

201. Harold A. Huckins
Princeton Advanced
Technology, Inc.
56 Finley Road
Princeton, NJ 08540

202. O. Richard Hughes
Celanese Research Company
86 Morris Avenue
Summit, NJ 07901

203. Joseph E. Hunter, Jr.
General Motors Corporation
12 Mile and Mound Roads
Warren, MI 48090-9055

204. Louis C. Ianniello
U.S. Department of Energy
Washington, DC 20545

205. Robert H. Insley
Champion Spark Plug Company
20000 Conner Avenue
Detroit, MI 48234

206. Curt A. Johnson
General Electric Company
Post Office Box 8
Schenectady, NY 12301

207. Douglas C. Johnson
Sundstrand Corporation
4400 Ruffin Road
Post Office Box 85757
San Diego, CA 92138-5757

208. Larry Johnson
Argonne National Laboratory
9700 S. Cass Avenue
Building 362
Argonne, IL 60439

209. R. A. Johnson
General Motors Corporation
Post Office Box 420
Indianapolis, IN 46206-0420

210. L. A. Joo
Great Lakes Research Corporation
Post Office Box 1031
Elizabethton, TN 37643

211. A. David Joseph
Sealed Power Corporation
100 Terrace Plaza
Muskegon, MI 49443

212. Roy Kamo
Adiabatics, Inc.
630 S. Mapleton
Columbus, IN 47201

213. Allan Katz
Air Force Wright Aeronautical
Laboratory
Materials Laboratory, AFWAL/MLLM
Wright-Patterson AFB, OH 45433

214. R. N. Katz
U.S. Army Materials Technology
Laboratory
Arsenal Street
Watertown, MA 02172

215. P. Victor Kelsey
Aluminum Company of America
Alcoa Technical Center B
Alcoa Center, PA 15061

216. Frederick L. Kennard, III
General Motors Corporation
1300 N. Dort Highway
Flint, MI 48556

217. J. R. Kidwell
Garrett Turbine Engine Company
111 S. 34th Street
Post Office Box 5217
Phoenix, AZ 85010

218. Max Klein
Gas Research Institute
8600 West Bryn Mawr Avenue
Chicago, IL 60631

219. C. E. Knapp
Norton Company
8001 Daly Street
Niagara Falls, Ontario
CANADA

220. A. S. Kobayashi
University of Washington
Seattle, WA 98195

221. David M. Kotchick
AiResearch Manufacturing Company
2525 W. 190th Street
Torrance, CA 90509

222. Bruce Kramer
George Washington University
Washington, DC 20052

223. Saunders B. Kramer
U.S. Department of Energy
Forrestal Building CE-151
1000 Independence Avenue
Washington, DC 20585

224. D. M. Kreiner
Garrett Turbine Engine Company
111 S. 34th Street
Post Office Box 5217
Phoenix, AZ 85010

225. Pieter Krijgsman
Ceramic Design Int. Hold., Ltd.
Post Office Box 68
8050 AB Hattem
THE NETHERLANDS

226. W. J. Lackey
Georgia Tech Research Institute
Atlanta, GA 30332

227. Everett A. Lake
Air Force Wright Aeronautical Laboratory
AFWAL/POOS
Wright-Patterson AFB, OH 45433

228. James Lankford
Southwest Research Institute
6220 Culebra Road
PO Drawer 28510
San Antonio, TX 78284

229. John G. Lanning
Corning Glass Works
Corning, NY 14831

230. David C. Larsen
Corning Glass Works
Sullivan Park, FR-51
Corning, NY 14831

231. Patrick Lauzon
National Research Council Canada
1411 Oxford Street
Halifax, N.S.
CANADA B3H 3Z1

232. Harry A. Lawler
Standard Oil Engineered Materials Company
Post Office Box 1054, Building 91-2
Niagara Falls, NY 14302

233. Alan Lawley
Drexel University
Philadelphia, PA 19104

234. Daniel Lee
Temescon
2850 7th Street
Berkeley, CA 94710

235. June-Gunn Lee
Korea Advanced Institute of Science and Technology
Post Office Box 131
Dong Dac Mun, Seoul
KOREA

236. E. M. Lenoe
Air Force Office of Scientific Research
APO San Francisco, CA 96503-0110

237. Stanley R. Levine
NASA Lewis Research Center
21000 Brookpark Road
Cleveland, OH 44135

238. David Lewis
Naval Research Laboratory
4555 Overlook Avenue, SW
Washington, DC 20375

239. Winston W. Liang
AMERCOM, Incorporated
8928 Fullbright Avenue
Chatsworth, CA 91311

240. Bill Long
Babcock and Wilcox
Post Office Box 1260
Lynchburg, VA 24505

241. L. A. Lott
EG&G, Inc.
Post Office Box 1625
Idaho Falls, ID 83415

242. Bryan K. Luftglass
Chem Systems, Inc.
303 S. Broadway
Tarrytown, NY 10591

243. Michael J. Lynch
General Electric Company
Post Office Box 414, 7B-36
Milwaukee, WI 53201

244. Vincent L. Magnotta
Air Products and Chemicals, Inc.
Post Office Box 538
Allentown, PA 18105

245. Tai-il Mah
Universal Energy Systems
4401 Dayton-Xenia Road
Dayton, OH 45432

246. L. Manes
Commission of the European Communities
Ispra Establishment
1-21020 Ispra (Varese)
ITALY

247. Gerald R. Martin
Fleetguard, Inc.
Cookeville, TN 38501

248. John Mason
The Garrett Corporation
9851 Sepulveda Boulevard
Post Office Box 92248
Los Angeles, CA 90009

249. J. McCauley
U.S. Army Materials Technology Laboratory
DRXMR-MC
Arsenal Street
Watertown, MA 02172

250. Robert R. McDonald
Boride Products, Incorporated
2879 Aero Park Drive
Traverse City, MI 49684

251. William J. McDonough
U.S. Department of Energy
Forrestal Building CE-151
1000 Independence Avenue
Washington, DC 20585

252. Thomas D. McGee
Iowa State University
Ames, IA 50011

253. Malcolm G. McLaren
Rutgers University
Bowser Road, Box 909
Piscataway, NJ 08854

254. Arthur F. McLean
Ford Motor Company
20000 Rotunda Drive
Dearborn, MI 48121

255. Brian L. Mehosky
Standard Oil Engineered Materials Company
4440 Warrensville Center Road
Cleveland, OH 44128

256. P. K. Mehrotra
Kennametal, Inc.
Post Office Box 639
Greensburg, PA 15601

257. Joseph J. Meindl
Reynolds International, Inc.
Post Office Box 27002
6603 W. Broad Street
Richmond, VA 23261

258. D. Messier
U.S. Army Materials Technology
Laboratory
DRXMR-MC
Arsenal Street
Watertown, MA 02172

259. Arthur G. Metcalfe
Solar Turbines, Inc.
2200 Pacific Highway
Post Office Box 80966
San Diego, CA 92138

260. Thomas N. Meyer
Aluminum Company of America
Alcoa Technical Center
Alcoa Center, PA 15069

261. W. Miloscia
Standard Oil Engineered
Materials Company
4440 Warrensville Center Road
Cleveland, OH 44128

262. Bill Moehle
Ethyl Corporation
451 Florida Boulevard
Ethyl Tower
Baton Rouge, LA 70801

263. Helen Moeller
Babcock and Wilcox
Post Office Box 11165
Lynchburg, VA 24506-1165

264. Frederick E. Moreno
Turbo Energy Systems, Inc.
350 Second Street, Suite 5
Los Altos, CA 94022

265. Peter E. D. Morgan
Rockwell International
1049 Camino Dos Rios
Post Office Box 1085
Thousand Oaks, CA 91360

266. Solomon Musikant
General Electric Company
Post Office Box 8555
Mail Stop U-1219
Philadelphia, PA 19101

267. Pero Nannelli
Pennwalt Corporation
900 First Avenue
Post Office Box C
King of Prussia, PA 19406-0018

268. Robert M. Neilson, Jr.
EG&G Idaho, Inc.
Post Office Box 1625
Idaho Falls, ID 83415

269. Dale E. Niesz
Battelle Columbus Laboratories
505 King Avenue
Columbus, OH 43201

270. William D. Nix
Stanford University
Stanford, CA 94305

271. Richard D. Nixdorf
American Matrix, Inc.
118 Sherlake Drive
Knoxville, TN 37922

272. Norton Company
HPC Library/DM Jacques
Goddard Road
Northboro, MA 01532-1545

273. Brian M. O'Connor
The Lubrizol Corporation
29400 Lakeland Boulevard
Wickliffe, OH 44092

274. W. Richard Ott
Alfred University
Alfred, NY 14802

275. Muktesh Paliwal
GTE Products Corporation
Hawes Street
Towanda, PA 18848

276. Hayne Palmour III
North Carolina State University
2158 Burlington Engineering Laboratories
Post Office Box 5995
Raleigh, NC 27607

277. Joseph N. Panzarino
Norton Company
Goddard Road
Northboro, MA 01532-1545

278. Pellegrino Papa
Corning Glass Works
Corning, NY 14831

279. James G. Paschal
Reynolds Metals Company
Post Office Box 76154
Atlanta, GA 30358

280. Arvid E. Pasto
GTE Laboratories, Inc.
40 Sylvan Road
Waltham, MA 02254

281. James W. Patten
Cummins Engine Company, Inc.
Box 3005, Mail Code 50183
Columbus, IN 47202-3005

282. Robert A. Penty
Eastman Kodak Company
901 Elmgrove Road
Rochester, NY 14650

283. Gary R. Peterson
U.S. Department of Energy
785 DOE Place
Idaho Falls, ID 83402

284. R. Byron Pipes
University of Delaware
2001 Spencer Laboratory
Newark, DE 19716

285. Robert C. Pohanka
Office of Naval Research
800 N. Quincy Street, Code 431
Arlington, VA 22217

286. Stephen C. Pred
ICD Group, Inc.
1100 Valley Brook Avenue
Lyndhurst, NJ 07071

287. Karl M. Prewo
United Technologies Corporation
Silver Lane, MS 24
East Hartford, CT 06108

288. Hubert B. Probst
NASA Lewis Research Center
21000 Brookpark Road
Cleveland, OH 44135

289. Carr Lane Quackenbush
Norton Company
High Performance Ceramics
Goddard Road
Northboro, MA 01532-1545

290. Brian Quigy
National Aeronautics and Space Administration
Washington, DC 20546

291. George Quinn
U.S. Army Materials Technology Laboratory
Arsenal Street
Watertown, MA 02172

292. Dennis T. Quinto
Kennametal, Inc.
Post Office Box 639
Greensburg, PA 15601

293. S. Venkat Raman
Air Products and Chemicals, Inc.
Post Office Box 538
Allentown, PA 18105

294. Dennis Readey
Ohio State University
2041 College Road
Columbus, OH 43210

295. Robert R. Reeber
U.S. Army Research Office
Post Office Box 12211
Research Triangle Park, NC 27709

296. K. L. Reifsnider
Virginia Polytechnic Institute
and State University
Blacksburg, VA 24061

297. Paul Rempes
Champion Spark Plug Company
20000 Conner Avenue
Detroit, MI 48234

298. T. M. Resetar
U.S. Army Materials Technology
Laboratory
DAXMA-MC
Arsenal Street
Watertown, MA 02172

299. K. T. Rhee
Rutgers University
Post Office Box 909
Piscataway, NJ 08854

300. Roy W. Rice
W. R. Grace and Company
7379 Route 32
Columbus, MD 21044

301. David W. Richerson
Ceramatec, Inc.
163 West 1700 South
Salt Lake City, UT 84115

302. Paul Rieth
Ferro Corporation
661 Willet Road
Buffalo, NY 14218

303. Michael A. Rigdon
Institute for Defense Analyses
1801 Beauregard Street
Alexandria, VA 22311

304. John E. Ritter, Jr.
University of Massachusetts
Amherst, MA 01003

305. Giulio A. Rossi
Norton Company
High Performance Ceramics
Goddard Road
Northboro, MA 01532-1545

306. Barry R. Rossing
Aluminum Company of America
Alcoa Technical Center
Alcoa Center, PA 15069

307. David J. Rowcliffe
SRI International
333 Ravenswood Avenue
Menlo Park, CA 94025

308. Donald W. Roy
Coors Porcelain Company
17750 N. 32 Street
Golden, CO 80401

309. Bruce Rubinger
Gobal
50 Milk Street, 15th Floor
Boston, MA 02109

310. Robert Ruh
Air Force Wright Aeronautical
Laboratory
Materials Laboratory, AFWAL/MLLM
Wright-Patterson AFB, OH 45433

311. Robert J. Russell, Sr.
Norton Company
High Performance Ceramics
Goddard Street
Northboro, MA 01532-1545

312. George P. Safol
Westinghouse Electric
Corporation
Pittsburgh, PA 15235

313. J. Sankar
North Carolina Agricultural and
Technical State University
Greensboro, NC 27411

314. Maxine Savitz
Garrett Ceramic Components
Division
19800 South Venice
Torrance, CA 90509

315. Richard Schapery
Texas A&M University
College Station, TX 77843

316. J. L. Schienle
Garrett Turbine Engine Company
111 S. 34th Street
Phoenix, AZ 85034

317. L. J. Schioler
Aerojet Tech Systems Company
Post Office Box 13222
Dept. 9990, Bldg. 2001
Sacramento, CA 95813

318. Richard A. Schmidt
Battelle Columbus Division
505 King Avenue
Columbus, OH, 43201-2693

319. Arnie Schneck
Deere & Co.
Post Office Box 128
Wood-Ridge, NJ 07075

320. Matthew Schreiner
Gas Research Institute
8600 W. Bryn Mawr Avenue
Chicago, IL 60631

321. John Schuldies
Industrial Ceramic Technology Inc.
141 Enterprise Drive
Ann Arbor, MI 48103

322-342. R. B. Schulz
U.S. Department of Energy
Forrestal Building CE-151
1000 Independence Avenue
Washington, DC 20585

343. Wesley J. C. Schuster
Thermo Electron Corporation
115 Eames Street
Post Office Box 340
Wilmington, MA 01887

344. Murray A. Schwartz
Bureau of Mines
2401 Eye Street, NW
Washington, DC 20241

345. Douglas B. Schwarz
Dow Chemical U.S.A.
52 Building
Midland, MI 48674

346. Thomas M. Sebestyen
U.S. Army Tank Automotive Command
AMSTA-RGRT
Warren, MI 48397-5000

347. Brian Seegmiller
Coors Porcelain Company
17750 North 32 Street
Golden, CO 80401

348. S. G. Seshadri
Standard Oil Engineered Materials Company
Post Office Box 832
Niagara Falls, NY 14302

349. Peter T. B. Shaffer
Advanced Refractory Technologies Inc.
699 Hertel Avenue
Buffalo, NY 14207

350. Maurice E. Shank
United Technologies Corporation
East Hartford, CT 06108

351. Laurel M. Sheppard
Advanced Materials and Processes
Route 87
Metals Park, OH 44073

352. Dinesh K. Shetty
The University of Utah
Salt Lake City, UT 84112

353. Jack D. Sibold
Coors Porcelain Company
17750 North 32 Street
Golden, CO 80401

354. Neal Sigmon
U.S. House of Representatives
Rayburn Building, Room B308
Washington, DC 20515

355. Richard Silberglitt
DHR, Inc.
6849 Old Dominion Drive
Suite 228
McLean, VA 22101

356. Maurice J. Sinnott
University of Michigan
438 W. Engineering Building
Ann Arbor, MI 48109

357. S. R. Skaggs
Los Alamos National Laboratory
Post Office Box 1663
Los Alamos, NM 87545

358. J. Thomas Smith
GTE Laboratories, Inc.
40 Sylvan Road
Waltham, MA 02254

359. Jay R. Smyth
Garrett Turbine Engine Company
Post Office Box 5217
MS 93-172/1302-2K
Phoenix, AZ 85010

360. Rafal Sobotowski
Standard Oil Engineered
Materials Company
3092 Broadway Avenue
Cleveland, OH 44115

361. Thomas M. Sopko
Lubrizol Enterprises, Inc.
29400 Lakeland Boulevard
Wickliffe, OH 44092

362. Boyd W. Sorenson
E. I. DuPont de Nemours &
Company
Wilmington, DE 19898

363. Richard M. Spriggs
National Research Council
2101 Constitution Avenue
Washington, DC 20418

364. M. Srinivasan
Standard Oil Engineered
Materials Company
Post Office Box 832
Niagara Falls, NY 14302

365. Gordon L. Starr
Cummins Engine Company, Inc.
Box 3005, Mail Code 50183
Columbus, IN 47202-3005

366. Harold L. Stocker
General Motors Corporation
Post Office Box 420, T-23
Indinapolis, IN 46206-0420

367. Roger Storm
Standard Oil Engineered
Materials Company
Post Office Box 832
Niagara Falls, NY 14302

368. E. E. Strain
Garrett Turbine Engine Company
111 S. 34th Street
Post Office Box 5217
Mail Stop 301-2N
Phoenix, AZ 85010

369. Thomas N. Strom
NASA Lewis Research Center
21000 Brookpark Road, 77-6
Cleveland, OH 44135

370. Richard Suddeth
Boeing Motor Airplane Company
Post Office Box 7730, MS K-76-67
Wichita, KS 67277

371. Paul Sutor
Midwest Research Institute
425 Volker Boulevard
Kansas City, MO 64116

372. J. J. Swab
U.S. Army Materials Technology
Laboratory
Arsenal Street
Watertown, MA 02172

373. Lewis Swank
Ford Motor Company
Post Office Box 2053
Building SRL, Room E3172
Dearborn, MI 48121

374. Stephen R. Tan
ICI Advanced Materials
Post Office Box 11
The Heath, Runcorn
Cheshire WA7 4QE
ENGLAND

375. Anthony C. Taylor
U.S. House of Representatives
Rayburn Building, Room 2321
Washington, DC 20515

376. W. H. Thielbahr
U.S. Department of Energy
550 2nd Street
Idaho Falls, ID 83401

377. John K. Tien
Columbia University
1137 SW Mudd Building
New York, NY 10027

378. T. Y. Tien
University of Michigan
Dow Building
Ann Arbor, MI 48109-2136

379. Julian M. Tishkoff
Air Force Office of Scientific Research
Bolling AFB
Washington, DC 20332

380. Louis E. Toth
National Science Foundation
1800 G Street, NW
Washington, DC 20550

381. Richard E. Tressler
The Pennsylvania State University
201 Steidle Building
University Park, PA 16802

382. Donald R. Uhlmann
Massachusetts Institute of Technology
Cambridge, MA 02139

383. Edward C. Van Reuth
Technology Strategies Incorporated
10722 Shingle Oak Court
Burke, VA 22015

384. Thomas Vasilos
Avco Corporation
201 Towell Street
Wilmington, MA 01887

385. V. Venkateswaran
Standard Oil Engineered Materials Company
Post Office Box 832
Niagara Falls, NY 14302

386. John B. Wachtman, Jr.
Rutgers University
Post Office Box 909
Piscataway, NJ 08854

387. Richard B. Wallace
General Motors Corporation
36880 Ecorse Road
Romulus, MI 48174

388. Harlan L. Watson
U.S. House of Representatives
Rayburn Building, Suite 2321
Washington, DC 20515

389. Albert R. C. Westwood
Martin Marietta Laboratories
1450 South Rolling Road
Baltimore, MD 21227

390. Thomas J. Whalen
Ford Motor Company
Dearborn, MI 48121

391. Sheldon M. Wiederhorn
National Bureau of Standards
Gaithersburg, MD 20899

392. James C. Williams
Carnegie-Mellon University
Schenley Park
Pittsburgh, PA 15213

393. Roger R. Wills
TRW, Inc.
Cleveland, OH 44110

394. J. M. Wimmer
Garrett Turbine Engine Company
111 S. 34th Street
Post Office Box 5217
Phoenix, AZ 85010

395. David Wirth
Coors Porcelain Company
17750 North 32 Street
Golden, CO 80401

396. Thomas J. Wissing
Eaton Corporation
26201 Northwestern Highway
Post Office Box 766
Southfield, MI 48037

397. George W. Wolter
Howmet Turbine Components Corporation
699 Benston Road
Whitehall, MI 49461

398. James C. Wood
NASA Lewis Research Center
21000 Brookpark Road
MS 500-210
Cleveland, OH 44135

399. Hun C. Yeh
AiResearch Casting Company
19800 Van Ness Avenue
Torrance, CA 90509

400. Thomas M. Yonushonis
Cummins Engine Company, Inc.
Box 3005, Mail Code 50183
Columbus, IN 47202-3005

401. Don Zabierek
Air Force Wright Aeronautical Laboratory
AFWAL/POTC
Wright-Patterson AFB, OH 45433

402. Charles Zeh
U.S. Department of Energy
Post Office Box 880
Morgantown, WV 26505

403. Anne Marie Zerega
U.S. Department of Energy
Forrestal Building CE-15
1000 Independence Avenue
Washington, DC 20585

404. Martin Zlotnick
Nichols Research Corporation
1764 Old Meadow Lane, Suite 150
McLean, VA 22102-4307

405. Klaus M. Zwilsky
National Research Council
2101 Constitution Avenue
Washington, DC 20418

406. Department of Energy
Oak Ridge Operations Office
Assistant Manager for Energy Research and Development
PO Box E
Oak Ridge, TN 37831

408-437. Department of Energy
Technical Information Center
Office of Information Services
PO Box 62
Oak Ridge, TN 37831

For distribution by microfiche as shown in DOE/TIC-4500, Distribution Category UC-95.

☆U.S. GOVERNMENT PRINTING OFFICE 1987—748-168/60093